



HAL
open science

Testing gravity in space: towards a realistic treatment of chameleon gravity in the MICROSCOPE mission

Martin Pernot-Borràs

► To cite this version:

Martin Pernot-Borràs. Testing gravity in space: towards a realistic treatment of chameleon gravity in the MICROSCOPE mission. General Relativity and Quantum Cosmology [gr-qc]. Sorbonne Université, 2020. English. NNT: 2020SORUS173 . tel-03333888

HAL Id: tel-03333888

<https://theses.hal.science/tel-03333888v1>

Submitted on 3 Sep 2021

HAL is a multi-disciplinary open access archive for the deposit and dissemination of scientific research documents, whether they are published or not. The documents may come from teaching and research institutions in France or abroad, or from public or private research centers.

L'archive ouverte pluridisciplinaire **HAL**, est destinée au dépôt et à la diffusion de documents scientifiques de niveau recherche, publiés ou non, émanant des établissements d'enseignement et de recherche français ou étrangers, des laboratoires publics ou privés.



Sorbonne Université

École Doctorale 564 - Physique en Ile-de-France

ONERA & Institut d'Astrophysique de Paris

Tester la gravité dans l'espace
Vers un traitement réaliste de la gravité Caméléon
dans la mission MICROSCOPE

par

Martin PERNOT-BORRÀS

Thèse de doctorat de Physique

Dirigée par M. Jean-Philippe Uzan
M. Joël Bergé

Présentée et soutenue publiquement le 4 novembre 2020

Devant le jury composé de :

M.	Serge Reynaud	Président du jury
Mme.	Clare Burrage	Rapporteuse
M.	David F. Mota	Rapporteur
M.	Eugeny Babichev	Examineur
M.	Philippe Brax	Membre invité
M.	Jean-Philippe Uzan	Directeur de thèse
M.	Joël Bergé	Co-encadrant

A la meva tieta.

Acknowledgment

Ce manuscrit est le résultat de trois années de thèse qui n’auraient pas pu aboutir sans le concours de nombreuses personnes. Je remercie d’abord mes encadrants Joël Bergé et Jean-Philippe Uzan, qui ont su m’apporter un encadrement de qualité me laissant une juste liberté et me poussant lorsque c’était nécessaire. Je veux aussi remercier Philippe Brax pour les collaborations m’ayant permis de produire les divers travaux publiés lors de cette thèse. Et je voudrais aussi exprimer ma reconnaissance à tous les membres du jury qui ont accepté et pris le temps de revoir mon travail. Je tiens aussi à exprimer ma gratitude à Isabelle Petitbon et au CNES dont le support financier a permis le bon déroulement de cette thèse.

Je souhaite aussi remercier l’ensemble de mes collègues de l’ONERA qui m’ont offert un environnement riche scientifiquement et agréable humainement. En particulier je remercie Bruno Christophe, Manuel Rodrigues et Françoise Liourzou qui ont toujours été là pour répondre à mes questions sur le domaine du spatial, sur l’accélérométrie et sur MICROSCOPE. Je remercie Ratana Chhun qui n’a cessé de compléter ma culture cinématographique, et qui m’a presque appris à désamorcer une bombe. Je remercie Phuong-Anh Huynh pour son effort de sensibilisation aux pratiques de l’écologie parisienne. Et je remercie Emilie Hardy avec qui nous avons affronté la froideur des palais des congrès américains. Je remercie Alexandre Reblay qui en plus d’amener une bonne humeur dans les couloirs, m’a apporté de nombreux détails sur l’usinage des pièces de MICROSCOPE. Et je remercie aussi les divers stagiaires qui ont défilé et animé nos bureaux durant les années, dont particulièrement Julien Delbosque et Sébastien Belis.

Je dirige aussi mes remerciements à l’ensemble des doctorants qui ont animé mon quotidien à l’ONERA et à l’IAP. Je remercie Arno Vantieghem, Matteo Rizzato, et Doogesh Kodi-Ramana avec qui j’ai partagé mon bureau dans les bas-fonds de l’IAP dans la meilleure des ambiances. Je remercie Océane Dhuicque, dont l’arrivée a comblé mon bureau bien vide de l’ONERA. Je remercie Amaël Ellien et Simon Rozier ainsi que Lucas Bonnin, avec qui les pauses cafés étaient très politiques et avec qui j’ai apprécié me promener dans les rues froides et embrumées de Paris. Je remercie Shweta Dalal pour m’avoir appris de belles paroles en hindi. Je remercie Marko Shuntov pour son café, co-bureau durant ma dernière année, mais avec qui j’ai dû partager plus de temps et de souffrance sur un vélo que dans notre bureau. Je remercie François Larrouturou dont je dois souligner “l’originalité” du surnom dont j’ai hérité de sa part. Je remercie Etienne Savalle avec qui tout congrès de physique se transforme en congrès cycliste. Je remercie Théo Lopez presque camarade doctorant depuis la classe de seconde. Et je remercie aussi Cynthia, sans qui la thèse à l’IAP aurait été bien plus triste.

Enfin je souhaite remercier ma famille qui m’a accompagné dans ce vieux projet de faire de la recherche. Je remercie particulièrement mes parents, mon frère, mon oncle et ma grande-tante qui ont été les premiers à me faire lever les yeux vers l’univers et ont su éveiller mon sens de la curiosité, qualité principale selon moi nécessaire à la pratique de la recherche. Et pour finir, je remercie la plus importante de toutes, Déborah, ma compagne qui depuis plus d’une décennie m’apporte son soutien indéfectible et m’a offert la stabilité nécessaire à la réussite de ce projet.

Contents

0	General introduction	9
1	The equivalence principle	13
1.1	The equivalence principle in Newtonian physics	13
1.1.1	Inertia	13
1.1.2	Gravity	14
1.1.3	The weak equivalence principle	15
1.2	The equivalence principle in General Relativity	16
1.2.1	Einstein equivalence principle	16
1.2.2	General relativity theory	18
1.3	History of the equivalence principle tests	20
1.3.1	Early tests	20
1.3.2	Torsion balances	21
1.3.3	The Earth-Moon system & the equivalence principle	23
1.4	MICROSCOPE	25
1.4.1	Mission and design	25
1.4.2	Capacitive detection	28
1.4.3	Measurement equation	32
1.4.4	Noise sources	35
1.4.5	Spectral analysis and results of the mission	36
2	Gravity beyond general relativity	39
2.1	Motivation for modifying general relativity	39
2.2	Scalar-Tensor theories	40
2.2.1	General theory	40
2.2.2	Newtonian limit	43
2.2.3	Non-universal scalar field coupling	44
2.2.4	Massless scalar field	45
2.2.5	Massive scalar field and the Yukawa approximation	48
2.2.6	Scalar-tensor theories in cosmology	50
2.3	Screening mechanisms and chameleon	50
2.3.1	Chameleon model principle	51
2.3.2	Chameleon & matter	52
2.3.3	Solution around a spherical ball and thin-shell effect	53
2.3.4	Interaction between two extended bodies and apparent WEP violation	55
2.3.5	Chameleon constraints and experimental cavities	57
2.3.6	Current constraints	57

3	Testing unscreened scalar field with MICROSCOPE	61
3.1	Assuming a spherical Earth	62
3.1.1	Introduction and summary	62
3.1.2	Article	63
3.2	Yukawa and the geoid	69
3.2.1	Introduction and summary	69
3.2.2	Article	69
4	Modelling the chameleon field in an experiment	107
4.1	Symmetrical set-ups	108
4.1.1	Introduction and summary	108
4.1.2	Article	109
4.2	Asymmetries in the geometry	125
4.2.1	Introduction and summary	125
4.2.2	Article	126
4.3	Additional content: exploring methods	144
4.3.1	Quasi-cylindrical method for nested cylinders	144
4.3.2	Adaptive mesh refinement methods for a 3D treatment	145
5	Application: testing the chameleon stiffness with MICROSCOPE	147
5.1	Measurement of the electrostatic stiffness in MICROSCOPE	148
5.1.1	Introduction and summary	148
5.1.2	Article	148
5.2	Use for constraining chameleon gravity	192
5.2.1	Introduction and summary	192
5.2.2	Article	192
6	Application to the motion of charged particles	201
6.1	Introduction and summary	201
6.2	Article	202
7	Conclusion and perspectives	219

Chapter 0

General introduction

The history of our understanding of gravity has been imprinted by a rich variety of experimental tests and observations. Tycho Brahe's observations of the celestial bodies' motion led Kepler to formulate his laws in the 17th century. These laws paved the ways to the inverse-square law of the gravitational force in Newtonian gravity in 1687. Two centuries later, the detection of an anomaly in the advance of Mercury's perihelion questioned Newton's theory and found its explanation in Einstein's theory of general relativity (GR) in 1915. This history has been paralleled by the formulation and evolution of the universality of free fall, a phenomenological principle that has been motivated by numerous experiments performed since Galileo. It led Einstein to its revolutionary consideration on gravity as a fictitious force that could not be distinguished from inertia. While a wide part of the physics community was not keen on putting Newton's prediction behind, general relativity encountered difficulties to be accepted. It is only when the deflection of light rays by the Sun has been observed by Eddington during an eclipse four years later, as forecast by Einstein's theory, that its acknowledgement gained ground. Since then many predictions of this theory have been confirmed experimentally, making it now our standard model for the gravitational interaction. A popular application is for instance gravitational redshift which is verified at a 10^{-17} level with atomic clocks and that allowed for satellite navigation systems.

Meanwhile many clues hinted to the fact that general relativity is not complete. In cosmology, the observations of anomalous velocities of stars in galaxy and of galaxies in galaxy clusters favoured the hypothesis of missing mass generically called dark matter. More recently the observational of the acceleration of the universe's expansion pleaded for the addition of cosmological constant to GR or the existence of a new component of matter named dark energy. An alternative to these new yet-undetected dark components of matter is to modify or extend general relativity. Parallel to these cosmological considerations, other motivations for such a modification come from the quantum world. Quantum physics describes the microscopic nature of the very matter responsible for the gravitation phenomenon. It has become a challenge to describe both these theories in the same framework. This pressing need comes partly from our incapacity to describe physics close to GR singularities such as the one of a black hole or the big bang.

Except for the aforementioned cosmological observations – whose explanation could not be fully due to a modification of our standard theory –, GR is in such a good agreement with all the numerous tests it has been submitted to, that there is not much clues on the ways of modifying or extending it. The current strategy is to extend it in any direction that are mathematically consistent and check for new observables that could discriminate the new theory against GR or provide solutions to the cosmological problem. With the same motivation to find such experimental hints it is crucial to increase the precision of the current test of GR, as detecting a discrepancy would represent a smoking-

gun for alternatives theories. The simplest example of such an extension are scalar-tensor theories that consider a new scalar degree of freedom in addition to the tensor field describing GR. Besides its simplicity, such scalar field is motivated by the fact that it represents a possible candidate to solve cosmological problems such as dark energy or because it naturally emerges from beyond-GR theories as string theory. This field – when coupling to ordinary matter – gives rise to a gravity-like fifth force in addition to classical gravity, electromagnetism and the weak and strong interactions from particle physics. This force is expected to be able to induce a deviation from Newton’s inverse-square law in the limit of weak gravitational fields or an apparent violation of one of the founding pillar of general relativity: the equivalence principle or more specifically the universality of free fall. For these reasons, the search of a fifth force has become essential to probe gravity theories beyond GR.

Given the current precisions on the tests of GR, only weak fifth forces are still viable. This makes them more difficult to detect. Many reasons are responsible for this. For instance, if very weak, in a given experiment it would be more likely to be lost in the noise. Space-borne experiments represent a possible breakthrough for this problem as they enjoy a more stable environment free from any perturbations inherent to human activity. To detect a fifth force, it is also crucial to have a precise understanding of all classical effects at play in a given experiment as otherwise one could consider some measured effects as due to a fifth force whereas it is only a classical effect. Such classical effects are numerous, with examples given by electromagnetic effects due to the experimental set-up or the need for modelling the classical gravitational effects as the one induced by the experiment’s self-gravity. To the latter issue is also related the need for knowing precisely the mass distribution of gravity source. While for self-gravity it is easily addressed through the metrology of the experimental parts, for the case of Earth, knowing its precise mass distribution is still an open problem. Of course geodesy provides a model for it but it usually assumes Newton’s gravity. When considering a fifth force such a model can be affected and the problem of determining Earth’s mass distribution becomes a degenerate problem.

Another problem in the search for fifth forces comes from their parametrisation. Such weak fifth forces are more likely to be found in the data of some experiment if we know how they behave. This is still an open issue for many models, specially for screened scalar field. This type of model has been introduced to provide a fifth force that could act significantly on cosmological scales while remaining weak on local scales and thus compatible with the high precision of current local tests. Screening mechanisms usually involve a non-linear dependency to the matter distribution in the theory. The prototype model of this theory is the chameleon model. In this theory, the magnitude of the fifth force is expected to be higher in an environment of low density such as space than in a high density environment such as Earth. The testability of such a force is thus highly dependent on the environment in which an experiment takes place. Quantifying this dependency requires to finely study the impact of a matter distribution on the field. A key effect is the influence of the experimental apparatus on it. The non-linearities of the theories make this evaluation difficult even if the matter distribution is known. Solutions to this are only available for idealised matter geometries. Going beyond these assumptions and evaluating precisely the fifth forces is still an open issue.

The aim of his PhD thesis is to investigate space-based experimental tests of these fifth forces, with an emphasise on the MICROSCOPE mission. This experiment represents the latest development in the long history of the test of the universality of free fall also known as the weak formulation of the equivalence principle. This type of test is one of the source of constraints on scalar fifth forces due to their ability to provide a violation of this principle. The MICROSCOPE mission recently improved the precision

on this test by an order of magnitude with an experiment in Earth's orbit. This PhD study focuses on two types of scalar fifth forces: unscreened scalar fields that have a linear coupling to matter and a screened scalar field exemplified by the chameleon model. The simplicity of the first type allows us to evaluate the constraints MICROSCOPE can provide and to study the experimental degeneracy of fifth force searches and the determination of the Earth mass distribution. We use the second model to study how the environmental dependency of screening affects the experimental search of screened fifth force. This type of model is particularly interesting in the case of MICROSCOPE as the fact that it is performed in space could potentially lead to new possible constraints.

This thesis is organised as follows. The first two chapters are dedicated to introducing the physics of this problem. Chapter 1 reviews the concept of the equivalence principle in Newton's and Einstein's theories and the history of the test of its weak formulation, the universality of free fall. It ends with the presentation of the MICROSCOPE mission. Chapter 2 is dedicated to gravity theories beyond GR. We focus on scalar-tensor theories. We present the general theory and explore many models from unscreened scalar field – such as the dilaton field or a massive field leading to a Yukawa-like fifth force – to screened scalar field with the chameleon model. In chapter 3, we explore the former type of models. We derive the constraints the MICROSCOPE results induce on these models when idealising the shape of the Earth. These constraints have been published in *Physical Review Letters*. We then go beyond these idealisations to study the way of solving the degeneracy between the determination of Earth's mass distribution and the search of a scalar fifth force. Study that has been published in *Classical Quantum Gravity*. In chapter 4 we analyse the chameleon field with the aim of solving its dynamics to determine its dependency to the environment. This was published in *Physical Review D*. We solve the field profile for many geometries. In particular we solve it for a geometry of nested cylinders very similar to the MICROSCOPE geometry. We find that despite being performed in space, the MICROSCOPE is expected to screen the field. We nonetheless show that forces due to the internal matter distribution of the satellite can occur. Such a force arises from asymmetries in its geometry; in the case of nested cylinders it occurs when a cylinder is shifted. We find that this force behaves as a stiffness as it is linear to the displacement of the cylinder. Its use for possible chameleon constraints by the MICROSCOPE experiment is then studied in Chapter 5. Setting such constraints requires in the first place to estimate any other source of stiffness in the MICROSCOPE experiment induced by classical interaction e.g. gravity and electromagnetism. These results are still to be published. Chapter 6 takes the advantage of the solution of the chameleon field obtained in Chapter 4, to elaborate a new type of experiment to test the existence of the chameleon field by looking at the modification of the trajectory of charged particles in an electromagnetic field. This proposal has been published in *Physical Review D*. We conclude with some perspectives in Chapter 7.

Chapter 1

The equivalence principle

The equivalence principle can be considered as the deepest key principle in gravity. It drove our understanding of this phenomenon from Galileo to Newton's theory to finally Einsteinian gravity. While our vision on the matter was evolving in history, the formulation of this principle kept on changing.

1.1 The equivalence principle in Newtonian physics

The first historical formulation of the equivalence principle emerges from the experimental observation of the universality of free fall. It is the fact that all test bodies, if dropped in the same gravity field, would fall exactly the same way independently of their masses and chemical compositions, provided that they are not submitted to any other force – e.g. air resistance, friction, ... In other words they would experience the exact same acceleration.

This observation has strong implications on our description of the motion of masses in a gravity field. In Newtonian physics [73], such motion results from the competition between two physical phenomena to which bodies are subjected, inertia and gravity. While being thought as distinct phenomena, they are parametrised by a common quantity: the mass of the bodies. In fact, due to this double role, the latter can be distinguished at least conceptually into two quantities: the inertial mass and gravitational mass. These are finally assumed to be equivalent only because of the observed universality of free fall.

1.1.1 Inertia

In Newton's Principia [73], inertia is defined as:

The vis insita, or innate force of matter, is a power of resisting, by which every body, as much as in it lies, endeavours to persevere in its present state, whether it be of rest, or of moving uniformly forward in a right line.

This force is ever proportional to the body whose force it is; and differs nothing from the inactivity of the mass, but in our manner of conceiving it.

It is the capacity a massive body has to resist to a change in its state of motion that is caused by an external force. It traduces both the difficulty to induce a movement to a motionless body and the impulse a moving object holds, that causes the difficulty to change its trajectory. Although it could be thought as a force, it is not, as emphasized by the second part of the definition. It is an innate feature of a mass that only appears when an external force is applied to it.

The inertial mass quantifies this resistance. This is encoded, in Newtonian kinematics, by Newton's second law. It states that in an inertial frame of reference the variation in time of the momentum of the body \mathbf{p} is given by the sum \mathbf{F} of all forces it is subjected to. The momentum of a body is defined in terms of its inertial mass m_i and velocity \mathbf{v} as $\mathbf{p} = m_i \mathbf{v}$ such that

$$\frac{d}{dt}(m_i \mathbf{v}) = \mathbf{F}. \quad (1.1)$$

Inertial or Galilean frames are those in which any object of constant mass and free of any forces – or submitted to forces of null resultant – would remain at rest or have a straight trajectory of constant velocity. Equivalently, these frames are those that have such a movement relative to the absolute space that Newton postulates. This defines the equivalence class of Galilean reference frames.

If the body has a constant mass in time its motion is then governed by

$$m_i \mathbf{a} = \mathbf{F} \quad (1.2)$$

where $\mathbf{a} = \frac{d\mathbf{v}}{dt}$ is the acceleration of the body. The inertial mass measures the strength of the inertial resistance. The more massive the body, the more it resists to some force i.e. the more substantial an external force is required to induce a given acceleration.

Note that these equations are only valid in inertial frames. In a non-inertial frame of reference, such as a rotating frame for instance, fictitious inertial forces appear in the previous equations to account for the fact that bodies tend to stay at rest or to follow straight lines of inertial frames. These forces: the one deriving from the linear acceleration of the frame, the centrifugal and Coriolis forces due to a rotation, and the Euler force that appears when the rotation is accelerated. All these forces are proportional to the inertial mass of the considered body.

1.1.2 Gravity

Gravity on the other hand is defined in Newton's Principia as:

There is a power of gravity tending to all bodies, proportional to the several quantities of matter which they contain. [...]

The force of gravity towards the several equal particles of any body is reciprocally as the square of the distance of places from the particles

This is the observed attractive interaction between all bodies that is proportional to their quantities of matter. The masses of the bodies represent these quantities of matter. The interaction between two bits of matter constituting these bodies decreases as the inverse square of their distance r such that its magnitude is equal to $\frac{G m_1 m_2}{r^2}$ where G is the gravitational constant, and m_1, m_2 are the masses of the bits of matter. The mass is the parameter of the gravitational force. This mass parameter is to be distinguished from the inertial mass, in this way it is called the gravitational mass m_g .

Note that this parameter plays a double role, of source and charge of the interaction. This is made explicit in a different outlook of this interaction. A given body, because of its active gravitational mass, sources a gravity field to which any other body would couple because of its passive gravitational mass. As all bodies play this role, they have both an active and passive gravitational mass. Nevertheless due to Newton's action/reaction law stating that the forces that two bodies exert mutually on each other are opposite in sign but equal in magnitude, these two masses are not to be distinguished.

Mathematically, the theory is described as follows. The gravitational field is governed by Poisson's equation that relates the spatial Laplacien of the Newtonian potential to

the distribution of matter that is encoded in the matter density distribution ρ

$$\Delta\Phi = 4\pi G\rho(\mathbf{x}, t) \quad (1.3)$$

where $G = 6.674 \times 10^{-11} \text{ m}^3.\text{kg}^{-1}.\text{s}^{-2}$ is the gravitational constant.

The integration of this equation around a static point particle or a static spherically symmetric source of matter provides their Newtonian potential

$$\Phi_{\mathcal{N}}(r) = -G\frac{m_{\mathcal{S}}}{r} \quad (1.4)$$

where $m_{\mathcal{S}}$ is the active gravitational mass of the source i.e. the integral of $\rho(\mathbf{x})$ over its volume, and r the distance to its mass barycentre. The gravity field of an object is simply the gradient of the Newtonian potential $\mathbf{g} = -\nabla\Phi$. The field of a point or spherical body is given by

$$\mathbf{g}(r) = G\frac{m_{\mathcal{S}}}{r^2}\mathbf{u} \quad (1.5)$$

where $\mathbf{u} = \mathbf{r}/r$ is the unitary vector directed towards the barycentre of the source body. For such bodies, the potential only depends on the distance r . Nevertheless, for more general objects of arbitrary shape or matter distribution, one would obtain a more complex non-radial gravity field with a dependency on the orientation relative to the source object and a different orientation. Earth for instance is not perfectly spherical nor homogeneous. Its gravity is complex and described in terms of a spherical harmonics expansion. It is however dominated by the spherical monopole that is given by Eq. (1.5). The next mode is the dipole that originates from the flattening of the poles. The latter is caused amongst other causes by inertial forces due to Earth's rotation.

Given an arbitrary gravity field \mathbf{g} created by some matter distribution, a test point particle then experiences a gravitational force proportional to the field

$$\mathbf{F}_{\mathcal{N}} = m_{\mathbf{g}}\mathbf{g} \quad (1.6)$$

where the coupling parameter $m_{\mathbf{g}}$ is the passive gravitational mass. Again, similarly to the creation of the gravitational field, if this test particle is extended, the force is more complex as one needs to integrate Eq. (1.6) over its volume to take into account its inhomogeneities and the gradient of the field.

To sum up, the gravitational mass is the key parameter of Newton's theory of gravity. It holds both roles of sourcing the gravity field and of charge of the interaction with a gravity field. The more massive the body, the stronger the gravity field it sources and the stronger the force it feels.

1.1.3 The weak equivalence principle

When considering the motion of a test body in a gravity field, both gravity and inertia are at play. One obtains an expression for the acceleration it experiences by using the gravitational force of Eq. (1.6) in Eq. (1.2)

$$\mathbf{a} = \frac{m_{\mathbf{g}}}{m_{\mathbf{i}}}\mathbf{g} \quad (1.7)$$

The gravity force being proportional to the gravitational mass, the acceleration of the body is proportional to the ratio of its gravitational and inertial masses. At first glance, these two definitions of the mass have no reason to be equal as they account for two distinct physical phenomena. One could always define two units of measure for both masses as discussed in Ref. [27]. One could define an 'inertial kilogram' – from a reference body whose mass would be for instance measured by collision experiments in which

any gravitational influence could be ignored – and a ‘gravitational kilogram’ – from a reference body whose mass would be for example deduced from a motionless experiment involving gravity such as the tension of a spring as in a weighing scales.

Nevertheless, in the case the two definitions of mass coincide, they cancel in Eq. (1.7) leaving the acceleration of the body independent of its mass. In that case two distinct bodies of different mass would follow the exact same trajectory dictated only by the gravity field: they fall in the same way. For example in a gravity field created by a spherical homogeneous object, if one were to drop with same velocity two objects at same height they would reach its surface at the exact same time.

This universality of free fall has been observed up to some precision on Earth, leading us to the assumption that inertial mass and gravitational mass are indeed equal for all bodies independently of their mass and chemical composition. The implications of this empirical assumption are so deep on our conception of mass, that it has been raised to the rank of principle, the weak equivalence principle (WEP). It makes gravity a privileged interaction in which trajectories and orbits of test bodies are independent of the bodies’ nature. It is nonetheless important to emphasise that in Newton’s theory it is only an empirical fact and it does not emerge naturally from it. This theory of gravity would still hold without this principle. In that case gravity would play a similar role than the electromagnetic interaction. For instance in the presence of an electric field \mathbf{E} , a particle of charge q feels the Lorentz force $\mathbf{F}_\mathcal{E} = q \mathbf{E}$. The particle would then have different trajectories depending on its charge-to-mass ratio $\frac{q}{m_i}$. In Newtonian gravity, the mass ratio $\frac{m_g}{m_i}$ would play the same role as $\frac{q}{m_i}$. It is however empirically not the case. While being fortuitous in Newton’s theory, in general relativity this principle is way more far-reaching as we will see in the next section.

Despite having assumed this principle, any experiment testing it, cannot exclude tiny violations that are smaller than their current precision. The precision on the test has been increasing over history [114]. The strength of such a violation is parametrised by the Eötvös parameter η defined as the normalised difference between the accelerations \mathbf{a}_1 and \mathbf{a}_2 of a pair of bodies of different mass ratios $\left(\frac{m_g}{m_i}\right)_j$

$$\eta_{1,2} = \frac{|\mathbf{a}_1 - \mathbf{a}_2|}{1/2|\mathbf{a}_1 + \mathbf{a}_2|} = 2 \frac{\left(\frac{m_g}{m_i}\right)_1 - \left(\frac{m_g}{m_i}\right)_2}{\left(\frac{m_g}{m_i}\right)_1 + \left(\frac{m_g}{m_i}\right)_2}. \quad (1.8)$$

Experimental tests of the WEP provide an upper bound on η for several different pairs of bodies. The main tests will be broached in Sec. 1.3

Finally it is worth mentioning that, as one can see in this equation, it is not necessary to have the ratio $\left(\frac{m_g}{m_i}\right)$ equal to one for all bodies. Assuming it to be constant is sufficient to obtain the universality of free fall i.e. $\eta = 0$. But this would be equivalent to rescale the gravitational constant, so we can by convention assume it to be equal to one.

1.2 The equivalence principle in General Relativity

1.2.1 Einstein equivalence principle

In Einstein’s theory of gravitation, the equivalence principle holds a completely different status, it is its corner stone. It inspired Einstein’s thoughts that resulted in his theory. The universality of free fall indeed paves the way to a geometrical description of gravity. The fact that the free fall of a test body in an external gravity field is independent of the nature of the body means that the gravitational interaction is only a feature of the gravity field and of the matter sourcing it. A little step further, it allows

the interpretation of gravity as the result of a new dynamical entity: a spacetime. As opposed to Newton's idea of a rigid absolute spacetime, this new spacetime is dynamical. It is unique and its dynamics is ruled by the distribution of mass and energy, spacetime is said to be curved by matter. Then any test body – whose self-gravity i.e. influence on spacetime is negligible – follows the same trajectories, these are the geodesics which are the curves of shortest path of this spacetime. In a flat spacetime, empty of any matter, these curves are straight lines of spacetime – just as uniform straight trajectories of Newton's theory in the absence of gravity. In a spacetime curved by the presence of matter, these geodesics are no longer straight lines but curved lines of spacetime. The curvature of trajectories is the manifestation of gravity. Without the weak equivalence principle, this outlook would not be possible, gravity would rely on the nature of the body we consider, and could not be described by a unique spacetime.

Yet, Einstein went a big step further in these considerations. When a body free falls in a gravity field, he wondered: if this body is an observer, what would he see and feel? As reported in Ref. [37], he argued that:

For an observer in free fall from the roof of a house there is during the fall – at least in his immediate vicinity – no gravitational field. Namely, if the observer lets go of any bodies, they remain relative to him, in a state of rest or uniform motion, independent of their special chemical or physical nature. The observer, therefore, is justified in interpreting his state as being “at rest”.

This is a direct consequence of the universality of free fall. The observer can only conclude the presence of gravity because he holds a point of reference by observing his environment. If instead, he and the body he drops, were enclosed in a box freely falling with them, having no external visual reference, he would have no way of detecting the presence of gravity, the outcome of any experiment would be consistent with gravity having disappeared. This is valid as long as air friction is negligible and the box is small enough to neglect the effects of gravity gradients due to a non-homogeneous gravity field. Finally consider this box to be instead placed far from any gravity source and with a rocket at its bottom that provides a constant acceleration to it. Both the observer and the objects he drops would now feel a constant inertial force that would drag them towards the bottom of the box. But still having no external reference, the observer would believe gravity has been in a way “switched on” again. In this thought experiment known as Einstein lift experiment, no one can tell the difference between a gravitational force and an inertial force. This leads to the assumption that not only the inertial mass and gravitational mass luckily happen to be equal, but gravity and inertia are completely equivalent and even unified. Gravity is now an inertial fictitious force that completely disappears in a new concept of inertial frames that are those that are freely falling.

This consideration resulted in two more advanced formulations of the equivalence principle. First the Einstein equivalence principle that states

(1) The universality of free-fall is verified by test bodies

(2) In any freely falling frame, independently of its position (local position invariance) and velocity (local Lorentz invariance) in spacetime, the outcome of a local non-gravitational experiment is given by the laws of special relativity;

Then the strong equivalence principle that generalises the universality of free fall to extended bodies – whose influence on the gravity field is no longer negligible –, and the second assertion to include gravitational experiment. This formulation of the equivalence principle implies that also gravitation binding energy falls the same way than matter. With Nordström theory [75] that describes gravity with a scalar field, general relativity is the only known field theory verifying this feature.

In other words no local experiment can locally distinguish two freely falling frames and characterise the gravity field it is falling in, spacetime is locally flat or Minkowski.

It is important to emphasize the fact that this only holds locally or when the gravity field is completely uniform. In real situations, for a spherical source for instance, the gravity field is both radially oriented towards its source and decreasing radially with the distance to the source. This means two things for the observer of the previous thought experiment. If he drops a body aside of himself, if the fall lasts long enough, he would eventually see it getting closer to himself, as both bodies would follow two separate geodesics that are radial. On top of that, if he were to drop the brush above himself, being further away of the source of gravity, it would experience a weaker acceleration leading to tidal effects that would tend to separate the observer from its dropped body. So by these observations he could still betray the presence of gravity. The statement of the Einstein equivalence principle is nonetheless local, spacetime is only locally flat, one can only suppress gravity locally. One could always perform an experiment on smaller length or time scales, in which these tidal effects would get smaller than its working precision.

To sum up the equivalence principle holds a very different and central place in Einstein's theory than in Newton's physics. Many features have been added to the universality of free fall. It is a necessary requirement to its metricity, without which the theory would fall.

1.2.2 General relativity theory

General relativity [33, 32] is described as follows. It is a geometrical theory in which gravity is expressed as the curvature of spacetime. It is said to be a metric theory as spacetime is a Lorentzian manifold described by a metric tensor $g_{\mu\nu}$. This object is used to define distances in this spacetime such that the distance ds between two infinitely close events in spacetime is expressed as

$$ds^2 = g_{\mu\nu} dx^\mu dx^\nu \quad (1.9)$$

where dx^μ is the separation vector separating these events. Following general relativity's convention, greek indices ($\mu, \nu = 0, \dots, 3$) denote the spacetime components of a vector or tensor, while latin ones ($i, j = 1, \dots, 3$) denote only spatial components. We also use the Einstein summation convention in which any indice that is contracted – i.e. that appear twice – is summed upon. We use the signature convention $(-, +, +, +)$ for $g_{\mu\nu}$.

This tensor field is the dynamical quantity of the theory. It is governed by the Einstein-Hilbert action

$$S = \frac{M_{\text{Pl}}^2}{2} \int d^4x \sqrt{-g} (R - \Lambda) + \int d^4x \sqrt{-g} \mathcal{L}_m(g_{\mu\nu}, \psi_m^{(i)}), \quad (1.10)$$

where g is the determinant of the metric, R the Ricci scalar defined below, Λ a cosmological constant, x the spacetime coordinates, $M_{\text{Pl}}^2 = \frac{c^4}{8\pi G}$ the Planck mass defined through the gravity constant G and the speed of light c , \mathcal{L}_m the Lagrangian density of matter depending on field matter $\psi_m^{(i)}$ labelled by i .

When varying this action with $g^{\mu\nu}$ – the dual metric tensor defined as $g^{\mu\sigma} g_{\sigma\nu} = \delta_\nu^\mu$ –, one obtains the Einstein field equations governing the dynamics of $g_{\mu\nu}$

$$R_{\mu\nu} - \frac{1}{2} R g_{\mu\nu} + \Lambda g_{\mu\nu} = \frac{8\pi G}{c^4} T_{\mu\nu} \quad (1.11)$$

where $R_{\mu\nu} = g^{\rho\sigma} R_{\rho\mu\sigma\nu}$ is the Ricci curvature tensor defined by the contraction of the Riemann tensor which is a combination of $g_{\mu\nu}$ and its first two derivatives with the spacetime coordinates. The factor $\frac{8\pi G}{c^4}$ coming from the Planck mass in the action, is chosen such that when taking the Newtonian limit – weak-field and non-relativistic

limit – of this equation, one retrieves Poisson equation Eq. (1.3) from Newton’s theory. Finally $T_{\mu\nu}$ is the stress-energy tensor defined as

$$T_{\mu\nu} = -\frac{2}{\sqrt{-g}} \frac{\delta(\sqrt{-g}\mathcal{L}_m)}{\delta g^{\mu\nu}} \quad (1.12)$$

and describes the matter content of the universe. Equation (1.11) tells how this matter content and the geometry of spacetime are related, the matter telling to spacetime how to curve. The total stress-energy tensor is divergence-free imposing energy conservation for matter

$$\nabla_\mu T^{\mu\nu} = 0, \quad (1.13)$$

where ∇_μ denotes the covariant derivative which is a way of defining a derivative on a manifold. In general relativity it is defined as $\nabla_\mu g^{\mu\nu} = 0$ and its action is explicit in terms of the Christoffel symbols defined below.

In such a spacetime, any test particle follows the geodesics of spacetime defined by the parametric equation

$$\frac{d^2 x^\sigma}{ds^2} + \Gamma_{\mu\nu}^\sigma \frac{dx^\mu}{ds} \frac{dx^\nu}{ds} = 0 \quad (1.14)$$

for $x^\sigma(s)$ the spacetime coordinates of the geodesic curve parametrised by the affine parameter s that can be chosen to be the proper time τ and $\Gamma_{\mu\nu}^\sigma$ the Christoffel symbols defined through the metric tensor as $\Gamma_{\mu\nu}^\rho = \frac{1}{2}g^{\rho\sigma}(\partial_\mu g_{\sigma\nu} + \partial_\nu g_{\mu\sigma} - \partial_\sigma g_{\mu\nu})$. These are the curves of shortest path in spacetime, in the sense of the definition of distance from Eq. (1.9). Particles follow these curves if they are freely falling i.e. submitted to no other interaction but gravity. In agreement with the WEP, they are independent of the mass of the particle. If the spacetime is flat, the Christoffel symbols cancel such that we get an equation of null acceleration that in Cartesian coordinates is the one of a straight line. Otherwise, the terms including the Christoffel symbols give the curvature of geodesic resulting in the manifestation of gravity. This equation can be simplified defining the 4-velocity vector along the curve $u^\mu = \frac{dx^\mu}{ds}$ and the action of the covariant derivative on it as $\nabla_\mu u^\nu = \partial_\mu u^\nu + \Gamma_{\mu\sigma}^\nu u^\sigma$, one obtains

$$a^\nu \equiv u^\mu \nabla_\mu u^\nu = 0. \quad (1.15)$$

This equation gives the kinetics of a test mass and defines the 4-acceleration a^μ in a curved spacetime. All effects of gravity are included in this kinetic term. If a test mass is submitted to a force, it would appear in the right part of this equation: $m_i a^\mu = F^\mu$. In the weak-field limit, for non-relativistic particles, this equation reduces to Newton’s equation of motion for gravity.

The equivalence principle is naturally included in general relativity so that neither m_i nor m_g appear in Eq. (1.15). In the neighbourhood of any observer that follows a geodesic of spacetime, one can always attach a non rotating frame to it and find a coordinate system x^μ [69] in which the metric takes the form

$$g_{\mu\nu}(x^\mu) = \eta_{\mu\nu} + \frac{1}{3}R_{\rho\mu\sigma\nu} x^\rho x^\sigma + \mathcal{O}(x^3), \quad (1.16)$$

Such a coordinate system is called Fermi normal coordinates. This reduces to the metric of a flat spacetime of special relativity $\eta^{\mu\nu}$ in the close neighbourhood i.e. $x^\mu \rightarrow 0$ of the observer. In the same way, the first derivatives of $g^{\mu\nu}$ cancel in that neighbourhood, leading the Christoffel symbols to cancel and thus the gravity to locally disappear. The second derivatives of the metric do not however cancel, they are included in the Riemann tensor. This term is responsible for tidal effects that would still be observable if the neighbourhood is not small enough as mentioned in Sec. 1.2’s last paragraph. These

effects are described by the geodesic deviation equation giving the relative acceleration of two nearby geodesics. In the Newtonian limit it reads

$$\frac{d^2 \delta x^i}{d\tau^2} = -R^i{}_{0j0} \delta x^j, \quad (1.17)$$

$\delta \mathbf{x}$ being the spatial separation vector between the geodesics. In this limit one can show that $R^i{}_{0j0} = \delta^i_k \frac{\partial^2 \Phi}{\partial x^k \partial x^j}$. One recognises the gravity gradient tensor or the Hessian of the Newtonian potential Φ . For a homogeneous spherical source of gravity of mass m_S , one can show that in spherical coordinates attached to it $R^i{}_{0j0} = \frac{Gm_S}{r^3} \text{diag}(-2, 1, 1)$. Inserting this into Eq. (1.17), one obtains equations accounting for the tidal effects mentioned in Sec. 1.2. Due to the relative signs of the radial and angular components of this tensor, the separation of two nearby free-falling objects increases if separated radially and decreases if separated angularly. This illustrates the locality of the equivalence principle in general relativity.

1.3 History of the equivalence principle tests

Before the implications of this equivalence principle it has become one of the more precisely tested physical principle. Many different types of tests have been developed to test the WEP. Their upperbound on the Eötvös parameter are summarized in Fig. 1.1 adapted from Ref. [114]. The history of this test has been marked by three periods: an early period, anterior to the tests shown in Fig. 1.1, where mainly pendulum were used reaching precisions up to 10^{-5} on η ; then during the whole 20th century, WEP tests made a big leap forward by use of the Eötvös experiment obtaining precisions of 10^{-8} in the late 19th century and reaching 10^{-13} in the early 21th; finally more recently the era of space-borne tests have been opened by the MICROSCOPE mission reaching the level of 10^{-14} and maybe soon 10^{-15} . The main tests are explained in the following sections.

1.3.1 Early tests

First measurements of the universality of free fall started during the Renaissance. Their precision was very limited by the unprecise metrology techniques of the time. Maybe the most popular test is Galileo's experiment dropping balls at the leaning tower in Pisa. Nevertheless this might be a popularising thought experiment. What Galileo really used [47] is inclined planes. He was indeed aware that vertical free-falling experiments such as the Pisa one, would be very limited by the action of air drag. Besides, even though the v^2 scaling of this drag was only known later, he knew that it was dependent on the velocity of the ball. Then to obtain slower falling balls while still having a long enough free-fall necessary to time measurement, he used slightly inclined planed on which he made roll balls of different matter such that the acceleration of gravity is $g \sin \alpha$ for an inclination angle α . He compared their fall by measuring the falling time by means of a water clock – similar to a hourglass but with water. To the precision this means could provide, he did not measure any violation.

Galileo also tested the universality of free fall using swinging pendulums of different composition. Such a pendulum consists of a massive body placed at the end of a thread. If the WEP is verified, the swinging frequency must be independent of the mass of the body and only a function of the length of the thread. This can be described in Newtonian physics. If we denote this length L and the inertial and gravitational mass as previously, the equation of motion is given by

$$\ddot{\theta} + \omega^2 \sin \theta = 0, \quad (1.18)$$

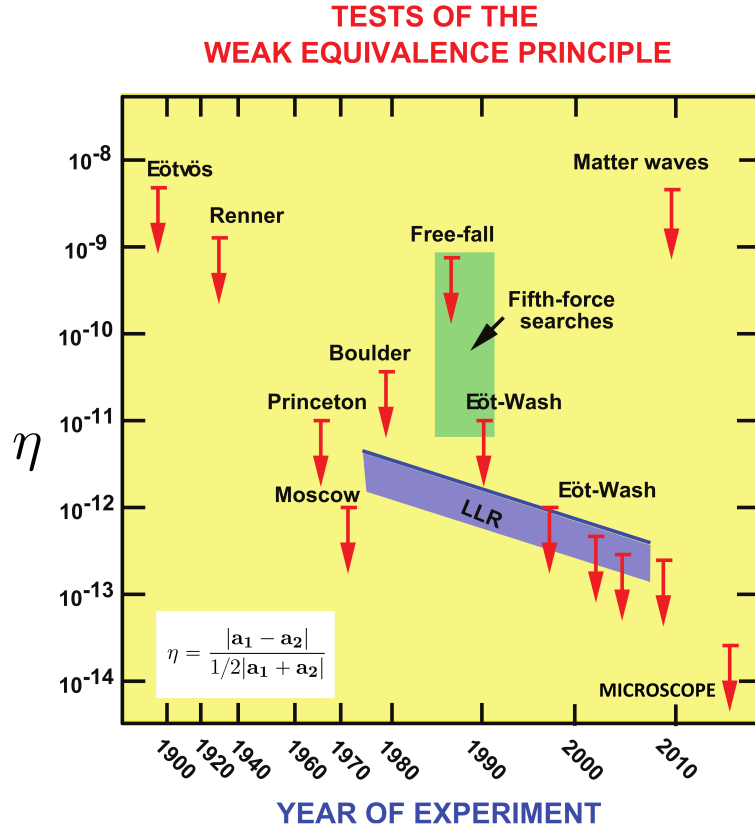


Figure 1.1: Evolution of upper bounds set on the Eötvös parameter η by different WEP tests. The base of an arrow denotes an upper bound. Figure adapted from Ref. [114].

where $\omega = \omega_0 \sqrt{m_g/m_i}$ with the proper angular frequency defined from the considered local gravity field value g by $\omega_0 = \sqrt{g/L}$. In the limit of small oscillations the solution of this equation is straightforward. One gets oscillation at the angular frequency of ω . Consequently if two bodies have different mass ratio they would oscillate at different frequencies. Such violation can be expressed by the Eötvös parameter as

$$\eta \simeq \frac{|\omega_1 - \omega_2|}{\omega_0} \quad (1.19)$$

where the numerator contains the pulsation of each pendulum. If the WEP holds, the mass ratio are equal and the movement would be independent of the mass, and they would both oscillate at ω_0 .

Galileo conducted this experiment in the 17th century comparing pendulums of cork and lead. He concluded [47] that after a hundred oscillations, the number of oscillations of the two pendulum did not differ by much that one. For the WEP, this implies that $\eta < 10^{-2}$. Not long after, Newton repeated the experiment using other types of matter [73]. He improved it [10], by replacing the two masses by two identical hollow spheres in which he would set different materials. This was done to minimise the difference in the air drag. At the same time he came to a better evaluation of the latter. He concluded that no violations were detected at a level of $\eta < 10^{-3}$. Finally Bessel made another improvement with this experiment reaching $\eta < 10^{-5}$.

1.3.2 Torsion balances

The precision on the WEP tests improved radically in the late 19th century with Eötvös' experiment [108]. The principle of this experiment is sketched in Fig. 1.2. It

consists in a torsion balance made of a rod suspended by a thread. At both ends of the rod are fixed two masses of different composition. Were the WEP violated, one would expect a torque that would twist the system. The explanation of such an outcome is straightforward in Newtonian physics.

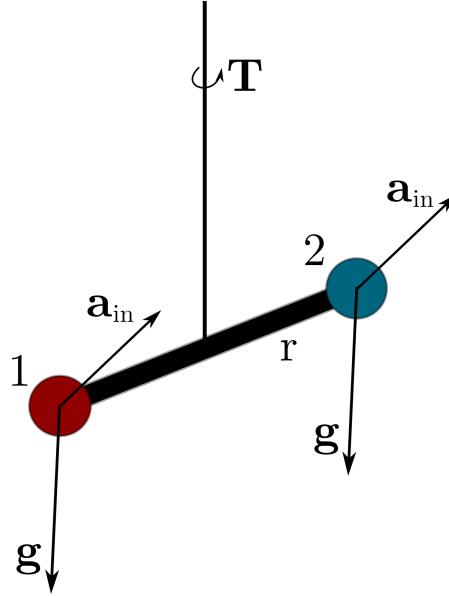


Figure 1.2: Sketch of a torsion balance from the Eötvös experiment.

Consider the wire to be perfect so that it opposes no rigidity to any torsion, and the rod to be homogeneous and symmetrical enough such that its contribution to the torsion is negligible, and finally that only the two masses are at play. Both masses are subjected to two forces: the gravity force that is proportional to the gravitational mass, and the inertial centrifugal force due to Earth's rotation that is proportional to the inertial mass. If we neglect the variation of the gravity field \mathbf{g} and of the inertial acceleration \mathbf{a}_{in} on the scale of the experiment, each mass experiences the total force $\mathbf{F}_j = m_g^j \mathbf{g} + m_i^j \mathbf{a}_{\text{in}}$, where $j = 1, 2$ labels the masses. Now if the WEP is not respected, each mass has a different gravitational-to-inertial-mass ratio so that the sum of the two forces gives two different forces \mathbf{F}_1 and \mathbf{F}_2 that are non collinear. This creates a constant torque

$$\mathbf{T} = \mathbf{r}_1 \times \mathbf{F}_1 + \mathbf{r}_2 \times \mathbf{F}_2. \quad (1.20)$$

If initially the torque is not aligned with the wire, it rapidly swings such that the wire gets naturally aligned with the sum of the forces. Then the torque is collinear to $\mathbf{F}_1 + \mathbf{F}_2$ and

$$\begin{aligned} \mathbf{T} \cdot (\mathbf{F}_1 + \mathbf{F}_2) &= \mathbf{r}_1 \times \mathbf{F}_1 \cdot \mathbf{F}_2 + \mathbf{r}_2 \times \mathbf{F}_2 \cdot \mathbf{F}_1 \\ &= \mathbf{r}_1 \cdot \mathbf{F}_1 \times \mathbf{F}_2 + \mathbf{r}_2 \cdot \mathbf{F}_2 \times \mathbf{F}_1 \\ \mathbf{T} \cdot (\mathbf{F}_1 + \mathbf{F}_2) &= \mathbf{r} \cdot \mathbf{F}_1 \times \mathbf{F}_2. \end{aligned}$$

where we defined $\mathbf{r} = \mathbf{r}_1 - \mathbf{r}_2$. Hence the torque is given by

$$\mathbf{T} = \frac{\mathbf{r} \cdot \mathbf{F}_1 \times \mathbf{F}_2}{|\mathbf{F}_1 + \mathbf{F}_2|}. \quad (1.21)$$

Clearly if the forces are collinear, the torque is null. Then if the WEP holds the rod is expected to stay still. However if they are not, that is if the WEP is not respected and the rod is not aligned with the meridian – as the total force would be in the apparatus

plane –, a constant torque would twist the apparatus. In this experiment the presence of a torque was checked by an optical telescope. In reality the actual experiment Eötvös used is more complex. It uses a balance whose masses are placed at two different heights separated by a few tenth of centimetres – as the apparatus was originally designed in the hope of measuring gravity gradients for geophysics. This provided a way to put an upper bound on the Eötvös parameter η . Eötvös team [109] and Renner [88] reached a precision of a few 10^{-9} on η in the 1920s.

Then, mainly motivated by the fact that Eötvös version could not provide a zero-check, the apparatus got improved in the 1960s by the Princeton group [90]. While they could suppress the effect of Earth’s gravity and Earth’s induced inertial forces by aligning the axis of the symmetry of the system with the meridian, they considered the motion of the apparatus around the sun, and compared the sun’s gravity with the centrifugal force whose intensity and direction is modulated by Earth rotation – the effective rotation velocity of the apparatus around the sun peaks at midnight and is minimal at midday. This leads to an anomalous total force that cancels at 6 am and 6 pm, this effective velocity being then the one of the orbit so that both forces are equal in magnitude and opposite in sign. All in all, a modulated torque with a 24 hours period would be expected if the weak equivalence principle is violated. The design got also modified. They added a third test mass of same composition than one of the masses, and put all of them on the same horizontal plane. This was motivated to limit the sensitivity to the gravity gradient to which the original Eötvös set-up was sensitive. They indeed estimated that Eötvös should have been sensitive to the presence of the nearby experimentalist. In the same spirit, taking advantage of new technical developments they used as rotation detection system an optical system coupled to electronics by a photomultiplier, so that they could suppress the necessity of a human operator. The influence of such a person have been shown to be negligible at more than 6 m from the apparatus. Finally they suppressed other sources of perturbations, placing the experiment in a vacuum chamber for instance, or in a pit to improve temperature stability – temperature gradients could indeed lead to parasitic forces –, or again in a magnetic shield to avoid magnetic contamination. They were able to perform their experiment during several continuous days. They reached a precision of a few 10^{-11} on η in the 1960s, that got improved to less than 10^{-12} by the Moscow group [11] in the 1970s enjoying a more quiet seismic environment noise.

Finally, having in mind to use again Earth’s gravity field to probe the existence of shorter-ranged Yukawa type fifth force, the EötWash group [3] implemented a turntable providing a precise constant rotation motion to the balance that would allow to control the modulation of Earth’s violation signal. They started with a precision of a few 10^{-11} on η in the 1990s [3] and reached in 2008 $\eta < 2.1 \times 10^{-13}$ at 1σ [93].

1.3.3 The Earth-Moon system & the equivalence principle

Alternatively to these laboratory tests conducted on Earth’s surface, another test was imagined based on celestial mechanics. The Earth-Moon system can indeed be seen as two bodies falling in the Sun’s gravity field. The description of this problem is nonetheless more complicated than the one of laboratory tests. Due to the importance of the mass of the bodies and to the shortness of the system compared with its distance to the sun, one cannot neglect the interaction of Earth and Moon. This then must be treated as a three-body problem. Its application to the test of the equivalence principle was first done in 1825 by Laplace [63] who only looked for a violation of the weak equivalence principle due to the different compositions of Earth and Moon – the Moon being mainly only composed of Earth’s mantle material, while Earth has an iron core. Later, in the 1960s, Nordtvedt [76, 77, 78] considered the possibility of a violation of the strong equivalence principle due to the different binding energies that the two bodies

hold.

Laplace effect

The first effect [63] known as Laplace effect is very well exposed in Ref. [27]. The problem is treated in Newtonian mechanics. By parametrising a WEP violation through the ϵ_j parameters defined as

$$\frac{m_g^j}{m_i^j} = 1 + \epsilon_j \quad (1.22)$$

with $j = \oplus, \mathbb{C}$ labelling Earth and the Moon, one can show that the accelerations Earth and Moon experience differ by

$$\delta \mathbf{a} = (\epsilon_{\oplus} - \epsilon_{\mathbb{C}}) \mathbf{g}_{\odot} \simeq \eta \mathbf{g}_{\odot}, \quad (1.23)$$

where $\mathbf{g}_{\odot} = Gm_{\odot}/r_{\oplus}^2$ is the Sun's gravity field at the level of Earth's orbit. Such an anomalous acceleration is shown to introduce a variation of the Earth-Moon distance r , given by

$$\delta r(t) = \delta a \frac{1 + 2\omega_{\mathbb{C}}/\Omega}{\omega_{\mathbb{C}}^2 - \Omega^2} \cos \Omega t \quad (1.24)$$

in which $\Omega = \omega_{\mathbb{C}} - \omega_{\oplus}$ defined in terms of the angular frequencies of the Moon and Earth orbits. The angular frequency Ω corresponds to the synodic lunar period that is the period at which the Moon retrieves a same position with respect to Earth and Sun while orbiting the Earth. This period differs from the period of its orbit due to the motion of the Earth around the Sun. This equation tells us that the variation of the Earth-Moon system due to a WEP violation should occur at this period. It leads to a polarisation of the Moon's orbit toward the Sun.

Laplace compared his theory with celestial observation. He used the measure of parallaxes that are the only way of measuring the distance to the Moon and the Sun at that time. He actually formulated his theory considering that the weak equivalence principle as Earth and Moon seeing a different solar mass. Nonetheless this is completely equivalent to the previous description. His conclusion corresponds to a precision on the WEP test of $\eta < 3 \times 10^{-7}$.

Lunar Laser Ranging (LLR) & the strong equivalence principle

A little more than one century after, Apollo missions provided a big technological leap for this test. Several laser retro-reflectors have indeed been left on Moon's surface allowing for a precise measurement of the Earth-Moon distance by laser ranging. Meanwhile, Einstein's considerations about the equivalence principle lead to its strong formulation. This latter implies that not only an anomalous acceleration in this system is due to the difference of composition of Earth and Moon, but also to their different gravitationnal binding energies that are no longer negligible for those bodies. This effect is known as the Nordtvedt effect [76, 77, 78].

A simple model helps understand such effect. Assume that the binding energy does not contribute equally to the gravitational mass and inertial mass in such a way that

$$m_g^j = m_i^j + \kappa m_b^j \quad (1.25)$$

where κ is the Nordtvedt parameter of this model and $m_b^j = \frac{1}{c^2} \frac{3G(m_g^j)^2}{5R}$ the mass associated to the binding energy here expressed for a spherical body of radius R . This model leads to an anomalous acceleration between Earth and Moon that is

$$\Delta \mathbf{a} = \kappa \left(\frac{m_b^{\oplus}}{m_i^{\oplus}} - \frac{m_b^{\mathbb{C}}}{m_i^{\mathbb{C}}} \right) \mathbf{g}_{\odot}. \quad (1.26)$$

If $\kappa = 0$, i.e. a gravitational binding energy contributing equally to inertial and gravitational mass, one obtains a null differential acceleration as long as WEP is respected – as WEP violation are not included in this model. On the other hand for $\kappa \neq 0$, this anomalous acceleration provides the same effect on the variation of Earth-Moon distance as previously given by Eq. (1.24).

This variation has been tested by the Lunar Laser Ranging by monitoring precisely this distance. The precision on the measurement of this distance has gone from a few tenth of centimetres to the level of the millimetre [72]. Of course this distance is observed to vary. Many other sources exist such as among others: tidal effects leading to an increase of about 3.8 cm.yr^{-1} , effects of other celestial bodies, effect of Earth's geoid. Ephemeris models are constructed to evaluate these effects. Subtracting these models to the LLR observations one obtains a residual variation. This residual went from tenth of centimetres to around 2 cm recently [111]. This result leads to a constraint on the difference of acceleration of Earth and Moon to a level of $\eta_{\text{LLR}} < 0.9 \times 10^{-13}$ at 1σ . Such a differential acceleration must be seen as the result of both the Laplace effect – WEP violation – and Nordtvedt effect – SEP violation. The former effect has been nonetheless evaluated by the EötWash group. They measured it using torsion balance with test masses mimicking the composition of Earth and Moon. They obtained the result $\eta_{\text{WEP}}^{\text{LLR}} < 4.5 \times 10^{-13}$ at 1σ [4]. This lead recently to a level of precision on the SEP test of the order of 5.4×10^{-13} at 1σ [111].

1.4 MICROSCOPE

The latest technology jump on the WEP test comes from space missions. Space indeed offers a stable environment allowing to free ourself from most parasit forces one suffers on Earth – mainly seismic perturbations due to human activity. Many concepts have been proposed in the late 1990s and early 2000s such as the STEP mission [70] aiming for a precision of 10^{-18} on η , Galileo Galilei (GG) mission [74] targeting a precision of 10^{-17} and the MICROSCOPE mission [100] whose goal was to achieve a precision of 10^{-15} . So far, only the latter flew.

The MICROSCOPE experiment – *MICRO-Satellite à Compensation de traînée pour l'Observation du Principe d'Équivalence* – is a French mission led by a CNES-ESA-ONERA-CNRS-OCA-DLR-ZARM collaboration. It has been launched in April 2016 and has been then performing its experiment until October 2018 when it has been passivated and removed from a stable orbit. The mission has been a success, providing a preliminary improvement of an order of magnitude on the WEP test [103, 104]. Final results shall be published soon.

1.4.1 Mission and design

Principle

The mission inherits the expertise ONERA has been developing in the field of ultra-sensitive electrostatic accelerometry that resulted in resounding successes obtained in Earth gravimetry [101] with CHAMP [86], GOCE [91, 80], GRACE [87].

MICROSCOPE's WEP test is based on a set of accelerometers that measures the difference in the acceleration that test masses of different compositions are experiencing as they orbit the Earth. The orbit is a quasi-circular sun-synchronous orbit with an eccentricity of 1.4×10^{-3} and an altitude of 710 km. The experiment is sketched in Fig. 1.3. It consists of two sensor units each composed of two nested cylindrical accelerometers. Such an accelerometer is designed to measure the acceleration experienced by a cylindrical test mass. While one sensor unit called SUEP performs the WEP tests, with two

test masses of different compositions – a platinum alloy and a titanium alloy, the other sensor unit called SUREF is used as a reference with two test masses of same composition – platinum alloy. This latter is made of 90% of platinum and 10% of rhodium and the titanium alloy of 90% of titanium, 6% of aluminium and 4% of vanadium.

In such a set-up, if the WEP was violated, the two test masses of different nature would tend to follow slightly different orbits. Actually, the accelerometer measurement is based on a capacitive measurement – that will be described in Sec. 1.4.2 – in which the test masses are forced to remain at a constant position with respect to the satellite. This is achieved by means of an electric field whose magnitude is modulated via a servo loop control. Then by measuring this magnitude one can reconstruct the acceleration that the test masses are experiencing.

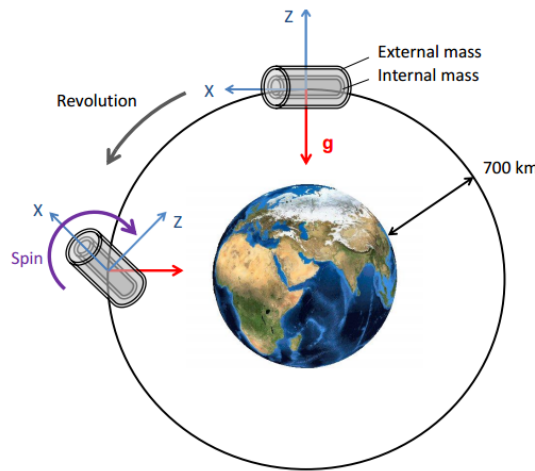


Figure 1.3: Sketch of the MICROSCOPE's detection principle. The orientation of its cylinders during its orbit is shown. The X and Z-axis are in the plane of the orbit. The evolution of their orientation is compared with the Earth's gravity field radial direction.

The accelerometers are able to measure the acceleration along the 6 degree of freedom of the test mass cylinders: 3 axis, one longitudinal denoted X along the main axis of the cylinders composing the accelerometers, and two other perpendicular directions radial to the cylinders; and 3 angles of rotation around these axis. One of these latter axes is always perpendicular to the plane of the orbit, such that if the WEP violation was to occur, a signal would appear only on the others two. Due to the orbital motion, a sinusoidal signal is expected. This is explained by comparing the direction of measurement and of the gravity. The source of the violation is indeed the Earth gravity field which is radial at first order in the Earth geoid. But while the satellite orbits, its axes are in rotation with respect to the direction of the gravity field. As a consequence the sensitive axes are successively aligned and perpendicular to the gravity field's axis as depicted in Fig. 1.3. For a sensitive axis of the accelerometers, this leads to a periodical gravitational acceleration and thus the WEP violation to be periodic. Even though the test can be performed on two axes, the analysis is only done on the X-axis for which the sensitivity is the better. The satellite can operate in two modes: an inertial mode where its axes remain constant compared to distant stars, and a spin mode where the satellite is spinning on itself in the orbital plane. In inertial mode, a hypothetical WEP violation would appear at the orbital frequency $f_{orb} = 1.6818 \times 10^{-4}$ Hz. In spin mode the frequency is modulated by the spinning frequency such that the WEP violation would appear at the frequency $f_{EP} = f_{orbit} + f_{spin}$. If the WEP was then violated, one would expect a line to appear at this frequency in the Fourier spectrum of the difference of

acceleration between the two test mass cylinders. This spin mode is a very important feature of the mission as it allows for a modulation of the expected violation signal and to perform the test at a frequency where the noise is minimal. All sources of noise will be discussed later.

The benefits of space

Performing this experiment in space is motivated by many benefits. Space provides a very stable environment. It indeed allows us to free ourselves from any non-gravitational perturbations encountered on Earth due to human activities or seismic perturbations. Besides, in the MICROSCOPE experiment, many other external perturbations are limited by the choice of the mission's design. For instance, by choosing an altitude of 710 km, the residual atmosphere is poor enough such that the satellite is submitted to a drag not greater than 10^{-8} m.s^{-2} . A higher altitude could have been used, but at the price of a smaller gravity acceleration and thus of a lower expected violation signal. This altitude is the result of the balance between both these considerations. Moreover the choice of a Sun-synchronous orbit, in which the satellite keeps showing the same face to the sun, induces a thermal stability of the set-up. This minimises the occurrence of temperature gradients that can cause perturbing forces due mainly to mechanical dilatation, radiation pressure and the radiometer effect – as will be discussed in Sec. 1.4.4. Finally to overcome the possibility of any other perturbation, the satellite is equipped by a drag-free system using a set of cold gas thrusters that can compensate any force that would be identified as non-gravitational.

This stability that the experiment enjoys allows it to be performed during an extended period of time. This is equivalent to a long free fall. The typical duration of a measurement series is of 8 days. This duration is limited mission operations. This permits to average out any stochastic errors.

Nevertheless space leads to some limitations. The first one is phenomenological. While in an experiment performed in a laboratory on Earth – such as the Eötvös experiment – the test masses can easily be changed to perform the WEP for different couples of matter, in the MICROSCOPE mission – due to the payload limitation that the cost of a space mission induces – the test is only done for one specific couple of material. This narrows the impact on the phenomenology of the WEP and the constraints on alternatives theories of gravity. A more expansive mission could however overcome this issue. The second limitation is technical. The mission is one-shot. If any damage happens to any system of the satellite, the mission would be impacted with no possibility to fix it. The MICROSCOPE mission suffered from this. At the beginning of the mission two capacitor components ceased to function. It has been attributed to overheating. Fortunately it did not paralyse the experiment, nevertheless it limited its operation. To avoid a new failure that could be fatal to the mission, it was decided not to turn on both sensors units at the same time, but to perform the measure on each sensor separately.

Experiment design

The instrument's design is depicted in Fig 1.4. The experiment is performed in a cylindrical cavity. This cavity is delimited by a hermetical invar shield designed to suppress any external electromagnetic field that could perturb the experiment. A vacuum system is present at the top of the cavity, which ensures a 10^{-5} Pa vacuum in the cavity.

The very heart of the cavity is composed of the two accelerometers made in total of 6 nested cylinders. Each accelerometer is composed of 3 cylinders. One is the test mass cylinder and is surrounded by two electrode cylinders. The latter cylinders are made

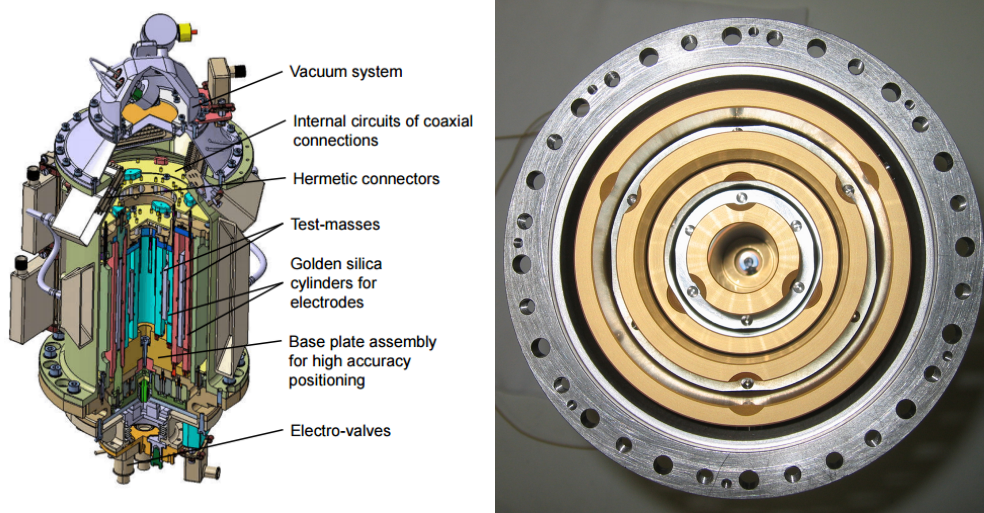


Figure 1.4: Left: scheme a sensor unit of the MICROSCOPE experiment. Right: picture of the inside of SUREF as viewed from above.

of silica covered by gold. On the side facing the test mass cylinder, this golden layer is engraved by a series of grooves resulting in several electrically isolated rectangular gold patches. Each of them constitutes an electrode. Its electric potential is controlled by a wire weld to its surface and crossing the silica cylinder through a drilled hole. The test mass potential on the other hand is controlled through a wire of a diameter of $7\ \mu\text{m}$. The control of these potentials is done by a system of electronics placed outside the vacuum cavity. This control allows to use the test mass and the two electrode cylinders as a set of two capacitors. This permits, by a process that will be explained in the next section, to control the position of the test mass and to measure its acceleration. The 2 sets of 3 cylinders that constitute an accelerometer are nested in each other, and enclosed in an inner holed invar ferule that is directly enclosed by the shield. The geometrical parameters of the cylinders as measured during integration are given by Tab. 1.1 for the test masses of both SU and by Tab. 1.2 for the electrode cylinders of SUEP. The density of the latter is of $2.203\ \text{g}\cdot\text{cm}^{-3}$. Finally the specifications about the ferrules are given by Tab.1.3, their density is of $8.125\ \text{g}\cdot\text{cm}^{-3}$.

Table 1.1: Result of the metrology performed on the test masses geometrical parameters during integration for both sensor units. IS1 and IS2 denotes respectively denotes the internal and external test masses.

Parameter	IS1-SUREF	IS2-SUREF	IS1-SUEP	IS2-SUEP
Inner diameter [mm]	30.801	60.799	30.801	60.802
Outer diameter [mm]	39.390	69.397	39.390	69.401
Length [mm]	43.331	79.821	43.330	79.831
Mass [kg]	0.401533	1.359813	0.401706	0.300939
Density @ 20°C [$\text{g}\cdot\text{cm}^{-3}$]	19.967	19.980	19.972	4.420

1.4.2 Capacitive detection

The measurement of the acceleration is based on a capacitive detection. It can be performed in three directions and three angles. The measurement in each direction

Table 1.2: Geometrical parameters of the electrodes cylinders from SUEP as measured during integration. ‘CylInt’ and ‘CylExt’ respectively denotes the internal and external cylinder surrounding a test mass.

Parameter	IS1-CylInt	IS1-CylExt	IS2-CylInt	IS2-CylExt
Inner diameter [mm]	17.998	40.600	50.305	70.610
Outer diameter [mm]	29.602	49.700	59.601	80.009
Length [mm]	78.001	81.002	115.002	118.002

Table 1.3: Specified geometrical parameters of the inner and outer ferrule surrounding all the cylinders.

Parameter	Inner Ferrule	Outer Ferrule
Inner diameter [mm]	86	115
Outer diameter [mm]	94	119

requires the use of at least a set of two electrodes that forms a pair of capacitors whose plates are made by one electrode and one face of the test mass. Fig. 1.5 shows for one test mass the different electrodes at play labelled X, Y, Z. Note that for Y and Z directions, instead of a single pair of electrodes, a set of two pairs of electrodes are used – labelled Y1, Y2 and Z1, Z2, respectively – to also control the orientation of the cylinder – here labelled by θ and Ψ .

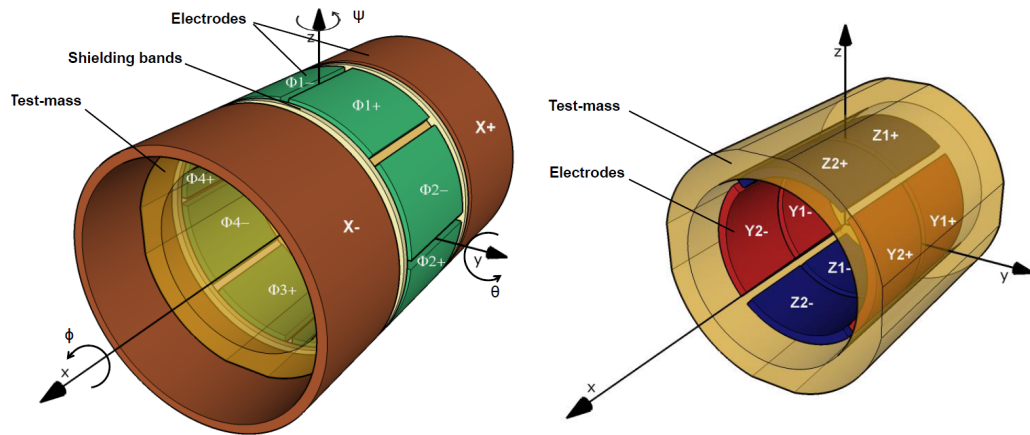


Figure 1.5: Scheme of the different electrodes at play for the measurement of the acceleration of a test mass. The Y and Z-axis are controlled by variation of the gaps. The X-axis is controlled by variation of the overlapping surfaces. The rotation of the test mass around X is controlled by the electrodes labelled Φ .

This measurement is achieved as follows. It can be decomposed in two processes: the detection of a displacement and the action to correct for this displacement. The test mass is levitated in the cage formed by the electrodes and maintained at a rest position equidistant with all electrodes with a gap of $600 \mu\text{m}$. Consider now one direction of measurement i.e. a pair of electrodes. The test mass is maintained at some potential – by a $7 \mu\text{m}$ wire – and the electrodes at some other potentials that are equal in magnitude

but opposite in sign. In the centred position, the situation is symmetrical such that the two capacitances are equal. If the test mass is shifted – as caused by some external acceleration for instance – the two capacitances are no longer equal. This variation is measured and converted in a detection voltage that can be converted in an information on the position of the test mass. From this voltage, a servo-control loop computes action voltage the system needs to apply – by tuning the potential of the electrodes – to bring back the test mass to the centred position. This action on the test mass is detailed in the case of a plane capacitor in the boxed section A. Both these processes are based on the imbalance of the capacitances due to the displacement. For the Y and Z directions this imbalance is due to a variation of the gaps of the capacitors while for the X axis to the variation of the overlapping area of the capacitors plates. In the details given in the box we only develop the former.

Finally the rotation around the axis of the cylinder is controlled by using a set of 4 pairs of electrodes – labelled by Φ . The measurement is possible thanks to the special design of the test masses which are not perfectly cylindrical but instead have, every 90° , a longitudinal part of its surface that is flatten. If one such part is not positioned symmetrically with respect to 2 electrodes, it again induces a difference in the capacitances leading to a force.

Box A: A model for the action: the plane capacitor

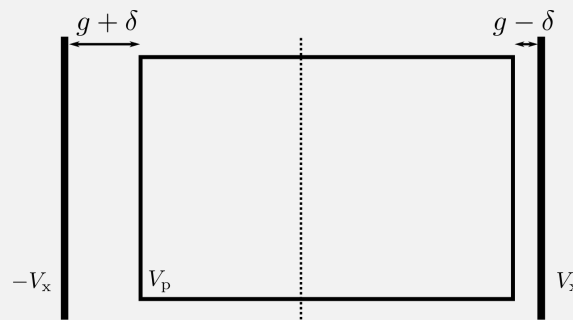


Figure 1.6: Sketch of the model of a plane capacitor. The system of the electrodes – thick black line – and the rectangular test masse – thinner lines forms a set of two capacitors.

For a better understanding of the capacitive action of the test mass, we consider the case of the plane capacitor shown in Fig. 1.6. This case is good to model the measurement on the Y and Z axis. We consider a parallelepiped test mass surrounded by two electrodes facing two opposite sides of the test mass. Consider the gap in-between to be filled by a perfect vacuum. The test mass is maintained at a constant electric potential V_p while the electrodes are maintained at respectively V_x and $-V_x$, that we can modulate. This difference of potential leads to a voltage through two capacitors. Due to this imposed difference of potential, a force appears between the plates and the test mass, that would cancel if the test mass is centred between the plates with a gap g on both sides. Now consider this test mass to be slightly shifted toward one of the electrodes by a distance δ so that it is separated by respectively $g + \delta$ and $g - \delta$ from each electrodes. This difference of gap leads to a non null force.

Consider one capacitor. This capacitor stores the energy $E = \frac{1}{2}C\Delta V^2$, where ΔV is the difference of potential between the two plates of the capacitor and $C = \epsilon_0 A/e$ is the capacitance linked to the capacitor's geometrical quantities: A , the area of the overlapping surface of the plates, and e , the distance between

the plates. This energy corresponds to the electrical work that has been needed to create the difference of potential ΔV , or microscopically to make the charge carriers migrate to one of the plate to create this difference of potential. This energy also represents the potential energy the charge carriers hold and would spend to restore electrical balance. This could occur electrically if the electrical voltage maintaining the difference of potential was turned off; or mechanically with a force if the plates were mobile as is the test mass in our case. This force derives from this potential energy as

$$F_{\text{cap}} = \frac{dE}{de} = \frac{1}{2} \frac{dC}{de} \Delta V^2, \quad (1.27)$$

where we assumed the difference of potential to remain constant. The force is directed along the axis of displacement and is attractive. Microscopically it corresponds to the attraction of the positive and negative charges that are respectively present at the surface of the two plates due to the voltage.

Using the above formula for the capacitance, one gets an expression of the magnitude of the force experienced by the plates of this plane capacitor – in the MICROSCOPE's case by the test mass–:

$$F_{\text{cap}}(e) = \frac{1}{2} \frac{\varepsilon_0 A}{e^2} \Delta V^2. \quad (1.28)$$

This attractive force increases if the plates get closer and if the difference of potential is being increased.

We use this in the full problem of the two capacitors shown in Fig. 1.6. For fixed electrodes, the test mass experiences two forces from the two electrodes with which it forms the two capacitors. If the test mass is centred, the two forces cancel. If instead it is shifted, the force are no longer balanced resulting in a total force. The force is directed in the direction of the displacement \mathbf{e}_δ and is expressed using Eq. (1.28) as

$$\begin{aligned} \mathbf{F}_{\text{el}} &= [F_{\text{cap}}(g - \delta) - F_{\text{cap}}(g + \delta)] \mathbf{e}_\delta \\ \mathbf{F}_{\text{el}} &= \frac{1}{2} \varepsilon_0 A \left[\frac{(V_x - V_p)^2}{(g - \delta)^2} - \frac{(V_x + V_p)^2}{(g + \delta)^2} \right] \mathbf{e}_\delta, \end{aligned} \quad (1.29)$$

where we have specified the difference of potential consistently with Fig. 1.6 and we have considered the same area A for both capacitors.

One can Taylor expand this expression for small δ . By also developing the difference of potential terms, one obtains at first order in $\frac{\delta}{g}$

$$\mathbf{F}_{\text{el}} \simeq \frac{2\varepsilon_0 A}{g^2} \left[-V_p V_x + (V_p^2 + V_x^2) \frac{\delta}{g} \right] \mathbf{e}_\delta. \quad (1.30)$$

This expression contains two terms. The first one is dominant for small displacement and is opposed to the direction of the displacement. It is independent of δ . One can act on V_x to tune this force that the test mass is experiencing such that it can compensate any acceleration the test mass is feeling and maintain it at the centred position. The MICROSCOPE measurement is based on this principle. The potential V_x is tuned using a servo-control loop, the acceleration being then deduced as $a = \frac{2\varepsilon_0 A_p}{g^2 m_{\text{TM}}} V_x$, m_{TM} being the mass of the test mass.

The second term is only dominant for large δ , it is directed in the direction of the displacement so that it destabilises the system. Being linear to the displacement it is called the electrostatic stiffness. The force is written $\mathbf{F}_k = -k \delta$

the stiffness is equal to $k = \frac{2\varepsilon_0 A}{g^3}(V_p^2 + V_x^2)$. Even if sub-dominant, this term is considered in MICROSCOPE servo-control loop.

Note that this is an idealised simple model. In the MICROSCOPE experiment, more proper electrostatic models are considered taking into account more complex features such as the curvatures of the electrodes for instance.

This principle is used to measure the acceleration on the Y and Z axes. The measurement on the longitudinal axis X is based on another principle. The test mass cylinder is nested in two cylindrical electrodes that do not cover the whole surface of the test mass. While in the symmetric position the overlapping surfaces with the two electrodes are equal, if the test mass cylinder is moving along the X-axis, the two surfaces differ and create an imbalance of the capacitances. This leads to a force similar to the previous. To evaluate it one can differentiate the capacitance in Eq. (1.27) with respect to the area only the gap e is kept constant with the Y and Z electrodes.

1.4.3 Measurement equation

We now derive the measurement equation for the experiment. We follow the same procedure as Refs. [50, 104, 5]. The question is to determine in the satellite's rest frame the electrostatic force that one needs to apply to the 4 test masses to maintain them at a fixed position. To that end we need to study the dynamics of both the test masses and the satellite. We treat this problem in Newtonian physics. In particular we assume gravity to be described in Newton's theory. Nevertheless this description is still valid in alternative theories of gravity as long as the gravity fields do not vary too rapidly at the level of the experiment. If they do not, they should be treated as a perturbing force.

The satellite's frame \mathcal{R}_{sat} centred on the satellite centre of mass O_c^{sat} is in rotation compared to the geocentric frame \mathcal{R}_{geo} centred on O. This rotation is described by the satellite angular velocity vector $\boldsymbol{\Omega}$ of components $(\Omega_x, \Omega_y, \Omega_z)$ in the geocentric frame. We denote O_c^i the centre of mass of the i^{th} test mass. The dynamics of each test mass is ruled by

$$m_i^i \frac{d^2 \mathbf{O}_c^{\text{sat}} \mathbf{O}_c^i}{dt^2} = \mathbf{F}_g^i + \mathbf{F}_e^i + \mathbf{F}_p^i - m_i^i \left(\frac{d^2 \mathbf{O} \mathbf{O}_c^{\text{sat}}}{dt^2} + [\text{In}] \cdot \mathbf{O}_c^{\text{sat}} \mathbf{O}_c^i + 2[\Omega] \cdot \frac{d \mathbf{O}_c^{\text{sat}} \mathbf{O}_c^i}{dt} \right) \quad (1.31)$$

where \mathbf{F}_g^i is the gravitational force experienced by the test mass as sourced by the Earth, \mathbf{F}_e^i is the electrostatic forces applied by the electrodes and described above, and \mathbf{F}_p^i any other perturbing forces. The last two terms describe the inertial forces that are due to the rotation of \mathcal{R}_{sat} . They depend on the distance between O_c^{sat} and O_c^i and are expressed by defining the rotation matrix $[\Omega]$ as

$$[\Omega] = \begin{pmatrix} 0 & -\Omega_z & \Omega_y \\ \Omega_z & 0 & -\Omega_x \\ -\Omega_y & \Omega_x & 0 \end{pmatrix} \quad (1.32)$$

and the gradient of inertia matrix as $[\text{In}] = [\Omega]^2 + [\dot{\Omega}]$. The term in $[\Omega]$ corresponds to the Coriolis force, the term in its squared $[\Omega]^2$ to the centrifugal force and the term in its time derivative to the Euler force. The dynamics includes the motion of the satellite that is ruled by

$$m_i^{\text{sat}} \frac{d^2 \mathbf{O} \mathbf{O}_c^{\text{sat}}}{dt^2} = \mathbf{F}_g^{\text{sat}} + \mathbf{F}_e^{\text{sat}} + \mathbf{F}_p^{\text{sat}} \quad (1.33)$$

resulting from the forces the satellite experiences: the gravitational force $\mathbf{F}_g^{\text{sat}}$, any perturbing force $\mathbf{F}_p^{\text{sat}}$ such as the residual air-drag of the atmosphere for instance and $\mathbf{F}_e^{\text{sat}} = -\sum_{j=1}^{N_{\text{TM}}} \mathbf{F}_e^j$ the reaction forces due to the forces applied to the different test masses by the electrodes.

The gravitational forces, which are the source for a possible WEP violation, are described as follow. The precision goal of MICROSCOPE is such, that we must treat the non homogeneity of the gravity field on the scale of the test masses and the satellite, by integrating the gravity field over their volume. We can nonetheless Taylor expand the gravity field around some arbitrary point A close to the center of mass O_c of the considered body, for any point P in this body

$$\mathbf{g}(P) \simeq \mathbf{g}(A) + \mathbf{T}(A) \cdot \mathbf{AP}, \quad (1.34)$$

where $\mathbf{T} = \nabla \mathbf{g}$ is the gradient of gravity evaluated at A. This object is an order 2 three-dimensional tensor whose components are linked to the Newtonian potential by $T^{ij} = \partial^i \partial^j \Phi$. Note that the fact we express it around an arbitrary point will be useful for considering the fact the center of mass of test masses, although they are nested, do not coincide perfectly. In the MICROSCOPE's data analysis the point A is chosen to be $\mathbf{O}_c^{\text{sat}}$ for all bodies, although it is not enclosed in any test cylinder, but this only introduces an error smaller than 10^{-8} m.s^{-2} on the local gravity field, and when considering the differential acceleration between two test masses the gravity gradient term would only depend on the separation between their mass centre that is independent of $\mathbf{O}_c^{\text{sat}}$.

When integrating gravitational force associated to the Earth gravity field, given by Eq. (1.6), over the volume of the considered body, one obtains the expression of the gravitational forces for the i^{th} test mass and the satellite

$$\mathbf{F}_g^i = m_g^i [\mathbf{g}(\mathbf{O}_c^{\text{sat}}) + \mathbf{T}(\mathbf{O}_c^{\text{sat}}) \cdot \mathbf{O}_c^{\text{sat}} \mathbf{O}_c^i] \quad (1.35a)$$

$$\mathbf{F}_g^{\text{sat}} = m_g^{\text{sat}} \mathbf{g}(\mathbf{O}_c^{\text{sat}}) \quad (1.35b)$$

where we have suppressed the spatial dependency in P by introducing the centres of masses of each body which by definition the mass barycentre verifies $\int_{\text{body}} \mathbf{O}_c^i \mathbf{P} dm(P) = \mathbf{0}$.

Putting all these equations together one obtains the electrostatic acceleration one needs to apply to keep a test mass at a fixed position and thus the acceleration it experiences $\mathbf{\Gamma}_{\text{app}}^i = \frac{1}{m_i^i} \mathbf{F}_e^i$ that can be expressed as

$$\begin{aligned} \mathbf{\Gamma}_{\text{app}}^i &= \frac{m_g^i}{m_i^i} [\mathbf{g}(\mathbf{O}_c^{\text{sat}}) + [\mathbf{T}](\mathbf{O}_c^{\text{sat}}) \cdot \mathbf{O}_c^{\text{sat}} \mathbf{O}_c^i] \\ &+ \frac{1}{m_i^i} \mathbf{F}_p^i - [\text{In}] \cdot \mathbf{O}_c^{\text{sat}} \mathbf{O}_c^i - 2[\Omega] \cdot \frac{d\mathbf{O}_c^{\text{sat}} \mathbf{O}_c^i}{dt} - \frac{d^2 \mathbf{O}_c^{\text{sat}} \mathbf{O}_c^i}{dt^2} \\ &- \frac{1}{m_i^{\text{sat}}} \left(m_g^{\text{sat}} \mathbf{g}(\mathbf{O}_c^{\text{sat}}) - \sum_{j=1}^{N_{\text{TM}}} \mathbf{F}_e^j + \mathbf{F}_p^{\text{sat}} \right). \end{aligned} \quad (1.36)$$

The first two lines depend on the considered test mass while the last does not. In theory this last line is not source of any difference in the acceleration of a pair test masses, and thus does not affect the measurement. Nevertheless as will be shown in the next paragraph, geometrical defects of the cylinders can lead to a contribution of these terms. But their contribution are limited by design of the instrument and by the drag-free control system. This system acts on the whole satellite through cold-gas thrusters. This latter are chosen to be operated to compensate the acceleration of one of the test mass. The residual acceleration this test mass experiences is at the level $10^{-13} \text{ m.s}^{-2}$.

Of course, with this choice, the other test mass is affected, but as we are only interested in measuring the differential acceleration it does not affect the test.

This model is idealised. One needs to take into account the stochastic errors and the systematics errors that are caused by the instrument's imperfections. These are modelled for each test mass by the following equation

$$\mathbf{\Gamma}_{\text{meas}}^i = \mathbf{K}_0^i + [A^i][\theta^i]\mathbf{\Gamma}_{\text{app}}^i + [\text{Coupl}] \frac{d\mathbf{\Omega}_{\text{TM}}}{dt} + \mathbf{\Gamma}_{\text{noise}}^i \quad (1.37)$$

where \mathbf{K}_0^i is a bias term containing the instrument bias and any other constant perturbation as the satellite self-gravity, $[\theta^i]$ a rotation matrix accounting for the slight misalignment between the axis of the cylinder and the satellite frame, $[A^i]$ the sensitivity matrix whose diagonal corresponds to scale factor of the instrument and off-diagonal terms model the parallelism default between the electrodes and the test mass cylinder, and $[\text{Coupl}]$ models the possible coupling between the angular acceleration $\frac{d\mathbf{\Omega}_{\text{TM}}}{dt}$ of a test mass and its linear acceleration. All those error parameters have been estimated during the mission with dedicated in-orbit calibration sessions, their estimations are presented in Refs. [50, 104] and their magnitude will be mentioned in Sec. 1.4.5. The last term corresponds to the stochastic noise sources that will be described in the next section.

Finally we can define, for two test masses 1 and 2 of the same sensor unit, the measured differential acceleration as

$$\mathbf{\Gamma}_{\text{meas}}^d = \mathbf{\Gamma}_{\text{meas}}^1 - \mathbf{\Gamma}_{\text{meas}}^2. \quad (1.38)$$

The differential acceleration $\mathbf{\Gamma}_{\text{meas}}^d$ is the aim of the MICROSCOPE measurement and is linked to the Eötvös parameter in the measurement equation as in Ref. [104] as

$$\begin{aligned} \mathbf{\Gamma}_{\text{meas}}^d \simeq [M_c] \left(\eta \mathbf{g}(O_{\text{sat}}) + ([T] - [\text{In}]) \mathbf{\Delta} - 2[\Omega] \dot{\mathbf{\Delta}} - \ddot{\mathbf{\Delta}} \right) \\ + \mathbf{K}_0^d + 2[M_d] \mathbf{\Gamma}_{\text{app}}^c + \mathbf{\Gamma}_{\text{quad}}^d + [\text{Coupl}_d] \mathbf{\Omega}_{\text{TM}} + \mathbf{\Gamma}_{\text{noise}}^d, \end{aligned} \quad (1.39)$$

where the dot and the double dot denotes the first and second time derivative, $\mathbf{\Delta} = \mathbf{O}_c^2 \mathbf{O}_c^1$ is the separation between the centre of mass of the two test masses, $[M_d] = 1/2 ([A^1][\theta^1] - [A^2][\theta^2])$ is the difference of geometrical defects of the two inertial sensors, following this, any other quantity labelled by d – apart from $\mathbf{\Gamma}_{\text{meas}}^d$ – is defined as the semi-difference of the value it takes for the two test masses and any quantity labelled by c is the mean of the associated quantity for the two test masses of a sensor unit. Finally the term $\mathbf{\Gamma}_{\text{quad}}^d$ accounts for any term quadratic in the electrical potentials in the electronics. An example are the terms quadratic in the potential of the electrodes, that is not considered in an electrostatic model of Eq. (1.30) or the geometrical defects that are not considered in $[A]$ and $[\theta]$ creates.

Note that two additional approximations led us to this equation. First in the definition of the Eötvös parameter η in Eq. (1.8) we only kept the numerator. This is justified by the fact that previous WEP test have shown the mass ratios $\frac{m_g^i}{m_i^i}$ to be very close to 1. Similarly, if we denote ϵ_{WEP}^i its discrepancy with 1, the gravity gradient term is expanded as

$$\begin{aligned} [T](O_c^{\text{sat}}) \cdot \left[\frac{m_g^1}{m_i^1} \mathbf{O}_c^{\text{sat}} \mathbf{O}_c^1 - \frac{m_g^2}{m_i^2} \mathbf{O}_c^{\text{sat}} \mathbf{O}_c^2 \right] = [T](O_c^{\text{sat}}) \cdot [\mathbf{O}_c^2 \mathbf{O}_c^1 + \epsilon_{\text{WEP}}^1 \mathbf{O}_c^{\text{sat}} \mathbf{O}_c^1 \\ - \epsilon_{\text{WEP}}^2 \mathbf{O}_c^{\text{sat}} \mathbf{O}_c^2] + o[(\epsilon_{\text{WEP}}^i)^2]. \end{aligned} \quad (1.40)$$

In the MICROSCOPE analysis we only consider the first term.

The measurement equation (1.39) is the basis of MICROSCOPE's data analysis. This equation describes the different contributors of a possible non-null differential acceleration. Besides a WEP violation described by η , many effects can lead to such a signal. These can be estimated and minimised as described in Refs. [50, 104]. The geometrical defects, coupling terms, quadratic terms and off-centring on Δ_y have been estimated during in-flight calibration sessions. Any term involving time derivatives are being kept under control by the servo-loop control keeping the test mass motionless. The inertial forces are well known by precisely monitoring the satellite attitude using star-sensors. The gravity gradient is estimated using Earth's geoid models from the previous gravity mission GRACE [98], the other off-centrings Δ_x and Δ_z are estimated in the data analysis. Note that Eq. (1.39) shows explicitly the contribution on the differential acceleration of the forces common to the two sensors described in Γ_{app}^c induced by the geometrical defects. Again these perturbing common forces are minimised by the drag-free system. Finally the noise whose contributor are described in the next section is being handled in the data analysis by doing a Fourier spectral analysis.

1.4.4 Noise sources

There are three main sources of noise affecting the measurement of the acceleration of the test masses. These have different signatures in the experiment acceleration spectrum leading them to dominate at different frequencies. These signatures are shown in Fig. 1.7 and are clearly visible in Fig. 1.8 showing the spectrum of the differential acceleration obtained for a measurement session on SUEP.

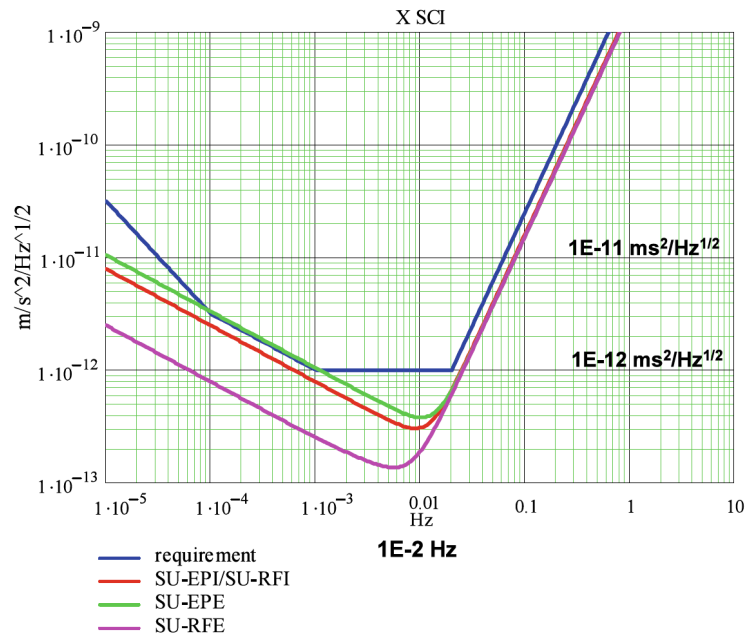


Figure 1.7: Expected noise signatures in the MICROSCOPE instrument. SU-EP stands for SUEP and SU-RF for SUREF. I and E denotes the internal and external accelerometer of each sensor unit. Figure adapted from Ref. [99].

Gold wire

The control of the electrical potential of the test mass requires a $7 \mu\text{m}$ -diametre gold wire. This wire acts mechanically as a spring that induces a perturbing force. This effect

has been studied with a torsion balance in Ref. [115]. Its stiffness has been estimated to a few 10^{-5} N.m^{-1} which leads to a negligible differential acceleration. Yet, this wire also leads to a damping term. This phenomenon described in [92] is explained by heat loss due to friction in the wire. This contributor of the noise can be evaluated using the fluctuation-dissipation theorem. It depends on the temperature of the wire. It has been shown that it can dominate the signal at low frequency, with a $f^{-1/2}$ -behaviour.

Electronic noise

The electronics used for the capacitive measurement is expected to create a stochastic noise on the position of the test masses. This leads to a f^2 -signal on the acceleration that dominates only at high-frequency.

Thermal noise

Finally variations of the temperature in a sensor unit cavity are a source of noise. Two main effects are responsible for this: the radiation pressure effect and the radiometer effect.

The first one is due to the infra-red thermal photons, emitted by the electrode cylinders because of their temperature, that hit the test masses and induce a pressure. Temperature variations can then lead to difference of pressure on each side of the test mass resulting in a force.

The radiometer effect is caused by the residual gas in the cavity. This effect appears in rarefied atmospheres when a body is submitted to a difference of temperature on two opposite sides of its volume.

The impact of these two effects depends on the thermal stability of the set-up. Many sessions have been dedicated to estimate them, using for instance heaters in the cavity to induce controlled temperature variations.

1.4.5 Spectral analysis and results of the mission

The analysis of the MICROSCOPE data is based on a spectral analysis using a fast Fourier transform of the differential acceleration. It is done on the X-axis longitudinal to the cylinders. As discussed before if a violation of the WEP was to be detected it would appear as a sinusoidal signal of frequency f_{EP} in the differential acceleration. This should appear in Fourier space as a line at this frequency. We discussed in the previous section the spectral signature of the different noise contributors. The gravity gradient has also an interesting signature. To see it, we need to express the gravity gradient tensor in the satellite's frame. In the Earth's spherical coordinates, if we only consider the monopole of Earth's geoid, only the diagonal-component contribute and are multiple of $2GM_{\text{Earth}}/r^3$. In the satellite's frame, given the quasi-circular orbit, the gravity gradient reads [102] in the satellite frame as

$$[T] = \frac{GM_{\text{Earth}}}{r^3} \begin{pmatrix} \frac{1}{2} + \frac{3}{2} \cos 2\alpha & 0 & -3 \sin 2\alpha \\ 0 & -1 & 0 \\ -3 \sin 2\alpha & 0 & \frac{1}{2} - \frac{3}{2} \cos 2\alpha \end{pmatrix} \quad (1.41)$$

where α is the angle defining the satellite's orientation in the Earth's reference of frame. One clearly sees that the gravity gradient has two contributions, one constant that is not distinguishable in spectral analysis and another at $2f_{\text{EP}}$. Note that in the measurement equation, the gravity gradient comes with the off-centring which, being constant in the satellite frame, does not affect the expected frequency at which this effect should appear.

During the mission, 24 120-orbits-long sessions have been performed on SUEP and 9 on SUREF. They have been operated with a satellite spin of 2.9432×10^{-3} Hz. This spin has been chosen such that the WEP signal would appear at a frequency $f_{\text{EP}} = 3.1113 \times 10^{-3}$ Hz where the contribution of the noise described previously is minimised. It was chosen during the in-flight characterisation sessions. As this thesis is being written the results of only two measurement sessions have been published [103, 104]: one session for each sensor units SUEP and SUREF. The analysis of the entire MICROSCOPE's data has since then been completed and the results are currently being validated for an upcoming publication.

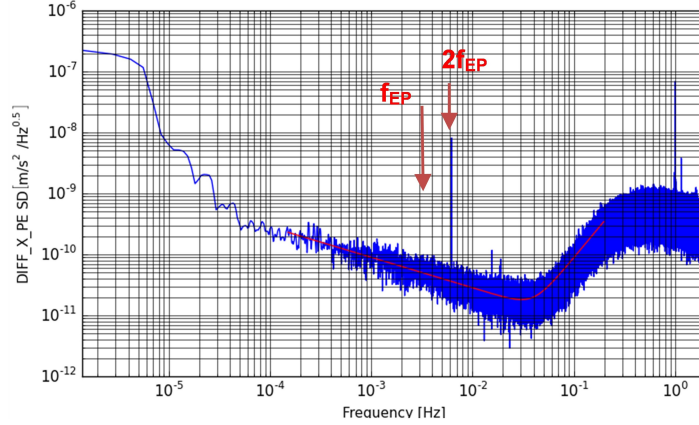


Figure 1.8: Power spectral density of the differential acceleration measured by SUEP during a measurement session. The red arrows show f_{EP} – at which a WEP violation would appear – and $2f_{\text{EP}}$ – at which the gradient gradient signal appear. Figure adapted from Ref. [103].

Figure 1.8 shows the power spectral density of the SUEP sensor unit for one session. The noise clearly has the expected behaviours at low and high frequencies. This figure shows clearly the expected gravity gradient ray at $2f_{\text{EP}}$. On the other hand, at f_{EP} where a WEP violation would appear, no line is visible.

A constraint on η is obtained by analysing the differential acceleration using the model given by Eq. (1.39) projected on the X-axis. The signal sampling rate is of 4 Hz. The analysis consists mainly in subtracting from the signal any effect described before that are found to contribute during the calibration session. Their estimation is given in Tab. 1.4. This leaves the measurement equation with three terms: η -term and the gravity gradient terms sourced by the off-centring along X and Z. The WEP violation term is expected to appear at frequency of f_{EP} and the off-centring term at $2f_{\text{EP}}$ respectively. To analyse them, a discrete Fourier transform is performed, then frequency bands are selected around f_{EP} and $2f_{\text{EP}}$ to perform a least square fit to estimate η , the off-centring Δ along X and Z, gravity models being used at this point to evaluate $\mathbf{g}(\text{O}_c^{\text{sat}})$ and $[\mathbf{T}](\text{O}_c^{\text{sat}})$.

The result [103, 104] on the SUEP sensor is

$$\eta_{\text{Ti,Pt}} = [-1 \pm 9 \text{ (stat)} \pm 9 \text{ (syst)}] \times 10^{-15} \quad (\text{at } 1\sigma), \quad (1.42)$$

where the second and third terms are the statistical uncertainty at 1σ and systematic uncertainty. The latter is obtained from Tab. 1.4 where it is derived from the systematics on $\mathbf{\Gamma}_{\text{meas}}^{\text{d}}$. η indeed appears in $\mathbf{\Gamma}_{\text{meas}}^{\text{d}}$ as multiplied by the gravity and $[M_c]$. The former has been estimated to $7.9 \text{ m}\cdot\text{s}^{-2}$ at the level of the satellite. The latter has been evaluated to differ from identity by less than a percent. To sum up, this result excludes any WEP

Table 1.4: Evaluation of systematic errors in the differential acceleration x-component for SUEP at f_{EP} .

Term in the Eq. (1.39) projected on the x-axis \mathbf{e}_x in phase with g_x at f_{EP}	Amplitude or upper bound in $\text{m}\cdot\text{s}^{-2}$
$T_{xx}\Delta x$	$< 10^{-18}$
$T_{xy}\Delta y$	$< 10^{-19}$
$T_{xz}\Delta z$	$< 10^{-17}$
$\dot{\Omega}_y\Delta z - \dot{\Omega}_z\Delta y$	5×10^{-17}
$\Omega_x\Omega_y\Delta y - \Omega_x\Omega_z\Delta z - (\Omega_y^2 + \Omega_z^2)\Delta x$	1.3×10^{-17}
$([M_d]\mathbf{\Gamma}_{\text{app}}^c)\cdot\mathbf{e}_x$	1.7×10^{-15}
$(\mathbf{\Gamma}_{\text{quad}}^d)\cdot\mathbf{e}_x$	5×10^{-17}
$([\text{Coupl}_d]\mathbf{\Omega}_{\text{TM}})\cdot\mathbf{e}_x$	$< 2 \times 10^{-15}$
Thermal systematics	$< 67 \times 10^{-15}$
Magnetic systematics	$< 2.5 \times 10^{-16}$
Total of systematics in $\mathbf{\Gamma}_{\text{meas}}^d\cdot\mathbf{e}_x$	$< 71 \times 10^{-15}$
Total of systematics in $\eta_{\text{Ti,Pt}}$	$< 9 \times 10^{-15}$

violations greater than 1.9×10^{-14} at 1σ . This represents an improvement of the precision on the WEP test of roughly one order of magnitude compared to the previous bound.

The result on the SUREF is the following

$$\eta_{\text{Pt,Pt}} = [+4 \pm 4(\text{stat}) \pm 8(\text{syst})] \times 10^{-15} \quad (\text{at } 1\sigma). \quad (1.43)$$

This is comforting as no violation is expected, the two test masses being of same composition. Note that the precision is slightly better, this is due to a better noise level on this instrument.

Chapter conclusion

The weak equivalence principle is one of the most well-tested physical principles. The history of its test is rich and goes back to Galileo's epoch. The most recent improvement of this test is the MICROSCOPE mission. By performing its test in orbit, this experiment improved the precision of this test by an order of magnitude.

The implications of the WEP on our vision of gravity are far-reaching. It is a founding pillar of general relativity. Thence testing it allows for probing gravity theories beyond GR. Such theories are the subject of the next chapter.

Chapter 2

Gravity beyond general relativity

While the equivalence principle is the corner stone of general relativity, many alternatives to this theory violate this principle. Some have already been ruled out by the current precision on the test of the equivalence principle or by other means. Other can predict a violation weaker than the current bound or provide a more complex phenomenology of such a violation. Understanding this phenomenology is a great opportunity to constraint these theories, by re-analysing WEP test data or imagining new experimental design for these tests.

Following the literature, we qualify these alternative theories to general relativity as *modified gravity* even if it is clear that it is only general relativity that is modified and not gravity itself.

2.1 Motivation for modifying general relativity

General relativity is our current standard theory for describing gravity. Its foundations are well tested [114]. It passes all experimental tests e.g. deflection of light by the Sun [34, 30, 61], precession of Mercury’s perihelion [34, 64], gravitational redshift [31, 110], Shapiro time delay [95], Lense–Thirring effect [65, 42], Hulse–Taylor binary pulsar’s gravitational radiation [54]. It also predicted the existence of black holes [94, 22]. More recently the long awaited direct detection [1] of the gravitational waves it predicted [35] has been a crowning achievement for the theory and gave a proof of the existence of astrophysical black holes. On cosmological scales, general relativity predicted the expansion of the universe [36] that was later confirmed observationally by Hubble [52]. Today it provides a framework to develop a theory reproducing most observations [55], with the exception of: galaxy clustering [117] and galaxy rotation curves [45] leading to the introduction of the so-far-undetected dark matter; and of the acceleration of the universe’s expansion [81, 89] only explained by a cosmological constant or a dark energy.

Despite these successes, the history of gravity has been marked by a rich variety of alternative theories of gravity. Most of these have been successively constrained experimentally. A possible way to modify general relativity is to introduce new gravity fields in addition to the metric field. The simplest field one can consider is a scalar field [46]. It has been widely studied phenomenologically as it could provide a fifth force that could violate the WEP. In cosmology it can provide a dynamical dark energy to explain late time cosmic acceleration and is also a possible model of inflation [66]. The next field that can be considered is a vector. It is used in Einstein-Aether theory [48] to reintroduce the concept of a preferred reference frame in general relativity that would violate local Lorentz invariance. In TeVeS theory [7] both scalar field and vector field are used to provide a relativistic version of MOND theory. The latter theory was introduced [71] as a modification of Newton’s gravity that would explain anomalies in the galaxy

rotation curves without the hypothesis of dark matter. Then the next possible field that can be introduced is a second metric tensor. Such a second tensor field is used for instance in massive gravity [26] to again resolve cosmological problems.

In the following we will only consider scalar-tensor theories and their role in the weak equivalence principle phenomenology.

2.2 Scalar-Tensor theories

2.2.1 General theory

In scalar-tensor theories, a new scalar field ϕ is introduced in addition to the metric tensor of general relativity. We follow the same convention as Refs. [40, 27].

Action in the Einstein and Jordan frames

The theory enjoys two different representations in the so called Einstein frame and Jordan frame. The Einstein frame is the one where the GR part of the action is given by the Einstein-Hilbert action. In this frame the action of scalar-tensor theory takes the form

$$S = \int d^4x \sqrt{-g} \left[\frac{M_{\text{Pl}}^2}{2} R - \frac{1}{2} g^{\mu\nu} \partial_\mu \phi \partial_\nu \phi - V(\phi) \right] + \int d^4x \sqrt{-\tilde{g}} \mathcal{L}_m(\Omega^2(\phi) g_{\mu\nu}, \psi_m^{(i)}), \quad (2.1)$$

where V is the potential of the field, \mathcal{L}_m is the matter Lagrangian as described in the standard model by matter fields $\psi_m^{(i)}$ that are labelled by i . R , $g_{\mu\nu}$, g are respectively the Einstein frame's Ricci scalar, the metric tensor and its determinant, and $\Omega^2(\phi)$ is the conformal factor function used to defined the Jordan frame metric $\tilde{g}_{\mu\nu}$ given as a function of the scalar field as

$$\tilde{g}_{\mu\nu}(\phi) = \Omega^2(\phi) g_{\mu\nu} \quad (2.2)$$

with $\Omega(\phi)$ the conformal factor function. By definition of the inverse metric tensor one also has $\tilde{g}^{\mu\nu} = \Omega^{-2}(\phi) g^{\mu\nu}$. \tilde{g} is the determinant of $\tilde{g}_{\mu\nu}$.

In the Einstein frame, the scalar field is minimally coupled to the metric through the term $\sqrt{-g}$ and its kinetic term. On the other hand the matter fields from \mathcal{L}_m get non-minimally coupled to the scalar field, leading to the fact that matter particles do not follow geodesics of spacetime. Instead each matter field sees the Jordan frame metric $\tilde{g}_{\mu\nu}$ leading it to follow curves modified by ϕ in the Einstein frame. One can obtain the action in the Jordan frame, by performing the conformal transform in Eq. (2.2). The Ricci scalar [112] transforms as

$$\tilde{R} = \Omega^{-2} \left[R - 3 \frac{1}{\sqrt{-g}} \partial_\mu (g^{\mu\nu} \sqrt{-g} \partial_\nu \ln \Omega^2) - \frac{3}{2} \left(\frac{\partial \ln \Omega^{-2}}{\partial \phi} \right)^2 g^{\mu\nu} \partial_\mu \phi \partial_\nu \phi \right], \quad (2.3)$$

such that by defining two arbitrary functions F and Z of ϕ , a new potential U and the scalar field rescaling $\phi \rightarrow \tilde{\phi}$ by the set of equations:

$$F(\tilde{\phi}) = \Omega^{-2}(\phi), \quad (2.4a)$$

$$\left(\frac{\partial \phi}{\partial \tilde{\phi}} \right)^2 = \frac{Z(\tilde{\phi})}{F(\tilde{\phi})} + 3 \frac{M_{\text{Pl}}^2}{2} \left(\frac{\partial \ln F}{\partial \tilde{\phi}} \right)^2, \quad (2.4b)$$

$$U(\tilde{\phi}) = V(\phi) F^2(\tilde{\phi}), \quad (2.4c)$$

one obtains the action in the Jordan frame

$$S = \int d^4x \sqrt{-\tilde{g}} \left[\frac{M_{\text{Pl}}^2}{2} F(\tilde{\phi}) \tilde{R} - \frac{1}{2} Z(\tilde{\phi}) \tilde{g}^{\mu\nu} \partial_\mu \tilde{\phi} \partial_\nu \tilde{\phi} - U(\tilde{\phi}) \right] + \int d^4x \sqrt{-\tilde{g}} \mathcal{L}_m(\tilde{g}_{\mu\nu}, \psi_m^{(i)}), \quad (2.5)$$

Note that second term of Eq. (2.3) involves a total derivative that provides, when integrated by part, a term that does not contribute to the dynamics of the theory.

These two descriptions are physically completely equivalent although one of them can be more convenient to perform some calculations, but when computing observables they provide the same result. Note that in the Einstein frame the scalar field has a dimension of a mass, while in the Jordan frame it is dimensionless.

Field's equations

One obtains the field's equations by varying the action with respect to each field. Leading this calculation in the Einstein frame is more convenient as we will retrieve equations similar to GR and lead to a more straightforward calculation when considering the Newtonian limit.

By varying the action with respect to $g^{\mu\nu}$, one gets the modified Einstein field equations

$$R_{\mu\nu} - \frac{1}{2}R g_{\mu\nu} = \frac{1}{M_{\text{Pl}}^2} \left[\Omega^2(\phi) \tilde{T}_{\mu\nu} - 2g_{\mu\nu} \partial^\rho \phi \partial_\rho \phi + \partial_\mu \phi \partial_\nu \phi - V(\phi) g_{\mu\nu} \right]. \quad (2.6)$$

Compared to Einstein equation from GR, the scalar field here provides a new source to curve spacetime geometry, besides it modifies the way matter curves space time through the factor Ω^2 in front of the stress-energy tensor. Note that here it is the Jordan frame stress-energy tensor

$$\tilde{T}_{\mu\nu} = \frac{2}{\sqrt{-\tilde{g}}} \frac{\partial(\sqrt{-\tilde{g}} \mathcal{L}_m)}{\partial \tilde{g}^{\mu\nu}} \quad (2.7)$$

that plays the role of source. This tensor is in fact the one describing ordinary matter as in the standard model. This is because, in the Jordan frame, the matter fields only couple to the metric and not to the scalar field. Consequently it is in this frame that matter respects energy conservation $\tilde{\nabla}_\mu \tilde{T}^{\mu\nu} = 0$ as in classic general relativity – i.e. in Eq. (1.13). On the contrary, in the Einstein frame the matter fields are affected by the scalar field. This induces a modification of the energy conservation equation with an additional term accounting for the coupling with ϕ . This coupling leads to an apparent modification of masses of the matter fields or equivalently of the gravitational constant when considering observables. Nonetheless in the Jordan frame, even if the masses are constant, by looking at the action, one can tell that the gravitational constant – in M_{Pl} – is modified, leading to an effective gravitational constant $G_{\text{eff}} = \Omega^2(\phi)G$. These frame-dependent considerations are however artificial. The important conclusion is obtained when looking at observables given by these theories as for instance the gravitational force one would measure. In such a case one would tell that the scalar field modifies the product of the gravitational constant and the masses of the considered bodies: Gm_1m_2 . One can then equivalently interpret this as a variation of G or of the masses. The variation depends on the local value of the field. An example will be given when studying Brans-Dicke theory in Sec. 2.2.4. Note that when considering a non-universal coupling, all physical constants will be subjected to variation from the scalar field [107].

When varying the action with ϕ , one obtains the Klein-Gordon equation governing the dynamics of the field

$$\partial^\mu \partial_\mu \phi = \frac{dV}{d\phi} - \frac{d \ln \Omega}{d\phi} T^{\mu\nu} g_{\mu\nu}. \quad (2.8)$$

The field couples to the trace of the Einstein frame stress-energy tensor - defined by removing the tilde in Eq. (2.7). It is linked to the Jordan frame one by $T^{\mu\nu} g_{\mu\nu} =$

$\Omega^4(\phi)\tilde{T}^{\mu\nu}\tilde{g}_{\mu\nu}$. From this we conclude that the scalar field sees ordinary matter affected by the factor of Ω^4 . This is justified by our previous discussion emphasising the fact that the ordinary matter we know from our description of nature without a scalar field is properly described by the Jordan frame quantity. It is important to note that the field is not sourced by traceless stress-energy tensor matter fields as for instance the electromagnetic field.

Geodesics in Einstein frame

As mentioned previously the matter fields see the Jordan frame metric. In this frame, as long as no additional coupling terms are added, the matter fields are indeed coupled minimally to the metric field through the term $\sqrt{-\tilde{g}}$. As a consequence matter particles follow geodesics of the Jordan frame metric so that

$$\frac{d^2x^\rho}{ds^2} + \tilde{\Gamma}_{\mu\nu}^\rho \frac{dx^\mu}{ds} \frac{dx^\nu}{ds} = 0 \quad (2.9)$$

where $\tilde{\Gamma}_{\mu\nu}^\sigma$ are the Christoffel symbols in the Jordan metric. Note that this does not mean that in the Jordan frame matter follows geodesics as in pure GR. In this frame the non-minimal coupling between the scalar field and the tensor field affects the gravity field in such a way that the trajectories of matter particles get in the end modified compared to pure GR.

The Christoffel symbols contain first derivatives of the metric that transform as

$$\partial_\sigma \tilde{g}_{\mu\nu} = \Omega^2(\phi) \left(\partial_\sigma g_{\mu\nu} + 2 \frac{\partial \ln \Omega}{\partial \phi} g_{\mu\nu} \partial_\sigma \phi \right). \quad (2.10)$$

Then the Christoffel symbols transform as

$$\begin{aligned} \tilde{\Gamma}_{\mu\nu}^\rho &= \frac{1}{2} \tilde{g}^{\rho\sigma} (\partial_\mu \tilde{g}_{\sigma\nu} + \partial_\nu \tilde{g}_{\mu\sigma} - \partial_\sigma \tilde{g}_{\mu\nu}) \\ &= \frac{1}{2} \Omega^{-2}(\phi) g^{\rho\sigma} \Omega^2(\phi) \left[(\partial_\mu g_{\sigma\nu} + \partial_\nu g_{\mu\sigma} - \partial_\sigma g_{\mu\nu}) \right. \\ &\quad \left. + 2 \frac{\partial \ln \Omega}{\partial \phi} (\partial_\mu \phi g_{\sigma\nu} + \partial_\nu \phi g_{\mu\sigma} - \partial_\sigma \phi g_{\mu\nu}) \right] \\ \tilde{\Gamma}_{\mu\nu}^\rho &= \Gamma_{\mu\nu}^\rho + \frac{\partial \ln \Omega}{\partial \phi} (\partial_\mu \phi \delta_\nu^\rho + \partial_\nu \phi \delta_\mu^\rho - g^{\rho\sigma} \partial_\sigma \phi g_{\mu\nu}). \end{aligned} \quad (2.11)$$

Using this in Eq. (2.9), one gets a modified geodesics equations in the Einstein frame

$$\frac{d^2x^\rho}{ds^2} + \Gamma_{\mu\nu}^\rho \frac{dx^\mu}{ds} \frac{dx^\nu}{ds} + \frac{\partial \ln \Omega}{\partial \phi} \left(2 \partial_\mu \phi \frac{dx^\mu}{ds} \frac{dx^\rho}{ds} - g^{\rho\sigma} \partial_\sigma \phi g_{\mu\nu} \frac{dx^\mu}{ds} \frac{dx^\nu}{ds} \right) = 0. \quad (2.12)$$

Similarly to Eq. (1.15), one can express this equation in the following form

$$u^\mu \nabla_\mu u^\rho = - \frac{\partial \ln \Omega}{\partial \phi} \perp^{\mu\rho} \partial_\mu \phi \quad (2.13)$$

where $u^\mu = \frac{dx^\mu}{ds}$ is the 4-velocity along the geodesic curve or its tangent vector and $\perp^{\mu\nu} = u^\mu u^\nu + g^{\mu\nu}$ is the projector on the 3-space normal to u^μ . Note that we used the fact that $u^\mu u_\mu = -1$ for massive particles.

From this new geodesics equation, one can thus conclude that the scalar field affects the geodesics of the Einstein frame by a term that depends on the gradient of the field. Doing so the scalar field creates a fifth force that can be expressed as

$$F_\phi^\rho = - \frac{\partial \ln \Omega}{\partial \phi} \perp^{\mu\rho} \partial_\mu \phi. \quad (2.14)$$

This force can lead to WEP violation when considering a non-universal coupling of the scalar field as will be discussed in Sec. 2.2.3.

A last feature that is worth mentioning in scalar-tensor theories, is that null geodesics are not affected by the scalar field. The reason to this is the structure of the conformal transformation from Eq. (2.2). As argued in Ref. [39], null geodesics are curves for which the tangent vector to the curve is null i.e. $\tilde{g}_{\mu\nu}u^\mu u^\nu = 0$. If this property of nullity holds in the Jordan frame, it holds also in the Einstein frame as $g_{\mu\nu}u^\mu u^\nu = \Omega^{-2}\tilde{g}_{\mu\nu}u^\mu u^\nu = 0$. As a consequence, null geodesics are the same in the two frames, so that they do not get affected by the scalar field. This implies that massless particles do not feel any force from the scalar field. An important phenomenological consequence concerns bending of light by the a massive body. In scalar-tensor theory, the result of such phenomena is still the same as described by general relativity, that is in agreement with observations.

2.2.2 Newtonian limit

Similarly to general relativity one can study the Newtonian limit of scalar-tensor theories. The procedure is the same as in pure GR. The Newtonian limit is the weak-field and non-relativistic limit. We assume the metric field to be close to Minkowski spacetime such that

$$g_{\mu\nu} = \eta_{\mu\nu} + h_{\mu\nu}, \quad (2.15)$$

where $\eta_{\mu\nu} = \text{Diag}(-1, 1, 1, 1)$ is Minkowski metric and $h_{\mu\nu}$ is a small perturbation.

Then to first order in $h_{\mu\nu}$ one gets [112]

$$\Gamma_{\mu\nu}^\rho = \frac{1}{2}\eta^{\rho\sigma}(\partial_\mu h_{\sigma\nu} + \partial_\nu h_{\mu\sigma} - \partial_\sigma h_{\mu\nu}), \quad (2.16a)$$

$$R_{\mu\nu} = \frac{1}{2}(\partial_\rho \partial_\mu h_{\rho\nu} + \partial_\rho \partial_\nu h_{\mu\rho} - \partial^\rho \partial_\rho h_{\mu\nu} - \partial_\mu \partial_\nu h), \quad (2.16b)$$

$$R = \partial^\mu \partial^\nu h_{\mu\nu} - \partial^\rho \partial_\rho h, \quad (2.16c)$$

where $h = h^\mu_\mu$ and $\eta_{\mu\nu}$ is used to contract indices. By posing $\bar{h}_{\mu\nu} = h_{\mu\nu} - \frac{1}{2}h\eta_{\mu\nu}$ and by fixing the freedom of coordinates system with the gauge $\partial^\nu \bar{h}_{\mu\nu} = 0$, Einstein field equation (2.6) in the case of scalar-tensor theory becomes

$$\partial^\rho \partial_\rho \bar{h}_{\mu\nu} = -\frac{2}{M_{\text{Pl}}^2} \left[\Omega^2(\phi) \tilde{T}_{\mu\nu} - 2\eta_{\mu\nu} \partial^\rho \phi \partial_\rho \phi + \partial_\mu \phi \partial_\nu \phi - V(\phi) \eta_{\mu\nu} \right]. \quad (2.17)$$

The 00-equation gives a modified Poisson equation. For non-relativistic matter we have $\tilde{T}_{00} = \tilde{\rho}$, where $\tilde{\rho}$ is the local density matter distribution function. Moreover as in pure general relativity the 00-component of $\bar{h}_{\mu\nu}$ is linked to Φ the equivalent of the Newtonian potential as $\bar{h}_{00} = -4\Phi$. We obtain the equation

$$\partial^\rho \partial_\rho \Phi = \frac{1}{2} \frac{1}{M_{\text{Pl}}^2} \left[\Omega^2(\phi) \tilde{\rho} + \partial_t \phi \partial_t \phi + 2\partial^\rho \phi \partial_\rho \phi + V(\phi) \right] \quad (2.18)$$

which for static configurations becomes

$$\Delta \Phi = 4\pi G \left[\Omega^2(\phi) \tilde{\rho} + 2(\nabla \phi)^2 + V(\phi) \right], \quad (2.19)$$

where Δ is the space Laplacian. From this modified Poisson equation, one concludes that the potential is no longer the classic Newton potential $\Phi_{\mathcal{N}} = GM/r$, instead it is modified by the scalar field through the norm of its gradient and its potential. Likewise the gravity potential sees a modified mass $\Omega^2(\phi)\tilde{\rho}$. Note that nonetheless those modifications of Newton's potential are negligible for most theories.

In the Newtonian limit the field's Klein-Gordon equation becomes

$$\square\phi = \frac{dV}{d\phi} + \frac{d\ln\Omega}{d\phi}\Omega^4(\phi)\tilde{\rho} \quad (2.20)$$

where \square denotes the d'Alembertian that reduces to the Laplacian for static configurations. Note that we have used the Newtonian limit of the trace of the stress-energy tensor $\tilde{T}^{\mu\nu}\tilde{g}_{\mu\nu} = -\tilde{\rho}$.

The geodesics equation also simplifies in the Newtonian limit. The motion of test particles is described by Eq. (2.12), again in the weak-field limit for non-relativistic matter and static configuration one has from Eq. (2.16a)

$$\Gamma_{00}^i = \frac{1}{2}\partial_{x^i}h_{00} = \partial_{x^i}\Phi \quad (2.21)$$

where we have used $h_{00} = 2\Phi$ and where i denotes the three spatial dimensions. We can then insert this in Eq. (2.12). By taking the proper-time τ as affine parameter and using the fact that in the non-relativistic limit $\frac{d\tau}{dt} \simeq 1$ and $\frac{dx^i}{dt} \simeq 1$, one gets

$$\frac{d^2x^i}{dt^2} = -\partial_{x^i}\Phi - \frac{\partial\ln\Omega}{\partial\phi}\partial_{x^i}\phi. \quad (2.22)$$

Hence in the Newtonian limit, the fifth force that the scalar field creates, scales exactly as the gradient of the field. For a test particle of mass m one has the 3-force

$$\mathbf{F}_\phi = -m\frac{\partial\ln\Omega}{\partial\phi}\nabla\phi. \quad (2.23)$$

We recall this formulation of the fifth force is only valid as long as the particles have velocities $v \ll c$ small compared to the speed of light. This force can lead to a violation of the WEP. It can be explicitated through different functions $\Omega_{(i)}$ if the field couples non-universally to each matter field as shown in the next section.

2.2.3 Non-universal scalar field coupling

Until now we have considered the scalar field to couple universally to each matter component. One can however consider that it couples differently to each matter field. This is described by associating a different conformal factor $\Omega_{(i)}$ to each matter field. This way one can associate a different Jordan frame metric for each field. But as matter follows the Jordan frame geodesics, in the Einstein frame matter particles follow curves that are different depending on their nature. Their equation is obtained by adding the matter field dependency in Eq. (2.13) such that for each i we have

$$u^\mu\nabla_\mu u^\rho = -\frac{\partial\ln\Omega_{(i)}}{\partial\phi}\perp^{\mu\rho}\partial_\mu\phi. \quad (2.24)$$

One concludes that particles of different nature experience different fifth forces. This force is expressed by the second member of this equation. It leads to a violation of the WEP. As a consequence WEP tests provide a great opportunity to constraint the existence of such scalar-fields.

For extended bodies or composite particles, besides the fact that their influence on the scalar field could not be negligible, one needs to integrate this force on their volume. One however needs to do this integration for each matter field contained in the body. This takes into account the possible inhomogeneities of the body. One gets the force it experiences as

$$F_{\text{extended}}^\rho = -\int_{\text{Vol}}\sum_i\tilde{\rho}_i(\mathbf{x})\frac{\partial\ln\Omega_{(i)}(\phi)}{\partial\phi}\perp^{\mu\rho}\partial_\mu\phi dV \quad (2.25)$$

where $\tilde{\rho}_i$ denotes the matter density function associated to the i^{th} matter component of the body.

This non-universal coupling also affects the dynamics of the scalar field. Similarly to the force, each matter field brings a contribution to the scalar field that is weighted by its coupling constant $\Omega_{(i)}$. The Klein-Gordon equation of the field in the Newtonian limit then becomes

$$\square\phi = \frac{dV}{d\phi} + \sum_i \frac{d \ln \Omega_{(i)}}{d\phi} \Omega_{(i)}^4(\phi) \tilde{\rho}_i(\mathbf{x}, t). \quad (2.26)$$

As a consequence the matter fields do not source equally to the field. We recall again that the electromagnetic field does not contribute to this equation.

2.2.4 Massless scalar field

In this section we explore different scalar-tensor theory models based on different potentials and the coupling constants.

Jordan-Brans-Dicke theory: a prototype massless scalar field

The first scalar-tensor theory is the Jordan-Brans-Dicke theory [12, 29]. It was introduced as a modification of General Relativity that respects Mach's principle [67]. This principle is motivated by considerations about Newton's bucket, a bucket filled with water whose surface curves due to inertial forces if the bucket is rotating. Newton's interpretation was that this was a proof to the existence of an absolute space in which the bucket would have an absolute rotation. Nonetheless, as relativity have ruled out such concept of an absolute space, what would then explain the existence of such inertial forces? Mach's idea to solve this problem, was that these apparent forces were caused by the gravitational interaction of the whole distribution of causally connected distant matter around the bucket that would appear as rotating in the bucket frame.

This principle leads to an effective inertial mass of bodies that would have a spatial and time dependence governed by the distribution of mass around it. One only having experimentally access to G times the gravitational mass, it is equivalent to consider that the gravitational constant G that varies. In Brans-Dicke theory, the variation of G is encoded in a scalar field.

In the general formalism introduced previously Brans-Dicke theory corresponds in the Jordan frame to

$$F(\tilde{\phi}) = \tilde{\phi}, \quad (2.27a)$$

$$Z(\tilde{\phi}) = M_{\text{Pl}}^2 \frac{\omega}{\tilde{\phi}}, \quad (2.27b)$$

$$U(\tilde{\phi}) = 0, \quad (2.27c)$$

with ω being a constant parameter of the theory. Eqs. (2.4) gives the theory in the Einstein frame with

$$\phi = \phi_0 + M_{\text{Pl}} \sqrt{\omega + 3/2} \ln \frac{\tilde{\phi}}{\tilde{\phi}_0}, \quad (2.28a)$$

$$\Omega(\phi) = \tilde{\phi}_0^{-1/2} e^{-\frac{\phi - \phi_0}{2M_{\text{Pl}}\sqrt{\omega + 3/2}}}, \quad (2.28b)$$

$$V(\phi) = 0 \quad (2.28c)$$

where ϕ_0 and $\tilde{\phi}_0$ are two constants. Note that the function Ω is, in this model, universal to all the matter fields so that the WEP is respected.

We want to see how this scalar field acts in the Newtonian limit around a spherical ball such as Earth. As long as ϕ is small compared to M_{Pl} we have $\Omega(\phi) = \tilde{\phi}_0^{-1/2}$. One can moreover verify that the contribution of the field to the classic gravitational potential is negligible so that it reduces to Newton's potential multiplied by Ω^2 . To evaluate the additional fifth force we need to determine the gradient of the field. For static situations, it is obtained by integrating the Klein-Gordon equation that with the above definition becomes

$$\Delta\phi = -\frac{\tilde{\phi}_0^{-2}}{M_{\text{Pl}}\sqrt{2(2\omega+3)}}\tilde{\rho}. \quad (2.29)$$

It is easily solved around a spherical body of mass M such as Earth, one obtains a result very similar to Newton's potential. And finally we obtain from Eq. (2.22) the total force created by both the Newtonian gravity field and the scalar field that a test body of mass m experiences

$$|\mathbf{F}| = \tilde{\phi}_0^{-1} \frac{2\omega+3+\tilde{\phi}_0^{-1}}{2\omega+3} \frac{GMm}{r^2}. \quad (2.30)$$

In conclusion the effect of Brans-Dicke scalar field in the Newtonian limit, is completely equivalent to a modification of the gravitational constant. The gravitational constant one would measure is given by

$$G_{\text{cav}} = \tilde{\phi}_0^{-1} \frac{2\omega+3+\tilde{\phi}_0^{-1}}{2\omega+3} G \quad (2.31)$$

where $\tilde{\phi}_0$ is the background value of the field determined by the distribution of mass around the considered location and G is the bare gravitational constant parameter of general relativity part of the theory. The effective gravitational constant G_{cav} is the gravitational constant one would measure from a gravity experiment conducted in a laboratory such as a Cavendish experiment for instance. In Brans-Dicke this value would vary depending on the location in space and time due to the local value of $\tilde{\phi}_0$. The most recent bound comes from the Cassini-Huygens mission [9] and shows that $\omega > 40000$.

General universal massless scalar-tensor theories

A convenient way of parametrising such massless theory is given in [41, 39]. This helps setting general constraints. It consists in developing the coupling function Ω around the background value ϕ_0 the field takes far from any massive source

$$\ln \Omega(\phi) = \ln \Omega(\phi_0) + \alpha_0(\phi - \phi_0) + \beta_0(\phi - \phi_0)^2 + o((\phi - \phi_0)^3) \quad (2.32)$$

where α_0 and β_0 are constants parametrising respectively the linear and quadratic coupling that the scalar field induces. In the language of Feynman diagrams, the former corresponds to the exchange of a scalar particle while the latter to the exchange of two particles. In this language Brans-Dicke theory corresponds to $\alpha_0^2 = 1/(2\omega+3)$ and $\beta_0 = 0$.

In such a model, in the Newtonian limit similarly to the Brans-Dicke case, due to the scalar field, one would experimentally measure an effective gravitational constant given as

$$G_{\text{cav}} = G \Omega(\phi_0)^2 (1 + \alpha_0^2). \quad (2.33)$$

Current constraints on massless scalar field in this language are given by Fig. 2.1. The main constraints come from solar-system tests of general relativity and from observations of distant binary pulsar systems.

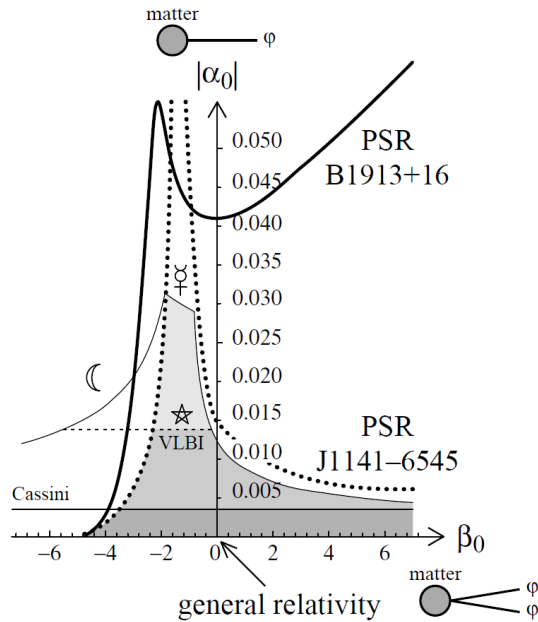


Figure 2.1: Constraints on a universal massless scalar-tensor theory as parametrised by Eq. (2.32). Binary pulsars constraints are denoted by their name beginning by PSR. \mathbb{C} denotes constraints from Laser Lunar Ranging, \mathbb{Q} constraints from measurement of Mercury’s precession of the perihelion, VLBI constraints from VLBI’s measurement of light deflection, and Cassini constraints from the measurement of the Shapiro effect with the Cassini spacecraft. The compilation of all constraints is shown in the darkest grey region. This figure is extracted from Ref. [39].

It is worth mentioning that, although a scalar field does not affect the trajectory of photons, a constraint is obtained from light deflection measurement. Such a constraint is the result of the modulation by the field of the gravitational constant. In general relativity, the deflection angle of photon by the sun is proportional to the gravitational constant. In scalar-tensor theory, as the trajectory of photon is not affected by the scalar field, this angle is still proportional to the bare gravitational constant G . On the other hand, processes involving massive test bodies, as for instance Keplerian orbits, depend on the effective gravitational constant G_{cav} , that depends on the value of the field. By comparing the consistency of the gravitational constant obtained from the latter process with the former, one can thus test scalar tensor theory. In other words, if one analyses light deflections observations considering the value of the gravitational constant measured from Keplerian orbits, one could measure a value of the deflection angle different from GR. This provides a way of testing such theories.

Massless field and non universal coupling

In the Brans-Dicke model, the scalar field couples universally to each matter field. A non-universal coupling would be created by a different function $\Omega_{(i)}$ for each matter field. Take

$$\Omega_{(i)}(\phi) = e^{\frac{\beta^i}{M_{\text{Pl}}}\phi}, \quad (2.34)$$

with β^i being a matter-field-dependent coupling constant. Again $\Omega(\phi) \simeq 1$, for small field compared to M_{Pl} . Now when considering the coupling between two bodies two different β^i appear: one in the Klein-Gordon equation for the body sourcing the field, and another one in the geodesic equation for the body falling in it. One obtains an

interaction between the bodies i and j deriving from the potential

$$V_{ij}(r) = \frac{GM}{r} (1 + 2\beta^i \beta^j). \quad (2.35)$$

that is parametrised by their coupling constant β^i .

This class of non universally coupled scalar field is often called *dilaton* field. This denomination comes from a scalar field that emerges from string theory in the low energy limit [25]. Many models exist for the composition dependent coupling constant. Amongst other one can mention for instance a phenomenological model using linear combinations of the baryonic and leptonic numbers of the atoms constituting the test masses at play [44, 43]; or a more theoretically motivated model using different coupling constant for each matter fundamental fields [23]. Such scalar fields being non universal, lead to a composition dependent force that induces a WEP violation, which in the case of two masses around Earth would give the Eötvös parameter

$$\eta = \frac{\beta_{\text{Earth}}(\beta^i - \beta^j)}{1 + \beta_{\text{Earth}}(\beta^i + \beta^j)} \quad (2.36)$$

Considerations about the naturalness problem of the coupling of this scalar field to matter and about its cosmological implications, hinted at a possible violation to appear in the range: $10^{-13} > \eta > 10^{-18}$ [79].

Another important feature of such a non-universal scalar field is that masses of elementary particles and fundamental constant vary [107]. Similarly to the Brans-Dicke case, the gravitational constant varies, but now it varies differently for each fundamental matter field, such that each field sees a different constant. Nonetheless, the mass of a field has no absolute signification, instead it is a way of parametrising physics and to compare the fundamental interactions between each other. As a consequence if the gravitational constant varies differently for each field, this is equivalent to vary the masses of the field and thus the other fundamental constants.

2.2.5 Massive scalar field and the Yukawa approximation

ϕ^2 -potential

In the previous section we have considered null potentials for the scalar field. When this potential is non zero, the field acquires a mass. The effect of such mass can be understood with the potential

$$V(\phi) = \frac{1}{2} m_\phi^2 \phi^2 \quad (2.37)$$

for a mass of the scalar field denoted m_ϕ . We still use the non universal coupling to matter $\Omega_{(i)}(\phi) = e^{\frac{\beta^i}{M_{\text{Pl}}}\phi}$. In this case, the field's Klein-Gordon equation in the Newtonian limit for static configurations reads

$$\Delta\phi = m_\phi^2 \phi + \frac{1}{M_{\text{Pl}}} \sum_i \beta^i \tilde{\rho}_i. \quad (2.38)$$

This equation can be solved using Green's function, the solution is defined as an integral over the source volume V_s

$$\phi(r) = \frac{1}{M_{\text{Pl}}} \int_{V_s} d^3\mathbf{r}' \frac{e^{-m_\phi|\mathbf{r}-\mathbf{r}'|}}{4\pi|\mathbf{r}-\mathbf{r}'|} \sum_i \beta^i \tilde{\rho}_i(\mathbf{r}'). \quad (2.39)$$

For a point source of mass M with $\tilde{\rho}_i = M\delta^3(\mathbf{r})$, this integral reduces to the field

$$\phi(r) = \frac{\beta^i M}{4\pi M_{\text{Pl}}} \frac{e^{-m_\phi r}}{r}, \quad (2.40)$$

β^i being the coupling constant associated to its composing matter. This field profile leads in Eq. (2.22) to a radial force $F_r = m \partial_r V_{\text{Yukawa}}$ which derives from the Yukawa potential

$$V_{\text{Yukawa}}(r) = \frac{GM}{r} (1 + 2\beta^i \beta^j e^{-m_\phi r}). \quad (2.41)$$

Hence the implication of this model of a massive scalar field is a modification of Newton's potential with a term scaling in $e^{-m_\phi r}$. This modification gets exponentially suppressed for $r \gg \lambda_\phi$, where λ_ϕ is the Compton wavelength of the field defined in SI units as

$$\lambda_\phi = \frac{\hbar}{c m_\phi}. \quad (2.42)$$

The force of such a massive scalar field has thus a finite-range λ_ϕ .

For extended bodies the interaction has an additional geometrical function due to the integral over the volume of the source body in Eq. (2.39) and over the volume of the falling body. One can show [2] that for two spherical bodies of radii r_1 and r_2 the force created by the only Yukawa field is given by

$$\frac{F_{\text{Yukawa}}}{m} = GM\beta^1\beta^2\Phi\left(\frac{r_1}{\lambda_\phi}\right)\Phi\left(\frac{r_2}{\lambda_\phi}\right)\left(1 + \frac{r}{\lambda_\phi}\right)\frac{e^{-r/\lambda_\phi}}{r^2}, \quad (2.43)$$

r being the separation between the two bodies and $\Phi(x) = 3(x \cosh x - \sinh x)/x^3$ a form factor functions coming from the above-mentioned integral. This formula is valid for homogeneous bodies. Otherwise one needs to take into account the sum involving different β_i 's in the integration.

Such a massive scalar field has been widely used in the search of a local fifth force with experiments performed on Earth and observations in the solar system. It has been extensively tested and short-ranged interactions are the less constrained. Current constraints on such a model will be given in Chapter 3.

Mass for an arbitrary potential

For an arbitrary potential with an arbitrary coupling to matter, one can still define a concept of mass of the field for a potential exhibiting a minimum. The mass is defined as the curvature of the potential at this minimum. Such that if this minimum is reached at ϕ_{\min} , we have

$$m_\phi^2 = \frac{d^2V}{d\phi^2}(\phi_{\min}). \quad (2.44)$$

This is due to the fact that when the field oscillates close to the minimum of its potential one can Taylor expand the potential

$$V(\phi) \simeq V(\phi_{\min}) + \frac{dV}{d\phi}(\phi_{\min})(\phi - \phi_{\min}) + \frac{1}{2} \frac{d^2V}{d\phi^2}(\phi_{\min})(\phi - \phi_{\min})^2 \quad (2.45)$$

$$V(\phi) \simeq V(\phi_{\min}) + \frac{1}{2} m_\phi^2 (\phi - \phi_{\min})^2 \quad (2.46)$$

leading to the same potential as previously, the constant $V(\phi_{\min})$ having no effect. Green's function for the scalar field's equation are the same and an exponential suppression similarly appears on a scale given by the Compton wavelength.

2.2.6 Scalar-tensor theories in cosmology

In the previous sections we have mainly been dealing with local effects of a scalar field that appear in the Newtonian limit. Nevertheless scalar-tensor theories play an important role in cosmology. As the simplest modification of GR, they are the first proposals that step in to explain cosmological problems. They are for instance a very good candidate for inflation as they naturally give rise to a phase of acceleration of the expansion of the universe followed by a period of reheating [83]. They are also useful in late time cosmology as they can be compatible with the currently observed acceleration of expansion of the universe [81, 89] as a substitute to a cosmological constant.

Such a scalar field, without a conformal coupling to GR, is called quintessence [20]. In cosmology it behaves as a perfect fluid of equation of state $P = w\rho$ linking its pressure to its energy density with

$$w = \frac{\frac{1}{2}(\partial_t\phi)^2 - V(\phi)}{\frac{1}{2}(\partial_t\phi)^2 + V(\phi)}. \quad (2.47)$$

If the field's dynamics at current time is dominated by its potential, the field is said to be slow-rolling. In this case it can behave as a cosmic fluid with $w < -1/3$ in Friedmann's equations that provide an accelerated expansion. It can even mimic a cosmological constant with $w = -1$. While it is currently dominant, if the potential is chosen wisely, the quintessence field can be sub-dominant in the early times and thus can be compatible with cosmological observations. Such potentials are known to explain the coincidence problem providing a natural mechanism to explain why it is only dominant now. These potentials are known as tracker solutions [116], one of the most studied being the Ratra-Peebles potential [85]

$$V(\phi) = \frac{\Lambda^{n+4}}{\phi^n}, \quad (2.48)$$

with Λ the energy scale of the potential and n its slope. The slow-roll of the field requires the potential to be very shallow such that the field must be very light $m_\phi < H_0 \simeq 10^{-33}$ eV, where H_0 is the value the Hubble constant takes today.

Quintessence has been extended to the framework of scalar-tensor theories in extended quintessence [82]. In that case, the condition on the potential holds. The field is required to evolve adiabatically by staying close to the minimum of its potential. The shallowness of the potential imposes the previous condition for the scalar field to be light. But in scalar-tensor theories, the scalar field being coupled to matter, this condition imposes that the induced fifth force must be long-range. Such a force is incompatible with current search of a fifth force, WEP tests, constancy of physical constants. Refs. [24, 25] propose a mechanism to overcome this problem. More generally, to reconcile scalar-tensor theories with local scale observations, one needs to hide the effects of the fifth force locally: this is achieved through screening mechanisms.

2.3 Screening mechanisms and chameleon

Screening mechanisms have been developed to hide the effects of the fifth force induced by the scalar field in Earth based and solar system experiments. Many mechanisms exist and are encrypted in the choice of potential and coupling functions $\frac{\partial \ln \Omega}{\partial \phi}$.

In the symmetron model [51], the coupling function is chosen to depend on the scalar field's value. Then the screening mechanism is obtained by choosing wisely the potential to lead to values of the field that would turn off the coupling function in high matter density environment while they would act in low density environment.

On the other hand in the chameleon model [60, 59], the field acquires a density-dependent mass that makes the fifth force short-range in high density environments while long-range in low density environments such as in cosmology.

2.3.1 Chameleon model principle

In this model, the coupling function is taken to be constant by choosing

$$\Omega_{(i)}(\phi) = e^{\frac{\beta^i}{M_{\text{Pl}}}\phi} \quad (2.49)$$

with β^i a coupling constant associated to the i^{th} matter field. It can be either universal to each matter component or not. Due to this coupling, the field acquires a local-mass-density-dependent effective potential

$$V_{\text{eff}}(\phi) = V(\phi) + \frac{1}{M_{\text{Pl}}} \sum_i \beta^i \tilde{\rho}_i \phi, \quad (2.50)$$

with the field's equation

$$\square\phi = \frac{dV_{\text{eff}}}{d\phi}. \quad (2.51)$$

This form of the effective potential is again valid for fields that are negligible compared to the Planck mass. Otherwise one should consider the term $e^{4\frac{\beta^i}{M_{\text{Pl}}}\tilde{\phi}}$ in factor of ρ in the field's equation. For the sake of clarity we will now only consider a universal coupling.

The screening mechanism is encoded in the field's potential. The idea is to choose the potential in a way that the effective potential exhibits a density-dependent minimum at which the curvature of the potential is variable. If the obtained curvature in high density environments is way larger than in low density ones, then the field acquires a large mass while remaining light for low density. This leads to a modulated range of the fifth force dependent on the environment as is required for screening.

The simplest model is obtained by taking a monotonically decreasing potential that tends to zero with null derivative at infinity and diverges in 0 with divergent derivative. This is achieved with a Ratra-Peebles like inverse power law as depicted in Fig. 2.2. The sum of this potential and the density-dependent coupling term provides the sought behaviour for the field's mass. The field's mass sensitivity to density is determined by the slope of the potential.

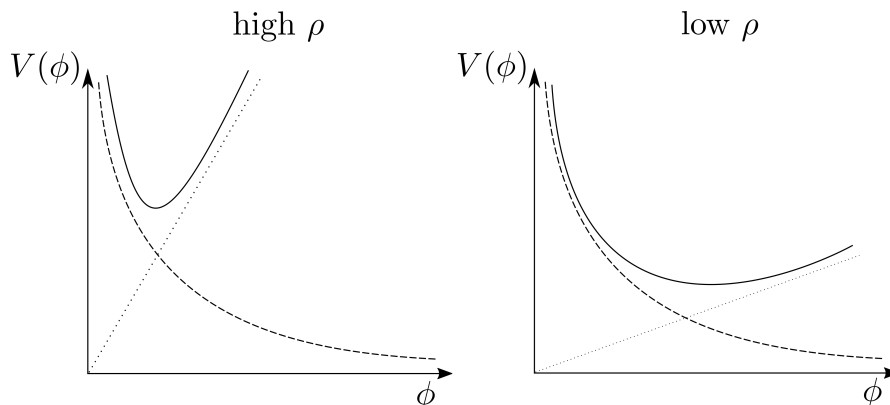


Figure 2.2: Sketch of the density-dependent chameleon effective potential (plain line). It is the sum of the bare potential (dashed line) and the coupling to density (dotted line).

Motivated by its use in cosmology the most studied potential is again the Ratra-Peebles potential that provides the desired form for screening. However it has been

proven [113] that the chameleon screening could not at the same time provide a late time cosmic acceleration and a suppression of the fifth force locally. Then cosmologically in the chameleon gravity a cosmological constant is still required, such that the most studied potential is given by

$$V(\phi) = \Lambda^4 \left(1 + \frac{\Lambda^n}{\phi^n} \right). \quad (2.52)$$

In consequence such a model encounters the same naturalness problem than the cosmological constant. Nonetheless it is important to study it to understand the phenomenology of screening mechanism.

2.3.2 Chameleon & matter

To better understand the chameleon screening, it is crucial to understand how the field is influenced by the distribution of matter. The question is to understand how the field propagates in the case of two interacting bodies in a background environment of a given uniform density ρ_{vac} lower than those of the bodies ρ_{in} . In the absence of these bodies, the field would be constant to the value ϕ_{vac} that minimises the potential associated to its density. If now these bodies are embedded in this environment they will perturb the field, as inside them the potential will be different and with a smaller value ϕ_{in} that minimises its potential. In the model considered above, these density-dependent values are given as

$$\phi_{\text{min}}(\rho) = \left(M_{\text{Pl}} \frac{n\Lambda^{n+4}}{\beta\rho} \right)^{\frac{1}{n+1}}, \quad (2.53)$$

such that it is indeed greater for low density environments.

Far from these bodies the field should retrieve its unperturbed behaviour, so we can expect the boundary conditions very far from the objects to be $\phi \rightarrow \phi_{\text{vac}}$ and $\phi' \rightarrow 0$. Getting closer to the bodies the field would slowly evolve towards the value ϕ_{in} . Depending on the size of the bodies this value will be reached more or less deeply inside the bodies or not. The question is the scale on which this evolution occurs. We know that away from the boundary of the objects, the field would eventually be close enough to its minimum that the effective potential could be approximated as in Eq. (2.46), so that the field will exponentially get closer to ϕ_{vac} or ϕ_{in} on a scale given by the Compton wavelength. We can then consider that the variations of the field are given by this scale. It is defined for the effective potential in natural units as

$$\lambda_c(\rho) = \left(\frac{d^2 V_{\text{eff}}}{d\phi^2}(\phi_{\text{min}}(\rho)) \right)^{-\frac{1}{2}}. \quad (2.54)$$

For the above inverse power-law potential, it is given by

$$\lambda_c(\rho) \equiv \sqrt{\frac{1}{n(n+1)\Lambda^{n+4}} \left(M_{\text{Pl}} \frac{n\Lambda^{n+4}}{\beta\rho} \right)^{\frac{n+2}{n+1}}}. \quad (2.55)$$

One sees that this scale is shorter in higher density environment. We denote $\lambda_{c,\text{vac}}$ and $\lambda_{c,\text{in}}$, the Compton wavelength associated to the two previous densities.

From this we can expect the field to reach ϕ_{in} inside the objects if the size of the considered object is much larger than $\lambda_{c,\text{in}}$. In the space in between the bodies, depending on the comparison of their separation with $\lambda_{c,\text{vac}}$ the field may or may not reach ϕ_{vac} . In the case it does, the field would retrieve its unperturbed value, then any mutual information between the two bodies would be suppressed such that no scalar interaction would appear. Then depending on the density of the background environment, screening will appear or not. For a high density environment, the bodies would have to be very close from each other to avoid screening.

2.3.3 Solution around a spherical ball and thin-shell effect

This modulated scale of variation of the field implying a modulated finite range of the force is responsible for the screening mechanism. Nevertheless, other aspects of screening appear in the chameleon theory. To understand them it is interesting to solve the field around a ball. We follow the same procedure as Refs. [59]. We consider a high density uniform spherical ball embedded in a low density background. We keep the same notation for the densities, minimum of the potential associated to the inside and the outside of the ball. The problem is to solve Eq. (2.51). We already got an idea of the solution in the previous section. We impose the same boundary conditions

$$\begin{cases} \phi \xrightarrow[r \rightarrow \infty]{} \phi_{\text{vac}} \\ \phi' \xrightarrow[r \rightarrow \infty]{} 0 \end{cases}. \quad (2.56)$$

These conditions are expected to be reached on scales given by the field Compton wavelength associated to the vacuum background environment.

Depending on the Compton wavelength in the ball, many regimes appear in this problem whether the field reaches the minimum of its effective potential deep inside the ball or not. If it does, we say the ball is screened. In the thin-shell regime, it is reached very quickly. In the partially screened regime, the variation of the field is slower. Instead in the thick-shell regime the variation is slow enough that ϕ_{in} is not reached at the center of the ball.

Thin-shell and partially screened solution

In the thin-shell regime and the partially screened regime, deep inside the ball, the field stay very close to ϕ_{in} . At some radius R_{TS} from the center, the field starts to depart from this value, in such a way that $\phi_{\text{vac}} > \phi > \phi_{\text{in}}$ due to the hierarchy between the minima of the two effective potentials. In that case in the region $R_{\text{TS}} \leq r \leq R_{\text{ball}}$, the field is in the part of its potential where it is greater than its minimum, so that the density-dependent term dominates

$$\frac{d^2\phi}{dr^2} + \frac{2}{r} \frac{d\phi}{dr} \simeq \frac{\beta}{M_{\text{Pl}}} \rho_{\text{in}}. \quad (2.57)$$

This equation is straightforward to solve with $\phi(R_{\text{TS}}) \simeq \phi_{\text{in}}$ and $\frac{d\phi}{dr}(r_{\text{TS}}) \simeq 0$, one obtains for $R_{\text{TS}} \leq r \leq R_{\text{ball}}$

$$\phi(r) = \phi_{\text{in}} + \frac{\beta}{3M_{\text{Pl}}} \rho_{\text{in}} \left(\frac{r^2}{2} + \frac{R_{\text{TS}}^3}{r} - \frac{3}{2} R_{\text{TS}}^2 \right). \quad (2.58)$$

Then, at the boundary of the object, the effective potential suddenly changes due to the dropping of the density. Now the field is in the potential dominant part of the effective potential. Nonetheless, it has acquired in the ball a "velocity" $\frac{d\phi}{dr}$ large enough to lead the second left-hand-side term to dominate the potential. This leads the field to keep increasing with a decaying first derivative. The difference between the field's value and ϕ_{vac} decreases as $1/r$. Then eventually the field's derivative decays enough such as the effective potential dominates again, however at this point the field would have reached a value close to its minimum. This allows one to approximate the effective potential as in Eq. (2.46).

Thus in the region outside the ball we can then approximate that the field follows the equation

$$\frac{d^2\phi}{dr^2} + \frac{2}{r} \frac{d\phi}{dr} \simeq m_\phi^2 \phi, \quad (2.59)$$

with $m_\phi^2 = \frac{d^2 V_{\text{eff}}}{d\phi^2}(\phi_{\text{min}})$.

One can integrate this equation from infinity where the field must be at ϕ_{vac} , and obtain

$$\phi(r) = \phi_{\text{vac}} - K \frac{e^{-m_\phi(r-R_{\text{ball}})}}{r}, \quad (2.60)$$

where K is a constant to be determined by reconnecting the two solutions at $r = R_{\text{ball}}$. The continuity of the field and its derivative at $r = R_{\text{ball}}$ provides a system of two equations whose solutions give K and R_{TS} . In the case the field's mass outside the ball m_ϕ is small enough – otherwise more complex term should be added – one obtains

$$R_{\text{TS}}^2 = R_{\text{ball}}^2 \left(1 - \frac{\Delta R}{R}\right), \quad (2.61a)$$

$$K = 3\beta M_{\text{Pl}} \frac{\Delta R}{R} GM_{\text{ball}} - \frac{\beta \rho_{\text{in}}}{3M_{\text{Pl}}} \left(\frac{R_{\text{ball}}^3}{2} + R_{\text{TS}}^3 - \frac{3}{2} R_{\text{TS}}^2 R_{\text{ball}} \right), \quad (2.61b)$$

where M_{ball} is the total mass of the ball and $\frac{\Delta R}{R}$ is called the thin-shell parameter and defined as

$$\frac{\Delta R}{R} = \frac{R_{\text{ball}}^2 - R_{\text{TS}}^2}{R_{\text{ball}}^2} = \frac{\phi_{\text{vac}} - \phi_{\text{in}}}{3\beta M_{\text{Pl}} \Phi_{\text{ball}}(R_{\text{ball}})}, \quad (2.62)$$

with $\Phi_{\text{ball}}(R_{\text{ball}})$ being the Newtonian potential of the ball at its surface. This thin-shell parameter determines how close R_{TS} is to R_{ball} , and then it distinguishes the thin-shell regime and partially screened regime. In the thin-shell regime, it is so small that all the variation of the field in the ball is concentrated on a very thin shell right under its surface as $R_{\text{TS}} \simeq R_{\text{ball}}$, for the remainder part of the ball the field is constant and equal to ϕ_{in} . In such a case the second term in K is negligible such that the outside field is well approximated by

$$\phi(r) = \phi_{\text{vac}} - 3\beta M_{\text{Pl}} \frac{\Delta R}{R} \frac{GM_{\text{ball}}}{r} e^{-m_\phi(r-R_{\text{ball}})}. \quad (2.63)$$

This solution is very similar to the Yukawa solution, it however includes the additional small factor $3\frac{\Delta R}{R}$. This factor weakens the force around this ball, one gets a force similar to the Yukawa interaction for a test particle around the ball

$$\frac{F_\phi}{m} = 3\beta^2 \frac{\Delta R}{R} \frac{GM_{\text{ball}}}{r^2} (1 + m_\phi r) e^{-m_\phi(r-R_{\text{ball}})}. \quad (2.64)$$

For a non-universal coupling the β^2 would be the product of the coupling constant of each body.

The $\frac{\Delta R}{R}$ -depletion term in this result is one of the reasons that leads to screening in the chameleon theory. It suppresses the interaction between bodies. Consider this ball to be the Earth. Around it, a test body – whose influence on the field is negligible – such as a satellite in some conditions, would feel a long-ranged fifth force that would be similar to a Yukawa interaction but depleted by the factor $3\frac{\Delta R}{R}$. It could then be very small and negligible compared to Newton's interaction. However a precise enough experiment may allow for its detection. Another interesting feature is if one instead considers celestial motions in the solar system as for instance the scalar interaction between two planets. This solution tells us that a planet perturbs the field in such a way that all the variation of the field in the object is concentrated in a thin shell leading to the fact that only a negligible volume of the planet feels the effect of a fifth force. This makes the influence of the scalar interaction possibly negligible and consistent with our observations. Note that in this problem of two planets, to obtain the force of their interaction, one needs to solve the field created by the two bodies simultaneously to catch together the effect of

the distant body and the influence of the studied body. This problem will be addressed in the next section.

These aspects of screening add to the one developed in the previous section, that are based only on the modulated range of the scalar interaction. The latter is nonetheless still relevant in the case of the Earth, if one were to conduct an experiment at its surface. In that case one needs to consider the atmosphere, which could also have a thin-shell if the mass of the field associated to its density is small enough. In that case the situation would be equivalent to the one discussed in the previous section and the field would evolve so rapidly that it would be constant in most of the atmosphere leading test particles to feel a null fifth force, and that any interaction between extended bodies would be suppressed.

All previous considerations have been developed in the thin-shell regime as screening is the strongest. If nonetheless, this screening factor $\frac{\Delta R}{R}$ is not negligible anymore, at the center of the ball the field still reaches ϕ_{in} but it varies on a larger part of its volume as $R_{\text{TS}} < R_{\text{ball}}$. In that case, as long as $R_{\text{TS}} > 0$ the above solution is still valid with additional term due to the second term in Eq. (2.61b). This regime can be called partially-screened. In that case, the chameleon screening is only partial, and effects could be detectable. For instance the Yukawa-like interaction would only be partially diminished, or in the atmosphere the range of the scalar interaction could be larger and thus detectable.

Thick-shell solution

The thick-shell regime occurs when the Compton wavelength of the field inside the ball is greater than its size. In such a case, the minimum of the potential is not reached at the centre of the ball. Instead the field starts at some other value ϕ_0 greater than ϕ_{in} that depends on the ratio between the Compton wavelength and the size of the ball. The field can be obtained by taking the limit $R_{\text{TS}} \rightarrow 0$ in Eqs. (2.58-2.60) and replacing ϕ_{in} by ϕ_0 . In that case, for the motion of a test body around this ball one retrieves completely the Yukawa interaction as $\frac{\Delta R}{R} \rightarrow 1$.

The occurrence of these regimes depends on the ratio between the Compton wavelength associated to the considered body and its size and potential. In the model of chameleon we are considering, one easily sees from Eq. (2.55) that the thin-shell regime is more likely to occur for large β and small Λ .

2.3.4 Interaction between two extended bodies and apparent WEP violation

In the previous section, we obtained the chameleon field around a spherical body. This profile gives the force a pure test mass – in the sense that it does not affect the chameleon field – would experience. In the case the mass is extended, the test mass sources the field and modifies it in its neighbourhood leading to a modification of the force it feels.

An expression for this force has been obtained in Refs. [17, 53] assuming the test mass is much smaller than the main source body, so that it only perturbs its associated profile and assuming their separation is smaller than the Compton wavelength of the medium in which they are embedded. The interaction between two spherical bodies is radial and expressed as

$$F_\phi = 2 Q^A Q^B F_N \quad (2.65)$$

where A and B label the two bodies and $Q^i = \beta^i \frac{\Delta R}{R} \Big|_i$ is for each body the product of the coupling constant associated to its composition and its thin-shell parameter defined above. This expression shows that the thin-shell of both bodies can deplete their interaction. In the case their separation exceed the Compton wavelength of the medium, a Yukawa-like suppression is expected.

From such a formula one can also deduce an important feature of the model for WEP phenomenology. Of course, as for any scalar-tensor theory, if the coupling to matter is non universal, with a different constant β^i for each types of matter, the WEP is not fulfilled. But in the chameleon model, in the case of a universal coupling, the chameleon model can still provide an apparent WEP violation. According to Eq. (2.65), the force a body experiences in the neighbourhood of a more massive body is a function of its own thin-shell parameter that depends on its mass density and Newton's potential. Two bodies of different compositions would hence feel different accelerations due to their different thin-shell parameters, leading to an apparent violation of the equivalence principle. Such a violation holds an uncommon feature. The WEP is indeed still holding as two pure test particles would fall the exact same way. Now as discussed before extended bodies affecting the field dynamics could fall at different rates. This violation is different from a violation of the strong equivalence principle, as extended bodies do not necessarily have a dominating gravitational bounding energy – as for instance MICROSCOPE's test masses. The violation of the equivalence principle induced by the chameleon is in a way between a WEP violation and a strong equivalence principle violation.

As discussed in Refs. [60, 59], such a violation would be more likely to appear in orbit as otherwise in the atmosphere the short Compton wavelength leads the profile sourced by Earth to be flat.

An important caveat to this apparent WEP violation is experimental. We assume such WEP violations to be very small as otherwise it would have measurable effects on the trajectory of planets. Those violations are thus expected to be observed in high precision experiments. Such experiments nonetheless suffer two features regarding this model. Just as the MICROSCOPE experiment, they are based on the comparison of the acceleration of two test masses. But to perform this comparison they must be placed in the same conditions, such as the same vacuum cavity or the same satellite similarly to MICROSCOPE. It implies the considered extended test masses to be rather close leading them to perturb each other such that the previous model may no longer be relevant. This perturbation could either be one mass screening the effects from Earth for the other or simply the interaction of the two test bodies to dominate. Besides such experiments involve means of measurement that cannot be dispensable so as the use of a vacuum cavity – this point will be discussed in the next section – to isolate the experiment of any perturbation. Both these systems are made of high density matter that usually encompass the experiment. The presence of matter is very likely to screen the apparent WEP violation described above. Nonetheless this does not exclude other effects that could originate from the inside of the experiment such as asymmetries due to experimental defects or simply a designed presence of a dense matter source in the cavity.

As a conclusion the chameleon model can provide apparent WEP violations in the sense that only extended test masses would experience different gravitational accelerations while proper test particles would follow the same geodesics. This WEP violation is nonetheless very difficult to observe as the experimental means used to detect it are very likely to screen it. Testing the chameleon by such an experiment hence requires a huge effort to model all effects of their design and thus to design them.

2.3.5 Chameleon constraints and experimental cavities

Except for tests coming from astrophysical or cosmological studies, all tests of the chameleon model are performed in a vacuum cavity. The profile in such a cavity can be guessed with our previous considerations.

Consider a spherical vacuum cavity delimited by a spherical wall of a given thickness of high density. This wall will be subjected to a similar screening than for the dense ball case. In the case, analogous to the thin-shell regime, where the associated Compton wavelength of the field is much smaller than its thickness, the field will develop two thin-shells on both its outer and inner sides. In these thin-shells the field will vary in such a way that deeply in the wall the field would be nearly constant and equal to the value ϕ_{in} of the field that minimises its associated potential. The field exterior to the system will be similar to the one of a spherical ball leading to the outer thin-shell to be similar. On the other hand, the magnitude of the variation in the inner thin-shell will depend on the size of the inner vacuum space.

In the cavity, as argued in Refs. [59, 17], the field would tend to evolve towards the value ϕ_{vac} of the field that minimises the potential in the vacuum. This value being greater than ϕ_{in} , the field would have a bubble like shape reaching a maximum ϕ_0 at its center. This latter value depends on the size of the cavity. If the size is larger than the Compton wavelength associated to the vacuum density, the field would have enough room to reach its minimum so we would have $\phi_0 = \phi_{\text{vac}}$. If the size is instead smaller, one would have $\phi_{\text{vac}} > \phi_0 \geq \phi_{\text{in}}$. An order of magnitude of ϕ_0 – given by Ref [59] for spherical cavities and by Ref. [15] for cylindrical cavities – is given by the value of the field whose mass equals the radius of the cavity, i.e. the value that solves

$$\frac{d}{2} = m^{-1}(\phi_0) = \frac{1}{\sqrt{V_{\text{eff}}''(\phi_0)}}, \quad (2.66)$$

d being the size of the cavity. This estimate is however only an order of magnitude. Its extremal behaviours – divergence for very wide cavities and nullity for infinitely small cavities – are not relevant for the actual asymptotic behaviour of ϕ_0 i.e. ϕ_{vac} for very wide cavities and ϕ_{in} for infinitely small cavities as in that case we should retrieve the case of a ball.

In the case the wall of the cavity is small enough compared with its Compton wavelength to have a thick-shell, the overall form of the profile is still the same. The field does however not reach its minimum in the wall, but a larger value. This affects ϕ_0 and in that case any outer body can affect the inner profile. Yet quantifying such an influence is a difficult problem to address. It requires to solve the field's Klein-Gordon equation. Due to non-linearities of this equation, numerical methods are mainly required. But in this problem as we need to catch at the same time the dynamics of the field inside and outside the cavity, this requires to solve the field in 3D for large spatial regions. Combined with the fact that in high-density environment the field can vary on very short scales, the solution to this problem requires computing resources that are consequent.

2.3.6 Current constraints

Many efforts have been done to constraint this model. These have been gathered in the reviews Refs. [19, 13]. Figure 2.3 shows them in the (β, Λ) plane for $n = 1$ and (β, n) plane for $\Lambda = \Lambda_{\text{DE}} = 2.4 \text{ meV}$, the energy scale of dark energy.

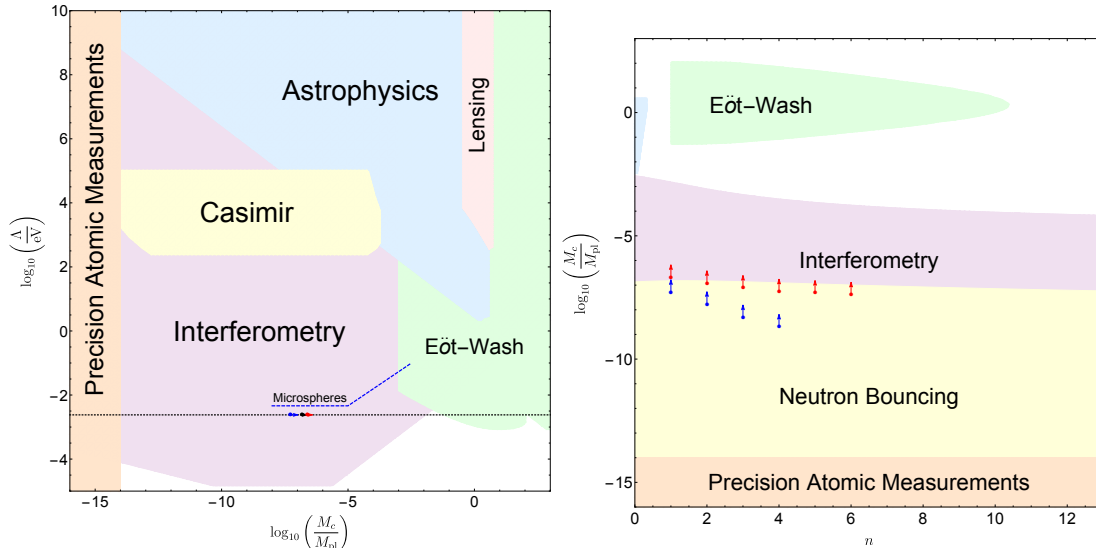


Figure 2.3: Current constraints on the existence of the chameleon field from several experiences as gathered by Refs. [19, 13]. Excluded regions are coloured. Left panel: constraints in the plane ($\beta = 1/M_c$, Λ) for $n = 1$. Right panel: constraints in the plane ($\beta = 1/M_c$, n) for $\Lambda = \Lambda_{\text{DE}} = 2.4 \text{ meV}$.

Among these, the most stringent constraints are the following.

Atom interferometry

Atom interferometry [17, 49, 38, 56] is the more competitive way of testing this model. The principle is to use the wave feature of clouds of atoms, to perform by means of interferometry a very precise measurement of the acceleration they are submitted to. The latest developmental of this experiment [56] provided a precision up to a few tenth of $\text{nm}\cdot\text{s}^{-2}$ on such acceleration.

Using clouds of atoms is very interesting for the chameleon problem. These test masses can indeed be considered as unscreened in a large part of the chameleon parameter space. This allows for a direct access to the profile inside the cavity by measuring the force its gradient creates. This allows those experiments to be the more competitive for testing the chameleon. They also use a matter ball in the cavity to source different features of the chameleon profile.

Casimir test

This test is based on the experiments performed to test the Casimir effect [97, 62]. This effect arises in quantum electrodynamics when considering two parallel conducting plates separated by a high-quality vacuum that are brought close enough. This is due to the fact that the presence of the conductors constrains in the inter-plate region the modes of the electromagnetic field that can emerge from quantum fluctuations. The result is a force that pushes the plates together and that is expected to scale as d^{-4} for d being the separation of the plates.

When considering the chameleon field, an additional force is expected to appear. It is generated by the profile sourced by the pair of plates. When considering a single plate far from any other matter, perpendicularly to the plate the field profile is very similar to the radial profile of a ball. The field is symmetrical around the axis of the plate such that any gradient of the field inside the plate cancel. If now a second plate is brought

close to the first one this will affect the profile in such a way that a bubble-like profile analogous to the one of cavity will settle. This leads to a reduction of the gradient on the side of a plate facing the other, leaving the profile asymmetric in the plates. This creates a force. This force is again pulling the plates closer.

Reference [14] provides an analytic model for this force. This model shows features that are phenomenologically interesting. First the force is constant for very small separations that are smaller than the Compton wavelength associated to the matter composing the plates. For larger separations it scales as $d^{-2n/(n+2)}$, n being the slope of the chameleon potential as defined before. This is valid as long as the separation is smaller than the Compton wavelength of the vacuum. Finally for the largest separation the force is exponentially suppressed as the field tends to reach the minimum of its potential in between the plates. This peculiar behaviour of the chameleonic interaction provides a way to distinguish it from the quantum-originated one.

Eöt-Wash test

Torsion balance experiments, such as the one performed by the Eöt-Wash group [58], use two rotating parallel disks pored with holes or radial grooves. These are designed to test deviation from the inverse-square-law of Newton's gravity. These grooves follow the same pattern, such that if they are perfectly aligned and symmetrical no torque is expected. If instead these are no longer aligned by for instance rotating one of the disks on its axis, the other disk should feel a torque that would tend to restore the alignment. By precisely modelling or cancelling the contribution of standard gravity to this torque, one could then measure a deviation to the Newtonian model of gravity.

Refs. [106, 105] provide a model for the chameleon contribution to this torque that allows to constrain it. The main limitation comes from the use of thin conducting foil acting as a Faraday cage to shield any electrostatic forces between the disks. While such a foil has no dominant effect on the Newtonian force or a Yukawa coupling of the disks, it can completely screen their chameleonic interaction.

Astrophysical tests

Many astrophysical observables are used to constraint the chameleon model. The main test [57] is based on the cosmic distance ladder, more precisely on use of Cepheid variable stars as distance indicators. The need of distance indicators in astrophysics is due to the fact that we do not have a direct access to the measurement of the distance of stars, but only on their apparent magnitude which is a function of their absolute magnitude and distance. One then needs an estimate of the absolute magnitude of an object to estimate its distance.

Cepheid stars are one of the possible solutions to answer this problem. Such stars have the distinctive feature to pulsate radially. This is due to a complex mechanism involving a variability in the radiative process leading to a fluctuating balance between these and the gravitational attraction. This process occurs in the outer shells of these stars, and involves a variation of their temperatures leading to a fluctuation of their magnitudes. This process occurs on a period that is directly linked to the star's mean brightness. The relation between the period of variation and the absolute magnitude is well understood such that it can be used to estimate their distance using the absolute magnitude deduced from the measurement of their period.

The interest for our problem, is that modifications of gravity in the outer shell of Cepheids affect this process. In the case of the chameleon model, these modifications would occur only if the considered star is unscreened or partially screened. This provides a way to test this model. Ref. [57] uses a set of screened and unscreened galaxies

whose distances are measured using Cepheids they contain. These distances are then compared to another distance indicator which is not sensitive to the chameleon field. If the chameleon model were to exist this would lead to a discrepancy between these two distance indicators in the unscreened cases.

Note that many other astrophysical tests exist. The most recent development is galaxy warping tests [28], that has not yet provided constraints.

Chapter conclusion

Scalar-tensor theories are one of the ways of modifying GR. When coupling to matter, the scalar field they consider gives rise to a fifth force, that can induce a violation of the WEP. Two main classes of such models are to be distinguished: unscreened scalar fields that lead to a WEP violation for non-universal couplings to matter; and screened scalar fields which can induce a WEP violation even for universal couplings. The next chapter explores the constraints MICROSCOPE can provide on the former class, while the latter class' test is studied in the remaining parts of the thesis with the case of the chameleon field.

Chapter 3

Testing unscreened scalar field with MICROSCOPE

Unscreened scalar fields are the most straightforward models to constrain with the MICROSCOPE results. The reason is that unlike screened interaction – for which taking into consideration the screening influence of the satellite is crucial – for unscreened scalar fields one can directly compare the accelerations of two test masses that are both created by Earth. In such a case, the influence of the satellite can be treated as a simple perturbation adding up to the latter interaction as linearity of such unscreened models leads to superposition principle. Following the pre-existing constraints on those models in the literature we nonetheless neglect this effect.

For those unscreened models, MICROSCOPE is only able to test those who have a non-universal coupling as otherwise they would not provide any WEP violation. Constraining those models comes down to independently study the interaction it creates between a given test mass and the Earth. We consider a massless field for which the force between two point-test-particles derives from the potential in Eq. (2.35) and a massive Yukawa-like field given by Eq. (2.41). We need to specify how the coupling functions β_i in those potential varies with the chemical composition of the object we study. Many models exist, some of which have a more phenomenological interest and other a more theoretical motivation. The next step is to integrate this force over the volume of the bodies – this can be delicate for Earth being an extended body. For massless fields treating this issue is similar to the Newtonian case as Gauss’ theorem is still valid, and we can reduce a sphere to a point by averaging β_i over the volume of the sphere if it is not radially uniform. For massive Yukawa fields, this is no longer the case due to the finite range of the interaction. Considering the Earth to be spherical leads to the form factors already mentioned in Eq. (2.43). These account for the fact that the side of the planet facing the test masses contributes more than the far side. This imbalance is due to the Yukawa exponential suppression term that modifies the inverse square law which no longer fulfil Gauss’ theorem. Nevertheless, when considering a more realistic shape for Earth this becomes a more intricate problem. The shape of Earth is described [84] by the geoid that consists in the components of the Earth gravity field in terms of spherical harmonics. But these components are unknown. Experimentally one only have access to the sum of those components, more specifically to the value it takes at the latitude, longitude and altitude at which an experiment is being performed. From such data one can then reconstruct the geoid. This reconstruction however depends on the gravity theory one considers. In the literature [87] the geoid is reconstructed only by considering Newton’s gravity. This geoid hence cannot be straightforwardly used as prior to constraint a Yukawa scalar interaction.

In this chapter, we present these considerations following two articles. In the first

one, we compute the constraints the MICROSCOPE's results provide if the Earth is assumed to be spherical. In the second article, we study the implication induced by the consideration of Earth's geoid on the test of massive Yukawa fields.

3.1 Assuming a spherical Earth

3.1.1 Introduction and summary

Several models are considered in this paper to study MICROSCOPE's constraints on them. They consist in different chemical dependence of the β^i coupling functions in Eq. (2.35) for massless fields, and in Eq. (2.41) for Yukawa-like massive fields. In this article this function is denoted α_i and two models are explored for it.

The first one, based on Ref. [43], decomposes the product of the coupling functions of the two interacting bodies into a universal dimensionless coupling constant α , and two coupling charges q that are functions of the isotopic composition of the bodies. We consider two models for this charge that are given in terms of the baryon and lepton number of the test masses. Besides this coupling, we consider the field to be massive through a Yukawa suppression term. The range of this interaction is denoted λ . The integration of this interaction over the test masses' volumes is straightforward as we precisely know their compositions and we can neglect the variation of the Yukawa term over their sizes. The Earth integration is more intricate. The above-mentioned form factors appear. They are denoted Φ and one needs to assume a model for Earth's composition. We consider it to be a sphere made of central iron core surrounded by a mantle made of silica. This model provides a way of constraining the remaining free parameters of the theory: (α, λ) . The constraints are depicted and compared with the current constraints. They show that the MICROSCOPE mission improves the bound of the constraints by roughly one order of magnitude for interaction ranges $\lambda > 10^2$ km, as the experiment is only sensitive to interaction whose range is greater than the altitude of its orbit.

The second model that we consider is the dilaton model as described in Ref. [23]. This model assumes that the scalar field couples differently to each components of matter. This is described by a set of five coupling dimensionless constants ($d_g, d_e, d_{m_e}, d_{m_u}, d_{m_d}$) parametrising respectively its coupling to the gluons, photons, electrons and quarks contained in matter. This model leads to a coupling functions α_i that is given by

$$\alpha_i \approx d_g^* + [(d_{\tilde{m}} - d_g) Q'_{\tilde{m}} + d_e Q'_e]_i, \quad (3.1)$$

where $d_g^* = d_g + 0.093(d_{\tilde{m}} - d_g) + 0.00027d_e$, $d_{\tilde{m}}$ is a linear combination of d_{m_u} and d_{m_d} , and finally $Q'_{\tilde{m}}$ and Q'_e are charges that are functions of the isotopic composition of the interacting body. This coupling function has a universal term d_g^* and a composition dependent member. By construction, the universal term is dominating such that when applying the formalism to the MICROSCOPE case, one can only consider the universal term for Earth's coupling function. This leads the difference of acceleration of the two test masses of MICROSCOPE to be independent of Earth's composition unlike the previous model. In this analysis we consider both massless and massive dilaton fields. The result shows that again the MICROSCOPE results narrow the constraints by an order of magnitude.

Finally, we consider the case where this dilaton field only couples to electromagnetism – i.e. to the photons. The MICROSCOPE constraints associated with it are compared with those obtained by experiments designed to monitor hyperfine transition frequencies of different atoms, for which a dilaton field is expected to cause variations. While MICROSCOPE being very competitive for heavy fields, atomic constraints are better for ultra-light fields.

3.1.2 Article

PHYSICAL REVIEW LETTERS **120**, 141101 (2018)**MICROSCOPE Mission: First Constraints on the Violation of the Weak Equivalence Principle by a Light Scalar Dilaton**Joel Bergé,^{1,*} Philippe Brax,² Gilles Métris,³ Martin Pernot-Borràs,^{1,4} Pierre Touboul,¹ and Jean-Philippe Uzan^{5,6}¹*DPHY, ONERA, Université Paris Saclay, F-92322 Châtillon, France*²*Institut de Physique Théorique, Université Paris-Saclay, CEA, CNRS, F-91191 Gif-sur-Yvette Cedex, France*³*Université Côte d'Azur, Observatoire de la Côte d'Azur, CNRS, IRD, Géoazur, 250 avenue Albert Einstein, F-06560 Valbonne, France*⁴*Sorbonne Université, CNRS, Institut d'Astrophysique de Paris, IAP, F-75014 Paris, France*⁵*Institut d'Astrophysique de Paris, CNRS UMR 7095, Université Pierre et Marie Curie–Paris VI, 98 bis Boulevard Arago, 75014 Paris, France*⁶*Sorbonne Universités, Institut Lagrange de Paris, 98 bis, Boulevard Arago, 75014 Paris, France* (Received 1 December 2017; revised manuscript received 9 January 2018; published 2 April 2018)

The existence of a light or massive scalar field with a coupling to matter weaker than gravitational strength is a possible source of violation of the weak equivalence principle. We use the first results on the Eötvös parameter by the *MICROSCOPE* experiment to set new constraints on such scalar fields. For a massive scalar field of mass smaller than 10^{-12} eV (i.e., range larger than a few 10^5 m), we improve existing constraints by one order of magnitude to $|\alpha| < 10^{-11}$ if the scalar field couples to the baryon number and to $|\alpha| < 10^{-12}$ if the scalar field couples to the difference between the baryon and the lepton numbers. We also consider a model describing the coupling of a generic dilaton to the standard matter fields with five parameters, for a light field: We find that, for masses smaller than 10^{-12} eV, the constraints on the dilaton coupling parameters are improved by one order of magnitude compared to previous equivalence principle tests.

DOI: [10.1103/PhysRevLett.120.141101](https://doi.org/10.1103/PhysRevLett.120.141101)

Scalar-tensor theories are a wide class of gravity theories that contain general relativity [1]. In the Newtonian limit, they imply the existence of a fifth force, that can be well described by a Yukawa deviation to Newtonian gravity. Its range depends mostly on the mass of the scalar field and can vary from submillimetric to cosmological scales [2,3]. It has so far been constrained on all scales from a few microns to the largest scales of the Universe (see, e.g., Refs. [1,4,5]).

This new force may or may not be composition dependent. A nonuniversal coupling implies both a violation of the weak equivalence principle (WEP) and a variation of the fundamental constants [6,7]. The former effect has already been exploited by the Eöt-Wash group to bring the current best constraints on Yukawa-type interactions and on light dilaton interactions [8–10], while the latter allows one to set constraints on cosmological to local scales [11].

The *MICROSCOPE* satellite aims to constrain the WEP in space [12,13] by measuring the Eötvös parameter, defined as the normalized difference of acceleration between two bodies i and j in the same gravity field, $\eta = (\Delta a/a)_{ij} = 2|\vec{a}_i - \vec{a}_j|/|\vec{a}_i + \vec{a}_j|$. First results [14] give

$$\eta = (-1 \pm 27) \times 10^{-15} \quad (1)$$

at a 2σ confidence level. *MICROSCOPE* tests the WEP by finely monitoring the difference of acceleration of freely falling test masses of different composition (platinum and

titanium) as they orbit Earth, measured along the principal axis of the (cylindrical) test masses. The measurement equation is given, e.g., in Ref. [14] as $a_{\text{Pt}} - a_{\text{Ti}} = g_x \eta + f(\vec{p}, n)$, where g_x is the projection of the Earth gravity field onto the axis of the test and $f(\vec{p}, n)$ is a function of the instrumental and environmental parameters and measurement noise.

The constraint (1) was obtained after analyzing only one measurement session; therefore, the error bars should be considered as the largest that can be expected from the whole *MICROSCOPE* mission. The statistical error is expected to decrease with increasing data and with the refinement of the data analysis by the end of the mission in 2018. In the meantime, this new constraint of the WEP can already be used to set new bounds on fifth force characteristics. This Letter focuses on the implications of the first results of *MICROSCOPE* for an interaction between matter and a light dilaton.

Scalar fifth force.—The existence of a light scalar field ϕ modifies the Newtonian interaction between two bodies i and j of masses m_i and m_j by a Yukawa coupling [4,15,16]:

$$V_{ij}(r) = -\frac{Gm_i m_j}{r} (1 + \alpha_{ij} e^{-r/\lambda}). \quad (2)$$

The scalar coupling to matter α_{ij} can be decomposed as the product $\alpha_i \alpha_j$ of the scalar couplings to matter for each test body measured by the dimensionless factors (e.g., [23])

$$\alpha_i \equiv \frac{\partial \ln m_i/M_P}{\partial \phi/M_P} \quad (3)$$

with $M_P^{-1} = \sqrt{4\pi G}$ the Planck mass. The range λ of the Yukawa interaction is related to the mass of the field by $\lambda = \hbar/m_\phi c$. The amplitude of the WEP violation is related to the presence of a scalar field that does not couple universally to all forms of energy, contrary to general relativity. The magnitude of the scalar force varies from element to element and is characterized by $\alpha_i(\phi)$, which requires the determination of $m_i(\phi)$ and thus the specification of the couplings of the scalar field to the standard model fields. Any dynamics or gradient of this scalar field thus induces a spatial dependence of the fundamental constants [6,7]. For two test masses in the external field of a body E , the Eötvös parameter reduces to

$$\eta = \frac{(\alpha_i - \alpha_j)\alpha_E}{1 + \frac{1}{2}(\alpha_i + \alpha_j)\alpha_E} \simeq (\alpha_i - \alpha_j)\alpha_E. \quad (4)$$

In order to set constraints, we need to specify the couplings of the field to matter as well as its masses.

Baryonic and leptonic charges.—The simplest analysis consists in assuming that the composition-dependent coupling α_{ij} depends on a scalar dimensionless ‘‘Yukawa charge’’ q , characteristic of each material as [8,9]

$$\alpha_{ij} = \alpha \left(\frac{q}{\mu} \right)_i \left(\frac{q}{\mu} \right)_j, \quad (5)$$

where α is a universal dimensionless coupling constant which quantifies the strength of the interaction with respect to gravity and μ is the atomic mass in atomic units (e.g., $\mu = 12$ for carbon-12, or $\mu = 47.948$ for titanium). Different definitions of the charge q are possible depending on the detailed microscopic coupling of the scalar field to the standard model fields. At the atomic levels, taking into account the electromagnetic and nuclear binding energies, the charge is usually reduced to the material’s baryon and/or lepton numbers (B and L) (see, e.g., Refs. [24,25]). Hence, for a macroscopic body, we must consider its isotopic composition. Hereafter, we shall set constraints on such interactions with either $q = B$ or $q = B - L$.

Following Ref. [14] and their approximations, it is straightforward to show [using Eqs. (2) and (4)] that, for *MICROSCOPE*, the Eötvös parameter due to a Yukawa potential is

$$\eta = \alpha \left[\left(\frac{q}{\mu} \right)_{\text{Pt}} - \left(\frac{q}{\mu} \right)_{\text{Ti}} \right] \left(\frac{q}{\mu} \right)_E \left(1 + \frac{r}{\lambda} \right) e^{-r/\lambda}, \quad (6)$$

where r is the mean distance from the satellite to the center of Earth [26]. The Earth charge takes into account the Earth differentiation between the core and mantle:

TABLE I. Baryonic, leptonic, and dilaton charges for *MICROSCOPE*’s test masses.

Material	B/μ	$(B-L)/\mu$	Q'_m	Q'_e
Pt/Rh	1.000 26	0.596 68	0.0859	0.0038
Ti/Al/V	1.001 05	0.540 44	0.0826	0.0019

$$\left(\frac{q}{\mu} \right)_E = \left(\frac{q}{\mu} \right)_{\text{core}} \Phi \left(\frac{R_c}{\lambda} \right) + \left(\frac{q}{\mu} \right)_{\text{mantle}} \left[\Phi \left(\frac{R_E}{\lambda} \right) - \Phi \left(\frac{R_c}{\lambda} \right) \right], \quad (7)$$

where R_E is the Earth mean radius and R_c the Earth core radius. The function $\Phi(x) \equiv 3(x \cosh x - \sinh x)/x^3$ [4] takes into account the fact that all Earth elements do not contribute similarly to the Yukawa interaction at the satellite’s altitude [27] ($\Phi = 1$ for the test masses, since their sizes are much smaller than the ranges λ that can be probed in orbit). We assume that the core of Earth is composed of iron and that the mantle is composed of silica (SiO_2) [28]. The baryonic and lepton charges for the *MICROSCOPE* experiment are summarized in Table I.

At the 2σ level, *MICROSCOPE*’s constraints on the Eötvös parameter are given by Eq. (1) and can readily be transformed into constraints on Yukawa parameters (α, λ). Figures 1 and 2 depict the corresponding exclusion regions, respectively, for $q = B$ and $q = B - L$. In both analyses, we compare our new constraint to the bounds from Eöt-Wash’s torsion pendulum experiments [8,9,29] and the constraints from the lunar-laser ranging (LLR) experiment [30,31]. Note that, while we plot only the latest, most competitive constraints, several other experimental constraints are available (e.g., [4,32–40]). Moreover, the LLR constraint could

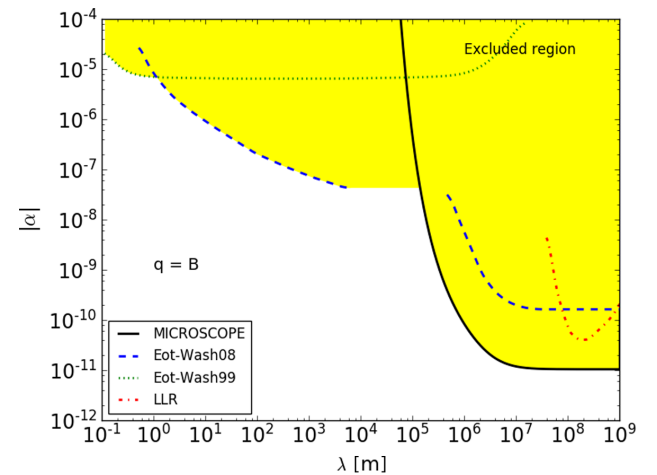


FIG. 1. Constraints on the Yukawa potential parameters (α, λ) with $q = B$. The excluded region is shown in yellow and compared to earlier constraints from Refs. [29] (dotted line), [8] (dashed line), and [30,31] (dot-dashed line). *MICROSCOPE* (solid line) improves on the Eöt-Wash constraints by one order of magnitude for $\lambda > \text{a few } 10^5 \text{ m}$.

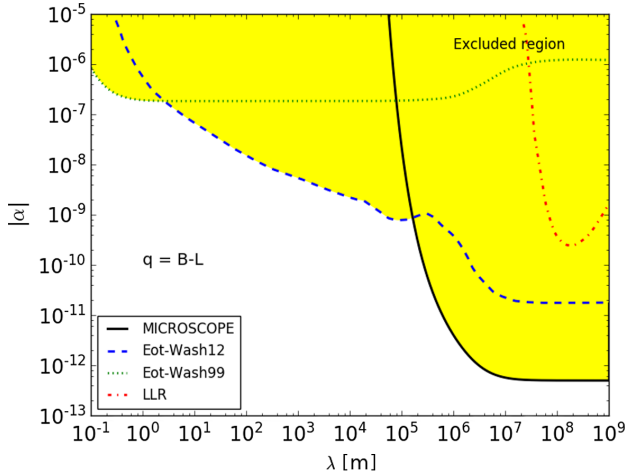


FIG. 2. The same as Fig. 1, but with $q = B - L$, compared to the earlier constraints from Refs. [29] (dotted line), [9] (dashed line), and [30,31] (dot-dashed line).

be slightly strengthened in the near future [41]. This shows that *MICROSCOPE*'s first results allow us to gain one order of magnitude compared to previous analyses for $\lambda > \text{a few } 10^5 \text{ m}$. As *MICROSCOPE* orbits Earth at about 7000 km from its center, one would naively expect that it can probe only interactions with $\lambda > \text{a few } 10^6 \text{ m}$; smaller ranges could not be probed, as they imply too much of a damping at *MICROSCOPE*'s altitude. However, if a fifth force with $\lambda \approx \text{a few } 10^5 \text{ m}$ were strong enough to affect *MICROSCOPE*, the contribution from the nearest point of Earth (as seen from *MICROSCOPE*) would be higher than that of the farthest point of Earth, implying an asymmetric behavior that can be probed by *MICROSCOPE* [as captured by the function $\Phi(x)$ above]. Hence, *MICROSCOPE* is sensitive to scalar interactions with ranges as low as a few hundreds of kilometers.

Dilaton models.—We now consider the characteristics of a generic dilaton with couplings described in Refs. [17,18,28]. The mass of an atom (atomic number Z and mass number A) can be decomposed as $m(A, Z) = Zm_p + (A - Z)m_n + Zm_e + E_1 + E_3$, where $m_{n,p}$ is the mass of the neutron or proton and E_1 and E_3 are the electromagnetic and strong interaction binding energies. Following Ref. [28], we consider that the coupling coefficients of the dilaton to the electromagnetic and gluonic fields are d_e and d_g , while d_{m_e} , d_{m_u} , and d_{m_d} are its coupling to the electron and u and d quark mass terms, respectively. The latter two can be replaced by the couplings $d_{\delta m}$ and $d_{\bar{m}}$ to the symmetric and antisymmetric linear combination of u and d . Assuming a linear coupling, one deduces that the variation of the fine structure constants and masses of the quarks are given by $\Delta\alpha_{\text{EM}}/\alpha_{\text{EM}} = d_e\phi/M_p$ and $\Delta m_{u,d}/m_{u,d} = d_{u,d}\phi/M_p$.

First, we consider a massless dilaton ($m_\phi = 0$), whose range λ_ϕ is infinite, as was done by the Eöt-Wash group [9].

The dilaton coupling to matter, and hence the fifth force, is parametrized by the five numbers (d_g , d_e , $d_{\bar{m}}$, $d_{\delta m}$, and d_{m_e}) so that the coupling to matter (3) takes the form

$$\alpha_i \approx d_g^* + [(d_{\bar{m}} - d_g)Q'_{\bar{m}} + d_e Q'_e]_i, \quad (8)$$

where $d_g^* = d_g + 0.093(d_{\bar{m}} - d_g) + 0.00027d_e$. The dilaton charges depend on the chemical composition of the test masses and on the local value of the dilaton. Following Ref. [28], they are well approximated by

$$Q'_{\bar{m}} = 0.093 - \frac{0.036}{A^{1/3}} - 1.4 \times 10^{-4} \frac{Z(Z-1)}{A^{4/3}} \quad (9)$$

and

$$Q'_e = -1.4 \times 10^{-4} + 7.7 \times 10^{-4} \frac{Z(Z-1)}{A^{4/3}}. \quad (10)$$

In the limit where λ is much larger than any other spatial scales, the Eötvos parameter reduces to Eq. (4) so that (at first order in dilaton charges Q'_j —given that $|Q'_j| \ll 1$) [28]

$$\eta_{\text{massless}} = D_{\bar{m}}([Q'_{\bar{m}}]_{\text{Pt}} - [Q'_{\bar{m}}]_{\text{Ti}}) + D_e([Q'_e]_{\text{Pt}} - [Q'_e]_{\text{Ti}}), \quad (11)$$

where the coefficients $D_{\bar{m}} = d_g^*(d_{\bar{m}} - d_g)$ and $D_e = d_g^*d_e$ are to be estimated. The values for $Q'_{\bar{m}}$ and Q'_e in the *MICROSCOPE* case are given in Table I.

Figure 3 summarizes our new constraints and compare them to the earlier ones from the Eöt-Wash [9] and the Moscow groups [42]. The different slopes of the allowed

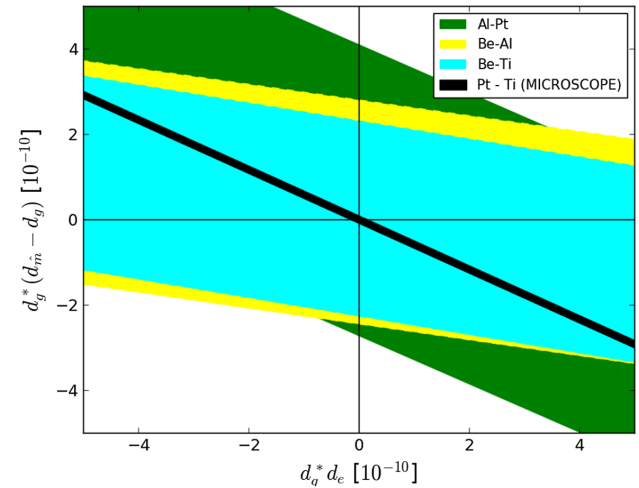


FIG. 3. Constraints on the couplings of a massless dilaton ($D_{\bar{m}}$, D_e). The region allowed by the *MICROSCOPE* measurement (black band) is compared to earlier constraints by torsion pendulum experiments from Refs. [42] (green) and [9] (yellow and cyan). The difference of slopes arises from the difference of material used in these three experiments. *MICROSCOPE* allows us to shrink the allowed region by one order of magnitude.

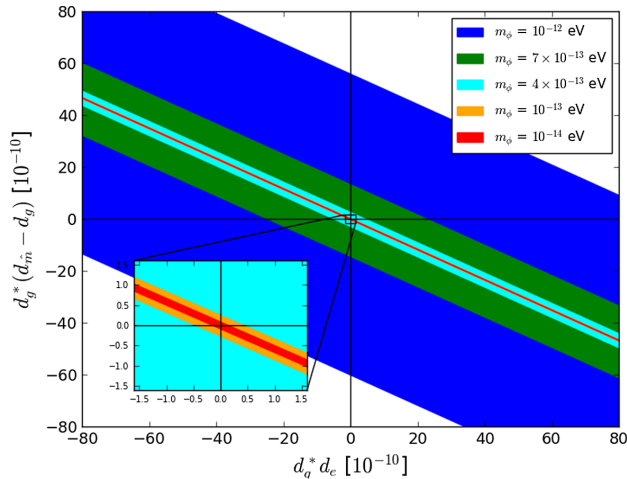


FIG. 4. Constraints on the couplings of a massive dilaton for various values of its mass. Each color shows the allowed $(D_{\bar{m}}, D_e)$ for a given mass of the scalar field. The inset is an enlargement of smaller $(D_{\bar{m}}, D_e)$. Constraints saturate for light fields $m_\phi < 10^{-14}$ eV. *MICROSCOPE* is not sensitive to masses larger than a few 10^{-12} eV.

regions are due to the different pairs of materials used by each experiment.

Massive dilaton.—The mass of the dilaton modifies the range of its interaction so that Eq. (11) is modified as

$$\eta = \eta_{\text{massless}} \times \Phi\left(\frac{R_E}{\lambda_\phi}\right) \left(1 + \frac{r}{\lambda_\phi}\right) e^{-r/\lambda_\phi}. \quad (12)$$

Note that this equation is simpler than Eq. (7), because Eq. (11) does not depend on the Earth dilaton charge, and it is therefore independent of the exact Earth model used.

From Figs. 1 and 2, we expect that *MICROSCOPE* shall mainly be sensitive to masses in the range 10^{-14} – 10^{-12} eV. Lower masses will result in constraints similar to those for a massless dilaton (see Fig. 3), while larger masses cannot be constrained, as they correspond to ranges that *MICROSCOPE* cannot probe. This is indeed what we conclude from our analysis summarized in Fig. 4. Constraints in the $(D_{\bar{m}}, D_e)$ plane are rather loose for high-enough masses, $m_\phi > 10^{-12}$ eV, and converge to those of a long-range dilaton for $m_\phi < 10^{-14}$ eV.

Finally, we assume that the dilaton field couples only to the electromagnetic field; i.e., the only nonvanishing coupling is d_e . The coupling to proton and neutron is then induced from their binding energy [43]. Several groups set constraints on such a dilaton from the fine structure constant oscillations in atomic frequency comparisons [44–46]. These results are based on the time evolution of the scalar field that oscillates within its self-potential. It has been argued that these oscillations may lead to oscillations of the Newtonian potentials if the scalar field behaves like cold dark matter [19] (thereby affecting *MICROSCOPE* in an unexpected way) or even break the

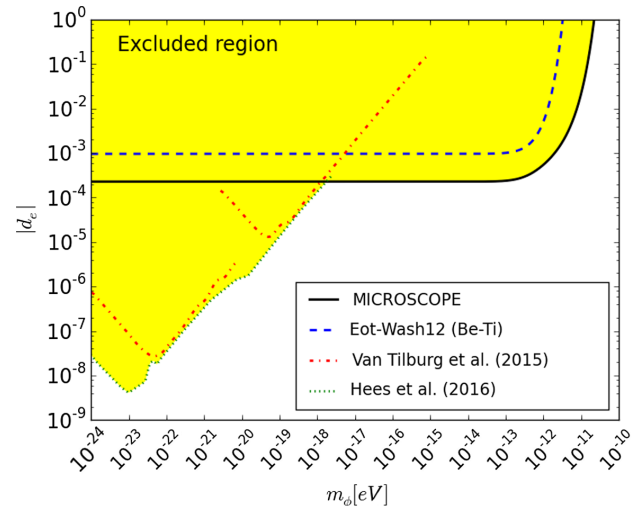


FIG. 5. Constraints on d_e , for a dilaton coupled only to the electromagnetic sector, compared with constraints from atomic spectroscopy (dot-dashed line [44,45]) and the Eöt-Wash WEP test (dashed line [8]).

Yukawa approximation [20]. Here, we do not tie our scalar field to describe dark matter, and we restrict our analysis to linear couplings, thence avoiding those possible pitfalls [47]. The *MICROSCOPE* constraints are obtained by considering the $D_{\bar{m}} = 0$ subspace of the parameter space $(D_{\bar{m}}, D_e, m_\phi)$ of Fig. 4 and recognizing that $D_e = d_g^* d_e = 0.00027 d_e^2$. Figure 5 shows our constraints, compared with those from the Eöt-Wash test of the WEP and with atomic spectroscopy [44,45]. *MICROSCOPE* allows us to exclude a new region above $|d_e| = 10^{-4}$, for a field of mass $10^{-18} < m_\phi/\text{eV} < 10^{-11}$. Atomic spectroscopy stays more competitive for lighter fields.

Conclusion.—This Letter gave the first constraints on a composition-dependent scalar fifth force from *MICROSCOPE*'s first measurement of the WEP [14]. We first considered the case of a massive scalar field coupled to either B or $B-L$ to conclude that *MICROSCOPE* is particularly competitive for a Yukawa potential of a range larger than 10^5 m (corresponding to a field of mass smaller than 10^{-12} eV). In that case, we improved existing constraints on the strength of the field by one order of magnitude. Below that range, torsion pendulum experiments remain unbeaten. Then, we considered a model describing the coupling of a generic dilaton to the standard matter field with five parameters, for both massless and massive fields. For $m_\phi < 10^{-14}$ eV, our constraints are similar to those for a massless field and better by one order of magnitude than the previously published ones.

From a theoretical perspective, a scalar long-range interaction is severely constrained by its effects on planetary motion. Since general relativity passes all tests on Solar System scales, many mechanisms have been designed to hide this scalar field in dense regions

(e.g., chameleons [48,49], symmetron [50], K-mouflage [51,52], or Vainshtein [53]). The generic dilaton model considered in this Letter corresponds to another type of screening (the least coupling principle [17]) and can incorporate the behavior of many theories, such as the string theory. The local prediction of the violation of the WEP can be compared to the variation of the fundamental constants on local and astrophysical scales (e.g., [54–57]). Better constraints can be obtained from modeling the profile (and time variation) of the scalar field along *MICROSCOPE*'s orbit, as well as its propagation inside the satellite up to the test masses; this is nontrivial, requires some care, and will be done in a further work. Constraints on the violation of the WEP will also have strong consequences for bigravity models [58].

From an experimental perspective, these new constraints were obtained from only two *MICROSCOPE*'s measurement sessions of the Eötvös parameter [14]. As the mission is scheduled to continue until 2018, new data are currently coming in, thereby offering the possibility of decreasing the statistical errors. We are also refining our data analysis procedures to optimize the measurement of the WEP. We therefore expect to improve on *MICROSCOPE*'s constraint on the Eötvös parameter by the end of the mission: 10 times as many data will be available than were used in Ref. [14]; furthermore, although we expect the data to become systematic dominated, the control on systematics will be improved compared to Ref. [14], since calibration sessions have been performed, whose results will be used in the next data analysis. Therefore, we could improve the constraints reported in that Letter by up to another order of magnitude (unless a WEP violation becomes apparent). But this forecast is valid only for $\lambda > \text{a few } 10^5 \text{ m}$ ($m_\phi < 10^{-12} \text{ eV}$). Probing lower-range (more massive) scalar fields can be done only using small scale experiments. Torsion pendulum and atomic interferometry experiments represent our best hopes to look for such extra fields. New, improved torsion pendulum will then be required to probe laboratory and smaller scale gravity, either through the measurement of the WEP or of the gravitational inverse square law. A torsion pendulum experiment in space seems the way forward to beat the current on-ground limits [59].

We thank the members of the *MICROSCOPE* Science Performance Group for useful discussions. We also thank Thibault Damour for useful comments on a first version of the manuscript. This work makes use of technical data from the CNES-ESA-ONERA-CNRS-OCA *Microscope* mission and has received financial support from ONERA and CNES. We acknowledge the financial support of the UnivEarthS Labex program at Sorbonne Paris Cité (ANR-10-LABX-0023 and ANR-11-IDEX-0005-02). The work of J.-P. U. done in the ILP LABEX (under reference ANR-10-LABX-63) was supported by French state funds managed by the ANR within the Investissements d'Avenir program under reference ANR-11-IDEX-0004-02. This

work is supported in part by the EU Horizon 2020 research and innovation program under the Marie-Sklodowska Grant No. 690575. This Letter is based upon work related to the COST Action CA15117 (CANTATA) supported by COST (European Cooperation in Science and Technology).

*joel.berge@onera.fr

- [1] C. M. Will, *Living Rev. Relativity* **17**, 4 (2014).
- [2] E. Fischbach, D. Sudarsky, A. Szafer, C. Talmadge, and S. H. Aronson, *Phys. Rev. Lett.* **56**, 3 (1986).
- [3] E. Fischbach and C. L. Talmadge, *The Search for Non-Newtonian Gravity, XVII* (Springer-Verlag, New York, 1999), p. 58.
- [4] E. G. Adelberger, B. R. Heckel, and A. E. Nelson, *Annu. Rev. Nucl. Part. Sci.* **53**, 77 (2003).
- [5] B. Jain and J. Khoury, *Ann. Phys. (Amsterdam)* **325**, 1479 (2010).
- [6] J.-P. Uzan, *Rev. Mod. Phys.* **75**, 403 (2003).
- [7] J.-P. Uzan, *Living Rev. Relativity* **14**, 2 (2011).
- [8] S. Schlamminger, K.-Y. Choi, T. A. Wagner, J. H. Gundlach, and E. G. Adelberger, *Phys. Rev. Lett.* **100**, 041101 (2008).
- [9] T. A. Wagner, S. Schlamminger, J. H. Gundlach, and E. G. Adelberger, *Classical Quantum Gravity* **29**, 184002 (2012).
- [10] T. Damour, *Classical Quantum Gravity* **29**, 184001 (2012).
- [11] J.-P. Uzan, *AIP Conf. Proc.* **736**, 3 (2005).
- [12] P. Touboul, G. Métris, V. Lebat, and A. Robert, *Classical Quantum Gravity* **29**, 184010 (2012).
- [13] J. Bergé, P. Touboul, and M. Rodrigues, *J. Phys. Conf. Ser.* **610**, 012009 (2015).
- [14] P. Touboul *et al.*, *Phys. Rev. Lett.* **119**, 231101 (2017).
- [15] T. Damour and G. Esposito-Farese, *Classical Quantum Gravity* **9**, 2093 (1992).
- [16] See Supplemental Material at <http://link.aps.org/supplemental/10.1103/PhysRevLett.120.141101>, which includes Refs. [17–22], for a derivation of the equation.
- [17] T. Damour and A. M. Polyakov, *Nucl. Phys.* **B423**, 532 (1994).
- [18] T. Damour and J. F. Donoghue, *Classical Quantum Gravity* **27**, 202001 (2010).
- [19] D. Blas, D. L. Nacir, and S. Sibiryakov, *Phys. Rev. Lett.* **118**, 261102 (2017).
- [20] T. A. de Pirey Saint Alby and N. Yunes, *Phys. Rev. D* **96**, 064040 (2017).
- [21] P. Brax, *Rep. Prog. Phys.* **81**, 016902 (2018).
- [22] L. Hui, A. Nicolis, and C. W. Stubbs, *Phys. Rev. D* **80**, 104002 (2009).
- [23] C. Schmid, J.-P. Uzan, and A. Riazuelo, *Phys. Rev. D* **71**, 083512 (2005).
- [24] P. Fayet, *Nucl. Phys.* **B347**, 743 (1990).
- [25] P. Fayet, *Eur. Phys. J. C* **77**, 53 (2017).
- [26] The orbit is nearly circular, and we can safely neglect any variation of r (estimated less than 0.1%).
- [27] Note that we ignore Earth's asphericity in this analysis.
- [28] T. Damour and J. F. Donoghue, *Phys. Rev. D* **82**, 084033 (2010).

- [29] G. L. Smith, C. D. Hoyle, J. H. Gundlach, E. G. Adelberger, B. R. Heckel, and H. E. Swanson, *Phys. Rev. D* **61**, 022001 (1999).
- [30] J. G. Williams, S. G. Turyshev, and D. H. Boggs, *Phys. Rev. Lett.* **93**, 261101 (2004).
- [31] C. Talmadge, J.-P. Berthias, R. W. Hellings, and E. M. Standish, *Phys. Rev. Lett.* **61**, 1159 (1988).
- [32] J. K. Hoskins, R. D. Newman, R. Spero, and J. Schultz, *Phys. Rev. D* **32**, 3084 (1985).
- [33] C. W. Stubbs, E. G. Adelberger, F. J. Raab, J. H. Gundlach, B. R. Heckel, K. D. McMurry, H. E. Swanson, and R. Watanabe, *Phys. Rev. Lett.* **58**, 1070 (1987).
- [34] V. P. Mitrofanov and O. I. Ponomareva, *Zh. Eksp. Teor. Fiz.* **94**, 16 (1988).
- [35] J. C. Long, H. W. Chan, and J. C. Price, *Nucl. Phys.* **B539**, 23 (1999).
- [36] C. D. Hoyle, U. Schmidt, B. R. Heckel, E. G. Adelberger, J. H. Gundlach, D. J. Kapner, and H. E. Swanson, *Phys. Rev. Lett.* **86**, 1418 (2001).
- [37] C. D. Hoyle, D. J. Kapner, B. R. Heckel, E. G. Adelberger, J. H. Gundlach, U. Schmidt, and H. E. Swanson, *Phys. Rev. D* **70**, 042004 (2004).
- [38] D. J. Kapner, T. S. Cook, E. G. Adelberger, J. H. Gundlach, B. R. Heckel, C. D. Hoyle, and H. E. Swanson, *Phys. Rev. Lett.* **98**, 021101 (2007).
- [39] M. Masuda and M. Sasaki, *Phys. Rev. Lett.* **102**, 171101 (2009).
- [40] A. O. Sushkov, W. J. Kim, D. A. R. Dalvit, and S. K. Lamoreaux, *Phys. Rev. Lett.* **107**, 171101 (2011).
- [41] V. Viswanathan, A. Fienga, O. Minazzoli, L. Bernus, J. Laskar, and M. Gastineau, *arXiv:1710.09167 [Mon. Not. R. Astron. Soc. (to be published)]*.
- [42] V. Braginsky and V.-I. Panov, *Zh. Eksp. Teor. Fiz.* **61**, 873 (1971).
- [43] J. Gasser and H. Leutwyler, *Phys. Rep.* **87**, 77 (1982).
- [44] K. Van Tilburg, N. Leefer, L. Bougas, and D. Budker, *Phys. Rev. Lett.* **115**, 011802 (2015).
- [45] A. Hees, J. Guéna, M. Abgrall, S. Bize, and P. Wolf, *Phys. Rev. Lett.* **117**, 061301 (2016).
- [46] T. Kalaydzhyan and N. Yu, *Phys. Rev. D* **96**, 075007 (2017).
- [47] See Supplemental Material at <http://link.aps.org/supplemental/10.1103/PhysRevLett.120.141101>, which includes Refs. [17–22].
- [48] J. Khoury and A. Weltman, *Phys. Rev. D* **69**, 044026 (2004).
- [49] J. Khoury and A. Weltman, *Phys. Rev. Lett.* **93**, 171104 (2004).
- [50] K. Hinterbichler and J. Khoury, *Phys. Rev. Lett.* **104**, 231301 (2010).
- [51] E. Babichev, C. Deffayet, and R. Ziour, *Int. J. Mod. Phys. D* **18**, 2147 (2009).
- [52] P. Brax, C. Burrage, and A.-C. Davis, *J. Cosmol. Astropart. Phys.* **01** (2013) 020.
- [53] A. I. Vainshtein, *Phys. Lett. B* **39**, 393 (1972).
- [54] F. Luo, K. A. Olive, and J.-P. Uzan, *Phys. Rev. D* **84**, 096004 (2011).
- [55] J. Guéna, M. Abgrall, D. Rovera, P. Rosenbusch, M. E. Tobar, P. Laurent, A. Clairon, and S. Bize, *Phys. Rev. Lett.* **109**, 080801 (2012).
- [56] N. Leefer, C. T. M. Weber, A. Cingöz, J. R. Torgerson, and D. Budker, *Phys. Rev. Lett.* **111**, 060801 (2013).
- [57] M. E. Tobar, P. L. Stanwix, J. J. McFerran, J. Guéna, M. Abgrall, S. Bize, A. Clairon, P. Laurent, P. Rosenbusch, D. Rovera, and G. Santarelli, *Phys. Rev. D* **87**, 122004 (2013).
- [58] A. De Felice, S. Mukohyama, and J.-P. Uzan, *Gen. Relativ. Gravit.* **50**, 21 (2018).
- [59] J. Bergé, in *Proceedings of the 52nd Rencontres de Moriond* (unpublished).

3.2 Yukawa and the geoid

3.2.1 Introduction and summary


This article furthers to the previous analysis to constraint a Yukawa-like deviation to Newton's gravity using Earth as a source for the interaction. The previous article started broaching the crucial subject of knowing the geometric structure of it. The problem is tackled by considering a simplistic model of Earth. When considering a more realistic model, the analysis encounters degeneracy. As mentioned in the introduction of this chapter, such a model is only known experimentally from geodesy. More specifically, what is modelled is the asperities of the gravitational field that reflects both Earth's density inhomogeneities and departure from a spherical shape. The reference geoid models are obtained from space missions such as GOCE [91, 80] and GRACE [87], that measure the value of the gravity field in orbit spanning all latitudes and longitudes at a specific altitude. In the standard analysis [84] one assumes the gravity field to be Newtonian and decomposes it over a basis of spherical harmonics. Its components are estimated by the set of measurements obtained in these missions. Nonetheless if an additional gravitational interaction was to exist it would necessary need to consider it in this analysis, otherwise discrepancy could appear between models obtained from different experiments. In the case of a Yukawa interaction for instance, due to the finite range of the interaction, geodesy experiments performed at different altitudes would obtain different geodetic components. As a consequence, one cannot just use the pre-obtained geodetic model to constraint modified gravity but instead reinterpret data including the deviation to Newton gravity in the analysis. This article explores this entanglement between geodesy and test of modified gravity.

For simplicity the problem is addressed by only considering a universal Yukawa coupling that is parametrised by the dimensionless constant α . In analogy with the Newtonian analysis, the modified gravity potential from Eq. (2.41) is decomposed over a spherical harmonics basis. In this equation the product of β_i is replaced by α . The obtained components can be expressed as the sum of a Newtonian contribution and Yukawa contribution. From this, the gravity field components are derived and a more simple description is obtained using spin-weighted spherical harmonics. This mathematical decomposition is the basis of the article. It is a generalisation of Eq. (2.43), to an arbitrary geometry of the considered body. This model is used to build statistical estimator to evaluate the impact of the existence of a Yukawa coupling on the estimation of a Newtonian geoid. We find that for breaking the degeneracy between the measurement of the geoid and the test a Yukawa interaction, we need to combine the results of different gravitational surveys performed at different altitudes. An estimator of the Yukawa parameters for such a combination of two experiments is given. A model of a homogeneous ellipsoidal Earth is used to provide numerical values for these estimators. The Yukawa interaction is found to be sub-dominant in geodesy experiment considering their current precisions. For the matter of testing the Yukawa force as we did in the previous section, considering the Earth to be a sphere is found to be a good approximation for experiments performed at high altitudes.

Parallel to that, this geodetic decomposition is used to express the impact of a Yukawa coupling on the orbital dynamics of a satellite – such as the one used to perform geodesy experiments – and is studied by deriving Lagrange-Gauss equations. In these equations the Yukawa interaction is treated as a perturbing force that would induce a secular change in the parameters of the Keplerian orbit.

3.2.2 Article

Interpretation of geodesy experiments in non-Newtonian theories of gravity

Joel Bergé¹ , Philippe Brax², Martin Pernot-Borràs^{1,3} and Jean-Philippe Uzan^{4,5}

¹ DPHY, ONERA, Université Paris Saclay, F-92322 Châtillon, France

² Institut de Physique Théorique, Université Paris-Saclay, CEA, CNRS, F-91191 Gif-sur-Yvette Cedex, France

³ Sorbonne Université, CNRS, Institut d'Astrophysique de Paris, IAP, F-75014 Paris, France

⁴ CNRS, Institut d'Astrophysique de Paris, IAP, F-75014 Paris, France

⁵ Institut Lagrange de Paris, 98 bis, Bd Arago, 75014 Paris, France

E-mail: joel.berge@onera.fr

Received 31 July 2018, revised 28 September 2018

Accepted for publication 19 October 2018

Published 7 November 2018



CrossMark

Abstract

This paper revisits deviations from Newtonian gravity described by a Yukawa interaction that can arise from the existence of a finite range fifth force. We show that the standard multipolar expansion of the Earth gravitational potential can be generalised. In particular, the multipolar coefficients depend on the distance to the centre of the Earth and are therefore not universal to the Earth system anymore. This offers new ways of constraining such Yukawa interactions and demonstrates explicitly the limits of the Newton-based interpretation of geodesy experiments. In turn, limitations from geodesy data restrict the possibility of testing gravity in space. The gravitational acceleration is described in terms of spin-weighted spherical harmonics allowing us to obtain the perturbing force entering the Lagrange–Gauss secular equations. This is then used to discuss the correlation between geodesy and modified gravity experiments and the possibility to break their degeneracy. Finally we show that, given the existing constraints, a Yukawa fifth force is expected to be sub-dominant in satellite dynamics and space geodesy experiments, as long as they are performed at altitudes greater than a few hundred kilometres. Gravity surveys will have to gain at least two orders of magnitude in instrumental precision before satellite geodesy could be used to improve the current constraints on modified gravity.

Keywords: modified gravity, experimental gravitation, orbital dynamics

(Some figures may appear in colour only in the online journal)

1. Introduction

The efforts to test Newton and Einstein gravity have been continuous in the last hundred years and lie at the crossroads between theoretical and experimental physics, laboratory and space physics. Celestial mechanics has historically been crucial in that respect, motivated mostly by the imperfect understanding of the shape of the Earth, the stability of the Solar system and the long lasting Newtonian problem of the anomalous drift of the perihelion of Mercury. A main difficulty arises from the fact that gravity is a long range interaction that cannot be screened. Hence, the knowledge of our environment (Earth gravitational field and its evolution, Solar system structure, cosmological model) is a limitation to these tests. In that respect, the developments of dedicated satellite missions have brought new insights on both possible deviations from general relativity (GR) and the Earth gravitational field.

Today, GR is well-tested on local scales [1, 2] whilst the need to improve the existing constraints is partly motivated by cosmology. The accelerated cosmic expansion and other evidences, such as the dynamics of spiral galaxies, have led to the conclusion that there should exist a dark sector, composed of dark matter and dark energy, representing respectively 26% and 70% of the energy budget of the universe. This dark sector can also be interpreted as a sign that GR may not be a good description of gravity on cosmological scales and on low acceleration regimes. Many extensions of GR have been proposed (see e.g. [3–5] for reviews) and many tests of GR and of Einstein’s equivalence principle on cosmological scales have been designed to test them [6–10]. No deviations from GR have been detected so far (see e.g. [2, 3, 11–13] for general reviews of laboratory and cosmological scales tests).

Concerning the recent experimental tests of GR, let us mention the Lense–Thirring effect [14–16], the pericentre anomaly [17–21], the gravitational redshift [22], the universality of free fall [23–27] and the constancy of fundamental constants [28–30], the last two involving Einstein’s equivalence principle. To these standard tests, let us add the new window opened by the detection of gravitational waves [31]. In particular, the detection of an electromagnetic counterpart to the gravitational-wave signal emitted by a binary neutron star merger [32] put severe constraints on a whole class of alternatives to GR [33–39].

Among all the extensions of GR, scalar–tensor theories [40], in which a scalar long range interaction that may be composition dependent, is added to the standard spin-2 interaction mediated by the gravitons, are still among the open alternatives. In particular, if this scalar is light, they may enjoy sizeable cosmological imprints. As a long range fifth force would then appear on Solar system scales, they need to include a screening or a decoupling mechanism [41–48]. While the parameter space of these models has been severely reduced (see e.g. [49] for up-to-date tests), they remain ideal candidates for extensions of GR. Even if the scalar field is heavy on Solar system scales, it is still responsible for a fifth force described, in the Newtonian regime, by a Yukawa potential (see e.g. the supplemental material of [50] and references therein). Many constraints on the mass and the amplitude of this extra-potential have been obtained so far (e.g. [3, 51] and references therein, and [50, 52–55] for more recent works).

The goal of this article is to revisit the constraints on such a Yukawa interaction drawn from the analysis of geodetic data. As already emphasised, it is a tautology to say that local GR tests are limited by our knowledge of the Earth gravitational field. Nevertheless, there have been extensive studies under the assumption of Newton’s gravity whilst the tests of Yukawa gravity have all been performed assuming at best a spherical and homogeneous Earth, but most often, assuming that the Yukawa interaction is sourced by a point-like Earth. We develop a method to describe the effects of such a modified gravity on the orbits of dedicated satellites in a realistic description of the Earth. Clearly, in that case our ignorance of the properties of the fifth force

does limit our reconstruction of the property of the mass distribution of the Earth, while the latter limits the constraints on this fifth force. We propose to analyze these interactions and provide tools to test GR in our terrestrial neighbourhood.

The shape and mass distribution of the Earth, and their variability, have so far been reconstructed from local measurements of the gravitational field (on-ground or airborne) and global satellite models of the full gravitational field. Recent satellite geodesy missions have allowed geophysicists to map the Earth gravity model with an exquisite precision: e.g. GOCE [56, 57] or GRACE [58–60] and combinations of (satellite) missions [61, 62]. GOCE and GRACE provide measurements of the spherical harmonics coefficients up to degree and order 250, whereas the EGM2008 model goes up to degree and order 2159 [63].

The uncertainties on the shape of the Earth add up to other systematic errors (such as Solar radiation pressure, atmospheric drag, Earth tides, Earth magnetic field, thermal instabilities—for discussions of systematics in both laboratory and space, see e.g. [20, 26, 64]). Then, they must be either shielded or corrected for during the data analysis process (see e.g. [26, 64–66]). This article focuses on satellite tests of gravity so that the main sources of gravitational error come from the zonal terms, and especially the first one, J_2 (which describes the Earth flattening) [15, 20]. Before the advent of the precise satellite measurements from GRACE and GOCE, the large uncertainty on J_2 was considered a show-stopper for precise tests of gravity. Techniques were then elaborated to cancel its effect. For instance, by empirically combining the perigee shift and precession of the line of nodes of LAGEOS and LAGEOS II, it was shown that the contribution of J_2 (and the associated error) to the perigee shift and to the Lense–Thirring effect could be cancelled [67]. The GRACE and GOCE missions changed the situation thanks to their remarkably precise measurements, giving the parameter J_2 to a 10^{-8} relative precision level when combined with LAGEOS data. In the case of the perigee shift measurement of the LAGEOS II satellite, Lucchesi and Peron [20] evaluate that using the errors on J_2 provided by the EIGEN-GRACE02S gravitational field model [60] allows for a percent level test of GR’s perigee shift with no further empirical correction.

However, correcting for the shape of the Earth when testing gravity in space relies on two pillars: (i) a model of the Earth gravitational field and (ii) accurate and precise values of the coefficients of the model. To the best of our knowledge, the model is always described as a spherical harmonics expansion derived from Laplace equation to solve for the Newtonian gravitational field sourced by the shape of the Earth. The values of the spherical harmonics coefficients are provided by Earth gravity surveys, such as GRACE, GOCE, LAGEOS, or local on-ground surveys.

The evaluation of the accuracy of coefficients estimator and of robust uncertainties is a highly non-trivial part of the data analysis needed to make a model of the gravitational field. Errors on spherical harmonic coefficients are commonly separated between formal and calibrated errors [20, 60]. Formal errors come from the data regression method and mainly include statistical errors as well as possible numerical uncertainties linked to the data analysis method itself. For instance, because of its Sun-synchronous orbit, GOCE never flew over the poles; the resulting polar gaps (whereby no data can constrain the spherical harmonics model in the polar regions) causes the least-square regression on spherical harmonics coefficients to be ill-conditioned, thus requiring a regularization technique. With no regularization, estimating the (near)-zonal terms is particularly difficult. These coefficients come with large error bars; after regularization, the error bars can be seen to shrink [57, 68] (for J_2 , the error shrinks from a few 10^{-9} to a few 10^{-12}). However, there does not seem to be any investigation about the possible bias introduced by the regularization technique.

Under the Newtonian gravity hypothesis (i.e. the static part of spherical harmonics coefficients should be consistent between different data subsets along the experiment’s time span,

Table 1. Constraints on the J_2 parameter by several experiments.

GRACE	$J_2 = 1.082\,635\,430\,912\,2197 \times 10^{-3} \pm 3.526\,362\,561\,283\,4223 \times 10^{-12}$	[62]
GOCE	$J_2 = 1.082\,626\,532\,640\,4513 \times 10^{-3} \pm 1.212\,794\,611\,655\,5258 \times 10^{-11}$	[57]
EIGEN-6C	$J_2 = 1.082\,626\,337\,689\,3369 \times 10^{-3} \pm 2.477\,786\,925\,867\,517 \times 10^{-13}$	[70]

or between different experiments), formal errors are *a posteriori* calibrated to account for systematic errors: for a single satellite model, subset solutions are generated from data covering different time periods, and the scattering of subset solutions is used as the calibrated error (see e.g. [60] for GRACE). The same method is applied to calibrate multi-satellite models, where an upper bounds for the systematic errors is derived from the difference between estimates of several satellite data [20]. In this case, it is implicitly assumed that any tension between different data sets comes from imperfectly controlled systematic errors. Although this is true if the underlying hypothesis (the Earth gravity is described by Newton's theory) is true, any tension may also provide a smoking gun for physics beyond Newton's inverse square law and GR. Indeed, a modified gravity model may very well predict non-universal spherical harmonics coefficients, e.g. coefficients whose value depends on the distance to the centre of the Earth (in this paper, we show that it is indeed the case). Along this line, it should be noted that despite very precise measurements of the static J_2 zonal term, the GRACE-only, GOCE-only and EIGEN-6C (combining LAGEOS, GOCE, GRACE and ground measurements) models provide inconsistent values (as was already noted by Wagner and McAduo [69]), which differ by at least 700σ ; see table 1.

Whether this tension is due to largely underestimated errors, to biases introduced by regularization techniques, to uncontrolled systematics, to inconsistent data sets, or to new physics beyond GR is not clear. However, it should invite us to extreme caution when using gravity surveys and geodesy results to model and correct for the Earth gravitational field when testing GR or looking for deviations to Newton's inverse square law.

This article investigates the effects of modified gravity on the Earth gravitational field and our ability to reconstruct the shape of the Earth and, in turn, the effect of an imperfect knowledge of the Earth gravitational field on searches for modified gravity. As explained, we base our discussion on phenomenological deviations from Newton gravity described by a Yukawa potential.

In particular, we shall show that although we can still describe the Earth gravitational field with a spherical harmonics expansion, a Yukawa interaction modifies the meaning of the expansion coefficients. They mix properties of the Earth and of gravity and get an explicit dependence on the distance to the centre of the Earth. As a consequence, they are not simply related to the Earth geometry any more, and should not be used to map the Earth mass distribution and geoid. For instance, the $J_2(r)$ zonal term does not only describe the Earth flattening, but is impacted by the Yukawa interaction. Furthermore, we should not expect coefficients measured by different satellites at different altitude (or even by a single satellite at different times, provided that satellite's orbit is not circular) to be consistent; combining different data sets should also be performed with great care.

Therefore, using geodesy results derived under the assumption that no deviation to GR (or to Newton's law) exists is prone to errors when constraining modified gravity, just because the Earth gravity model used to correct for the Newtonian contribution may be incorrect. This may be the case if using (possibly inconsistent) multi-satellite models, or a model set with a satellite at an altitude other than the altitude of the gravity test. The underlying question is that of the model to use. When looking for modified gravity in terms of a Yukawa

interaction, two parameters are added to the Newtonian gravity sector (the strength and range of the interaction), *de facto* changing the model. Using geodesy results derived assuming a simple Newtonian model must then be seen as inconsistent with the task at hand, and will introduce biases and uncertainties that must be quantified and accounted for in the modified gravity constraints.

The way out of this difficulty is, as usual, to set all analyses within the same theoretical framework to ensure consistency. The Earth gravitational field should be measured under the assumption that a Yukawa interaction may exist. The Earth gravitational field models would then explicitly contain information about the Yukawa interaction, either explicit or marginalised upon. In the former case, they would provide constraints on modified gravity; in the latter case, their estimated coefficients would have larger uncertainty, but would be unbiased and could safely be used by modified gravity experiments.

This paper is organised as follows. We first derive the spherical harmonic expansion of the Earth gravitational field in presence of a Yukawa interaction and give expressions for the gravitational acceleration and for the Gauss–Lagrange equations of motion in section 2; we give a worked-out example in section 3. Section 4 provides a general discussion of the entanglement between geodesy and modified gravity measurements; in particular, we discuss the statistics of geodesy and non-Newtonian gravity estimators built from the combination of different space geodesy missions; this section may be skipped at first reading. The impatient reader is directed to section 5, where we provide order-of-magnitude estimates derived with a simple Earth model. In particular, we show in section 5.1 that given their instrumental precision, current space geodesy experiments are immune to a Yukawa interaction (given the current experimental constraints) as long as they fly high enough; we then show in section 5.2 that the effect of a Yukawa interaction on satellites orbits is at most of the same level as that from relativistic effects and planetary effects; finally, section 5.3 shows that our limited knowledge of the Earth’s interior and geometry is not yet a limiting factor when constraining the presence of a Yukawa interaction with the estimators defined in section 4.

2. Earth gravity in presence of a Yukawa potential

2.1. Gravitational potential

Among the various ways to modify Newton’s gravity, the introduction of a Yukawa potential describes the effect of an extra-massive degree of freedom that can appear, e.g. in scalar–tensor gravity [2]. Assuming that the coupling of this new degree of freedom to the standard model fields is universal, the associated potential created by a point-mass source of mass M at a distance r is

$$U_{\text{pm}}(r) = -\frac{GM}{r} \left[1 + \alpha \exp\left(-\frac{r}{\lambda}\right) \right], \quad (1)$$

where α is the strength of the Yukawa deviation with respect to gravity and λ its range. G is a constant that matches Newton’s gravitational constant, as it would be measured in a Cavendish experiment in the limit $r \gg \lambda$.

It follows that the gravitational potential generated by an extended source is obtained by integrating equation (1) over the source

$$U(\mathbf{r}) = \int_V U_{\text{pm}}(\mathbf{r} - \mathbf{s}) d^3V, \quad (2)$$

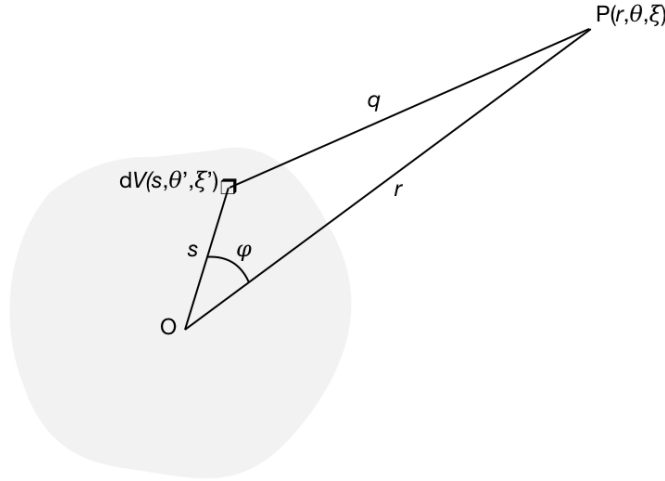


Figure 1. Geometry of the problem. We compute the gravitational potential at point P due to a source (grey area) whose centre-of-mass is O . In a spherical coordinates system centered on O , θ (resp. θ') is the co-latitude of P (resp. of the infinitesimal volume that sources the field at P') and ξ (resp. ξ') its longitude. We define the orthonormal basis $(\mathbf{u}_r, \mathbf{u}_\theta, \mathbf{u}_\xi)$ in such a way that $\mathbf{OP} = r\mathbf{u}_r$ and $\mathbf{OP}' = s\mathbf{u}_{r'}$ so that $\cos \varphi = \mathbf{u}_r \cdot \mathbf{u}_{r'}$.

where \mathbf{s} is the position-vector of the infinitesimal element of volume d^3V and $\mathbf{r} = (r, \theta, \xi)$ are the spherical coordinates of the point P where the potential is evaluated (see figure 1), where θ is the co-latitude, and ξ the longitude.

As usual, we relate the multipolar decomposition of this potential to that of the source. To that purpose, we use the standard expansion

$$\frac{1}{q} = \frac{1}{r} \sum_{\ell=0}^{\infty} \left(\frac{s}{r}\right)^{\ell} P_{\ell}(\cos \varphi), \quad (3)$$

where $q \equiv |\mathbf{r} - \mathbf{s}|$ and P_{ℓ} are Legendre polynomials. r and s are the distances between the centre of mass O of the source and, respectively, the point P where we compute the gravitational potential or the infinitesimal volume element P' of the source so that $s/r < 1$. In conventional spherical coordinates centered on O , $(\mathbf{u}_r, \mathbf{u}_\theta, \mathbf{u}_\xi)$, $\mathbf{OP} = r\mathbf{u}_r$, $\mathbf{OP}' = s\mathbf{u}_{r'}$ or equivalently the coordinates of P (resp. P') are (r, θ, ξ) (resp. (s, θ', ξ')); see figure 1 for the definitions. The Yukawa contributions can be expanded in a similar way thanks to (see [71])

$$\frac{e^{-q/\lambda}}{q} = \frac{1}{\sqrt{rs}} \sum_{\ell=0}^{\infty} (2\ell + 1) K_{\ell+\frac{1}{2}}\left(\frac{r}{\lambda}\right) I_{\ell+\frac{1}{2}}\left(\frac{s}{\lambda}\right) P_{\ell}(\cos \varphi), \quad (4)$$

where $I_{\ell+\frac{1}{2}}$ and $K_{n+\frac{1}{2}}$ are modified spherical Bessel functions of the second and third kinds.

Inserting the decompositions (3) and (4) in equation (2) and expanding the Legendre polynomials in spherical harmonics $Y_{\ell m}$ ⁶ as

$$P_{\ell}(\cos \varphi) = \frac{1}{2\ell + 1} \sum_{m=-\ell}^{\ell} Y_{\ell m}^*(\theta', \xi') Y_{\ell m}(\theta, \xi), \quad (5)$$

⁶ Another common normalization for spherical harmonics is $P_{\ell}(\cos \varphi) = \frac{4\pi}{2\ell+1} \sum_{m=-\ell}^{\ell} Y_{\ell m}^*(\theta', \xi') Y_{\ell m}(\theta, \xi)$: we use equation (5) to ensure that in the case of a homogeneous sphere, we recover $y_{00}^N = 1$.

the gravitational potential can be expressed as a multipolar decomposition as

$$U(P) = U(r, \theta, \xi) = -\frac{GM_{\oplus}}{r} \sum_{\ell=0}^{\infty} \sum_{m=-\ell}^{\ell} \left(\frac{R_{\oplus}}{r}\right)^{\ell} y_{\ell m}(r) Y_{\ell m}(\theta, \xi), \quad (6)$$

where M_{\oplus} and R_{\oplus} are the mass and equatorial radius of the Earth. We shall use equivalently the notations $Y_{\ell m}(\theta, \xi)$ or $Y_{\ell m}(\mathbf{u}_r)$ in the following.

The introduction of a Yukawa interaction does not modify the general multipolar expansion of the Earth gravitational potential. Indeed, the multipolar coefficients $y_{\ell m}$ now enjoy two contributions and split as

$$y_{\ell m}(r) = y_{\ell m}^N + y_{\ell m}^Y(r) \quad (7)$$

where the superscripts N and Y stand for the Newton and Yukawa contributions. After trivial algebra, one gets that

$$y_{\ell m}^N = \frac{1}{(2\ell+1)M_{\oplus}} \int_V d^3V \rho(\mathbf{s}\mathbf{u}_{r'}) \left(\frac{s}{R_{\oplus}}\right)^{\ell} Y_{\ell m}^*(\mathbf{u}_{r'}) \quad (8)$$

and

$$y_{\ell m}^Y(r) = \frac{\alpha}{M_{\oplus}} \left(\frac{r}{\lambda}\right)^{\ell+\frac{1}{2}} K_{\ell+\frac{1}{2}}\left(\frac{r}{\lambda}\right) \int_V d^3V \rho(\mathbf{s}\mathbf{u}_{r'}) \left(\frac{s}{R_{\oplus}}\right)^{\ell} \left(\frac{\lambda}{s}\right)^{\ell+\frac{1}{2}} I_{\ell+\frac{1}{2}}\left(\frac{s}{\lambda}\right) Y_{\ell m}^*(\mathbf{u}_{r'}) \quad (9)$$

where $\rho(\mathbf{s}\mathbf{u}_{r'})$ is the Earth's density in P' and $d^3V = s ds d^2\mathbf{u}_{r'}$ is the volume element around P' . The Earth density can then be expanded in spherical harmonics as

$$\rho(\mathbf{s}\mathbf{u}_{r'}) = \sum_{\ell m} \rho_{\ell m}(s) Y_{\ell m}(\mathbf{u}_{r'}), \quad (10)$$

so that we finally get, after integrating over $d^2\mathbf{u}_{r'}$,

$$y_{\ell m}(r) = \frac{1}{(2\ell+1)M_{\oplus}} \int s^2 \left(\frac{s}{R_{\oplus}}\right)^{\ell} \rho_{\ell m}(s) \left[1 + \alpha \mathcal{A}_{\ell}\left(\frac{s}{\lambda}\right) \mathcal{B}_{\ell}\left(\frac{r}{\lambda}\right)\right] ds, \quad (11)$$

with the two functions

$$\mathcal{A}_{\ell}(x) = x^{-(\ell+1/2)} I_{\ell+1/2}(x) \quad (12)$$

$$\mathcal{B}_{\ell}(x) = (2\ell+1)x^{\ell+1/2} K_{\ell+1/2}(x). \quad (13)$$

As expected, the kernel is m -independent so that the m -dependence arises only from the one of the density. Note that in equation (11) the integral is 1-dimensional. Indeed s is defined by the Earth surface $R_{\oplus}(\mathbf{u}_{r'})$ so is directionally dependent. Since we have performed a multipolar expansion, we need to take this boundary conditions into account in the function ρ so that

$$\rho(\mathbf{s}\mathbf{u}_{r'}) = \rho_{\oplus}(\mathbf{s}\mathbf{u}_{r'}) \{1 - \Theta[s - R_{\oplus}(\mathbf{u}_{r'})]\} \quad (14)$$

where Θ is the Heaviside function. The shape of the Earth is thus contained in the multipoles $\rho_{\ell m}$.

2.2. Gravitational acceleration

The gravitational acceleration is defined, as usual, as

$$\mathbf{g}(r, \theta, \xi) = -\nabla U(r, \theta, \xi). \quad (15)$$

We thus need to evaluate the gradient of equation (6) in spherical coordinates. It decomposes on the spherical basis as

$$\mathbf{g} = \mathbf{g}_{\parallel} + \mathbf{g}_{\perp}, \quad \text{with} \quad \mathbf{g}_{\parallel} \equiv g_r \mathbf{u}_r, \quad \mathbf{g}_{\perp} \equiv g_{\theta} \mathbf{u}_{\theta} + g_{\xi} \mathbf{u}_{\xi}. \quad (16)$$

2.2.1. Radial component. The derivation with respect to r does not act on the spherical harmonics so that

$$g_r(r\mathbf{u}_r) \equiv \sum_{\ell m} g_r^{\ell m}(r) Y_{\ell m}(\mathbf{u}_r) \quad (17)$$

with

$$g_r^{\ell m}(r) = -\frac{GM_{\oplus}}{r^2} \left(\frac{R}{r}\right)^{\ell} \left[(\ell + 1) (y_{\ell m}^N + y_{\ell m}^Y) - \frac{r}{\lambda} \dot{y}_{\ell m}^Y \right] \quad (18)$$

where a dot refers to a derivative with respect to $x = r/\lambda$. Since

$$(\ell + 1) y_{\ell m}^Y - \frac{r}{\lambda} \dot{y}_{\ell m}^Y = y_{\ell m}^Y \left[\ell + 1 + \frac{r}{\lambda} \frac{K_{\ell-1/2}(r/\lambda)}{K_{\ell+1/2}(r/\lambda)} \right]. \quad (19)$$

Then, it is clear that equation (18) recasts as

$$g_r^{\ell m} = -\frac{GM_{\oplus}}{r^2} (\ell + 1) \left(\frac{R_{\oplus}}{r}\right)^{\ell} z_{\ell m}(r) \quad (20)$$

where $z_{\ell m}$ is a radial function that differs from $y_{\ell m}$ only by its Kernel,

$$z_{\ell m}(r) = \frac{1}{(2\ell + 1)M_{\oplus}} \int s^2 \left(\frac{s}{R_{\oplus}}\right)^{\ell} \rho_{\ell m}(s) \left[1 + \alpha \mathcal{A}_{\ell} \left(\frac{s}{\lambda}\right) \mathcal{C}_{\ell} \left(\frac{r}{\lambda}\right) \right] ds \quad (21)$$

where we have introduced the function

$$\mathcal{C}_{\ell}(x) = (2\ell + 1)x^{\ell+1/2} K_{\ell+1/2}(x) \left[1 + \frac{x}{\ell + 1} \frac{K_{\ell-1/2}(x)}{K_{\ell+1/2}(x)} \right]. \quad (22)$$

2.2.2. Angular part. The angular components are given by

$$g_{\theta}(r\mathbf{u}_r) = \frac{GM_{\oplus}}{r^2} \sum_{\ell m} \left(\frac{R_{\oplus}}{r}\right)^{\ell} y_{\ell m}(r) \partial_{\theta} Y_{\ell m}(\mathbf{u}_r) \quad (23)$$

$$g_{\xi}(r\mathbf{u}_r) = \frac{GM_{\oplus}}{r^2} \sum_{\ell m} \left(\frac{R_{\oplus}}{r}\right)^{\ell} y_{\ell m}(r) \frac{1}{\sin \theta} \partial_{\xi} Y_{\ell m}(\mathbf{u}_r), \quad (24)$$

with $y_{\ell m}(r)$ given by equation (11). However such a decomposition does not give a proper multipolar expansion since $\partial_{\theta} Y_{\ell m}$ mixes different multipoles. Indeed, after derivation the expansion is no more in an orthonormal basis. The standard way to express the gravitational acceleration in a good frame is to use recursion properties between spherical harmonics (see e.g. [72–75]). Here, we propose to use a simpler way by introducing spin-weighted spherical harmonics.

To that purpose, we first define the two complex vectors

$$\mathbf{u}_{\pm} \equiv \frac{1}{\sqrt{2}} (\mathbf{u}_{\theta} \mp j\mathbf{u}_{\xi}), \quad (25)$$

where $j^2 = -1$ so that

$$\mathbf{g}_\pm = g_+ \mathbf{u}_+ + g_- \mathbf{u}_- \quad \text{with} \quad g_\pm = \frac{1}{\sqrt{2}} (g_\theta \pm j g_\xi). \quad (26)$$

With our notations, we get

$$g_\pm = \frac{1}{\sqrt{2}} \frac{GM_\oplus}{r^2} \sum_{\ell m} \left(\frac{R_\oplus}{r} \right)^\ell y_{\ell m}(r) \left[\partial_\theta \pm \frac{j}{\sin \theta} \partial_\xi \right] Y_{\ell m}(\mathbf{u}_r). \quad (27)$$

Now acting s -times with the complex derivative in the square brackets on the spherical harmonics defines the spin-weighted spherical harmonics ${}_s Y_{\ell m}(\theta, \xi)$ [76, 77].

From equation (2.7) of [77]), we have

$$\left[\partial_\theta \pm \frac{j}{\sin \theta} \partial_\xi \right] Y_{\ell m}(\theta, \xi) = \pm \sqrt{\ell(\ell+1)}_{\pm 1} Y_{\ell m}(\theta, \xi) \quad (28)$$

from which it follows that the proper multipolar expansion of the gravitational acceleration is

$$g_\pm = \sum_{\ell m} g_{\pm \pm 1}^{\ell m} Y_{\ell m}(\theta, \xi) \quad (29)$$

with

$$g_{\pm \pm 1}^{\ell m} = \pm \frac{1}{\sqrt{2}} \frac{GM_\oplus}{r^2} \sqrt{\ell(\ell+1)} \left(\frac{R_\oplus}{r} \right)^\ell y_{\ell m}(r). \quad (30)$$

2.2.3. Summary. Equation (20) for the radial component and (30) for the angular component allow us to compute directly the contribution of the (ℓ, m) multipole to the gravitational acceleration of any extended body once $\rho(\mathbf{su}, r)$ is known. They now need to be translated to non-Keplerian perturbations applied to bodies orbiting around the Earth.

2.3. Orbital perturbations and secular effect on satellites osculating parameters

Given perturbing forces acting on a satellite, the Lagrange–Gauss equations allow one to compute the secular variations of the satellite’s orbital parameters [78–80]. They can be also used to deduce the characteristics of a perturbing source from a measurement of the satellite’s dynamics. In particular, they can be used to estimate the Earth gravitational field spherical harmonic coefficients. This section establishes the Lagrange–Gauss equations and the expression of the perturbing force arising from the shape of the Earth and a non-Newtonian gravity modelled by a Yukawa potential.

2.3.1. Expression of the perturbing force. Let us define a perturbing force acting on an orbiting body as the difference between the actual force applied to the body and the pure Newtonian monopole gravitational force. We ignore all non-gravitational forces, as well as gravity from the Sun, the Moon and other Solar system planets, so that the perturbing force is

$$\mathbf{F}_{\text{pert}} = \mathbf{g} + \frac{GM_\oplus}{r^2} \mathbf{u}_r = \mathcal{R} \mathbf{e}_R + \mathcal{S} \mathbf{e}_S + \mathcal{W} \mathbf{e}_W \quad (31)$$

where \mathcal{R} , \mathcal{S} and \mathcal{W} are the radial, tangential (in the orbital plane) and orthogonal components of the perturbing force per unit of reduced mass. The unit vectors \mathbf{e}_R , \mathbf{e}_S , \mathbf{e}_W are defined in

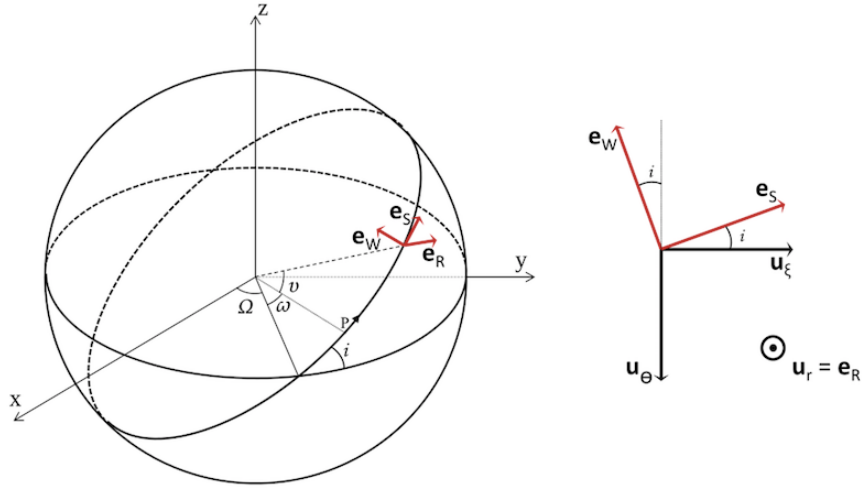


Figure 2. Left: comoving frame associated to the orbit and in which we decompose the perturbation. Notice that we have introduced i the inclination, Ω the longitude of the ascending node, ω the argument of the perigee P and ν the true anomaly. Right: a rotation to transform the spherical coordinates unit vectors \mathbf{u}_θ and \mathbf{u}_ξ into the comoving unit vectors \mathbf{e}_S and \mathbf{e}_W .

figure 2. Since $\mathbf{e}_R = \mathbf{u}_r$, the change of coordinates between the two frames reduce to a rotation so that the components of the force are

$$\mathcal{R} = \frac{m_{\text{sat}}}{\mu} \left[g_r(r, \theta, \xi) + \frac{GM_\oplus}{r^2} \right] \quad (32)$$

$$\mathcal{S} = -\frac{m_{\text{sat}}}{\mu} [g_\theta(r, \theta, \xi) \sin i - g_\xi(r, \theta, \xi) \cos i] \quad (33)$$

$$\mathcal{W} = -\frac{m_{\text{sat}}}{\mu} [g_\theta(r, \theta, \xi) \cos i + g_\xi(r, \theta, \xi) \sin i] \quad (34)$$

where $\mu = M_\oplus m_{\text{sat}} / (M_\oplus + m_{\text{sat}})$ is the reduced mass of the Earth-satellite system.

The perturbation force can also be decomposed in the basis $(\mathbf{u}_r, \mathbf{u}_+, \mathbf{u}_-)$ as

$$\mathbf{F}_{\text{pert}} = \mathcal{R}\mathbf{u}_r + \sum_{s=\pm} \mathcal{R}^s \mathbf{u}_s \quad (35)$$

so that its angular component can be decomposed in spin-weighted harmonics as

$$\mathcal{R}^\pm = \frac{1}{\sqrt{2}} (\mathcal{S} \pm j\mathcal{W}) = \mp \frac{m_{\text{sat}}}{\mu} \exp \left[j \left(\frac{\pi}{2} \mp i \right) \right] g_\pm. \quad (36)$$

It follows that the multipolar decomposition is now well-defined as

$$\mathbf{F}_{\text{pert}} = \sum_{\ell m} \left[\mathcal{R}_{\ell m} Y_{\ell m} \mathbf{u}_r + \sum_{s=\pm} \mathcal{R}_{\ell m}^s Y_{\ell m}^s \mathbf{u}_s \right] \quad (37)$$

with

$$\mathcal{R}_{\ell m} = \frac{GM_{\text{tot}}}{r^2} \left[-(\ell + 1) \left(\frac{R_\oplus}{r} \right)^\ell z_{\ell m}(r) + \delta_{\ell 0} \delta_{m 0} \right], \quad (38)$$

$$\mathcal{R}_{\ell m}^{\pm} = \mp \frac{1}{\sqrt{2}} \frac{GM_{\text{tot}}}{r^2} \sqrt{\ell(\ell+1)} \left(\frac{R_{\oplus}}{r} \right)^{\ell} y_{\ell m}(r) \exp \left[j \left(\frac{\pi}{2} \mp i \right) \right], \quad (39)$$

where $M_{\text{tot}} = M_{\oplus} + m_{\text{sat}}$ and $y_{\ell m}(r)$ and $z_{\ell m}(r)$ are defined in equations (11) and (21) respectively.

It immediately follows that the radial, tangential and othogonal components of the perturbing force (equations (32)–(34)) are

$$\mathcal{R}(r, \theta, \xi) = \frac{GM_{\text{tot}}}{r^2} \sum_{\ell m} \left[-(\ell+1) \left(\frac{R_{\oplus}}{r} \right)^{\ell} z_{\ell m}(r) + \delta_{\ell 0} \delta_{m 0} \right] Y_{\ell m}(\theta, \xi) \quad (40)$$

$$\mathcal{S}(r, \theta, \xi) = -\frac{j}{2} \frac{GM_{\text{tot}}}{r^2} \sum_{\ell m} \sqrt{\ell(\ell+1)} \left(\frac{R_{\oplus}}{r} \right)^{\ell} y_{\ell m}(r) \left[e^{-ji} {}_{+1}Y_{\ell m}(\theta, \xi) + e^{ji} {}_{-1}Y_{\ell m}(\theta, \xi) \right] \quad (41)$$

$$\mathcal{W}(r, \theta, \xi) = -\frac{1}{2} \frac{GM_{\text{tot}}}{r^2} \sum_{\ell m} \sqrt{\ell(\ell+1)} \left(\frac{R_{\oplus}}{r} \right)^{\ell} y_{\ell m}(r) \left[e^{-ji} {}_{+1}Y_{\ell m}(\theta, \xi) - e^{ji} {}_{-1}Y_{\ell m}(\theta, \xi) \right]. \quad (42)$$

In Newtonian gravity, the perturbations arise only from the shape of the Earth, from the gravitational perturbations of other celestial bodies (Sun, Moon, planets, etc) and of friction forces from the atmosphere and radiation pressure. They all have been studied in details and shown to cause secular drifts such as the precession of the line of nodes (the latter being mostly sourced by the Earth equatorial bulge through the $J_2 \equiv -\sqrt{5}y_{20}$ zonal term) [80]. In a theory gravity beyond Einstein (or, on small scales, Newton), the existence of an extra gravitational potential causes a new set of perturbations, also related to the shape of the Earth. In our model at hand, the Yukawa potential mixes the shape of the Earth contributions and the non-Newtonian interaction.

2.3.2. Lagrange–Gauss equations and secular effects. Secular effects due to a perturbing force on osculating parameters for a given orbit configuration can be computed from the Lagrange–Gauss equations once the component of the perturbative force (37) are known.

The Lagrange–Gauss equations then read

$$\frac{da}{dt} = 2 \sqrt{\frac{a^3}{GM_{\text{tot}}(1-e^2)}} [\mathcal{R}e \sin \nu + (1+e \cos \nu)\mathcal{S}] \quad (43)$$

$$\frac{de}{dt} = \sqrt{\frac{a(1-e^2)}{GM_{\text{tot}}}} \left[\mathcal{R} \sin \nu + \frac{e+2 \cos \nu + e \cos^2 \nu}{1+e \cos \nu} \mathcal{S} \right] \quad (44)$$

$$\frac{di}{dt} = \sqrt{\frac{a(1-e^2)}{GM_{\text{tot}}}} \frac{\cos(\omega+\nu)}{1+e \cos \nu} \mathcal{W} \frac{d\Omega}{dt} = \sqrt{\frac{a(1-e^2)}{GM_{\text{tot}}}} \frac{\sin(\omega+\nu)}{1+e \cos \nu} \frac{\mathcal{W}}{\sin i} \quad (45)$$

$$\frac{d\omega}{dt} = \sqrt{\frac{a(1-e^2)}{GM_{\text{tot}}}} \left[-\frac{\mathcal{R}}{e} \cos \nu + \frac{(2+e \cos \nu) \sin \nu}{e(1+e \cos \nu)} \mathcal{S} - \frac{\sin(\omega+\nu) \cos i}{1+e \cos \nu} \frac{\mathcal{W}}{\sin i} \right] \quad (46)$$

$$\frac{d\ell}{dt} = n + \sqrt{\frac{a}{GM_{\text{tot}}}} \frac{1-e^2}{e(1+e \cos \nu)} [\mathcal{R}(-2e + \cos \nu + 2 \cos^2 \nu) - \sin \nu(2+e \cos \nu)\mathcal{S}] \quad (47)$$

where a is the semi-major axis of the orbit, e its eccentricity, i its inclination, Ω the longitude of the ascending node, ω the argument of the perigee and $\ell = n(t - T)$ ⁷ with $n \equiv \sqrt{\mu/a^3}$. Additionally, the true anomaly variation is given by

$$\frac{d\nu}{dt} = \sqrt{\frac{\mu}{a^3(1-e^2)^3}}(1 + e \cos \nu)^2, \quad (48)$$

and does not depend on the perturbing force. The Ω , ω , i and ν angles are shown in the left panel of figure 2.

2.3.3. Summary. This provides all the equations for studying the orbital motion of a satellite in a theory of gravity including a Yukawa interaction together with the Newtonian force. The Lagrange–Gauss equations (43)–(47) can be solved for the secular effects caused by a Yukawa interaction on satellites dynamics, once the perturbing force (37) is known. The latter depends on the shape and mass distribution of the Earth, given by equation (10) through the $y_{\ell m}(r)$ functions, explicitly given in equation (11). As we have already emphasised, the parameter $\rho_{\ell m}$ describing the Earth and (α, λ) describing the non-Newtonian gravity are entangled. This formalism paves the way to many investigations to which we now turn.

3. Worked-out example: N -layer, rotationally symmetric Earth model

This section applies our previous formalism to a simple model of the Earth. It will allow us to better grasp the impact of the Yukawa interaction on the Earth gravitational field and the way it mixes with the usual perturbing effects arising from the shape of the Earth.

To that purpose, we consider a N -layer Earth, where each layer, of radius $R_i(\theta, \xi)$, is homogeneous with density ρ_i , such that

$$\rho(\mathbf{s}\mathbf{u}_{r'}) = \sum_{i=1}^N \rho_i \{ \Theta[s - R_{i-1}(\mathbf{u}_{r'})] - \Theta[s - R_i(\mathbf{u}_{r'})] \}, \quad (49)$$

where $R_0(\mathbf{u}_{r'}) = 0$. In the case $N = 4$, we recover the conventional figure of the Earth's interior divided into inner and outer core, mantle and crust (e.g. [81]); increasing N allows one to approximate better the slow density variations of each of the main layers.

3.1. Monopole and quadrupole

Here, we provide explicit expressions for the first two non-zero spherical harmonics coefficients (monopole and quadrupole), y_{00} and y_{20} , usually called \overline{C}_{00} and \overline{C}_{20} in the literature. Note that with our normalization, $y_{00} = \overline{C}_{00}$ and $y_{20} = \overline{C}_{20}$. The quadrupole y_{20} is linked to the J_2 flattening of the Earth via $J_2 = -\sqrt{5}y_{20}$ if we ignore the rotation of the Earth.

Appendix A derives the expression of $y_{\ell 0}(r)$ under the assumption that the Earth is made of N concentric, homogeneous ellipsoidal, rotationally symmetric layers. The computation involves integrating hypergeometric functions over θ , which can easily be done numerically, but requires further assumptions to allow for an analytic expression. Assuming that the flattening of the Earth layers $f_i = (R_{\text{eq},i} - R_{\text{pole},i})/R_{\text{eq},i}$ are small ($f_i \ll 1$), we can Taylor expand the ϕ_ℓ functions, and we obtain the monopole (at first order in f_i)

⁷Note that this ℓ is not to be confused with the multipole of the spherical harmonics expansion. We will not use it in the remainder of this paper.

$$\begin{aligned}
y_{00}(r) = & \frac{4\pi R_{\oplus}^3}{3M_{\oplus}} \sum_{i=1}^N \rho_i \left[(1-f_i) \frac{R_{\text{eq},i}^3}{R_{\oplus}^3} - (1-f_{i-1}) \frac{R_{\text{eq},i-1}^3}{R_{\oplus}^3} \right] \\
& + \frac{4\pi\alpha}{3M_{\oplus}} e^{-r/\lambda} R_{\oplus}^3 \sum_{i=1}^2 \rho_i \left\{ 3 \frac{\lambda^3}{R_{\oplus}^3} \left[\frac{R_{\text{eq},i}}{\lambda} \cosh \frac{R_{\text{eq},i}}{\lambda} - \left(\frac{f_i R_{\text{eq},i}^2}{3\lambda^2} + 1 \right) \sinh \frac{R_{\text{eq},i}}{\lambda} \right] \right. \\
& \left. - 3 \frac{\lambda^3}{R_{\oplus}^3} \left[\frac{R_{\text{eq},i-1}}{\lambda} \cosh \frac{R_{\text{eq},i-1}}{\lambda} - \left(\frac{f_{i-1} R_{\text{eq},i-1}^2}{3\lambda^2} + 1 \right) \sinh \frac{R_{\text{eq},i-1}}{\lambda} \right] \right\}, \quad (50)
\end{aligned}$$

where the first term is the Newtonian contribution (also computed under the assumption $f_i \ll 1$).

In the simple case of a homogeneous ellipsoid ($N = 1$), equation (50) reduces to

$$y_{00}(r) = 1 + \frac{\alpha}{1-f} \Phi \left(\frac{R_{\oplus}}{\lambda}, f \right) e^{-r/\lambda}, \quad (51)$$

where we used that, for a homogeneous ellipsoid

$$M_{\oplus} = \frac{4}{3} \pi R_{\oplus}^3 \rho (1-f), \quad (52)$$

and where

$$\Phi(x, f) = 3 \frac{x \cosh(x) - \sinh(x)}{x^3} - \frac{\sinh x}{x} f \quad (53)$$

generalises the usual sphere's form factor [3] to an ellipsoid of flatness f . In the case of a homogeneous sphere, we thus recover the result from the direct integration over the sphere [3], and in the case of a two-layer spherical Earth, we recover the expression given in [50]. The Φ function is discussed in appendix C.

Under the same assumption, at first order in f_i , we find the quadrupole

$$\begin{aligned}
y_{20}(r) = & -\frac{8\pi R_{\oplus}^3}{15\sqrt{5}M_{\oplus}} \sum_{i=1}^N \rho_i \left[\frac{R_{\text{eq},i}^5}{R_{\oplus}^5} f_i - \frac{R_{\text{eq},i-1}^5}{R_{\oplus}^5} f_{i-1} \right] + \frac{8\pi\alpha R_{\oplus}^3}{3\sqrt{5}M_{\oplus}} e^{-r/\lambda} \left(3 + 3 \frac{r}{\lambda} + \frac{r^2}{\lambda^2} \right) \\
& \times \sum_{i=1}^N \rho_i \left\{ 3f_i \frac{\lambda^5}{R_{\oplus}^5} \left[\frac{R_{\text{eq},i}}{\lambda} \cosh \frac{R_{\text{eq},i}}{\lambda} - \left(\frac{R_{\text{eq},i}^2}{3\lambda^2} + 1 \right) \sinh \frac{R_{\text{eq},i}}{\lambda} \right] \right. \\
& \left. - 3f_{i-1} \frac{\lambda^5}{R_{\oplus}^5} \left[\frac{R_{\text{eq},i-1}}{\lambda} \cosh \frac{R_{\text{eq},i-1}}{\lambda} - \left(\frac{R_{\text{eq},i-1}^2}{3\lambda^2} + 1 \right) \sinh \frac{R_{\text{eq},i-1}}{\lambda} \right] \right\} \quad (54)
\end{aligned}$$

where the first term is the Newtonian contribution.

For a homogeneous Earth of density ρ and flattening f , equation (54) simplifies to

$$y_{20}(r) = -\frac{2f}{5\sqrt{5}(1-f)} \left[1 - 5\alpha e^{-r/\lambda} \kappa \left(\frac{r}{\lambda} \right) \Phi_2 \left(\frac{R_{\oplus}}{\lambda} \right) \right], \quad (55)$$

where we used equation (52), $\kappa(x) = 3 + 3x + x^2$ and where the function

$$\Phi_2(x) = 3 \frac{x \cosh(x) - (x^2/3 + 1) \sinh(x)}{x^5} \quad (56)$$

is a form factor akin to the Φ function above (see appendix C).

Equations (11), (50) and (54) make the role of the Yukawa term clearer. The coefficients of the potential's spherical harmonic expansion obviously depend on where they are estimated,

through the exponential decrease of the Yukawa interaction with respect to distance. Another major impact is the presence of a form factor, which emerges because Gauss' theorem does not apply to a Yukawa interaction (even for a spherical Earth). In other words, it quantifies the fact that for a short-range Yukawa interaction, regions of the Earth close to the experiment play a bigger part in the gravitational field than regions further away, so that the Yukawa interaction created by an extended body is not equal to the Yukawa interaction created by a point-mass of the same mass as the body's. Hence, measurements of the gravitational field made on the ground, in low earth orbit, or at a greater distance of Earth, will provide different coefficients; we then should be careful when combining different gravity measurements.

In particular, the y_{00} coefficient is not equal to 1 by definition (as in pure Newtonian gravity), but is affected by a supplementary, distance-dependent term $y_{00}(r) = 1 + y_{00}^Y(r)$. Therefore, it should not be set *a priori* to 1 when measuring the Earth potential, but estimated like other coefficients. Actually, estimating it is akin to estimating an effective Newton constant that depends on the distance to the centre of the Earth, with the 'real' Newton constant being estimated by Cavendish-like experiments on the ground.

Similar conclusions can be drawn for the y_{20} term. It is affected by the Yukawa term, whose value will depend on α and on the ratio between the Yukawa range and the characteristic scales of the experiment (r and R_\oplus), with a maximum effect around $\lambda \sim r$. As shown in appendix C, $\Phi_2(R_\oplus/\lambda)$ is of order a few percent in this regime, so that the Yukawa contribution to the y_{20} measured by a satellite orbiting the Earth at a low altitude amounts to a few percent of α .

We should finally note that under the assumptions used to obtain equations (50) and (54), higher terms ($y_{40}, y_{60}...$) vanish. We need to Taylor expand to higher orders in f_i to get non-zero coefficients. We checked that the approximations (50)–(54) provide accurate numbers (up to the percent accuracy) by comparing them to the numerical integration of equation (A.2) and the corresponding equation for the Newtonian part.

3.2. Gravitational acceleration

The expressions above for the first spherical harmonic coefficients can be inserted in equations (20) and (30) to derive the expression of the gravitational acceleration of an N -layer rotationally symmetric Earth (for which all $m \neq 0$ multipoles cancel). However, this requires tedious algebra, so we will restrain ourselves to the homogeneous ellipsoid case $N = 1$, and consider that only the $\ell = 0$ and $\ell = 2$ multipoles are non-negligible (this is a reasonable assumption since the measured J_2 is 1000 times higher than the following spherical harmonic coefficients). We find that the norm of the radial and tangential components are

$$g_{||}(r, \theta, \xi) = -\frac{GM_{\text{tot}}}{r^2} \left[1 + \frac{\alpha}{1-f} \left(1 + \frac{r}{\lambda} \right) e^{-r/\lambda} \Phi \left(\frac{R_\oplus}{\lambda}, f \right) \right] - \frac{3\sqrt{5}}{2} \frac{GM_{\text{tot}}}{r^2} z_{20}(r) (3 \cos^2 \theta - 1) \quad (57)$$

where we made $z_{00}(r)$ explicit, and

$$|g_{\perp}(r, \theta, \xi)| = \sqrt{\frac{5}{2}} \frac{GM_\oplus}{r^2} \left(\frac{R_\oplus}{r} \right)^2 |y_{20}(r)| = \frac{1}{\sqrt{2}} \frac{GM_\oplus}{r^2} \left(\frac{R_\oplus}{r} \right)^2 |J_{20}(r)| \quad (58)$$

where we used that

$$\pm_1 Y_{20}(\theta, \xi) = \mp \frac{1}{4} \sqrt{\frac{15}{2\pi}} \sin 2\theta. \quad (59)$$

Note that the J_2 contribution is formally identical to the Newtonian case, although now J_2 is a function of r . Following the rotational symmetry of our model, those components are indeed independent of the longitude ξ . We provide order-of-magnitude estimates of the Yukawa accelerations and compare them with usual gravitational and non-gravitational perturbations, for a homogeneous Earth, in section 5.2.

3.3. Perturbations and secular effects on satellite dynamics

The Lagrange–Gauss equations (equations (43)–(47)) can be trivially obtained for a N -layer rotationally symmetric Earth in a way similar to that used to get the gravitational acceleration above, by inserting equations (A.7) and (A.8) in (40)–(42). As for the gravitational acceleration, we restrain ourselves to the homogeneous ellipsoid. In this case, the components of the perturbing force are

$$\mathcal{R}(r, \theta, \xi) = -\frac{GM_{\text{tot}}}{r^2} \left[\frac{\alpha}{1-f} \left(1 + \frac{r}{\lambda}\right) e^{-r/\lambda} \Phi\left(\frac{R_{\oplus}}{\lambda}, f\right) + \frac{3\sqrt{5}}{2} z_{20}(r)(3 \cos^2 \theta - 1) \right] \quad (60)$$

$$\mathcal{S}(r, \theta, \xi) = \frac{3}{2\sqrt{2\pi}} \frac{GM_{\text{tot}}}{r^2} \left(\frac{R_{\oplus}}{r}\right)^2 J_{20}(r) \sin 2\theta \sin i \quad (61)$$

$$\mathcal{W}(r, \theta, \xi) = -\frac{3}{2\sqrt{2\pi}} \frac{GM_{\text{tot}}}{r^2} \left(\frac{R_{\oplus}}{r}\right)^2 J_{20}(r) \sin 2\theta \cos i. \quad (62)$$

As was the case for the gravitational acceleration, those components are indeed independent of the longitude ξ .

Although we do not solve the Lagrange–Gauss equations in this paper, it is instructive to express the components of the perturbing force as a function of the satellite’s unperturbed orbit’s Keplerian parameters (which is required to solve the equations). Using that $r = a(1 - e^2)/(1 + e \cos \nu)$ and that (following some algebra based on [82])

$$\sin 2\theta = 2 \sin(\omega + \nu) \sin i \sqrt{1 - \sin^2(\omega + \nu) \sin^2 i} \quad (63)$$

$$\cos \theta = \sin(\omega + \nu) \sin i, \quad (64)$$

we find that

$$\begin{aligned} \mathcal{R} = & GM_{\text{tot}} \frac{(1 + e \cos \nu)^2}{a^2(1 - e^2)^2} \left\{ \frac{3}{5} \left(\frac{R_{\oplus}(1 + e \cos \nu)}{a(1 - e^2)}\right)^2 \frac{f}{1-f} (3 \sin^2(\omega + \nu) \sin^2 i - 1) \right. \\ & - \frac{\alpha}{1-f} \exp\left(-\frac{a(1 - e^2)}{\lambda(1 + e \cos \nu)}\right) \left[\left(1 + \frac{a(1 - e^2)}{\lambda(1 + e \cos \nu)}\right) \Phi\left(\frac{R_{\oplus}}{\lambda}, f\right) \right. \\ & \left. \left. + 3 \left(\frac{R_{\oplus}(1 + e \cos \nu)}{a(1 - e^2)}\right)^2 f \sigma \left(\frac{a(1 - e^2)}{\lambda(1 + e \cos \nu)}\right) \Phi_2\left(\frac{R_{\oplus}}{\lambda}\right) (3 \sin^2(\omega + \nu) \sin^2 i - 1) \right] \right\} \quad (65) \end{aligned}$$

$$\begin{aligned} \mathcal{S} = & \frac{6}{5\sqrt{2\pi}} GM_{\text{tot}} R_{\oplus}^2 \left(\frac{1 + e \cos \nu}{a(1 - e^2)}\right)^4 \frac{f}{1-f} \sin(\omega + \nu) \sin^2 i \sqrt{1 - \sin^2(\omega + \nu) \sin^2 i} \\ & \times \left[1 - 5\alpha \exp\left(-\frac{a(1 - e^2)}{\lambda(1 + e \cos \nu)}\right) \kappa \left(\frac{a(1 - e^2)}{\lambda(1 + e \cos \nu)}\right) \Phi_2\left(\frac{R_{\oplus}}{\lambda}\right) \right] \quad (66) \end{aligned}$$

$$\mathcal{W} = -\frac{3}{5\sqrt{2\pi}}GM_{\text{tot}}R_{\oplus}^2 \left(\frac{1+e\cos\nu}{a(1-e^2)}\right)^4 \frac{f}{1-f} \sin(\omega+\nu) \sin(2i) \sqrt{1-\sin^2(\omega+\nu)\sin^2 i} \\ \times \left[1 - 5\alpha \exp\left(-\frac{a(1-e^2)}{\lambda(1+e\cos\nu)}\right) \kappa\left(\frac{a(1-e^2)}{\lambda(1+e\cos\nu)}\right) \Phi_2\left(\frac{R_{\oplus}}{\lambda}\right)\right], \quad (67)$$

where $\sigma(x) = 3 + 3x + 2/3x^2 - x^3/3$ and $\kappa(x)$ is defined above.

Equations (65)–(67) clearly show the impact of a Yukawa interaction on a satellite's orbit. The first line of each equation provides the Newtonian part, while the Yukawa contribution is shown in the remaining terms. Not surprisingly, the Yukawa interaction impacts the perturbing force in a similar way it impacts the spherical harmonic coefficients (see section 3.1), through form factors and a complex radial dependence that couples an exponential decay with polynomials $\sigma(r/\lambda)$ and $\kappa(r/\lambda)$ which tend to maximise the effect for $r \sim \lambda$.

As aforementioned, it is well known that the J_2 zonal term sources a precession of the line of nodes through the \mathcal{S} and \mathcal{W} components of the perturbing force in the pure Newtonian case [80]. Equations (66) and (67) show that a Yukawa interaction adds up to this effect. Its impact will depend on the strength α of the Yukawa interaction, but also on how its range λ compares to the orbit's semi-major axis and to the radius of the Earth. We can therefore expect to measure different rates of precession for satellites orbiting at different altitudes. Even for a homogeneous sphere ($f = 0$), although the tangential components vanish $\mathcal{S} = \mathcal{W} = 0$, the radial component remains affected by the form factor of the Earth: it simplifies to contain only the usual exponential decay coupled to the Earth's form factor.

We can therefore expect observable effects of the coupling of the Yukawa interaction to the shape of the Earth on the dynamics of satellites. Hence, not taking the shape of the Earth into account to predict the very effects that are looked for to constrain a Yukawa interaction in orbit ends up in wrong predictions, and is likely to prevent reliable constraints.

In other words, it is incorrect to consider the perturbation due to the Yukawa interaction as a purely radial interaction sourced by a point-mass when working with satellite dynamics. Most existing works that aim to constrain a Yukawa interaction with satellites dynamics focused on measuring the perigee precession under this incorrect assumption [83–87]. Nevertheless, although those works miss the contribution of the tangential components of the Yukawa interaction, we should note that since they focus their analyses on $\lambda \approx$ a few R_{\oplus} (where $\Phi \approx 1$, see figure C1) their simplifying assumption only marginally affects the radial component of the perturbation. However, if aiming to constrain short range Yukawa interaction, one has to take into account the fact that the Earth is an extended body, since in this regime the form factor is significantly greater than 1 and hence dramatically impacts the Gauss equations.

4. Entanglement of geodesy and gravitation experiments in the Earth gravitational field

The discussion above shows that modified gravity affects the spherical harmonic coefficients of the Earth gravitational field, and in turn gravity observables (such as the motion of satellites). Although this comes hardly as a surprise, to the best of our knowledge, this has never been seriously taken into account, neither to survey and invert the Earth gravity (to estimate the shape of the Earth) nor to constrain the Yukawa parameters in orbit. In the former case, geophysicists assume that the Earth gravitational field is described by Newtonian gravity (hence, they ignore any Yukawa deviation altogether, see e.g. [57, 63]). In the latter case, for a Yukawa-like modification of gravitation, its effects on Keplerian parameters are most often computed under the assumption that the Yukawa acceleration is sourced by a point-mass Earth

[83, 84, 86, 88], or at best by a uniform, spherical Earth [50]. And yet, a Yukawa deviation has explicit effects such as a dependence of spherical harmonic coefficients on the radial distance from the Earth. Conversely, our imperfect knowledge of the Earth geometry may impact experimental constraints of the Yukawa parameters.

Hagiwara [89] investigated the effect of a non-Newtonian contribution to the Earth gravitational field on geodesy experiments. He found that non-Newtonian terms could safely be ignored to measure the Earth geoid. However, he was considering 1980s experiments precision, and as modern in-orbit gravity experiments such as GRACE, GOCE and GRACE-FO bring unprecedented precision on the measurement of the Earth gravitational field, it is timely to revisit his work. This is the purpose of this section and the next one. In this section, we first show the limitations that modified gravity brings to geodesy measurements, then those that geodesy uncertainties bring to tests of modified gravity, before giving recommendations on how to go beyond current limitations. Order-of-magnitude estimates are then given in section 5.

Figure 3 shows the entanglement between modified gravity (illustrated with a Yukawa interaction) and the shape of the Earth when testing gravity or measuring the Earth geometry with experiments in the Earth gravity. For simplicity, we still ignore relativistic effects, the influence of the Moon and other planets and the rotation of the Earth. We will compare the contribution of a Yukawa interaction with those effects in section 5.2; a rigorous data analysis should of course take all known effects into account (i.e. correct for relativistic and Newtonian tidal effects before constraining the Yukawa interaction). The system of interest is the Earth, whose geometry is coupled to a possible Yukawa potential; we aim to measure the Earth geometry and/or the Yukawa parameters. In the sense of Kant, they are noumenons (the ‘true’ system), *a priori* not accessible to human senses, but which we can approximate by analyzing observable ‘phenomenons’. Those phenomenons can be as diverse as the value of the gravitational field acceleration \mathbf{g} , its gradient $[T]$, the equivalence principle, or the secular variations of Keplerian parameters (perigee drift $\Delta\omega$, regression of the line of nodes $\Delta\Omega$, variation of the eccentricity Δe). Experiments provide us with ‘measurements’ of those phenomenons, that are affected by statistical and systematic uncertainties. For instance, GOCE measured the gravitational gradient $[T]$, LAGEOS measured the perigee drift $\Delta\omega$ and the regression of the line of nodes $\Delta\Omega$, and MICROSCOPE tested the weak equivalence principle. We may perform several measurements (each with its own expected value for the phenomenons under scrutiny, and each with its own uncertainties—stacked boxes in the figure), that we can then combine, e.g. simply by averaging their individual results ($\langle \dots \rangle$ is the ensemble average). Finally, those measurements can be used under some hypotheses and with some priors Π on parameters to get estimates (possibly biased, and likely up to a given estimation error) of the underlying ‘true’ parameters. The three boxes in the lower part of the figure show three different possible uses of Earth gravity measurements: geodesy (hypothesis H1—section 4.1), tests of gravity (hypothesis H2—section 4.2) and simultaneous geodesy and tests of gravity (hypothesis H3—section 4.3).

In this section, based on figure 3, we quantify the limitations on parameter estimations given some hypotheses. We do not try to be exhaustive and only give examples based on the measurement of the Newtonian spherical harmonic coefficients (section 4.1) and on the estimation of the Yukawa strength for a given range λ from the combination of two satellite measurements (section 4.2). Section 4.3 discusses how to go beyond the limitations shown in sections 4.1 and 4.2 for modified gravity experiments. Our discussion can be generalised to other observables (e.g. secular variations of Keplerian parameters), but we refrain from providing a full analysis of all possible experiments. Such analyses shall be presented in future works.

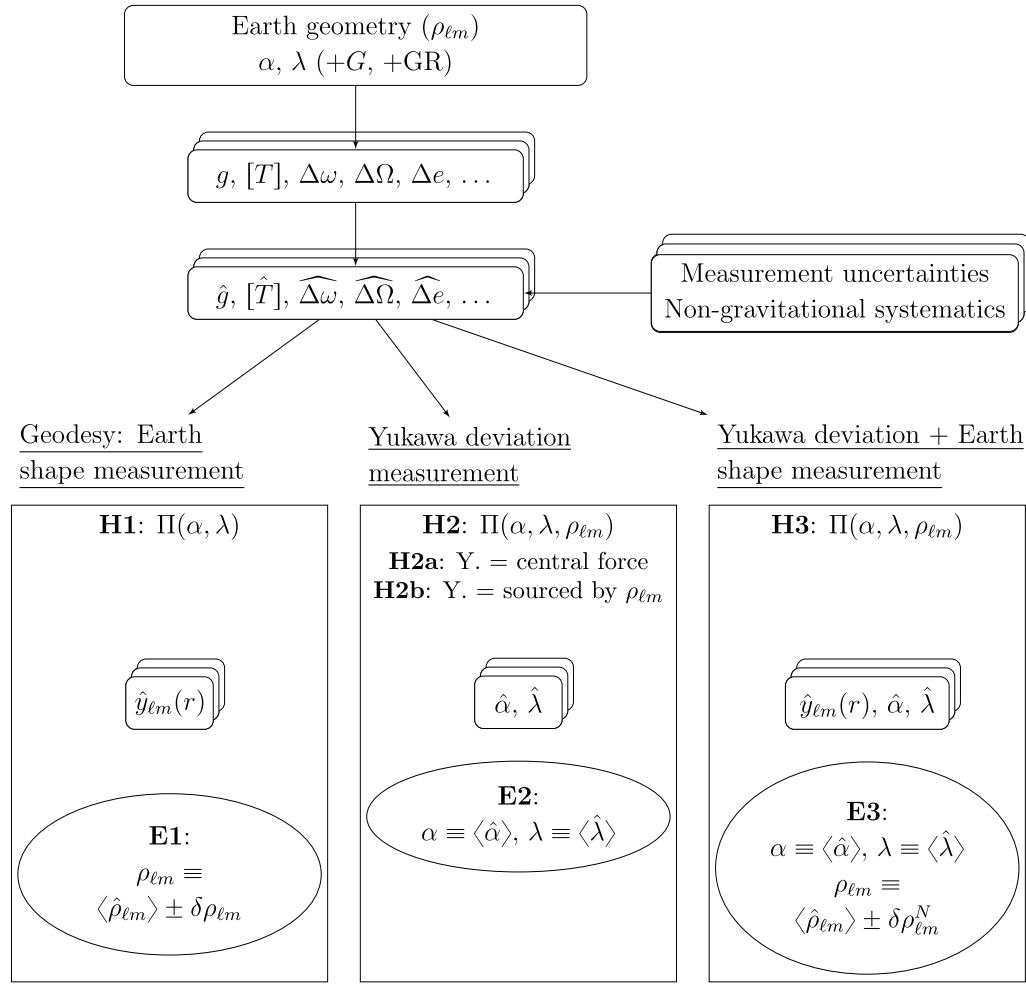


Figure 3. Gravity experiments in the Earth gravitational field. The Earth (universal) geometry as described by the density spherical harmonics coefficients $\rho_{\ell m}$ (equation (10)), the gravitation constant and modified gravity parameters are unavailable to our senses (noumenons); they are the parameters of the theoretical model that can be used to try to know them. They can be observed through phenomenons (gravity acceleration, secular variations of satellites’ osculating parameters) whose values depend on the values of the parameters of the model. Measurements provide us with estimates of those phenomenons (affected by statistical and systematic uncertainties). Depending on what hypotheses we make, we can use those measurements to estimate the parameters of the model: geodesy (H1), modified gravity experiments (H2), or both (H3); the estimates E1–E3 may be biased and known with some error depending on the hypothesis made.

We note measurements and estimates with a hat: e.g. $\hat{\alpha}$ is the estimate of the Yukawa interaction strength. Modeled quantities are noted with a tilde: e.g. $\tilde{\alpha}$ is the strength of the Yukawa interaction for some *a priori* model. We use the term ‘prior’ loosely to denote an *a priori*, possibly subjective information on a parameter, and do not restrict its use to the Bayesian ‘prior probability density function’.

4.1. Impact of Yukawa interaction on geodesy measurements (H1)

Geodesy surveys are shown in figure 3 by the left-hand-side panel. They aim to map the Earth geometry and mass distribution, as well as their time variations (estimates E1) through the measurement of the static and/or variable gravitational field [56–63]: their goal is hence to estimate the spherical harmonics coefficients $\rho_{\ell m}(s)$ of the Earth density, as defined in equation (10).

Let us consider a satellite gravity survey performed at a distance r from the centre of the Earth. The survey provides estimates of the coefficients $y_{\ell m}$ of a spherical harmonic expansion, *a priori* independently of any underlying gravity model (as long as the Earth gravitational potential in a modified gravity model can be expanded in spherical harmonics): in our case, they contain both a Newtonian and a Yukawa contribution.

A gravity model hypothesis H1 is then required to extract $\rho_{\ell m}$ from the measured $\hat{y}_{\ell m}$. It can either be a pure Newtonian field, or explicitly contain modified gravity. In the former case, $\hat{y}_{\ell m}$ is supposed to be given by equation (8); in the latter case, it is supposed to be given by equation (11). If modified gravity is considered, the best way to proceed is the latter: invert equation (11) with some prior $\Pi(\alpha, \lambda)$ on the Yukawa interaction to obtain $\rho_{\ell m}$. However, to the best of our knowledge, all geodesy works use a Newtonian hypothesis and invert equation (8) (e.g. [90, 91]). In this case, a non-zero Yukawa contribution will contaminate the analysis. A possible way to use the existing inversion codes based on Newtonian gravity is then to consider the Yukawa contribution as a systematic error, and just remove it from the estimated $\hat{y}_{\ell m}$ to then invert an estimated Newtonian coefficient. We thus assume a prior on the Yukawa parameters, which may be biased ($E(\tilde{\alpha}) = \alpha + \delta\alpha$, $E(\tilde{\lambda}) = \lambda + \delta\lambda$), where (α, λ) are the true values and $(\delta\alpha, \delta\lambda)$ are the prior's bias; we finally assume some uncertainty ($\text{Var}(\tilde{\alpha})$, $\text{Var}(\tilde{\lambda})$) on our prior. The Newtonian coefficient estimator then reads

$$\hat{y}_{\ell m}^N = \hat{y}_{\ell m} - \tilde{\alpha} \widetilde{f_{\ell}(r, \lambda)} q_{\ell m}^Y / q_{00}^N \quad (68)$$

where the function $f_{\ell}(r, \lambda) = \mathcal{B}_{\ell}(r/\lambda)/(2\ell + 1)$ encapsulates the prior on λ (which affects the gravitational field model in a non-trivial way that we do not attempt to compute) and the quantities

$$q_{\ell m}^N = \int s^2 \left(\frac{s}{R_{\oplus}} \right)^{\ell} \rho_{\ell m}(s) ds \quad (69)$$

$$q_{\ell m}^Y = \int s^2 \left(\frac{s}{R_{\oplus}} \right)^{\ell} \rho_{\ell m}(s) \mathcal{A}_{\ell} \left(\frac{s}{\lambda} \right) ds \quad (70)$$

are the integrals over the volume of the Earth that appear in equations (8) and (9), whose dependence on the geoid and mass density are not yet important, but will be developed below. In the remainder of this section, we do not attempt to obtain $\rho_{\ell m}$, but use $\hat{y}_{\ell m}^N$ as a proxy. Note that trivially, $q_{00}^N = M_{\oplus}$.

The expected value and variance of the estimator (68) are

$$E(\hat{y}_{\ell m}^N) = y_{\ell m}^N - \alpha \delta \left[f_{\ell}(r, \lambda) \frac{q_{\ell m}^Y}{q_{00}^N} \right] - \delta \alpha \left(f_{\ell}(r, \lambda) \frac{q_{\ell m}^Y}{q_{00}^N} \right) - \delta \alpha \delta \left[f_{\ell}(r, \lambda) \frac{q_{\ell m}^Y}{q_{00}^N} \right] \quad (71)$$

and

$$\text{Var}(\hat{y}_{\ell m}^N) = \text{Var}(\hat{y}_{\ell m}) + \tilde{\alpha}^2 \text{Var}(\widetilde{f_{\ell}(r, \lambda)} \frac{q_{\ell m}^Y}{q_{00}^N}) + \left(\widetilde{f_{\ell}(r, \lambda)} \frac{q_{\ell m}^Y}{q_{00}^N} \right)^2 \text{Var}(\tilde{\alpha}) + \text{Var}(\tilde{\alpha}) \text{Var} \left(\widetilde{f_{\ell}(r, \lambda)} \frac{q_{\ell m}^Y}{q_{00}^N} \right) \quad (72)$$

where we assume that the measurement itself is unbiased ($\mathbb{E}(\hat{y}_{\ell m}) = y_{\ell m}$), that it is independent of the prior on the Yukawa interaction and where, for clarity, we ignore all other possible systematic errors (e.g. solar radiation pressure, atmospheric drag, tidal effects, mass motion on the Earth surface...).

We should also note that beside a prior on the Yukawa interaction, a prior on the Earth mass distribution is implicitly used in $f_{\ell}(r, \lambda) \widetilde{q_{\ell m}^Y} / q_{00}^N$ (see equation (70)). It may as well come from experiments completely independent of the gravitational field (e.g. seismology surveys) or from gravitational field measurements, through the estimation of the spherical harmonic coefficients. In the latter case, the problem becomes non-linear, since the prior is based on knowledge similar to what we wish to measure. Although we should keep that in mind, we ignore this aspect and assume that the prior is indeed uncorrelated with the measurement.

Equations (71) and (72) allow us to conclude on the effect of a Yukawa interaction on the estimation of $\hat{y}_{\ell m}^N$. Equation (71) shows that a prior on the Yukawa interaction too far from the real characteristics of the Yukawa interaction (or simply ignoring the possibility of a Yukawa interaction if it actually exists) leads to a biased estimate of the Newtonian contribution to the Earth gravitational field. Equation (72) shows that a physically-motivated prior increases the variance of the estimator (i.e. which is not anymore equal to the variance of the measured $\hat{y}_{\ell m}$ as when ignoring the possibility of a Yukawa interaction): this is the price to pay to have an unbiased estimate $\hat{y}_{\ell m}^N$. With those observations in mind, one must be aware that using (as usual) the Newtonian framework for geodesy (i.e. assuming $\alpha = 0$ and $\delta\alpha = 0$) may lead to biased estimations of the Earth geometry if in reality $\alpha \neq 0$; furthermore, in this case, the uncertainties on the estimates are underestimated.

We can also note that the bias and variance of the $\hat{y}_{\ell m}^N$ estimator depend on the distance of the experiment to the centre of the Earth through the radial dependence of $f_{\ell}(r, \lambda)$. Therefore, if modified gravity is real, then under the incorrect hypothesis that gravity is purely Newtonian (in which case it is assumed that the measured coefficients $\hat{y}_{\ell m} = \hat{y}_{\ell m}^N$), we may expect that different estimators $\hat{y}_{\ell m}^N$ obtained at different altitudes will be inconsistent, each with a non-zero bias and an underestimated variance coming from an incorrect hypothesis, even if the measurements are perfect. This is reminiscent of the inconsistent measurements of the y_{20} parameter between the GOCE-only, GRACE-only and EIGEN-6C models mentioned in the introduction. Answering the question of whether the tension between those measurements stems from data analyses or from the presence of a Yukawa interaction is beyond the scope of this paper, but could be done by re-analyzing all the concerned data with a model that takes into account the possible presence of a Yukawa potential and using realistic priors on the Yukawa interaction⁸.

Moreover, as shown by equation (72), the Yukawa interaction increases the variance of the $\hat{y}_{\ell m}$ estimator for non-circular orbits through the $f_{\ell}(r, \lambda)$'s dependence on r . This increase is also non-zero when combining several measurements made with satellites at different altitudes.

We give order-of-magnitude estimates of the effect of a non-zero Yukawa interaction on the $y_{\ell m}$ coefficients in section 5.

⁸ Quick-and-dirty constraints of the Yukawa interaction from the 700 σ tension mentioned in the introduction provide results highly inconsistent with published constraints. The most likely reason is an incorrect error analysis from gravity surveys. See section 4.2 for a discussion on how to constrain the Yukawa interaction by combining GOCE and GRACE measurements.

4.2. Impact of Earth's gravity and shape errors on the measurement of Yukawa parameters (H2)

Tests of gravity are shown by the middle panel of figure 3. The aim is to measure the Yukawa interaction parameters E2 (other applications can be e.g. to measure any relativistic effect) under some hypotheses H2 and priors on the Yukawa parameters (α, λ) and/or the Earth shape $(\rho_{\ell m})$ and/or a direct measurement of the gravitational field with no explicit discrimination between the Newtonian and Yukawa contributions $(y_{\ell m})$. An extra prior consists in how the Yukawa interaction is modeled. Independently of the assumptions on the Newtonian gravitational field, we can either assume that it is sourced by a point-mass-like Earth (H2a) or by the full, complex shape of the Earth (H2b). As aforementioned, to our knowledge, most works [83–85, 88] use the H2a hypothesis, when a handful either briefly discuss or effectively use a spherical Earth (simplified H2b hypothesis—[50, 87]), but we could not find any use of a non-spherical Earth to constrain a Yukawa interaction. Similarly, to our knowledge, no prior on α nor λ has ever been used, although it is common practice to consider at least the measured y_{20} zonal term of the Earth gravitational field to correct for its Newtonian contribution.

Several observables can be used to constrain a Yukawa interaction with experiments in the Earth gravitational field. Published works use the secular variation of Keplerian parameters of orbiting satellites like LAGEOS I and II [83–85, 88] under the H2a hypothesis (the Yukawa interaction is sourced by a point-mass Earth), or the measured (absence of) violation of the equivalence principle [50]. Given the link between the spherical harmonics coefficients and the Yukawa interaction, we could also think of constraining the Yukawa parameters directly from the measured $\hat{y}_{\ell m}$, either from a single experiment or from a combination of experiments and/or different $\hat{y}_{\ell m}$. To the best of our knowledge, such an analysis, based on hypothesis H2b, has never been performed. As already mentioned, we do not try to be exhaustive, and will only provide details for one possible way to constrain the Yukawa parameter. Therefore, in the remainder of this section, we propose to combine the $\hat{y}_{\ell m}$ coefficient measured by two experiments at different altitudes (for a given pair (ℓ, m)) and show how it can shed light on the Yukawa interaction.

Let us assume that $y_{\ell m}$ is estimated by two different experiments at distances r_1 and r_2 from the centre of the Earth, to provide two estimators $\hat{y}_{\ell m,1}$ and $\hat{y}_{\ell m,2}$. Using equation (11), we can form the following estimator of α , for a given range λ , from the difference between the two $\hat{y}_{\ell m}$ estimators:

$$\hat{\alpha}_{\ell m} = \frac{q_{00}^N(\tilde{\rho}(\mathbf{x}), \tilde{h}(\mathbf{x}))}{[f_{\ell}(r_1, \lambda) - f_{\ell}(r_2, \lambda)]q_{\ell m}^Y(\tilde{\rho}(\mathbf{x}), \tilde{h}(\mathbf{x}))} (\hat{y}_{\ell m,1} - \hat{y}_{\ell m,2}), \quad (73)$$

where the functions $q_{\ell m}^N$ and $q_{\ell m}^Y$ were defined above and $q_{00}^N = M_{\oplus}$; we now write their explicit dependence on the mass density distribution $\rho(\mathbf{x})$ and on the geoid $h(\mathbf{x})$ —just another way to see the information contained in $\rho_{\ell m}(s)$. This estimator is clearly Earth-model-dependent. Although different in its purpose, it is related to Wagner and McAdoo's error factor [69]; in that case, it serves as a way to calibrate different (Newtonian) gravitational field models, while we treat it as a measure of non-Newtonian deviations. We should also note that a better estimator would be to average (73) over all (ℓ, m) pairs, but for the sake of clarity, we only discuss (73) in the following.

The prior on the Earth model propagates in a non-trivial way to a bias and uncertainty on the $q_{\ell m}$ functions. We do not try to perform this computation (which should be done numerically and requires specifying a model for the Earth), but assume that instead of dealing with priors on the mass distribution and the geoid, we have (biased) priors on the $q_{\ell m}$ functions (for clarity, we drop the ρ and h dependences), such as $E(\tilde{q}_{\ell m}) = q_{\ell m} + \delta q_{\ell m}$, which applies both

to the Newtonian and to the Yukawa contributions to the gravitational field. Additionally, we assume that the Earth model is based only on data independent of the gravitational field (e.g. seismology surveys); otherwise, the problem is non-linear since (as seen in section 4.1) the model depends on our knowledge of the Yukawa interaction.

Under those hypotheses, the expected value of the $\hat{\alpha}_{\ell m}$ estimator is

$$E(\hat{\alpha}_{\ell m}) = \frac{q_{\ell m}^Y}{q_{\ell m}^Y + \delta q_{\ell m}^Y} \left\{ \alpha_{\ell m} + \frac{q_{00}^N}{[f_\ell(r_1, \lambda) - f_\ell(r_2, \lambda)] q_{\ell m}^Y} \left[\left(1 + \frac{\delta q_{00}^N}{q_{00}^N} \right) (\delta y_{\ell m,1} - \delta y_{\ell m,2}) + \frac{\delta q_{00}^N}{q_{00}^N} (y_{\ell m,1} - y_{\ell m,2}) \right] \right\}. \quad (74)$$

We should note that the bias in the measured $\hat{y}_{\ell m}$ may not be the same for the two satellites. It is then apparent that a biased $\hat{y}_{\ell m}$ contributes an additive bias to $\hat{\alpha}_{\ell m}$, while a biased Earth model contributes both an additive and a multiplicative bias to $\hat{\alpha}_{\ell m}$. These biases can be minimised by minimizing $\delta y_{\ell m}$ and $\delta q_{\ell m}^{N,Y}$ (i.e. improving the accuracy of the $y_{\ell m}$ measurement and of the Earth model).

The variance of this estimator can then be shown to be

$$\begin{aligned} \text{Var}(\hat{\alpha}_{\ell m}) &= \left(\frac{q_{00}^N + \delta q_{00}^N}{[f_\ell(r_1, \lambda) - f_\ell(r_2, \lambda)] (q_{\ell m}^Y + \delta q_{\ell m}^Y)} \right)^2 \\ &\times \left[\left(1 + \frac{\text{Var}(\tilde{q}_{00}^N)}{(q_{00}^N + \delta q_{00}^N)^2} - 2 \frac{\text{Cov}(\tilde{q}_{00}^N, \tilde{q}_{\ell m}^Y)}{(q_{00}^N + \delta q_{00}^N)(q_{\ell m}^Y + \delta q_{\ell m}^Y)} + \frac{\text{Var}(\tilde{q}_{\ell m}^Y)}{(q_{\ell m}^Y + \delta q_{\ell m}^N)^2} \right) [\text{Var}(\hat{y}_{\ell m,1}) + \text{Var}(\hat{y}_{\ell m,2})] \right. \\ &\left. + \left(\frac{\text{Var}(\tilde{q}_{00}^N)}{(q_{00}^N + \delta q_{00}^N)^2} - 2 \frac{\text{Cov}(\tilde{q}_{00}^N, \tilde{q}_{\ell m}^Y)}{(q_{00}^N + \delta q_{00}^N)(q_{\ell m}^Y + \delta q_{\ell m}^Y)} + \frac{\text{Var}(\tilde{q}_{\ell m}^Y)}{(q_{\ell m}^Y + \delta q_{\ell m}^N)^2} \right) (y_{\ell m,1} + \delta y_{\ell m,1} - y_{\ell m,2} - \delta y_{\ell m,2})^2 \right]. \quad (75) \end{aligned}$$

Now assuming that the spherical harmonics coefficients measurements are unbiased and the biases on the Earth model are small, then at first order, equation (75) reads

$$\begin{aligned} \text{Var}(\hat{\alpha}_{\ell m}) &\approx \left(\frac{q_{00}^N}{[f_\ell(r_1, \lambda) - f_\ell(r_2, \lambda)] q_{\ell m}^Y} \right)^2 \left(1 - 2 \frac{\delta q_{\ell m}^Y}{q_{\ell m}^Y} + 2 \frac{\delta q_{00}^N}{q_{00}^N} \right) \\ &\times \left\{ \left[1 + \frac{\text{Var}(\tilde{q}_{00}^N)}{(q_{00}^N)^2} \left(1 - 2 \frac{\delta q_{00}^N}{q_{00}^N} \right) - 2 \frac{\text{Cov}(\tilde{q}_{00}^N, \tilde{q}_{\ell m}^Y)}{q_{00}^N q_{\ell m}^Y} \left(1 - \frac{\delta q_{\ell m}^Y}{q_{\ell m}^Y} - \frac{\delta q_{00}^N}{q_{00}^N} \right) \right. \right. \\ &\quad \left. \left. + \frac{\text{Var}(\tilde{q}_{\ell m}^Y)}{(q_{\ell m}^Y)^2} \left(1 - 2 \frac{\delta q_{\ell m}^Y}{q_{\ell m}^Y} \right) \right] [\text{Var}(\hat{y}_{\ell m,1}) + \text{Var}(\hat{y}_{\ell m,2})] \right. \\ &\quad \left. + \left[\frac{\text{Var}(\tilde{q}_{00}^N)}{(q_{00}^N)^2} \left(1 - 2 \frac{\delta q_{00}^N}{q_{00}^N} \right) - 2 \frac{\text{Cov}(\tilde{q}_{00}^N, \tilde{q}_{\ell m}^Y)}{q_{00}^N q_{\ell m}^Y} \left(1 - \frac{\delta q_{\ell m}^Y}{q_{\ell m}^Y} - \frac{\delta q_{00}^N}{q_{00}^N} \right) \right. \right. \\ &\quad \left. \left. + \frac{\text{Var}(\tilde{q}_{\ell m}^Y)}{(q_{\ell m}^Y)^2} \left(1 - 2 \frac{\delta q_{\ell m}^Y}{q_{\ell m}^Y} \right) \right] (y_{\ell m,1} - y_{\ell m,2})^2 \right\}. \quad (76) \end{aligned}$$

Similarly to what happened for the expected value, equations (75) and (76) show that several contributions make up the variance of $\hat{\alpha}_{\ell m}$: the variance and bias of the measured $\hat{y}_{\ell m}$ as well as the uncertainties and biases on the Earth model used for the analysis (which go in the H2b hypotheses of figure 3). In particular, a biased Earth model affects the variance of $\hat{\alpha}_{\ell m}$ in a non-trivial way, whereby the bias on the mass (remember that $q_{00}^N = M_\oplus$) may or may not be counterbalanced by the bias on $q_{\ell m}^Y$, so that the impact of the Earth model bias will depend on

the multipole (ℓ, m) considered for the analysis. However, exploring the details of this question is far beyond the scope of this paper.

Equations (74)–(76) are the bases for a signal-to-noise analysis to optimise the significance of the estimation of α for a given λ , for a given mission made of two satellites; for example, given a model of the Earth, it allows us to define the satellites' altitude or the optimal $y_{\ell m}$ that should be used to constrain α with a given precision and accuracy. Furthermore, by comparing both contributions to the variance, it directly provides clues about the limitations brought by our imperfect knowledge of the Earth, and can therefore set a lower bound on the measurement precision and accuracy required to reach a given precision on the Yukawa parameters.

Such an analysis, linked to a given mission concept, should be done numerically, and goes beyond the scope of this paper. Nevertheless, we can give some crude order of magnitude estimate. More realistic estimates for equations (74)–(76) are given in section 5. For instance, ignoring the covariance between q_{00}^N and $q_{\ell m}^Y$ and the bias on the Earth model, we can compare the relative contribution to the variance of the $\hat{y}_{\ell m}$ measurements and of our imperfect model of the Earth. For instance, considering $(\ell, m) = (2, 0)$, and assuming that $\text{Var}(\tilde{q}_{20}^Y)/q_{20}^Y \approx \text{Var}(y_{20})/y_{20} \approx 10^{-16}$ [57] and that $\text{Var}(q_{00}^N)/q_{00}^N = \text{Var}(M_{\oplus})/M_{\oplus} \approx 10^{-8}$, we find that the variance of the Yukawa strength estimator is limited by the y_{20} measurement if $\text{Var}(\hat{y}_{20}) > 10^{-8}(y_{20,1} - y_{20,2})$. Further assuming that $y_{20,1} - y_{20,2} \sim 10^{-13}$,⁹ we find that unless we have an improved Earth model, the error on $\hat{\alpha}$ will saturate as soon as we measure y_{20} with a precision (square root of the variance) better than 10^{-17} . As the current measured uncertainty on y_{20} is of order 10^{-12} [62], this crude order of magnitude estimate shows that were we to use the difference of J_2 between two satellite measurements made at different altitudes, we can improve the instrumental precision by five orders of magnitude before our constrain on α would become dominated by the Earth model. The limitation due to the Earth model would be even farther down if $y_{20,1} - y_{20,2}$ happens to be less than our assumed 10^{-13} .

As already mentioned, we consider the 700 σ tension between the y_{20} coefficient measured by GOCE and GRACE dubious, and hence refrain from deriving any constrain on the Yukawa interaction, since the most likely cause for the tension is linked to error analyses. We present a better motivated example for the y_{20} case, in a homogeneous Earth model, in section 5.

Although similar considerations could be made when constraining a Yukawa interaction from the measurement of satellite orbits and secular variations of Keplerian parameters, we only mention that given the dependence of the Lagrange–Gauss equations on the shape of the Earth, constraints will undoubtedly be impacted by the model of the Earth used for the analysis.

4.3. Going beyond current hypotheses and analyses in modified gravity experiments

The discussion above allowed us to identify limitations inherent to current experiments in geodesy and modified gravity in the vicinity of the Earth. For instance, although Earth gravity surveys are almost model-independent (apart from the facts that it is assumed that the gravitational field can be expanded on a spherical harmonics basis and that by definition $y_{00} = 1$ and is not estimated), geodesy experiments must choose a model to invert a gravity map into a model of the Earth. On the one hand, ignoring the possibility for modified gravity may end up on a biased Earth model. On the other hand, modified gravity experiments based on an explicit Earth model (like the estimator presented in section 4.2) are impacted by a biased and imprecise model of the Earth. This is most likely the case if they rely on a model derived from

⁹For illustrative purpose. Given the current experimental limits on the Yukawa interaction, this value is about the maximum that could still be measured by two satellites, at altitudes of 250 km and 2500 km, for $\lambda \sim 1.2 \times 10^5$ m—see section 5.

a global gravity survey (small scale ground tests relying on the modeling of the laboratory surroundings are less prone to this kind of errors). This process is shown by the left arm of the flowchart depicted in figure 4: from a gravity survey and its measured $y_{\ell m}$ coefficients, a (biased) model of the Earth is derived under the assumption that gravity has only a Newtonian contribution (H1 hypothesis of figure 3 with no prior on modified gravity), then (biased) constraints on modified gravity are derived (H2 hypothesis).

As the bias and uncertainty of the Earth model propagate to the constraints on modified gravity only if those constraints are model-dependent, a possibility to avoid this limitation is to define model-independent constraints. Other combinations of spherical harmonic coefficients may be thought of that, in principle, cancel the contributions from the model of the Earth. For instance, the ratio of \hat{y}_{20} measured by two satellites is independent of the Earth details. However, this is true only for spherical harmonics coefficients as defined in section 2, where y_{00} is not universally equal to 1 but depends on the distance to the Earth. On the contrary, spherical harmonic coefficients provided by gravity surveys give $y_{00} = 1$ by definition. This discrepancy, beside implicitly combining inconsistent models, would force us to renormalise our y_{20} by y_{00} , making them effectively depend on the Earth characteristics, with a different dependence for both satellites. Therefore, given the current gravity surveys measurements, it is not possible to avoid Earth model uncertainties.

Those difficulties arise in the H2b hypothesis, whereby we compute the Yukawa contribution sourced by the shape of the Earth. Most published constraints on the Yukawa interaction use the H2a hypothesis and ignore the shape of the Earth altogether, besides the effect of the Earth flattening. This is no better than using a biased Earth model, since it amounts to using inconsistent gravity models (extended Earth for the Newtonian part of the gravity field, and point-mass Earth for the Yukawa contribution). We then claim that the H2a hypothesis should be dropped and replaced by the H2b hypothesis.

At this point, it should be clear that we are currently facing two main problems. The first one is the use of inconsistent models in geodesy and in modified gravity experiments. The second one is the entanglement of geodesy and modified gravity experiments, which ends up in non-linear error propagation and interdependent models, priors and constraints.

A natural solution to the inconsistent models problem is simply to derive geodesy results from gravity surveys with modified gravity in mind. Instead of considering the measured spherical harmonics coefficients as pure representations of the (Newtonian) geometry, the contribution from modified gravity should be taken into account. This is shown by the H1' frame in the right arm of figure 4's flowchart. By assuming a gravity model to which both the Newtonian and the Yukawa interaction contribute and using an appropriate prior on the Yukawa parameters, the Earth model becomes unbiased, though its variance is increased, as shown in section 4.1. Then, we can safely use this Earth model to derive unbiased constraints on modified gravity (H2' frame). The dashed line between H2 and the H1' prior on modified gravity show how existing constraints on the Yukawa interaction can readily be used and marginalised over to obtain a better Earth model, from which updated constraints on the Yukawa interaction can be derived.

Another possibility is not only to derive geodesy results with modified gravity in mind, but to perform geodesy and modified gravity experiments simultaneously. This is shown by the H3 hypothesis in figures 3 and 4. This option has the advantage to allow for the use of the same data set for both analyses, thereby lowering the risk of errors coming from incompatible data sets. Moreover, as shown by the dashed lines in the H3 frame of figure 4, such a solution allows for easy iterations between priors, Earth models and modified gravity constraints, which solves the 'non-linear error propagation' problem. For instance, we could fly two satellites at different altitudes at the same time to break directly the degeneracy between the Newtonian and the Yukawa contributions to the spherical harmonic expansion of the gravitational field.

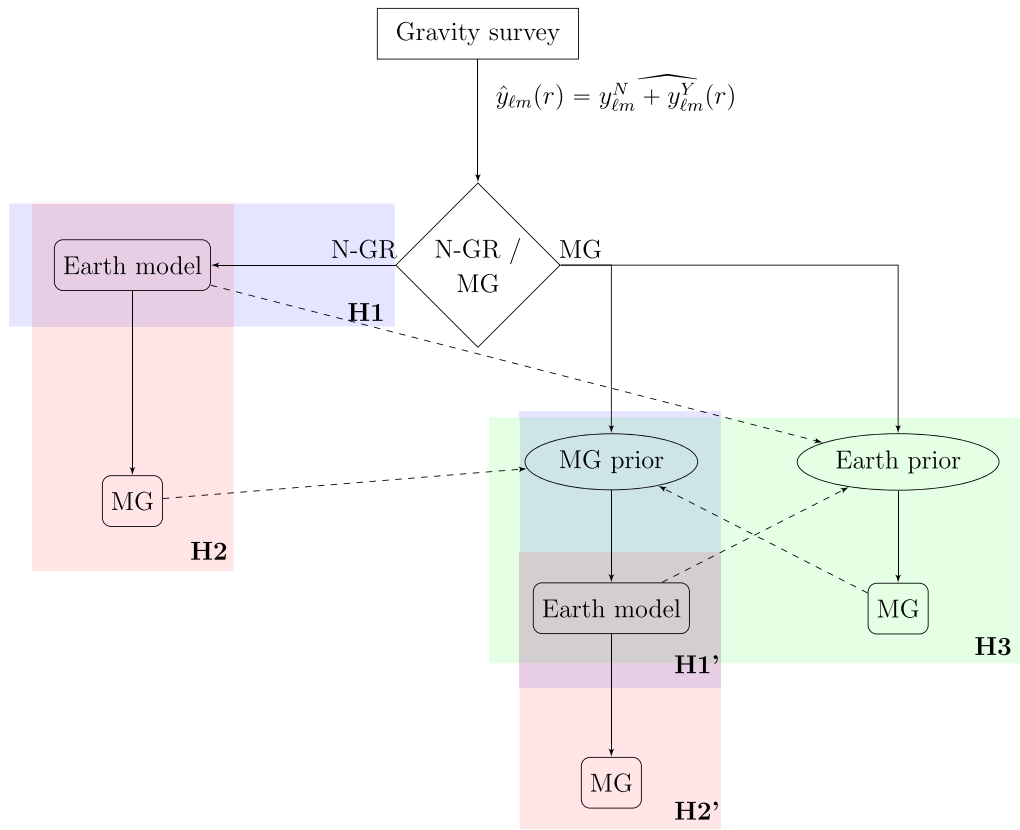


Figure 4. Flowchart for modified gravity experiments in the Earth gravitational field with at least one aspect of data analysis based on an external gravity model. An external gravity survey provides the measured coefficients of a spherical harmonic expansion; they contain the contributions from the Newtonian (Earth shape) and the modified gravitational fields. A model is then decided upon to extract information from those $\hat{y}_{\ell m}$ coefficients: either we assume gravity is Newtonian (N-GR), or we include modified gravity in the model (MG). In the former case, we can derive a (possibly biased, if modified gravity actually exists) model of the Earth (figure 3’s H1 hypothesis), from which we can constrain (possibly biased) estimators for modified gravity (H2 hypothesis). In the latter case, priors on modified gravity allow for an (unbiased) model of the Earth (H1’ hypothesis), from which (unbiased) constraints on modified gravity can be drawn (H2’ hypothesis). Using both priors on modified gravity and on the shape of the Earth, we can get an updated Earth model and modified gravity constraints simultaneously (H3 hypothesis). Dashed lines show the interplay between priors and measurements, and show that we can iterate to improve upon the analysis; a Bayesian approach is even better in the H3 case.

Assuming that systematic errors are well-controlled, any difference between measurements done simultaneously would stem from modified gravity, which would naturally be accounted for in the underlying model.

We shall close this discussion by noting that we only discussed explicitly Earth-model-dependent constraints of modified gravity. For completeness, we briefly mention that some tests of (modified) gravity do not require any explicit Earth model. This is for instance the case of experiments that aim to look for a model-independent deviation to Newtonian gravity or GR and only need a gravity model as provided by gravity surveys to correct for systematics,

with no explicit link to the real Earth geometry. For example, MICROSCOPE is sensitive to the Earth gravity gradient (GGT) [26], which is therefore corrected for with published ITSG-GRACE14s spherical harmonic coefficients [62]. No error nor bias from any Earth model can thereby enter in the search for a violation of the equivalence principle. However, we warn that if a Yukawa interaction is present, then its effect at the MICROSCOPE altitude should not be the same than that at the altitude where the gravity model was measured by GRACE, potentially creating a bias in the GGT correction. However, from the orders of magnitude derived in section 5, we expect this possible bias to be negligible. On the opposite, the constraints on the Yukawa interaction estimated from the first MICROSCOPE results [50] rely on an explicit model of the Earth; its impact will be assessed in a future work.

Finally, where possible, the most promising way to go beyond limitations from gravity surveys performed at different altitudes and from imperfect Earth models may be to embark a gravitational field measurement device onboard any satellite mission that aims to test modified gravity. For example, would a gradiometer surround the MICROSCOPE instrument, it could directly measure the actual GGT affecting the measurement, which could then be corrected for without relying on any external gravity model. However, we do not see how to go pass the limitations from our imperfect knowledge of the Earth model in tests that are explicitly model-dependent (e.g. the expected Yukawa interaction-induced equivalence principle violation explicitly depends on the Earth physical characteristics—and not only its local gravitational field). An in-depth analysis of those limitations will be done in a future work.

5. Order of magnitude estimates: homogeneous ellipsoidal Earth model

In this section, we provide order-of-magnitude estimates of the impact that the imperfect knowledge of the shape of the Earth and a Yukawa interaction have on each other, as applications of the discussion in section 4. Without loss of generality, we consider a very simple Earth model, where the Earth is a rotationally symmetric, homogeneous ellipsoid. We can therefore use the results of section 3, with $N = 1$. We assume numerical values listed in table 2. We should note that our model's flattening is not equal to the actual measured one: we chose it in order to recover the mass and J_2 measured for the actual Earth, despite having an overly simple Earth model.

5.1. Impact of the Yukawa interaction on the measured Earth gravitational field

5.1.1. Impact on the quadrupole. We start with order-of-magnitude estimates of the contribution of the Yukawa interaction in the bias and variance of the Newtonian estimator of the y_{20} coefficients, as an application of the discussion in section 4.1.

Using equation (55) for the y_{20} coefficient of a homogeneous Earth, the \hat{y}_{20}^N estimator of equation (68) becomes

$$\hat{y}_{20}^N = \hat{y}_{20}(r) + \frac{2\tilde{f}\tilde{\alpha}k(r, \lambda, R_{\oplus})}{5\sqrt{5}(1-\tilde{f})} \quad (77)$$

where $k(r, \lambda, R_{\oplus}) = 5e^{-r/\lambda}\kappa\left(\frac{r}{\lambda}\right)\Phi_2\left(\frac{R_{\oplus}}{\lambda}\right)$ and where we assume that we experimentally measured $\hat{y}_{20}(r)$. As before, the tilde symbols represents priors.

The expected value and variance of this estimator, derived from equations (71) and (72) give

$$\mathbb{E}(\hat{y}_{20}^N) = y_{20}^N + \frac{2fk(r, \lambda, R_{\oplus})}{5\sqrt{5}(1-f)}\delta\alpha \quad (78)$$

Table 2. Homogeneous Earth model parameters: equatorial radius R_{\oplus} , density ρ and (inverse) flatness $1/f$.

R_{\oplus}	ρ	$1/f$
6378.1 km	$5.51 \times 10^6 \text{ g m}^{-3}$	370 ± 10

where we assume that the measurement and flattening model are unbiased but the prior on α is biased ($E(\tilde{\alpha}) = \alpha + \delta\alpha$), and

$$\sigma_{y_{20N}}^2 = \sigma_{y_{20}}^2 + \frac{4k^2(r, \lambda, R_{\oplus})}{125(1-\tilde{f})} \left[\frac{\tilde{f}\tilde{\alpha}}{(1-\tilde{f})^2} \sigma_{\tilde{f}}^2 + \sigma_{\tilde{\alpha}}^2 \right]. \quad (79)$$

We can note that when ignoring the possibility of a non-zero Yukawa interaction, the bias in equation (78) is just the Yukawa contribution to the $y_{20}(r)$ coefficient (equation (55)).

Figure 5 shows the bias on the estimated \hat{y}_{20}^N as given by equation (78), when (incorrectly) assuming $\alpha = 0$, for a low-earth orbit experiment (altitude of GOCE—left panel) and a hypothetical mid-earth orbit (2500 km—right panel) in the $\alpha - \lambda$ plane. The black line shows the current best constraints on the existence of a Yukawa interaction [50, 86]: the region of the plane above the line is excluded by previous experiments. It is clear that the effect of a given (α, λ) pair affects the measurement of y_{20} differently depending on the altitude, due to the exponential dependence of the Yukawa interaction. For instance, $(\alpha, \lambda) \approx (2 \times 10^{-8}, 1.2 \times 10^5 \text{ m})$, i.e. for $\delta\alpha = 2 \times 10^{-8}$, brings a bias of about 10^{-13} for an experiment at the GOCE altitude, while it barely affects an experiment at 2500 km ($\delta y_{20} \approx 10^{-16}$). The exact value for a 250 km and 500 km altitude satellites is given in table 3.

Assuming a prior $\tilde{\alpha} = 0 \pm \sigma_{\tilde{\alpha}}$, and still assuming that the model of the flattening is unbiased, equation (79) shows that the increase in the measured y_{20}^N 's uncertainty is equal to the maximum bias that can be brought by allowed values for the Yukawa parameters. This once again shows that choosing a good prior on α helps to minimise the bias on y_{20}^N (at the price of increasing its error bar).

5.1.2. Impact on higher zonal terms. Table 3 lists the expected deviations for y_{n0} ($n = 2, 4, 6, 8$) due to a Yukawa interaction, for a rotationally symmetric, homogeneous ellipsoidal Earth, at altitudes of 250 km and 500 km, and compares them with current uncertainties on the measured coefficients for GOCE-only and GRACE-only gravitational field models [57, 62]. Those numbers are normalised such that the Newtonian contributions correspond to the measurements for the actual Earth, to account for our oversimplified Earth model. The first column gives the expected bias from a Yukawa interaction with $(\alpha, \lambda) = (2 \times 10^{-8}, 1.2 \times 10^5 \text{ m})$, or equivalently the increase in rms for $(\alpha, \lambda) = (0 \pm 2 \times 10^{-8}, 1.2 \times 10^5 \text{ m})$; the third and fourth columns give up-to-date tabulated values.

The results listed in the table show that current space geodesy missions, which fly higher than a few hundred kilometers, are immune to a Yukawa interaction (as currently constrained by other experiments). Currently allowed values of Yukawa parameters only marginally affect the measurement of the Newtonian spherical harmonics: the expected bias (equivalently, uncertainty increase would a Yukawa interaction be absent, but our imperfect knowledge about it considered) is between two and three orders of magnitude smaller than the current errors on the first few zonal terms. Nevertheless, should the measurement errors be decreased by two orders of magnitude (even for high-altitude satellites), care should be taken to include the Yukawa interaction in the model.

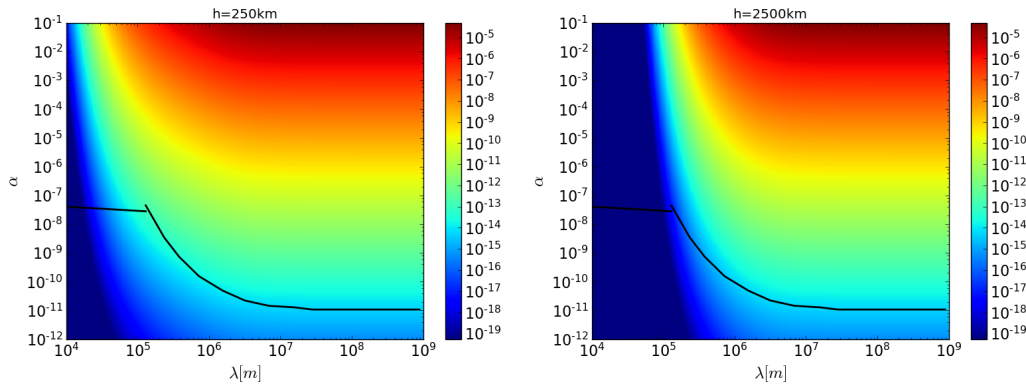


Figure 5. Bias on the estimated y_{20}^N Newtonian zonal term from a Yukawa deviation for a homogeneous Earth (equation (78)) when incorrectly assuming $\alpha = 0$ if a non-zero Yukawa interaction actually exists, in the $\alpha - \lambda$ plane, for two experiments orbiting the Earth at different altitudes: 250 km (like GOCE) and 2500 km. In this case, the bias is just the Yukawa contribution to the $y_{20}(r)$ coefficient (equation (55)). The black contour shows the best existing exclusion constraints on a Yukawa interaction [25, 50].

Table 3. Bias on the first few estimated Newtonian zonal terms from a Yukawa deviation for a rotationally symmetric, homogeneous ellipsoidal Earth, when incorrectly assuming $\alpha = 0$ if a non-zero Yukawa interaction actually exists with $(\alpha, \lambda) = (2 \times 10^{-8}, 1.2 \times 10^5 \text{ m})$, at an altitude of 250 km (GOCE [57]) and 500 km (GRACE [62]).

	Yukawa bias (rms increase— $E(\hat{\alpha}) = 0$)	Tabulated value	Tabulated uncertainty
GOCE			
y_{20}	7.4×10^{-14}	$-4.841\ 653\ 042\ 45 \times 10^{-4}$	5.423×10^{-12}
y_{40}	1.3×10^{-15}	$5.399\ 505\ 09 \times 10^{-7}$	2.758×10^{-12}
y_{60}	2.5×10^{-15}	$-1.499\ 796\ 81 \times 10^{-7}$	3.556×10^{-12}
y_{80}	4.1×10^{-15}	$4.944\ 8989 \times 10^{-8}$	3.972×10^{-12}
GRACE			
y_{20}	1.0×10^{-14}	$-4.841\ 692\ 836\ 73 \times 10^{-4}$	1.577×10^{-12}
y_{40}	1.8×10^{-16}	$5.399\ 933\ 70 \times 10^{-7}$	3.35×10^{-13}
y_{60}	3.8×10^{-16}	$-1.499\ 746\ 14 \times 10^{-7}$	1.88×10^{-13}
y_{80}	6.7×10^{-16}	$4.947\ 7947 \times 10^{-8}$	1.35×10^{-13}

5.2. Impact of a Yukawa interaction on orbital dynamics

We now quantify the perturbing accelerations created by a Yukawa interaction on an orbiting satellite (see section 3.2). Figure 6 compares the Yukawa monopole (i.e. the term in $z_{00}(r)$ in \mathbf{g}_{\parallel}) and quadrupole accelerations (i.e. the term in $J_{20}(r)$ in \mathbf{g}_{\perp}), to other usual gravitational and non-gravitational accelerations. The blue lines correspond to our fiducial $(\alpha, \lambda) = (2 \times 10^{-8}, 1.2 \times 10^5 \text{ m})$ model, and the red lines represent a long-range Yukawa interaction $(\alpha, \lambda) = (5 \times 10^{-12}, \infty)$, as still allowed by experiments. In each case, the solid line corresponds to the monopole acceleration and the dashed line shows the quadrupole acceleration.

The other lines show the acceleration of the Earth Newtonian monopole (GM), and several gravitational (Newtonian Earth quadrupole— J_{20} —, gravitational pull of the Moon, Sun, Venus and Jupiter, relativistic effects—GR—, Earth tides) and non-gravitational (solar

radiation pressure—SRP—, atmospheric drag, Earth albedo) perturbations. We followed [82] to compute those perturbations. The line showing the atmospheric drag is based on an upper limit of the atmospheric density, and therefore shows the maximum drag expected. The vertical dotted lines show the altitude of GOCE, GRACE, LAGEOS and geostationary satellites from left to right.

A long-ranged Yukawa interaction is largely subdominant for altitudes higher than a few thousands kilometers; below that, its perturbation is of the order of those of Venus and Jupiter. In particular, the perturbation due to the coupling between the Earth's quadrupole and a long-ranged Yukawa interaction is several orders of magnitude lower than the perturbation caused by Jupiter.

Perturbations caused by a mid-ranged Yukawa interaction (as still allowed by experiments) fall off quickly with the altitude, so that they are ever more subdominant than a long-ranged Yukawa interaction for satellites orbiting the Earth higher than 500 km. However, they may have an impact similar to that of relativistic effects on low-earth satellites; the quadrupole acceleration, although less significant, can be of the same order as the perturbations caused by Venus and Jupiter.

Finally, figure 6 clearly shows the strong radial dependence of the Yukawa interaction that we mentioned throughout this paper. It means that satellites like GOCE and GRACE are not affected in the same way by a Yukawa interaction, although other perturbations (leaving apart the atmospheric drag) impact both of them in a similar manner. This confirms the possibility to use two such satellites to constrain a Yukawa interaction in low-earth orbit, as we have sketched in section 5.3, or directly through the comparison of their dynamics. This can be done by solving Lagrange–Gauss equations, which we will present in a future work.

5.3. Impact of the Earth geometry and mass distribution on the constraints on Yukawa parameters

We consider the impact of our imperfect knowledge of the Earth shape and compute an order of magnitude estimate of the level of error that we may expect on the estimation of α . In this section, we consider that we constrain α for fixed λ (then the $\alpha - \lambda$ plane can be constrained by binning it along λ) and use the estimator (73).

We keep the same Earth model (table 2), where we assume some error on the flattening ($\delta f/f = 0.027$). In the case of an homogeneous Earth, the estimator's expected value is given by

$$E(\hat{\alpha}) = \alpha - \frac{5\sqrt{5}}{2f[k(r_1, \lambda, R_{\oplus}) - k(r_2, \lambda, R_{\oplus})]} \frac{\delta f}{f} (y_{20}(r_1) - y_{20}(r_2)) \quad (80)$$

where we assumed that the \hat{y}_{20} measurements are unbiased, and that the model of the flattening is biased by δf . Assuming that $\alpha = 2 \times 10^{-8}$ and $\lambda = 1.2 \times 10^5$ m, and that the satellites orbit the Earth at 250 km and 2500 km (which allow for the larger difference $y_{20}(r_1) - y_{20}(r_2)$ in the allowed region of the (α, λ) plane—see figure 5), we find a 40% bias $\delta\alpha = 8 \times 10^{-9}$ on the estimation of α . This is a significant bias, that may point to a close limitation due to our knowledge of the Earth. However, our homogeneous Earth model is deliberately simplistic and implies a large error on the flattening. Since the bias on α scales linearly with the relative uncertainty on the flattening, we can expect that better Earth models (e.g. 2-layer models), with smaller error on the flattening, will have a less significant bias on the constraints on α .

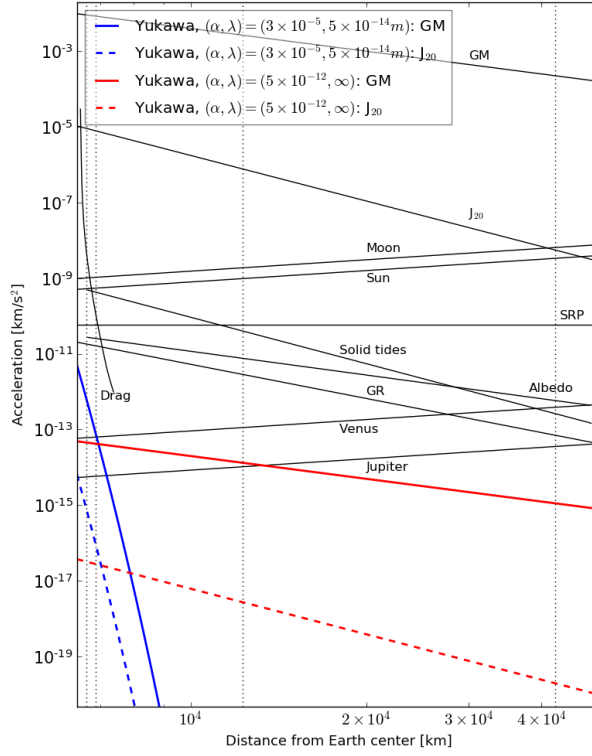


Figure 6. Comparison of Yukawa interaction perturbation with usual gravitational and non-gravitational perturbations, for satellites up to geostationary altitude. Black solid lines represent usual perturbations, as can be computed e.g. from [82] (see main text). Colored lines show the Yukawa perturbation for two different allowed configurations: short-range, relatively strong interaction (blue) and long-range, weak interaction (red); solid lines show the acceleration of the Yukawa interaction monopole, and dashed lines show the acceleration due to the Yukawa interaction quadrupole. Dotted lines show the altitude of GOCE, GRACE, LAGEOS and geostationary satellites from left to right.

The uncertainty on the $\hat{\alpha}$ estimator is given (at first order) by

$$\sigma_{\alpha} = \frac{5\sqrt{5}(1-f)}{2f[k(r_1, \lambda, R_{\oplus}) - k(r_2, \lambda, R_{\oplus})]} \sqrt{\frac{\hat{y}_{20}(r_1) - \hat{y}_{20}(r_2)}{(1-f)^2} \frac{\sigma_f^2}{f^2} + 2\sigma_{y_{20}}^2} \quad (81)$$

where we assumed $\sigma_{y_{20}}^2(r_1) = \sigma_{y_{20}}^2(r_2)$ and ignored any bias on the flattening, but consider some uncertainty σ_f on it. As discussed in section 4.2, the uncertainty on the α estimator has contributions from the measurement errors and from the uncertainty on the Earth model. Figure 7 compares those two contributions. It should be noted that in our simple example, if we assume a percent error on the flattening, the y_{20} measurement errors dominate down to $\sigma_{y_{20}} \approx 10^{-15}$. As soon as gravity surveys reach a better precision, then the Earth model will limit experiments aiming to constraints a Yukawa interaction.

Since the relative error on the mass of the Earth scales linearly with the relative error on the flattening, figure 7 can be used to confirm the crude estimate that we made in section 4.2: with $\sigma_f/f \approx \sigma_{M_{\oplus}}/M_{\oplus} \approx 10^{-4}$, this uncertainty will dominate over the y_{20} measurement errors as soon as the latter are better than 10^{-17} (in the case presently under consideration, where $(\alpha, \lambda) = (2 \times 10^{-8}, 1.2 \times 10^5 \text{ m})$).

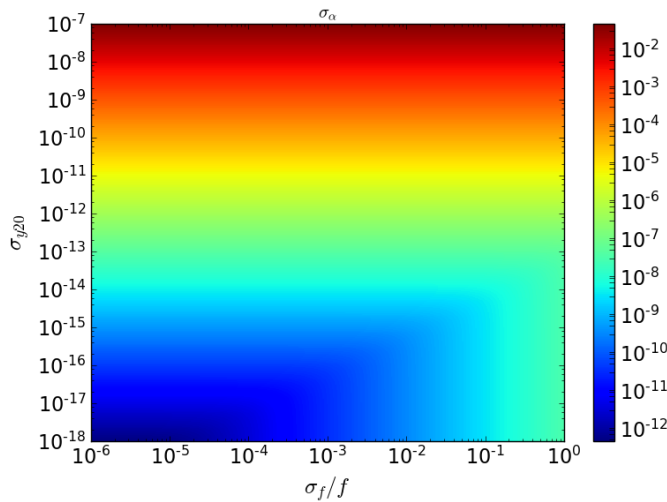


Figure 7. Contribution to the $\hat{\alpha}$ estimator variance of the relative error on the modeled Earth flattening and of measurement error on y_{20} , for $\lambda = 1.2 \times 10^5$ m.

Although the numbers given in this section are meant for rough order-of-magnitude estimates, they show that current experiments are not yet limited by our ability to reliably model the Earth.

6. Conclusion

We have investigated the entanglement between the shape of the Earth and modified gravity. Describing deviations to Newtonian gravity with a Yukawa interaction, we showed that the Earth gravitational field potential can still be expanded in spherical harmonics, just like in the pure Newtonian realm. We derived explicit expressions for the spherical harmonic coefficients, that we used to compute the (modified) gravity acceleration. We finally considered the Lagrange–Gauss equations, that describe the effect of a perturbing force on a satellite’s orbital dynamics, in the case where the Yukawa interaction is sourced by the complex shape of the Earth. To perform those calculations, we introduced a new method to compute a multipolar decomposition of the gravity acceleration with spin-weighted spherical harmonics, which greatly simplifies the required algebra.

We showed that although formally the coefficients of the spherical harmonic expansion keep the same form as in the Newtonian case, they acquire a new meaning and are not universal to the Earth system anymore, since they become explicitly dependent on the distance from the centre of the Earth. Consequently, the gravitational acceleration and the perturbing force due to the shape of the Earth also acquire a new radial dependence.

This behavior has many implications both in geodesy and in modified gravity experiments:

- in presence of a non-zero Yukawa interaction, measurements of the Earth gravitational field performed at different altitudes inevitably provide inconsistent results (up to measurement errors).
- in presence of a non-zero Yukawa interaction, using a Newtonian gravity model to map the Earth mass distribution by inverting the spherical harmonic coefficients measured for the gravitational field is prone to be biased; using a prior on modified gravity, considered

as a systematic error, should help to minimise the bias, although the uncertainty on the mass distribution estimator will increase.

- Earth-model-dependent measurements of a Yukawa interaction are inevitably affected by any bias or uncertainty on the Earth model (e.g. coming from geodesy data). Model-independent estimators might be constructed but require that gravity surveys go beyond the implicit assumption that the underlying field is Newtonian.
- even experiments that rely only on the measured Earth gravitational field (with no need to detail its source) are prone to errors if they are performed at an altitude different from that where the gravitational field was measured.

We proposed to combine gravitational surveys to define a new estimator of the Yukawa interaction strength α . Taking advantage of the radial dependence of the spherical harmonic coefficients in presence of a Yukawa interaction, we can simply take the difference of the values of a given coefficient as measured by two satellites at different altitude. We discussed the limitations caused by our imperfect knowledge of the Earth. Despite a significant bias in α if the model of the Earth is too simplistic, we found that we can increase the instrumental precision by several orders of magnitude before being limited by our knowledge of the Earth. However, we restrained from deriving new constraints on the Yukawa interaction from the strong tension in the J_2 zonal term as measured by GOCE and GRACE, since we find it dubious and its most probable cause is underestimated measurement errors.

Although the limitations listed above seem profound, we showed that they are subdominant compared to other usual gravitational and non-gravitational perturbations. We based our conclusion on order-of-magnitude estimates using a simple Earth model and taking into account those values of the Yukawa interaction that are still allowed by experiments but that give the strongest effects. For instance, the strength of the perturbation imparted by the coupling of the Earth quadrupole with a Yukawa interaction on a satellite is smaller than that due to Jupiter. Very-low-altitude satellites could be affected by a mid-range, still undetected Yukawa interaction, at the level of usual relativistic effects (which should obviously be corrected for before one can detect and characterize a Yukawa interaction). Thus, it is from low-altitude experiments that it seems most likely to improve our knowledge about a possible Yukawa interaction, provided that the atmospheric drag can be correctly taken into account (e.g. through a drag-free system).

We can therefore expect that although we should rigorously take into account the complex shape of the Earth when constraining modified gravity in orbit, especially for experiments performed in a low-Earth orbit, considering the Earth as a sphere remains a very good approximation for high-altitude satellites. Nevertheless, it would be sound to gather geodesy and modified gravity to minimise any modeling limitation. This can be done by performing geodesy experiments with modified gravity in mind (i.e. using a beyond-Newton gravity model), or even by designing experiments aiming to measure the shape of the Earth and modified gravity simultaneously.

Acknowledgments

We thank Phuong-Anh Huynh and Bernard Foulon for useful and stimulating discussions. We acknowledge the financial support of CNES through the APR program ('GMscope+' project) and of the UnivEarthS Labex program at Sorbonne Paris Cité (ANR-10-LABX-0023 and ANR-11-IDEX-0005-02). The work of JPU is made in the ILP LABEX (under reference ANR-10-LABX-63) was supported by French state funds managed by the ANR within the Investissements d'Avenir programme under reference ANR-11-IDEX-0004-02. This work is supported in part

by the EU Horizon 2020 research and innovation programme under the Marie-Sklodowska grant No. 690575. This article is based upon work related to the COST Action CA15117 (CANTATA) supported by COST (European Cooperation in Science and Technology).

Appendix A. Multipolar coefficients $y_{\ell 0}(r)$ for a layered Earth

The $y_{\ell m}$ coefficients are defined in equation (11) and have two components given in equations (8) and (9). Introducing the term $q_{\ell m}^Y$ such that

$$y_{\ell m}^Y(r) \equiv \frac{\alpha}{M_{\oplus}} \left(\frac{r}{\lambda}\right)^{\ell+\frac{1}{2}} K_{\ell+\frac{1}{2}} \left(\frac{r}{\lambda}\right) q_{\ell m}^Y$$

and making explicit the volume integral in spherical coordinates (we detail the computation only for $y_{\ell m}^Y$ since the one of $y_{\ell m}^N$ derives trivially from it), we write

$$q_{\ell m}^Y = \int_0^{2\pi} d\xi \int_0^{\pi} d\theta \sin \theta Y_{\ell m}^*(\theta, \xi) Q_{\ell}^Y(\theta, \xi) \quad (\text{A.1})$$

with

$$Q_{\ell}^Y(\theta, \xi) \equiv \int_0^{R(\theta, \xi)} ds \rho(s, \theta, \xi) \frac{s^{\ell+2}}{R_{\oplus}^{\ell}} \left(\frac{\lambda}{s}\right)^{\ell+\frac{1}{2}} I_{\ell+\frac{1}{2}} \left(\frac{s}{\lambda}\right). \quad (\text{A.2})$$

Then, we introduce the function

$$\phi_{\ell}(x, k) = 2^{-\ell-\frac{3}{2}} x^{\ell+3} \frac{\Gamma\left(\frac{\ell+3}{2}\right)}{\Gamma\left(\ell+\frac{3}{2}\right)\Gamma\left(\frac{\ell+5}{2}\right)} {}_1F_2\left(\frac{\ell+3}{2}; \ell+\frac{3}{2}, \frac{\ell+5}{2}; \frac{k^2 x^2}{4}\right), \quad (\text{A.3})$$

where Γ is the Gamma function and ${}_1F_2$ is a generalised hypergeometric function. We note that (see appendix B for an explicit proof)

$$\int_a^b dx x^{\ell+2} \left(\frac{\lambda}{R_{\oplus} x}\right)^{\ell+\frac{1}{2}} I_{\ell+\frac{1}{2}} \left(\frac{R_{\oplus} x}{\lambda}\right) = \phi_{\ell}\left(b, \frac{R_{\oplus}}{\lambda}\right) - \phi_{\ell}\left(a, \frac{R_{\oplus}}{\lambda}\right), \quad (\text{A.4})$$

and letting $x = s/R_{\oplus}$, equation (A.2) becomes

$$Q_{\ell}^Y(\theta, \xi) = R_{\oplus}^3 \sum_{i=1}^N \left[\phi_{\ell}\left(\frac{R_i(\theta, \xi)}{R_{\oplus}}, \frac{R_{\oplus}}{\lambda}\right) - \phi_{\ell}\left(\frac{R_{i-1}(\theta, \xi)}{R_{\oplus}}, \frac{R_{\oplus}}{\lambda}\right) \right]. \quad (\text{A.5})$$

We now further assume that the Earth is made of N concentric, homogeneous ellipsoidal, rotationally symmetric layers. Noting $f_i = (R_{\text{eq},i} - R_{\text{pole},i})/R_{\text{eq},i}$ the i th layer's flattening, where $R_{\text{eq},i}$ and $R_{\text{pole},i}$ are its equatorial and polar radiuses, we get

$$R_i(\theta, \xi) = \frac{R_{\text{eq},i}(1-f_i)}{\sqrt{1-(2f_i-f_i^2)\sin^2\theta}}. \quad (\text{A.6})$$

Under the rotational symmetry assumption, $y_{\ell m} = 0$ for all $m \neq 0$, and

$$y_{\ell 0}^N = \frac{2\pi}{\sqrt{2\ell+1}(\ell+3)M_{\oplus}} \int_0^{\pi} d\theta \sin \theta P_{\ell 0}(\cos \theta) R_{\oplus}^3 \times \sum_{i=1}^N \rho_i \left[\left(\frac{R_{\text{eq},i}(1-f_i)}{R_{\oplus} \sqrt{1-(2f_i-f_i^2)\sin^2\theta}} \right)^{\ell+3} - \left(\frac{R_{\text{eq},i-1}(1-f_{i-1})}{R_{\oplus} \sqrt{1-(2f_{i-1}-f_{i-1}^2)\sin^2\theta}} \right)^{\ell+3} \right] \quad (\text{A.7})$$

and

$$y_{\ell 0}^Y(r) = \frac{2\pi\alpha}{M_{\oplus}} \sqrt{2\ell + 1} \left(\frac{r}{\lambda}\right)^{\ell + \frac{1}{2}} K_{\ell + \frac{1}{2}}\left(\frac{r}{\lambda}\right) \int_0^{\pi} d\theta \sin\theta P_{\ell 0}(\cos\theta) R_{\oplus}^3$$

$$\times \sum_{i=1}^N \rho_i \left[\phi_{\ell} \left(\frac{R_{\text{eq},i}(1-f_i)}{R_{\oplus} \sqrt{1-(2f_i-f_i^2)\sin^2\theta}}, \frac{R_{\oplus}}{\lambda} \right) - \phi_{\ell} \left(\frac{R_{\text{eq},i-1}(1-f_{i-1})}{R_{\oplus} \sqrt{1-(2f_{i-1}-f_{i-1}^2)\sin^2\theta}}, \frac{R_{\oplus}}{\lambda} \right) \right] \quad (\text{A.8})$$

where $P_{\ell 0}(\cos\theta)$ is an associated Legendre polynomial.

Appendix B. Proof of equation (A.4)

We wish to compute

$$H \equiv \int_a^b x^{n+2} \left(\frac{\lambda}{R_{\oplus}x}\right)^{n+\frac{1}{2}} I_{n+\frac{1}{2}}\left(\frac{R_{\oplus}x}{\lambda}\right) dx. \quad (\text{B.1})$$

Let us first introduce the new variables $k = R_{\oplus}/\lambda$ and $y = kx$, such that

$$H = k^{-n-3} \int_{ak}^{bk} y^{3/2} I_{n+\frac{1}{2}}(y) dy. \quad (\text{B.2})$$

We then define

$$\phi_{\ell}(x, k) = k^{-n-3} \int_0^{kx} y^{3/2} I_{n+\frac{1}{2}}(y) dy \quad (\text{B.3})$$

such that $H = \phi_{\ell}(b, k) - \phi_{\ell}(a, k)$. Using [92]

$$I_{\alpha}(x) = \frac{\left(\frac{x}{2}\right)^{\alpha}}{\Gamma(\alpha + 1)} {}_0F_1\left(; \alpha + 1; \frac{x^2}{4}\right), \quad (\text{B.4})$$

where ${}_0F_1()$ is the confluent hypergeometric limit function, and setting $u = \frac{y}{kx}$, we get

$$\phi_{\ell}(x, k) = \frac{2^{-n-\frac{1}{2}}x^{n+3}}{\Gamma\left(n + \frac{3}{2}\right)} \int_0^1 u^{n+2} {}_0F_1\left(; n + \frac{3}{2}; \frac{k^2x^2}{4}u^2\right) du. \quad (\text{B.5})$$

An extra change of variable $v = u^2$ provides

$$\phi_{\ell}(x, k) = \frac{2^{-n-\frac{3}{2}}x^{n+3}}{\Gamma\left(n + \frac{3}{2}\right)} \int_0^1 v^{\frac{n+1}{2}} {}_0F_1\left(; n + \frac{3}{2}; \frac{k^2x^2}{4}v\right) dv. \quad (\text{B.6})$$

Finally, using [92]

$${}_{A+1}F_{B+1}(a_1, \dots, a_A, c; b_1, \dots, b_B, d; z) = \frac{\Gamma(d)}{\Gamma(c)\Gamma(d-c)} \int_0^1 t^{c-1} (1-t)^{(d-c-1)} {}_A F_B(a_1, \dots, a_A; b_1, \dots, b_B; tz) dt, \quad (\text{B.7})$$

we obtain

$$\phi_{\ell}(x, k) = 2^{-n-\frac{3}{2}}x^{n+3} \frac{\Gamma\left(\frac{n+3}{2}\right)}{\Gamma\left(n + \frac{3}{2}\right) \Gamma\left(\frac{n+5}{2}\right)} {}_1F_2\left(\frac{n+3}{2}; n + \frac{3}{2}, \frac{n+5}{2}; \frac{k^2x^2}{4}\right), \quad (\text{B.8})$$

which proves equation (A.4).

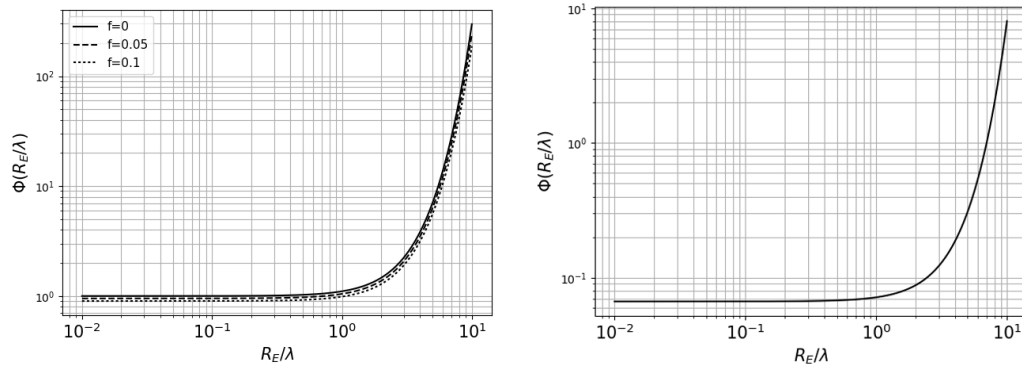


Figure C1. Left: form factor $\Phi(x, f)$, as a function of the ratio R_{\oplus}/λ . Right: form factor $\Phi_2(x)$, as a function of the ratio R_{\oplus}/λ . Long-range Yukawa interaction set on the left of the plots, while short-range Yukawa interaction are on the right.

Appendix C. Form factors

This appendix discusses some aspects of the form factors introduced in section 3 for a homogeneous, rotationally symmetric ellipsoid of flatness f and equatorial radius R_E

$$\Phi(x, f) = 3 \frac{x \cosh(x) - \sinh(x)}{x^3} - \frac{\sinh x}{x} f \quad (\text{C.1})$$

$$\Phi_2(x) = 3 \frac{x \cosh(x) - (x^2/3 + 1) \sinh(x)}{x^5}. \quad (\text{C.2})$$

They are shown in figure C1, as a function of R_E/λ . The left panel shows $\Phi(R_E/\lambda, f)$ for three different flatnesses, and the right panel shows $\Phi_2(R_E/\lambda)$. For long-range interactions ($R_E/\lambda \rightarrow 0$), both functions tend to a finite limit: $\Phi(R_E/\lambda, f) \rightarrow 1 - f$ and $\Phi_2(R_E/\lambda) \rightarrow -1/15$. In this case, the form factor does not play a role in the monopole acceleration (up to the flatness), but it limits the quadrupole acceleration. Short-range interactions are more strongly affected by those form factors, highlighting the fact that Gauss theorem does not apply to a Yukawa interaction. In particular, for $\lambda \sim 0.1 R_E$, the Yukawa monopole acceleration is boosted by two orders of magnitude, meaning that it does not scale naively as αg_{Newton} , but as $100 \alpha g_{\text{Newton}}$. Therefore, correctly taking this form factor into account is important to get correct constraints on the Yukawa interaction.

ORCID iDs

Joel Bergé  <https://orcid.org/0000-0002-7493-7504>

References

- [1] Will C M 1993 *Theory and Experiment in Gravitational Physics* (Cambridge: Cambridge University Press)
- [2] Will C M 2014 *Living Rev. Relativ.* **17** 4
- [3] Adelberger E G, Heckel B R and Nelson A E 2003 *Annu. Rev. Nucl. Part. Sci.* **53** 77–121
- [4] Clifton T, Ferreira P G, Padilla A and Skordis C 2012 *Phys. Rep.* **513** 1–189
- [5] Joyce A, Jain B, Khoury J and Trodden M 2015 *Phys. Rep.* **568** 1–98

- [6] Uzan J P and Bernardeau F 2001 *Phys. Rev. D* **64** 083004
- [7] Uzan J P 2003 *Ann. Henri Poincaré* **4** S347–69
- [8] Uzan J P 2007 *Gen. Relativ. Gravit.* **39** 307–42
- [9] Uzan J P 2010 *Gen. Relativ. Gravit.* **42** 2219–46
- [10] Jain B et al 2013 arXiv:1309.5389
- [11] Jain B and Khoury J 2010 *Ann. Phys.* **325** 1479–516
- [12] Safronova M S, Budker D, DeMille D, Kimball D F J, Derevianko A and Clark C W 2018 *Rev. Mod. Phys.* **90** 025008
- [13] Delva P, Hees A and Wolf P 2017 *Space Sci. Rev.* **212** 1385–421
- [14] Everitt C W F et al 2011 *Phys. Rev. Lett.* **106** 221101
- [15] Ciufolini I, Paolozzi A, Koenig R, Pavlis E C, Ries J, Matzner R, Gurzadyan V, Penrose R, Sindoni G and Paris C 2013 *Nucl. Phys. B* **243** 180–93
- [16] Ciufolini I, Moreno Monge B, Paolozzi A, Koenig R, Sindoni G, Michalak G and Pavlis E C 2013 *Class. Quantum Grav.* **30** 235009
- [17] Iorio L, Ciufolini I and Pavlis E C 2002 *Class. Quantum Grav.* **19** 4301–9
- [18] Lucchesi D M 2003 *Phys. Lett. A* **318** 234–40
- [19] Lucchesi D M and Peron R 2010 *Phys. Rev. Lett.* **105** 231103
- [20] Lucchesi D M and Peron R 2014 *Phys. Rev. D* **89** 082002
- [21] Li Z W, Yuan S F, Lu C and Xie Y 2014 *Res. Astron. Astrophys.* **14** 139–43
- [22] Bertotti B, Iess L and Tortora P 2003 *Nature* **425** 374–6
- [23] Williams J G, Turyshev S G and Boggs D H 2004 *Phys. Rev. Lett.* **93** 261101
- [24] Schlamminger S, Choi K Y, Wagner T A, Gundlach J H and Adelberger E G 2008 *Phys. Rev. Lett.* **100** 041101
- [25] Wagner T A, Schlamminger S, Gundlach J H and Adelberger E G 2012 *Class. Quantum Grav.* **29** 184002
- [26] Touboul P et al 2017 *Phys. Rev. Lett.* **119** 231101
- [27] Viswanathan V, Fienga A, Minazzoli O, Bernus L, Laskar J and Gastineau M 2018 *Mon. Not. R. Astron. Soc.* **476** 1877–88
- [28] Uzan J P 2003 *Rev. Mod. Phys.* **75** 403
- [29] Uzan J P 2011 *Living Rev. Relativ.* **14** 2
- [30] Uzan J P 2004 *AIP Conf. Proc.* **736** 3–20
- [31] Abbott B P et al 2016 *Phys. Rev. Lett.* **116** 061102
- [32] Abbott B P et al 2017 *Phys. Rev. Lett.* **119** 161101
- [33] Brax P, Burrage C and Davis A C 2016 *J. Cosmol. Astropart. Phys.* JCAP03(2016)004
- [34] Lombriser L and Taylor A 2016 *J. Cosmol. Astropart. Phys.* JCAP03(2016)031
- [35] Lombriser L and Lima N A 2017 *Phys. Lett. B* **765** 382–5
- [36] Baker T, Bellini E, Ferreira P G, Lagos M, Noller J and Sawicki I 2017 *Phys. Rev. Lett.* **119** 251301
- [37] Creminelli P and Vernizzi F 2017 *Phys. Rev. Lett.* **119** 251302
- [38] Ezquiaga J M and Zumalacárregui M 2017 *Phys. Rev. Lett.* **119** 251304
- [39] Sakstein J and Jain B 2017 *Phys. Rev. Lett.* **119** 251303
- [40] Damour T and Esposito-Farese G 1992 *Class. Quantum Grav.* **9** 2093–176
- [41] Vainshtein A I 1972 *Phys. Lett. B* **39** 393–4
- [42] Damour T and Nordtvedt K 1993 *Phys. Rev. Lett.* **70** 2217–9
- [43] Damour T and Polyakov A M 1994 *Nucl. Phys. B* **423** 532–58
- [44] Khoury J and Weltman A 2004 *Phys. Rev. D* **69** 044026
- [45] Khoury J and Weltman A 2004 *Phys. Rev. Lett.* **93** 171104
- [46] Babichev E, Deffayet C and Ziour R 2009 *Int. J. Mod. Phys. D* **18** 2147–54
- [47] Hinterbichler K and Khoury J 2010 *Phys. Rev. Lett.* **104** 231301
- [48] Brax P, Burrage C and Davis A C 2013 *J. Cosmol. Astropart. Phys.* JCAP01(2013)020
- [49] Burrage C and Sakstein J 2018 *Living Rev. Relativ.* **21** 1
- [50] Bergé J, Brax P, Métris G, Pernot-Borràs M, Touboul P and Uzan J P 2018 *Phys. Rev. Lett.* **120** 141101
- [51] Fischbach E and Talmadge C L 1999 *The Search for Non-Newtonian Gravity* (New York: Springer-Verlag)
- [52] Kapner D J, Cook T S, Adelberger E G, Gundlach J H, Heckel B R, Hoyle C D and Swanson H E 2007 *Phys. Rev. Lett.* **98** 021101
- [53] Masuda M and Sasaki M 2009 *Phys. Rev. Lett.* **102** 171101
- [54] Sushkov A O, Kim W J, Dalvit D A R and Lamoreaux S K 2011 *Phys. Rev. Lett.* **107** 171101

- [55] Klimchitskaya G L and Mostepanenko V M 2014 *Gravit. Cosmol.* **20** 3–9
- [56] Rummel R, Yi W and Stummer C 2011 *J. Geod.* **85** 777–90
- [57] Pail R et al 2011 *J. Geod.* **85** 819–43
- [58] Tapley B D, Bettadpur S, Watkins M and Reigber C 2004 *Geophys. Res. Lett.* **31** L09607
- [59] Tapley B et al 2005 *J. Geod.* **79** 467–78
- [60] Reigber C, Schmidt R, Flechtner F, König R, Meyer U, Neumayer K H, Schwintzer P and Zhu S Y 2005 *J. Geodyn.* **39** 1–10
- [61] Pail R et al 2010 *Geophys. Res. Lett.* **37** L20314
- [62] Mayer-Gurr T, Eicker A and Ilk K H 2006 *Proc. 1st Symp. Int. Gravity Field Service*
- [63] Pavlis N K, Holmes S A, Kenyon S C and Factor J K 2012 *J. Geophys. Res.* **117** B04406
- [64] Hoyle C D, Kapner D J, Heckel B R, Adelberger E G, Gundlach J H, Schmidt U and Swanson H E 2004 *Phys. Rev. D* **70** 042004
- [65] Fischbach E, Sudarsky D, Szafer A, Talmadge C and Aronson S H 1986 *Phys. Rev. Lett.* **56** 3–6
- [66] Tóth G 2018 arXiv:1803.04720
- [67] Ciufolini I 1996 *Nuovo Cimento A* **109** 1709–20
- [68] Metzler B and Pail R 2005 *Stud. Geophys. Geod.* **49** 441–62
- [69] Wagner C A and McAadoo D C 2012 *J. Geod.* **86** 99–108
- [70] Shako R, Frste C, Abrykosov O, Bruinsma S, Marty J C, Lemoine J M, Flechtner F, Neumayer K H and Dahle C 2014 EIGEN-6C: a high-resolution global gravity combination model including GOCE data *Geotechnologies Science Report; No. 20 (Advanced Technologies in Earth Sciences)* 1st edn (Berlin: Springer) pp 155–61
- [71] Abramowitz M and Stegun I A 1964 *Handbook of Mathematical Functions with Formulas, Graphs, and Mathematical Tables* (New York: Dover) (9th Dover printing, 10th GPO printing)
- [72] Cunningham L E 1970 *Celest. Mech.* **2** 207–16
- [73] Métris G, Xu J and Wytrzyśczak I 1998 *Celest. Mech. Dyn. Astron.* **71** 137–51
- [74] Fantino E and Casotto S 2009 *J. Geod.* **83** 595–619
- [75] Petrovskaya M S and Vershkov A N 2010 *J. Geod.* **84** 165–78
- [76] Newman E T and Penrose R 1966 *J. Math. Phys.* **7** 863–70
- [77] Goldberg J N, Macfarlane A J, Newman E T, Rohrlich F and Sudarshan E C G 1967 *J. Math. Phys.* **8** 2155–61
- [78] Kaula W M 1966 *Theory of Satellite Geodesy: Applications of Satellites to Geodesy* 1st edn (New York: Dover)
- [79] Deruelle N and Uzan J P 2014 *Théories de la Relativité* 1st edn (Paris: Belin)
- [80] Roy A E 2005 *Orbital Motion* 4th edn (Bristol: Institute of Physics)
- [81] Mathez E, Webster J and Webster J 2004 *The Earth Machine: the Science of a Dynamic Planet* (New York: Columbia University Press)
- [82] Montenbruck O and Gill E 2000 *Satellite Orbits: Models, Methods, and Applications (Physics and Astronomy Online Library)* (Berlin: Springer)
- [83] Iorio L 2002 *Phys. Lett. A* **298** 315–8
- [84] Haranas I and Ragos O 2011 *Astrophys. Space Sci.* **331** 115–9
- [85] Haranas I, Ragos O and Mioc V 2011 *Astrophys. Space Sci.* **332** 107–13
- [86] Kolosnitsyn N I and Melnikov V N 2004 *Gen. Relativ. Gravit.* **36** 1619–24
- [87] Haranas I, Kotsireas I, Gómez G, Fullana M J and Gkigkitzis I 2016 *Astrophys. Space Sci.* **361** 365
- [88] Lucchesi D M 2011 *Adv. Space Res.* **47** 1232–7
- [89] Hagiwara Y 1989 *J. Geod. Soc. Japan* **35** 319–24
- [90] Grombein T, Seitz K and Heck B 2013 *J. Geod.* **87** 645–60
- [91] Casenave F, Métivier L, Pajot-Métivier G and Panet I 2016 *J. Geod.* **90** 655–75
- [92] Cuyt A A, Petersen V, Verdonk B, Waadeland H and Jones W B 2008 *Handbook of Continued Fractions for Special Functions* 1st edn (New York: Springer)

Chapter conclusion

The MICROSCOPE results provided new bounds on the existence of many models of unscreened scalar massless or massive field. For massive fields, those constraints have been obtained by assuming some models for the Earth’s mass distribution. Going beyond those models suffers from degeneracy as this distribution is only known via the measurement of the gravity fields variation. We proposed a way of breaking this degeneracy by performing gravitational experiments at different altitudes.

Chapter 4

Modelling the chameleon field in an experiment

While constraining unscreened scalar fields with MICROSCOPE's results is pretty straightforward, the case of the chameleon field is more tricky. Unlike the cases developed in the previous chapter, this is due to the fact that the gravitational effects of the satellite and of the measurement device and the possible interaction between the test masses might no longer be negligible.

As discussed in Chapter 2 the screening mechanism is the reason to this. The high density material constituting both the satellite and the means of measure are indeed to be considered when solving the field's Klein-Gordon equation Eq. (2.51). In the same way, MICROSCOPE's test being performed with extended bodies, their influence on the chameleon's dynamics is also to be considered. This latter point is central, as we concluded from the previous discussion in Sec. 2.3.4 that this is this effect that can create an apparent WEP violation in the case of a universally coupled chameleon through different screening factors. Note that moreover the chameleon theory being non-linear it does not verify the superposition principle. As a consequence these effects cannot be treated as perturbations. Evaluating those contributions is a complex problem due to the non-linearities of the equation and the lack of symmetries in the realistic geometrical configuration.

Two kinds of effects are expected in the MICROSCOPE experiment. The first one, similar to the case of a Yukawa interaction explored in the previous chapter, is a force created by a source of the chameleon field placed at the exterior of the experiment. The Earth – that MICROSCOPE is orbiting – is for such an effect playing the role of the main source for the field. The question is thus to consider the chameleon interaction of both test masses with it. Such an effect requires the satellite not to be completely screened, as otherwise the walls of the satellite would suppress the force. Instead the satellite needs to be only partially screened and the satellite influence is limited. The field must not nonetheless be in a regime in which the screening is too weak. As otherwise this would mean that the coupling to matter is too loose such that one would expect the force created by the Earth to be too small. In any case this effect is difficult to evaluate. One needs to model at the same time the influence of the Earth and the satellite. Due to the lack of symmetry, this is a 3D problem for which an analytic solution is difficult to find and a numerical solution is very costly in computing resources.

The second effect that could occur is sourced by the inside of the satellite. Such an effect arises from the distribution of matter in the satellite and thus depends on the geometry of the experiment. An asymmetry in this geometry could cause the field to propagate in a way that each element of a test mass volume would unevenly be pulled. Such an asymmetry can for instance be caused by wisely placing a big ball of heavy

matter inside the experiment, such that its influence on the field would be consequent. The MICROSCOPE mission has not been designed to maximise such asymmetry. On the contrary, its design has a cylindrical symmetry. This symmetry can be broken by the movement of the test masses, leading the cylinder to no longer be coaxial respectively to the others. But this motion is controlled by the servo-control loop. This system is so efficient that the displacement of the test masses as compared with their centred position is less than a micron, such effect is thus not expected during WEP tests sessions. However during the mission, measurement sessions have been dedicated by imposing a sinusoidal motion to the test masses via the electrostatic forces. The goal of these sessions was to measure the electrostatic stiffness inherent to the capacitive measurement system. This stiffness has been presented previously with the idealised model in Eq. (1.30). When interpreting these sessions, more realistic models are considered to compute the expected values for the stiffness. Nonetheless a discrepancy has been measured between the expected and measured values. This represents an opportunity to test the chameleon theory as a chameleonic force is expected to appear in this asymmetric configuration. Putting constraints on the chameleon using this measurement requires us to finely understand how the fields propagate inside the experiment.

It is important to note that these effects are not to be treated separately as they might take place at the same time. In the case where the MICROSCOPE satellite is screened, one would nevertheless expect only the latter. Note also that the chameleon articles by Khoury & Weltman [60, 59] studied the possibility of a WEP violation in space-borne experiments. They considered it through the interaction of the two test masses. But their model does not take into account the effects of the matter present in between the test masses e.g. the electrodes cylinders in MICROSCOPE. Besides, to obtain a WEP violation they treat the case of a non-universal coupling of the chameleon field. Such model could exist but it would not be comparable with the current constraint that has been presented in Sec. 2.3.6. The work presented in this chapter aims to study only universal coupling effects in MICROSCOPE.

This chapter intends to model the propagation of the chameleon field in an experiment such as MICROSCOPE. It is organised around two articles. The first one focuses on symmetrical geometries and aims to study the range of chameleon parameters at which MICROSCOPE is screened. To that end, an effort is done to solve the field numerically with as few approximations as possible in the chameleon's Klein-Gordon equation and a particular care on the way of posing boundary conditions of the problem. This way, we verify the literature's criterion for screening that were based mainly on approximated analytic models. In the second article, we explore the effect of non-coaxiality in nested-cylinders-like geometries. We find a way of treating this 2D problem at 1D. We find that to small displacement of a cylinder the chameleonic force behaves as a destabilising stiffness. We study the properties of this force.

Note that in the articles we denote the chameleon conformal function $A(\phi)$ while we have denoted it $\Omega(\phi)$ in Chapter 2.

4.1 Symmetrical set-ups

4.1.1 Introduction and summary

The central thread of this article is to evaluate the influence of a system of matter – that can correspond to a satellite – on the dynamics of the chameleon field. We consider a background environment of low density in which we embed a matter system. We consider symmetrical geometries. We start considering 1D situations, as the structure of the Klein-Gordon in this case allows us to integrate once the equation on the exterior

of the system. This provides a condition on the first derivative at some place that leads the field to evolve at infinity to the minimum of the potential in the background environment such that it verifies strictly the boundary conditions of the field. We choose this place to be the boundary of the considered system and we use it as the initial point of a numerical integration. Having obtained this condition, the value of the field at this place is still a free parameter that we impose by a shooting method in such a way that the solution we obtain in the system is consistent with what is expected. For instance we expect the field derivative to cancel at the center of the system as justified by the symmetry.

From this method we obtain the exact numerical profiles of the chameleon field associated to the configuration of a single wall of a given thickness and of a pair of walls separated by vacuum of the same type than the background environment. We analyse those profiles to verify the aspects of screening that have been addressed in Chapter 2. In the first case, by solving the field for different wall thicknesses we measure the difference between the effective minimal value reached by the field in the wall and the value that minimises its potential. We conclude that we can safely consider the wall to be screened for a thickness greater than 100 times the Compton wavelength of the field associated to its constituting matter. We also analyse the range of influence of a wall depending on its thickness. Of course if the wall is screened it has a farer influence, but at most its influence can be considered as null for distances to the wall greater than 10 times the Compton wavelength associated to the background environment. This confirms the exponential suppression behaviour of the field.

Having verified this latter behaviour, we then explore 2D and 3D configurations. We cannot use the same procedure as the 1D case because the structure of the Klein-Gordon no longer permits a first integration. But knowing now that we can safely set boundary conditions at finite distance of the system, this gives the opportunity of proceeding to a shooting method. We choose the center of the system to set the initial condition of a numerical integration as we know the derivative cancels by symmetry. Then we act by dichotomy on the initial value of the field to obtain the field that verifies the proper boundary conditions at some large distance from the system. The result of the method in 1D is in very good agreement with the previous. From this method we obtain the field profile for a cylindrical and spherical vacuum cavity and the profile of a spherical ball.

We use all these profiles to check several points of the chameleon's literature. First we study the profile inside both types of cavities and verify the expected value of the field at its centre that was given by Eq. (2.66). We find that this criterion only gives a rough order of magnitude. We then verify the Casimir-like force that appears between two plates. We found a very good agreement at small separation d and slight divergence at large separation. We find that the d^{-4} behaviour of the force at intermediate separation is only an approximation of a smoother curve. We also verify the Khoury & Weltman's profile of a spherical ball [59].

Finally we come back to MICROSCOPE and solve the field for coaxial nested cylinders. Because of the cylindrical symmetry no force is expected on any cylinder. The occurrence of an externally sourced force is studied. The screening criterion provides the region of the chameleon's parameter space on which the experiment is screened. This reveals that the MICROSCOPE mission is not competitive with the current bounds. In the unscreened region a force could appear but its quantification is beyond the scope of this article as it requires a 3D treatment. A method has been explored to answer this problem but without any conclusive success as will be addressed in Sec. 4.3.

4.1.2 Article

General study of chameleon fifth force in gravity space experiments

Martin Pernot-Borràs^{1,2,*}, Joel Bergé¹, Philippe Brax³, and Jean-Philippe Uzan^{2,4}

¹*DPHY, ONERA, Université Paris Saclay, F-92322 Châtillon, France*

²*Institut d'Astrophysique de Paris, CNRS UMR 7095, Sorbonne Université,
98 bis Bd Arago, 75014 Paris, France*

³*Institut de Physique Théorique, Université Paris-Saclay,
CEA, CNRS, F-91191 Gif-sur-Yvette Cedex, France*

⁴*Sorbonne Université, Institut Lagrange de Paris, 98 bis, Bd Arago, 75014 Paris, France*



(Received 30 July 2019; published 2 October 2019)

In this article we investigate the profile of the scalar field of a scalar-tensor theory subject to the chameleon mechanism in the context of gravity space missions like the MICROSCOPE experiment. We analyze the experimental situations for models with an inverse power-law potential that can in principle induce a fifth force inside the satellite, and hence either be detected or constrained. As the mass of the scalar field depends on the local matter density, the screening of the scalar field depends crucially on both the parameters of the theory (potential and nonminimal coupling to matter) and the geometry of the satellite. We calculate the profile of the scalar field in one-, two- and three-dimensional satellite configurations without relying on the thick- or thin-shell approximations for the scalar field. In particular, we consider the typical geometry with nested cylinders which is close to the MICROSCOPE design. In this case we evaluate the corresponding fifth force on a test body inside the satellite. This analysis clarifies previous claims on the detectability of the chameleon force by space-borne experiments.

DOI: [10.1103/PhysRevD.100.084006](https://doi.org/10.1103/PhysRevD.100.084006)

I. INTRODUCTION

General relativity (GR) has successfully passed all experimental tests from the Solar System scale [1] to cosmology [2], including the recent confirmation of the existence and properties of gravitational waves [3,4]. However, GR has to be endowed with a dark sector (including dark matter and a cosmological constant) to provide a cosmological model consistent with observations [5,6]. The absence of convincing models for the dark sector has revived the interest for gravity theories beyond GR [1,7]. These theories introduce new degrees of freedom, the effects of which need to be suppressed on small scales, although they may play an important role on cosmological scales.

The simplest extension of GR posits the existence of a nonminimally coupled scalar field. Such a theory, with only one extra degree of freedom, involves at least two free functions (a potential and a universal coupling function when enforcing the weak equivalence principle). These scalar-tensor theories are currently well constrained from local scales observations [1,8] to cosmology [9,10]. When the potential and the coupling function enjoy the same minimum these theories can exhibit a cosmological attraction mechanism toward GR in such a way that they are in agreement with local experimental constraints [11].

The new degree of freedom can then be considered as a valid dark-energy candidate [12].

On small scales, the scalar field is responsible for a fifth force that has to be shielded in order to pass existing experimental tests. Several screening mechanisms have been proposed in the case of scalar-tensor theories, including the least coupling principle [13], the symmetron [14], and the chameleon mechanism [15,16]. The latter model assumes that the coupling and potential functions do not have the same minimum. It follows that the minimum of the effective potential depends on the local density of matter. Hence, in high-density environments, the field is heavier and the fifth force may have a range that is too small to be detected, while in low-density environments the fifth force can be long ranged.

Local gravity experiments on the existence of a fifth force already provide strong constraints on the existence of the chameleon field [17,18] (see Sec. VID). The main bounds typically come from atom interferometry [19,20], Casimir effect measurements [21], or torsion balance experiments to detect short-scale forces [22]. Other efforts could lead to new advances by improving sensitivity or by imagining more original signatures [23]. It was originally expected [15,16] that space-based experiments could be highly competitive, as they would be performed in a lower-density environment.

However, all of these experiments suffer from the problem that their setups can screen the fifth force. The

*martin.pernot_borras@onera.fr

recent results on the test of the weak equivalence principle by the MICROSCOPE mission [24] orbiting the Earth have long been expected to provide new constraints on chameleon theories (as argued in Refs. [15,16]). In this experiment, even with a universal coupling, the proof masses can show different screenings of the field, leading to different accelerations. As a consequence, one would expect the equivalence principle to be violated for macroscopic extended objects, while it still holds at the fundamental level. The question is thus to determine how screened the chameleon field is at the level of a proof mass under the influence of the geometry of a given experiment, a study that has not been performed so far and for which this article is a first step. This is an intricate problem as the distribution of matter is often complex and the chameleon's dynamics is highly nonlinear. Most of the experiments cited above typically consist of a vacuum cavity enclosed in a shield that can contain experimental devices, such as electrodes or test masses. As these test masses are extended bodies, they must be taken into account in the profile of the field when computing the force they experience.

Two kinds of effects are expected depending on whether a cavity can be considered isolated or not. On the one hand, in the so-called “thin-shell” regime, the field inside the cavity is decoupled from the exterior since the cavity walls exponentially damp the field on a scale smaller than their thickness; in this case, the force applied to a test mass inside the cavity is local and is mostly determined by the structure and geometry of the cavity. On the other hand, in the so-called “thick-shell” regime, the exterior field can penetrate the cavity as it is marginally influenced by the matter constituting the cavity. The limit between these two regimes depends on the model parameters and the geometry of the experiments. In this article, we shall investigate these two dependences and compute the force exerted on a test mass in different settings.

To this end, we must determine the chameleon profile inside the experiment. This is a complex problem mostly because of the structure of the boundary conditions and the attraction of the profile toward a fixed point. It has been addressed in various ways in the literature. Analytic models suffer from the nonlinearities of the chameleon equation; to overcome them, the Klein-Gordon equation is often approximated by neglecting some terms or by linearizing the chameleon potential [16,21,25–32]. Numerical models [22,33–36] suffer from the limited resources they have, leading to solving the equation in a bounded region, setting the boundary conditions at a finite distance, or neglecting some short-scale variations of the field. Besides the fact that this last point may lead to an incorrect field even where the field varies slowly, this is very problematic for experiments using extended test masses. Short-scale variations are indeed more likely to happen in matter, impacting the very gradient responsible for the force that is being measured. This caveat is also encountered in analytic approaches.

This article overcomes these approximations. We tackle the problem numerically and consider all of the terms in the chameleon equation. To comply with the necessity to set boundary conditions at infinity, we consider a low-density background environment in which we embed a high-density system whose complexity increases throughout the paper. Our final goal is to approach the concentric-cylinder geometry of the MICROSCOPE instrument [24]. Although we restrict ourselves to static configurations with symmetries that are simpler than those in realistic cases, this paper will pave the way to further studies that include asymmetries and dynamics. We should note that most configurations studied in this article have already been partly explored in the literature, whether in specific regimes or with assumed boundary conditions. Here we investigate general profiles to clarify the boundary condition problem and to infer robust criteria to legitimize the approximations encountered in the literature.

This article is organized as follows. The first part of the paper focuses on one-dimensional (1D) geometries. In Sec. II, we discuss the dynamics of the chameleon field, paying particular attention to the role of boundary conditions. In Sec. III we analyze the case of an infinite wall, and in Sec. IV we consider the case of a one-dimensional cavity. Following these 1D configurations, we explore two-dimensional (2D) and three-dimensional (3D) symmetrical configurations in Sec. V. Finally, in Sec. VI we notice that the exact numerical integration of the field profile in a cavity leads to discrepancies with the analytic approximations used to evaluate the Casimir pressure induced by the chameleon field. We also consider the effect of the chameleon force on the motion of atoms in a cavity and the corresponding drift time, which could serve as a testing ground for such models. Finally, we present the field profile in nested cylindrical configurations close to the MICROSCOPE setting as a first step toward a more thorough investigation of the constraints from MICROSCOPE on chameleons, which is left for future work. We conclude in Sec. VII.

II. THE CHAMELEON'S PROFILE AND INITIAL CONDITIONS

A. Theoretical model

The chameleon mechanism is given in the Einstein frame by

$$S = \int d^4x \sqrt{-g} \left[\frac{M_{\text{Pl}}^2}{2} R - \frac{1}{2} \partial^\mu \phi \partial_\mu \phi - V(\phi) \right] - \int d^4x \mathcal{L}_m(\tilde{g}_{\mu\nu}, \psi_{\text{matter}}, \dots), \quad (1)$$

where ϕ is the chameleon field, V is its potential, M_{Pl} is the reduced Planck mass, R is the Ricci scalar, $g_{\mu\nu}$ is the Einstein frame metric, g is its determinant, and \mathcal{L}_m is the

matter Lagrangian with ψ_{matter} the matter fields. The field couples nonminimally to matter through the Jordan frame $\tilde{g}_{\mu\nu} = A^2(\phi)g_{\mu\nu}$, where A is a universal coupling function. We define the dimensionless coupling constant $\beta = M_{\text{Pl}} \frac{d \ln A}{d\phi}$. The field could have different coupling functions for each component of matter, but here we restrict to a universal coupling.

For static configurations of nonrelativistic matter, the field follows the Klein-Gordon equation

$$\nabla^2 \phi = V_{\text{eff},\phi} \equiv V_{,\phi} + \frac{\beta}{M_{\text{Pl}}} \rho_{\text{mat}}, \quad (2)$$

where ρ_{mat} is the mass density function. For nonstatic configurations, the Laplacian would be a d'Alembertian. We use the Ratra-Peebles inverse power-law potential of energy scale Λ and exponent n [17,37] as a typical example of a chameleon model,

$$V(\phi) = \Lambda^4 \left(1 + \frac{\Lambda^n}{\phi^n} \right). \quad (3)$$

The effective potential V_{eff} has a minimum given by

$$\phi_{\text{min}}(\rho_{\text{mat}}) = \left(M_{\text{Pl}} \frac{n\Lambda^{n+4}}{\beta\rho_{\text{mat}}} \right)^{\frac{1}{n+1}}. \quad (4)$$

It plays a central role in the chameleon dynamics.

We recall that in a medium with constant density, the field is expected to relax exponentially to the minimum of its potential. It varies on a typical scale of the order of its local Compton wavelength,

$$\lambda_{\text{c}}(\rho_{\text{mat}}) \equiv m^{-1}(\rho_{\text{mat}}) = \frac{1}{\sqrt{V''_{\text{eff}}(\phi_{\text{min}})}}, \quad (5)$$

which is explicitly given, in the models considered in this article, by

$$\lambda_{\text{c}}(\rho_{\text{mat}}) = \sqrt{\frac{1}{n(n+1)\Lambda^{n+4}} \left(\frac{nM_{\text{Pl}}\Lambda^{n+4}}{\beta\rho_{\text{mat}}} \right)^{\frac{n+2}{n+1}}}. \quad (6)$$

The fifth force induced by the coupling to the chameleon field on a test point mass is proportional to the gradient of the scalar field and given by

$$\vec{F} = -\frac{\beta}{M_{\text{Pl}}} m_{\text{test}} \vec{\nabla} \phi. \quad (7)$$

Nevertheless an extended body cannot *a priori* be considered as a test body since its own matter density impacts the field profile inside and outside its volume. Hence, to properly evaluate the force one needs to solve consistently for the field profile including the extended body and integrate this force over the whole volume of the body.

In what follows, it is convenient to rewrite the chameleon's Klein-Gordon equation (2) in terms of ϕ_{min} as

$$\nabla^2 \phi = n\Lambda^{n+4} \left[\frac{1}{\phi_{\text{min}}^{n+1}(\rho_{\text{mat}})} - \frac{1}{\phi^{n+1}} \right], \quad (8)$$

where the dependence on the local mass density is now contained in ϕ_{min} .

If we consider a region of space with local density ρ_{vac} that is large compared to the corresponding chameleon's Compton wavelength and far from any perturbing body, we can assume that the field is uniform with a value $\phi_{\text{vac}} = \phi_{\text{min}}(\rho_{\text{vac}})$. We shall now study the way a one-dimensional material structure affects this uniform profile as experiencing the different ϕ_{min} associated to the different environments the field should depart from ϕ_{vac} .

B. Initial conditions in one dimension

The chameleon profile is a solution to a boundary value problem. Given the previous discussion, the field shall relax to its minimum value in the external space, such that

$$\begin{cases} \phi \xrightarrow{x \rightarrow +/\infty} \phi_{\text{min}}(\rho_{\text{vac}}), \\ \phi' \xrightarrow{x \rightarrow +/\infty} 0. \end{cases} \quad (9)$$

Such a boundary value problem can be solved using finite-difference methods. However, due to the finite extent of computational memory we cannot set boundary conditions at infinity. We then need to set the boundary conditions at a finite distance from the considered object, and make a compromise between computational memory limits and the distance at which we can consider that the gap between the value that the field takes and ϕ_{vac} becomes negligible. The Compton wavelength in vacuum $\lambda_{\text{c,vac}}$ is an estimate of this distance [16,17]. This is an approximate criterion; a more accurate one will be determined in the following by the direct integration of an initial value problem.

Initial conditions cannot be chosen to be at ϕ_{vac} with a null derivative. To understand this we must note the key role played by ϕ_{min} as a fixed point of the theory. One can check that for $n > 0$ we have

$$\frac{d^2 \phi}{dx^2} \begin{cases} > 0 & \text{if } \phi > \phi_{\text{min}}, \\ = 0 & \text{if } \phi = \phi_{\text{min}}, \\ < 0 & \text{if } \phi < \phi_{\text{min}}, \end{cases} \quad (10)$$

so that the field derivative increases (decreases) for $\phi > \phi_{\text{min}}$ ($\phi < \phi_{\text{min}}$). For $\phi = \phi_{\text{min}}$, the field's derivative will not vary.

Hence, if we choose the initial conditions $\phi'_i = 0$, as in Fig. 1, the field will diverge monotonically toward $+\infty$ or $-\infty$ at large x , for an initial value $\phi_i > \phi_{\text{min}}$ or $\phi_i < \phi_{\text{min}}$, respectively. For an initial value $\phi_i = \phi_{\text{min}}$, since ϕ_{min} is a fixed point the field remains constant.

If we choose $\phi'_i \neq 0$, the considerations in Eq. (10) do not change and the ϕ' evolution remains the same. Nevertheless,

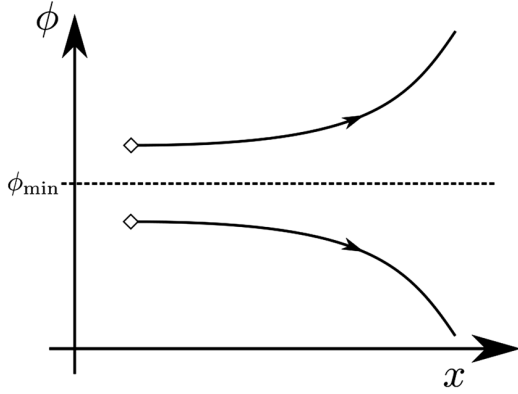


FIG. 1. Sketch of the field profiles for null initial derivatives: $\phi'_i = 0$. Different behaviors are obtained depending on the magnitude of ϕ_i compared to ϕ_{\min} .

the field evolution will no longer be monotonic and will eventually show maxima and minima. In the case where $\phi_i > \phi_{\min}$, if $\phi'_i > 0$, the field will diverge more rapidly than if $\phi'_i = 0$, if $\phi_i < 0$, new behaviors will occur. The different possible evolutions for $\phi'_i \neq 0$ are sketched in Fig. 2. For small values of $|\phi'_i|$, the field does not have enough “speed” to reach ϕ_{\min} , and thus it will reach a minimum and then diverge. For high values of $|\phi'_i|$, the field can reach ϕ_{\min} . When crossing ϕ_{\min} , ϕ' will still be negative, but as we now have $\phi < \phi_{\min}$ it will decrease and make the field diverge negatively. For a given ϕ_i , there is only one value of ϕ'_i (in between these two behaviors) that will cause ϕ' to vanish precisely when the field reaches ϕ_{\min} . In this case, ϕ_i is fixed by the considered matter distribution.

Note that the case where $\phi_i < \phi_{\min}$ is completely symmetric with the case where $\phi_i > \phi_{\min}$, as shown by the light grey curves in Fig. 2.

In 1D, the problem can be treated relatively easily. The chameleon equation can indeed be integrated once, from

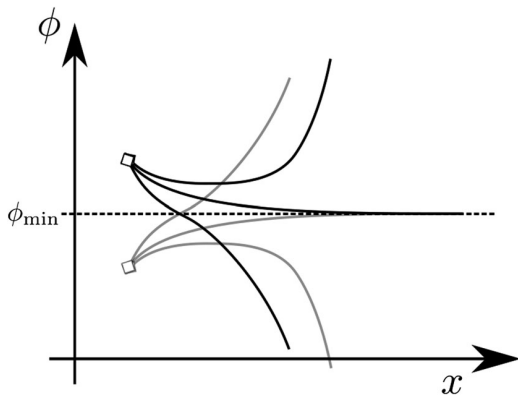


FIG. 2. Sketch of the field profiles for nonzero initial derivatives: $\phi'_i \neq 0$. Different behaviors (each line) are obtained depending on the magnitude and sign of ϕ'_i . Grey lines correspond to $\phi_i < \phi_{\min}$.

infinity—where boundary conditions are verified—to the place we want to set the initial conditions. This gives a condition on ϕ'_i in terms of ϕ_i ,

$$\frac{1}{2}\phi_i'^2 = \frac{n}{\phi_{\text{vac}}^{n+1}}(\phi_i - \phi_{\text{vac}}) + \left(\frac{1}{\phi_i^n} - \frac{1}{\phi_{\text{vac}}^n}\right). \quad (11)$$

This leaves us with only one initial parameter to deal with. We can use shooting methods, varying ϕ_i to obtain the proper solution for the considered configuration.

III. EFFECT OF AN INFINITE WALL ON THE CHAMELEON'S DYNAMICS

A. An interface between two infinite domains

As a first step, we consider the simple case of an interface between two infinitely extended domains of different densities, for instance, a high-density wall and a low-density vacuum of density ρ_{wall} and ρ_{vac} , respectively.

Far from the interface, the field will tend toward the value that minimizes the potential in each environment: ϕ_{wall} and ϕ_{vac} , respectively. Note that Eq. (4) implies $\phi_{\text{vac}} > \phi_{\text{wall}}$. In between, the field will evolve smoothly and cross the interface with a value ϕ_I and a continuous derivative, with $\phi_{\text{wall}} < \phi_I < \phi_{\text{vac}}$. To solve for the profile numerically, we set the initial conditions at this interface. In the wall since $\phi_I > \phi_{\text{wall}}$, the profile is analogous to the case shown by the black line that asymptotically tends toward ϕ_{\min} in Fig. 2. In the other domain, the symmetric dotted line is more relevant, as now $\phi_I < \phi_{\text{vac}}$.

In this configuration, no shooting methods are required. This is because the asymptotic conditions on both sides of the interface give two different conditions [equivalent to Eq. (11)] on ϕ_I and ϕ'_I , given by

$$\frac{1}{2}\phi_I'^2 = \frac{n}{\phi_{\text{vac}}^{n+1}}(\phi_I - \phi_{\text{vac}}) + \left(\frac{1}{\phi_I^n} - \frac{1}{\phi_{\text{vac}}^n}\right), \quad (12)$$

$$\frac{1}{2}\phi_I'^2 = \frac{n}{\phi_{\text{wall}}^{n+1}}(\phi_I - \phi_{\text{wall}}) + \left(\frac{1}{\phi_I^n} - \frac{1}{\phi_{\text{wall}}^n}\right). \quad (13)$$

Combining these two equations gives ϕ_I and ϕ'_I in terms of ϕ_{wall} and ϕ_{vac} . We can then integrate numerically in both domains. Figure 3 depicts such a solution with the interface at $x = 0$. Note that for this profile and for every other profile computed in the following, if not stated otherwise, we consider the case where $n = 2$, $\beta = 1$, $\Lambda = 1$ eV, $\rho_{\text{wall}} = 8.125$ g cm $^{-3}$, and $\rho_{\text{vac}} = 10^{-3}\rho_{\text{wall}}$ ($\phi_{\text{vac}} = 10\phi_{\text{wall}}$ for $n = 2$). In each domain, the field reaches the corresponding minimum of its potential within scales given by the Compton wavelength $\lambda_c(\rho_{\text{mat}})$. For the set of parameters and densities considered throughout the article, we have $\lambda_{c,\text{vac}} \simeq 2$ m and $\lambda_{c,\text{wall}} \simeq 0.02$ m. Note that for the sake of clarity, we chose ρ_{vac} and ρ_{wall} values that are not vastly different. For more realistic vacuum cavities, $\rho_{\text{vac}} = 10^{-15}\rho_{\text{wall}}$, implying a more significant difference between $\lambda_{c,\text{vac}}$ and $\lambda_{c,\text{wall}}$.

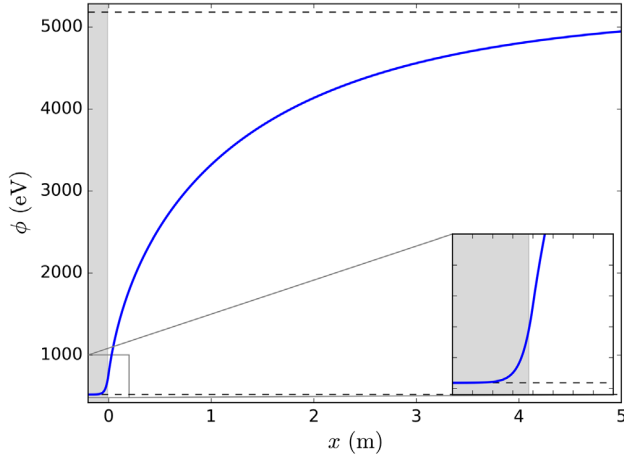


FIG. 3. Example of field profiles with an interface at $x = 0$. ϕ_{\min} values are shown with the two dashed lines. The grey zone is the higher density domain.

B. A single wall

We then consider a single wall of uniform density embedded in the low-density background environment. We denote its thickness by e . On both sides of the wall, the field will evolve similarly as in the previous section. We set the initial conditions on one of the borders of the wall, say, on the right side. We denote them by ϕ_e and ϕ_e' . By symmetry, the field value will be the same on the other border of the wall, with a derivative of opposite sign. As in the previous section, we know that $\phi_{\text{wall}} < \phi_e < \phi_{\text{vac}}$ with $\phi_e' > 0$, and by direct integration the boundary conditions give a condition on ϕ_e' in terms of ϕ_e ,

$$\phi_e' = \pm \sqrt{2 \left[\frac{n}{\phi_{\text{vac}}^{n+1}} (\phi_e - \phi_{\text{vac}}) + \left(\frac{1}{\phi_e^n} - \frac{1}{\phi_{\text{vac}}^n} \right) \right]}, \quad (14)$$

where we choose the positive sign in this case.

If we look toward the wall, the initial field derivative ϕ_e' will look negative. As $\phi_e > \phi_{\text{wall}}$, the field will be similar to the black line that shows a minimum in Fig. 2. The field will then evolve from ϕ_e to a minimum value reached at the center of the wall. The scale of this evolution will depend on the magnitude of ϕ_e . Consequently, there is a one-to-one mapping between e and ϕ_e : the larger the value of ϕ_e , the smaller the value of e .

Figure 4 depicts the numerical integration of a series of profiles for different values of e . Dotted lines delimit the frontiers of the considered wall. As expected, the thicker the wall gets, the more space the field has to evolve inside the wall, so the closer it gets to ϕ_{wall} .

1. $\phi_e(e)$ relation

To compute the profile associated with any wall thickness we need to determine the relation $\phi_e(e)$, which can be

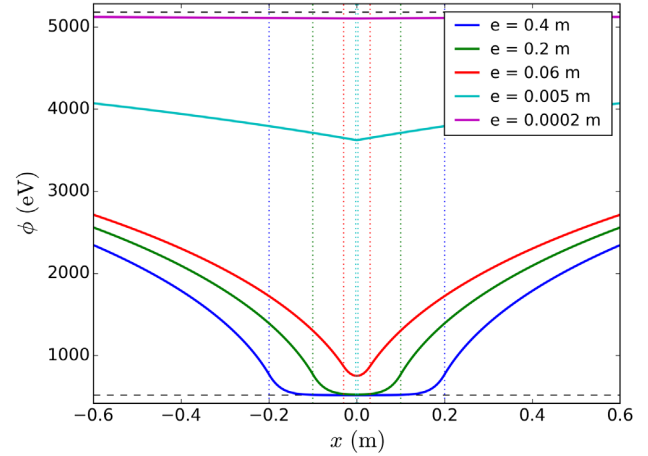


FIG. 4. Field profiles for different wall thicknesses e . The two values of ϕ_{\min} are shown by the two dashed lines. Dotted lines show the extent of the walls.

obtained by a shooting method. Figure 5 shows an example of such a relation for our fiducial parameters (n, β, Λ), and $\phi_{\text{wall}}, \phi_{\text{vac}}$.

This figure shows that a limited range for $\phi_e \in [\phi_1, \phi_{\text{vac}}]$ realizes all possible value of $e \in \mathbb{R}^+$. The bounds of this range are given by two limiting regimes:

- (i) ϕ_{vac} corresponds to the limiting case where the wall becomes infinitely thin and represents a very tiny perturbation to the background field.
- (ii) ϕ_1 corresponds to the other limiting case where the field tends to reach ϕ_{wall} at the center of the wall: we say that the field is completely screened inside the wall. The profile can be seen as two concatenated profiles of the case in Sec. III A, which explains the value ϕ_1 as the lower boundary. This behavior is consistent with the fact that the field is exponentially

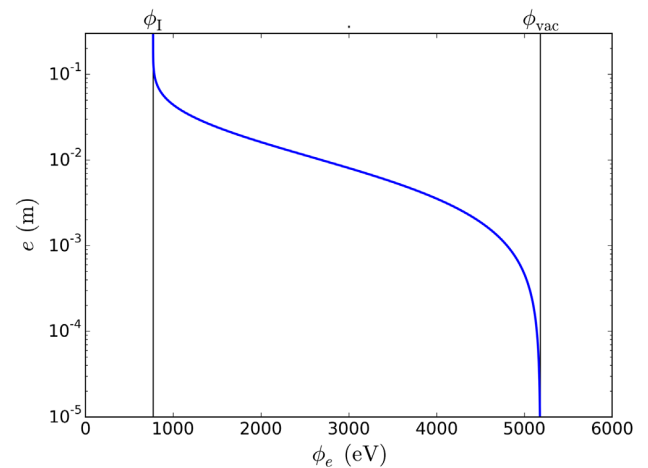


FIG. 5. Example of the relation $\phi_e(e)$. The black lines denote ϕ_1 and ϕ_{vac} .

suppressed in the wall on scales of the Compton wavelength $\lambda_{c,\text{wall}}$ in the wall.

2. $\phi_e(e)$'s dependence on Λ and β

ϕ_I and ϕ_{vac} depend on Λ and β in such a way that the interval $[\phi_I, \phi_{\text{vac}}]$ spreads or shrinks. It spreads logarithmically with Λ and shrinks logarithmically with β . Figure 6 shows how the $\phi_e(e)$ relation depends on Λ . Here the interval $[\phi_I, \phi_{\text{vac}}]$ is normalized to the interval $[0, 1]$.

This figure shows that when varying Λ , the $\phi_e(e)$ relations have the same slope, but are just shifted on the e axis. The dependence on β is similar, albeit in the opposite direction. To understand this variation, we can choose a specific value in the $[\phi_I, \phi_{\text{vac}}]$ interval, say, $\frac{\phi_e - \phi_I}{\phi_{\text{vac}} - \phi_I} = 0.5$, and see how e varies with Λ and β . We can fit this variation as

$$e(\Lambda, \beta) = A \times \Lambda \times \beta^{-\frac{2}{3}}, \quad (15)$$

where A is a coefficient that depends in a nontrivial way on ρ_{wall} and ρ_{vac} . In the cases considered in this figure, $A = 2.15 \times 10^{-3} \text{ m eV}^{-1}$.

3. Screening of the wall

As mentioned before, when the wall gets thicker, it gets screened so that the field tends to the value that minimizes the potential inside the wall ϕ_{wall} at the center of the wall. In this case, we can consider that the field's dynamics on both sides of the wall decouple, such that if the matter distribution were to change on one side of the wall it would not influence the field on the other side. This will be important for the case of a cavity.

This was expected to happen for walls thicker than $\lambda_{c,\text{wall}}$ [17]. Nevertheless, we can deduce from our simulations a more accurate criterion. We can indeed measure the

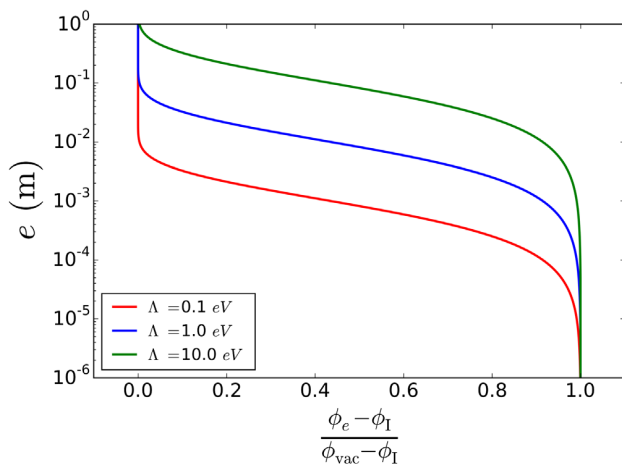


FIG. 6. Variation of $\phi_e(e)$ with Λ , for $\Lambda = 0.1, 1, 10 \text{ eV}$. The interval on which $\phi_e(e)$ is defined is normalized to $[0, 1]$.

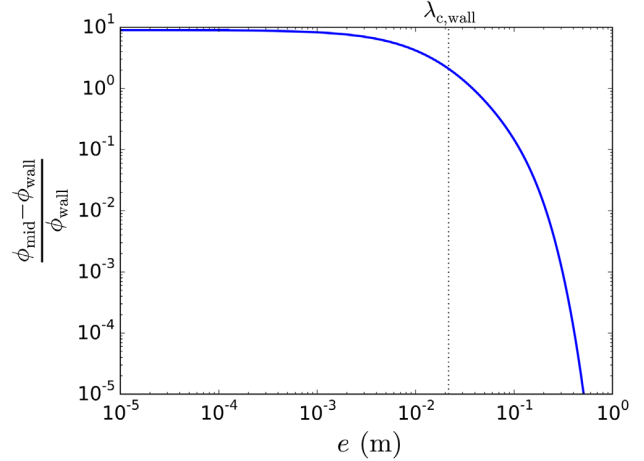


FIG. 7. Variation with the wall thickness e of the difference between the value of the field at the center of the wall and ϕ_{wall} .

difference between ϕ_{wall} and the effective minimum value the field reaches at the center of the wall. Figure 7 shows its evolution with the wall thickness.

As expected, we observe that this difference slowly decreases as the wall gets thicker. It then suddenly decreases when the wall thickness exceeds $\lambda_{c,\text{wall}}$. We can consider that this gap becomes negligible when it reaches a thickness of roughly $100\lambda_{c,\text{wall}}$, as it gets smaller than typical numerical precisions. This criterion is useful for other numerical methods such as finite-difference methods, in which one can only solve the field in a bounded region. For instance, when considering a system totally surrounded by walls, one can safely set initial conditions for the field to be at its minimum deeply inside these walls, as long as these walls have thicknesses greater than $100\lambda_{c,\text{wall}}$.

4. Range of influence of a wall

We can also deduce the scale of influence of a wall. Outside the wall, the field slowly relaxes to its asymptotic value ϕ_{vac} .

The typical relaxation scale L_e at which the gap between the field and ϕ_{vac} becomes negligible is given by

$$\frac{\phi(e/2 + L_e) - \phi_{\text{vac}}}{\phi_{\text{vac}}} = \epsilon, \quad (16)$$

where we take ϵ to be small. We can then consider that for distances to the wall larger than L_e , the dynamics of the field is no longer influenced by the wall.

Figure 8 shows how this scale of influence varies with the wall thickness, for $\epsilon = 1\%$. We observe that it increases when the wall gets thicker, and finally reaches a plateau when the wall is totally screened, i.e., its thickness exceeds $\lambda_{c,\text{wall}}$.

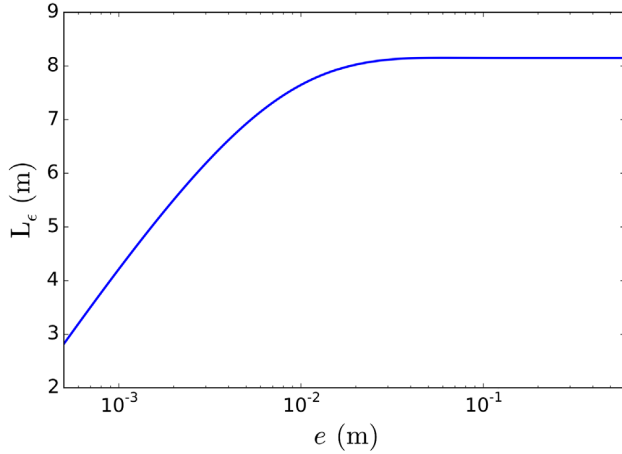


FIG. 8. Scale of influence L_e of a wall as a function of e , for $\epsilon = 1\%$.

We can infer a useful criterion from such a figure. We can safely assume that the influence of the wall cannot be felt farther than $10\lambda_{e,\text{vac}}$ from it.

IV. ONE-DIMENSIONAL CAVITY

A. Profile and $\phi_d(d)$ relation

The experimental case of a cavity in one dimension is modeled as two walls of equal thickness e , separated by an empty space of size d , as illustrated in Fig. 9. For simplicity we assume that the cavity has the same density as the background environment ρ_{vac} .

We follow the same approach as in the previous section. We impose initial conditions at the external border of a wall, say, the right one. When fixing the thickness of the wall, the initial conditions will be determined by the size of the cavity d , so we denote them by ϕ_d and ϕ'_d . The same first integration in the external vacuum region gives a condition on ϕ'_d in terms ϕ_d to satisfy the boundary condition at infinity. The magnitude of ϕ_d determines

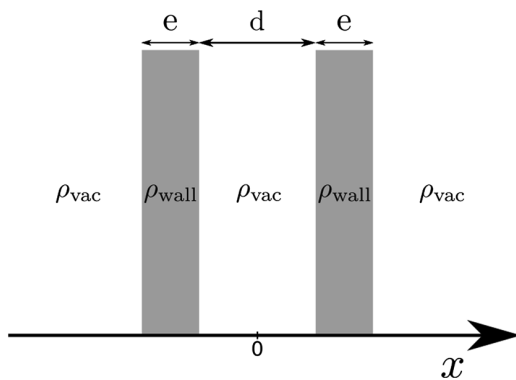


FIG. 9. 1D cavity.

the dynamics of the field inside the walls/cavity system. The overall profile will still be symmetric around the cavity center.

Inside the walls, the field is no longer symmetric. It must indeed reach a value smaller than ϕ_d on the inside border of the wall, as otherwise it would have the same asymptotic behavior as in the external vacuum region or diverge. Thus, if $\phi_e(e)$ is the initial value of the field given in the previous section for a wall of thickness e , we should now choose $\phi_d < \phi_e(e)$. In this way, the field will not have enough “speed” to reach ϕ_d again at the border of the cavity, but it will instead reach a value $\phi(d/2) < \phi_d < \phi_{\text{vac}}$, with a positive derivative. Then, in the cavity the field will have the same kind of dynamics with a maximum as for the bottom grey line in Fig. 2, and reach $\phi(d/2)$ again at the other side of the cavity.

For a fixed wall thickness e , ϕ_d will determine the value of $\phi(d/2)$, which will determine the maximum field

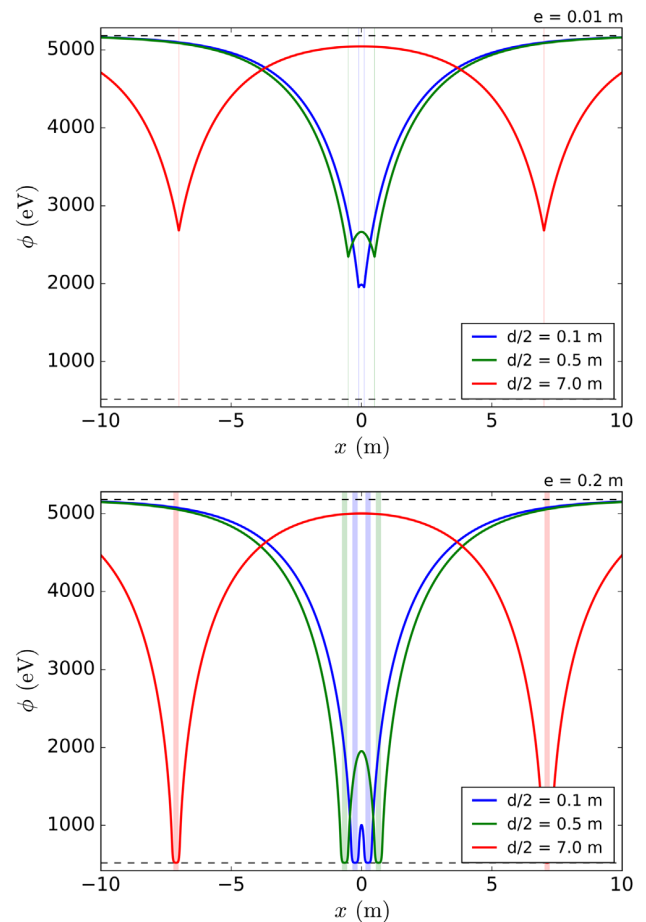


FIG. 10. Field profiles for different cavity sizes with unscreened (upper panel) and screened (lower panel) walls of thickness $e = 0.01$ m and $e = 0.2$ m, respectively. The values of ϕ_{min} are shown as dashed lines. The walls are represented by vertical colored strips.

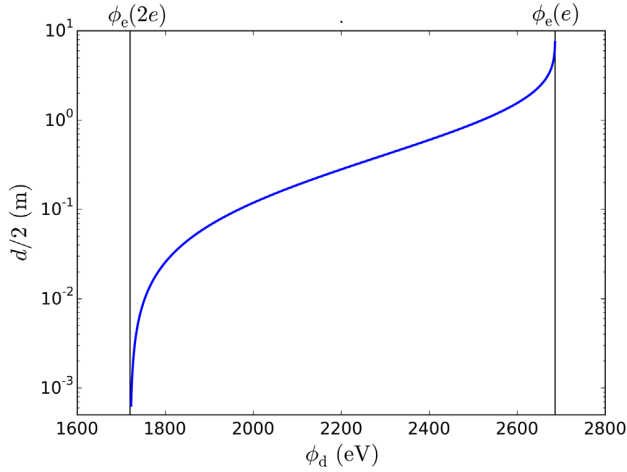


FIG. 11. Relation $\phi_e(d)$, for $e = 1$ cm. ϕ_{\min} values are shown with the two black lines.

value ϕ_0 at the cavity center. Thus, we will obtain the corresponding cavity size d . We use the same shooting method as in the previous section to numerically determine how ϕ_d varies with d , and hence the $\phi_d(d)$ relation. Note that the larger the value of d , the larger the value of ϕ_0 .

Figure 10 shows profiles corresponding to different cavity sizes, with a thin wall of size $e = 1$ cm (upper panel) and a thick screened wall of size $e = 20$ cm (lower panel). We find bubble profiles inside the cavity similar to Refs. [25,26].

Figure 11 shows an example of the $\phi_d(d)$ relation with thin unscreened walls of size $e = 1$ cm. As for the case of a single wall, the whole interval for $d \in \mathbb{R}$ is spanned by a restrained interval for ϕ_d , $[\phi_e(2e), \phi_e(e)]$, where $\phi_e(2e)$ corresponds to the initial condition associated with a single wall of size $2e$.

The curve for $\phi_d(d)$ is similar to $\phi_e(e)$ in the previous section, with two regimes. For $d \gg \lambda_{c,vac}$, the field has enough space in the cavity to reach a value ϕ_0 at its center close to the potential minimum ϕ_{vac} . In this regime, and as the cavity grows larger the two walls can be considered to be isolated, so the dynamics of the field is very similar to the one seen in Sec. III B. This explains why ϕ_d varies very slowly with d , with $\phi_d \simeq \phi_e(e)$.

On the other hand, as the size of cavity decreases the field has less and less space to evolve, such that ϕ_0 gets smaller. In this regime, as the two walls get closer, the dynamics of the field tends to the dynamics of a single wall of thickness $2e$. This explains why small values of d are obtained for ϕ_d tending towards $\phi_e(2e)$.

B. Chameleonic force in a cavity

Using the field profiles in a cavity, we can deduce the fifth force that a test point mass would feel using Eq. (7).

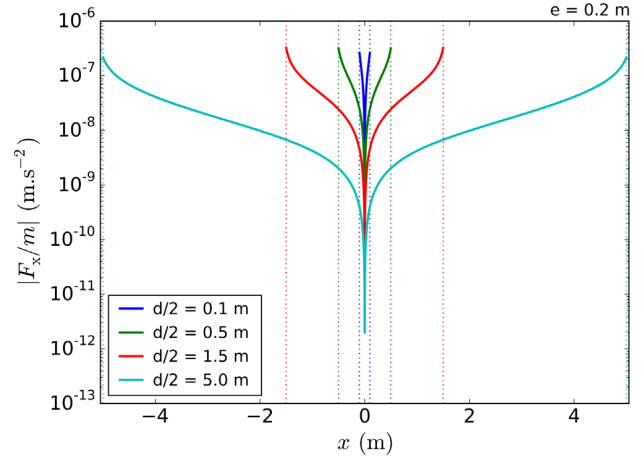


FIG. 12. Force experienced by a test mass for different cavity sizes, for screened walls with $e = 1$ m.

Figure 12 shows the magnitude of the fifth force experienced by a test mass inside cavities of different sizes for a constant wall thickness as expressed by Eq. (7). This force is directed outward. The wall is chosen here to be screened with $e = 0.2$ m. It shows that the force profile does not vary much, but just stretches with the cavity. The maximum force value reached at the border of the cavity varies slightly.

Conversely, Fig. 13 shows how the force profile changes as a function of the wall thickness, at constant cavity size. One can see that the magnitude of the force increases as the walls get thicker. In agreement with previous considerations, it stops varying when the wall thickness exceeds $\lambda_{c,wall} = 2.2$ cm, as the screened walls isolate the inner dynamics from the outside. Thus, larger forces are expected in cavities separated by thick walls. Nevertheless, in the case of thin walls, we expect it to be overtaken by effects sourced by external objects.

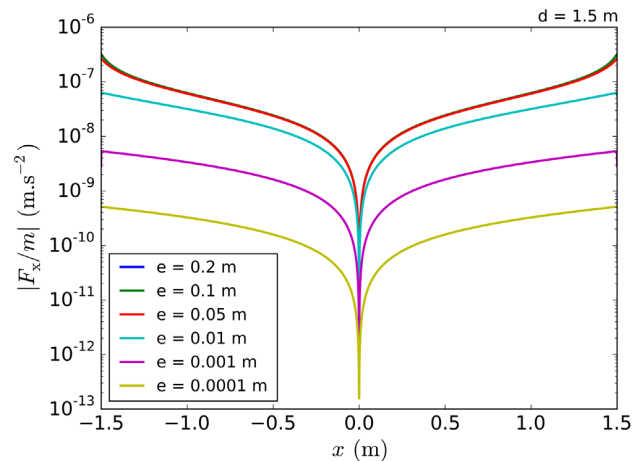


FIG. 13. Force experienced by a test mass for different wall sizes, for a fixed cavity size $d = 1.5$ m.

V. CYLINDRICAL AND SPHERICAL SYSTEMS

In 2D and 3D, the method previously used is no longer applicable. The chameleon's Klein-Gordon equation (8) indeed becomes in cylindrical or spherical symmetries

$$\frac{d^2\phi}{dr^2} + \frac{(D-1)}{r} \frac{d\phi}{dr} = n\Lambda^{n+4} \left[\frac{1}{\phi_{\min}^{n+1}(\rho_{\text{mat}})} - \frac{1}{\phi^{n+1}} \right], \quad (17)$$

where D is the dimension of the symmetry. For $D \geq 2$, the first field's derivative term prevents us from obtaining a condition on the initial field derivative by integrating the chameleon equation once. Thus, we cannot follow the same scheme as before, and we need to adjust the two initials conditions ϕ_i and ϕ'_i .

Nevertheless, it is convenient to set the initial conditions at the symmetry center, as by symmetry the derivative of the field cancels. We thus have to determine a single parameter—the value of the field ϕ_0 —to obtain the correct profile. A dichotomy algorithm can be used to determine the correct ϕ_0 that satisfies the correct asymptotic boundary conditions (9). A more complex analysis of the chameleon's dynamics than the one in Sec. II B shows that if the value of ϕ_0 is greater (weaker) than its correct value, the field will asymptotically diverge positively (negatively). Then, by solving the field for some ϕ_0 , we can evaluate whether the field is greater or lesser than ϕ_{vac} at some large distance far greater than $\lambda_{\text{c,vac}}$ from the considered system, and then adjust ϕ_0 as a dichotomy and reproduce the same procedure.

This converges rapidly toward the correct profile. It is important to note that, because the symmetry center is the origin of the coordinate system ($r = 0$), we cannot impose initial conditions at this point as the second term in Eq. (17) diverges numerically due to its dependence on r . We instead impose them very close to $r = 0$, with $\phi_i = \phi_0$ and $\phi'_i = 0$. This should lead to an error on the obtained field. The fields obtained in a 1D cavity with this method agree with the fields obtained with the previous method to less than 0.1%.

A. Cylindrical and spherical cavity

Analogously to Sec. IV, the cases of a cavity in 2D and 3D are, respectively, an infinitely extended cylinder and an empty sphere. Here we still denote the diameter of the cavity by d and the wall thickness by e .

The radial profiles in such cases are very similar to the 1D case. For equal cavity size, the effect of cylindrical and spherical symmetry decreases the values reached in the cavity. Figure 14 shows examples of radial profiles for 1D, 2D, and 3D cavities in the cases of screened walls and unscreened walls.

When the wall is screened the nature of the cavity does not affect the field outside. The field tends to reach lower values in the cavity for larger cavity sizes, leading to a weaker force. When the wall is not screened, the behavior

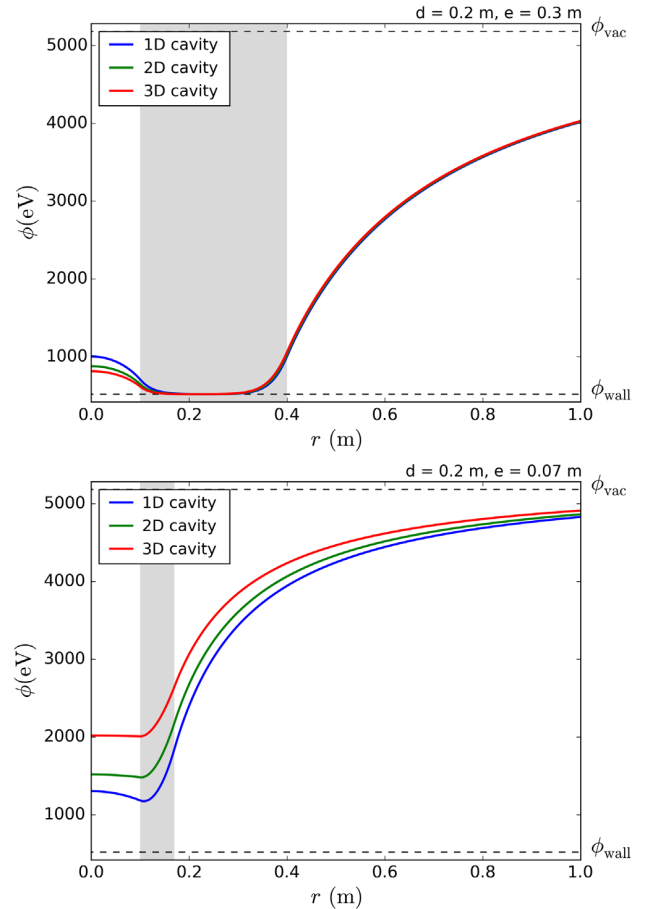


FIG. 14. Field profiles for 1D, 2D, and 3D cavities in the case of screened walls of thickness $e = 30$ cm and unscreened walls of thickness $e = 7$ cm. Values of ϕ_{\min} are shown as dashed lines. The wall is shown by the grey region.

becomes inverted and the size of the cavity has an impact on the exterior field.

B. ϕ_0 variation

As for the 1D cavity, the larger the cavity, the larger the value of ϕ_0 reached by the field at the center of the cavity. In the literature (e.g., Ref. [16] for a sphere or Refs. [18,38] for a cylinder), this value was expected to be that of the field whose mass matches the radius of the cavity, i.e., that is given by

$$\frac{d}{2} = m^{-1}(\phi_0) = \frac{1}{\sqrt{V''(\phi_0)}}. \quad (18)$$

In Fig. 15 the value of ϕ_0 obtained with this approximate criterion is compared to the actual value given by these simulations for 1D, 2D, and 3D cavities. All curves have the same global monotony. Nevertheless, whereas simulations show that $\phi_0 \in [\phi_{\text{wall}}, \phi_{\text{vac}}]$, the approximated criterion does not give a bounded range for ϕ_0 .

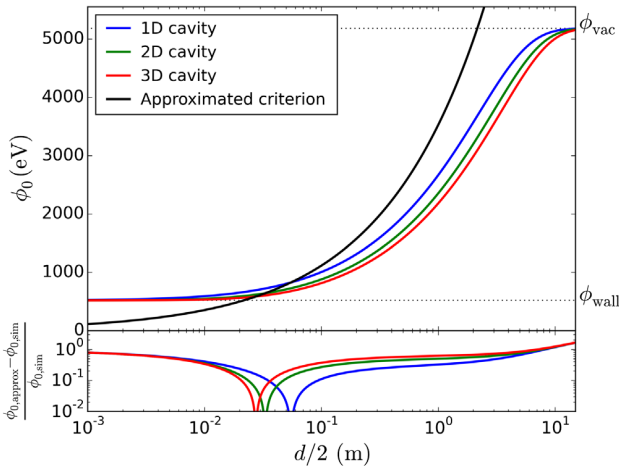


FIG. 15. Central value of the field in the cavity as a function of the cavity size d for screened walls of thickness $e = 0.1$ m. The colored lines correspond to 1D, 2D, and 3D cavities. The black line is an approximated estimation from Ref. [16]. ϕ_{\min} values are shown by the two dotted lines. The lower panel shows the relative difference between the two curves.

The comparison of the curves shows that they mainly diverge by 100%, such that the approximated criterion turns out to be very weak.

VI. APPLICATIONS AND DISCUSSION

A. Chameleonic Casimir-like force

The one-dimensional configuration in Sec. IV is similar to the typical experimental setup in Casimir effect measurements in which two nearby plates experience a force of quantum origin [39,40]. In the case of the chameleon field, one expects an extra effect that would add up to the conventional Casimir force. In both cases, the force between the walls is attractive. The walls play the role of the plates, and the effect originates from the fact that the field in the walls is not symmetrical and thus its gradient does not cancel. The global behavior of the force as a function of the distance between the walls was computed with an approximate analytic model in Ref. [21].

The force a wall feels can be computed by integrating the gradient of the field over the whole wall. Knowing the profile associated with a two-wall configuration, a 1D integration gives the pressure,

$$\begin{aligned} F_s &= -c^2 \frac{\beta}{M_{\text{Pl}}} \int_{\frac{d}{2}}^{\frac{d}{2}+e} \nabla_x \phi \rho_{\text{wall}} dx \\ &= -c^2 \frac{\beta}{M_{\text{Pl}}} \rho_{\text{wall}} [\phi_d - \phi(d/2)]. \end{aligned} \quad (19)$$

Figure 16 shows the evolution of this pressure in the case of our simulations and in the case of Ref. [21], as a function of the separation of the walls. Both curves have the same

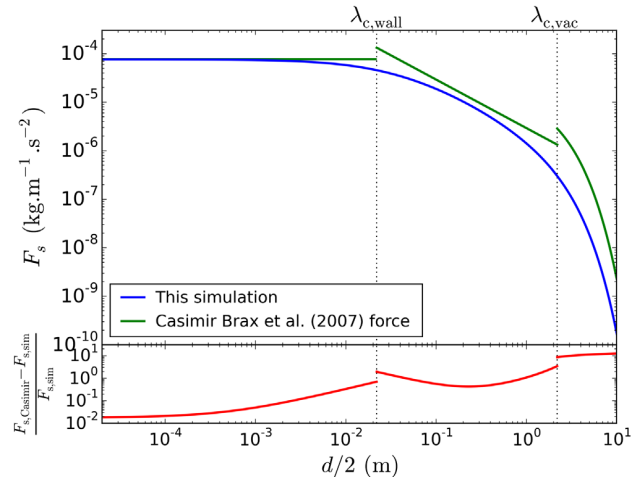


FIG. 16. Upper panel: chameleon-originated Casimir force as a function of the separation d of the walls for screened walls with $e = 0.2$ m. The blue curve is the result of this simulation. The green lines come from the analytical model of Ref. [21]. Lower panel: Relative difference. Dotted lines show $\lambda_{c,\text{vac}}$ and $\lambda_{c,\text{wall}}$.

global behavior, with a plateau for small separations and an exponential suppression for separations greater than $\lambda_{c,\text{vac}}$. This latter behavior is consistent with Sec. VB, as we saw that for large separations the walls can be considered as isolated, so the field tends to the symmetrical case of Sec. III B.

Despite their similar behavior, the two curves do not match perfectly. For small separations they agree within a few percent. In the intermediate regime $\lambda_{c,\text{wall}} < \frac{d}{2} < \lambda_{c,\text{vac}}$, they diverge by a few tenths of a percent, and for larger separations they diverge more severely. The force we find is weaker, and this might slightly relax current Casimir measurement constraints on the chameleon [21].

B. Thin- and thick-shell approximations of a ball

Another important case is a spherical uniform ball. In the chameleon's original article [16], the profile around a ball was approximated in two extremal regimes: the thick-shell regime in which the ball is too small for the field to reach the minimum of the potential in the ball; and the thin-shell regime in which the ball is large enough for the field to remain mainly at the minimum of the potential throughout most of the ball. Our simulations can provide the field around a ball in any regime.

Figure 17 compares our simulations with the thin-shell and thick-shell approximations, with different contrasts between the vacuum and the ball density (then different values of ϕ_{vac}). In the thick-shell regime, our simulation and the thick-shell model are in very good agreement (to less than a percent) when the density contrast is low. When the density contrast is larger, the agreement is even better (to less than 0.01%). In the thin-shell regime, the two profiles agree to within a few percent, except inside a zone

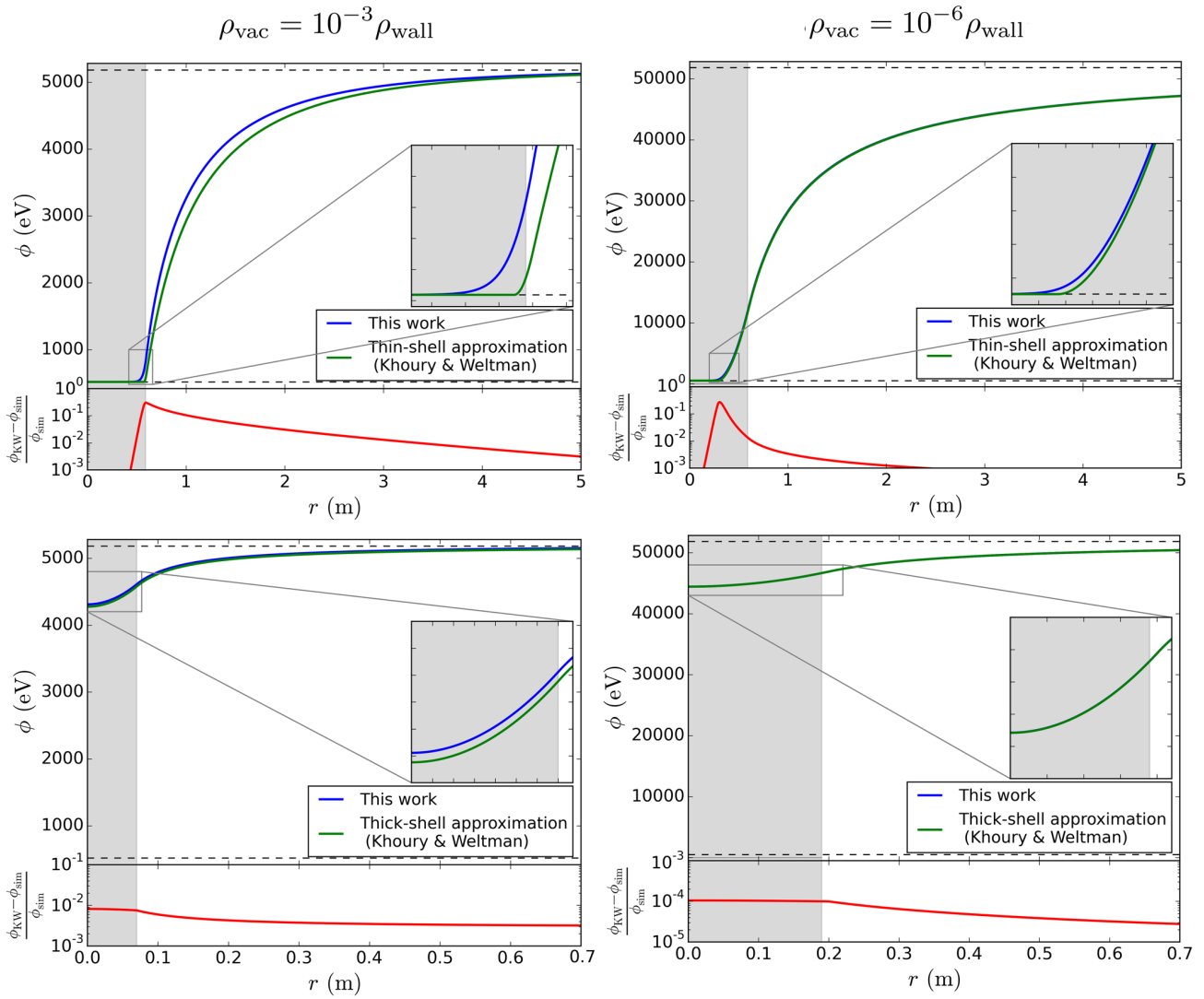


FIG. 17. Radial field profiles of a ball embedded in vacuum. The shaded zone corresponds to the inside of the ball. These simulations are compared to the models of Ref. [16] in the thin-shell regime (upper panels) and thick-shell regime (lower panels). The left and right panels correspond to different matter contrasts between the ball and the vacuum. ϕ_{\min} values are shown as dashed lines.

around the interface between the ball and the vacuum, where they agree to within a few tenths of a percent. This comes mainly from the difference in the skin depth of the wall on which the field varies. For higher density contrasts, the agreement is globally better, but there is still a slight difference where the field starts to vary inside the ball.

We can therefore assume that, except for inside the ball, the models are globally accurate in the thin-shell regime. In between the two regimes, when the ball has an intermediate radius, these two models are less accurate, particularly for low density contrasts.

C. Radial drift of test masses in a cylinder

As shown above, the chameleon inside a cavity creates a radial outward force that affects test masses (like atoms).

For instance, the profile of the force created in the cylindrical case of Fig. 14 is shown in the upper panel of Fig. 18. This force may affect any experiment based on monitoring the trajectory of atoms inside a cylindrical cavity [41], even if measuring it is not the primary objective of the experiment (in which case it should be considered as a source of systematic uncertainty).

Let us consider an experiment where atoms (test masses) are dropped at a distance R_0 from the main symmetry axis of the cylinder (either alongside the axis, or radially): the atoms will experience an outward radial drift, with a drift rate depending on the parameters (β, Λ, n) of the model. For instance, in the screened cylindrical case of Fig. 14, if they are dropped with a null velocity at $R_{\text{vac}}/10$, the atoms will reach the border of the cavity in 2498 s. The middle panel of Fig. 18 shows the total drift time for the atoms to reach

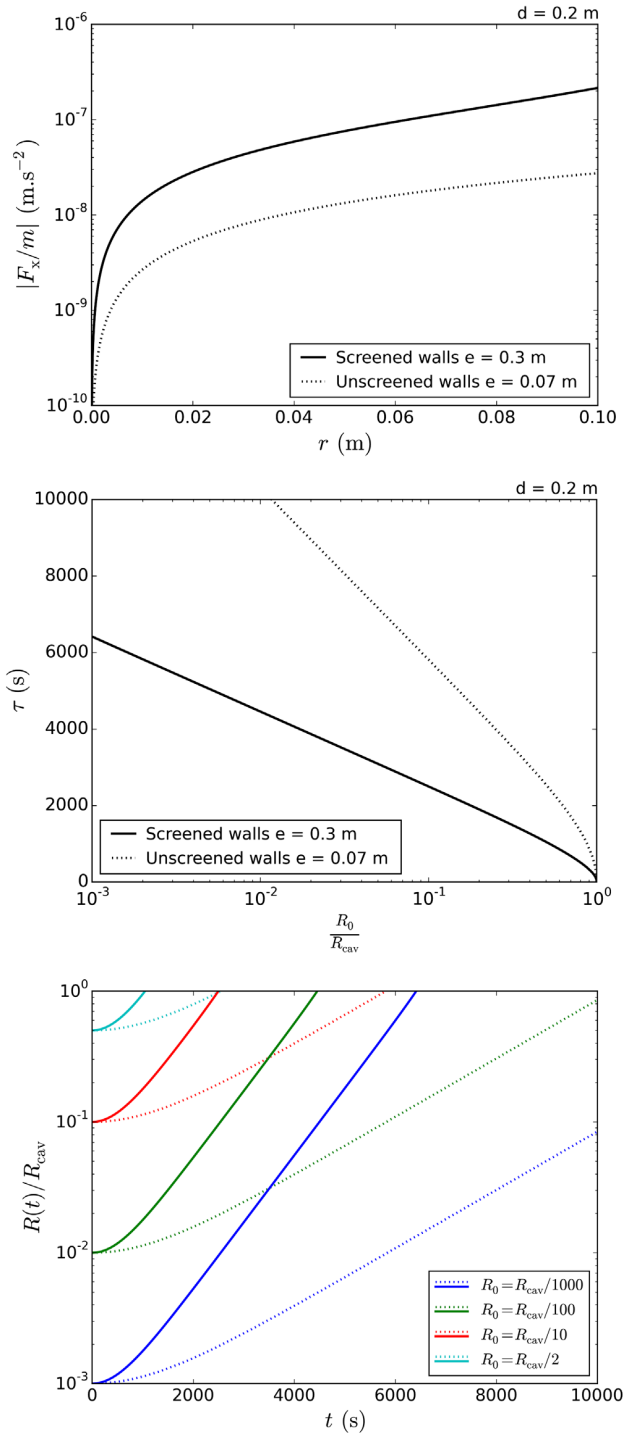


FIG. 18. Upper panel: Fifth force associated with the cylindrical cavity in Fig. 14. Middle panel: Total drift time from some initial position R_0 to the border of the cavity R_{cav} . Lower panel: Radial position of atoms R as they drift with time t for different initial positions. Solid lines correspond to screened walls ($e = 0.3$ m) and dotted lines to unscreened walls ($e = 0.07$ m).

R_{cav} as a function of R_0 . In the unscreened case, as the profile is flatter, the force is weaker than in the screened case, so that the drift time is typically longer. Trivially, the smaller R_0 , the longer the drift time. The lower panel shows the evolution with time t of the radial position R of atoms in the cavity for different initial positions R_0 .

In more realistic setups, the drift should be estimated in view of typical integration times as it may become non-negligible, even in experiments not specifically looking for a chameleon inside the cavity. For instance, we could conceive of an experiment where the motion of atoms under the influence of the Earth's gravitational field is measured. If the chameleon force inside the cavity is strong enough to impart a detectable drift on the atoms, it should be considered as a source of systematic error (though its detection would be a significant breakthrough). Another typical case is where we drop two types of atoms, e.g., to test the equivalence principle in the Earth's gravitational field; if the chameleon coupling β is not universal, then the chameleon inside the cavity will make the atoms drift differentially, thereby mimicking a violation of the equivalence principle, though it would be considered as a systematic uncertainty on the main measurement.

D. Nested cylinders: Toward the MICROSCOPE configuration

Our computation generalizes to more complex configurations, such as the case of nested infinite cylinders. Figure 19 compares different profiles for two nested cylinders of either same or different matter densities.

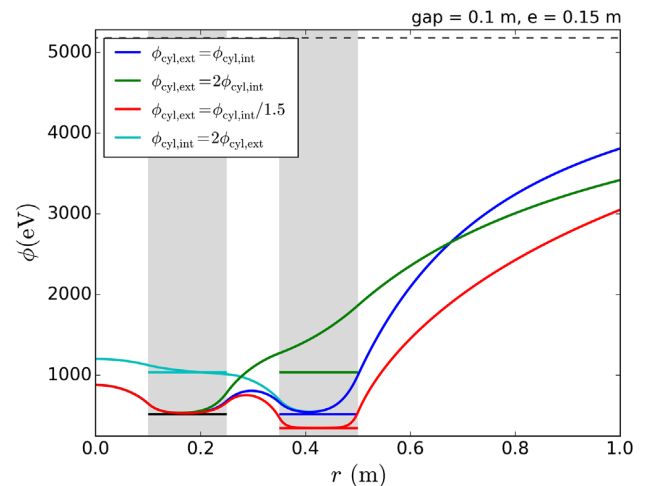


FIG. 19. Radial profiles for two nested cylinders of thickness e and different matter densities, to which correspond different values of ϕ_{min} . These ϕ_{min} values are represented by the horizontal segments. Cylinders are delimited by the shaded regions and separated by a distance gap .

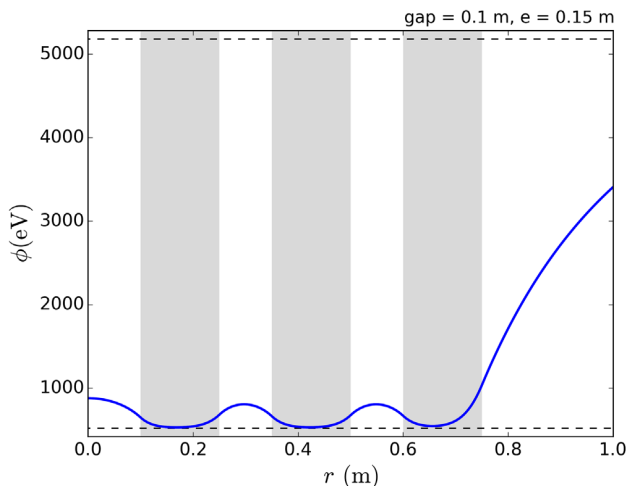


FIG. 20. Radial profile for three nested cylinders of thickness e with the same matter density. Cylinders are delimited by the shaded regions and separated by a distance gap . The ϕ_{\min} values are represented by the horizontal segments.

Consistently with our 1D study, the nature of the outer cylinder has no influence on the profile inside the inner cylinder when the cylinders are screened. Besides, in the empty inter-cylinder space, atoms experience a drift similar to the one discussed previously. But whereas in the cylindrical cavity a change in the direction in the force occurs at the center of the cavity, here it no longer occurs at the middle of the empty space but rather at some other location (at the maxima of the field) that depends on the densities of the cylinders and on the parameters of the model. This change of direction can even disappear, as it does for the green line. Then, different signatures are expected for different cylinders' features and chameleon parameters.

Figure 20 shows the radial profile obtained for three nested cylinders. This configuration is similar to the MICROSCOPE experiment's design in which cylindrical test masses are nested in cylindrical sensors. The middle cylinder experiences a chameleonic fifth force from the cylinders; nevertheless, when integrated over the whole cylinder it vanishes due to the cylindrical symmetry. We expect a force to appear when the symmetry is broken, e.g., when one of the cylinders is not perfectly centered. While this would require more intricate computations, (which will be described in a follow-up article), we can estimate the magnitude of such a force. To that purpose, we consider the force exerted on a cylindrical element (of opening angle $d\theta$ and height dl) of a cylinder. In the case shown in Fig. 20, this force is $\frac{dF}{d\theta dl} = 6.3 \times 10^{-6} \text{ N m}^{-1} \text{ rad}^{-1}$, and is directed towards the center. We expect the total force in a decentered configuration to be of the same order of magnitude up to a geometry factor.

In Ref. [16] it was claimed that MICROSCOPE could detect a clear violation of the weak equivalence principle

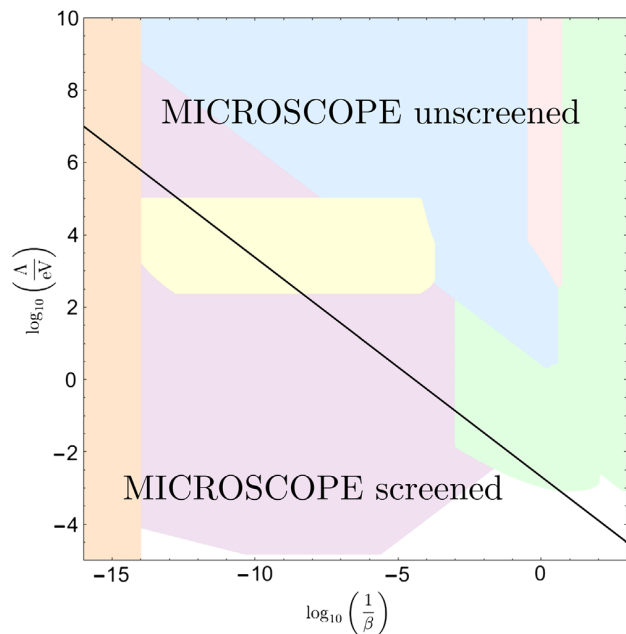


FIG. 21. The chameleon's parameter space adapted from Refs. [17,18]. The black line corresponds to parameters for which $100\lambda_{c,\text{shield}} = e_{\text{shield}}/2$ and delimits two regimes, i.e., whether the MICROSCOPE setup is screened or not. The colored regions correspond to current constraints from other experiments: atomic interferometry (purple [42]), Eöt-Wash (green [22,43]), Casimir effect measurements (yellow [21,44]), astrophysics tests (blue [45–47]), lensing (pink [48]), and precision atomic tests (orange [49,50]).

from the chameleon field sourced by the Earth. However, the screening due to the experimental setup itself was neglected. The MICROSCOPE setup is actually enclosed in a shield of thickness $e_{\text{shield}} \simeq 1 \text{ cm}$. Using the screening criterion of Sec. III B 3, we show in Fig. 21 that the chameleon parameter space (for $n = 1$) is divided into two regions: above the black line (which shows where $100\lambda_{c,\text{shield}} = e_{\text{shield}}/2$, where $\lambda_{c,\text{shield}}$ stands for the Compton wavelength associated with the shield's density) MICROSCOPE is not screened, but it is screened below the line. Thus, no violation of the weak equivalence principle can be expected below the line, while it could still be expected above it. The colored regions in Fig. 21 correspond to regions that have already been experimentally excluded [17]. It is then clear that the constraining potential of MICROSCOPE is much less than anticipated. It could only improve our current knowledge about the chameleon in a small region. This will be the subject of future work where the effect of the Earth on the chameleon profile will be included.

VII. CONCLUSION

In this article, we treated the problem of solving the chameleon scalar field's profile by paying special attention

to the boundary conditions. We found that it is possible to deal with this problem numerically without using any approximations. Our approach considers a matter system embedded in a background environment. We first considered 1D symmetrical systems. We treated the cases of a single wall and a cavity modeled as two separated walls. We determined a refined criterion which guarantees that screening occurs within a cavity. For instance, we checked that we can safely consider that the field reaches its minimum inside a matter wall, as long as the wall thickness exceeds 100 times the Compton wavelength associated with the wall matter. In this case we can consider that such a wall would screen the field. In the case of a cavity, we computed the profiles of forces that test masses would experience inside the cavity. We also computed the Casimir-like force and found discrepancies with analytic approximations in the literature. We then explored 2D and 3D symmetrical geometries. The case of a ball was compared to the thin-shell and thick-shell models from Ref. [16]. We found it to be in very good agreement, except in the region close to the ball's boundary. In a cylindrical cavity, we studied how point masses like atoms could experience a drift between the cylinders which may either lead to an experimental method of detecting chameleons or create a new source of systematic uncertainty in future experiments.

Finally, we treated the case of nested cylinders of different matter densities suited to the setup of the MICROSCOPE mission. Despite the symmetry considered here, which leads to a null force experienced by the cylinders, we provided an estimate of the magnitude of

the force when the symmetry is broken. This effect will be explored by simulating nonsymmetric configurations in a follow-up article. Moreover, our analysis challenges the previous claim on the ability of space experiments to detect chameleon-sourced violations of the weak equivalence principle sourced by the Earth [15,16]. Using the refined screening criterion for cavities, we deduced that for a large region of the parameter space such an effect would be screened by the experimental setup. The Earth should be included in simulations of the remaining region. This will be the subject of a forthcoming article.

ACKNOWLEDGMENTS

We thank Manuel Rodrigues, Gilles Métris, and Pierre Touboul for useful discussions and technical information about the MICROSCOPE experiment. We thank the members of the MICROSCOPE Science Working Group for allowing us to start this project and encouraging us to pursue it. We acknowledge the financial support of CNES through the APR program (“GMscope+” project). M. P. B. is supported by a CNES/ONERA PhD grant. This work uses technical details of the T-SAGE instrument, installed on the CNES-ESA-ONERA-CNRS-OCA-DLR-ZARM MICROSCOPE mission. This work is supported in part by the EU Horizon 2020 research and innovation programme under the Marie-Sklodowska Grant No. 690575. This article is based upon work related to the COST Action CA15117 (CANTATA) supported by COST (European Cooperation in Science and Technology).

-
- [1] C. M. Will, The confrontation between general relativity and experiment, *Living Rev. Relativity* **17**, 4 (2014).
 - [2] M. Ishak, Testing general relativity in cosmology, *Living Rev. Relativity* **22**, 1 (2019).
 - [3] LIGO Scientific and Virgo Collaborations, Observation of Gravitational Waves from a Binary Black Hole Merger, *Phys. Rev. Lett.* **116**, 061102 (2016).
 - [4] LIGO Scientific and Virgo Collaborations, Multi-messenger observations of a binary neutron Star merger, *Astrophys. J. Lett.* **848**, L12 (2017).
 - [5] Y. Akrami, F. Arroja, M. Ashdown, J. Aumont, C. Baccigalupi, M. Ballardini, A. J. Banday, R. B. Barreiro, and N. Bartolo (Planck Collaboration), Planck 2018 results. I. Overview and the cosmological legacy of Planck, [arXiv:1807.06205](https://arxiv.org/abs/1807.06205).
 - [6] P. Peter and J.-P. Uzan, *Primordial Cosmology*, Oxford Graduate Texts (Oxford University Press, Oxford, 2009).
 - [7] B. Jain *et al.*, Novel probes of gravity and dark energy, [arXiv:1309.5389](https://arxiv.org/abs/1309.5389).
 - [8] P. C. C. Freire, N. Wex, G. Esposito-Farèse, J. P. W. Verbiest, M. Bailes, B. A. Jacoby, M. Kramer, I. H. Stairs, J. Antoniadis, and G. H. Janssen, The relativistic pulsarwhite dwarf binary PSR J1738 + 0333 II. The most stringent test of scalartensor gravity, *Mon. Not. R. Astron. Soc.* **423**, 3328 (2012).
 - [9] A. Riazuelo and J.-P. Uzan, Cosmological observations in scalar-tensor quintessence, *Phys. Rev. D* **66**, 023525 (2002).
 - [10] A. Coc, K. A. Olive, J.-P. Uzan, and E. Vangioni, Big bang nucleosynthesis constraints on scalar-tensor theories of gravity, *Phys. Rev. D* **73**, 083525 (2006).
 - [11] T. Damour and K. Nordtvedt, General Relativity as a Cosmological Attractor of Tensor-Scalar Theories, *Phys. Rev. Lett.* **70**, 2217 (1993).
 - [12] J.-P. Uzan, Cosmological scaling solutions of nonminimally coupled scalar fields, *Phys. Rev. D* **59**, 123510 (1999).
 - [13] T. Damour and A. Polyakov, The string dilation and a least coupling principle, *Nucl. Phys.* **B423**, 532 (1994).
 - [14] K. Hinterbichler and J. Khoury, Screening Long-Range Forces Through Local Symmetry Restoration, *Phys. Rev. Lett.* **104**, 231301 (2010).

- [15] J. Khoury and A. Weltman, Chameleon Fields: Awaiting Surprises for Tests of Gravity in Space, *Phys. Rev. Lett.* **93**, 171104 (2004).
- [16] J. Khoury and A. Weltman, Chameleon cosmology, *Phys. Rev. D* **69**, 044026 (2004).
- [17] C. Burrage and J. Sakstein, Tests of chameleon gravity, *Living Rev. Relativity* **21**, 1 (2018).
- [18] P. Brax, C. Burrage, and A.-C. Davis, Laboratory constraints, *Int. J. Mod. Phys. D* **27**, 1848009 (2018).
- [19] C. Burrage and E. J. Copeland, Using atom interferometry to detect dark energy, *Contemp. Phys.* **57**, 164 (2016).
- [20] D. Sabulsky, I. Dutta, E. A. Hinds, B. Elder, C. Burrage, and E. J. Copeland, Experiment to Detect Dark Energy Forces Using Atom Interferometry, *Phys. Rev. Lett.* **123**, 061102 (2019).
- [21] P. Brax, C. van de Bruck, A.-C. Davis, D. F. Mota, and D. Shaw, Detecting chameleons through Casimir force measurements, *Phys. Rev. D* **76**, 124034 (2007).
- [22] A. Upadhye, Dark energy fifth forces in torsion pendulum experiments, *Phys. Rev. D* **86**, 102003 (2012).
- [23] S.-w. Chiow and N. Yu, Multiloop atom interferometer measurements of chameleon dark energy in microgravity, *Phys. Rev. D* **97**, 044043 (2018).
- [24] P. Touboul *et al.*, Microscope Mission: First Results of a Space Test of the Equivalence Principle, *Phys. Rev. Lett.* **119**, 231101 (2017).
- [25] P. Brax, G. Pignol, and D. Roulier, Probing strongly coupled chameleons with slow neutrons, *Phys. Rev. D* **88**, 083004 (2013).
- [26] A. N. Ivanov, R. Höllwieser, T. Jenke, M. Wellenzohn, and H. Abele, Influence of the chameleon field potential on transition frequencies of gravitationally bound quantum states of ultracold neutrons, *Phys. Rev. D* **87**, 105013 (2013).
- [27] C. Burrage, E. J. Copeland, and E. A. Hinds, Probing dark energy with atom interferometry, *J. Cosmol. Astropart. Phys.* **03** (2015) 042.
- [28] C. Burrage, E. J. Copeland, and J. A. Stevenson, A proposed experimental search for chameleons using asymmetric parallel plates, *J. Cosmol. Astropart. Phys.* **08** (2016) 070.
- [29] A. Ivanov, G. Cronenberg, R. Hllwieser, T. Jenke, M. Pitschmann, M. Wellenzohn, and H. Abele, Exact solution for chameleon field, self-coupled through the Ratra-Peebles potential with $n = 1$ and confined between two parallel plates, *Phys. Rev. D* **94**, 085005 (2016).
- [30] T. Nakamura, T. Ikeda, R. Saito, and C.-M. Yoo, Chameleon field in a spherical shell system, *Phys. Rev. D* **99**, 044024 (2019).
- [31] L. Kraiselburd, S. J. Landau, M. Salgado, D. Sudarsky, and H. Vucetich, Equivalence principle in chameleon models, *Phys. Rev. D* **97**, 104044 (2018).
- [32] L. Kraiselburd, S. Landau, M. Salgado, D. Sudarsky, and H. Vucetich, Thick shell regime in the chameleon two-body problem, *Phys. Rev. D* **99**, 083516 (2019).
- [33] P. Hamilton, M. Jaffe, P. Haslinger, Q. Simmons, H. Miller, and J. Khoury, Atom-interferometry constraints on dark energy, *Science* **349**, 849 (2015).
- [34] B. Elder, J. Khoury, P. Haslinger, M. Jaffe, H. Miller, and P. Hamilton, Chameleon dark energy and atom interferometry, *Phys. Rev. D* **94**, 044051 (2016).
- [35] S. Schlögel, S. Clesse, and A. Fzfa, Probing modified gravity with atom-interferometry: A numerical approach, *Phys. Rev. D* **93**, 104036 (2016).
- [36] C. Burrage, E. J. Copeland, A. Moss, and J. A. Stevenson, The shape dependence of chameleon screening, *J. Cosmol. Astropart. Phys.* **01** (2018) 056.
- [37] B. Ratra and P. J. E. Peebles, Cosmological consequences of a rolling homogeneous scalar field, *Phys. Rev. D* **37**, 3406 (1988).
- [38] P. Brax, C. van de Bruck, A.-C. Davis, D. F. Mota, and D. Shaw, Testing chameleon theories with light propagating through a magnetic field, *Phys. Rev. D* **76**, 085010 (2007).
- [39] A. O. Sushkov, W. J. Kim, D. A. R. Dalvit, and S. K. Lamoreaux, Observation of the thermal Casimir force, *Nat. Phys.* **7**, 230 (2011).
- [40] A. Lambrecht and S. Reynaud, Casimir effect: Theory and experiments, *Int. J. Mod. Phys. A* **27**, 1260013 (2012).
- [41] C. Llinares and P. Brax, Detecting Coupled Domain Walls in Laboratory Experiments, *Phys. Rev. Lett.* **122**, 091102 (2019).
- [42] M. Jaffe, P. Haslinger, V. Xu, P. Hamilton, A. Upadhye, B. Elder, J. Khoury, and H. Miller, Testing sub-gravitational forces on atoms from a miniature in-vacuum source mass, *Nat. Phys.* **13**, 938 (2017).
- [43] D. J. Kapner, T. S. Cook, E. G. Adelberger, J. H. Gundlach, B. R. Heckel, C. D. Hoyle, and H. E. Swanson, Tests of the Gravitational Inverse-Square Law Below the Dark-Energy Length Scale, *Phys. Rev. Lett.* **98**, 021101 (2007).
- [44] R. S. Decca, D. López, E. Fischbach, G. L. Klimchitskaya, D. E. Krause, and V. M. Mostepanenko, Tests of new physics from precise measurements of the casimir pressure between two gold-coated plates, *Phys. Rev. D* **75**, 077101 (2007).
- [45] B. Jain, V. Vikram, and J. Sakstein, Astrophysical tests of modified gravity: Constraints from distance indicators in the nearby universe, *Astrophys. J.* **779**, 39 (2013).
- [46] A. Cabré, V. Vikram, G.-B. Zhao, B. Jain, and K. Koyama, Astrophysical tests of gravity: A screening map of the nearby universe, *J. Cosmol. Astropart. Phys.* **07** (2012) 034.
- [47] V. Vikram, J. Sakstein, C. Davis, and A. Neil, Astrophysical tests of modified gravity: Stellar and gaseous rotation curves in dwarf galaxies, *Phys. Rev. D* **97**, 104055 (2018).
- [48] H. Wilcox, R. C. Nichol, G.-B. Zhao, D. Bacon, K. Koyama, and A. K. Romer, Simulation tests of galaxy cluster constraints on chameleon gravity, *Mon. Not. R. Astron. Soc.* **462**, 715 (2016).
- [49] P. Brax and C. Burrage, Atomic precision tests and light scalar couplings, *Phys. Rev. D* **83**, 035020 (2011).
- [50] J. Jaeckel and S. Roy, Spectroscopy as a test of coulomb's law: A probe of the hidden sector, *Phys. Rev. D* **82**, 125020 (2010).

4.2 Asymmetries in the geometry

4.2.1 Introduction and summary

This article focusses on the eventuality of the appearance of chameleonic forces sourced by asymmetries in the geometry of an experiment. With MICROSCOPE's case in mind we want to estimate the force a cylinder nested in other cylinders would feel if it is shifted in such a way that the cylinders are no longer coaxial. This problem cannot be treated as those described in the previous article as it is a 2-dimensional problem.

We start exploring this problem of asymmetries in 1D. We develop a way of treating the case of a freely moving wall surrounded by two fixed parallel walls with methods similar to those of the previous article. We obtain the profile for different displacements of the middle wall and compute the force it experiences. We conclude that this force is linear to the displacement as long as it is small. It thus behaves as a destabilising stiffness just as MICROSCOPE's electrostatic stiffness.

In the cylindrical case, we consider two nested cylinders where the inner one is freely moving. Two methods are used to solve the field. The first is semi-analytical and uses a cylindrical multipoles decomposition of the field. In this formalism we can decompose the Klein-Gordon equation on this basis as a set of 1D equations. Due to the non-linearities of the equation, all modes are coupled. We find that for small displacements of the inner cylinder we can neglect these inter-modes coupling and consider each mode equation as decoupled. We can then apply the methods from the previous article to solve these 1D equations. We obtain a profile for each mode that we can reconstruct in a 2D profile and we also compute the force from the multipoles. Parallel to this method we implement a full numerical 2D method. We follow the idea proposed for the chameleon problem by Ref. [38]. It consists in a finite-difference method in which from an initial guess the algorithm iteratively converges towards the right solution. This method provides results even for significant displacements. The two methods agree on the force that they both provide. Besides, the accelerations one computes from those forces in the cylindrical geometry are very close to the acceleration one obtains in 1D for comparable configurations. This demonstrates that the cylindrical geometry does not bring any additional effect. For large displacements we find that the force is no longer linear.

We study the chameleonic stiffness in the small displacement regime. Its dependency to the chameleon parameter is given. We find that the stiffness is increasing with β even if for large values of this parameter the cylinders are screened. We also study its dependency on the geometrical parameters. First we show that the result for the force is independent of the density of the vacuum in between the cylinders as long as the associated Compton wavelength of the field is significantly larger than the typical inter-cylinder-gaps. Secondly we study its dependency on the size of the cylinder. By analysing the Klein-Gordon equation we find a scaling relation that relates the solutions of geometrical situations that are related by a homothetic transformation. We deduce a force scaling that shows that smaller systems are more likely to provide a detectable force.

The results of this article on the chameleon stiffness give an opportunity of an additional force in MICROSCOPE data. Testing it requires applying the formalism with the correct number of cylinders and the correct geometrical parameters presented in Chapter 1. Testing modified gravity with the measurement of the test mass stiffness is the subject of the next chapter.

4.2.2 Article

PHYSICAL REVIEW D **101**, 124056 (2020)**Fifth force induced by a chameleon field on nested cylinders**Martin Pernot-Borràs^{1,2,*}, Joel Bergé,¹ Philippe Brax,³ and Jean-Philippe Uzan^{2,4}¹*DPHY, ONERA, Université Paris Saclay, F-92322 Châtillon, France*²*Institut d'Astrophysique de Paris, CNRS UMR 7095, Université Pierre & Marie Curie—Paris VI, 98 bis Bd Arago, 75014 Paris, France*³*Institut de Physique Théorique, Université Paris-Saclay, CEA, CNRS, F-91191 Gif-sur-Yvette Cedex, France*⁴*Sorbonne Universités, Institut Lagrange de Paris, 98 bis, Bd Arago, 75014 Paris, France*

(Received 1 May 2020; accepted 9 June 2020; published 25 June 2020)

This article investigates the properties of a scalar fifth force that arises in a scalar tensor-theory with a chameleon screening mechanism in the context of gravity space missions like the MICROSCOPE experiment. In such an experiment, the propagation of the chameleon field inside the nested cylinders of the experiment causes a fifth force when the cylinders are not perfectly coaxial. We propose a semianalytic method to compute the field distribution and the induced fifth force and compare it to a full numerical simulation, in settings where the cylindrical symmetry is broken. The scaling of the fifth force with both the parameters of the model and the geometry of the experiment is discussed. We show that the fifth force is repulsive, hence adds a destabilizing stiffness that should be included in the force budget acting on the detector. This opens the way to a new method to constrain a scalar fifth force in screened models.

DOI: [10.1103/PhysRevD.101.124056](https://doi.org/10.1103/PhysRevD.101.124056)**I. INTRODUCTION**

Scalar-tensor theories represent a large class of extensions of general relativity (GR) that are widely studied [1–3] to constrain deviations from GR and to investigate the physical effects of a potential scalar partner to the graviton, which may arise from high-energy theories, e.g., string theory. On large scales, coupled scalars modify the evolution of the universe and its structure. They have attracted a lot of attention in connection with the modeling of the late acceleration of the Universe, i.e., as possible dark energy candidates [4]. On smaller scales, the extra-degree of freedom is responsible for a fifth force. The properties of this fifth force depends on the nature of the couplings of the scalar field to standard matter, universal or not, on the mass of the scalar field, and more generally on its potential. While light field models can be attracted toward general relativity [5,6] and are constrained in laboratory and space gravity experiments, local tests are more difficult for models exhibiting screening as they require to take into account the effects of the environment [7]. Amongst such models, let us cite the symmetron [8] and the chameleon [9,10] mechanisms. In both cases, the profile of the scalar field and thus the associated fifth force depends on the local mass density: the field acquires a large mass in high density environments responsible for the suppression of the fifth

force, whereas in low density environments the force can be long-ranged.

The main goal of this article is to continue our investigation on the possibility to test such scalar-tensor theories with a screening mechanism in gravity space experiments. Even if the coupling of the field is universal, it can generate composition dependent fifth force between macroscopic objects since the profile of the scalar field, and thus the fifth force that derives from it, inside the object depends on its density, and thus on this composition. So far, many experiments [11–13] have set constraints on the existence of a chameleon field among which atom interferometry [14,15], Casimir effect measurements [16] or torsion balance experiments [17]. Space-borne experiments—as the MICROSCOPE mission [18] testing the weak equivalence principle in orbit—were originally argued to be a possible smoking gun for the chameleon mechanism [9,10] as the local density in space is much smaller than at the surface of the Earth, hence leading to a lighter field and a stronger fifth force. However, this intuitive argument requires to be analyzed in depth, in particular to take into account the fact that the experimental set-up can itself screens the chameleon. Understanding this screening and the propagation of the scalar field inside the measurement device is a key issue to detect or constrain such a mechanism. It requires to determine the field profile for nontrivial matter distributions as the theory is highly nonlinear and a special attention to the boundary conditions must be paid. Multiple approaches have been used

*martin.pernot_borras@onera.fr

involving both analytic [10,16,19–26] and numerical methods [17,27–30].

In a previous paper [31], we considered an idealized experimental setting modeled by cylindrically or spherically nested geometries, and studied the propagation of a chameleon field inside such a setting. This clarified the occurrence of the screening mechanism and led us to conclude that for experiments similar to the MICROSCOPE mission, the screening induced by the experiment’s cavity steps in for most of the parameter space of the chameleon model, hence reducing the hope of constraining chameleons with this space experiment. Nevertheless, the different parts of the detector are subject to a series of nongravitational forces that need to be compensated. It follows that the inner cylinders of the device can move and thus depart from the cylindrical symmetry. This can induce an internal source for the fifth force that needs to be modeled and constrained in the force budget of the experiment.

To that purpose, we consider a model configuration similar to the MICROSCOPE geometry involving an accelerometer composed of nested test mass cylinders and electrode cylinders. A force on a test mass appears when the cylindrical symmetry is broken by shifting the cylinder from its axis. The goal of this article is to quantify the fifth force induced by this noncoaxiality. Thus, we consider a static configuration of two infinite nested cylinders. After summarizing briefly the theoretical context in Sec. II, we start by a simplified exercise in Sec. II in which we restrict to 1-dimensional configurations. Then we tackle the case of nested cylinders by first developing a semianalytical multipolar expansion in Sec. IV and the full numerical integration in Sec. V. Both methods have their own domain of validity and are compared when they both apply. Once the profiles are determined, we compute in Sec. VI the resulting force on the inner cylinder and then discuss its scaling with the geometry of the model and the parameters of the theory.

This provides the first analysis of the fifth force stiffness induced by a chameleon field on an idealized gravity experiment with a design similar to the MICROSCOPE mission. It shows that the fifth force being repulsive, it adds a destabilizing stiffness that would require to be compared to the other forces acting on the detector, from electrostatic and Newtonian origin (since the Newtonian force vanishes only for infinite cylinders). Hence, this work paves the way to the analysis of the MICROSCOPE experiment that shall be presented in a companion article [32].

II. GENERAL EQUATIONS

A. Theory

Let us consider the theory defined by the general scalar-tensor action in the Einstein frame,

$$S = \int d^4x \sqrt{-g} \left[\frac{M_{\text{Pl}}^2}{2} R - \frac{1}{2} \partial^\mu \phi \partial_\mu \phi - V(\phi) \right] - \int d^4x \sqrt{-\tilde{g}} \mathcal{L}_m(\tilde{g}_{\mu\nu}, \phi, \dots), \quad (1)$$

where ϕ is a scalar field, V its potential, M_{Pl} the reduced Planck mass, R the Ricci scalar, $g_{\mu\nu}$ the Einstein frame metric, g its determinant, and \mathcal{L}_m the matter Lagrangian. The field couples nonminimally to matter through the Jordan frame metric

$$\tilde{g}_{\mu\nu} = A^2(\phi) g_{\mu\nu}, \quad (2)$$

where $A(\phi)$ is a universal coupling function, from which the dimensionless coupling constant

$$\beta(\phi) = M_{\text{Pl}} \frac{d \ln A}{d\phi} \quad (3)$$

can be defined. It characterizes the magnitude of the coupling to the scalar field to standard matter, and hence the magnitude of the fifth force. Note that the coupling may not be universal, so that the field could have different couplings, $A_i(\phi)$ for the different components of matter. Such models involve spacetime variations of fundamental constants that have been well-constrained [33–35] so that we restrict our analysis to a universal coupling. The method proposed here generalizes itself easily to nonuniversal couplings.

In the Einstein frame, the scalar field dynamics follows from the Klein-Gordon equation,

$$\square \phi = \frac{dV}{d\phi} - \frac{\beta(\phi)}{M_{\text{Pl}}} T_{\mu\nu} g^{\mu\nu}, \quad (4)$$

so its source term depends both on the potential and the local value of the trace of the matter stress-energy tensor, which reduces to the local energy density for a non-relativistic matter.

B. Chameleon models

Chameleon models posits that the potential V and coupling function A do not have the same convexity so that the minimum of the effective potential depends on the local matter density. We shall assume that the coupling function is of the form

$$A = e^{\beta\phi/M_{\text{Pl}}} \quad (5)$$

and the potential is of the form

$$V = \Lambda^4 \left(1 + \frac{\Lambda^n}{\phi^n} \right) \quad (6)$$

where Λ is a mass scale, n a natural number and β a positive constant. It follows that the Klein-Gordon equation (4) reduces to

$$\square\phi = \frac{dV_{\text{eff}}}{d\phi} \quad (7)$$

with the effective potential

$$V_{\text{eff}} = V(\phi) + \frac{\beta}{M_{\text{Pl}}} \rho \phi, \quad (8)$$

ρ being the mass density configuration. This equation enjoys a density-dependent minimum

$$\phi_*(\rho) = \left(n \frac{M_{\text{Pl}} \Lambda^{n+4}}{\beta \rho} \right)^{\frac{1}{n+1}}. \quad (9)$$

In media of constant density ρ the field would tend to reach this minimal value. This would occur on scales given by the density dependent Compton wavelength,

$$\lambda_c(\rho) \equiv \sqrt{\frac{1}{n(n+1)\Lambda^{n+4}} \left(\frac{nM_{\text{Pl}}\Lambda^{n+4}}{\beta\rho} \right)^{\frac{n+2}{n+1}}}, \quad (10)$$

which becomes shorter as ρ is larger.

Finally, if we assume static configurations, the field is governed by the Laplace equation

$$\Delta\phi = n\Lambda^{n+4}[\phi_*^{-(n+1)} - \phi^{-(n+1)}]. \quad (11)$$

With the rescalings $\phi/\Lambda \rightarrow \phi$, $\beta/\Lambda^3 \rightarrow \beta$ and $\Lambda\mathbf{r} \rightarrow \mathbf{r}$, it reduces to

$$\Delta\phi = \frac{\beta}{M_{\text{Pl}}} \rho(x) - n\phi^{-(n+1)}. \quad (12)$$

From such a rescaling, a profile computed for specific Λ , β and matter configurations specified by ρ , could directly lead to profiles for different Λ and β and a rescaled geometry.

III. ONE-DIMENSIONAL ASYMMETRIC CONFIGURATIONS

Let us first start by considering a nonsymmetrical one-dimensional model. It consists of 3 infinite parallel walls of the same thickness. The central wall can move and thus is not necessarily at the same distance from the other two external fixed walls.

The configuration is characterized by the thickness e of the walls, the gap g between the walls in the symmetric case, the distance $2g + e$ between the two external walls and the displacement δ of the central wall with respect to the middle position. The density of the walls and of the interwall regions are respectively denoted by ρ_{in} and ρ_{vac} .

Throughout this work, if not stated otherwise, we shall assume

$$\rho_{\text{in}} = 8.125 \text{ g.cm}^{-3},$$

and

$$\rho_{\text{vac}} = 10^{-3} \rho_{\text{in}}$$

for which the corresponding Compton wavelengths are $\lambda_{c,\text{in}} \simeq 2 \text{ cm}$ and $\lambda_{c,\text{vac}} \simeq 2 \text{ m}$.

A. Resolution method

The profile of the field in the symmetrical case ($\delta = 0$) has already been described in our former work [31]. We can adapt the method to deal with the nonsymmetrical case and solve Eq. (12) for a nonsymmetrical configuration.

The main problem is to determine the boundary conditions for the numerical integration. When $\delta = 0$, it is obvious, by symmetry, that the field's derivative cancels at the center of the central wall. Under that condition, one can proceed by dichotomy on the value of the field at the center to determine the value that is compatible with the boundary conditions at large distance.

When $\delta \neq 0$, the derivative of the field does not vanish at the center but at a slightly shifted location that depends on δ . Again, it can be determined by dichotomy. Since the central wall is separated from the two external walls by distances of respectively $g - \delta$ and $g + \delta$, we start at some initial position x_0 in the central wall. We then determine the profile that corresponds to the condition $\phi'(x_0) = 0$ with the same procedure as for the symmetrical case. The different configurations encountered in each direction—i.e., a gap of respective width $g - \delta$ and $g + \delta$ —and the boundary conditions, give two different values of $\phi(x_0)$. Depending on the sign of the difference of these values we adjust x_0 , and repeat the procedure until convergence when this difference gets negligible. This way we obtain the correct position x_0 and initial value $\phi(x_0)$ corresponding to the profile satisfying the correct boundary conditions at large distance.

B. Profile of the field and resulting force on the central wall

The profile of the field for a configuration in which $e = 0.2 \text{ m}$ and $g = 0.25 \text{ m}$ is depicted in Fig. 1 for different displacement δ . Since the profile is no more symmetrical inside the central wall, it implies that the integration of the fifth force $-\beta\nabla\phi/M_{\text{Pl}}$ does not vanish. Figure 2 depicts the evolution of the fifth force with δ . For small displacements it is linear with a positive sign, i.e., a repulsive force that tends to destabilize the configuration. It develops a nonlinear scaling for large δ . Note, for comparison, that the Newtonian force on the central wall remains zero whatever δ .

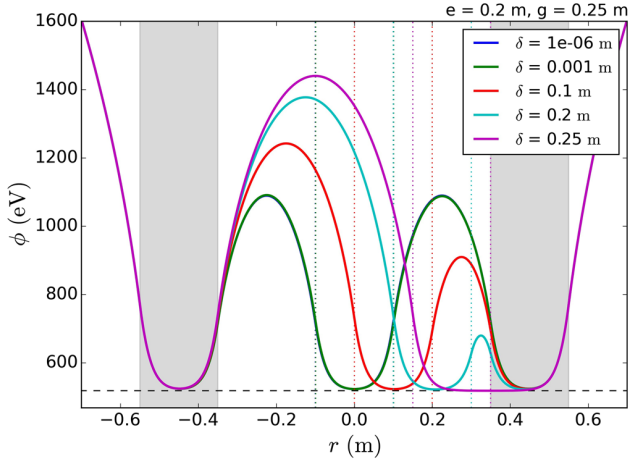


FIG. 1. Profiles of ϕ for a three-wall asymmetric configuration for walls of thickness $e = 0.2$ m and for different displacements δ of the central wall. The dotted lines delimit the borders of the central walls. The shaded zones correspond to the two fixed external walls. The blue and green curves are superposed. The model parameters have been chosen to $n = 2$, $\beta = 1$, $\Lambda = 1$ eV.

This result can be compared to the one obtained by considering this problem as two joined Casimir-like configurations—two sets of parallel plates whose chameleonic force has been analytically computed in Ref. [16]—where the central wall is pulled by each external walls resulting in a total destabilizing force. The agreement between our numerical computation and this analytical form is excellent for almost all the range of displacements. The Casimir-like force scales for one pair of plates as d^{-1} for $n = 2$. Then applied to our cases here it scales as $\frac{2\delta}{(g+\delta)(g-\delta)}$. So it is linear as long $\delta \ll g$. For larger displacements the agreement is not as good since our result departs from linearity for larger δ . This is indeed not surprising

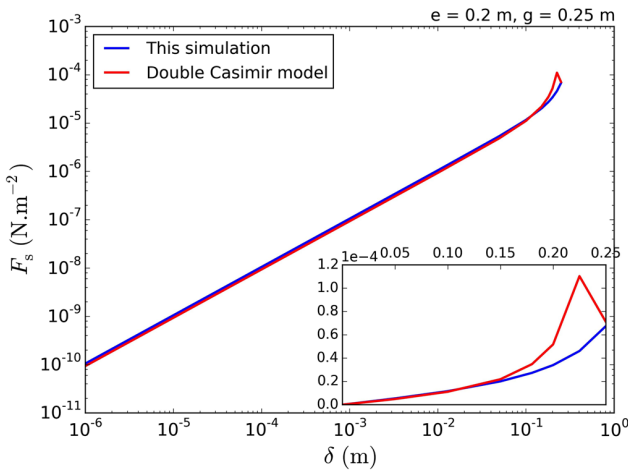


FIG. 2. The pressure on the central wall for the configuration described in Fig. 1 as a function of the displacement δ . The red line corresponds to the two-Casimir-like configuration as computed in Ref. [16].

as for small displacements this is the regime where $\lambda_{c,in} \ll d \ll \lambda_{c,vac}$ for both sets of plates, for which a good agreement already exists [16]. For large displacements this is no longer the case, explaining the discrepancy.

IV. TWO-DIMENSIONAL CYLINDRICAL ASYMMETRIC CONFIGURATION: SEMIANALYTIC MULTIPOLAR APPROXIMATION

Let us now turn to the less academic case of two infinite nested cylinders. This geometry is close to the one of MICROSCOPE's accelerometers even though we still assume that the cylinders are infinite to simplify the analysis. The transverse geometry is detailed in Fig. 3 and the goal is to compute the force on the inner cylinder once shifted from the center. This is indeed a more complex problem than previously as it requires to treat the full 2 dimensions in Eq. (12) and cannot be reduced to 1-dimensional problem as for configurations with cylindrical symmetry. Nevertheless, as we shall now see, for small displacements the problem can be simplified using a multipolar expansion of the field configuration.

The geometry we consider is described on Fig. 3 and consists of two cylinders:

- (i) an outer cylinder of radius \bar{R} and width \bar{e} centered on O and with density ρ_{out} ;
- (ii) an inner cylinder of radius R and width e centered on O' and with density ρ_{in} . We assume that

$$\mathbf{OO}' = \delta \mathbf{e}_x, \quad (13)$$

where δ is the displacement of the inner cylinder with respect to the axis of symmetry and \mathbf{e}_x the unit vector in this direction, arbitrarily chosen to be the x -axis.

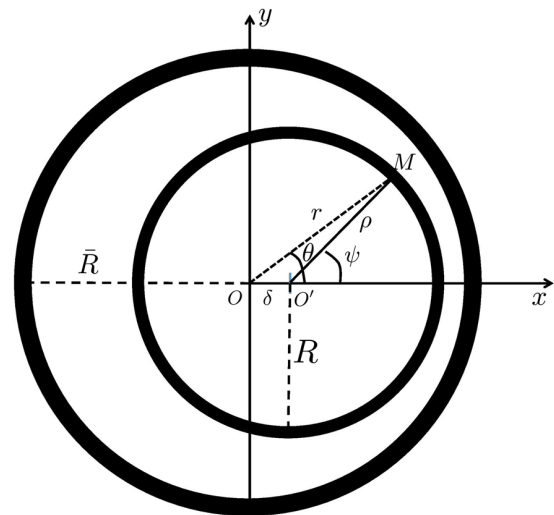


FIG. 3. Geometry of the 2-dimensional configuration of the two nested cylinders and definition of the notations of the problem.

We define the basis of the Cartesian coordinates as $(\mathbf{e}_x, \mathbf{e}_y)$ and the polar coordinates system $(\mathbf{e}_r, \mathbf{e}_\theta)$ with

$$\mathbf{e}_x \cdot \mathbf{e}_r = \cos \theta, \quad \mathbf{e}_y \cdot \mathbf{e}_r = \sin \theta, \quad (14)$$

and

$$\mathbf{e}_x \cdot \mathbf{e}_\theta = -\sin \theta, \quad \mathbf{e}_y \cdot \mathbf{e}_\theta = \cos \theta. \quad (15)$$

In complex notations, it is clear that the equation of the inner cylinder is $r(\theta)e^{i\theta} = \delta + Re^{i\psi}$ so that $R^2 = r^2 + \delta^2 - 2\delta r \cos \theta$, from which we determine the equation of the inner disk in polar coordinates

$$r(\theta) = R \left(\frac{\delta}{R} \cos \theta + \sqrt{1 - \frac{\delta^2}{R^2} \sin^2 \theta} \right), \quad (16)$$

this defines the inner and outer borders of the inner cylinder as $r_-(\theta)$ and $r_+(\theta)$, respectively with R and $R + e$ in Eq. (16). It follows that the matter density is distributed as

$$\rho(r, \theta) = \rho_{\text{vac}} + \begin{cases} \rho_{\text{in}} - \rho_{\text{vac}} & \text{if } r \in [r_-(\theta), r_+(\theta)] \\ \rho_{\text{out}} - \rho_{\text{vac}} & \text{if } r \in [\bar{R}, \bar{R} + \bar{e}] \\ 0 & \text{otherwise} \end{cases}. \quad (17)$$

It will be convenient to define the function Ξ such that $\Xi(x; a, b) = 1$ is $x \in [a, b]$ and 0 otherwise, i.e., it is defined in terms of the Heaviside distribution H as

$$\Xi(x; a, b) = H(x - a) - H(x - b). \quad (18)$$

It follows that

$$\rho(r, \theta) = \rho_{\text{vac}} + (\rho_{\text{out}} - \rho_{\text{vac}})\Xi(r; \bar{R}, \bar{R} + \bar{e}) + (\rho_{\text{in}} - \rho_{\text{vac}})\Xi[r; r_-(\theta), r_+(\theta)]. \quad (19)$$

A. Mode decomposition

In cylindrical coordinates, forgetting about the z -dimension since by symmetry $\phi = \phi(r, \theta)$, the gradient is given by $\nabla = (\partial_r, \partial_\theta/r)$ and the Laplacian by

$$\Delta f = \partial_r^2 f + \frac{1}{r} \partial_r f + \frac{1}{r^2} \partial_\theta^2 f. \quad (20)$$

for any function $f(r, \theta)$. One can always decompose f in modes as

$$f(r, \theta) = \sum_{\ell \in \mathbb{Z}} \frac{u_\ell(r)}{\sqrt{r}} e^{i\ell\theta} \quad (21)$$

with

$$\frac{u_\ell(r)}{\sqrt{r}} = \int \frac{d\theta}{2\pi} f(r, \theta) e^{-i\ell\theta}. \quad (22)$$

It follows that

$$\Delta f = \frac{1}{\sqrt{r}} \sum_{\ell \in \mathbb{Z}} \left[u_\ell'' + \frac{(1 - \ell^2)}{r^2} u_\ell \right] e^{i\ell\theta}. \quad (23)$$

Let us now turn to integration. We will have to integrate functions $f(r, \theta)$, such as the components of the force, on the inner cylinder as

$$\int f(M) dm = \rho_{\text{in}} h \int_{\text{inner cyl.}} f(r, \theta) r d\theta dr,$$

h being the length of the cylinder. For each θ , r varies between r_- and r_+ so that

$$\int f(M) dm = \rho_{\text{in}} h \int_0^{2\pi} d\theta \int_{r_-(\theta)}^{r_+(\theta)} f(r, \theta) r dr. \quad (24)$$

It is then ‘‘easily’’ checked that for $f = 1$ we get the mass of the cylinder $\rho_{\text{in}} \pi h e (2R + e)$. Indeed this is a tricky integral which turns out to be trivial in terms of the angle ψ defined in Fig. 3.

B. One cylinder

We start by considering only the outer cylinder. The density profile has been fully described in our former work [31] and is denoted by $\bar{\phi}(r)$. It is solution of

$$\bar{\phi}'' + \frac{1}{r} \bar{\phi}' = \frac{\beta}{M_{\text{pl}}} [\rho_{\text{vac}} + (\rho_{\text{out}} - \rho_{\text{vac}})\Xi(r; \bar{R}, \bar{R} + \bar{e})] - \frac{n}{\bar{\phi}^{n+1}} \quad (25)$$

with the boundary conditions

$$\bar{\phi}(\infty) = \phi_*(\rho_{\text{vac}}), \quad \bar{\phi}'(0) = 0. \quad (26)$$

C. Two cylinder configuration

Starting from the previous profile $\bar{\phi}(r)$, we consider the effect of the second cylinder and decompose ϕ as

$$\phi(r, \theta) = \bar{\phi}(r) + \psi(r, \theta). \quad (27)$$

Indeed, if the inner cylinder is centered in O then ψ is only a function of r . Such configurations were also studied in our previous work [31]. Now by subtracting Eq. (25) to the Klein-Gordon equation (12) we get

$$\begin{aligned} \psi'' + \frac{1}{r}\psi' + \frac{1}{r^2}\partial_\theta^2\psi &= \frac{\beta}{M_{\text{Pl}}}(\rho_{\text{in}} - \rho_{\text{vac}})\Xi[r; r_-(\theta), r_+(\theta)] \\ &+ \frac{n}{\bar{\phi}^{n+1}(r)} - \frac{n}{[\bar{\phi}(r) + \psi(r, \theta)]^{n+1}}. \end{aligned} \quad (28)$$

This equation is fully general and no approximation has been made so far. It is a 2-dimensional nonlinear partial differential equation. There is no way it can be analytically solved in full generality.

D. Multipolar hierarchy

To go further, we decompose ψ in multipoles as in Eq. (21) and we single out the monopole $\ell = 0$,

$$\psi(r, \theta) = \psi_0(r) + \sqrt{\frac{\delta}{r}} \sum_{\ell \neq 0} u_\ell(r) e^{i\ell\theta}. \quad (29)$$

This decomposition is fully general. Since ψ is a real-valued function, $u_\ell^* = u_{-\ell}$. We introduce the dimensionless

factor δ/r as it is clear that the nonradial terms all vanish when $\delta = 0$ and that $\delta/R \sim \delta/(R + e)$ will serve as a small parameter for our expansion. Thus, the generic Klein-Gordon equation takes the form

$$\begin{aligned} \psi_0'' + \frac{1}{r}\psi_0' + \sqrt{\frac{\delta}{r}} \sum_{\ell \neq 0} \left[u_\ell'' + \frac{(\frac{1}{4} - \ell^2)}{r^2} u_\ell \right] e^{i\ell\theta} \\ = \frac{\beta}{M_{\text{Pl}}}(\rho_{\text{in}} - \rho_{\text{vac}})\Xi[r; r_-(\theta), r_+(\theta)] \\ + \frac{n}{\bar{\phi}^{n+1}(r)} - \frac{n}{[\bar{\phi}(r) + \psi(r, \theta)]^{n+1}}. \end{aligned} \quad (30)$$

The goal is thus to determine the functions $\psi_0(r)$ and $u_\ell(r)$. It is clearly a difficult task as the last term of the right-and side (rhs) couples to all the modes.

The evolution of each mode can be obtained by integrating Eq. (30) times $e^{-i\ell\theta} d\theta/2\pi$ over θ and singling out the monopole from the $\ell \neq 0$ modes so that Eq. (29) splits as

$$\begin{aligned} \psi_0'' + \frac{1}{r}\psi_0' &= \frac{n}{\bar{\phi}^{n+1}(r)} - \int \frac{n}{\left[\bar{\phi}(r) + \psi_0(r) + \sqrt{\frac{\delta}{r}} \sum_{\ell \neq 0} u_{\ell'}(r) e^{i\ell'\theta} \right]^{n+1}} \frac{d\theta}{2\pi} \\ &+ \frac{\beta}{M_{\text{Pl}}}(\rho_{\text{in}} - \rho_{\text{vac}}) \begin{cases} \Xi[r; R, R + e] & \text{if } \delta = 0 \\ \int \Xi[r; r_-(\theta), r_+(\theta)] \frac{d\theta}{2\pi} & \text{if } \delta \neq 0 \end{cases} \end{aligned} \quad (31)$$

$$\begin{aligned} \sqrt{\frac{\delta}{r}} \left[u_\ell'' + \frac{(\frac{1}{4} - \ell^2)}{r^2} u_\ell \right] &= \frac{\beta}{M_{\text{Pl}P}}(\rho_{\text{in}} - \rho_{\text{vac}}) \int \Xi[r; r_-(\theta), r_+(\theta)] e^{-i\ell\theta} \frac{d\theta}{2\pi} \\ &- n \int \frac{e^{-i\ell\theta}}{\left[\bar{\phi}(r) + \psi_0(r) + \sqrt{\frac{\delta}{r}} \sum_{\ell' \neq 0} u_{\ell'}(r) e^{i\ell'\theta} \right]^{n+1}} \frac{d\theta}{2\pi} \end{aligned} \quad (32)$$

Let us note that (1) this hierarchy is highly nonlinear and that (2) the complex integrals on the rhs of Eqs. (31)–(32) cannot be performed as one would need to know the poles of its integrand, which depend on the whole solution and because, due to the displacement, the radial width of the inner cylinder depends on θ . Nevertheless as shown in the Appendix A, the integral of $\Xi e^{-i\ell\theta}$ over θ can be computed analytically so that the only big issue is the complex integral involving u_ℓ .

E. Small displacement approximation

So far, the system (31)–(32) is fully general since we made no approximation. Now, keeping in mind our goal, we want the force on the inner cylinder, so that we are interested on the field configuration on the cylinder, that is

close to $r \sim R$. Since we assume $\delta \ll R$, we can expand our solutions in e/R .

First, we define $e(\theta)$ as

$$e(\theta) = r_+(\theta) - r_-(\theta) \quad (33)$$

with the definition (16). At lowest order in δ/R , it reduces to

$$e(\theta) = e \left(1 + \frac{\delta^2}{R(R + e)} \sin^2 \theta \right). \quad (34)$$

Then, consider Eq. (31). The computation of the integral of Ξ is obtained by taking the limit $\ell \rightarrow 0$ in Eq. (A3) as $[\vartheta_+(r) - \vartheta_-(r)]/\pi$ where $\vartheta_+(r)$ and $\vartheta_-(r)$ are two angles

in $[0, \pi]$ at which the circle of radius r centered on O intersects the circle centered on O' of radius R and $R + e$ respectively. They are defined only for $r \in [R - \delta, R + \delta]$ and $r \in [R + e - \delta, R + e + \delta]$ respectively so that this term vanishes outside of the support $[R - \delta, R + E + \delta]$. It can be checked that in the limit $\delta \rightarrow 0$ it reduces to the function equal to 1 on this support, that is precisely $\Xi[r; R, R + e]$. So, we get

$$\frac{\beta}{M_{\text{Pl}}}(\rho_{\text{in}} - \rho_{\text{vac}}) \begin{cases} \Xi[r; R, R + e] & \text{if } \delta = 0 \\ \frac{\vartheta_+(r) - \vartheta_-(r)}{\pi} & \text{if } \delta \neq 0 \end{cases} \quad (35)$$

for the source term.

Then, consider Eq. (32). The multipolar components of Ξ are derived in Appendix A, see Eq. (A3).

Now, we need to treat the nonlinear term. To that purpose we consider an expansion in powers of δ/r . The dominant term involves only functions of r so that the integral over θ vanishes. It follows that

$$\int e^{-i\ell\theta} \left[\bar{\phi}(r) + \psi_0(r) + \sqrt{\frac{\delta}{r}} \sum_{\ell' \neq 0} u_{\ell'}(r) e^{i\ell'\theta} \right]^{-(n+1)} \frac{d\theta}{2\pi}$$

reduces to

$$-(n+1) \sqrt{\frac{\delta}{r}} \frac{u_{\ell}(r)}{[\bar{\phi}(r) + \psi_0(r)]^{n+2}}$$

at lowest order. Then, the first nonlinear term is given by

$$\frac{(n+1)(n+2)\delta}{2} \frac{\sum_{L \neq 0} u_L(r) u_{\ell-L}(r) |_{\ell-L \neq 0}}{r [\bar{\phi}(r) + \psi_0(r)]^{n+3}}. \quad (36)$$

In the equation for ψ_0 we have the contribution of the monopole $-n/[\bar{\phi}(r) + \psi_0(r)]^{n+1}$ and then the linear term in u_{ℓ} vanishes so that the first correction is the nonlinear term involving the sum $\sum_{L \neq 0} u_L(r) u_{-L}(r) = \sum |u_{\ell}(r)|^2$.

In conclusion, we get the hierarchy for the modes as a set of 1-dimensional differential equations to which we need to add the equation for $\bar{\phi}$, so that the full system is described by

$$\bar{\phi}'' + \frac{1}{r} \bar{\phi}' = \frac{\beta}{M_{\text{Pl}}} [\rho_{\text{vac}} + (\rho_{\text{out}} - \rho_{\text{vac}}) \Xi(r; \bar{R}, \bar{R} + \bar{e})] - \frac{n}{\bar{\phi}^{n+1}} \quad (37)$$

$$\begin{aligned} \psi_0'' + \frac{1}{r} \psi_0' &= \frac{n}{\bar{\phi}^{n+1}(r)} - \frac{n}{[\bar{\phi}(r) + \psi_0(r)]^{n+1}} + \frac{n(n+1)(n+2)\delta}{2} \frac{\sum_{L \neq 0} |u_L(r)|^2}{r [\bar{\phi}(r) + \psi_0(r)]^{n+3}} \\ &+ \frac{\beta}{M_{\text{Pl}}} (\rho_{\text{in}} - \rho_{\text{vac}}) \begin{cases} \Xi[r; R, R + e] & \text{if } \delta = 0 \\ \frac{\vartheta_+(r) - \vartheta_-(r)}{\pi} & \text{if } \delta \neq 0 \end{cases}. \end{aligned} \quad (38)$$

$$\begin{aligned} u_{\ell}'' + \frac{(\frac{1}{4} - \ell^2)}{r^2} u_{\ell} &= \frac{\beta}{M_{\text{Pl}}} (\rho_{\text{in}} - \rho_{\text{vac}}) \sqrt{\frac{r}{\delta}} \frac{[\sin \ell \vartheta_+(r) - \sin \ell \vartheta_-(r)]}{\pi \ell} \\ &+ n(n+1) \frac{u_{\ell}(r)}{[\bar{\phi}(r) + \psi_0(r)]^{n+2}} - \frac{n(n+1)(n+2)}{2} \sqrt{\frac{\delta}{r}} \frac{\sum_{L \neq 0} u_L(r) u_{\ell-L}(r) |_{\ell-L \neq 0}}{[\bar{\phi}(r) + \psi_0(r)]^{n+3}}, \end{aligned} \quad (39)$$

where $\Xi(r; \bar{R}, \bar{R} + \bar{e})$ is defined in Eq. (18), $\vartheta_{\pm}(r)$ in Eq. (A1). The equation for $\bar{\phi}$ is closed and can be solved easily numerically following the same method as in our previous work [31]. Then, the equation for ψ_0 is coupled to all the modes. But, if we restrict to $\mathcal{O}(\delta/R)$ it becomes closed. Then, the infinite set of equations for the u_{ℓ} becomes again linear if we work at order $\mathcal{O}(\sqrt{\delta/R})$, and we can solve it having previously solved for ψ_0 . Note that this set of equations is only valid for $\delta < e/2$.

F. Numerical scheme

To completely specified the system, we need to define properly the boundary conditions for (ψ_0, u_{ℓ}) .

The total field ϕ must verify the same asymptotic boundary condition than $\bar{\phi}$: $\phi(\infty) = \phi_*(\rho_{\text{vac}})$. Consequently, both the monopole and the multipoles must asymptotically cancel,

$$\psi_0(\infty) = 0, \quad u_{\ell}(\infty) = 0. \quad (40)$$

We now have all the elements to integrate numerically the set of equations (37)–(39). In the following all numerical examples will assume, if not specified otherwise, that the cylinders are of same density ρ_{in} and that the parameters of the geometry are $R = 0.2$ m, $e = 0.05$ m and $\bar{R} = 0.6$ m, $\bar{e} = 0.1$ m.

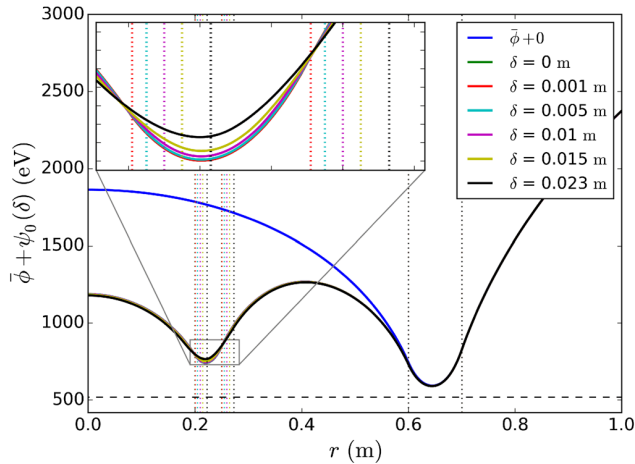


FIG. 4. Profiles of the field including the monopole correction for an asymmetric system of two nested cylinders for different displacements δ of the inner cylinder. The blue line shows the one-cylinder profile $\bar{\phi}$. The green line is the centered two-nested-cylinder profile. The dotted lines delimit the border of the cylinders.

1. Monopole ψ_0

The contribution of the monopole being cylindrically symmetric, its derivative shall cancel at $r = 0$: $\psi_0'(0) = 0$. We can therefore follow the same numerical resolution scheme as we performed for $\bar{\phi}$ in Ref. [31].

Figure 4 shows the profile of the monopole for various values of δ . It is compared to the one-cylinder profile $\bar{\phi}$ and to the symmetrical two-cylinder profile. As expected, it can be checked that the monopole profile tends to the former profile when δ tends to 0. As δ gets larger, the minimum value of the field reached in the inner cylinder departs slightly from the corresponding value in the two-centered-cylinders case. The total field might then leak in the multipoles.

2. Multipoles u_ℓ

The integration of the multipoles is more complex. Indeed, we do not know the position at which the field's derivative cancels, position used previously as a starting point to integrate $\bar{\phi}$ and ψ_0 . Nevertheless Eq. (29) gives useful information. The factor in front of the multipole sum scales as $1/\sqrt{r}$. For the total field not to diverge at $r = 0$, each u_ℓ must then scale at least as $r^{1/2}$ at $r = 0$. We thus deduce that we must have for all ℓ : $u_\ell(0) = 0$. Similarly to the method used to integrate $\bar{\phi}$ and ψ_0 , this leaves us with one parameter $u_\ell'(0)$ for the dichotomy which determines the correct initial condition giving the proper profile that verifies $u_\ell(\infty) = 0$.

Figure 5 depicts the first multipoles for several displacements of the inner cylinder δ . We observe that, as expected, the contribution of the multipoles is more important for

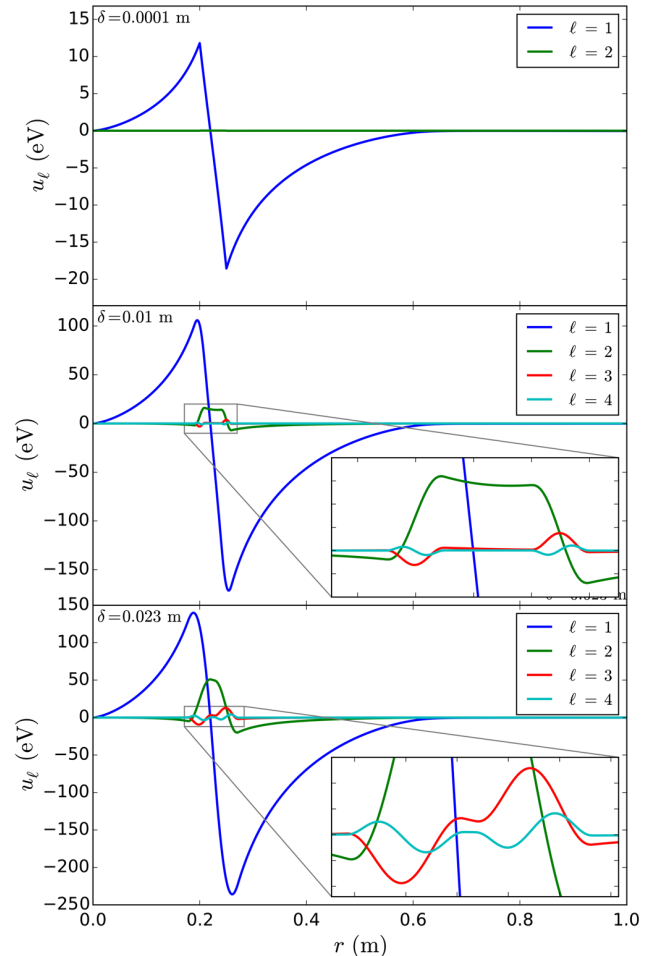


FIG. 5. Multipoles of order ℓ obtained for a set of displacement $\delta = 0.0001, 0.01, 0.023$ m from top to bottom.

large δ . We also notice that for small δ the dipole ($\ell = 1$) is the main contribution whereas for larger δ , the $\ell = 4$ term still provides a contribution to the field. We will see in Sec. VI that this hierarchy is preserved when computing the force on the inner cylinder, such that the contribution of the $\ell = 4$ multipole is always negligible. This justifies the fact that we do not consider multipoles of higher order.

Now, from these multipoles we can reconstruct 2-dimensional maps of the field using Eq. (29). Figure 6 shows such maps for different values of δ . Figure 7 gives a clearer view of these maps showing slices of the field profile in the plane $y = 0$. One can notice that asymmetry in the field appears along the axis of displacement. This is significant in the inter-cylinder space, where the field gets shrunk on the right side of the inner cylinder while expanding on the left. Similarly, the maximum of the field in the space enclosed by the inner cylinder departs from $x = 0$. When integrating over the whole cylinder this will be responsible for a force on the inner cylinder.

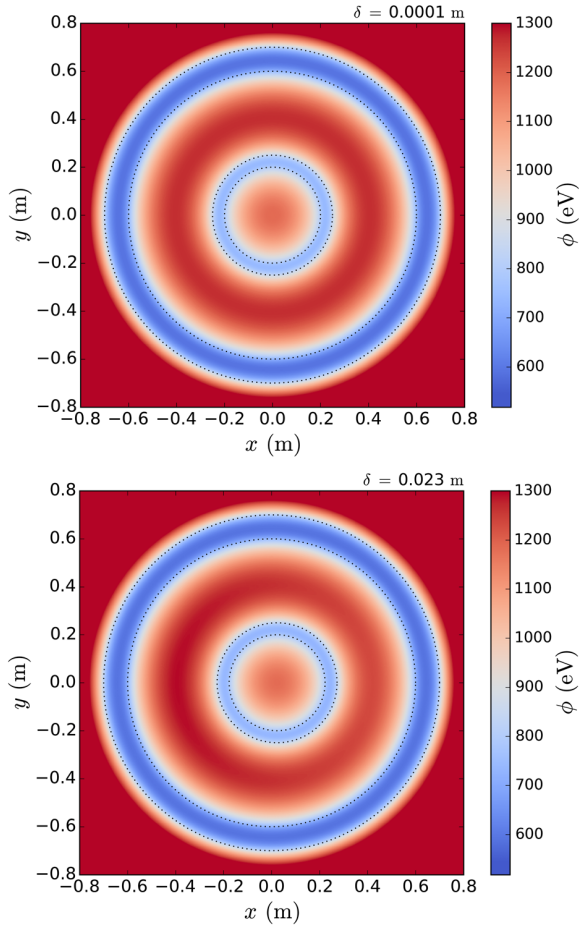


FIG. 6. Total field maps obtained by summing $\bar{\phi}$, ψ_0 and the multipoles for a set of displacement $\delta = 0.0001, 0.023$ m from top to bottom. The dotted lines delimit the cylinders. The field is truncated at 1300 eV in this scale.

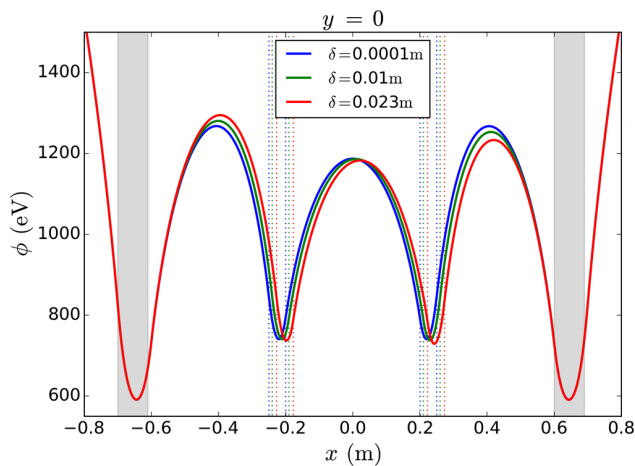


FIG. 7. Field profile slices for $y = 0$ for a set of displacement $\delta = 0.0001, 0.01, 0.023$ m. The shaded zones and the dotted lines delimit the cylinders.

G. Accuracy of the approximation

When solving Eqs. (38)–(39), we neglected the nonlinear terms in u_ℓ —3rd in the rhs of both Eqs. (38) and (39). Unfortunately, when evaluating them with the solution we have obtained, we notice that despite the suppression at high r caused by the powers of $\frac{\delta}{r}$, they can dominate close to the inner cylinder. This occurs for multipoles of order $l \geq 2$.

To verify the impact of this terms, we solve again the multipole equations (38)–(39) taking into account the nonlinear terms that we evaluate with the solution we first obtained by neglecting them. These terms involve a sum over all multipoles and we only keep terms up to $\ell = 4$ which is justified by the hierarchy of the multipoles observed on Fig. 5. As expected, this procedure leaves the monopole and the dipole unchanged, whereas for higher relative multipole there is a subsequent change in their relative magnitude while their global shape is conserved. This however has a limited impact on the total field and on the associated force as we will show that the monopole and the dipole are the dominant contributions to the force. The impact lessen for smaller displacement δ . The multipole shown in Fig. 5 take into account these nonlinear corrections.

V. TWO-DIMENSIONAL CYLINDRICAL ASYMMETRIC CONFIGURATION: FULL NUMERICAL COMPUTATION

We can also address the problem of the nested cylinders by a full numerical 2-dimensional simulation, that will not rely on the approximations of the previous section. We follow the same approach as Ref. [28] that uses an iterative relaxation algorithm which, from an initial guess, converges slowly to the solution. We apply it to the 2-dimensional chameleon equation

$$\frac{\partial^2 \phi}{\partial x^2} + \frac{\partial^2 \phi}{\partial y^2} = \frac{\beta}{M_{\text{Pl}}} \rho(x, y) - n \phi^{-(n+1)}, \quad (41)$$

which is discretized over a Cartesian 2D mesh by Taylor expanding to get

$$\begin{aligned} & \frac{\phi_{i+1,j} - 2\phi_{i,j} + \phi_{i-1,j}}{(\Delta x)^2} + \frac{\phi_{i,j+1} - 2\phi_{i,j} + \phi_{i,j-1}}{(\Delta y)^2} \\ & = \frac{\beta}{M_{\text{Pl}}} \rho(x_i, y_j) - n(\phi_{i,j})^{-(n+1)}, \end{aligned} \quad (42)$$

where $\phi_{i,j}$ denotes the field in the cell (i, j) of the mesh, Δx and Δy the resolutions of the mesh along the two axis. Here, we use a square mesh so that $\Delta x = \Delta y$. Then, starting from an initial guess we can iteratively redefine the field over the mesh as

$$\Phi_{i,j}^{(k+1)} = \frac{\phi_{i+1,j}^{(k)} + \phi_{i-1,j}^{(k)} + \phi_{i,j+1}^{(k)} + \phi_{i,j-1}^{(k)}}{4} - \frac{(\Delta x)^2}{4} \left[\frac{\beta}{M_{\text{Pl}}} \rho(x_i, y_j) - n(\phi_{i,j}^{(k)})^{-(n+1)} \right] \quad (43)$$

where k denotes the iteration. The process thus consists, at each iteration, in taking the mean value of the field on the 4 closest neighbors to which one subtracts $(\Delta x)^2$ times the second member of the equation evaluated with the current solution. After enough iterations this converges to the solution as long as the resolution of the mesh is fine enough. Having a resolution a tenth smaller than the smallest Compton wavelength of the field in the considered setup—here $\lambda_{c,\text{in}}$ —is sufficient by inspection.

Nevertheless, due to the nonlinearity of the equation, instabilities can appear. To overcome them we use an underrelaxation process, by adding a part of the k th solution in the redefinition the $k+1$ th as

$$\phi_{i,j}^{(k+1)} = (1 - \omega)\phi_{i,j}^{(k)} + \omega\Phi_{i,j}^{(k+1)} \quad (44)$$

where ω is the overrelaxation parameter that we take as $\omega = 0.9$ and Φ is defined by the previous equation.

In this method, due to the finite extent of the mesh, we must set boundary conditions at finite distance unlike the method used in the previous section. In our case, this requires the external cylinder to be thick enough for the field to reach the minimum of its potential, so that the internal field becomes screened. In our previous work [31], we showed that for a wall to be safely screened, its thickness needs to be roughly larger than $100 \lambda_{c,\text{wall}}$. Here, for the parameters we consider, due to the limited computing resources, we have only been able to use a mesh allowing one to have an external cylinder of thickness $80 \lambda_{c,\text{wall}}$, which appears to be sufficient.

Note that we are also limited by the facts we need to have a large enough mesh to treat the boundary conditions correctly and to have a precise enough mesh to model the small variations of the field that are more likely to happen inside the cylinders, which are the very quantity needed to evaluate the force. This limits us for exploring the chameleon parameter space, and makes this method complementary to the one presented in the previous section. This problem is less likely to be encountered in Ref. [28] as it focused on the field variations in the vacuum gaps and thus could neglect all variations smaller than Δx , which anyway have a limited impact on the larger scale variations.

A. Results

The results of this method are displayed in Figs. 8 and 9. This method allows us to simulate larger displacements than the multipole method. The structure is faithful to the one observed in the previous section. We observe the different behaviors for $r > 0.6$ m, due to the different ways

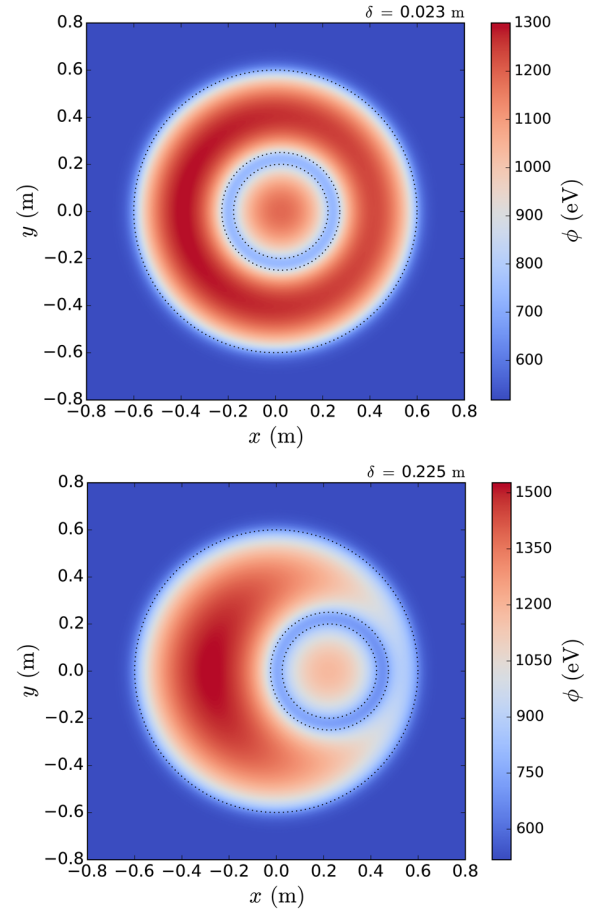


FIG. 8. Total field maps obtained by a full numerical simulation for a set of displacements $\delta = 0.023, 0.225$ m from top to bottom. The dotted lines delimit the cylinders.

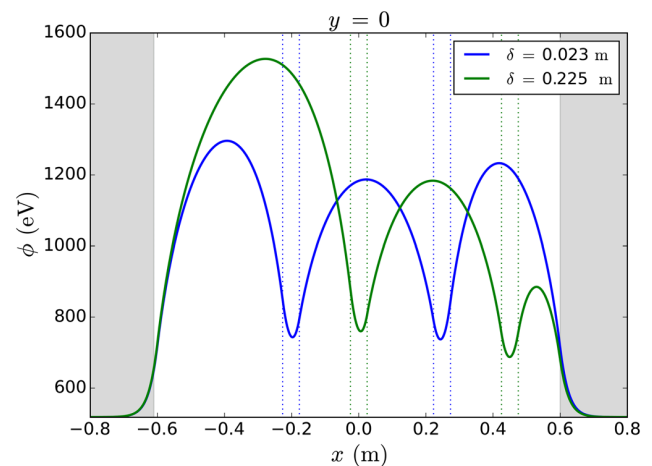


FIG. 9. Field profile slices in the plane $y = 0$ obtained by a full numerical simulation for a set of displacements $\delta = 0.023, 0.225$ m. The shaded zones and the dotted lines delimit the cylinders.

of setting boundary conditions. The departure from cylindrical symmetry is more clearly apparent for large δ , specially on both sides of the inner cylinder testifying of a more intense force.

B. Comparison of the two methods

With the full numerical method we can treat any displacements that are larger than the resolution of the mesh. This overlaps with the previous semianalytical method and enables us to compare them. To that end, we must increase the thickness of the external cylinder in the multipolar method. We are however limited by the numerical precision, we use a thickness of 0.2 m. Figure 10 compares the first multipoles computed in the previous section by considering or not the correction of the nonlinear terms discussed in Sec. IV G to the multipoles extracted from the 2D simulation.

We observe that, as expected, the nonlinear corrections have no impact on the monopole and the dipole. And the agreement is such that the largest difference between the multipoles obtain by the method amounts to less than a percent whether we considered nonlinear corrections or not. For the modes $\ell = 2$ and $\ell = 3$, without nonlinear corrections, the multipolar expansion fails at reproducing the result of the 2D simulation, reaching differences in the multipoles that represent an error of 69%. Fortunately, when we consider nonlinear corrections this differences

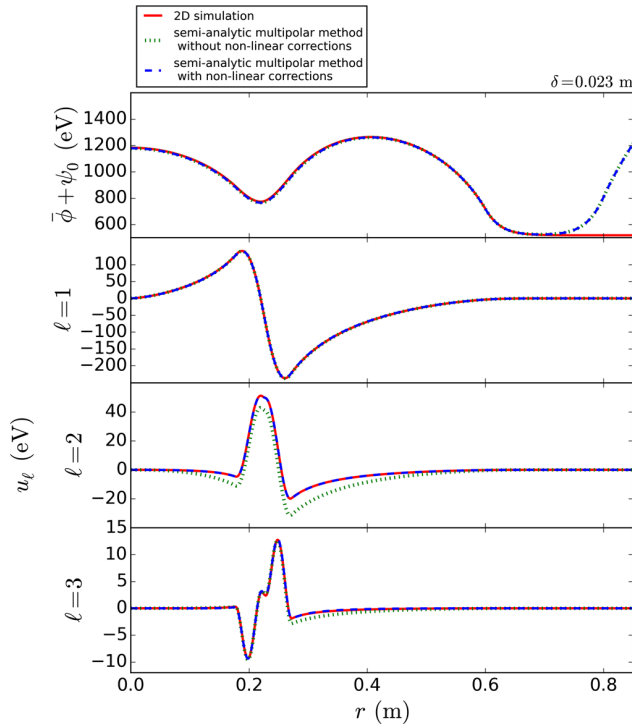


FIG. 10. Comparison of the multipoles computed by a full numerical method and the multipolar expansion method with and without considering terms nonlinear in u_ℓ in Eq. (39).

falls to respectively less than a percent for $\ell = 2$ and 9% for $\ell = 3$. This is a very strong confirmation of the validity of the multipolar approximation. The difference of 9% for $\ell = 3$ will be negligible when considering the force exerted on the inner cylinder, as we shall discuss.

VI. FORCE BETWEEN CYLINDERS

Now, we have all the elements to study the force that the cylinders are experiencing when shifting the inner one by δ .

A. Definition of the force

The force on the inner cylinder, is obtained by integrating the fifth force on the cylinder, hence

$$\mathbf{F} = -\frac{\beta}{M_{\text{Pl}}} \int \nabla \phi dm = -\frac{\beta}{M_{\text{Pl}}} \rho_{\text{in}} h \mathcal{F}[\delta] \quad (45)$$

with

$$\mathcal{F}[\delta] \equiv \int_0^{2\pi} d\theta \int_{r_-(\theta)}^{r_+(\theta)} \nabla \phi r dr. \quad (46)$$

We denote $\mathbf{F}_h = \frac{\mathbf{F}}{h}$. \mathbf{F}_h and \mathcal{F} only differ by a constant factor of $-\beta \rho_{\text{in}} / M_{\text{Pl}}$.

Since we assume a displacement along the x -axis, the y -components on two symmetric elements (i.e., on θ and $2\pi - \theta$) are equal and opposite so that

$$\mathcal{F}_x = \mathcal{F}, \quad \mathcal{F}_y = 0. \quad (47)$$

It follows that

$$\mathcal{F}[\delta] \equiv \int_0^{2\pi} d\theta \int_{r_-(\theta)}^{r_+(\theta)} \left[\cos \theta \partial_r \phi - \frac{\sin \theta}{r} \partial_\theta \phi \right] r dr. \quad (48)$$

Replacing the multipolar expansion of the field we obtain

$$\begin{aligned} \mathcal{F}[\delta] &= \int_0^{2\pi} \cos \theta \int_{r_-(\theta)}^{r_+(\theta)} [\bar{\phi}' + \psi'_0] r dr \\ &+ \sum_{\ell \neq 0} \int_0^{2\pi} e^{i\ell\theta} \int_{r_-(\theta)}^{r_+(\theta)} \sqrt{\frac{\delta}{r}} \left[\left(u'_\ell - \frac{u_\ell}{2r} \right) \cos \theta \right. \\ &\left. - i\ell \frac{u_\ell}{r} \sin \theta \right] r dr. \end{aligned} \quad (49)$$

We see that $\bar{\phi}' + \psi'_0$ will contribute to all the multipoles of the force.

B. Computation of the force

Let us proceed with a series of approximations that will allow us to get to the full generic expression of the force. Those approximations turn to be useful to understand the magnitude of the force.

1. Test inner cylinder

First, we consider that the inner cylinder as a test cylinder in the sense that its presence does not affect the scalar field profile inside the cavity. The latter is thus purely dictated by the outer cylinder, thus is axially symmetric and given by $\bar{\phi}(r)$ alone. It follows that the expression (48) reduces to

$$\mathcal{F}|_{\bar{\phi}}[\delta] \equiv \int_0^{2\pi} \cos \theta d\theta \int_{r_-(\theta)}^{r_+(\theta)} \bar{\phi}'(r) r dr. \quad (50)$$

Now, since

$$r_-(\theta) \equiv R + h_-(\theta) = R + \delta \cos \theta - \frac{1}{2} \frac{\delta^2}{R} \sin^2 \theta + \dots$$

and

$$\begin{aligned} r_+(\theta) &\equiv R + e + h_+(\theta) \\ &= R + e + \delta \cos \theta - \frac{1}{2} \frac{\delta^2}{R+e} \sin^2 \theta + \dots \end{aligned}$$

where the dots contain terms which are higher powers of $\sin^2 \theta$, we split the integral over r as

$$\int_R^{R+e} - \int_R^{r_-} + \int_{R+e}^{r_+}.$$

Obviously, the first does not depend on θ and gives 0 after angular integration. The other two reduce to $\bar{\phi}'(R)R[r_+(\theta) - R]$ and $\bar{\phi}'(R+e)(R+e)[r_+(\theta) - R - e]$. When integrating over θ only the linear term in δ survives so we get

$$\mathcal{F}|_{\bar{\phi}, \text{lin}}[\delta] = [\bar{\phi}'(R+e)(R+e) - \bar{\phi}'(R)R] \frac{\delta}{2}. \quad (51)$$

In this approximation we can get the force directly from our the results of our former work [31]. Even though we assumed staticity, we can write down the equation of motion for the inner cylinder as $m\ddot{\delta} = F$ so that

$$\ddot{\delta} + \frac{\beta}{2\pi M_p} \left[\frac{\bar{\phi}'(R+e)(R+e) - \bar{\phi}'(R)R}{(2R+e)e} \right] \delta = 0,$$

i.e we expect a typical pulsation of order

$$\omega^2 = \frac{\beta}{2\pi M_p} \left[\frac{\bar{\phi}'(R+e)(R+e) - \bar{\phi}'(R)R}{(2R+e)e} \right]. \quad (52)$$

Note that this does not assume that ω^2 is positive. If the slope of $\mathcal{F}[\delta]$ is positive then the force destabilizes the system and ω has to be thought as the inverse of a stability time.

TABLE I. Magnitude of the force and of the associated (inverse) of the stability time defined in Eq. (52) in the inner cylinder test approximation.

$\delta(\text{m})$	$ \mathbf{F}_h _{\bar{\phi}} (\text{N.m}^{-1})$	$ \mathbf{F}_h _{\bar{\phi}, \text{lin}} (\text{N.m}^{-1})$	$ \omega (\text{rad.s}^{-1})$
10^{-6}	9.57×10^{-11}	3.57×10^{-11}	1.18×10^{-4}
10^{-4}	9.57×10^{-9}	3.57×10^{-9}	1.18×10^{-4}
10^{-2}	9.57×10^{-7}	3.57×10^{-7}	1.18×10^{-4}
0.023	2.20×10^{-6}	8.21×10^{-7}	1.18×10^{-4}

Table I summarizes the force for different δ by the integration of $\bar{\phi}$ through both Eqs. (50)–(51), with or without the linear approximation. Both methods reproduce the same order of magnitude. We conclude that the force is positive so that the fifth force destabilizes the system of cylinders.

2. Inner cylinder with radial backreaction

To go one step further, we consider the change of the profile of the field induced by the inner cylinder but neglect the $\ell \neq 0$ modes so that $\psi_0(r)$ is taken as the symmetric configuration when $\delta = 0$. It follows that the expression (48) reduces to

$$\mathcal{F}|_{\bar{\phi}+\psi_0}[\delta] \equiv \int_0^{2\pi} \cos \theta d\theta \int_{r_-(\theta)}^{r_+(\theta)} [\bar{\phi}'(r) + \psi_0'(r)] r dr. \quad (53)$$

This leads us to a similar computation as the previous one with a modified profile

$$\mathcal{F}|_{\bar{\phi}+\psi_0, \text{lin}}[\delta] = [(\bar{\phi}' + \psi_0')_{(R+e)}(R+e) - (\bar{\phi}' + \psi_0')_R R] \frac{\delta}{2}. \quad (54)$$

Table II contains the values of the force applied to the inner cylinder corrected by the back reaction contribution of ψ_0 , again by integrating it with or without the linear approximation for the force. Now for all δ , the force is negative and the linear approximation fails to give the correct force by one order of magnitude. It shows that the

TABLE II. Magnitude of the force and of the associated pulsation taking into the cylindrically symmetric backreaction. To be compared to Table I. Note the change of sign in the force that shows the stabilizing effect of the monopole.

$\delta(\text{m})$	$ \mathbf{F}_h _{\bar{\phi}+\psi_0} (\text{N.m}^{-1})$	$ \mathbf{F}_h _{\bar{\phi}+\psi_0, \text{lin}} (\text{N.m}^{-1})$	$ \omega (\text{rad.s}^{-1})$
10^{-6}	-2.71×10^{-9}	-3.20×10^{-10}	3.54×10^{-4}
10^{-4}	-2.80×10^{-7}	-3.20×10^{-8}	3.54×10^{-4}
10^{-2}	-2.18×10^{-5}	-2.87×10^{-6}	3.35×10^{-4}
0.023	-3.55×10^{-5}	-5.76×10^{-6}	3.13×10^{-4}

monopole induces a stabilizing force, as can actually be seen directly from Fig. 4 on which it can clearly be seen that the gradient of the scalar field becomes positive.

3. Generic case

The general expression (49) includes the sum

$$\sum_{\ell} \int_0^{2\pi} e^{i\ell\theta} \int_{r_-(\theta)}^{r_+(\theta)} \sqrt{\frac{\delta}{r}} \left[\left(u'_{\ell} - \frac{u_{\ell}}{2r} \right) \cos\theta - i\ell \frac{u_{\ell}}{r} \sin\theta \right] r dr. \quad (55)$$

Again in the small δ limit, this can be computed by splitting the integral over r as

$$\begin{aligned} & \cos\theta \int_R^{R+e} \sqrt{\frac{\delta}{r}} \left(u'_{\ell}(r) - \frac{u_{\ell}(r)}{2r} \right) r dr - i\ell \sin\theta \int_R^{R+e} \sqrt{\frac{\delta}{r}} u_{\ell}(r) dr + \cos\theta \int_{R+e}^{R+e+h_+(\theta)} \sqrt{\frac{\delta}{r}} \left(u'_{\ell}(r) - \frac{u_{\ell}(r)}{2r} \right) r dr \\ & - i\ell \sin\theta \int_{R+e}^{R+e+h_+(\theta)} \sqrt{\frac{\delta}{r}} u_{\ell}(r) dr - \cos\theta \int_R^{R+h_-(\theta)} \sqrt{\frac{\delta}{r}} \left(u'_{\ell}(r) - \frac{u_{\ell}(r)}{2r} \right) r dr + i\ell \sin\theta \int_R^{R+h_-(\theta)} \sqrt{\frac{\delta}{r}} u_{\ell}(r) dr. \end{aligned}$$

Hence, \mathcal{F} is obtained by integrating over θ the following expression

$$\begin{aligned} & e^{i\ell\theta} \cos\theta \int_R^{R+e} \sqrt{\frac{\delta}{r}} \left(u'_{\ell}(r) - \frac{u_{\ell}(r)}{2r} \right) r dr - i\ell e^{i\ell\theta} \sin\theta \int_R^{R+e} \sqrt{\frac{\delta}{r}} u_{\ell}(r) dr \\ & + e^{i\ell\theta} \cos\theta h_+(\theta) \left(\sqrt{\frac{\delta}{r}} \left(u'_{\ell}(r) - \frac{u_{\ell}(r)}{2r} \right) r \right)_{r=R+e} - i\ell e^{i\ell\theta} \sin\theta h_+(\theta) \left(\sqrt{\frac{\delta}{r}} u_{\ell}(r) \right)_{r=R+e} \\ & - e^{i\ell\theta} \cos\theta h_-(\theta) \left(\sqrt{\frac{\delta}{r}} \left(u'_{\ell}(r) - \frac{u_{\ell}(r)}{2r} \right) r \right)_{r=R} + i\ell e^{i\ell\theta} \sin\theta h_-(\theta) \left(\sqrt{\frac{\delta}{r}} u_{\ell}(r) \right)_{r=R}. \end{aligned} \quad (56)$$

The first two terms have a contribution of $\ell = \pm 1$ which scales as $\sqrt{\delta}$. The terms in $\delta \cos\theta$ in h_{\pm} leads to terms linear in δ for $\ell = 2$. Then higher multipoles arise from the shape $h_{\pm}(\theta)$. Basically we will have a series with terms scaling as $[\delta^2 \sin^2(\theta)]^p$ each of which will involve multipoles up to $\ell = 2p + 1$ and each term is a higher power of δ^2 . This is good news since it better justifies the approximation scheme.

The expected tendency, deduced from our analytical analysis, that the contributions decrease with ℓ is numerically confirmed. Table III shows the force computed for each multipole, as shown in Fig. 5, up to $\ell = 4$, i.e., the contribution to the force resulting from the integration of Eq. (55) $|\mathbf{F}_h|_{u_{\ell}+u_{-\ell}}$ compared to the integration of Eq. (56) $|\mathbf{F}_h|_{u_{\ell}+u_{-\ell},\text{lin}}$ in the linear approximation. In both cases the multipole ℓ contains the contribution of u_{ℓ} and $u_{-\ell}$ to get a real-valued quantity. We observe, as expected, that the magnitudes of the multipoles decrease with higher ℓ . This decrease is slower than what expected in the linear approximation of Eq. (56). For small δ , we can consider that only the dipole contributes significantly to the total force. For larger δ the contributions are more balanced, but

still, the multipoles with $\ell > 2$ can be neglected. In any case, the main contribution to the force are the monopole and dipole of the field and none can be neglected.

TABLE III. Magnitude of the first multipoles of the force taking into account nonlinearities (top) and in the linear approximation (bottom).

$\delta(m)$	$ \mathbf{F}_h _{u_{\ell}+u_{-\ell}} (\text{N}\cdot\text{m}^{-1})$			
	$\ell = 1$	$\ell = 2$	$\ell = 3$	$\ell = 4$
10^{-6}	2.75×10^{-9}	1.14×10^{-16}
10^{-4}	2.74×10^{-7}	9.77×10^{-11}	1.29×10^{-11}	...
10^{-2}	2.11×10^{-5}	8.71×10^{-7}	1.11×10^{-7}	7.40×10^{-9}
0.023	3.12×10^{-5}	4.27×10^{-6}	5.42×10^{-7}	3.65×10^{-8}
$\delta(m)$	$ \mathbf{F}_h _{u_{\ell}+u_{-\ell},\text{lin}} (\text{N}\cdot\text{m}^{-1})$			
	$\ell = 1$	$\ell = 2$	$\ell = 3$	$\ell = 4$
10^{-6}	2.74×10^{-9}	5.06×10^{-17}
10^{-4}	2.74×10^{-7}	5.06×10^{-11}	1.16×10^{-15}	...
10^{-2}	2.41×10^{-5}	6.80×10^{-7}	1.16×10^{-10}	7.49×10^{-23}
0.023	4.67×10^{-5}	3.28×10^{-6}	2.44×10^{-9}	0

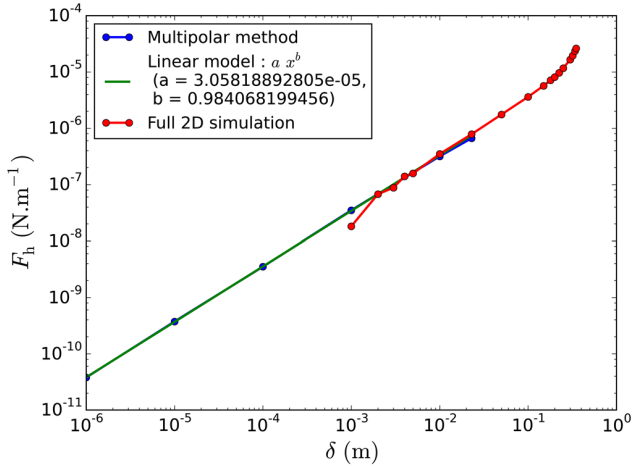


FIG. 11. Total linear force as a function δ . The blue line refers to the result of the multipolar expansion method while the red line is the result of the full numerical simulation. The green line is a linear model fitted on the two first points.

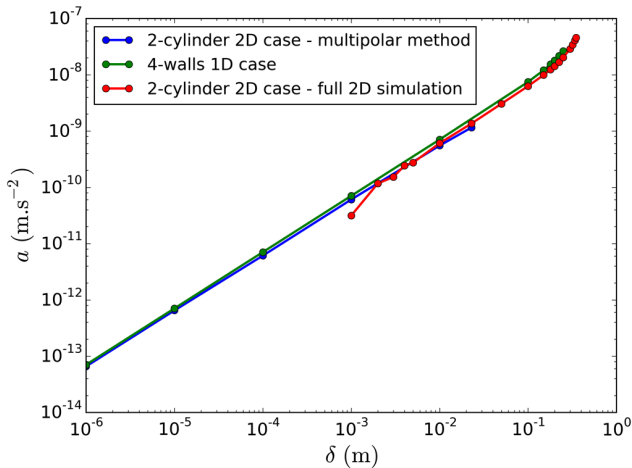


FIG. 12. Acceleration experienced by the inner cylinder of a 2-cylinders configuration computed by the multipolar expansion method (blue) and the full numerical simulation (red). The green line represents the acceleration experienced by the two central wall of a 4-wall configuration, i.e., of the analog 1-dimensional problem.

C. Dependence of the total force on δ

We can now gather all the different contributions and calculate the total force on the inner cylinder. Figure 11 depicts how it behaves with δ . The sum on ℓ is truncated to $\ell = 2$ included. The force is repulsive and linear in the displacement. The force obtained by both methods have been compared: there is an overlap for δ between 10^{-3} and $2 \cdot 10^{-2}$ m, where both methods agree. At each limit of this interval, each method starts to show some of its limits by departing from linearity. For the full numerical method, it is due to the fact that the mesh is too coarse compared to δ . For the multipolar method, it is due to the fact that some higher nonlinear terms we have not considered become non-negligible for large δ . Nevertheless, both methods are consistent and show the same global linear behavior and magnitude. The linearity of the force occurs for $\delta \lesssim 10^{-1}$ m and has a linear stiffness of $k_h = -3 \cdot 10^{-5}$ N.m $^{-2}$ —assuming the convention $\mathbf{F} = -k\delta$, and $k_h = k/h$.

These results can also be compared with the one-dimensional simulation of asymmetry from Sec. III. To be comparable to this cylindrical case, we consider a 4-wall configuration where the two internal walls move together. We compute the acceleration experienced by respectively the two walls and the internal cylinder. Figure 12 shows that both cases are in excellent agreement. The linearity of the force occurs for the same range of δ and the departure from linearity for large δ are very much similar. The magnitude of the accelerations using both methods differ by a factor smaller than 2, so that the cylindrical geometry does not bring any major additional contribution to the force—it even lowers it slightly.

D. Total force variation with β and λ

Let us investigate the dependence of this fifth force on the chameleon parameters β and Λ . We run the multipolar method for different parameters for $\delta = 10^{-6}$ m, and compare k_h that we estimate as the linear slope of $F(\delta)$.

Table IV summarizes the values of k_h obtained for different couples of parameters (β, Λ) . For each k_h , the sum of the multipole contribution is truncated at $\ell = 2$ as the next contributions are negligible. Figure 13 shows graphically its variation with β for $\Lambda = 1$ eV, and with Λ

TABLE IV. Dependence of the slope per unit of length of the cylinder, $k_h = -F/(h\delta)$, of the pressure with the parameters β and Λ of the chameleon model.

		Λ				
k_h N.m $^{-2}$		0.4	1	3	5	10
β	0.01	6.72×10^{-10}	2.81×10^{-10}	2.31×10^{-10}	2.26×10^{-10}	2.24×10^{-10}
	0.1	1.25×10^{-6}	5.13×10^{-7}	3.91×10^{-8}	3.01×10^{-8}	2.65×10^{-8}
	1	5.55×10^{-6}	3.78×10^{-5}	1.69×10^{-4}	3.67×10^{-5}	5.55×10^{-6}
	4	4.37×10^{-5}	8.78×10^{-5}	8.85×10^{-4}	2.20×10^{-3}	1.57×10^{-3}
	10	...	3.03×10^{-4}	1.41×10^{-3}	4.46×10^{-3}	1.51×10^{-3}

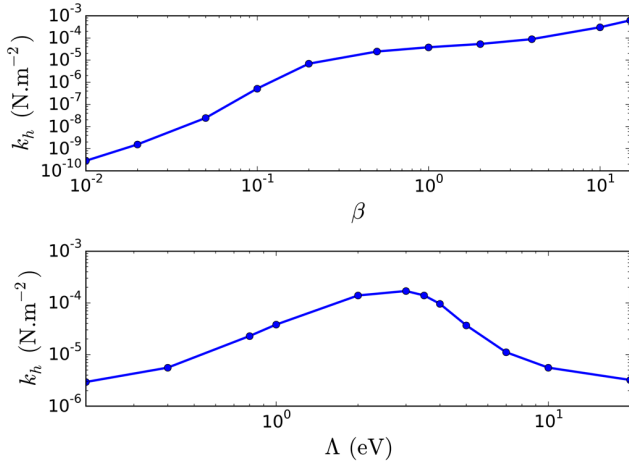


FIG. 13. Dependence of the chameleon stiffness k_h to β and Λ for $\Lambda = 1$ eV and $\beta = 1$ respectively.

for $\beta = 1$. The force increases with β and exhibits a maximum along the Λ -axis, that flattens for small values of β . Notice that the behavior of the stiffness is similar for the 1-dimensional case of 4-walls. This behavior is interesting considering screening. The cylinders indeed tend to be screened for large β and small Λ , as the Compton wavelength decreases. The behavior of the force shows that it can still be relevant even when the system of cylinders is screened— β large. This is promising as this could still lead to a detectable internal effect even when screening occurs, i.e., when externally sourced effects are shielded, see Ref. [31].

E. Dependence on the geometry

For now, we have fixed the geometry with specific sizes of cylinders, gaps, and matter densities. Varying these parameters will indeed change the value of the force and its stiffness, as well as shifting the sensitivity curves displayed in Fig. 13.

1. Effect of the densities

In most experiments, the vacuum density is much smaller than the one used in our analysis. Here, we estimate how this impacts the force by varying the density of the intercylinder vacuum. Figure 14 shows the result for a displacement $\delta = 10^{-6}$ m—for higher δ , the curve remains similar. The intercylinder vacuum density is expressed as a multiple of the cylinder density ρ_{in} , which we keep fixed. So far we used $\rho_{\text{vac}}/\rho_{\text{in}} = 10^{-3}$.

We observe that on the one hand, improving the vacuum quality leaves unchanged the magnitude of the force. This is due to the fact that the field is in fact unchanged in the intercylinder and exterior regions. When lowering ρ_{vac} the associated Compton wavelength stretches such that the field has less room to vary, but the associated minimum of the potential ϕ_* gets stretched at the same time. These

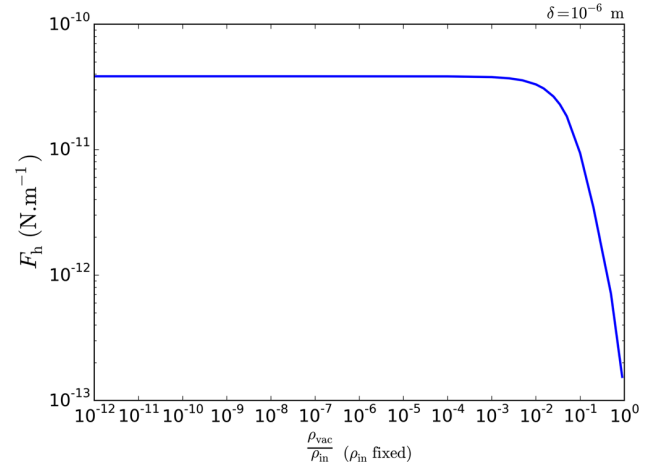


FIG. 14. Evolution of the force with the intercylinder vacuum density while the cylinder density is kept fixed, for $\delta = 10^{-6}$ m and $n = 2$, $\beta = 1$, $\Lambda = 1$ eV.

two effects compensate so that the profile and the force remains unchanged. On the other hand, when worsening the vacuum quality the force gets exponentially suppressed. This occurs when the Compton wavelength associated to ρ_{vac} becomes of same order of magnitude as the intercylinder gap, as then the field has enough room to reach its minimum so that the previous argument is no longer valid. The force becomes null when the vacuum density equals the density of the cylinders. This is natural as, in this case, the system can be considered as a solid cylinder in which the field is flat and equal $\phi_*(\rho_{\text{in}})$ deeply inside the cylinder at the level of where the inner cylinder was. This confirms that everything we obtained previously with $\rho_{\text{vac}}/\rho_{\text{in}} = 10^{-3}$ is directly transposable to case of a better vacuum quality.

2. Scaling of the geometry

Considering smaller scales in the geometry by reducing the sizes of the cylinders and the gaps would also affect the force. The scaling mentioned in Eq. (12) should give us the answer to this question. Indeed, it gives a correspondence between two geometries with constant matter densities, as long as the chameleon parameters are changed accordingly. This can be generalized to a scaling of the type

$$\begin{aligned}
 \mathbf{x} &\rightarrow \mathbf{x}' = \alpha_x \mathbf{x}, \\
 \Lambda &\rightarrow \Lambda' = \alpha_\Lambda \Lambda, \\
 \beta &\rightarrow \beta' = \alpha_\beta \beta, \\
 \phi &\rightarrow \phi' = \alpha_\phi \phi \\
 \rho &\rightarrow \rho' = \alpha_\rho^3 \rho,
 \end{aligned} \tag{57}$$

keeping the Planck mass unchanged. In order for the field equation to be unchanged, we need to impose that

$$\alpha_\phi = \alpha_\rho \alpha_\rho^3 \alpha_x^2, \quad \text{and} \quad \alpha_\phi^{n+2} = \alpha_\Lambda^{4+n} \alpha_x^2. \quad (58)$$

Hence, Eq. (12) corresponds to $\alpha_\rho = 1$, $\alpha_\Lambda = \alpha_\phi = \alpha$, $\alpha_x = 1/\alpha$ and $\alpha_\beta = \alpha^3$. It follows that the masses of the cylinders scale as $m \rightarrow m' = \alpha_\rho^3 \alpha_x^3 m$. Since the force is given by $\mathbf{F}_h = -\frac{\beta}{M_{\text{Pl}}} \frac{m}{h} \nabla_{\mathbf{x}} \phi$, it follows that it scales as

$$\mathbf{F} \rightarrow \mathbf{F}' = \alpha_\rho \alpha_\rho^3 \alpha_x \alpha_\phi \mathbf{F},$$

and that, given the constraint (58) the profile of the field is obtained from a simple rescaling as the Klein-Gordon equation remains unchanged, up to a general conformal factor. Hence, in the particular case of Eq. (12), $\mathbf{F}' = \alpha^3 \mathbf{F}$. This tells us that small systems are more likely to provide detectable forces since shrinking all physical dimensions by a factor α (keeping the same materials; $\alpha_\rho = 1$) would increase the force by a factor α^3 . On the other hand, this corresponds to another theory as β has also been changed. It follows that the dependence of the force on β and Λ is impacted accordingly so that the curves of Sec. VID should be shifted along the β - and Λ -axis in a way consistent with the above scaling relations. All these scalings have been checked using our simulations.

VII. CONCLUSIONS

This article investigated the fifth force that arises on the detector of a gravity experiment, in the case of chameleon models. As the profile of the scalar field is affected by the local matter density, this requires us to determine solutions of the Klein-Gordon equation inside the instrument. To that goal, we modeled the accelerometer in the simplest way as two nested cylinders. We then extended our previous work [31] to take into account the fact that the cylinders may move, violating the axial symmetry, and hence creating a nonvanishing fifth force on the cylinders.

The computation of this force requires full numerical simulations but we estimated its magnitude and dependence on the geometry and the parameters of the model by first assuming that the cylinders are infinite. In such a situation, the Newton force between the two cylinders vanishes exactly. First, we considered an analog 1-dimensional model with 2 parallel walls containing a third wall that can move from its central position. Then, we explored the case of 2 infinite nested cylinders. We developed a semianalytic method based on a multipolar expansion of the field. It allowed us to solve the Klein-Gordon equation iteratively. While the hierarchy of equations for the multipoles is a coupled system due to the nonlinearity of the chameleon model, we showed that they decoupled for small displacement. We thus solved these equation numerically, first in the linear approximation and then with the first nonlinear term, and compared them with the profiles obtained from a full numerical simulation using a finite difference relaxation method. The two approaches

are complementary and agree perfectly inside their common domain of applicability.

In all the cases studied, 1- or 2-dimensional, the force is linear in the displacement, as long as it is small compared to the radius of the cylinders. The fifth force is repulsive so that it does not stabilize the system by restoring the symmetry. Interestingly, the accelerations induced by this force in 1 or 2 dimensions are in very good agreement, testifying that there is no significant effect created by the cylindrical geometry. Then, we studied the dependence of this force on the chameleon parameters. We mainly showed that the force was increasing with β leading to the conclusion that one could expect detectable effects even when the cylinders are screened. We exhibited some scaling relations between the geometry and the parameters of the model and explored the sensitivity of the force to geometrical parameters. Two features have been explored: (1) we showed that the force was constant regardless of the magnitude of the density in the vacuum of the intercylinder gaps as long as this density is small enough, i.e., the Compton wavelength of the field in vacuum is smaller than the sizes of the gaps. This makes all our results valid for realistic densities of vacuum. Finally (2) we showed that reducing the size of the cylinders simultaneously would affect the force in such a way that dividing them by a factor α would multiply the force by a factor α^3 , leading to forces more likely to be detectable for smaller system.

While this analysis gives a first insight on the effect of a chameleon fifth force on a space detector with a geometry close to the MICROSCOPE accelerometer, it is still simplified. First it assumes infinite cylinders. Indeed, with finite cylinders one expects edge effects which would require full 3-dimensional simulations. Besides, while the Newtonian force is strictly zero for 2 infinite nested cylinders, it will be nonvanishing for finite cylinders. This study allows us to control such simulations in the limits $h/R \gg 1$. Then, we assume that the configuration of cylinders is static. While this is fine to compute the fifth force, it may not be adapted for a dynamical analysis. Such an analysis would require to study the relaxation of the field when the inner cylinder is moving and would challenge the hypothesis of a frozen field. Nevertheless, our formalism paves the way to study the effects of a chameleon fifth force on the detector of gravity experiments such as the MICROSCOPE mission. An application to this experiment will be presented, with more faithful geometrical parameters, in a follow-up article [32].

ACKNOWLEDGMENTS

We thank Manuel Rodrigues, Gilles Métris and Pierre Touboul for useful discussions and technical information about the MICROSCOPE instrument. We thank Arno Vantighem for useful and friendly discussion about numerical aspects. We thank the members of the MICROSCOPE Science Working Group for allowing us

to start this project and encouraging us to pursue it. We acknowledge the financial support of CNES through the APR program (“GMscope+” project). M. P. B. is supported by a CNES/ONERA PhD grant. This work uses technical details of the T-SAGE instrument, installed on the CNES-ESA-ONERA-CNRS-OCA-DLR-ZARM MICROSCOPE mission. This work is supported in part by the EU Horizon 2020 research and innovation program under the Marie-Sklodowska grant No. 690575. This article is based upon work related to the COST Action CA15117 (CANTATA) supported by COST (European Cooperation in Science and Technology).

APPENDIX: COMPUTATION OF $I_\ell(r)$

To obtain Eq. (35), we need to compute integrals of $e^{i\ell\theta}\Xi$ that contains terms like

$$I_\ell(r) = \int \frac{d\theta}{2\pi} H[r - f(\theta)] e^{i\ell\theta}$$

where H is the Heaviside function and f stands for r_- or r_+ .

At constant r , the equation $r = f(\theta)$ has then 2 opposite solutions in θ as $f(\theta)$ is the polar equation of a circle of radius R displaced of δ . These solutions exist only when $r \in [R - \delta, R + \delta]$ and are given by

$$\cos \vartheta(r) = \frac{r^2 + \delta^2 - R^2}{2\delta r}, \quad (\text{A1})$$

for which we keep only the positive root, the second being $-\vartheta(r)$. Then it is clear that $H[r - f(\theta)] = 1$ for $\theta \in [-\vartheta(r), \vartheta(r)]$ so that

$$I_\ell(r) = \int_{\vartheta(r)}^{-\vartheta(r)} \frac{d\theta}{2\pi} e^{i\ell\theta}$$

and thus

$$I_\ell(r) = -\frac{\sin \ell \vartheta(r)}{\pi \ell}.$$

It follows that

$$\int \Xi[r; r_-(\theta), r_+(\theta)] e^{-i\ell\theta} \frac{d\theta}{2\pi} = \frac{\sin \ell \vartheta_+(r)}{\pi \ell} - \frac{\sin \ell \vartheta_-(r)}{\pi \ell} \quad (\text{A2})$$

from which we deduce that

$$\int \Xi[r; r_-(\theta), r_+(\theta)] \frac{d\theta}{2\pi} = \frac{\vartheta_+(r) - \vartheta_-(r)}{\pi}. \quad (\text{A3})$$

-
- [1] C. M. Will, *Theory and Experiment in Gravitational Physics* (Cambridge University Press, Cambridge, England, 2018).
 - [2] C. M. Will, The confrontation between general relativity and experiment, *Living Rev. Relativity* **17**, 4 (2014).
 - [3] T. Damour and G. Esposito-Farese, Nonperturbative Strong Field Effects in Tensor–Scalar Theories of Gravitation, *Phys. Rev. Lett.* **70**, 2220 (1993).
 - [4] B. Jain *et al.*, Novel probes of gravity and dark energy, [arXiv:1309.5389](https://arxiv.org/abs/1309.5389).
 - [5] T. Damour and K. Nordvedt, General Relativity as a Cosmological Attractor of Tensor Scalar Theories, *Phys. Rev. Lett.* **70**, 2217 (1993).
 - [6] T. Damour and A. Polyakov, The string dilation and a least coupling principle, *Nucl. Phys.* **B423**, 532 (1994).
 - [7] J. Bergé, P. Brax, M. Pernot-Borràs, and J.-P. Uzan, Interpretation of geodesy experiments in non-Newtonian theories of gravity, *Classical Quantum Gravity* **35**, 234001 (2018).
 - [8] K. Hinterbichler and J. Khoury, Screening Long-Range Forces Through Local Symmetry Restoration, *Phys. Rev. Lett.* **104**, 231301 (2010).
 - [9] J. Khoury and A. Weltman, Chameleon Fields: Awaiting Surprises for Tests of Gravity in Space, *Phys. Rev. Lett.* **93**, 171104 (2004).
 - [10] J. Khoury and A. Weltman, Chameleon cosmology, *Phys. Rev. D* **69**, 044026 (2004).
 - [11] C. Burrage and J. Sakstein, Tests of chameleon gravity, *Living Rev. Relativity* **21**, 1 (2018).
 - [12] P. Brax, C. Burrage, and A.-C. Davis, Laboratory tests of screened modified gravity, *Int. J. Mod. Phys. D* **27**, 1848009 (2018).
 - [13] J. Bergé, P. Brax, G. Métris, M. Pernot-Borràs, P. Touboul, and J.-P. Uzan, Microscope Mission: First Constraints on the Violation of the Weak Equivalence Principle by a Light Scalar Dilaton, *Phys. Rev. Lett.* **120**, 141101 (2018).
 - [14] C. Burrage and E. J. Copeland, Using atom interferometry to detect dark energy, *Contemp. Phys.* **57**, 164 (2016).
 - [15] D. Sabulsky, I. Dutta, E. A. Hinds, B. Elder, C. Burrage, and E. J. Copeland, Experiment to Detect Dark Energy Forces Using Atom Interferometry, *Phys. Rev. Lett.* **123**, 061102 (2019).
 - [16] P. Brax, C. van de Bruck, A.-C. Davis, D. F. Mota, and D. Shaw, Detecting chameleons through Casimir force measurements, *Phys. Rev. D* **76**, 124034 (2007).
 - [17] A. Upadhye, Dark energy fifth forces in torsion pendulum experiments, *Phys. Rev. D* **86**, 102003 (2012).
 - [18] P. Touboul *et al.*, Microscope Mission: First Results of a Space Test of the Equivalence Principle, *Phys. Rev. Lett.* **119**, 231101 (2017).
 - [19] P. Brax, G. Pignol, and D. Roulier, Probing strongly coupled chameleons with slow neutrons, *Phys. Rev. D* **88**, 083004 (2013).

- [20] A. N. Ivanov, R. Höllwieser, T. Jenke, M. Wellenzohn, and H. Abele, Influence of the chameleon field potential on transition frequencies of gravitationally bound quantum states of ultracold neutrons, *Phys. Rev. D* **87**, 105013 (2013).
- [21] C. Burrage, E. J. Copeland, and E. A. Hinds, Probing dark energy with atom interferometry, *J. Cosmol. Astropart. Phys.* **03** (2015) 042.
- [22] C. Burrage, E. J. Copeland, and J. A. Stevenson, A proposed experimental search for chameleons using asymmetric parallel plates, *J. Cosmol. Astropart. Phys.* **08** (2016) 070.
- [23] A. Ivanov, G. Cronenberg, R. Hollwieser, T. Jenke, M. Pitschmann, M. Wellenzohn, and H. Abele, Exact solution for chameleon field, self-coupled through the Ratra-Peebles potential with $n = 1$ and confined between two parallel plates, *Phys. Rev. D* **94**, 085005 (2016).
- [24] T. Nakamura, T. Ikeda, R. Saito, and C.-M. Yoo, Chameleon field in a spherical shell system, *Phys. Rev. D* **99**, 044024 (2019).
- [25] L. Kraiselburd, S. J. Landau, M. Salgado, D. Sudarsky, and H. Vucetich, Equivalence principle in chameleon models, *Phys. Rev. D* **97**, 104044 (2018).
- [26] L. Kraiselburd, S. Landau, M. Salgado, D. Sudarsky, and H. Vucetich, Thick shell regime in the chameleon two-body problem, *Phys. Rev. D* **99**, 083516 (2019).
- [27] P. Hamilton, M. Jaffe, P. Haslinger, Q. Simmons, H. Müller, and J. Khoury, Atom-interferometry constraints on dark energy, *Science* **349**, 849 (2015).
- [28] B. Elder, J. Khoury, P. Haslinger, M. Jaffe, H. Müller, and P. Hamilton, Chameleon dark energy and atom interferometry, *Phys. Rev. D* **94**, 044051 (2016).
- [29] S. Schlogel, S. Clesse, and A. Fuzfa, Probing modified gravity with atom-interferometry: A numerical approach, *Phys. Rev. D* **93**, 104036 (2016).
- [30] C. Burrage, E. J. Copeland, A. Moss, and J. A. Stevenson, The shape dependence of chameleon screening, *J. Cosmol. Astropart. Phys.* **01** (2018) 056.
- [31] M. Pernot-Borràs, J. Bergé, P. Brax, and J.-P. Uzan, General study of chameleon fifth force in gravity space experiments, *Phys. Rev. D* **100**, 084006 (2019).
- [32] J. Bergé, P. Brax, M. Pernot-Borràs, and J.-P. Uzan, Microscope mission: Constraining the chameleon (2020) (to be published).
- [33] J.-P. Uzan, The fundamental constants and their variation: Observational status and theoretical motivations, *Rev. Mod. Phys.* **75**, 403 (2003).
- [34] J.-P. Uzan, Varying constants, gravitation and cosmology, *Living Rev. Relativity* **14**, 2 (2011).
- [35] J.-P. Uzan, Variation of the constants in the late and early universe, *AIP Conf. Proc.* **736**, 3 (2004).

4.3 Additional content: exploring methods

4.3.1 Quasi-cylindrical method for nested cylinders

In Sec. 4.2, we obtained the profile associated to a geometry of two nested cylinders whose axes do not coincide by two methods. Before that, we tried to solve the problem of computing the force the inner cylinder feels by making the assumption that the field is quasi-cylindrical in the limit small displacements.

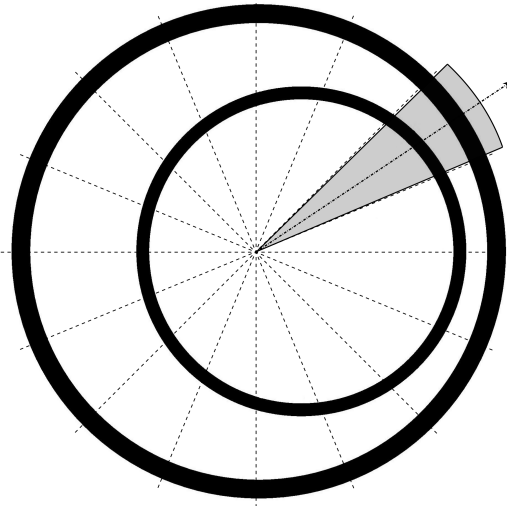


Figure 4.1: Sketch of the quasi-cylindrical method. The geometry is subdivided in radial ‘pie slices’ delimited by the dashed lines, one of them is shown with the shaded region, its central radius is depicted with the dashed arrow.

The starting point of this method is the ones developed in the first article of this chapter that allowed us to compute the field of a cylindrically symmetric geometry. The principle of the method is sketched in Fig. 4.1. We subdivide the geometry in ‘pie slices’ zones and consider that in each of these zones, the field can be approximated by the one of a cylindrically symmetric geometry of two centred nested cylinders whose boundaries are given by those of the decentred cylinders at the level of the central radius of the zone – dashed arrow in Fig. 4.1. Mathematically this corresponds to take as boundaries for the inner cylinder

$$R_{\text{in/out}}^{\text{approx}}(\alpha) = R_{\text{in/out}} \left(\frac{\delta}{R_{\text{in/out}}} \cos \alpha + \sqrt{1 - \frac{\delta^2}{R_{\text{in/out}}^2} \sin^2 \alpha} \right), \quad (4.1)$$

with δ the displacement of the inner cylinder, α the angle of the considered zone and $R_{\text{in/out}} = R$ or $R + e$ the real inner and outer radius of the cylinder. In each zone, the approximated field can be computed with the methods of the first paper. But the aim is to compute the force experienced by the inner cylinder. We compute it by summing over each element of the cylinder the forces obtained in each zones with the approximated field.

The results of this method were unsatisfying. While in the 1D case the force was destabilising, here we found that it was stabilising. This has motivated the development of the two others methods. These methods confirmed that this method was indeed wrong and that the force was destabilising.

4.3.2 Adaptive mesh refinement methods for a 3D treatment

In Sec. 4.1 we showed that MICROSCOPE is screened for most of the unconstrained part of the chameleon parameter space. In the remaining part, where the field is only partially screened, a WEP violation can appear. This effect is caused by the influence on the field profile of both the Earth and the test masses. As discussed in Sec. 2.3.4, two test masses are differently screened due to their different mass densities, thence they experience different fifth forces. But in the case of MICROSCOPE, the two tests masses interact and the matter from the satellite affects the field. To quantify the magnitude of such WEP violation we need to solve simultaneously the field behaviour as sourced by the Earth and the satellite. Solving this problem requires to run a 3D large simulation containing both of them. Besides, the boundary conditions must be set at some large distance of the system given by the scale of Compton wavelength associated to the low density background environment. This imposes to the simulation to span a very large region of space.

We attempted to answer this problem by using the relaxation method used in the Sec. 4.2. In this method, the simulated region is subdivided in a regular Cartesian mesh grid made of equal squared cells. A value of the field is attributed to each cell and is redefined by the solver at each iteration of the method until convergence. In Sec. 4.2, we used this method in 2D for a very limited region delimited by the outer cylinder of the geometry we were studying – the screening of this cylinder allowed for imposing the boundary conditions in it. Here, we need the simulation to be 3D and larger, this requires a number of cells significantly larger. Given that resolution of the grid is dictated by the size of the satellite and the magnitude of smallest Compton wavelength of the field associated to the matter at play, the number of required cells is way over the capacities of a computer and even maybe of a computer cluster.

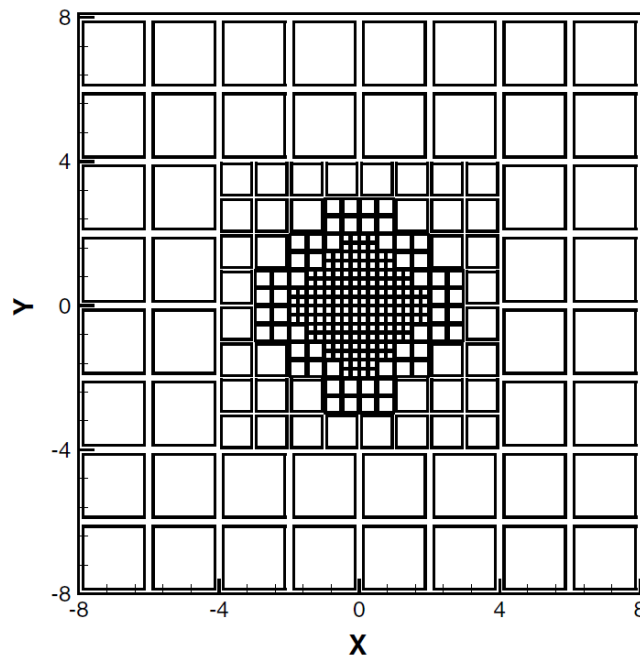


Figure 4.2: Sketched of an adaptive refined mesh grid obtained from Ref.[16].

The idea to overcome this problem is to use an adaptive mesh refinement technique. In these methods, instead of using a regular mesh grid, we use an adaptive mesh grid with cells of variable sizes. An example of such a grid is sketched in Fig. 4.2. This method optimises the usage of computing resources by focusing them where needed.

In the chameleon problem, the computing resources need to be focussed where the field varies sharply i.e. at the boundaries of matter in the satellite and in Earth. We implemented this method for the chameleon problem by following Ref. [16] who already applied it to elliptic equations problems i.e. Laplace-like equations. We used the package PARAMESH [68] to generate the grid.

This investigation of 3D simulations was not convincing. We applied it to the 2D case of nested cylinders to obtain their profile for chameleon parameters for which the cylinders are more screened compared to those shown in Sec. 4.2. We found that it did not provide a significant improvement to our ability of computing our chameleon problem, given our computing resources. This is mainly caused by the fact that between a coarse and a finely refined regions of the grid, the sizes of the cells must decrease step by step, as depicted in Fig. 4.2. The reason to this is the treatment of the information transmission at the transition between two levels of refinement. Thus, for our case, the power of AMR to reduce the computing needs is limited. We concluded that solving this problem is beyond our computing resources and, it seems to us, maybe beyond even those of computing clusters. As a point of comparison, the typical grids we used in the 2D problem of Sec. 4.2 were made of 500^2 cells, while an example of a large simulation such as the TNG300 cosmological simulation [96] uses 2500^3 cells. Of course in the 3D case we study, the field is less screened in the satellite such that we need less cells to treat the dynamics in the satellite, but due to the boundary conditions treatment, we need a simulation at least a thousand times larger. This problem might thus require a number of cells far larger than 2500^3 , which seems currently unreachable. The problem of the numerical treatment of the chameleon problem is thus still an open issue, it may require a closer collaboration with numericians. As discussed in Ref. [18], finite element methods should be privileged.

Chapter conclusion

We have numerically solved the chameleon profile associated to different geometries. The MICROSCOPE experiment has been found to be screened for most of the unconstrained parameter space. Despite this screening, an internally sourced force is expected to appear when a test mass cylinder is shifted from its rest position. This force behaves as a destabilising stiffness.

This new stiffness is used in the next chapter to constraint the chameleon model with measurement sessions dedicated to measure the electrostatic stiffness.

Chapter 5

Application: testing the chameleon stiffness with MICROSCOPE

As already mentioned the measurement of the electrostatic stiffness in MICROSCOPE may represent a novel and original opportunity for testing the chameleon theory. The reason for it is both the existence of a chameleonic stiffness that we characterised in the previous chapter and the discrepancy that has been observed between the measured stiffness and the expected stiffness from electrostatic models. Nevertheless before concluding on potential constraints, one needs to study all the source for such a stiffness and apply the formalism developed in the previous chapter to obtain the chameleon stiffness to a realistic case accounting for MICROSCOPE's geometrical parameters.

The MICROSCOPE mission has performed four sessions dedicated to the measurement the electrostatic stiffness one expects from the electrostatic forces involved in the capacitive measurement of the acceleration. A simple model for such a stiffness has been introduced by Eq. (1.30) in Chapter 1. The measurement sessions consist in displacing a test mass around its rest position and measure the force acting on it. This displacement is sinusoidal with a frequency of 3 MHz and an amplitude of $5\ \mu\text{m}$. The result is compared to a more complex model than the one given in Eq. (1.30) that corresponds to the geometrical specificities of the MICROSCOPE's test masses and electrode cylinders. As Ref. [21] shows, the result of the measured and the expected values of stiffness disagree by more than 15%. The electrostatic model has been verified by numerical calculation and shown to overestimate the electrostatic stiffness by a bit less than 10%. This leaves a discrepancy that needs to be explained.

This chapter explores this discrepancy. The first part of the chapter re-analyses the stiffness-measurement-sessions by including other possible sources of such a linear force. The main new contributor comes from the mechanical action of the $7\ \mu\text{m}$ -gold-wire used to maintain the test masses at a desired electrical potential and that acts as a spring. The action of this wire is actually not completely quantified. This article evaluates its possible contribution to the stiffness. It also explores that this discrepancy could be caused by a Yukawa-like fifth force and pulls constraints from it by attributing the whole residual discrepancy budget to it. The second part of the chapter intends to do the same procedure to the case of the chameleonic fifth force. The procedure is less straightforward as it requires the complex methods from last chapter.

5.1 Measurement of the electrostatic stiffness in MICROSCOPE

5.1.1 Introduction and summary

The aim of this article is to evaluate the magnitude of all possible classical source of discrepancy between the measured and expected electrostatic stiffness in the MICROSCOPE experiment before considering the interpretation of the observed discrepancy as the result of a modified gravity effect. The analysis of these sessions presented here goes beyond the original analysis [21] that consisted in measuring the amplitude of the excess sinusoidal acceleration that a test mass is experiencing when it is sinusoidally shifted from its rest position. In this work, we derive a measurement equation for the acceleration the test mass experiences. The main new contributor comes from the gold-wire to which it is connected. This wire acts as a spring that generates a stiffness term and two damping terms. This damping consists of the internal damping that is already known to be a contributor to the noise of the mission – see Sec.1.4.4 – and a viscous damping. The former provides an out-of-phase acceleration whose phase is determined by the quality factor of the wire. The latter provides an acceleration in opposition of phase.

The question is to determine the contributions of these effects and more particularly the physical parameters of the wire: stiffness on the j^{th} -axis k_{wj} , quality factor Q and viscous damping factor. The degeneracy between these parameters is discussed. By fitting the slope of the acceleration noise of the detector one can have access to the ratio $\frac{k_{wj}}{Q}$. Under some assumptions we show that we can use this information to disentangle the problem and estimate from the stiffness-measurement-sessions the parameters of the wire. In the axes perpendicular to the MICROSCOPE's cylinders, the contribution of this mechanical stiffness is shown to be too small to explain the measured stiffness discrepancy.

Then the possibility that the discrepancy is caused by a Yukawa fifth force is explored. Such a force does indeed lead to a stiffness when a cylinder is not centred in the same way as the Newton force does. This is due to the interaction of the test mass with the diverse parts of the apparatus. The contributions are diverse: the cylinders in which the test mass is nested provide a destabilising stiffness while the part on the top of these cylinders contribute as a stabilising stiffness. These effects are finely understood by deriving a total Yukawa force. The discrepancy-budget can then be transformed in a constraint on the (α, λ) -plane of the Yukawa interaction. The constraints are shown to be eight orders of magnitude looser than the current best upper bounds for the considered ranges of interaction. This is not surprising since MICROSCOPE was not designed to that purpose. Note that the equivalent effect from local Newtonian gravity has also been evaluated to demonstrate it is negligible. The ambition of the next section of this chapter is to perform the same analysis for the chameleon field.

5.1.2 Article

MICROSCOPE’s constraint on a short-range fifth force

Joel Bergé¹, Martin Pernot-Borràs¹², Jean-Philippe Uzan³⁴,
Philippe Brax⁵, Ratana Chhun¹, Gilles Métris⁶, Manuel
Rodrigues¹, Pierre Touboul¹

¹ DPHY, ONERA, Université Paris Saclay, F-92322 Châtillon, France

² Sorbonne Université, CNRS, Institut d’Astrophysique de Paris, IAP, F-75014 Paris, France

³ CNRS, Institut d’Astrophysique de Paris, IAP, F-75014 Paris, France

⁴ Institut Lagrange de Paris, 98 bis, Bd Arago, 75014 Paris, France

⁵ Institut de Physique Théorique, Université Paris-Saclay, CEA, CNRS, F-91191 Gif-sur-Yvette Cedex, France

⁶ Université Côte d’Azur, Observatoire de la Côte d’Azur, CNRS, IRD, Géoazur, 250 avenue Albert Einstein, F-06560 Valbonne, France

E-mail: joel.berge@onera.fr

July 2020

Abstract. The MICROSCOPE experiment was designed to test the weak equivalence principle in space, by comparing the low-frequency dynamics of cylindrical “free-falling” test masses controlled by electrostatic forces. We use data taken during technical sessions aimed at estimating the electrostatic stiffness of MICROSCOPE’s sensors to constrain a short-range Yukawa deviation from Newtonian gravity. We take advantage of the fact that in the limit of small displacements, the gravitational interaction (both Newtonian and Yukawa-like) between nested cylinders is linear, and thus simply characterised by a stiffness. By measuring the total stiffness of the forces acting on a test mass as it moves, and comparing it with the theoretical electrostatic stiffness (expected to dominate), it is *a priori* possible to infer constraints on the Yukawa potential parameters. However, we find that measurement uncertainties are dominated by the gold wires used to control the electric charge of the test masses, though their related stiffness is indeed smaller than the expected electrostatic stiffness. Moreover, we find a non-zero unaccounted for stiffness that depends on the instrument’s electric configuration, hinting at the presence of patch field effects. Added to significant uncertainties on the electrostatic model, they only allow for poor constraints on the Yukawa potential. This is not surprising, as MICROSCOPE was not designed for this measurement, but this analysis paves the way to new experimental searches for non-Newtonian gravity.

Keywords: Experimental Gravitation, Modified Gravity, Yukawa potential, Electrostatic accelerometer

Submitted to: *Class. Quantum Grav.*

1. Introduction

A hundred years after its invention, Einstein’s theory of General Relativity (GR) still passes all experimental tests [1], from early tests (the Mercury perihelion puzzle and the measurement of the gravitational deflection of stars’ light passing near the Sun by Eddington) to current tests (gravitational lensing [2, 3], gravitational redshift [4, 5], gravitational waves direct detection [6]). However, in order to stand still in front of (not so recent) astrophysical and cosmological observations, GR must be supplemented by dark matter and dark energy. The former explains the flat rotation curve of galaxies and their dynamics in clusters [7, 8], while the latter explains the acceleration of the cosmic expansion [9, 10]. Whether our theory of gravitation must be revised or the content of our Universe better understood is still an open discussion [11, 12]. In this article, we adopt the former possibility.

Theories beyond the standard model propose the existence of new fields and particles. For instance, string-inspired theories introduce a spin-0 dilaton-like particle (e.g. Refs. [13, 14]), while scalar-tensor models modify GR’s equations via the introduction of a new scalar field (see e.g. Refs. [11, 15, 16]). Although a new very light scalar field should entail the appearance of a new long-range force incompatible with current Solar system tests, its existence can be made compatible with experimental constraints by virtue of a screening mechanism that makes the field’s mass environment-dependent, thereby hiding it from local experimental tests [13, 17–24]. Those models can nevertheless have measurable effects, such as an apparent violation of the equivalence principle (e.g. Refs. [20, 25]) or a variation of fundamental constants [26, 27].

Looking for short-range deviations from Newtonian gravity is essential to test low-energy limits of high-energy alternative theories (such as string theory or extra dimensions) and is the goal of several experimental efforts (see Refs. [28–30] for reviews and references therein, and Refs. [31, 32] for recent results). While most of them are highly optimised to look for specific minute signals, we propose, in this article, to search for a short-range deviation from Newtonian gravity as a byproduct of MICROSCOPE data.

The MICROSCOPE space experiment tested the weak equivalence principle (WEP) to an unprecedented accuracy [33, 34] via the comparison of the acceleration of two test masses freely falling while orbiting the Earth. If the WEP is violated, a signal is expected at a well-known frequency depending on the satellite’s orbital and spinning frequencies (since the motion of the satellite modulates the Earth gravity field –which is the source of the measured acceleration). Since MICROSCOPE orbits the Earth at a 700 km altitude, the experiment is then sensitive to long-ranged (more than a few hundred kilometers) modifications of gravitation. Its first results thus allowed us to set new limits on beyond-GR models involving long-range deviations from Newtonian gravity parametrised by a Yukawa potential, a light dilaton [35] and a U-boson [36, 37]. Updates of those works are under way following the final MICROSCOPE results [38, 39].

In this article, we use MICROSCOPE sessions dedicated to the in-flight

Fifth force stiffness

3

characterisation of its instrument to look for short-range deviations of Newtonian gravity. Although in WEP-test configuration, the MICROSCOPE test masses are kept almost motionless by the electrostatic measurement apparatus and are (by design) barely affected by the satellite's and instrument's self-gravity, this is not the case in some technical sessions where they are set in a sinusoidal motion. In this situation, they are sensitive to other forces such as the instrument's electrostatic stiffness and the gravitational force from other parts of the instrument. Given the geometry of the MICROSCOPE instrument, we can expect to see deviations from Newtonian gravity ranging from the millimetre to the decimetre scales once all other environmental interactions are accounted for (we recover the fact that gravity tests are degenerate with the environment, as shown e.g. in Ref. [40]). Nevertheless, we must note that MICROSCOPE was not designed for this experiment, and we cannot expect to obtain competitive results. The intent of this paper is then to present this new experimental concept and show how we could improve MICROSCOPE to test short-range gravity in space.

The layout of this paper is as follows. After a brief introduction to the Yukawa deviation from Newtonian gravity in Sect. 2, we introduce our experiment measurement principle in Sect. 3. Sect. 4 provides an exhaustive account of the forces acting on the experiment. We present the data analysis procedure and the measurement of relevant parameters in Sect. 5. We then provide new (albeit not competitive) constraints in Sect. 6, before concluding in 7. Appendices give a pedagogical derivation of the electrostatic force at play along MICROSCOPE's cylinders' radial axes, and an analytical expression for the gravitational (both Newtonian and Yukawa) interaction between two cylinders.

2. Yukawa gravity

We parametrise a deviation from Newtonian gravity with a Yukawa potential, which is simply added to the Newtonian potential. The total gravitational potential created by a point-mass of mass M at distance r is then

$$V(r) = -\frac{GM}{r} \left[1 + \alpha \exp\left(-\frac{r}{\lambda}\right) \right], \quad (1)$$

where G is Newton's gravitational constant, α is the strength of the Yukawa deviation compared to Newtonian gravity and λ is the range of the corresponding fifth force.

Despite its simplicity, the Yukawa parametrisation is useful as it describes the fifth force created by a massive scalar field in the Newtonian regime (see e.g. the Supplemental material of Ref. [35] and references therein). The range λ corresponds to the Compton wavelength of the scalar field, and α is linked to its scalar charge. Phenomenologically, this charge can depend on the composition of the interacting bodies in various ways, e.g. through combinations of their baryon and lepton numbers [28]. In this paper, we consider composition-independent Yukawa interactions only (thereby, we assume a universal scalar charge), and we do not relate to any phenomenological subatomic model, but instead consider only α as the parameter to constrain.

Fifth force stiffness

4

Many experiments have already provided tight constraints on its range and strength, from sub-millimeter to solar system scales (e.g. Refs. [28,29] and references therein, and Refs. [35,41–44] for more recent works). In this article, we are concerned with ranges between $\lambda \approx 10^{-3}$ m and $\lambda \approx 10^{-1}$ m, corresponding to the scale of MICROSCOPE’s instrument. The best constraints on the strength of a Yukawa potential for such ranges are $|\alpha| \leq 10^{-3}$ [31,45,46].

3. MICROSCOPE measurement principle

3.1. Instrumental apparatus

The core of MICROSCOPE’s instrument consists of two differential accelerometers (or Sensor Units – SU), the test masses of which are co-axial cylinders kept in equilibrium with electrostatic actuation [47]. The test masses’ materials were chosen carefully so as to maximize a potential violation of the WEP from a light dilaton [13,48,49] and to optimise their industrial machining: the SUEP test masses are made of alloys of platinum-rhodium (PtRh10 – 90% Pt, 10% Rh) and titanium-aluminium-vanadium (TA6V – 90% Ti, 6% Al, 4% V), while the SUREF test masses are made of the same PtRh10 alloy.

The test masses of each SU are controlled electrostatically, through electrodes, without any mechanical contact; only a thin 7 μ m-diameter gold wire, used to fix the masses’ electrical potential to the electronics reference voltage, provides a mechanical contact between the test masses and their cage. The test masses’ control is performed by an electronic servo-loop. Two Front-End Electronics Unit (FEEU) boxes (one per SU) include the capacitive sensing of masses, the reference voltage sources and the analog electronics to generate the electrical voltages applied to the electrodes; an Interface Control Unit (ICU) includes the digital electronics associated with the servo-loop digital control laws, as well as the interfaces to the satellite’s data bus. Additionally, the same electronics’ output is used by the drag-free system of the satellite responsible for the cancellation of non-gravitational forces applied to the satellite, such as atmospheric drag and solar radiation pressure [50].

Fig. 1 shows a cut out view of one SU, with its two test masses, their surrounding electrodes-bearing cylinders, cylindrical invar shield, base plate, upper clamp and vacuum system.

3.2. MICROSCOPE’s test mass measured acceleration

The electrostatic (control) force applied by the electronics servo-control to maintain the j th test mass motionless ($j = 1, 2$ for the internal and external test masses) is [51]

$$\vec{\Gamma}_{\text{cont},j} = \frac{\vec{F}_{\text{el},j}}{m_{I_j}} = \vec{\Gamma}_{\oplus,j} + \vec{\Gamma}_{\text{cin},j} - \frac{\vec{F}_{\text{loc},j}}{m_{I_j}} - \frac{\vec{F}_{\text{pa},j}}{m_{I_j}} + \frac{\vec{F}_{\text{ext}}}{M_{I_{\text{sat}}}} + \frac{\vec{F}_{\text{th}}}{M_{I_{\text{sat}}}} \quad (2)$$

where m_{I_j} and $M_{I_{\text{sat}}}$ are the inertial masses of the j th test mass and of the satellite, \vec{F}_{ext} are non-gravitational forces affecting the satellite (atmospheric drag, Solar radiation

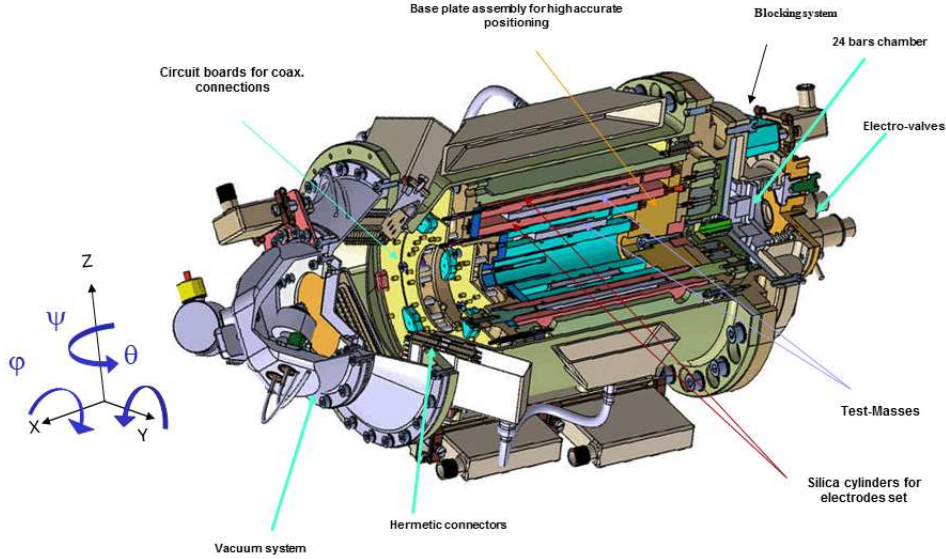


Figure 1. Cut out view of a MICROSCOPE sensor, with its two test masses, their surrounding electrodes-bearing cylinders, cylindrical invar shield, base plate, upper clamp and vacuum system. The reference system is shown on the left of the figure. Figure from Ref. [34].

pressure), \vec{F}_{th} are forces applied by the thrusters (to compensate for external forces) and $\vec{F}_{\text{loc},j}$ and $\vec{F}_{\text{pa},j}$ are local forces (inside the sensor) that we can consider explicitly (e.g. electrostatic stiffness, gold wire stiffness, self-gravity) or implicitly (e.g. electrostatic parasitic forces), respectively. The Earth gravitational acceleration

$$\vec{\Gamma}_{\oplus,j} = \frac{M_{G_{\text{sat}}}}{M_{I_{\text{sat}}}} \vec{g}(O_{\text{sat}}) - \frac{m_{G_j}}{m_{I_j}} \vec{g}(O_j) \quad (3)$$

where m_{G_j} and $M_{G_{\text{sat}}}$ are the gravitational masses of the test mass and of the satellite, $\vec{g}(O_{\text{sat}})$ (resp. $\vec{g}(O_j)$) is the Earth gravity acceleration at the center of mass of the satellite (resp. test mass). We assume that the test mass are homogeneous. Moreover, since we are concerned with short-range Yukawa deviations only, we assume that the Yukawa contribution to the Earth's gravity acceleration acting on the test-masses is negligible. Finally, the second term of the r.h.s. of the Eq. (2) contains the contribution from the satellite's inertia and from the motion of the test-mass,

$$\vec{\Gamma}_{\text{cin},j} = [\text{In}] \overrightarrow{O_{\text{sat}} O_j} + 2[\Omega] \overrightarrow{O_{\text{sat}} O_j} + \overrightarrow{O_{\text{sat}} O_j}, \quad (4)$$

where $[\text{In}] \equiv [\dot{\Omega}] + [\Omega][\Omega]$ is the gradient of inertia matrix of the satellite and $[\Omega]$ its angular velocity.

From Eq. (2), we show in Appendix A that the measured acceleration of a test

Fifth force stiffness

6

mass, expressed in the instrument frame, is

$$\vec{\Gamma}_{\text{meas},j|\text{instr}} = \vec{B}_{0,j} + \vec{\Gamma}_{\oplus,j|\text{sat}} + \vec{\Gamma}_{\text{cin},j|\text{sat}} - \frac{\vec{F}_{\text{loc},j|\text{instr}}}{m_{I_j}} + \vec{n}_j, \quad (5)$$

where \vec{n}_j is the measurement noise and $\vec{B}_{0,j}$ is the scale-factor-dependent bias, defined from the local parasitic forces and measurement bias. This equation is the core of our analysis.

In the remainder of this paper, we correct the measured acceleration for the Earth gravity modeled as described in Ref. [53], and for the cinematic acceleration inferred from satellite's attitude measurements. We thus deal with the acceleration

$$\vec{\Gamma}_j \equiv \vec{\Gamma}_{\text{meas},j|\text{instr}} - \vec{\Gamma}_{\oplus,j|\text{sat}} - \vec{\Gamma}_{\text{cin},j|\text{sat}} \quad (6)$$

$$= \vec{B}_{0,j} - \frac{\vec{F}_{\text{loc},j}}{m_{I_j}} + \vec{n}_j, \quad (7)$$

where we also dropped the subscripts “|instr” and “|sat” for simplicity.

4. Stiffness measurement

4.1. Electrostatic stiffness measurement sessions

The stiffness is the component of the force undergone by a test mass proportional to the offset of the mass from its equilibrium. Measurement sessions were dedicated to measure MICROSCOPE's instrument stiffness [52], the stiffness being expectedly dominated by an electrostatic stiffness (see Sect. 4.3 and Ref. [47]). The principle of the measurement is to impart a $f = 3$ mHz sinusoidal excitation of amplitude $x_0 = 5 \mu\text{m}$ to the test mass and measure its acceleration (Fig. 2). The position of the test mass is thus forced to be

$$x(t) = x_0 \sin(\omega t + \psi), \quad (8)$$

where $x(t)$ is any axis (x, y, z) of the instrument (along which we aim to estimate the electrostatic stiffness), $\omega = 2\pi f$ and ψ a given phase. Measurements lasted 1750 s for each axis of each test mass.

In Ref. [52], it was assumed that only the electrostatic stiffness k_ϵ played a significant role, such that $\vec{F}_{\text{loc},j} = -k_{\epsilon,j}\vec{x}$, where \vec{x} is the displacement of the test mass with respect to its equilibrium position, and Eq. (6) became (ignoring the quadratic factor)

$$\vec{\Gamma}_j = \vec{B}_{0,j} + \frac{k_{\epsilon,j}}{m_{I_j}}\vec{x} + \vec{n}_j. \quad (9)$$

Under these assumptions, the electrostatic stiffness is simply the slope of the $\vec{\Gamma}_j - \vec{x}$ relation (up to the factor m_{I_j}), as shown in the right panel of Fig. 2. Chhun *et al.* [52] used this simple technique to estimate the electrostatic stiffness on the three axes of each MICROSCOPE's test mass. They found significant disagreements with expectations from the theoretical model summarised in Sect. 4.3, which they explained by model inaccuracies and contribution from the gold wire aimed to control the charge of the test masses (Sect. 4.4). We discuss their results in Sect. 5.2.

Fifth force stiffness

7

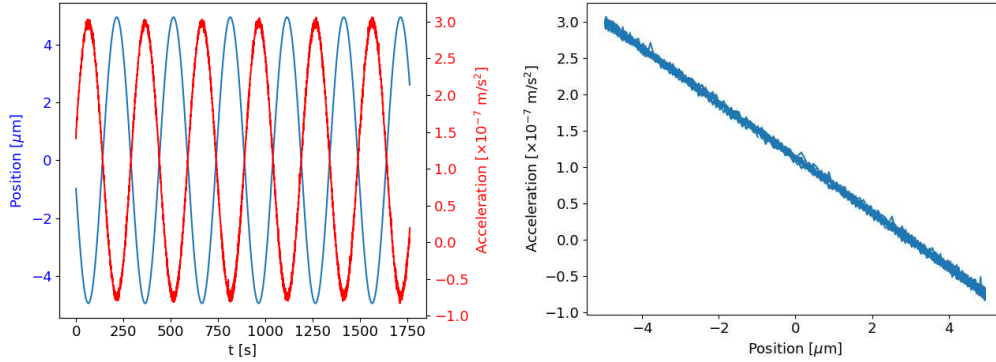


Figure 2. Experimental process to measure a MICROSCOPE's sensor's stiffness (here, the stiffness of SUREF's internal mass is estimated along its Y axis): the test mass is excited in position with a known amplitude of $5 \mu\text{m}$, and we measure its response in acceleration (left panel). Right panel: test mass' acceleration as a function of its position.

4.2. Local forces budget

In what follows, we go beyond the simple assumptions of Ref. [52] and explore how the same measurement could shed light on short-range non-Newtonian gravity.

To that goal, we need to take into account all the different local forces applied to the test mass as it moves inside its electrode cage during sessions dedicated to the measurement of the stiffness. Our central equation then follows from Eq. (6):

$$\vec{\Gamma}_j = \vec{\Gamma}_{\text{exc}} + \vec{B}_{0,j} - \frac{\vec{F}_{\text{loc},j}}{m_{I_j}} + \vec{n}_j, \quad (10)$$

where $\vec{\Gamma}_{\text{exc}} = x_0 \omega^2 \sin(\omega t + \psi)$ is the excitation acceleration imparted to the test mass from the electronics control loop, and the local force is the sum of the following contributors discussed in this section:

$$\vec{F}_{\text{loc}} = \vec{F}_{\text{el}} + \vec{F}_{\text{w}} + \vec{F}_{\text{p}} + \vec{F}_{\text{r}} + \vec{F}_{\text{N}} + \vec{F}_{\text{Y}} \quad (11)$$

where we ignored the j subscript for clarity. Here, \vec{F}_{el} is the electrostatic force (Sect. 4.3), \vec{F}_{w} is the force due to the gold wire (Sect. 4.4), \vec{F}_{p} is the radiation pressure (Sect. 4.5), \vec{F}_{r} is the radiometric effect (Sect. 4.6), \vec{F}_{N} and \vec{F}_{Y} are the Newtonian and non-Newtonian (Yukawa) gravity (Sect. 4.8).

4.3. Electrostatic force

The electrostatic force used to control the test mass is discussed at length in Ref. [47]. Here, we shall only state that it consists of a bias \vec{b}_ϵ and a stiffness k_ϵ ,

$$\vec{F}_{\text{el}} = \vec{b}_\epsilon - k_\epsilon \vec{x}. \quad (12)$$

Fifth force stiffness

8

Those factors depend on the geometry of the test mass and of the electrodes, and on the electric configuration (voltages applied to the different parts of the sensor). In particular, the electrostatic stiffness along the X -axis is expected to be zero for all sensors. For completeness, and since this paper particularly focuses on the stiffness, we provide below the electrostatic force imparted by the full set of electrodes on the radial axes when the test mass moves along the Y -axis [47]:

$$\begin{aligned}
F_{\text{el}}(y) \approx & -\frac{4\epsilon_0 S_y \sin(\alpha_y/2)}{e_i^2} (V'_{p_y} - V_p) v_y \\
& + \frac{2\epsilon_0 S}{e_i^3} \left(1 + \frac{\sin \alpha_y}{\alpha_y}\right) [(V'_{p_y} - V_p)^2 + V_d^2] y \\
& + \frac{2\epsilon_0 S}{e_i^3} \left(1 - \frac{\sin \alpha_z}{\alpha_z}\right) [(V'_{p_z} - V_p)^2 + V_d^2] y \\
& + \frac{\pi\epsilon_0 L_x (R_x + R_p)}{e_e^3} [(V'_{p_x} - V_p)^2 + V_d^2] y \\
& + \frac{\pi\epsilon_0 R_\phi L_\phi}{e_e^3} [(V'_{p_\phi} - V_p)^2 + V_d^2] y, \quad (13)
\end{aligned}$$

where ϵ_0 is the vacuum permittivity, e_i (e_e) is the gap between the inner (outer) electrode cylinder and the test-mass, and where we assumed that all control voltages listed in Ref. [47] are small compared to the V_p and V_d voltages. Those two voltages describe the electric configuration. Two configurations are available: high-resolution mode (HRM) and full-range mode (FRM). They are detailed in Ref. [47] and summarised in Appendix B.

The first term of the r.h.s. of Eq. (13) defines the gain of the detector (the force being proportional to the control voltage v_y); the other terms define the stiffness created by the Y , Z , X and ϕ electrodes. In this equation, S is the surface of the Y and Z electrodes, R_x and R_ϕ are the inner radius of the X and ϕ electrodes, and h and L_ϕ are their length. The angles α_y and α_z are defined by the angle between the displacement of the test mass and the Y and Z axes, respectively. Appendix C proves the form of the stiffness created by the Y electrodes (2nd term of the r.h.s. of the equation).

We assessed the accuracy of the stiffness terms of the model (13) with finite elements simulations. We found it to be biased high: finite elements models provide an electrostatic stiffness 7% to 10% lower than the model (13). Nevertheless, in the remainder of this paper, instead of relying on finite elements simulations, we use Eq. (13) corrected by a 8.5% bias. This allows us to easily propagate metrology and voltage uncertainties in the electrostatic stiffness model, without the need to run a time-consuming simulation for each allowed set of parameters. We then add an extra 3% statistical error to those uncertainties to reflect the uncertainty on the bias of the model. The 7th column of Table 3 lists the electrostatic stiffness expected for each test mass of MICROSCOPE.

Fifth force stiffness

9

4.4. Gold wire

The electric charge on test masses is controlled via a gold wire linking them to the satellite. The wire can be modelled as a spring acting on the test mass with the force

$$\vec{F}_w = -k_w[1 + i\phi(f)]\vec{x} - \lambda_w\dot{\vec{x}}, \quad (14)$$

where λ_w describes the viscous damping of the wire, k_w is the wire's stiffness and $\phi(f)$ describes the internal damping; note that ϕ can depend on the frequency. The wire's quality factor $Q = 1/\phi$.

For a sinusoidal motion of the test mass (along the j th axis) $x_j(t) = x_{j0} \sin(\omega t + \psi)$, the force exerted by the gold wire is the sum of an out-of-phase sinusoidal signal [54] and a (velocity-proportional) quadrature signal

$$F_{w,j}(t) = -k_{w,j}x_{j0} \sin(\omega t + \psi - \phi) + \lambda_w x_{j0} \omega \cos(\omega t + \psi). \quad (15)$$

Thermal dissipation in the wire is at the origin of the f^{-1} low-frequency noise that limits MICROSCOPE's test of the WEP [33]. With the dissipation-fluctuation theorem, it can be shown that this acceleration noise reads [54, 55]

$$\Gamma_{n,w}(f) = \frac{1}{m} \sqrt{\frac{4k_B T}{2\pi} \frac{k_w}{Q(f)}} f^{-1/2} \text{ ms}^{-2}/\sqrt{\text{Hz}}, \quad (16)$$

where m is the mass of the test mass, T is the temperature and k_B is the Boltzmann constant. This allows for an estimation of the k_w/Q ratio from the spectral density of long measurement sessions (see Sect. 5.3).

4.5. Radiation pressure

The electrode-bearing cylinders, being at temperature T , emit thermal radiation through photons that eventually hit the test mass and transfer their impulsion to it, thus creating a pressure. A gradient of temperature and a difference of temperature ΔT between the electrodes surrounding the test mass will therefore cause a force directed from the hottest to the coldest regions [56, 57]:

$$\vec{F}_p = \frac{16}{3c} S \sigma \Delta T T^3 \vec{e}, \quad (17)$$

where T is the average temperature, c the speed of light, σ the Stefan-Boltzmann constant, S the surface of the test mass, and \vec{e} is the vector directed from the hottest to the coldest region.

The temperature and its gradient did not evolve in time during the measurement sessions used in this paper (six temperature probes are positioned on each sensor in such a way that we can monitor the temperature and have a glimpse at its gradient [58]; in the worst case, we could note a 0.003K evolution of the temperature during the measurement –while its mean is about 280K–, with all probes affected by the same evolution, entailing

Fifth force stiffness

10

an unmeasurably small variation of the temperature gradients). Therefore, as far as we are concerned, we can consider the radiation-pressure-induced force as a simple bias. Given the measured temperatures, an order of magnitude estimation allows us to expect the corresponding acceleration at a level of $a_p \lesssim 10^{-10} \text{ ms}^{-2}$.

4.6. Radiometer effect

Taking its name from Crookes' radiometer, originally thought to prove the photon pressure, the radiometer effect is actually a residual gas effect affecting test masses in rarefied atmospheres whose mean free path exceed the size of the container. In this case, equilibrium conditions do not happen when pressure is uniform, but when the ratios of pressure to square root of temperature equal one another [56,57].

This entails a force on the test mass proportional to temperature gradient about its faces ΔT ,

$$\vec{F}_r = \frac{1}{2}PS\frac{\Delta T}{T}\vec{e}, \quad (18)$$

where P is the pressure in the container, S the surface of the test mass orthogonal to the temperature gradient, T the average temperature in the container and, as before, \vec{e} is the vector directed from the hottest to the coldest regions.

Even when stationary, a non-linear temperature profile can cause a position-dependent radiometric effect and potentially a stiffness. However, the sparse temperature measurements in MICROSCOPE sensors do not allow us to go beyond the linear temperature profile hypothesis, thereby limiting the radiometric effect to a constant acceleration. Orders of magnitude estimates provide a level of acceleration of the same order as the radiation pressure, $a_r \lesssim 10^{-10} \text{ ms}^{-2}$.

4.7. Other non-gravitational effects

Other non-gravitational forces could be considered, but are ignored due to their negligible effect.

4.7.1. Residual gas drag: The test mass moves in an imperfect vacuum, so that drag may be expected. Orders of magnitude estimates provide a related acceleration $\approx 10^{-23} \text{ ms}^{-2}$, well below our capacity to detect it.

4.7.2. Outgassing: Gas molecules are released from the materials of the instrument's parts (in particular the electrode bearing cylinders) and can impact the test mass and modify the pressure inside the instrument [56]. However, the vacuum system was designed, and the materials chosen, such that outgassing can be safely ignored [47].

4.7.3. Lorentz force: Test masses have a non-zero magnetic moment, and can therefore be affected by Lorentz forces, either from the Earth magnetic field or local magnetic fields. The former applies a periodic signal at the orbital frequency and therefore does

Fifth force stiffness

11

not affect the stiffness measurements (besides the fact that the Earth magnetic field is largely suppressed by MICROSCOPE's instrument magnetic shield). Local magnetic fields are more difficult to assess. However, noting that their effect on the test of the WEP is subdominant [58], we ignore them in this paper.

4.7.4. Contact-potential differences and patch fields Inhomogeneous distributions of surface potentials create a force between charged surfaces. MICROSCOPE's instrument can be affected by such patch effects, which act as an additional stiffness dependent on the test masses' voltages, thus on the electric configuration [59]. It goes beyond the scope of this article to develop a model of patch effects in MICROSCOPE, and we will not try to quantify them. Note that they may affect MICROSCOPE only in the stiffness measurement sessions used in this paper, where test masses are set in motion; in MICROSCOPE's test of the WEP, test masses are kept motionless, and thus immune to patch effects.

4.7.5. Misalignments and geometrical defects Very small misalignments between MICROSCOPE's cylinders can be estimated [58]. As they break the cylindrical symmetry, they can introduce additional terms in the electrostatic stiffness [60]. However, as we show below, the error budget in stiffness measurement sessions is largely dominated by the gold wire, so that we can safely ignore them for the purpose of this paper (thereby justifying our $[\theta_j] = \text{Id}$ assumption in Appendix A).

4.8. Local gravity

The local gravity force applied to a MICROSCOPE test mass is the sum of the forces between that test mass and the parts making the corresponding sensor (Fig. 1):

- seven co-axial cylinders: two silica electrode-bearing cylinders surrounding the test mass, the second test mass and two other silica electrode-bearing cylinders surrounding it and two cylindrical invar shields,
- and four plain cylinders: a silica base plate, an invar base plate, an invar upper clamp, and a vacuum system.

The characteristics of those elements can be found in Ref. [47]. As we show below, the gravity force is dominated by the closest elements, so that we can safely neglect the contribution from the other sensor and from the satellite itself.

The gravitational interaction between two bodies centered on O_1 and O_2 is

$$\vec{F} = - \int_{V_1} dV_1 \int_{V_2} dV_2 \frac{\partial V}{\partial r} (\vec{r}_1 - \vec{r}_2) \overrightarrow{O_1 O_2}, \quad (19)$$

where the 3-dimensional integrals are taken over the volume of the two bodies, and $\vec{r}_i = (x_i, y_i, z_i)$ is the coordinate vector of an infinitesimal volume element of the i th

Fifth force stiffness

12

body. Noting ρ_i the i th body's density, the Newtonian potential between infinitesimal volumes

$$V_N(\vec{r}_1 - \vec{r}_2) = -\frac{G\rho_1\rho_2 dV_1 dV_2}{|\vec{r}_1 - \vec{r}_2|}, \quad (20)$$

and the Yukawa potential of strength α and range λ between infinitesimal volumes

$$V_Y(\vec{r}_1 - \vec{r}_2) = -\alpha \frac{G\rho_1\rho_2}{|\vec{r}_1 - \vec{r}_2|} \exp\left(-\frac{|\vec{r}_1 - \vec{r}_2|}{\lambda}\right) dV_1 dV_2. \quad (21)$$

In the present case, as shown in Fig. 1, all contributions are interactions between cylinders, either empty (test masses, electrode bearing cylinders, shield) or full (base plate, upper clamp). For simplicity, we also assume that the vacuum system is a full cylinder. Computing the gravitational force applied to the test mass then boils down to computing the interaction between perfectly aligned cylinders (as we assumed in Sect. 3), and therefore computing the 6-dimensional integral (19).

Appendix D shows that, in the limit of small displacements with which we are concerned in that article, the 6D integral (19) can be reduced to a 1D integral depending on the geometry of the pair of cylinders. In these cases, the gravitational force can be Taylor-expanded, and is dominated by a stiffness term K_1 . The expressions given below apply both to the Newtonian ($\alpha = 1$, $\lambda \rightarrow \infty$) and Yukawa forces. They give the force exerted by any one of MICROSCOPE's cylinders on a test mass.

4.8.1. Longitudinal force In the limit of small displacements δ of the test mass along the cylinders' axis, the force is given by

$$\mathcal{F}_x(x_0, \delta) \approx -16\pi^2 G\rho\rho'\alpha \sum_i K_i(x_0)\delta^i, \quad (22)$$

where x_0 is the distance between the center of the test mass and the center of the source cylinder along their longitudinal axis ($x_0 = 0$ when the source is either an electrode-bearing cylinder or the other test mass, but $|x_0| > 0$ if the source is one cylinder of the base or the vacuum system –in which case the source and the test mass are above each other), and where the x subscript corresponds to MICROSCOPE's (longitudinal) X -axis but is referred to as z in the more conventional cylindrical coordinate system used in Appendix D. The K_i coefficients depend on the geometry of the test mass – source pair as follows. If a and b are the inner and outer radii of the cylinder source, 2ℓ its height and ρ its density; and if a' and b' are the inner and outer radii of the test mass, $2L$ its height and ρ' its density, then:

- (i) if the test mass is shorter than the source and they are concentric (which is the case

Fifth force stiffness

13

e.g. of the pair made of the internal test mass and any electrode-bearing cylinder),

$$\left\{ \begin{array}{l} K_0(x_0) = 0 \end{array} \right. \quad (23a)$$

$$\left\{ \begin{array}{l} K_1(x_0) = \int_0^\infty \frac{W(k; a', b')W(k; a, b)}{\kappa k} e^{-\kappa \ell} \sinh(\kappa L) dk \end{array} \right. \quad (23b)$$

$$\left\{ \begin{array}{l} K_2(x_0) = 0 \end{array} \right. \quad (23c)$$

$$\left\{ \begin{array}{l} K_3(x_0) = \int_0^\infty \frac{\kappa}{6} \frac{W(k; a', b')W(k; a, b)}{k} e^{-\kappa \ell} \sinh(\kappa L) dk, \end{array} \right. \quad (23d)$$

where J_i are Bessel functions of the first kind and where we introduced the parameter

$$\kappa = \sqrt{k^2 + 1/\lambda^2} \quad (24)$$

and the function

$$W(k; a, b) = bJ_1(kb) - aJ_1(ka). \quad (25)$$

- (ii) if the test mass is longer than the source and they are concentric (which is the case of the pair made of the internal test mass as the source and the external test mass): the force is formally identical to that of the previous case, with ℓ and L switching roles.
- (iii) if the test mass and the source are above each other,

$$\left\{ \begin{array}{l} K_0(x_0) = \frac{x_0}{|x_0|} \int_0^\infty \frac{W(k; a', b')W(k; a, b)}{\kappa^2 k} e^{-\kappa|x_0|} \sinh(\kappa \ell) \sinh(\kappa L) dk \end{array} \right. \quad (26a)$$

$$\left\{ \begin{array}{l} K_1(x_0) = - \int_0^\infty \frac{W(k; a', b')W(k; a, b)}{\kappa k} e^{-\kappa|x_0|} \sinh(\kappa \ell) \sinh(\kappa L) dk \end{array} \right. \quad (26b)$$

$$\left\{ \begin{array}{l} K_2(x_0) = \frac{x_0}{|x_0|} \int_0^\infty \frac{W(k; a', b')W(k; a, b)}{2k} e^{-\kappa|x_0|} \sinh(\kappa \ell) \sinh(\kappa L) dk \end{array} \right. \quad (26c)$$

$$\left\{ \begin{array}{l} K_3(x_0) = - \int_0^\infty \frac{\kappa}{6k} W(k; a', b')W(k; a, b) e^{-\kappa|x_0|} \sinh(\kappa \ell) \sinh(\kappa L) dk, \end{array} \right. \quad (26d)$$

4.8.2. Radial force Similarly, at 3rd order in δ/a' , where δ is the displacement of the test mass along a radial axis (Y or Z), the radial force created by any one of the other cylinders is

$$\mathcal{F}_r(x_0, \delta) \approx -2\pi^2 G \rho \rho' \alpha (K_1(x_0)\delta + K_3(x_0)\delta^3), \quad (27)$$

where the K_i coefficients depend on the geometry of the test mass – source pair:

- (i) if the test mass is shorter than the source and they are nested (which is the case

Fifth force stiffness

14

e.g. of the pair made of the internal test mass and any electrode-bearing cylinder),

$$\begin{cases} K_1(x_0) = 4 \int_0^\infty \frac{kW(k; a', b')W(k; a, b)}{\kappa^2} \left[L - \frac{e^{-\kappa\ell}}{\kappa} \sinh(\kappa L) \cosh(\kappa|x_0|) \right] dk \\ K_3(x_0) = - \int_0^\infty \frac{k^3W(k; a', b')W(k; a, b)}{\kappa^2} \left[L - \frac{e^{-\kappa\ell}}{\kappa} \sinh(\kappa L) \cosh(\kappa|x_0|) \right] dk, \end{cases} \quad (28a)$$

(28b)

with $x_0 \approx 0$ in this case.

- (ii) if the test mass is longer than the source and they are nested (which is the case of the pair made of the internal test mass as the source and the external test mass): the force is formally identical to that of the previous case, with ℓ and L switching roles.
- (iii) if the test mass and the source are above each other,

$$\begin{cases} K_1(x_0) = 4 \int_0^\infty \frac{kW(k; a', b')W(k; a, b)}{\kappa^2} \frac{e^{-\kappa|x_0|}}{\kappa} \sinh(\kappa\ell) \sinh(\kappa L) dk & (29a) \\ K_3(x_0) = - \int_0^\infty \frac{k^3W(k; a', b')W(k; a, b)}{\kappa^2} \frac{e^{-\kappa|x_0|}}{\kappa} \sinh(\kappa\ell) \sinh(\kappa L) dk & (29b) \end{cases}$$

4.8.3. Total gravitational force The gravity force applied to a MICROSCOPE test mass is just the sum of the Newton and Yukawa forces created by the aforementioned instruments' parts,

$$\vec{F}_g = (\mathcal{F}_{N,x} + \mathcal{F}_{Y,x}) \vec{e}_x + (\mathcal{F}_{N,r} + \mathcal{F}_{Y,r}) \vec{e}_r \quad (30)$$

$$= \sum_j (\mathcal{F}_{N,x,j} + \mathcal{F}_{Y,x,j}) \vec{e}_x + \sum_j (\mathcal{F}_{N,r,j} + \mathcal{F}_{Y,r,j}) \vec{e}_r, \quad (31)$$

where the r subscript stands for the Y and Z axes, and where the forces created by the j th part of the instrument $\mathcal{F}_{N,x,j}$ and $\mathcal{F}_{Y,x,j}$ are given by Eq. (22) and $\mathcal{F}_{N,r,j}$ and $\mathcal{F}_{Y,r,j}$ by Eq. (27).

As shown in Appendix D, a first order Taylor expansion of Eqs. (22) and (27) is enough to precisely account for the gravitational interactions in the present article, where displacements are limited to $5 \mu\text{m}$. This means that the local gravitation effectively acts as a stiffness on the test masses. We thus define the Newtonian and Yukawa, radial and longitudinal stiffnesses such as

$$\mathcal{F}_{N,r} = -k_{N,r}r \quad (32)$$

$$\mathcal{F}_{N,x} = -k_{N,x}x \quad (33)$$

$$\mathcal{F}_{Y,r} = -k_{Y,r}r \quad (34)$$

$$\mathcal{F}_{Y,x} = -k_{Y,x}x, \quad (35)$$

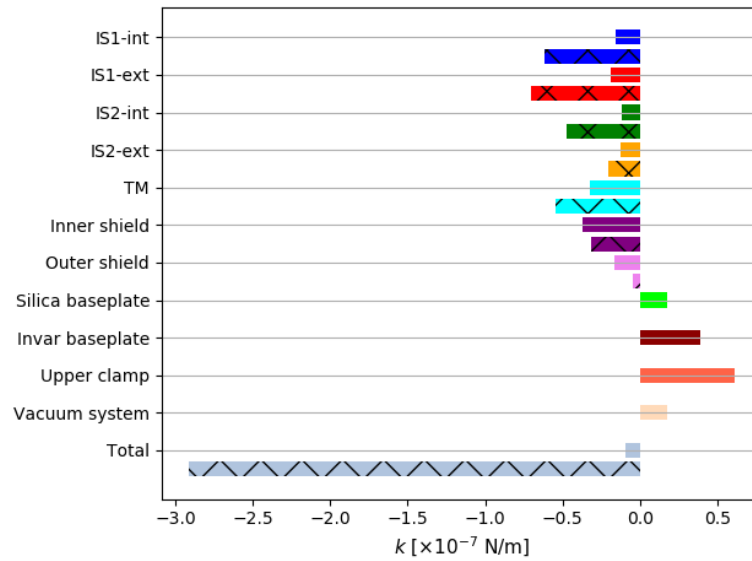


Figure 3. Newtonian (plain bars) and Yukawa (hashed bars) stiffnesses acted by the SUEP’s parts (the external test mass –TM–, the four electrode-bearing cylinders –IS1-int, IS1-ext, IS2-int, IS2-ext–, and the shielding cylinders) on its internal test mass. The Yukawa potential is set such that $(\alpha, \lambda) = (1, 0.01 \text{ m})$. The contribution of the base plates, upper clamp and vacuum system to the Yukawa interaction is too small to appear on the plot.

where x and r are the displacement of the test mass along the longitudinal and radial axes of the instrument.

Newtonian gravity The plain bars of Fig. 3 show the Newtonian stiffnesses from all cylinders on SUEP’s internal test mass along its radial axis. The force between nested cylinders is destabilising (negative stiffness), whereas the force from the base plates, upper clamp and vacuum system stabilises the test mass, with the total radial force being destabilising. It can also be shown that the Newtonian gravitational interaction along the X (longitudinal) axis acts as a stabilising stiffness.

Finally, it can be seen from the figure that the contribution from the outer shield is subdominant. Thence, those from the other differential sensor and from the other parts of the satellite are even more subdominant, and we ignore them.

The next-to-last column of Table 3 lists the Newtonian gravity stiffness of the four MICROSCOPE test masses along their radial and longitudinal axes.

Yukawa gravity The hashed bars of Fig. 3 show the Yukawa stiffnesses from all cylinders on SUEP’s internal test mass along its radial axis, for $(\alpha, \lambda) = (1, 0.01 \text{ m})$. It can be noted that only co-axial cylinders contribute, since the base, upper clamp and vacuum system are more distant than 0.01 m from the test mass. Similarly, the closest

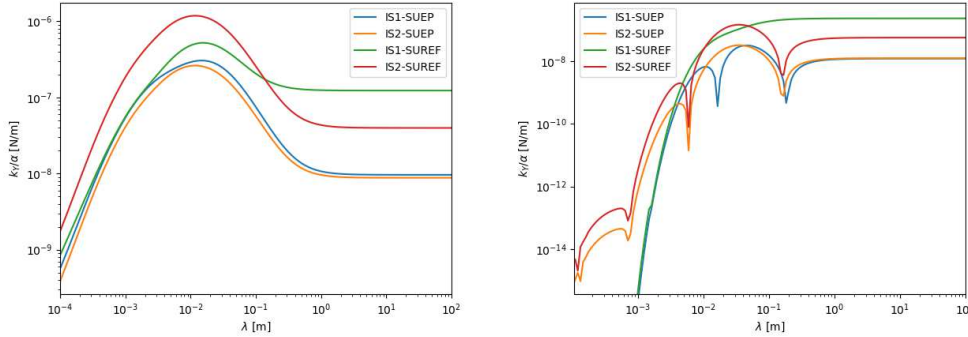


Figure 4. Yukawa stiffness (normalised by α) for the four MICROSCOPE test masses, on the radial (left) and longitudinal (right) axes, as a function of Yukawa's range.

cylinders provide most of the signal. It can be noted that the Yukawa stiffness of the closest cylinders is larger than their Newtonian stiffness. This difference comes from the fact that with $\lambda = 1$ cm, only a restricted part of the cylinders interact, causing an effect more complex than just an exponential decay proportional to the Newtonian stiffness.

Fig. 4 shows Yukawa gravity's stiffness as a function of Yukawa's range λ for all MICROSCOPE test masses, along their radial (left panel) and longitudinal (right panel) axes. Starting from the smaller λ reachable (linked to the distance between a test mass and its closest cylinder), the radial stiffness increases steadily as more and more co-axial cylinders are within reach of λ and contribute to the gravity signal. The stiffness peaks around $\lambda \approx 0.01$ m, where the base and upper cylinders start to contribute but with an opposite sign stiffness, thereby decreasing it until the Newtonian regime is reached when λ becomes larger than the sensor's largest scale. The longitudinal stiffness shows a similar behaviour, though it changes sign while more and more cylinders contribute to the signal.

Comparing Fig. 4 with Table 3, it is clear that the gravity stiffness (and therefore, signal) is largely subdominant. We put it at test in Sect. 5.

4.9. Summary: measured acceleration

Taking all the forces above into account, the acceleration of the j th test mass measured along the i th axis during a stiffness characterisation session is

$$\begin{aligned} \Gamma_{ji}(t) = & b_{\epsilon,ji} + a_{p,ji} + a_{r,ji} + \frac{m_j \omega^2 + k_{\epsilon,ji} + k_{N,ji}}{m_j} x_{i0} \sin(\omega t + \psi) \\ & + \frac{k_{w,ji}}{m_j} x_{i0} \sin(\omega t + \psi - \phi) + \frac{\lambda_{w,ji}}{m_j} \omega x_{i0} \cos(\omega t + \psi) + \frac{k_{Y,ji}(\alpha, \lambda)}{m_j} x_{i0} \sin(\omega t + \psi), \end{aligned} \quad (36)$$

where we singled out the Yukawa gravity contribution and made its stiffness' dependence on (α, λ) explicit, since it is this very dependence that we aim to constrain in the

Fifth force stiffness

17

remainder of this article. The first line of the equation comprises the effect of the measurement bias, radiation pressure and photometric effect (all three acting as a constant bias) and of the in-phase stiffnesses (excitation, electrostatic and Newtonian gravity). The second line of the equation gives the effect of the gold wire (internal and viscous damping), with the last term giving the Yukawa gravity contribution.

5. Data analysis

This section presents least-square estimates of the parameters introduced in the previous section. We measure the electrostatic stiffness, that of the gold wire, the quality factor of the gold wire, and a velocity-dependent coefficient for each axis of each sensor. We perform the exercise in the two electrical configurations (HRM and FRM) summarised in Appendix B.

5.1. Measurement equation

The measurement equation (36) could be used in its original form to extract the unknown parameters from the data and simultaneously constrain Yukawa interaction's parameters. However, since the Yukawa contribution is expected to be at most of the order of the Newtonian contribution, which is itself largely less than the electrostatic stiffness, its parameters have a small constraining power on the data, and we find more suited to first estimate an overall stiffness, from which we can eventually extract the (α, λ) parameters.

Moreover, Eq. (36) requires the estimation of two phases. The first one, ψ , is that of the excitation signal and can be estimated *a priori* by fitting the position data, then used as a known parameter in the following analysis. The second, ϕ , is the phase-offset induced by the gold wire's internal damping. Instead of trying to estimate it from the data (which may be difficult given the 4 Hz sampling of data, when assuming that the quality factor of the wire is in the range $Q \approx 1 - 100$, corresponding a time offset less than 2 s), we recast Eq. (36) as

$$\Gamma(t) \approx b + (\kappa_0 + \kappa_w \cos \phi) \sin(\omega t + \psi) - (\kappa_w \sin \phi - \kappa_\lambda) \cos(\omega t + \psi), \quad (37)$$

where $b \equiv b_\epsilon + a_p + a_r$, $\kappa_0 \equiv x_0(m\omega^2 + k_\epsilon + k_N + k_Y)/m$, $\kappa_w \equiv x_0 k_w/m$ and $\kappa_\lambda \equiv x_0 \lambda_w \omega/m$, and we dropped the i and j indices for clarity.

Five parameters are left for estimation: b , κ_0 , κ_w , κ_λ and $\phi = 1/Q$. It is however clear that fitting Eq. (37) will provide only three independent constraints. If estimating b will be easy, the other parameters will remain degenerate unless we can use some prior knowledge. We show in Sect. 5.3 that we can obtain an independent estimate of the $\kappa_w/Q = \kappa_w \phi$ combination.

Before going further in the parameters estimation in Sect. 5.4, we discuss Ref. [52]'s stiffness measurement process and compare it with ours.

Table 1. Total stiffness (identified as the electrostatic stiffness) measured in Ref. [52]. The expected values can be found in Table 3.

	$k_{\epsilon,x} [\times 10^{-3} \text{ N/m}]$	$k_{\epsilon,y} [\times 10^{-2} \text{ N/m}]$	$k_{\epsilon,z} [\times 10^{-2} \text{ N/m}]$
IS1-SUREF	0.837 ± 0.003	-1.515 ± 0.000	-1.514 ± 0.000
IS2-SUREF	4.424 ± 0.010	-8.170 ± 0.001	-7.144 ± 0.001
IS1-SUEP	1.396 ± 0.003	-1.494 ± 0.001	-1.478 ± 0.002
IS2-SUEP	0.639 ± 0.002	-6.424 ± 0.001	-6.310 ± 0.001

5.2. Preliminary note: discussion of Chhun *et al.* [52] analysis

In Ref. [52], Chhun *et al.* compute the electrostatic stiffness in HRM, using the same measurement sessions as those used here, with a simple ratio of sines amplitudes. They neglect the local gravity stiffness and assume a negligible gold wire's stiffness $k_w \approx 0$ and no velocity-dependent term ($\lambda_w = 0$), and they fit the position and acceleration as

$$x(t) = x_0 \sin(\omega t + \psi_x) \quad (38)$$

$$\Gamma(t) = \Gamma_0 \sin(\omega t + \psi_\Gamma), \quad (39)$$

and infer $k_\epsilon = m\Gamma_0/x_0 - m\omega^2$, with the implicit assumption that $\psi_x = \psi_\Gamma$. Table 1 sums up their results.

Two important points need to be highlighted. First, the stiffnesses estimated under the very restrictive assumptions of Ref. [52] are close to (yet inconsistent with) the expected electrostatic stiffnesses (with an accuracy ranging from a few to a dozen percent, especially on the radial axes, see Table 3). Second, the stiffness estimated on the radial axes are consistent with each other, thus showing a good degree of cylindrical symmetry; this symmetry is clearly expected for the electrostatic stiffness, but may seem accidental for the gold wires. Unless coincidental, those facts hint towards a total stiffness indeed dominated by the electrostatic stiffness, with negligible other contributors (e.g. gold wires).

It is instructive to consider Eq. (37) in view of Ref. [52] analysis. However, instead of assuming that the gold wire has no stiffness, we now assume that its quality factor $Q \gg 1$ (this is equivalent from the point of view of MICROSCOPE's test of the WEP, where only the ratio k_w/Q enters the measurement). Thus assuming $\phi \rightarrow 0$, we re-write Eq. (37) as (Taylor expanding the sine and cosine at first order in ϕ)

$$\Gamma(t) = \pm \sqrt{\kappa_0^2 + 2\kappa_0\kappa_w + \kappa_w^2(1 + \phi^2)} \sin\left(\omega t + \psi - \arctan \frac{\kappa_w\phi}{\kappa_0\kappa_w}\right), \quad (40)$$

which tends to $\lim_{\phi \rightarrow 0} \Gamma(t) = \pm |\kappa_0 + \kappa_w| \sin(\omega t + \psi)$. It is thus clear that using Eq. (38), Ref. [52] estimates the total stiffness. Nevertheless, a subtlety remains. Rigorously, although the phase in Eq. (40) should be that of the excitation, $\psi = \psi_x$, which may (and does) differ from the phase of the acceleration ψ_Γ , Ref. [52] assumes $\psi_x = \psi_\Gamma$ (which

Fifth force stiffness

19

is consistent with the assumption that the gold wire has zero stiffness). Unfortunately, the experiment contradicts this assumption (at least on the radial axes).

Relaxing the $\psi_x = \phi_\Gamma$ hypothesis of Eq. (38), we find almost unchanged total stiffnesses (with percent-level modifications), but a small residual with a $\pi/2$ phase offset remains after removing the best fit from the acceleration. This remaining small signal may be the sign of a non-zero contribution of the gold wires. Indeed, Eq. (37) shows that at first order, the amplitude of this residual signal is proportional to the k_w/Q ratio of the gold wires (when assuming $\lambda_w = 0$). Alas, this does not teach us anything about the absolute order of magnitude of either k_w or Q . We investigate the gold wires' characteristics below, before going back to Eq. (37) in Sect. 5.4.

5.3. Gold wire's k_w/Q ratio

As shown in Sect. 4.4, fitting the low-frequency part of the spectral density of the acceleration measured along a given axis can provide an estimate of the ratio k_w/Q for this axis once temperature data are available (which is the case for all measurement sessions). Performing this task for the three linear axes, we can get an estimate of the gold wire stiffness along each axis, and the orientation of the force due to the wire. This force is presumably collinear with the wire, although the glue clamping process may complexify it. Noting φ the angle between the force and the test mass longitudinal axis (X -axis), and θ the angle between the Y -axis and the projection of the wire on the (y, z) plane (Fig. 5), the three stiffnesses that can be measured are

$$k_{w,x} = |k_w| \cos \varphi \quad (41)$$

$$k_{w,y} = |k_w| \sin \varphi \cos \theta \quad (42)$$

$$k_{w,z} = |k_w| \sin \varphi \sin \theta \quad (43)$$

from which we can recover the modulus of the stiffness and the orientation of the wire. Fig. 6 shows the fit corresponding to SUEP-IS1's X -axis from the session used to estimate the WEP in Ref. [33]. Values obtained for the internal sensor of both SU are given in Table 2. We checked that estimates from different sessions are consistent. Note that rigorously, since the drag-free system is controlled by the external sensor, fitting the internal sensor's spectral density only provides information about the sum of the k_w/mQ ratios of both sensors (where m is their mass). Nevertheless, under the assumptions that their masses are similar (which is enough given the goals of this article), that their wires have similar k_w/Q ratios, and that their spectral density are uncorrelated, fitting the internal sensor's spectral density indeed provides a constraint on each sensor's wire's k_w/Q ratio.

Willemenot & Touboul [55] used a torsion pendulum to characterise a gold wire similar to those used by MICROSCOPE. Assuming that the wire is deformed perpendicular to its principal axis (i.e. in flexion), they give a convenient scaling to

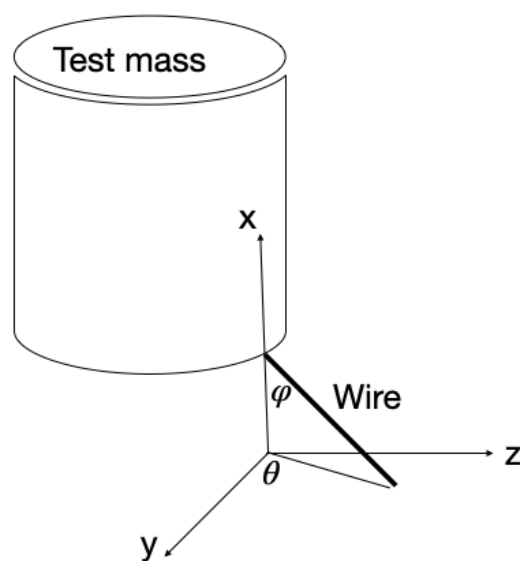


Figure 5. Gold wire and test mass geometry.

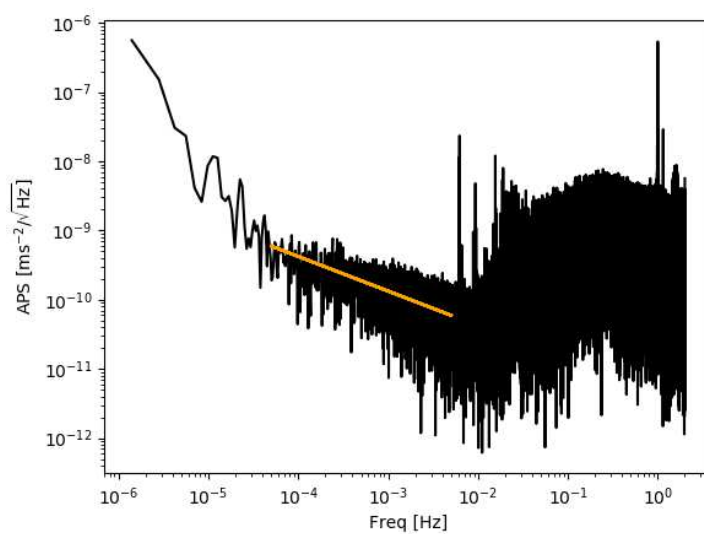


Figure 6. Typical spectral density of the acceleration measured along the X -axis of SUEP-IS1. The orange line is the best fit of the low-frequency part.

Fifth force stiffness

21

Table 2. Gold wire stiffness [10^{-3}Nm^{-1}] and orientation of the force [deg] estimated from long measurement sessions' acceleration noise spectral density.

	$k_{w,x}/Q$	$k_{w,y}/Q$	$k_{w,z}/Q$	k_w/Q	φ	θ
IS1-SUREF	0.07 ± 0.01	0.22 ± 0.1	0.66 ± 0.06	0.7 ± 0.08	84.4 ± 0.6	66 ± 30
IS1-SUEP	1.14 ± 0.2	0.31 ± 0.05	1.26 ± 0.2	1.73 ± 0.1	48 ± 4	70 ± 25

quantify the wire's stiffness

$$k_w = 2.91 \times 10^{-5} \left(\frac{r_w}{3.75 \mu\text{m}} \right)^4 \left(\frac{1.7 \text{ cm}}{l_w} \right)^3 \left(\frac{E}{7.85 \times 10^{10} \text{ Nm}^2} \right), \quad (44)$$

where r_w is the radius of the wire, l_w its length and E its Young modulus. Using MICROSCOPE's gold wires' characteristics ($r_w = 3.5 \mu\text{m}$, $l_w = 2.5 \text{ cm}$ and $E = 7.85 \times 10^{10} \text{ Nm}^2$), we expect $k_w \approx 9 \times 10^{-6}$. Combined with a quality factor $Q \approx 100$ as measured in Ref. [55], this scaling provides $k_w/Q \approx 10^{-7} \text{ N/m}$, in flagrant contradiction with the values estimated from flight data (Table 2).

Two explanations can be proposed: (i) the wire does not behave as shown in Ref. [55] or (ii) its quality factor is much lower than expected. In the former explanation, the wire may work in compression (i.e. it is deformed along its principal axis), which potentially increases its stiffness. In the latter, the mounting process (wires being glued to the test masses) may decrease the overall quality factor; differences between the glu points in MICROSCOPE and in Ref. [55] may explain a significant difference of quality factor.

Assuming that the electrostatic model of the instrument is correct and that the measured stiffness is dominated by the electrostatic stiffness hints at a low quality factor $Q \approx 1$. Note however that, even if the quality factor is really that low, MICROSCOPE's main results (the test of the WEP) depend on the k_w/Q ratio, and are thus unaffected by the current analysis.

5.4. Stiffness estimation

We now come back to Eq. (37), with the aim to estimate the model parameters for the four sensors, starting with radial axes.

5.4.1. Radial axes (Y and Z) The following assumptions allow us to break the degeneracy between the parameters mentioned in Sect. 5.1:

- for a given sensor and a given axis j , the gold wire's ratio $k_{w,j}/Q$ is independent of the electrical configuration (HRM or FRM), and can be estimated as shown in Sect. 5.3 for the internal sensors. We further assume that the mounting of gold wires is general enough to assume that the external sensors' $k_{w,j}/Q$ ratio is the same as that of the internal sensor.

Fifth force stiffness

22

- the ratio $k_{w,j}/Q$ varies from one axis to another, but the quality factor Q is a true constant for a given sensor. In other words, since $k_{w,j}$ and Q are degenerate, we assume that only the stiffness depends on the direction.
- by cylindrical symmetry, the total stiffness of the radial axis j ($j = y, z$) $k_{0,j} = m\omega^2 + k_{\epsilon,j} + k_N + k_Y$ is independent of the axis, and depends on the electrical configuration only through the electrostatic stiffness k_{ϵ} .

Noting $\hat{\chi}_y = k_{w,y}/Q$ and $\hat{\chi}_z = k_{w,z}/Q$ the radial gold wire's ratios estimated in Table 2, and combining constraints from the model (37), where we add the subscripts 'F' and 'H' for measurements in FRM and HRM modes, we obtain the following system of equations for a given sensor:

$$\left\{ \begin{array}{l} \hat{a}_{0yF} = \kappa_{0rF} + \kappa_{wy} \cos \phi \\ \hat{a}_{0yH} = \kappa_{0rH} + \kappa_{wy} \cos \phi \\ \hat{a}_{0zF} = \kappa_{0rF} + \kappa_{wz} \cos \phi \\ \hat{a}_{0zH} = \kappa_{0rH} + \kappa_{wz} \cos \phi \\ \hat{a}_{wyF} = -\kappa_{wy} \sin \phi + \kappa_{\lambda yF} \\ \hat{a}_{wyH} = -\kappa_{wy} \sin \phi + \kappa_{\lambda yH} \\ \hat{a}_{wzF} = -\kappa_{wz} \sin \phi + \kappa_{\lambda zF} \\ \hat{a}_{wzH} = -\kappa_{wz} \sin \phi + \kappa_{\lambda zH} \\ \hat{\chi}_y = \frac{k_{wy}}{Q} \\ \hat{\chi}_z = \frac{k_{wz}}{Q}, \end{array} \right. \quad \begin{array}{l} (45a) \\ (45b) \\ (45c) \\ (45d) \\ (45e) \\ (45f) \\ (45g) \\ (45h) \\ (45i) \\ (45j) \end{array}$$

where we recall that $\phi = 1/Q$, $\kappa_{wj} = x_0 k_{wj}/m$, and similarly for κ_{0r} (with the subscript $r = y, z$) and κ_{λ} and the \hat{a}_0 and \hat{a}_w coefficients are the estimates of the coefficients the sine and cosine of Eq. (37).

On the one hand, Eqs. (45e-45h) trivially give the velocity-dependent terms as a functions of the unknown Q and estimated χ_j and a_{wj} . On the other hand, Eqs. (45a-45d), (45i-45j) can be combined to give

$$2(\hat{\chi}_y - \hat{\chi}_z) \frac{x_0}{m} Q \cos \left(\frac{1}{Q} \right) = \hat{a}_{0yF} + \hat{a}_{0yH} - \hat{a}_{wzF} - \hat{a}_{wzH}, \quad (46)$$

thus providing the equation

$$x \cos \left(\frac{1}{x} \right) - \xi = 0 \quad (47)$$

of which Q is a root, where ξ is defined through parameters estimated from Table 2 and fitting Eq. (37) for the sensor's two radial axes in each electrical configuration.

Once Q is estimated, Eqs. (45a-45d) readily provide κ_{0rF} and κ_{0rH} . Actually, they give two estimates of each, which we checked to be consistent.

Fifth force stiffness

23

5.4.2. Longitudinal axis X Under the same assumptions, it is then straightforward to estimate the X -axis stiffness from Eq. (37) and Table 2, for a given electrical configuration (that we do not make explicit in the equations below for simplicity):

$$\left\{ \begin{array}{l} \kappa_{0x} = \hat{a}_{0x} - \frac{x_0}{m} \hat{\chi}_x Q \cos\left(\frac{1}{Q}\right) \\ \kappa_{\lambda x} = \hat{a}_{wx} + \frac{x_0}{m} \hat{\chi}_x Q \sin\left(\frac{1}{Q}\right). \end{array} \right. \quad (48a)$$

$$\left\{ \begin{array}{l} \kappa_{0x} = \hat{a}_{0x} - \frac{x_0}{m} \hat{\chi}_x Q \cos\left(\frac{1}{Q}\right) \\ \kappa_{\lambda x} = \hat{a}_{wx} + \frac{x_0}{m} \hat{\chi}_x Q \sin\left(\frac{1}{Q}\right). \end{array} \right. \quad (48b)$$

5.4.3. Results Our results are listed in Table 3 for each sensor, in their two electrical configurations. The left group's four columns show the instrumental parameters: total in-phase stiffness k_0 , gold wire stiffness k_w and quality factor Q , and velocity-dependent coefficient λ_w . The next two columns give the theoretical electrostatic stiffness $k_{\epsilon, \text{th}}$ and the Newtonian gravity stiffness. The last column lists the difference between the theoretical and the estimated electrostatic stiffness $\Delta k = \hat{k}_0 - k_N - m\omega^2 - k_{\epsilon, \text{th}}$. Error bars give 1σ uncertainties.

The electrostatic stiffness estimated in the HRM electrical configuration is consistent with the theoretical one for most sensors and axes, with at most a $\approx 2\sigma$ discrepancy. However, we note a significant difference in the FRM configuration (Fig. 7). Being dependent on the electrical configuration, this discrepancy hints at the existence of an electric potential-dependent additional stiffness completely degenerate with the electrostatic one. Patch effects could be at its origin: the discrepancy being significant for higher voltages is indeed consistent with the voltage-dependence of patch effects' stiffness. Disentangling this puzzle would require modeling patch effects in MICROSCOPE's sensors. As this goes far beyond the scope of this paper, and since our experiment is not competitive with other short-ranged forces searches (as we discuss below), we let the question of this discrepancy open. In the remainder of this paper, we thence use HRM measurements only.

The gold wire's quality factor is lower than could be expected from Ref. [55]. Nevertheless, Q being close to 1 is consistent with our discussion in Sect. 5.3. Correspondingly, the gold wires' stiffness is small and negligible compared to the electrostatic stiffness of the radial axes, as was assumed by Ref. [52]; however, they remain significantly degenerate in the longitudinal axis, giving a total stiffness similar to that estimated in Ref. [52]. Moreover, this degeneracy, that also exists for the radial axes, explains that the total error bars are dominated by the uncertainty on the gold wire's stiffness (k_0 and k_w are degenerate in the amplitude of Eq. (37)'s sine, meaning that \hat{k}_0 error bars actually come from those on k_w/Q).

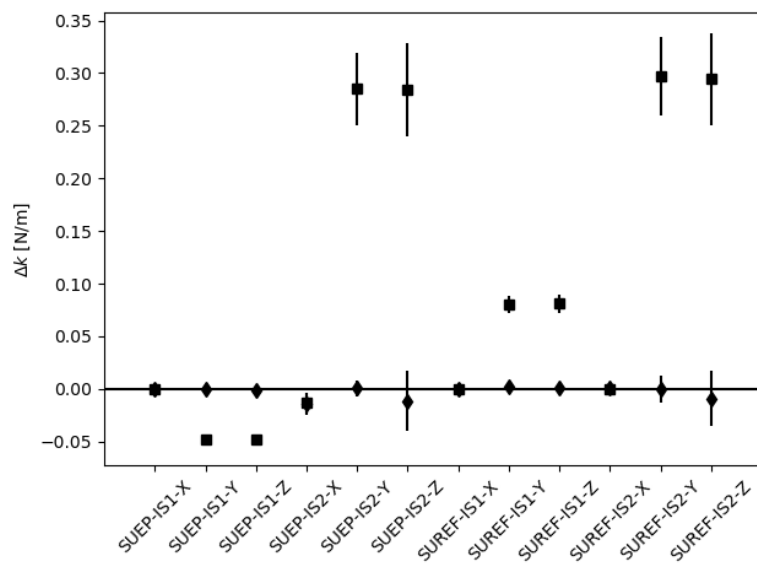


Figure 7. Difference between theoretical electrostatic stiffness and measured total in-phase stiffnesses corrected for the excitation and Newtonian gravity stiffnesses, $\Delta k = \hat{k}_0 - k_N - m\omega^2 - k_{\epsilon, \text{th}}$, for all axes (longitudinal and radial) of each sensor, in the HRM (diamonds) and FRM (squares) electric configurations.

Table 3. Estimated model parameters.

Sensor	Axis (mode)	\bar{k}_0	\bar{k}_w	\bar{Q}	$\bar{\lambda}_w$	k_ϵ	k_N	Δk
		$[\times 10^{-2} \text{ N/m}]$	$[\times 10^{-2} \text{ N/m}]$		$[\times 10^{-2} \text{ Ns/m}]$	$[\times 10^{-2} \text{ N/m}]$	$[\times 10^{-8} \text{ N/m}]$	$[\times 10^{-2} \text{ N/m}]$
SUEP IS1	X (HRM)	-0.00±0.12	0.16±0.08	1.5±0.7	4.23±3.82	0.00±0.01	1.22	-0.021±0.119
	Y (HRM)	-1.55±0.06	0.04±0.08	1.5±0.7	1.87±1.87	-1.57±0.05	-0.96	0.009±0.081
	Z (HRM)	-1.65±0.26	0.19±0.31	1.5±0.7	5.50±7.49	-1.57±0.05	-0.96	-0.095±0.260
	X (FRM)	0.04±0.12	0.16±0.08	1.5±0.7	2.88±3.89	0.00±0.01	1.22	0.024±0.120
	Y (FRM)	-18.85±0.06	0.04±0.08	1.5±0.7	1.35±1.89	-14.08±0.46	-0.96	-4.795±0.460
	Z (FRM)	-18.87±0.26	0.19±0.31	1.5±0.7	4.94±7.53	-14.08±0.46	-0.96	-4.809±0.523
SUEP IS2	X (HRM)	-1.35±1.01	1.41±1.01	12.8±8.9	5.60±2.93	0.00±0.01	1.27	-1.366±1.015
	Y (HRM)	-6.96±0.73	0.40±0.73	13.4±9.5	5.03±2.38	-7.01±0.23	-0.88	0.039±0.760
	Z (HRM)	-8.20±2.94	1.74±2.95	13.4±9.5	9.65±9.53	-7.01±0.23	-0.88	-1.201±2.949
	X (FRM)	-1.32±1.02	1.41±1.01	12.8±8.9	5.96±2.97	0.00±0.01	1.27	-1.337±1.015
	Y (FRM)	-78.47±0.68	0.38±0.69	12.7±8.6	2.25±2.39	-107.02±3.37	-0.88	28.538±3.440
	Z (FRM)	-78.56±2.77	1.66±2.78	12.7±8.6	7.03±9.53	-107.03±3.37	-0.88	28.456±4.366
SUREF IS1	X (HRM)	0.06±0.09	0.02±0.01	2.3±1.3	-0.52±4.35	0.00±0.01	23.65	0.041±0.092
	Y (HRM)	-1.58±0.08	0.05±0.08	2.5±1.3	1.60±1.33	-1.81±0.06	-12.32	0.209±0.095
	Z (HRM)	-1.71±0.12	0.18±0.12	2.5±1.3	3.80±1.40	-1.81±0.06	-12.32	0.082±0.133
	X (FRM)	0.06±0.09	0.02±0.01	2.3±1.3	-0.92±4.51	0.00±0.01	23.65	0.042±0.095
	Y (FRM)	-19.25±0.07	0.05±0.08	2.5±1.3	5.72±1.33	-27.31±0.86	-12.32	8.047±0.862
	Z (FRM)	-19.16±0.12	0.18±0.12	2.5±1.3	7.79±1.41	-27.31±0.86	-12.32	8.134±0.866
SUREF IS2	X (HRM)	0.20±0.35	0.20±0.17	28.9±20.9	0.85±14.57	0.00±0.01	5.72	0.144±0.347
	Y (HRM)	-8.91±1.09	0.68±1.09	33.9±19.2	5.81±1.44	-9.09±0.29	-3.98	0.111±1.126
	Z (HRM)	-9.56±1.69	2.38±1.68	33.9±19.2	9.34±2.00	-9.08±0.29	-3.98	-0.540±1.710
	X (FRM)	0.15±0.34	0.20±0.17	28.9±20.9	-2.96±14.45	0.00±0.01	5.72	0.089±0.345
	Y (FRM)	-80.24±1.04	0.65±1.04	32.4±19.3	21.79±1.45	-110.17±3.47	-3.98	29.877±3.629
	Z (FRM)	-80.09±1.66	2.27±1.66	32.4±19.3	24.64±1.88	-110.13±3.47	-3.98	29.988±3.847

Fifth force stiffness

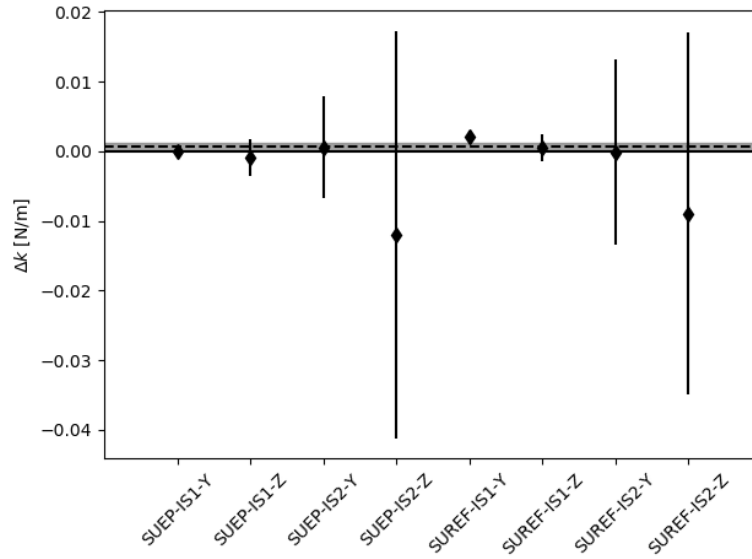


Figure 8. Difference between theoretical electrostatic stiffnesses and measured total in-phase stiffness corrected for the excitation and Newtonian gravity stiffnesses, $\Delta k = \hat{k}_0 - k_N - m\omega^2 - k_{\epsilon, \text{th}}$, for the radial axes of each sensor, in the HRM electric configuration. The dashed line is the Δk weighted average and the grey area shows its 1σ weighted uncertainty.

6. Constraints on short-ranged Yukawa deviation

In the previous section, we invoked patch effects to account for the non-zero difference between theoretical electrostatic stiffness and measured total in-phase stiffness corrected for the excitation and Newtonian gravity stiffnesses, $\Delta k = \hat{k}_0 - k_N - m\omega^2 - k_{\epsilon, \text{th}}$. Actually, Δk also contains the putative Yukawa potential that we aim to constrain in this paper.

Given the obvious dependence of Δk on the electric configuration, which cannot be explained by a Yukawa-like gravity interaction, we exclude the obviously biased FRM measurements from our analysis below. Furthermore, as shown in Fig. 4, a Yukawa potential has a stronger signature on the radial axes than on the longitudinal one. Therefore, we use only the stiffness estimated on the radial axes in the HRM configuration to infer constraints on the Yukawa interaction. Fig. 8 shows the corresponding Δk , together with their weighted average and 1σ uncertainty (dashed line and grey area), $\langle \Delta k \rangle = (7.1 \pm 6.0) \times 10^{-4}$ N/m.

The marginal offset from 0 is surely due to unaccounted for patch effects and a possible suboptimal calibration of our electrostatic model. However, as error bars are largely dominated by gold wires, and are significantly larger than the remaining bias, we use this estimation of $\langle \Delta k \rangle$ to infer the 95% upper bound on the Yukawa potential in Fig. 9, noting that a positive $\langle \Delta k \rangle$ corresponds to a negative α .

The curves in the lower part of Fig. 9 show the current best upper bounds on a

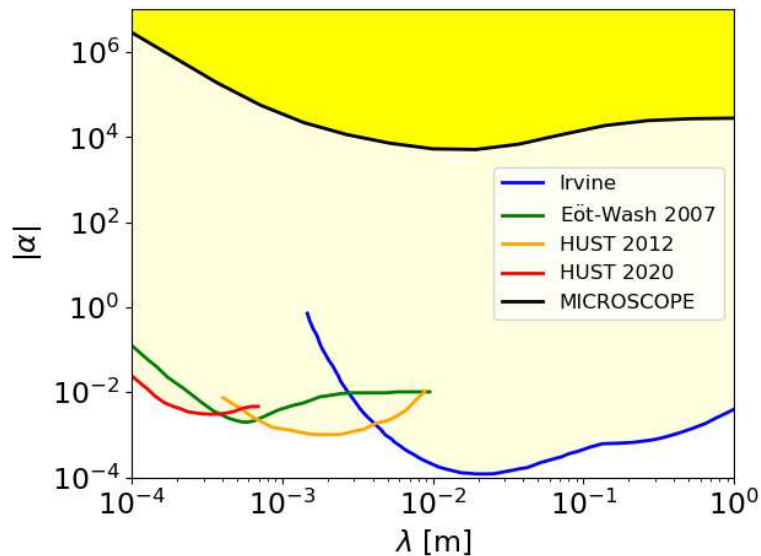


Figure 9. 95% confidence contour for a Yukawa potential. The light grey area shows the excluded region by various experiments: Irvine [61], Eöt-Wash 2007 [41], HUST 2012 [45], HUST 2020 [31], and the yellow area shows the region excluded by the current work.

Yukawa potential, inferred from dedicated torsion balance experiments [31, 41, 45, 61]. Note that the Eöt-Wash group recently updated its constraints [32]; however, since they have been improved below the ranges considered here, we do not show them in Fig. 9. Our constraints are clearly poor compared to the state of the art. It would have been surprising otherwise, since MICROSCOPE was not designed to look for short-range deviations from Newtonian gravity. However, our results suggest that thanks to its non-trivial geometry, an experiment looking like MICROSCOPE, if highly optimised, may allow for new constraints of gravity through the measurement of the interaction between several bodies.

7. Conclusion

We used in-flight technical measurements aimed to characterise MICROSCOPE’s instrument to search for short-ranged Yukawa deviations from Newtonian gravity. MICROSCOPE not being designed for this task, this article serves as a proposal for a new experimental concept in the search of small-scale modifications of gravitation, as well as a first proof of concept. The analysis is based on the estimation of the stiffness of the force underwent by MICROSCOPE’s test masses as they are set in motion in their cage.

We listed all forces possibly intervening in the measurement, and computed the total stiffness. We found that estimation uncertainties are dominated by those coming

Fifth force stiffness

28

from the gold wires' stiffness and quality factor (those wires being used to control the potential of the test masses). As the electrostatic stiffness is expected to dominate over other stiffnesses, we compared it with the estimated total stiffness. We found a non-zero difference depending on the instrument's electric configuration, hinting at unaccounted for patch field forces. Due to the complexity of their modeling, we removed those measurements with a significant bias from our inference of the Yukawa potential parameters.

Not surprisingly, our constraints on the Yukawa potential parameter space (α, λ) are not competitive with the published ones, obtained with dedicated laboratory tests. We find $|\alpha| < 10^4 - 10^6$ for $10^{-4} \text{ m} \leq \lambda \leq 1 \text{ m}$, eight orders of magnitude above the best current upper bounds. Nevertheless, our work can be the starting point for optimisations to be implemented in the proposed MICROSCOPE's follow up. The gold wire should be replaced by a contactless charge control management, as envisioned for LISA [62,63]; this replacement is already planned, since the gold wire is the main limiting factor for MICROSCOPE's test of the WEP [33, 34]. Furthermore, patch effects will need to be either controlled or measurable. Finally, a possible Yukawa interaction at ranges $10^{-4} \text{ m} \leq \lambda \leq 1 \text{ m}$ is expected to have a strength $\alpha < 10^{-4}$, corresponding to a stiffness seven orders of magnitude lower than the electrostatic stiffness. Since MICROSCOPE's capacitive control and measurement prevents us from using an electrostatic shield similar to that used by torsion pendulum experiments, a competitive experimental constrain will thus require a control of the instrument's theoretical model of one part in 10 millions. Whether this endeavour is possible remains an open question.

In the meantime, we use the measurements presented in this paper to provide new constraints on the chameleon model in a companion paper [64] based on Refs. [65,66].

Acknowledgments

We acknowledge useful discussions with Bruno Christophe and Bernard Foulon, and thank Vincent Lebat for comments on this article. We acknowledge the financial support of CNES through the APR program ("GMscope+" and "Microscope 2" projects). MPB is supported by a CNES/ONERA PhD grant. This work uses technical details of the T-SAGE instrument, installed on the CNES-ESA-ONERA-CNRS-OCA-DLR-ZARM MICROSCOPE mission. This work is supported in part by the EU Horizon 2020 research and innovation programme under the Marie-Sklodowska grant No. 690575. This article is based upon work related to the COST Action CA15117 (CANTATA) supported by COST (European Cooperation in Science and Technology).

References

- [1] Will C M 2014 *Living Reviews in Relativity* **17** 4 (*Preprint* 1403.7377)
- [2] Bartelmann M and Schneider P 2001 *Physics Reports* **340** 291–472 (*Preprint* astro-ph/9912508)
- [3] Hoekstra H and Jain B 2008 *Annual Review of Nuclear and Particle Science* **58** 99–123 (*Preprint* 0805.0139)

- [4] Delva P, Puchades N, Schönemann E, Dilssner F, Courde C, Bertone S, Gonzalez F, Hees A, Le Poncin-Lafitte C, Meynadier F, Prieto-Cerdeira R, Sohet B, Ventura-Traveset J and Wolf P 2018 *Physical Review Letters* **121** 231101 (*Preprint* 1812.03711)
- [5] Herrmann S, Finke F, Lülff M, Kichakova O, Puetzfeld D, Knickmann D, List M, Rievers B, Giorgi G, Günther C, Dittus H, Prieto-Cerdeira R, Dilssner F, Gonzalez F, Schönemann E, Ventura-Traveset J and Lämmerzahl C 2018 *Physical Review Letters* **121** 231102 (*Preprint* 1812.09161)
- [6] Abbott B P *et al.* 2016 *Phys. Rev. Lett.* **116** 061102
- [7] Zwicky F 1933 *Helvetica Physica Acta* **6** 110–127
- [8] Rubin V C and Ford Jr W K 1970 *Astrophysical Journal* **159** 379
- [9] Riess A G, Filippenko A V, Challis P, Clocchiatti A, Diercks A, Garnavich P M, Gilliland R L, Hogan C J, Jha S, Kirshner R P, Leibundgut B, Phillips M M, Reiss D, Schmidt B P, Schommer R A, Smith R C, Spyromilio J, Stubbs C, Suntzeff N B and Tonry J 1998 *Astronomical Journal* **116** 1009–1038 (*Preprint* astro-ph/9805201)
- [10] Perlmutter S, Aldering G, Goldhaber G, Knop R A, Nugent P, Castro P G, Deustua S, Fabbro S, Goobar A, Groom D E, Hook I M, Kim A G, Kim M Y, Lee J C, Nunes N J, Pain R, Pennypacker C R, Quimby R, Lidman C, Ellis R S, Irwin M, McMahon R G, Ruiz-Lapuente P, Walton N, Schaefer B, Boyle B J, Filippenko A V, Matheson T, Fruchter A S, Panagia N, Newberg H J M, Couch W J and Project T S C 1999 *Astrophysical Journal* **517** 565–586 (*Preprint* astro-ph/9812133)
- [11] Joyce A, Jain B, Khoury J and Trodden M 2015 *Physics Reports* **568** 1–98 (*Preprint* 1407.0059)
- [12] Joyce A, Lombriser L and Schmidt F 2016 *Annual Review of Nuclear and Particle Science* **66** 95–122 (*Preprint* 1601.06133)
- [13] Damour T and Polyakov A M 1994 *Nucl. Phys. B* **423** 532–558 (*Preprint* hep-th/9401069)
- [14] Damour T, Piazza F and Veneziano G 2002 *Physical Review Letters* **89** 081601 (*Preprint* gr-qc/0204094)
- [15] Damour T and Esposito-Farese G 1992 *Classical and Quantum Gravity* **9** 2093–2176
- [16] Clifton T, Ferreira P G, Padilla A and Skordis C 2012 *Physics Reports* **513** 1–189 (*Preprint* 1106.2476)
- [17] Vainshtein A I 1972 *Physics Letters B* **39** 393–394
- [18] Damour T and Nordtvedt K 1993 *Phys. Rev. Lett.* **70** 2217–2219
- [19] Khoury J and Weltman A 2004 *Phys. Rev. D* **69** 044026 (*Preprint* astro-ph/0309411)
- [20] Khoury J and Weltman A 2004 *Phys. Rev. Lett.* **93** 171104 (*Preprint* astro-ph/0309300)
- [21] Babichev E, Defayet C and Ziour R 2009 *Int. J. Mod. Phys. D* **18** 2147–2154 (*Preprint* 0905.2943)
- [22] Hinterbichler K and Khoury J 2010 *Phys. Rev. Lett.* **104** 231301 (*Preprint* 1001.4525)
- [23] Brax P, Burrage C and Davis A C 2013 *JCAP* **1** 020 (*Preprint* 1209.1293)
- [24] Burrage C and Sakstein J 2018 *Living Reviews in Relativity* **21** 1 (*Preprint* 1709.09071)
- [25] Damour T 2012 *Classical and Quantum Gravity* **29** 184001 (*Preprint* 1202.6311)
- [26] Uzan J P 2003 *Rev. Mod. Phys.* **75** 403 (*Preprint* hep-ph/0205340)
- [27] Uzan J P 2011 *Living Rev. Rel.* **14** 2 (*Preprint* 1009.5514)
- [28] Fischbach E and Talmadge C L 1999 *The Search for Non-Newtonian Gravity*
- [29] Adelberger E G, Heckel B R and Nelson A E 2003 *Annual Review of Nuclear and Particle Science* **53** 77–121 (*Preprint* hep-ph/0307284)
- [30] Adelberger E G, Gundlach J H, Heckel B R, Hoedl S and Schlamminger S 2009 *Progress in Particle and Nuclear Physics* **62** 102–134
- [31] Tan W H, Du A B, Dong W C, Yang S Q, Shao C G, Guan S G, Wang Q L, Zhan B F, Luo P S, Tu L C and Luo J 2020 *Physical Review Letters* **124** 051301
- [32] Lee J G, Adelberger E G, Cook T S, Fleischer S M and Heckel B R 2020 *Physical Review Letters* **124** 101101 (*Preprint* 2002.11761)
- [33] Touboul P, Métris G, Rodrigues M, André Y, Baghi Q, Bergé J, Boulanger D, Bremer S, Carle P, Chhun R, Christophe B, Cipolla V, Damour T, Danto P, Dittus H, Fayet P, Foulon B, Gageant C, Guidotti P Y, Hagedorn D, Hardy E, Huynh P A, Inchauspe H, Kayser P, Lala S, Lämmerzahl

- C, Lebat V, Leseur P, Liorzou F, List M, Löffler F, Panet I, Pouilloux B, Prieur P, Rebray A, Reynaud S, Rievers B, Robert A, Selig H, Serron L, Sumner T, Tanguy N and Visser P 2017 *Physical Review Letters* **119** 231101 (*Preprint* 1712.01176)
- [34] Touboul P, Métris G, Rodrigues M, André Y, Baghi Q, Bergé J, Boulanger D, Bremer S, Chhun R, Christophe B, Cipolla V, Damour T, Danto P, Dittus H, Fayet P, Foulon B, Guidotti P Y, Hardy E, Huynh P A, Lämmerzahl C, Lebat V, Liorzou F, List M, Panet I, Pires S, Pouilloux B, Prieur P, Reynaud S, Rievers B, Robert A, Selig H, Serron L, Sumner T and Visser P 2019 *Classical and Quantum Gravity* **36** 225006 (*Preprint* 1909.10598)
- [35] Bergé J, Brax P, Métris G, Pernot-Borràs M, Touboul P and Uzan J P 2018 *Physical Review Letters* **120** 141101 (*Preprint* 1712.00483)
- [36] Fayet P 2018 *Phys. Rev. D* **97** 055039 (*Preprint* 1712.00856)
- [37] Fayet P 2019 *Phys. Rev. D* **99**(5) 055043 URL <https://link.aps.org/doi/10.1103/PhysRevD.99.055043>
- [38] Touboul P in prep *Class. Quant. Grav.*
- [39] Métris G in prep *Class. Quant. Grav.*
- [40] Bergé J, Brax P, Pernot-Borràs M and Uzan J P 2018 *Classical and Quantum Gravity* **35** 234001 (*Preprint* 1808.00340)
- [41] Kapner D J, Cook T S, Adelberger E G, Gundlach J H, Heckel B R, Hoyle C D and Swanson H E 2007 *Physical Review Letters* **98** 021101 (*Preprint* hep-ph/0611184)
- [42] Masuda M and Sasaki M 2009 *Physical Review Letters* **102** 171101 (*Preprint* 0904.1834)
- [43] Sushkov A O, Kim W J, Dalvit D A R and Lamoreaux S K 2011 *Physical Review Letters* **107** 171101 (*Preprint* 1108.2547)
- [44] Klimchitskaya G L and Mostepanenko V M 2014 *Gravitation and Cosmology* **20** 3–9 (*Preprint* 1403.5778)
- [45] Yang S Q, Zhan B F, Wang Q L, Shao C G, Tu L C, Tan W H and Luo J 2012 *Physical Review Letters* **108** 081101
- [46] Tan W H, Yang S Q, Shao C G, Li J, Du A B, Zhan B F, Wang Q L, Luo P S, Tu L C and Luo J 2016 *Physical Review Letters* **116** 131101
- [47] Liorzou F, Touboul P, Rodrigues M, Bergé J, Boulanger D, Chhun R, Christophe B, Foulon B, Hardy E, Huynh P A, Lebat V, Métris G and Robert A in prep *Class. Quant. Grav.*
- [48] Damour T and Donoghue J F 2010 *Physical Review D* **82** 084033 (*Preprint* 1007.2792)
- [49] Damour T and Donoghue J F 2010 *Class. Quant. Grav.* **27** 202001 (*Preprint* 1007.2790)
- [50] Cipolla V, Prieur P, Robert A, Touboul P, Métris G, Rodrigues M, Joël, Boulanger D, Chhun R, Christophe B, Guidotti P Y, Hardy E, Lebat V, Liorzou F and Pouilloux B in prep *Class. Quant. Grav.*
- [51] Touboul P, Métris G, Rodrigues M, Bergé J, Boulanger D, Chhun R, Christophe B, Cipolla V, Damour T, Dittus H, Fayet P, Foulon B, Guidotti P Y, Hardy E, Huynh P A, Lämmerzahl C, Lebat V, Liorzou F, List M, Pouilloux B, Prieur P, Reynaud S, Rievers B, Robert A, Serron L, Sumner T and Visser P in prep *Class. Quant. Grav.*
- [52] Chhun R in prep *Class. Quant. Grav.*
- [53] Bergé J, Baghi Q, Hardy E, Métris G, Robert A, Rodrigues M, Touboul P, Chhun R, Guidotti P Y, Pires S, Serron L, Travert J M, Damour T, Dittus H, Fayet P, Lämmerzahl C, Panet I, Reynaud S, Sumner T and Visser P in prep *Class. Quant. Grav.*
- [54] Saulson P R 1990 *Physical Review D* **42** 2437–2445
- [55] Willemenot E and Touboul P 2000 *Review of Scientific Instruments* **71** 302–309
- [56] Nofrarias i Serra M 2007 *Thermal Diagnostics in the LISA Technology Package Experiment* Ph.D. thesis Departament de Física Fonamental. Universitat de Barcelona
- [57] Carbone L, Cavalleri A, Ciani G, Dolesi R, Hueller M, Tombolato D, Vitale S and Weber W J 2007 *Physical Review D* **76** 102003 (*Preprint* 0706.4402)
- [58] Hardy E a TBP *Class. Quant. Grav.*
- [59] Speake C C 1996 *Classical and Quantum Gravity* **13** A291–A297
- [60] Hudson D 2007 *Investigation expérimentale et théorique du prototype du capteur inertielle pour*

Fifth force stiffness

31

la vérification du principe d'équivalence dans la mission spatiale MICROSCOPE Ph.D. thesis
 Université Pierre et Marie Curie

- [61] Hoskins J K, Newman R D, Spero R and Schultz J 1985 *Physical Review D* **32** 3084–3095
- [62] Sumner T J, Shaul D N A, Schulte M O, Waschke S, Hollington D and Araújo H 2009 *Classical and Quantum Gravity* **26** 094006
- [63] Armano M, Audley H, Baird J, Binetruy P, Born M, Bortoluzzi D, Castelli E, Cavalleri A, Cesarini A, Cruise A M, Danzmann K, de Deus Silva M, Diepholz I, Dixon G, Dolesi R, Ferraioli L, Ferroni V, Fitzsimons E D, Freschi M, Gesa L, Gibert F, Giardini D, Giusteri R, Grimani C, Grzymisch J, Harrison I, Heinzl G, Hewitson M, Hollington D, Hoyland D, Hueller M, Inchauspé H, Jennrich O, Jetzer P, Karnesis N, Kaune B, Korsakova N, Killow C J, Lobo J A, Lloro I, Liu L, López-Zaragoza J P, Maarschalkerweerd R, Mance D, Meshksar N, Martín V, Martín-Polo L, Martino J, Martín-Porqueras F, Mateos I, McNamara P W, Mendes J, Mendes L, Nofrarias M, Paczkowski S, Perreur-Lloyd M, Petiteau A, Pivato P, Plagnol E, Ramos-Castro J, Reiche J, Robertson D I, Rivas F, Russano G, Slutsky J, Sopena C F, Sumner T, Texier D, Thorpe J I, Vetrugno D, Vitale S, Wanner G, Ward H, Wass P J, Weber W J, Wissel L, Wittchen A and Zweifel P 2018 *Physical Review Letters* **120** 061101
- [64] Pernot-Borràs M, Bergé J, Brax P and Uzan J P in prep *Physical Review D*
- [65] Pernot-Borràs M, Bergé J, Brax P and Uzan J P 2019 *Physical Review D* **100** 084006 (*Preprint* 1907.10546)
- [66] Pernot-Borràs M, Bergé J, Brax P and Uzan J P 2020 *Physical Review D* **101** 124056 (*Preprint* 2004.08403)
- [67] Lockerbie N A, Veryaskin A V and Xu X 1996 *Journal of Physics A Mathematical General* **29** 4649–4663

Appendix A. Test mass dynamics

Equation (2) is an idealised version of the more realistic description of Ref. [51]. First, the sensor is not perfectly aligned with the satellite’s frame; this is described by the $[\theta_j]$ matrix

$$\vec{\Gamma}_{\text{cont},j|\text{instr}} = [\theta_j] \left(\vec{\Gamma}_{\oplus,j|\text{sat}} + \vec{\Gamma}_{\text{cin},j|\text{sat}} + \frac{\vec{F}_{\text{ext}|\text{sat}}}{M_{I_{\text{sat}}}} + \frac{\vec{F}_{\text{th}|\text{sat}}}{M_{I_{\text{sat}}}} \right) - \frac{\vec{F}_{\text{loc},j|\text{instr}}}{m_{I_j}} - \frac{\vec{F}_{\text{pa},j|\text{instr}}}{m_{I_j}}, \quad (\text{A.1})$$

where the subscripts “|instr” and “|sat” mean that forces and accelerations are expressed in the instrument or satellite frame, respectively.

Finally, the measured acceleration is given by the control acceleration (A.1) affected by the matrix $[A_j]$ containing the instrument’s scale factors, by electrostatic parasitic forces (since the applied electrostatic forces are the sum of the measured and parasitic electrostatic forces $m_{I_j} \vec{\Gamma}_{\text{cont},j|\text{instr}} = \vec{F}_{\text{el},j} = \vec{F}_{\text{el,meas},j} + \vec{F}_{\text{elec,par},j}$), by the measurement bias $\vec{b}_{0,j}$ due to the read-out circuit and by noise \vec{n}_j :

$$\vec{\Gamma}_{\text{meas},j|\text{instr}} = \vec{b}_{0,j} + [A_j] \left(\vec{\Gamma}_{\text{cont},j|\text{instr}} - \frac{\vec{F}_{\text{elec,par},j|\text{instr}}}{m_{I_j}} \right) + K_{2,j} \left[\vec{\Gamma}_{\text{cont},j|\text{sat}} \right]^2 + \vec{n}_j. \quad (\text{A.2})$$

Table B1. High-resolution mode (HRM) electric configuration. All voltages are in V.

	V_d	V_p	V'_{px}	$V'_{py/z}$	$V'_{p\phi}$
IS1-SUREF	5	5	-5	2.5	-10
IS2-SUREF	5	5	-10	0	-10
IS1-SUEP	5	5	-5	2.5	-10
IS2-SUEP	5	5	0	2.5	-10

We can then wrap up and write the measured acceleration explicitly:

$$\vec{\Gamma}_{\text{meas},j|\text{instr}} = \vec{B}_{0,j} + [A_j][\theta_j] \left(\vec{\Gamma}_{\oplus,j|\text{sat}} + \vec{\Gamma}_{\text{cin},j|\text{sat}} + \frac{\vec{F}_{\text{ext}|\text{sat}}}{M_{I_{\text{sat}}}} + \frac{\vec{F}_{\text{th}|\text{sat}}}{M_{I_{\text{sat}}}} \right) - [A_j] \frac{\vec{F}_{\text{loc},j|\text{instr}}}{m_{I_j}} + K_{2,j} \left[\vec{\Gamma}_{\text{cont},j|\text{sat}} \right]^2 + \vec{n}_j, \quad (\text{A.3})$$

where

$$\vec{B}_{0,j} \equiv \vec{b}_{0,j} - [A_j] \left(\frac{\vec{F}_{\text{pa},j|\text{instr}}}{m_{I_j}} + \frac{\vec{F}_{\text{elec,par},j|\text{instr}}}{m_{I_j}} \right) \quad (\text{A.4})$$

is the scale-factor-dependent bias and $K_{2,j}$ is the quadratic factor accounting for nonlinearities in the electronics.

In this article, following the measurements of Ref. [34], we assume that $[A_j] = [\theta_j] = \text{Id}$, that the drag-free perfectly cancels the external forces and we ignore the quadratic factor (see Refs. [33, 50, 52]), so that our main measurement equation is

$$\vec{\Gamma}_{\text{meas},j|\text{instr}} = \vec{B}_{0,j} + \vec{\Gamma}_{\oplus,j|\text{sat}} + \vec{\Gamma}_{\text{cin},j|\text{sat}} - \frac{\vec{F}_{\text{loc},j|\text{instr}}}{m_{I_j}} + \vec{n}_j. \quad (\text{A.5})$$

Appendix B. Electric configurations

MICROSCOPE can be used with two electric configurations: in the full-range mode (FRM), voltages are high enough to be able to acquire the test masses, while the high-resolution mode (HRM), with lower voltages, allows for an optimal control of the test masses. Tables B1 and B2 summarise the corresponding voltages (which appear in Eq. 13).

Appendix C. Radial electrostatic stiffness due to the Y electrodes

In this appendix, we give a detailed computation of the electrostatic stiffness created by MICROSCOPE's Y electrodes on a given test mass as the test mass moves along the Y-axis (but remains at $z = 0$). Although this is textbook physics, this section allows us to clarify the model of the electrostatic stiffness. See Ref. [60] for the detailed general case. See Ref. [47] for details about the geometry involved in this computation. In short,

Table B2. Full-range mode (FRM) electric configuration. All voltages are in V.

	V_d	V_p	V'_{px}	$V'_{py/z}$	$V'_{p\phi}$
IS1-SUREF	1	42	0	0	0
IS2-SUREF	1	42	0	0	0
IS1-SUEP	1	42	0	0	0
IS2-SUEP	1	42	0	0	0

a given test mass is controlled along its Y -axis by two pairs of diametrically-opposed Y electrodes (at potential V_{e+} and V_{e-}), completed by two pairs of Z -electrodes, as shown in Fig. C1.

Appendix C.1. Electrostatic force between the plates of a capacitor

At constant potential, the electrostatic force between conductors reads $F_{\text{elec}} = \nabla U$, where U is the electrostatic energy. For a capacitor,

$$U = \frac{1}{2}CV^2, \quad (\text{C.1})$$

where C is its capacitance and V the potential difference between its plates. The electrostatic force created along the y -axis is then

$$F(y) = \frac{1}{2} \frac{\partial C}{\partial y} V^2. \quad (\text{C.2})$$

Appendix C.2. Capacitance of one Y electrode – test mass pair

Assuming electrodes are on an infinite cylinder (this assumption is reasonable since electrodes are far enough from the edges of the cylinder) and using the Gauss theorem, it is easy to show that the electric field of an electrode (of surface charge σ) at a distance r from the axis of the cylinder is

$$E(r) = \frac{\sigma R_{ey}}{\epsilon_0 r}. \quad (\text{C.3})$$

The electric potential of the electrode is thus

$$V(r) = \frac{R_{ey}\sigma}{\epsilon_0} \ln r. \quad (\text{C.4})$$

Finally, the capacitance of the electrode-test mass pair

$$C = \frac{Q}{\Delta V} = \frac{1}{4} \left(2\pi - 4 \frac{d_3}{R_{ey}} \right) \frac{L_y \epsilon_0}{\ln \frac{R_{mi}}{R_{ey}}}, \quad (\text{C.5})$$

where the charge

$$Q = \sigma S = \frac{\sigma}{4} \left(2\pi - 4 \frac{d_3}{R_{ey}} \right) R_{ey} L_y, \quad (\text{C.6})$$

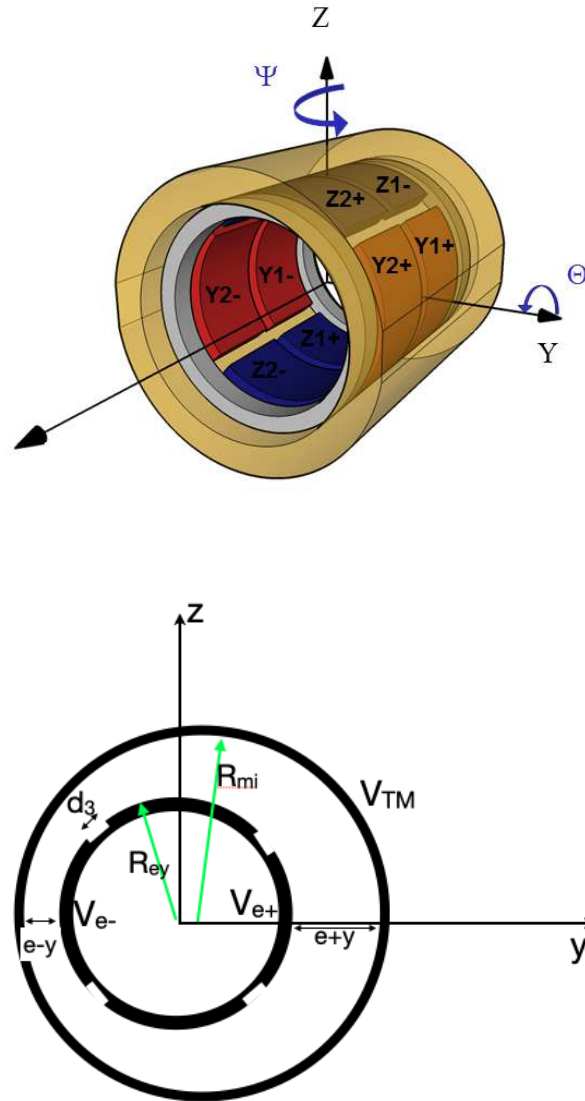


Figure C1. Test mass' Y- and Z-axes control geometry. Upper panel: test mass (light brown) and inner electrode-bearing silica cylinder, with its two rings of pairs of electrodes to control the Y-axis (red) and the Z-axis (blue). The outer electrode-bearing silica cylinder controls the X-axis and is not shown here (see Ref. [47]). Lower panel: Radial cut of a ring of Y and Z electrodes geometry, when the test mass is offset by y along the Y-axis, with e being the gap between the electrodes and the test mass in equilibrium. The inner cylinder carries the electrodes (Y and Z along the corresponding axes $-Y$ electrodes are shown at potential V_{e+} and V_{e-}) of external radius R_{ey} ; electrodes are separated by dips of width d_3 . The test mass (of inner radius R_{mi} and potential V_{TM}) surrounds this inner cylinder, and can move about it.

Fifth force stiffness

35

where S is the surface of an electrode (of length L_y).

Noting $e \equiv R_{mi} - R_{ey}$ the gap between the cylinder and the test mass, in the limit $e \ll R_{ey} \sim R_{mi}$, Eq. (C.5) reads

$$C = \frac{1}{4} \left(2\pi - 4 \frac{d_3}{R_{ey}} \right) L_y \epsilon_0 \frac{R_{mi} + R_{ey}}{2e}. \quad (\text{C.7})$$

Appendix C.3. Y electrodes electrostatic stiffness

When moving the test mass by an amount y along the Y -axis, the electrostatic force between the electrodes and the test mass is the sum of the forces between the test mass and the V_{e+} and V_{e-} electrodes, $F = F_+ + F_-$ (so far we consider only one pair of electrodes).

Those forces are, from Eq. (C.2),

$$F_+ = \frac{1}{2} \frac{\partial C_+}{\partial y} (V_{\text{TM}} - V_{e+})^2, \quad (\text{C.8})$$

$$F_- = \frac{1}{2} \frac{\partial C_-}{\partial y} (V_{\text{TM}} + V_{e-})^2, \quad (\text{C.9})$$

with

$$C_{\pm} = \frac{1}{4} \left(2\pi - 4 \frac{d_3}{R_{ey}} \right) L_y \epsilon_0 \frac{R_{mi} + R_{ey}}{2(e \pm y)}. \quad (\text{C.10})$$

The total force is thus

$$F = k' \left[-\frac{(V_{\text{TM}} - V_{e+})^2}{(e + y)^2} + \frac{(V_{\text{TM}} - V_{e-})^2}{(e - y)^2} \right], \quad (\text{C.11})$$

where

$$k' \equiv \frac{1}{16} \left(2\pi - 4 \frac{d_3}{R_{ey}} \right) L_y \epsilon_0 (R_{mi} + R_{ey}). \quad (\text{C.12})$$

Assuming $y \ll e$, the force reads, at first order in y/e ,

$$F = \frac{k'}{e^2} \left[(V_{\text{TM}} - V_{e-})^2 \left(1 + 2 \frac{y}{e} \right) - (V_{\text{TM}} - V_{e+})^2 \left(1 - 2 \frac{y}{e} \right) \right]. \quad (\text{C.13})$$

Keeping only the (stiffness) terms proportional to the displacement y and expanding the square sums, we get

$$F = 2 \frac{k'}{e^3} \left[-2(V_{e+} + V_{e-})V_{\text{TM}} + V_{e-}^2 + V_{e+}^2 + 2V_{\text{TM}}^2 \right] y, \quad (\text{C.14})$$

with [47]

$$\begin{cases} V_{e-} = V_p' - v_y \\ V_{e+} = V_p' + v_y \\ V_{\text{TM}} = V_p + \sqrt{2}V_d \sin \omega_d t, \end{cases} \quad (\text{C.15})$$

Fifth force stiffness

36

of which we take the mean value $\langle V_{\text{TM}} \rangle = V_p$ and $\langle V_{\text{TM}}^2 \rangle = V_p^2 + V_d^2$ (and omit the $\langle \dots \rangle$ symbol hereafter), such that the stiffness contribution to the force is

$$F = 4 \frac{k'}{e^3} [(V_p - V_p')^2 + V_d^2] y. \quad (\text{C.16})$$

Considering now the two pairs of electrodes, and substituting Eq. (C.12) to k' ,

$$F = \frac{1}{2} \left(2\pi - 4 \frac{d_3}{R_{ey}} \right) L_y \epsilon_0 \frac{R_{mi} + R_{ey}}{e^3} [(V_p - V_p')^2 + V_d^2] y. \quad (\text{C.17})$$

Since $R_{mi} \approx R_{ey}$, using the expression for the surface of an electrode (Eq. C.6), we find the expression given in Eq. (13), with $\alpha_y = 0$.

Appendix D. Gravitational force between hollow cylinders

Ref. [67] derives the longitudinal $F_z(r, z)$ and axial $F_r(r, z)$ forces between two hollow cylinders by a Yukawa gravitation. In this appendix, we use those results to complement them with the cases at hand in that paper. Note that contrary to the MICROSCOPE reference frame used in the main text, we use a more intuitive coordinate frame, where the z -axis is along the main axis of the cylinders, so that the natural cylindrical system (r, φ, z) holds. This is the convention of Ref. [67].

The gravitational force created along the z -axis on a unit mass at (r, θ, z) by a hollow cylinder of inner and outer radii a and b , height 2ℓ and density ρ is [67]

$$F_z(r, z) = -2\pi G \alpha \rho \int_0^\infty \frac{J_0(kr) dk}{\kappa} [bJ_1(kb) - aJ_1(ka)] \times \begin{cases} h_2(z; k) & \text{if } -\ell \leq z \leq \ell \\ h_1(z; k) & \text{if } z > \ell \\ h_3(z; k) & \text{if } z < -\ell \end{cases} \quad (\text{D.1})$$

where κ is defined in Eq. (24), with λ the Yukawa interaction range, J_i are Bessel functions of the first kind and the h_i functions depend on the altitude of the unit mass and are defined below ‡. The Newtonian interaction is straightforward to recover by setting $\lambda \rightarrow \infty$ (and $\alpha = 1$).

The corresponding radial force is given by

$$F_r(r, z) = -2\pi G \alpha \rho \int_0^\infty \frac{k J_1(kr) dk}{\kappa^2} [bJ_1(kb) - aJ_1(ka)] \times \begin{cases} h_4(z; k) & \text{if } -\ell \leq z \leq \ell \\ h_1(z; k) & \text{if } z > \ell \\ -h_3(z; k) & \text{if } z < -\ell \end{cases} \quad (\text{D.2})$$

The h_i functions are defined as

$$\begin{aligned} h_1(z; k) &= \exp[-\kappa(z - \ell)] - \exp[-\kappa(\ell + z)] \\ h_2(z; k) &= \exp[-\kappa(\ell - z)] - \exp[-\kappa(\ell + z)] \\ h_3(z; k) &= \exp[\kappa(z - \ell)] - \exp[\kappa(\ell + z)] \\ h_4(z; k) &= 2 - \exp[-\kappa(\ell - z)] - \exp[-\kappa(\ell + z)]. \end{aligned} \quad (\text{D.3})$$

‡ Note that h_1 and h_3 are confused in Ref. [67]

Fifth force stiffness

37

Appendix D.1. Forces on a full cylinder

The forces exerted by the previous cylinder (called the “source”, centered on $(x, y, z) = (0, 0, 0)$) on another full cylinder (called the “target”, centered on $(x_s, 0, z_s)$) of radius a' , height $2L$ and density ρ' , is obtained by integrating Eqs. (D.1) and (D.2) on the volume of the target (at this point in the computation, we do not care whether the geometry is physically sound –i.e. cylinders may overlap; this will be done below):

$$\mathcal{F}_z(x_s, z_s) = \rho' \iint dx dy \int_{z_{\min}}^{z_{\max}} dz F_z(r, z), \quad (\text{D.4})$$

and similarly for $\mathcal{F}_r(x_s, z_s)$, where, for convenience, we express the volume in Cartesian coordinates (though we will quickly return to cylindrical coordinates below), with $r = \sqrt{x^2 + y^2}$. The z -integral is taken from the base z_{\min} to the top z_{\max} of the target cylinder, and the (x, y) -integral is taken over the disk section of the cylinder. We explicit them below.

Appendix D.1.1. z -integral $F_z(r, z)$ and $F_r(r, z)$ depend on z only through the h_i functions, so it is enough to compute $H_i(k) = \int_{z_{\min}}^{z_{\max}} h_i(z; k) dz$. Several cases depending on the position of the target with respect to the source must be considered:

- (i) Target’s z -extend fully contained in source’s z -extend: in this case, $z_s - L > -\ell$ and $z_s + L < \ell$, and only h_2 and h_4 are defined. Their integrals are straightforward to compute, with $z_{\min} = z_s - L$ and $z_{\max} = z_s + L$:

$$H_2(z_s, k) = \frac{4e^{-\kappa\ell}}{\kappa} \sinh(\kappa L) \sinh(\kappa z_s) \quad (\text{D.5})$$

and

$$H_4(z_s, k) = 4L - \frac{4e^{-\kappa\ell}}{\kappa} \sinh(\kappa L) \cosh(\kappa z_s). \quad (\text{D.6})$$

- (ii) Target’s z -extend fully covering source’s z -extend ($z_s - L < -\ell$ and $z_s + L > \ell$): in this case, all h_i are defined, and

$$H_1(z_s, k) = -\frac{2}{\kappa} (e^{-\kappa(z_s+L)} - e^{-\kappa\ell}) \sinh(\kappa\ell), \quad (\text{D.7})$$

$$H_3(z_s, k) = -\frac{2}{\kappa} (e^{-\kappa\ell} - e^{\kappa(z_s-L)}) \sinh(\kappa\ell), \quad (\text{D.8})$$

$$H_4(z_s, k) = 4\ell - 4\frac{e^{-\kappa\ell}}{\kappa} \sinh(\kappa\ell) \quad (\text{D.9})$$

and $H_2(z_s, k) = 0$ by symmetry.

- (iii) Target fully above source ($z_s - L > \ell$): in this case, only h_1 is defined and

$$H_1(z_s, k) = \frac{4e^{-\kappa z_s}}{\kappa} \sinh(\kappa\ell) \sinh(\kappa L). \quad (\text{D.10})$$

Fifth force stiffness

38

(iv) Target fully below source ($z_s + L < -\ell$): in this case, only h_3 is defined and

$$H_3(z_s, k) = -\frac{4e^{\kappa z_s}}{\kappa} \sinh(\kappa\ell) \sinh(\kappa L). \quad (\text{D.11})$$

(v) Other cases correspond to the target's and the source's z -extend overlapping, with none completely covering the other. Since they are not of use in MICROSCOPE, we do not consider them here.

Appendix D.1.2. (x, y) -integral With no loss of generality, we can set the target cylinder on $(x_s, y_s) = (x_s, 0)$ in the (x, y) -plane ($y_s \neq 0$ cases are recovered by a simple rotation). For an arbitrary function f ,

$$\iint dx dy f(x, y) = \int_{\theta_-}^{\theta_+} d\theta \int_{R_-(\theta)}^{R_+(\theta)} r dr f(r, \theta), \quad (\text{D.12})$$

where the integration boundaries depend on the geometry of the problem. Let us assume that the disk over which we take the integral is centered on $(x_s, y_s) = (x_s, 0)$ and has a radius a (not to be confused with the radius of the source –which is of no use here).

(i) $|x_s| > a$

This case is illustrated by the left panel of Fig. D1. It is easy to show that the θ integral runs from $\theta_- = -\arcsin(a/|x_s|)$ to $\theta_+ = \arcsin(a/|x_s|)$. For a given θ in that domain, the r -integration then runs from $R_-(\theta)$ to $R_+(\theta)$ which are solutions of the quadratic equation

$$R^2 - 2x_s R \cos \theta + x_s^2 - a^2 = 0, \quad (\text{D.13})$$

and are given by

$$R_{\pm}(\theta) = x_s \cos \theta \pm \sqrt{a^2 - x_s^2 \sin^2 \theta}. \quad (\text{D.14})$$

(ii) $|x_s| \leq a$

In this case, shown in the right panel of Fig. D1, the θ boundaries are trivially $\theta_- = 0$ and $\theta_+ = 2\pi$. It is also trivial that for a given θ , $R_-(\theta) = 0$. Finally, it can be shown that the upper r -boundary is the same as that of the previous case, $R_+(\theta) = x_s \cos \theta + \sqrt{a^2 - x_s^2 \sin^2 \theta}$.

Appendix D.1.3. Longitudinal and radial forces Noting that the r -dependence of the $\mathcal{F}_z(x_s, z_s)$ force appears only in the J_0 Bessel function, and using Eq. (D.1) we re-write Eq. (D.4) as

$$\mathcal{F}_z(x_s, z_s) = -2\pi G \rho \rho' \alpha \int_0^\infty \frac{K_z(k)}{\kappa} [bJ_1(kb) - aJ_1(ka)] [H_1(z_s, k) + H_2(z_s, k) + H_3(z_s, k)] dk, \quad (\text{D.15})$$

where we abusively sum the H_i functions (setting them to 0 outside their definition range).

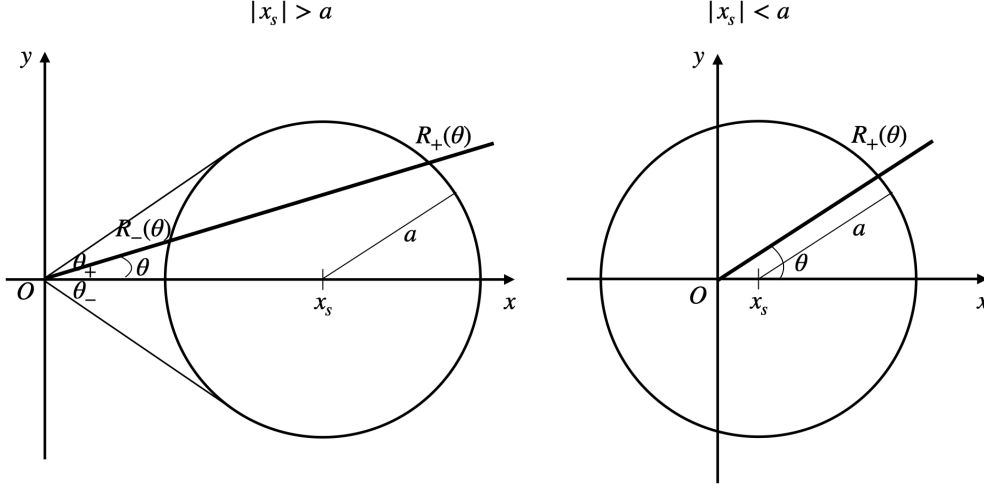


Figure D1. (x, y) -integration geometry.

Since all cylinders of a given MICROSCOPE's sensor unit are co-axial, we consider only the $|x_s| \leq a$ case in this paper, so that the (x, y) -integration is

$$K_z(k) = \int_0^{2\pi} d\theta \int_0^{R_+(\theta)} J_0(kr) dr, \quad (\text{D.16})$$

and we note that

$$I_z(k, \theta) \equiv \int_0^{R_+(\theta)} r J_0(kr) dr = \frac{R_+(\theta) J_1[kR_+(\theta)]}{k}. \quad (\text{D.17})$$

Similarly, the radial force

$$\mathcal{F}_r(x_s, z_s) = -2\pi G \rho \rho' \alpha \int_0^\infty \frac{K_r(k)}{\kappa} [bJ_1(kb) - aJ_1(ka)] [H_1(z_s, k) + H_4(z_s, k) - H_3(z_s, k)] dk, \quad (\text{D.18})$$

with

$$K_r(k) = \int_0^{2\pi} \cos \theta d\theta \int_0^{R_+(\theta)} kr J_1(kr) dr, \quad (\text{D.19})$$

and

$$\begin{aligned} I_r(k, \theta) &\equiv \int_0^{R_+(\theta)} kr J_1(kr) dr \\ &= \frac{\pi}{2} \{R_+(\theta) J_1[kR_+(\theta)] H_0[kR_+(\theta)] - R_+(\theta) J_0[kR_+(\theta)] H_1[kR_+(\theta)]\}, \end{aligned} \quad (\text{D.20})$$

where H_0 and H_1 are Struve functions (not to be confused with the previous H_i functions).

Without any further assumptions, we cannot integrate Eqs. (D.16) and (D.19) over θ analytically, and we end up with a 2D integral for the force between the two

Fifth force stiffness

40

cylinders. We show below that in the limit of small displacements, we can integrate them analytically. Nevertheless, in the general case, the θ integrations are easily performed numerically.

Appendix D.1.4. Small displacements limit: longitudinal force We assume that the target cylinder (of radius a') moves about a “reference” position $(\bar{x}, 0, \bar{z})$, with a small displacement δ along the z -axis. Assuming that $\bar{x} \ll a'$, at first order in \bar{x}/a' ,

$$I_z(k, \theta) \approx a' \frac{J_1(ka')}{k} + a' J_0(ka') \cos \theta \bar{x}, \quad (\text{D.21})$$

so that

$$K_z(k) \approx 2\pi \frac{a' J_1(ka')}{k}. \quad (\text{D.22})$$

Noting $z_s = \bar{z} + \delta$ the altitude of the target’s center, and expanding the H_i functions in the limit of small δ , taking care of their definition ranges of Sect. Appendix D.1.1, we find that the longitudinal force created on the cylinder of radius a' is, at 3rd order:

- (i) if $\bar{z} \ll (\ell, L)$ and $\ell > L$ (target’s z -extend fully covered by that of the source):

$$\mathcal{F}_z(\bar{z}, \delta) \approx -16\pi^2 G \rho \rho' \alpha (K_1 \delta + K_3 \delta^3), \quad (\text{D.23})$$

where

$$K_1 = \int_0^\infty \frac{a' J_1(ka') [b J_1(kb) - a J_1(ka)]}{\kappa k} e^{-\kappa \ell} \sinh(\kappa L) dk \quad (\text{D.24})$$

and

$$K_3 = \int_0^\infty \frac{\kappa a' J_1(ka') [b J_1(kb) - a J_1(ka)]}{6k} e^{-\kappa \ell} \sinh(\kappa L) dk \quad (\text{D.25})$$

- (ii) if $\bar{z} \ll (\ell, L)$ and $\ell < L$ (source’s z -extend fully covered by that of the target): the force is formally identical to that of the previous case, with ℓ and L switching roles.
 (iii) if $|\bar{z}| > \ell + L$ (cylinders above each other):

$$\mathcal{F}_z(\bar{z}, \delta) \approx 16\pi^2 G \rho \rho' \alpha (K_0 + K_1 \delta + K_2 \delta^2 + K_3 \delta^3), \quad (\text{D.26})$$

with

$$K_0 = -\frac{\bar{z}}{|\bar{z}|} \int_0^\infty \frac{a' J_1(ka') [b J_1(kb) - a J_1(ka)]}{\kappa^2 k} e^{-\kappa |\bar{z}|} \sinh(\kappa \ell) \sinh(\kappa L) dk, \quad (\text{D.27})$$

$$K_1 = \int_0^\infty \frac{a' J_1(ka') [b J_1(kb) - a J_1(ka)]}{\kappa k} e^{-\kappa |\bar{z}|} \sinh(\kappa \ell) \sinh(\kappa L) dk, \quad (\text{D.28})$$

$$K_2 = -\frac{\bar{z}}{|\bar{z}|} \int_0^\infty \frac{a' J_1(ka') [b J_1(kb) - a J_1(ka)]}{2k} e^{-\kappa |\bar{z}|} \sinh(\kappa \ell) \sinh(\kappa L) dk, \quad (\text{D.29})$$

and

$$K_4 = \int_0^\infty \frac{\kappa}{6k} a' J_1(ka') [b J_1(kb) - a J_1(ka)] e^{-\kappa |\bar{z}|} \sinh(\kappa \ell) \sinh(\kappa L) dk, \quad (\text{D.30})$$

Fifth force stiffness

41

Appendix D.1.5. Small displacements limit: radial force We assume that the target cylinder (of radius a') moves about a “reference” position $(\bar{x}, 0, \bar{z})$, with a small displacement δ along the X -axis. Assuming that $\bar{x} \ll a'$, at 3rd order in δ/a' ,

$$\begin{aligned} I_r(k, \theta) \approx & \frac{\pi a'}{2} [J_1(ka')H_0(ka') - J_0(ka')H_1(ka')] + ka' J_1(ka') \cos \theta \delta \\ & + \frac{k}{2} [ka' J_0(ka') \cos^2 \theta - J_1(ka') \sin^2 \theta] \delta^2 \\ & + \frac{k^2}{6} [J_0(ka') \cos(3\theta) - ka' J_1(ka') \cos^3 \theta] \delta^3, \end{aligned} \quad (\text{D.31})$$

so that

$$K_r(k) \approx \pi ka' J_1(ka') \delta - \frac{\pi k^2}{8} ka' J_1(ka') \delta^3. \quad (\text{D.32})$$

The radial force created on the cylinder of radius a' is thus, at 3rd order

$$\mathcal{F}_r(\bar{z}, \delta) \approx -2\pi^2 G \rho \rho' \alpha (K_1 \delta + K_3 \delta^3), \quad (\text{D.33})$$

where, in the definition ranges of Sect. Appendix D.1.1:

(i) if $\bar{z} \ll (\ell, L)$ and $\ell > L$ (target’s z -extend fully covered by that of the source):

$$K_1 = 4 \int_0^\infty \frac{ka' J_1(ka') [bJ_1(kb) - aJ_1(ka)]}{\kappa^2} \left[L - \frac{e^{-\kappa \ell}}{\kappa} \sinh(\kappa L) \cosh(\kappa \bar{z}) \right] dk \quad (\text{D.34})$$

and

$$K_3 = - \int_0^\infty \frac{k^3 a' J_1(ka') [bJ_1(kb) - aJ_1(ka)]}{\kappa^2} \left[L - \frac{e^{-\kappa \ell}}{\kappa} \sinh(\kappa L) \cosh(\kappa \bar{z}) \right] dk \quad (\text{D.35})$$

(ii) if $\bar{z} \ll (\ell, L)$ and $\ell < L$ (source’s z -extend fully covered by that of the target): the force is formally identical to that of the previous case, with ℓ and L switching roles.

(iii) if $|\bar{z}| > \ell + L$ (cylinders above each other):

$$K_1 = 4 \int_0^\infty \frac{ka' J_1(ka') [bJ_1(kb) - aJ_1(ka)]}{\kappa^2} \frac{e^{-\kappa |\bar{z}|}}{\kappa} \sinh(\kappa \ell) \sinh(\kappa L) dk \quad (\text{D.36})$$

$$K_3 = - \int_0^\infty \frac{k^3 a' J_1(ka') [bJ_1(kb) - aJ_1(ka)]}{\kappa^2} \frac{e^{-\kappa |\bar{z}|}}{\kappa} \sinh(\kappa \ell) \sinh(\kappa L) dk \quad (\text{D.37})$$

Appendix D.2. Forces between hollow cylinders

We finally come back to the problem at hand: the gravitational force between the two hollow cylinders defined at the beginning of this appendix. By virtue of the superposition principle, it is given by subtracting the force between the hollow source cylinder and two full target cylinders of radii a and b . Thus, in the limit of small displacements, the longitudinal and radial forces are formally given by Eqs. (D.23), (D.26) and (D.33), with the K_i coefficients given below (they are obviously identical to those given in the main text in the MICROSCOPE coordinates system, where the x and z -axes are inverted).

Fifth force stiffness

42

Appendix D.2.1. Longitudinal force

(i) if $\bar{z} \ll (\ell, L)$ and $\ell > L$ (target's z -extend fully covered by that of the source):

$$\mathcal{F}_z(\bar{z}, \delta) \approx -16\pi^2 G \rho \rho' \alpha (K_1 \delta + K_3 \delta^3), \quad (\text{D.38})$$

where

$$K_1 = \int_0^\infty \frac{[b' J_1(kb') - a' J_1(ka')][b J_1(kb) - a J_1(ka)]}{\kappa k} e^{-\kappa \ell} \sinh(\kappa L) dk \quad (\text{D.39})$$

$$K_3 = \int_0^\infty \frac{\kappa [b' J_1(kb') - a' J_1(ka')][b J_1(kb) - a J_1(ka)]}{6k} e^{-\kappa \ell} \sinh(\kappa L) dk \quad (\text{D.40})$$

(ii) if $\bar{z} \ll (\ell, L)$ and $\ell < L$ (source's z -extend fully covered by that of the target): the force is formally identical to that of the previous case, with ℓ and L switching roles.

(iii) if $|\bar{z}| > \ell + L$ (cylinders above each other):

$$\mathcal{F}_z(\bar{z}, \delta) \approx 16\pi^2 G \rho \rho' \alpha (K_0 + K_1 \delta + K_2 \delta^2 + K_3 \delta^3), \quad (\text{D.41})$$

with

$$K_0 = -\frac{\bar{z}}{|\bar{z}|} \int_0^\infty \frac{[b' J_1(kb') - a' J_1(ka')][b J_1(kb) - a J_1(ka)]}{\kappa^2 k} e^{-\kappa |\bar{z}|} \sinh(\kappa \ell) \sinh(\kappa L) dk \quad (\text{D.42})$$

$$K_1 = \int_0^\infty \frac{[b' J_1(kb') - a' J_1(ka')][b J_1(kb) - a J_1(ka)]}{\kappa k} e^{-\kappa |\bar{z}|} \sinh(\kappa \ell) \sinh(\kappa L) dk \quad (\text{D.43})$$

$$K_2 = -\frac{\bar{z}}{|\bar{z}|} \int_0^\infty \frac{[b' J_1(kb') - a' J_1(ka')][b J_1(kb) - a J_1(ka)]}{2k} e^{-\kappa |\bar{z}|} \sinh(\kappa \ell) \sinh(\kappa L) dk \quad (\text{D.44})$$

$$K_4 = \int_0^\infty \frac{\kappa}{6k} [b' J_1(kb') - a' J_1(ka')][b J_1(kb) - a J_1(ka)] e^{-\kappa |\bar{z}|} \sinh(\kappa \ell) \sinh(\kappa L) dk, \quad (\text{D.45})$$

Appendix D.2.2. Radial force

$$\mathcal{F}_r(\bar{z}, \delta) \approx -2\pi^2 G \rho \rho' \alpha (K_1 \delta + K_3 \delta^3), \quad (\text{D.46})$$

(i) if $\bar{z} \ll (\ell, L)$ and $\ell > L$ (target's z -extend fully covered by that of the source):

$$K_1 = 4 \int_0^\infty \frac{k [b' J_1(kb') - a' J_1(ka')][b J_1(kb) - a J_1(ka)]}{\kappa^2} \left[L - \frac{e^{-\kappa \ell}}{\kappa} \sinh(\kappa L) \cosh(\kappa \bar{z}) \right] dk \quad (\text{D.47})$$

$$K_3 = - \int_0^\infty \frac{k^3 [b' J_1(kb') - a' J_1(ka')][b J_1(kb) - a J_1(ka)]}{\kappa^2} \left[L - \frac{e^{-\kappa \ell}}{\kappa} \sinh(\kappa L) \cosh(\kappa \bar{z}) \right] dk \quad (\text{D.48})$$

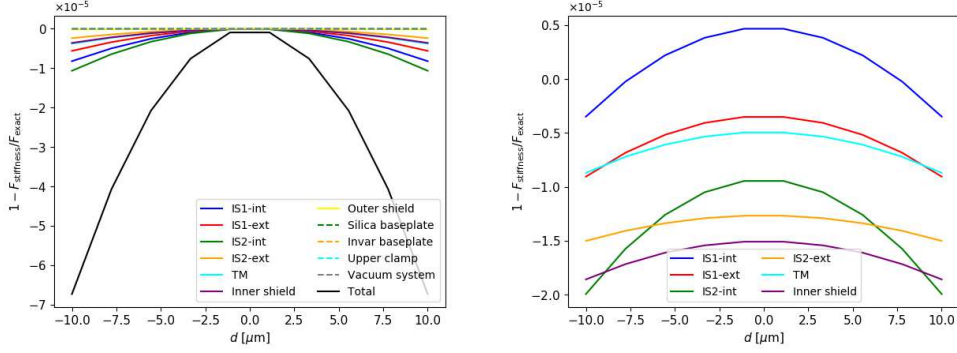


Figure D2. Relative difference between the exact expression (D.2) and its first order Taylor expansion (first term of Eq. D.46) for the radial force created by the parts of MICROSCOPE’s SUEP on the inner test mass, as a function of the displacement of the test mass. Left: Newtonian force. Right: Yukawa force, for $(\alpha, \lambda) = (1, 0.01 \text{ m})$; only those cylinders which create a non-negligible Yukawa force allowing for a well-behaved $F_{\text{stiffness}}/F_{\text{exact}}$ ratio are shown.

- (ii) if $\bar{z} \ll (\ell, L)$ and $\ell < L$ (source’s z -extend fully covered by that of the target): the force is formally identical to that of the previous case, with ℓ and L switching roles.
- (iii) if $|\bar{z}| > \ell + L$ (cylinders above each other):

$$K_1 = 4 \int_0^\infty \frac{k[b'J_1(kb') - a'J_1(ka')][bJ_1(kb) - aJ_1(ka)]}{\kappa^2} \frac{e^{-\kappa|\bar{z}|}}{\kappa} \sinh(\kappa\ell) \sinh(\kappa L) dk \quad (\text{D.49})$$

$$K_3 = - \int_0^\infty \frac{k^3[b'J_1(kb') - a'J_1(ka')][bJ_1(kb) - aJ_1(ka)]}{\kappa^2} \frac{e^{-\kappa|\bar{z}|}}{\kappa} \sinh(\kappa\ell) \sinh(\kappa L) dk \quad (\text{D.50})$$

Appendix D.3. MICROSCOPE gravitational stiffness

Fig. D2 shows the relative difference between the exact expression (D.2) and its first order Taylor expansion (first term of Eq. D.46) for the radial force created by the parts of MICROSCOPE’s SUEP on the inner test mass, when the test mass moves within the range used to estimate the stiffness in flight. A first order approximation provides a 10^{-5} accuracy on the gravitational forces, and can thus be safely used.

5.2 Use for constraining chameleon gravity

5.2.1 Introduction and summary

This article is dedicated to obtain equivalent constraints, using the MICROSCOPE's stiffness measurement sessions, for the chameleon field. We proceed exactly the same way as for the Yukawa interaction. We compute the chameleonic stiffness we showed to exist in Chapter 4, and compare it to the discrepancy observed on the MICROSCOPE's stiffness in the previous section.

Computing this stiffness requires the numerical methods we developed in Chapter 4. We modify it to include more cylinders and the correct physical parameters associated to the MICROSCOPE geometry. To span the larger part of the parameter space of chameleon field, we use numerous 1D and 2D methods. This is justified by the fact that we show that these two types of methods provide the same order of magnitude on the acceleration for a test mass. As in the Yukawa case, we obtain constraints by comparing the result of our simulation and the stiffness discrepancy from Tab. 3 of the previous article. The obtained constraints are shown not to be competitive with current constraints and are 2 orders of magnitude looser.

5.2.2 Article

Constraints on chameleon gravity from the measurement of the electrostatic stiffness of the MICROSCOPE mission accelerometers

Martin Pernot-Borràs,^{1,2,*} Joel Bergé,¹ Philippe Brax,³ Jean-Philippe Uzan,^{2,4} Gilles Métris,⁵ Manuel Rodrigues,¹ and Pierre Touboul¹

¹*DPHY, ONERA, Université Paris Saclay, F-92322 Châtillon, France*

²*Institut d'Astrophysique de Paris, CNRS UMR 7095, Université Pierre & Marie Curie - Paris VI, 98 bis Bd Arago, 75014 Paris, France*

³*Institut de Physique Théorique, Université Paris-Saclay, CEA, CNRS, F-91191 Gif-sur-Yvette Cedex, France*

⁴*Sorbonne Universités, Institut Lagrange de Paris, 98 bis, Bd Arago, 75014 Paris, France*

⁵*Université Côte d'Azur, Observatoire de la Côte d'Azur, CNRS,*

IRD, Géozur, 250 avenue Albert Einstein, F-06560 Valbonne, France

(Dated: today)

This article is dedicated to the use the MICROSCOPE mission's data to test chameleon theory of gravity. We take advantage of the technical sessions aimed to characterize the electrostatic stiffness of MICROSCOPE's instrument intrinsic to its capacitive measurement system. Any discrepancy between the expected and measured stiffness may result from unaccounted-for contributors, i.e. extra-forces. This work considers the case of chameleon gravity as a possible contributor. It was previously shown that in situations similar to these measurement sessions, a chameleon fifth force appears and acts as a stiffness for small displacements. The magnitude of this new component of the stiffness is computed over the chameleon's parameter space. It allows us to derive constraints by excluding any force inconsistent with the MICROSCOPE data. As expected –since MICROSCOPE was not designed for the purpose of such an analysis–, these new bounds are not competitive with state-of-the-art constraints, but they could be improved by a better estimation of all effects at play in these sessions. Hence our work illustrates this novel technique as a new way of constraining fifth forces.

I. INTRODUCTION

This article follows up from a series of articles [1–3] aiming to test modified gravity theories with data from the MICROSCOPE mission. This mission provided the tightest constraint to date on the weak equivalence principle (WEP) [4, 5]. Its instrument is based on a couple of accelerometers measuring the differential acceleration of two cylindrical test masses of different compositions. It contains four test masses: two cylinders of different composition in the SUEP (Equivalence Principle test Sensor Unit) sensor unit that is used to perform the WEP test and two cylinders of same composition in the SUREF (Reference Sensor Unit) sensor unit used as a reference. In Ref. [6], we directly used the WEP test results to improve the current constraints on the existence of un-screened scalar fifth forces, a massive Yukawa fifth force and a light dilaton field [7].

In Ref. [8], we proposed a new way of testing such theories by using sessions dedicated to measuring the electrostatic stiffness inherent to the capacitive measurement system of MICROSCOPE. An electrostatic destabilizing force appears when a test mass is displaced from its rest position: in the limit of small displacements it is a linear dependence. We call *stiffness* its associated linear factor. It has been measured by deliberately displacing each test mass separately with an amplitude of 5 μm . The

result of this series of tests has been compared to electrostatic models and a discrepancy has been pinpointed [9]. In Ref. [8], we modeled the total stiffness and studied all possible sources of forces to explain this discrepancy. They consist of mainly: (1) the satellite Newtonian self-gravity and (2) the stiffness of a 7- μm -thick-gold-wire used to control the electrical potential of the test masses that acts as a spring. We found that the contribution of the former is sub-dominant. After determining the parameters of the latter to evaluate its contribution to the stiffness, we found an unexplained residual component that depends on the electrical configuration, hinting at patch field effects. We nonetheless considered the possibility that this discrepancy may originate from modified gravity fifth forces sourced by the satellite and experimental apparatus. We have already [8] been able to set constraints on a Yukawa-like interaction by excluding any parameters of the interaction that lead to a stiffness larger than the discrepancy. As expected, since MICROSCOPE was not originally designed to such a test –leading to a loose estimation of the gold-wire-stiffness for instance–, the constraints are not competitive with state-of-the-art constraints but it opens a possible novel way of testing fifth force and demonstrate that its effect has to be modeled in details at each step of the experiment.

This article aims to extend this analysis to the chameleon gravity model [10, 11]. Unlike Yukawa model, this scalar field enjoys a screening mechanism that makes its fifth force more sensitive to the matter environment

* martin.pernot_borras@onera.fr

and more subtle to compute. We use the numerical methods developed in Refs. [1, 2] to compute the chameleon profile associated to a geometry of nested cylinders. In these articles, we studied the case of dis-centering one of the cylinders and showed that it should experience a chameleonic force acting as a stiffness for small displacements. Its magnitude depends on the geometrical parameters of the cylinders and on the parameters of the chameleon theory. This study was performed for only two nested cylinders. Here, we extend this methods to compute the field and the force associated to the geometry of the MICROSCOPE's instrument with the proper geometrical parameters. Each sensor unit is composed of eight cylinders: two cylindrical test mass cylinders, each of which is surrounded by two electrode cylinders; and two ferrule cylinders encompassing all the six cylinders [5]. The end of these ferrules are closed by two "lids" that we do not consider in this study.

This article is organized as follows. In Section II, we detail the methods used to compute the chameleon stiffness, and more particularly the necessity of different approximations for the different regimes of the chameleon gravity. In Section III, we present the constraints obtained by combining the results of these computations and the analysis of the MICROSCOPE stiffness measurement sessions from Ref. [8]. To finish, in Section IV, we discuss our results and the limits of this new approach.

II. CHAMELON STIFFNESS

A. Methods

We use three different methods to compute the chameleon stiffness depending on the regimes of the chameleon field. These regimes occur for the MICROSCOPE geometry for different zones of the chameleon parameter space [1]. The chameleon field is parameterized by three parameters: its coupling constant to matter β , and the energy scale Λ and index n of its inverse-power law potential. We can distinguish three main regimes: the *screened regime* in which a test mass and the two electrode cylinders surrounding it can be considered as an isolated system due to the fact that the electrode cylinders screen the field; a *deeply screened regime* in which the screening of the test mass is too deep to compute the profile associated to three cylinders and instead we need to consider it as two separate pairs of screened cylinders; and a *unscreened regime* in which the field penetrates all cylinders so that all of them must be taken into account when computing the field profile. Let us detail the computation techniques used in each regime.

a. Screened regime. This regime appears when the Compton wavelengths of the field in the cylinders are of the order of a twentieth of their thickness. It can be addressed by using the semi-analytic 2D model we developed in Ref. [2]. This method was initially applied to two cylinders. Here, we modify it to include a third

one. We impose the boundary conditions in the two external cylinders in such a way that the field must reach the minimum of the potentials associated to their densities. We displace the central test mass cylinder and solve the field's multipole from which we compute the force.

b. Deeply screened regime. This regime occurs when the Compton wavelengths are smaller than a twentieth of the cylinder's thickness. In this regime the screening of the test mass makes it impossible to use the previous method, as the value of the field reached deep in the test mass is so close to the value that minimizes its potential, that it is smaller than the typical numerical precision of a computer. We instead use a 1D method, and consider the three cylinders as two distinct pairs of screened parallel walls. To mimic two opposite sides of the cylinders, we consider two such systems. This 1D approximation is justified by the fact that we showed, in Ref. [2], that the chameleonic force computed in these planar and cylindrical configurations lead to the order of magnitude for the acceleration experienced by a test mass. We thus postulate, for these analogous situations, that the test masses' accelerations verify $a_{2D} = \alpha a_{1D}$, where α is a geometrical factor that is expected to be of order unity.

From this equality, by using Newton's law, one can obtain a relation between the surface force $F_{s,1D}$ experienced by the two walls in a planar configuration and the force per unit length $F_{l,2D}$ experienced by a cylinder in the corresponding 2D configuration. The ratio of masses leads to the ratio of the wall thicknesses and the transverse section area of the cylinder in the relation

$$F_{l,2D} \approx \alpha \frac{\pi [(d+e)^2 - d^2]}{2e} F_{s,1D}, \quad (1)$$

where d and e are respectively the internal radius and the thickness of the test mass cylinder. The value of α is discussed in Fig. 1 and below.

c. Unscreened regime. This regime takes place when the Compton wavelengths of the field in the cylinders are larger than their thicknesses. In this case the boundary conditions must be set at some distance much larger than the Compton wavelength associated to the density outside the cylinders. In this regime, this Compton wavelength is likely to be so large that one must perform large steps in terms of the numerical resolution in this zone, hence losing the accuracy on the result. To overcome this issue we again addressed this regime with a 1D resolution. In a 1D problem, as discussed in Ref. [1], the chameleon equation can indeed be integrated once in the region external to the cylinders and obtain, at the boundary of the external cylinder, a condition $\phi'[\phi(x_b)]$ giving the field derivative as a function of the field value that leads the boundary conditions to be respected far from it. We can use this condition to perform a dichotomy method to adjust the initial condition of our numerical method. We proceed in the same way as the case of asymmetrical parallel walls in Ref. [2], with the difference that instead of using for the dichotomy method the verification at some large distance from the cylinders that

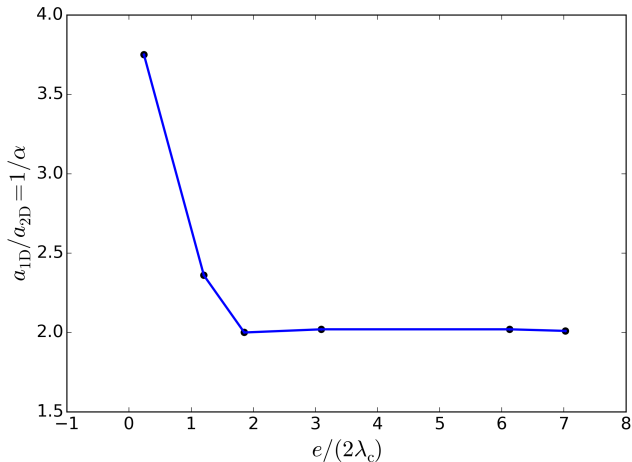


FIG. 1. Result of the comparison of the acceleration experienced by a test mass in planar and cylindrical configurations in different regimes of screening quantified by $\frac{e}{2\lambda_c}$, where e is the thickness of the cylinder and λ_c the Compton wavelength of the field associated to it.

the boundary conditions are respected, we check that the aforementioned condition is verified at the boundary of the outer cylinder. These two conditions are equivalent but the latter allows us to bypass solving the field in the external region.

Similarly to the previous regime, in this 1D resolution, to mimic two opposite radial directions of a 8-nested-cylinder-configuration, we consider a set of 16 parallel walls. In this 1D configuration a test mass is represented by two of these walls. We again use Eq. (1) to compute the corresponding 2D force. Note that due to the symmetry breaking by the shifting of the walls, the initial conditions cannot be set at the center of the 16 walls but instead at a slightly shifted location that we determine similarly as in Ref. [2].

To evaluate α in Eq. (1), we compare the forces computed in 1D and 2D. This requires to extend the method used in the screened regime to the other regimes. To overcome the problem encountered in these regimes, we considered an unrealistic configuration of 3 cylinders of same density with a external vacuum much denser than the vacuum of space. This allows us to avoid the numerical resolution issue encountered in the unscreened regime. Even if unrealistic, it allows us to quantify the geometrical factor between planar and cylindrical geometries, that we expect to be independent of the densities.

As depicted in Fig.1, the numerical comparison strongly hints at $\alpha = 1/2$, a value reached in most of the screening range but that appears to be smaller for unscreened situations. We interpret this latter behavior as the 2D method reaching its limits and we instead expect $\alpha = 1/2$ also this regime. This is justified by the longer Compton wavelength in this regime, that leads the

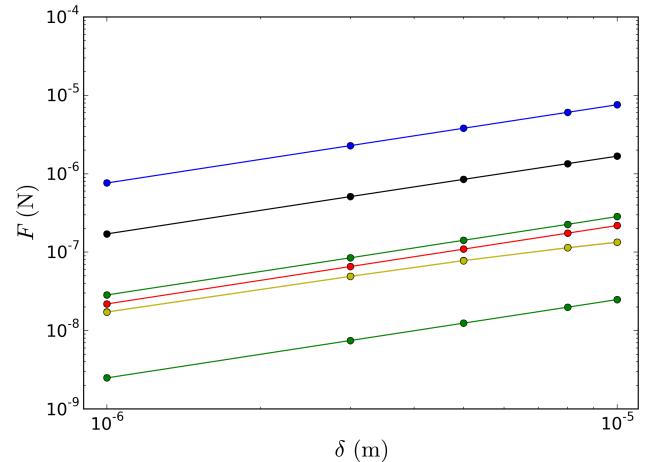


FIG. 2. Scaling of the chameleon fifth force as a function of the displacement in the range $\delta = 1 \dots 10 \mu\text{m}$ for different set of parameters (Λ, β) assuming $n = 1$. Λ are chosen in the range $10^{-1} - 3 \times 10^2$ eV and β in the range $6 - 10^7$. This shows that $\log F = \log k_{\text{chameleon}}(\Lambda, \beta) + \log \delta$ is a good approximation to the behavior of the force at small displacements. We use a log-log plot for convenience but it is easily checked that the slope is unity so that linearity is confirmed.

field's gradient to vary slowly within the cylinder. By approximating this gradient by the one obtained in planar situations, one directly obtains Eq.(1) with $\alpha = 1/2$ ¹. Hence we choose to generalize this result to all regimes in our present study.

B. Results

First, we check numerically that the force is linear for small displacements. As shown in Ref. [2], this is expected to be the case even though the theory is non-linear. Figure 2 depicts the behavior of $F(\delta)$ in the range $\delta = 1 \dots 10 \mu\text{m}$ relevant for our study. Besides, we know that by symmetry $F(0) = 0$. Hence it confirms that in this range of displacements it is safe to model the chameleon fifth force by a stiffness $k_{\text{chameleon}}(\Lambda, \beta)$ (measured in N.m^{-1}) so that

$$F = k_{\text{chameleon}}(\Lambda, \beta) \times \delta + \mathcal{O}(\delta^2). \quad (2)$$

Even though one can witness a small deviation of this linear relation for $\delta \sim 10 \mu\text{m}$ for the largest values of Λ ,

¹ The origin of this value comes from the fact that while for planar situations all parts of a wall are submitted to a force, for cylindrical configurations, only the parts of the cylinder that are closer to the axis of displacement contribute to the acceleration. This is due to the projection of the force that is mainly radially directed and to the effective radial displacement of the cylinder that varies with the cylindrical angle.

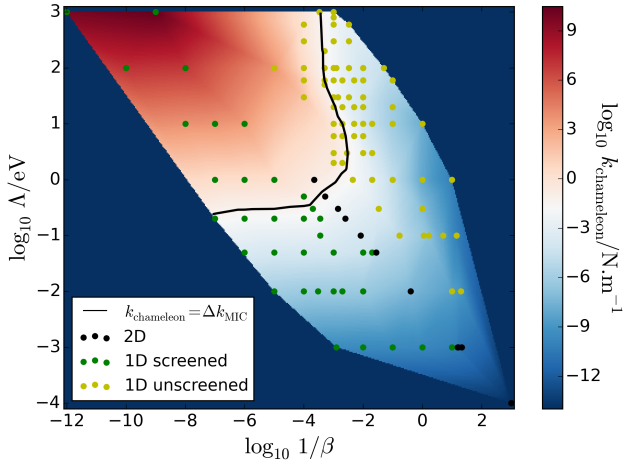


FIG. 3. Evolution with the parameters β and Λ of the chameleonic stiffness $k_{\text{chameleon}}$ of the external test mass of the sensor unit SUEP from the MICROSCOPE mission for $n = 1$. Its magnitude is shown by the background colors. This function is obtained by linearly interpolating the data points. These points are the result of the three numerical methods discussed in the main text that are here distinguished by different points of colors. This is represented in log-scale for β , Λ , $k_{\text{chameleon}}$. The black line is the contour line at which the stiffness is equal to the measured $2\text{-}\sigma$ uncertainty on the discrepancy Δk_{MIC} in the MICROSCOPE experiment.

these results comfort us in the linearity assumption in the range of displacements compatible with the MICROSCOPE data we are using and the parameter space we consider.

Then, we present the numerical results in Fig. 3. We computed the chameleonic stiffness $k_{\text{chameleon}}(\Lambda, \beta)$ experienced by a test mass when displaced radially by $1\ \mu\text{m}$. This figure shows the result for SUEP-IS2, the external test mass of SUEP. We spanned the parameter space (β, Λ) for $n = 1$, we denote each computation by a point with a color code that labels which of the three method were used. To obtain the continuous evolution of the stiffness with (β, Λ) , we performed a linear interpolation of the simulation points in log-scale. We show with the black solid line, the contour line at which the obtained chameleonic stiffness equals the $2\text{-}\sigma$ uncertainty on the discrepancy Δk_{MIC} on the stiffness measured in the MICROSCOPE sessions as presented in Ref. [8]. This latter article presents two distinct estimations over two perpendicular radial axis of the cylinder; the chameleonic stiffness being expected to be the same over these axes, we choose to average these two estimations and quadratically average the error bars.

III. CONSTRAINTS ON THE CHAMELEON'S PARAMETERS

The results shown in Fig. 3 mean that above the black line the chameleonic stiffness is too large to explain the observed stiffness residual in MICROSCOPE. This stiffness could be compatible with these measurements, if a stabilizing stiffness of the same magnitude were to exist. Nevertheless standard physics combined with our understanding of the instrument do not provide any such contribution. Thence we interpret these results as excluding the existence of a chameleon field for these parameters. Below the black line, the chameleonic stiffness is within the error bars of the observed discrepancy so that we cannot exclude its existence.

Note that we have not been able to span the whole parameter space. Our methods are unable to determine the stiffness for large β and Λ . We expect this to be caused by the fact that the field magnitude becomes so large that our numerical precision fails at describing the gradient in the test mass. Thus, the force vanishes. Nevertheless we can guess the behavior of the stiffness in these unexplored regions. For very large Λ , the field tends to be completely unscreened such that we expect it to converge towards a flat field providing a lower force. For very large β , on the contrary, the field tends to be more screened. At some point we expect the field to be able to reach the minimum of its potential in the inter-cylinder vacuum gaps, such that the cylinders would not interact through the scalar field anymore. In this case the field is equivalent to the field of an infinitely thick cylinder and gap. Given the inter-cylinder gaps of $600\ \mu\text{m}$ for MICROSCOPE, we expect this to happen for $\beta \gtrsim 10^{19}$. We thus expect the MICROSCOPE constraint to have a rectangular shape.

We applied the same procedure to the other three test masses. The result are summarized in Fig. 4. It shows the 2σ -constraints from each test mass: the internal mass of each sensor unit is called IS1 and the external IS2. We compare the MICROSCOPE constraints to the current constraints summarized in Refs.[12, 13]. They overlap the constraints from atom interferometry [14, 15], torsion balances [16, 17] and Casimir effect experiments [18, 19]. Nevertheless, they are not competitive with current constraints. This is not surprising since MICROSCOPE was not designed for this test.

IV. DISCUSSION

The best constraints are obtained from the internal test masses –IS1. This is explained by a better estimation – by one order of magnitude – of the gold-wire-stiffness [8] leading to a lower residual stiffness. The competitiveness of the internal masses is nonetheless depleted by the shortness of these test masses relative to the external ones [5]. We observe that the constraints from the internal test masses are very similar, their slight difference is only caused by a slightly different residual stiffness. They in-

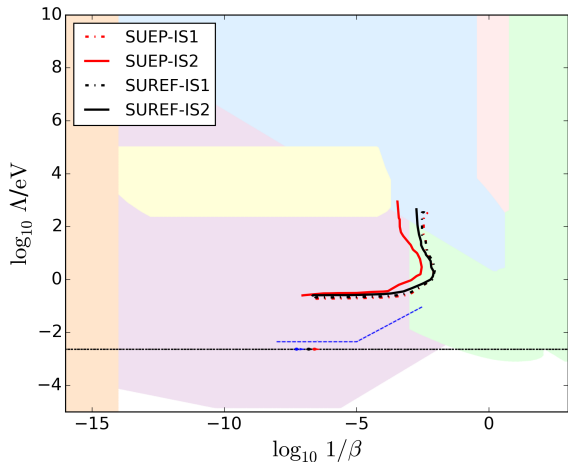


FIG. 4. Constraints on the chameleon model for $n = 1$ from the MICROSCOPE experiment using stiffness measurement sessions: the region excluded at $2\text{-}\sigma$ is above the four lines described in the legend. They correspond to the different test masses: IS1 (resp. IS2) denotes the the internal (resp. external) test masses of the SUREF and SUEP sensor units. Their constraints are compared to the current constraints from other experiments denoted with the colored regions as presented in Refs. [12, 13]. They come from atomic interferometry (purple, [14, 15]), Eöt-Wash group’s torsion balance experiments (green, [16, 17]), Casimir effect measurements (yellow, [18, 19]), astrophysics tests (blue, [20–22]) and lensing (pink, [23]), precision atomic tests (orange, [24, 25]), microsphere (blue line, [26]) and neutron interferometry (blue and red point, [27, 28]). The horizontal dotted line denotes the energy scale of dark energy.

deed experience the same chameleonic stiffness, which is consistent with the fact that they have the same geometrical parameters and are of the same composition. This tells us that the effect on the inner masses from the external test mass –of different compositions for the two sensor units– is negligible even in the unscreened regime –upper part of the constraint.

Comparing the chameleonic forces of the external test masses –that have same geometrical parameters but different densities– is interesting for the phenomenology of a WEP violation. This requires to normalize them by their masses. Doing so reveals that they each experience, in these dis-centered configurations, a different acceleration in both screened and unscreened regime. This confirms the ability of the chameleon field to provide an apparent WEP-violation-signal as the only result of the different densities of test masses through their different screening factors [11]. This has no direct repercussion on MICROSCOPE’s WEP test as: (1) it is performed in a situation where coaxiality of all cylinders is well controlled [5], (2) it is performed on a couple of test masses –IS1 and IS2– belonging to the same sensor unit for which the different geometrical parameters could also be the source of a differential acceleration. This dependence of

the force to the test masses’ densities nonetheless hints at an apparent-chameleonic-WEP-violation to appear in MICROSCOPE’s WEP test. Note that the common wisdom about chameleon inducing apparent WEP violation in screened regimes [10, 11] is not applicable to MICROSCOPE’s test of the WEP, since in this case, the satellite itself screens the Earth’s chameleon field [1], preventing any WEP violation signal at the frequency aimed by MICROSCOPE. Instead, we expect such a signal to appear in a lightly screened regime where the Earth’s chameleon profile can penetrate the instrument. Of course in such a regime the density dependence of the force would be depleted but the signal it induces might still be detectable if the precision of the experiment is high enough. Estimating this effect is beyond the scope of this article.

We obtained these new constraints from numerical simulations of the chameleon profiles in the nested-cylinder-geometry of the MICROSCOPE experiment. Some approximations must be discussed. Firstly, when evaluating the chameleonic stiffness, we used the profiles of infinitely extended cylinders. In MICROSCOPE, the cylinders being finite, we expect edge effects to appear that would require 3D simulations to quantify and that are beyond the scope of this study. Nevertheless, we expect these effects to decrease the computed stiffness. We indeed predict the field to behave as follows. On the one hand far from the ends of a cylinder, the transverse profile should be close to the one of infinite cylinders. On the other hand, at its ends, it should be influenced by the two cylindrical “lids” that close the ends of the electrode cylinders. We expect the presence of this matter to affect the chameleon profile in such a way that it is flattened in comparison to the profile of infinite cylinders. This flattening would reduce the gradients in the test mass at its ends, leading our computed stiffness to be overestimated. This would induce our constraints to be slightly decreased.

Another assumption is that we computed the profile for a static configuration while the stiffness measurement sessions involve a periodic motion of the test mass. The validity of this quasi-static assumption depends on the relaxation time of the field in response to a change in the matter distribution. We expect this assumption to stay valid as long as the movement are slow compared to the relaxation speed of the field. In analogy with gravitational waves [29], and consistently with the discussion from Ref. [30], we expect this speed to be close to the speed of light for light fields and lower for massive fields. This assumption could thus be questionable for chameleon parameters providing the heaviest fields such as in the deeply screened regime. Nevertheless, this regime is not accessible to our methods.

Finally, we idealized the MICROSCOPE geometry by not taking into account the influence of MICROSCOPE’s satellite but only the effect of the instrument. This is debatable in the regime where the field is unscreened. The complex geometry of the satellite could introduce peculiar effects on the chameleonic force. Nonetheless, given the null-effect on the internal test mass of the external

ones, and the low factor of 100 between the mass of the cylinders and of the satellite, we expect the influence of mass distribution closest to the test masses, i.e. the electrodes cylinders, to be dominant. This has for instance been demonstrated for a Yukawa fifth force in Ref. [8].

To conclude, this work extends the search for new methods to test chameleon models in the laboratory [3] or in space [31, 32]. Here we took advantage of MICROSCOPE’s instrumental characterization measurements to draw constraints on the chameleon field. An unexplained discrepancy between the measured and expected electrostatic stiffness might hint at a non-zero chameleonic force. The constraints we obtained are not competitive with state-of-the-art constraints. This is not a surprise. MICROSCOPE was not designed for testing short-ranged modified gravity theories. The main limitations of this test come from modeling uncertainties of the theoretical electrostatic stiffness and from the poor knowledge of the gold-wire characteristics. A better estimation of these physical parameters would reduce the error bars on the stiffness discrepancy. An alternative, under study for a next mission [33], is to suppress this gold wire as done in LISA Pathfinder [34]. Besides, patch field effects may be the most likely phenomenon to explain the observed

discrepancy on the measurement of the stiffness [8]. Estimating these effects would deplete this discrepancy and thus improve the sensitivity of the test. While awaiting these developments, the constraints we have provided are conservative.

ACKNOWLEDGMENT

We thank the members of the MICROSCOPE Science Working Group for allowing us to start this project and encouraging us to pursue it. We acknowledge the financial support of CNES through the APR program (“GMscope+” project). MPB is supported by a CNES/ONERA PhD grant. This work uses technical details of the T-SAGE instrument, installed on the CNES-ESA-ONERA-CNRS-OCA-DLR-ZARM MICROSCOPE mission. This work is supported in part by the EU Horizon 2020 research and innovation programme under the Marie-Sklodowska grant No. 690575. This article is based upon work related to the COST Action CA15117 (CANTATA) supported by COST (European Cooperation in Science and Technology).

-
- [1] M. Pernot-Borràs, J. Bergé, P. Brax, and J.-P. Uzan, “General study of chameleon fifth force in gravity space experiments,” *Phys. Rev. D*, vol. 100, p. 084006, Oct 2019.
 - [2] M. Pernot-Borràs, J. Bergé, P. Brax, and J.-P. Uzan, “Fifth force induced by a chameleon field on nested cylinders,” *Phys. Rev. D*, vol. 101, p. 124056, Jun 2020.
 - [3] J.-P. Uzan, M. Pernot-Borràs, and J. Bergé, “Effects of a scalar fifth force on the dynamics of a charged particle as a new experimental design to test chameleon theories,” *Phys. Rev. D*, vol. 102, no. 4, p. 044059, 2020.
 - [4] P. Touboul *et al.*, “Microscope mission: First results of a space test of the equivalence principle,” *Phys. Rev. Lett.*, vol. 119, p. 231101, Dec. 2017.
 - [5] P. Touboul *et al.*, “Space test of the equivalence principle: first results of the MICROSCOPE mission,” *Classical and Quantum Gravity*, vol. 36, p. 225006, oct 2019.
 - [6] J. Bergé, P. Brax, G. Métris, M. Pernot-Borràs, P. Touboul, and J.-P. Uzan, “Microscope mission: First constraints on the violation of the weak equivalence principle by a light scalar dilaton,” *Phys. Rev. Lett.*, vol. 120, p. 141101, Apr 2018.
 - [7] T. Damour and J. F. Donoghue, “Equivalence principle violations and couplings of a light dilaton,” *Phys. Rev. D*, vol. 82, p. 084033, Oct 2010.
 - [8] J. Bergé, M. Pernot-Borràs, J.-P. Uzan, P. Brax, R. Chhun, G. Métris, M. Rodrigues, and P. Touboul, “Microscopes constraint on a short-range fifth force,” to be submitted to *CQG*, 2020.
 - [9] R. Chhun *Classical and Quantum Gravity*, in prep.
 - [10] J. Khoury and A. Weltman, “Chameleon Fields: Awaiting Surprises for Tests of Gravity in Space,” *Phys. Rev. Lett.*, vol. 93, p. 171104, Oct. 2004.
 - [11] J. Khoury and A. Weltman, “Chameleon cosmology,” *Phys. Rev. D*, vol. 69, p. 044026, Feb. 2004.
 - [12] C. Burrage and J. Sakstein, “Tests of chameleon gravity,” *Living Rev. Relativ.*, vol. 21, p. 1, Dec. 2018.
 - [13] P. Brax, C. Burrage, and A.-C. Davis, “Laboratory tests of screened modified gravity,” *International Journal of Modern Physics D*, 06 2018.
 - [14] P. Hamilton, M. Jaffe, P. Haslinger, Q. Simmons, H. Mller, and J. Khoury, “Atom-interferometry constraints on dark energy,” *Science*, vol. 349, pp. 849–851, Aug. 2015. arXiv: 1502.03888.
 - [15] M. Jaffe, P. Haslinger, V. Xu, P. Hamilton, A. Upadhye, B. Elder, J. Khoury, and H. Mller, “Testing sub-gravitational forces on atoms from a miniature in-vacuum source mass,” *Nature Physics*, vol. 13, p. 938, July 2017.
 - [16] A. Upadhye, “Dark energy fifth forces in torsion pendulum experiments,” *Phys. Rev. D*, vol. 86, p. 102003, Nov. 2012.
 - [17] D. J. Kapner, T. S. Cook, E. G. Adelberger, J. H. Gundlach, B. R. Heckel, C. D. Hoyle, and H. E. Swanson, “Tests of the gravitational inverse-square law below the dark-energy length scale,” *Phys. Rev. Lett.*, vol. 98, p. 021101, Jan 2007.
 - [18] P. Brax, C. van de Bruck, A.-C. Davis, D. F. Mota, and D. Shaw, “Detecting chameleons through Casimir force measurements,” *Phys. Rev. D*, vol. 76, p. 124034, Dec. 2007.
 - [19] R. S. Decca, D. López, E. Fischbach, G. L. Klimchitskaya, D. E. Krause, and V. M. Mostepanenko, “Tests of new physics from precise measurements of the casimir pressure between two gold-coated plates,” *Phys. Rev. D*, vol. 75, p. 077101, Apr 2007.

- [20] B. Jain, V. Vikram, and J. Sakstein, “Astrophysical tests of modified gravity : constraints from distance indicators in the nearby universe,” *The Astrophysical Journal*, vol. 779, p. 39, nov 2013.
- [21] A. Cabré, V. Vikram, G.-B. Zhao, B. Jain, and K. Koyama, “Astrophysical tests of gravity: a screening map of the nearby universe,” *Journal of Cosmology and Astroparticle Physics*, vol. 2012, pp. 034–034, jul 2012.
- [22] V. Vikram, J. Sakstein, C. Davis, and A. Neil, “Astrophysical tests of modified gravity: Stellar and gaseous rotation curves in dwarf galaxies,” *Phys. Rev. D*, vol. 97, p. 104055, May 2018.
- [23] H. Wilcox, R. C. Nichol, G.-B. Zhao, D. Bacon, K. Koyama, and A. K. Romer, “Simulation tests of galaxy cluster constraints on chameleon gravity,” *Monthly Notices of the Royal Astronomical Society*, vol. 462, pp. 715–725, 07 2016.
- [24] P. Brax and C. Burrage, “Atomic precision tests and light scalar couplings,” *Phys. Rev. D*, vol. 83, p. 035020, Feb 2011.
- [25] J. Jaeckel and S. Roy, “Spectroscopy as a test of coulomb’s law: A probe of the hidden sector,” *Phys. Rev. D*, vol. 82, p. 125020, Dec 2010.
- [26] A. D. Rider, D. C. Moore, C. P. Blakemore, M. Louis, M. Lu, and G. Gratta, “Search for screened interactions associated with dark energy below the 100 μm length scale,” *Phys. Rev. Lett.*, vol. 117, p. 101101, Aug 2016.
- [27] H. Lemmel, P. Brax, A. Ivanov, T. Jenke, G. Pignol, M. Pitschmann, T. Potocar, M. Wellenzohn, M. Zawisky, and H. Abele, “Neutron interferometry constrains dark energy chameleon fields,” *Physics Letters B*, vol. 743, pp. 310 – 314, 2015.
- [28] K. Li, M. Arif, D. G. Cory, R. Haun, B. Heacock, M. G. Huber, J. Nsofini, D. A. Pushin, P. Saggi, D. Sarenac, C. B. Shahi, V. Skavysh, W. M. Snow, and A. R. Young, “Neutron limit on the strongly-coupled chameleon field,” *Phys. Rev. D*, vol. 93, p. 062001, Mar 2016.
- [29] C. M. Will, “Bounding the mass of the graviton using gravitational-wave observations of inspiralling compact binaries,” *Phys. Rev. D*, vol. 57, pp. 2061–2068, Feb 1998.
- [30] C. Burrage, E. J. Copeland, and E. A. Hinds, “Probing dark energy with atom interferometry,” *J. Cosmol. Astropart. Phys.*, vol. 2015, no. 03, p. 042, 2015.
- [31] J. Bergé *et al.*, “The local dark sector. Probing gravitation’s low-acceleration frontier and dark matter in the Solar System neighborhood,” 9 2019.
- [32] J. Bergé, P. Brax, M. Pernot-Borràs, and J.-P. Uzan, “Interpretation of geodesy experiments in non-Newtonian theories of gravity,” *Class. Quant. Grav.*, vol. 35, no. 23, p. 234001, 2018.
- [33] B. Battelier *et al.*, “Exploring the foundations of the universe with space tests of the equivalence principle,” 2019.
- [34] M. Armano *et al.*, “Sub-femto- g free fall for space-based gravitational wave observatories: Lisa pathfinder results,” *Phys. Rev. Lett.*, vol. 116, p. 231101, Jun 2016.

Chapter conclusion

We proposed a new test of modified gravity by measuring the stiffness it induces in asymmetrical geometries. We used the stiffness measurement sessions of MICROSCOPE to perform this test. This requires the estimation of all other classical sources of such a stiffness. We found a residual stiffness unexplained by the electrostatic models, classical gravity nor the gold-wire stiffness. The best explanation is patch field effects between the cylinders. We nonetheless explored the hypothesis that the discrepancy is caused by a modified gravity effect. We obtained a bound on a Yukawa force and a chameleon force. MICROSCOPE being not designed for this test, the bounds are, not surprisingly, not competitive.

Chapter 6

Application to the motion of charged particles

This chapter explores another application of the chameleon profiles inside cavities that have been obtained in Chapter 4. We consider the effect of a scalar field fifth force on the motion of charged particles in a uniform magnetic field. In the absence of a fifth force this dynamics is well known. The charged particles follow helix trajectories that are coiled around the lines of the magnetic field. If a fifth force is present, as long as it is large enough compared with its electromagnetic counterpart, these latter trajectories will be modified leading to new drifting effects of the particles.

6.1 Introduction and summary

In this article, to obtain these effects, we derive the general equations of motion of a relativistic charged particle in an arbitrary electromagnetic field and a scalar field from a scalar-tensor theory. We analyse the effect of the general scalar fifth force obtained in Eq. (2.14). From this general formalism we apply it to the non-relativistic case of a uniform magnetic field. We introduce an analytic solution for the dynamics of charged particles in the present of a scalar field.

We then analyse their trajectories. To continue this analytic treatment we use a generic unrealistic form of the scalar field inside the cavity. The trajectories show some peculiar features. For cylindrically symmetric scalar profiles, while without scalar field the particles follow closed circles, with a weak scalar field these trajectories get opened leading to an orthoradial drift or a precession of the trajectory. If the field is stronger, the trajectories are even more modified through a gain of their amplitude. The case of non cylindrically symmetric scalar field profiles is also studied. We show that such a profile can now lead to a radial drift of the charged particles that could induce the walls of the cavity to get charged.

From the drift of the trajectories of charged particles, we also consider the collective effect they create on macroscopic scales. The idea is to consider some density of charged particles between two parallel walls or two nested cylinders. If a magnetic field is present the microscopic drift induces a global current of charges inside the cavity. In the first case the current is parallel to the walls, in the second case, if the cylinders are co-axial, the current is orthoradial and has a radial component if a cylinder is shifted. Such a current could large enough to be detectable. An application to the chameleon field is provided for the case of parallel plates. We consider the current created by the profiles simulated in Chap. 4. From such a phenomena one could expect, if one were able to segment in the direction transverse to the cavity the measurement of the current, to have access the profile of the chameleon itself. The possible limitations of such an experiment

are discussed. We show that a perturbation from a gravity field can be suppressed by aligning it with the magnetic field of the experiment.

In short this article provides a new testable effect from a scalar fifth force. The electrical current it creates are modelled for a chameleon field. It is however important to note that the chameleonic effects have been studied for an idealised situation of infinite parallel walls. In a more realistic set-up, one should also study edge effects and the impact of the means of measurement that should impact the current.

6.2 Article

Effects of a scalar fifth force on the dynamics of a charged particle as a new experimental design to test chameleon theories

Jean-Philippe Uzan,^{1,2,*} Martin Pernot-Borràs,^{3,1,†} and Joel Berge^{3,‡}

¹*Institut d'Astrophysique de Paris, CNRS UMR 7095, Université Pierre & Marie Curie - Paris VI, 98 bis Bd Arago, 75014 Paris, France*

²*Sorbonne Universités, Institut Lagrange de Paris, 98 bis, Bd Arago, 75014 Paris, France*

³*DPHY, ONERA, Université Paris Saclay, F-92322 Châtillon, France*



(Received 25 June 2020; accepted 30 July 2020; published 31 August 2020)

This article describes the dynamics of a charged particle in an electromagnetic field in presence of a scalar fifth force. Focusing to the fifth force that would be induced by a chameleon field, the profile of which can be designed properly in the laboratory, it draws its physical effects on the cyclotron motion of a particle in a static and uniform magnetic field. The fifth force induces a drift of the trajectory that is estimated analytically and compared to numerical computations for profiles motivated by the ones of a chameleon field within two nested cylinders. The magnitude of the effect and the detectability of this drift are discussed to argue that this may offer a new experimental design to test small fifth force in the laboratory. More important, at the macroscopic level it induces a current that can in principle also be measured, and would even allow one to access the transverse profile of the scalar field within the cavity. In both cases, aligning the magnetic field with the local gravity field suppresses the effects of Newtonian gravity that would be several orders larger than the ones of the fifth force otherwise and the Newtonian gravity of the cavity on the particle is also argued to be negligible. Given this insight, this experimental setup, with its two effects—on a single particle and at the macroscopic level—may require attention to demonstrate its actual feasibility in the laboratory.

DOI: [10.1103/PhysRevD.102.044059](https://doi.org/10.1103/PhysRevD.102.044059)

I. INTRODUCTION

The search for a fifth force of nature has a long history [1–3] related to the developments of the theories of gravitation beyond Newton and Einstein gravity. The existence of a scalar interaction [4] has been revived by the development of theories of gravitation beyond general relativity since the existence of any new field may lead to a new long range force, depending on the nature of this new degree of freedom.

Within the framework of scalar-tensor theories of gravitation [5], the extra scalar degree of freedom, ϕ , is characterized by its potential $V(\phi)$ and its coupling to matter $A(\phi)$, so that the action of the theory, in the Einstein frame, is

$$S = \int dx^4 \sqrt{-g} \left[\frac{M_{\text{Pl}}^2}{2} R - \frac{1}{2} \partial^\mu \phi \partial_\mu \phi - V(\phi) \right] - \int d^4x \mathcal{L}_m(\tilde{g}_{\mu\nu}, \text{matter}) \sqrt{-\tilde{g}}, \quad (1)$$

with M_{Pl} the reduced Planck mass, R the Ricci scalar, $g_{\mu\nu}$ the Einstein frame metric, g its determinant and \mathcal{L}_m the matter Lagrangian. The field couples nonminimally to matter through the Jordan frame metric $\tilde{g}_{\mu\nu} = A^2(\phi)g_{\mu\nu}$, where $A(\phi)$ is a universal coupling function.

If this field is massless, or its Compton wavelength is larger than the size of the Solar system, one can constrain its effects thanks to the parametrized post-Newtonian formalism [6,7]. If the field is heavier, its action can be well described by a Yukawa deviation from Newtonian gravity. Such Yukawa deviations, composition independent or dependent, have been tested from the submillimeter scales to the Solar system scales and cosmology [8–12], with recent stringent constraints obtained from the MICROSCOPE experiment [13,14].

If the coupling is universal then the scalar-tensor theory satisfies the weak equivalence principle. Besides, among those theories of gravity, general relativity and Nordström theory which describes it by a scalar field in flat spacetime, share the unique property to embody the strong equivalence principle; see, e.g., Ref. [15]. If the coupling is not universal, then the weak equivalence principle is violated and one expects a space-time variation of the fundamental constants, that can be tested in their own way [16–18]. Light scalar field models can survive only if their coupling

*uzan@iap.fr

†martin.pernot_borras@onera.fr

‡joel.berge@onera.fr

is extremely weak today, which can be ensured in a large class of models by an attraction mechanism toward general relativity during the cosmic history [19,20]. Another class of models, including the symmetron [21] and the chameleon [22,23] mechanisms, enjoy a screening mechanism in which the coupling or the mass of the field depends of the local matter density of matter. It follows that the environment can suppress the scalar force.

Many experimental setups have been proposed to test the chameleon mechanism in the laboratory, see Ref. [13, 24–27] for reviews. This includes atomic spectroscopy [28]; atom interferometry [29–34], Casimir force measurement between plates [35,36], that have extensively been used to test the inverse square law on submillimeter scales [37,38]; the spectrum of ultracold neutrons in the Earth gravitational field [39,40]; torsion balance experiments [41–43]; neutron interferometry [44].

A. Goal

The driving idea we want to investigate in this article, is to use the environmental setup to design the profile of the scalar field inside the experiment, and hence the one of the fifth force. To that end, we rely on the results we obtained recently [45,46] to determine the propagation of the chameleon field inside the MICROSCOPE satellite experiment. Hence, we have been able to compute the chameleon profiles (1) for one-dimensional systems made of parallel plates and (2) two-dimensional systems as inside a set of nested cylinders. Indeed when the axes of the cylinders are parallel but not coincident, hence shifted by δ , the field distribution is no more cylindrically symmetric. It follows that the fifth force will modify the trajectory of any particle trapped between the cylinders. It is important to stress that in the chameleon situation, we can screen the experiment from the outside and design the profile of the fifth force inside the cavity. It will depend on the geometry of the cavity, the density inside the cavity and the parameters of the theory. This is a major difference with a light dilaton. The idea is thus to consider a charged particle in an electromagnetic field and determine the effect of the fifth force. Then, the system we shall consider is the trajectory of a particle orbiting inside two cylinders, or two parallel walls. This can be easily achieved thanks to a magnetic field. This latter case may offer an interesting setup to design an experiment. The Appendix gives equations for the acceleration of a particle by an electric field in a capacitor with parallel walls, and adding a magnetic field, in order to determine if the fifth force affects the Hall tension. As we shall see, this does not offer an interesting method.

To that goal, we first derive in Sec. II the general expression of the fifth force acting on a relativistic particle and its equation of motion in presence of an electromagnetic field; note that some subtleties concerning the fifth force have to be considered. We shall then focus in Sec. III

on the case of a static and uniform magnetic field and study the effect of the fifth force on the trajectory of the particle. As we shall explain, the fifth force induces a drift of the cyclotron motion with an amplitude and direction that depends on the characteristics of the fifth force. In Sec. IV we describe the macroscopic consequences of this drift. We will give estimates in order to discuss whether this can be measured and we will also compare it, in Sec. V, to the reaction force arising from the radiation emitted by any charge particle. This will provide all the elements for discussion on the possibility to use such a setup as a new experiment to constrain the existence of a fifth force. This analysis provides the first elements to discuss this possibility but also to estimate the possible effects of this scalar field on the propagation of high energy charged particle in the universe.

B. Setup

While most of our results will not depend on the specific choice of the coupling and the potential, let us be more specific on the choices that will be used for our numerics. We consider that the coupling function and potential are of the form

$$A = e^{\beta\phi/M_{\text{Pl}}}, \quad V = \Lambda^4 \left(1 + \frac{\Lambda^n}{\phi^n} \right) \quad (2)$$

where Λ is a mass scale, n a natural number and β a positive constant. It follows that the Klein-Gordon equation involves an effective potential that depends on the local the mass density ρ ,

$$\square\phi = \frac{dV_{\text{eff}}}{d\phi}, \quad V_{\text{eff}} = V(\phi) + \frac{\beta}{M_{\text{Pl}}} \rho\phi. \quad (3)$$

In our previous works, we have determined the profile of the scalar field for two parallel walls and two nested coaxial cylinders [45,46] and when their axes is shifted [46]. In the latter case, the profile is no more cylindrically symmetric so that a force appears between the two cylinders. In this work, we consider the trajectory of a particle of charge q and mass m .

Let us emphasize that the electromagnetic field does not modify the scalar field profile since external matter enters the Klein-Gordon equation only by a coupling to the trace of the stress-energy tensor through $T \ln A(\phi)$ in the effective potential (3). We consider the Cartesian basis $(\mathbf{e}_x, \mathbf{e}_y, \mathbf{e}_z)$ and cylindrical basis $(\mathbf{e}_r, \mathbf{e}_\theta, \mathbf{e}_z)$ aligned with the magnetic field.

II. DYNAMICS OF A CHARGED PARTICLE

A. Fifth force

Since the matter fields couple to the metric $A^2(\phi)g_{\mu\nu}$ the equation of a point particle of mass m and charge q derives from the action

$$S_{\text{pp}} = -c^2 \int m(\phi) \sqrt{-g_{\mu\nu} u^\mu u^\nu} d\tau + q \int A_\mu u^\mu d\tau \quad (4)$$

where τ is the proper time and u^μ the tangent vector to the worldline, i.e., $u^\mu = dX^\mu/d\tau$ and satisfies $u_\mu u^\mu = -c^2$ and A_μ the potential vector. Since we are considering particle, i.e., weakly self-gravitating bodies, the mass function $m(\phi)$ reduces to $mA(\phi)$ with m constant, the Jordan mass, such that particles with $q = 0$ follow geodesic of the metric $\tilde{g}_{\mu\nu}$. The equation of motion is

$$mc^2 \gamma^\mu = \frac{q}{A(\phi)} F^\mu{}_\nu u^\nu - mc^2 \frac{\partial \ln A}{\partial \phi} \perp^{\mu\nu} \nabla_\nu \phi \quad (5)$$

with $\gamma^\mu \equiv u^\nu \nabla_\nu u^\mu = du^\mu/d\tau$ is the 4-acceleration and satisfies $\gamma^\mu u_\mu = 0$, $F_{\mu\nu} = \partial_\mu A_\nu - \partial_\nu A_\mu$ the Faraday tensor, $\perp_{\mu\nu} \equiv g_{\mu\nu} + u_\mu u_\nu / c^2$ the projector on the 3-space normal to u^μ , which indeed ensures that $u^\mu u_\mu = -c^2$; see e.g., Ref. [17]. It follows that the fifth force,

$$F^\mu = -mc^2 \frac{\beta(\phi)}{M_{\text{P}}} \perp^{\mu\nu} \nabla_\nu \phi, \quad (6)$$

remains perpendicular to the 4-velocity, $u_\mu F^\mu = 0$. Indeed, this equation is 4-dimensional and we shall see below that in the 3-dimensional language, it is associated to a non-vanishing work. β , defined by

$$\beta(\phi) = M_{\text{P}} \frac{d \ln A}{d\phi}, \quad (7)$$

characterizes the sensitivity of the mass to a variation of the scalar field; it is dimensionless. Clearly, in the Galilean limit the projector plays no role. Note also that the Lorentz force is proportional to $q/A(\phi)$, the factor A arising from the fact that the Einstein mass is $mA(\phi)$. From now on, we work in units in which $c = 1$.

B. Equations of motion

In the Newtonian limit $g_{\mu\nu}$ reduces to the Minkowski metric $\eta_{\mu\nu}$ and the geodesic is given in 3-dimensional notations $X^\mu = (T, \mathbf{X})$. We define the 3-velocity and 3-acceleration as

$$\mathbf{V} = \frac{d\mathbf{X}}{dT}, \quad \mathbf{a} = \frac{d\mathbf{V}}{dT}, \quad (8)$$

where we use the convention that \mathbf{V} have coordinates V^i with $i = 1 \dots 3$. With these notations (see Ref. [47] for details), the scalar product is indeed $\mathbf{a} \cdot \mathbf{V} = \delta_{ij} a^i V^j$ and we have

$$u^0 = \frac{dX^0}{d\tau} = \frac{1}{\sqrt{1-V^2}}, \quad u^i = \frac{dX^i}{d\tau} = \frac{V^i}{\sqrt{1-V^2}}$$

with $V^2 = \delta_{ij} V^i V^j$ and

$$\gamma^0 = \frac{\mathbf{a} \cdot \mathbf{V}}{(1-V^2)^2}, \quad \gamma^i = \frac{1}{1-V^2} \left(a^i + \frac{\mathbf{a} \cdot \mathbf{V}}{1-V^2} V^i \right).$$

The scalar force reduces to the Nordström force [4] (see also Sec. 10.3 of Ref. [47]) and, once the Faraday tensor is decomposed as $F_{0i} = -E_i$, $F_{jk} = e_{ijk} B^i$ with e_{ijk} the Levi-Civita symbol, the Lorentz force has components

$$F_L^0 = \frac{q/A(\phi)}{\sqrt{1-V^2}} \mathbf{E} \cdot \mathbf{V}, \quad \mathbf{F}_L = \frac{q/A(\phi)}{\sqrt{1-V^2}} (\mathbf{E} + \mathbf{V} \wedge \mathbf{B}) \quad (9)$$

and the equation of motion (5) splits as

$$\frac{m\mathbf{a} \cdot \mathbf{V}}{(1-V^2)^2} = \frac{q/A(\phi)}{\sqrt{1-V^2}} \mathbf{E} \cdot \mathbf{V} - \frac{m}{M_{\text{P}}} \beta \frac{\mathbf{V} \cdot \nabla \phi}{1-V^2}, \quad (10)$$

$$\frac{m}{1-V^2} \left(\mathbf{a} + \frac{\mathbf{a} \cdot \mathbf{V}}{1-V^2} \mathbf{V} \right) = \frac{q/A(\phi)}{\sqrt{1-V^2}} [\mathbf{E} + \mathbf{V} \wedge \mathbf{B}] \quad (11)$$

$$- \frac{m}{M_{\text{P}}} \beta \left(\nabla \phi + \frac{(\mathbf{V} \cdot \nabla \phi)}{1-V^2} \mathbf{V} \right),$$

respectively for the time and space components. Equation (11) can be rewritten in a more compact form as

$$\begin{aligned} \frac{d}{dT} \left(\frac{m\mathbf{V}}{\sqrt{1-V^2}} \right) &= \frac{q}{A(\phi)} [\mathbf{E} + \mathbf{V} \wedge \mathbf{B}] \\ &- \frac{m}{M_{\text{P}}} \beta \sqrt{1-V^2} \left(\nabla \phi + \frac{(\mathbf{V} \cdot \nabla \phi)}{1-V^2} \mathbf{V} \right). \end{aligned} \quad (12)$$

This form makes explicit the 3-momentum $\mathbf{P} \equiv m\mathbf{V}/\sqrt{1-V^2}$ so that the right-hand side (rhs) is just the sum of the 3-dimensional form of the 2 forces, $\mathbf{f}_{\text{em}} + \mathbf{f}_5$. Note also that once multiplied by \mathbf{V} and using Eq. (10), it takes a form closer to the standard Newton third law,

$$\frac{m\mathbf{a}}{1-V^2} = \frac{q/A(\phi)}{\sqrt{1-V^2}} [\mathbf{E} + \mathbf{V} \wedge \mathbf{B} - (\mathbf{E} \cdot \mathbf{V}) \mathbf{V}] - \frac{m}{M_{\text{P}}} \beta \nabla \phi. \quad (13)$$

This provides the general relativistic equations of propagation of a charged particle in an electromagnetic field in presence of a fifth force.

C. Conservation of energy

For a static field with $A^\mu = (\Phi_E, \mathbf{A})$, it is easily checked that Eq. (10), with use of the definition (7), implies that

$$\frac{d}{dT} \left[\frac{mA(\phi)}{\sqrt{1-V^2}} + q\Phi_E \right] = 0 \quad (14)$$

for any static configuration of the fields, hence the conservation of the energy of the particle

$$\mathcal{E} \equiv \frac{mA(\phi)}{\sqrt{1-V^2}} + q\Phi_E. \quad (15)$$

The point particle action is easily rewritten as $\int \mathcal{L} dT$ defining the Lagrangian

$$\mathcal{L} = -mA(\phi)\sqrt{1-V^2} + q\mathbf{A}\cdot\mathbf{V} - q\Phi_E \quad (16)$$

from which we deduce the conjugate momenta

$$\boldsymbol{\pi} = \frac{mA(\phi)}{\sqrt{1-V^2}} \mathbf{V} + q\mathbf{A}. \quad (17)$$

Indeed, the Hamiltonian $\mathcal{H} = \boldsymbol{\pi}\cdot\mathbf{V} - \mathcal{L}$ reduces to the expression (15) of the energy or equivalently to

$$\mathcal{H} = \sqrt{m^2A^2(\phi) + (\boldsymbol{\pi} - q\mathbf{A})^2} + q\Phi_E. \quad (18)$$

As we shall see, the Lagrange equations

$$\frac{d\boldsymbol{\pi}}{dT} = \nabla\mathcal{L}$$

will provide additional conserved quantities once the symmetries of the problem are specified.

III. PARTICLE IN A MAGNETIC FIELD

We now assume that the particle is subject to a static and uniform magnetic field, parallel to the axis of the cylinders, $\mathbf{B} = B\mathbf{e}_z$. It follows that

$$\mathbf{A}(\mathbf{r}) = \frac{1}{2}\mathbf{B} \wedge \mathbf{r} = \frac{1}{2}Bre_\theta \quad (19)$$

and the cyclotron pulsation

$$\omega_0 = \frac{qB}{m}, \quad (20)$$

is of the order of

$$\omega_0 = 9.5 \times 10^7 Z \left(\frac{B}{1 \text{ T}} \right) \left(\frac{m}{m_p} \right)^{-1} \text{ s}^{-1}, \quad (21)$$

m_p being the proton mass and Z the charge number.

A. Cyclotron motion

When the fifth force vanishes, the equations of motion are easily integrated to give

$$\frac{du^{0,3}}{d\tau} = 0, \quad \frac{du^1}{d\tau} = \omega_0 u^2, \quad \frac{du^2}{d\tau} = -\omega_0 u^1, \quad (22)$$

the solution of which is

$$\begin{aligned} X &= R_0 \sin \omega_0 \tau, & Y &= R_0 \cos \omega_0 \tau, \\ Z &= U_Z \tau, & T - T_0 &= \frac{\omega_0}{\Omega} \tau. \end{aligned} \quad (23)$$

with U_Z , T_0 and R_0 constants of integration and

$$\Omega = \frac{\omega_0}{\sqrt{1 + R_0^2 \omega_0^2 + U_Z^2}}. \quad (24)$$

The charge travels on an helix of radius R_0 and pitch $2\pi U_Z/\omega_0$ about \mathbf{B} with an angular velocity ω_0 (the cyclotron frequency) when measured with its proper time and Ω (the synchrotron frequency) when measured with the coordinate time T of the inertial frame. Note that since $V^2 = (R_0^2 \omega_0^2 + U_Z^2)/(1 + R_0^2 \omega_0^2 + U_Z^2)$ we have $\Omega = \omega_0 \sqrt{1 - V^2}$. We deduce that the Larmor radius is given by

$$R_0 = \frac{V}{\omega_0 \sqrt{1 - V^2}} \sin \psi, \quad U_Z = \frac{V}{\sqrt{1 - V^2}} \cos \psi, \quad (25)$$

ψ being the pitch angle.

B. Conserved quantities

In the configuration considered here, the electric field vanishes and the magnetic field has been chosen as $\mathbf{B} = B\mathbf{e}_z$ and the field configuration as $\phi(x, y)$. It follows from Eq. (13) that

$$a \cdot \mathbf{e}_z = 0 \quad (26)$$

so that V_z remains constant. In the following we shall assume $V_z = 0$ so that the motion is reduced to a plane perpendicular to z .

Then, Eq. (17) implies that the motion satisfies the constraint

$$\frac{d\pi_\theta}{dT} = -mA(\phi)\sqrt{1-V^2}\partial_\theta \ln A \quad (27)$$

so that π_θ , given by

$$\pi_\theta = mr^2 \left(\frac{A(\phi)\dot{\theta}}{\sqrt{1-V^2}} + \frac{1}{2}\omega_0 \right), \quad (28)$$

can be identified with the angular momentum and conserved if ϕ has an axial symmetry, i.e., if the fifth force is radial. We also recall that the energy

$$\mathcal{E} = \frac{mA(\phi)}{\sqrt{1-V^2}} \quad (29)$$

will be conserved.

C. Nonrelativistic cyclotron motion

1. Nonrelativist equations

In the nonrelativistic regime the equation of motion (13) reduces to

$$\mathbf{a} = \frac{\omega_0}{A(\phi)} \mathbf{v} \wedge \mathbf{e}_z - \beta \nabla \phi,$$

with $\phi = \phi/M_p$. Even if the gradient of ϕ can be important, A remains close to unity because $\phi \ll 1$ (see Fig. 8 below for a concrete numerical example). So we shall approximate the dynamics by

$$\mathbf{a} = \omega_0 \mathbf{v} \wedge \mathbf{e}_z - \beta \nabla \phi, \quad \text{with} \quad \omega_0 = \frac{qB}{m}, \quad (30)$$

i.e., $A \sim A_0 = 1$. We assume that the two cylinders have axis parallel to \mathbf{e}_z so that the scalar field profile is independent of z , i.e., $\phi(x, y)$ or $\phi(r, \theta)$ in either Cartesian coordinates or cylindrical coordinates. Hence, we got the system

$$\begin{cases} \ddot{x} = \omega_0 \dot{y} - \beta c^2 \partial_x \phi \\ \ddot{y} = -\omega_0 \dot{x} - \beta c^2 \partial_y \phi \end{cases} \quad (31)$$

It can trivially be checked that the conserved quantities reduce to

$$\mathcal{E} = \frac{1}{2}(\dot{x}^2 + \dot{y}^2) + \beta c^2 \phi = \frac{1}{2}(\dot{r}^2 + r^2 \dot{\theta}^2) + \beta c^2 \phi \quad (32)$$

for the massic energy (29), that is indeed conserved and the angular momentum per unit mass (28)

$$\ell_z = r^2 \left(\dot{\theta} + \frac{1}{2} \omega_0 \right) \quad (33)$$

is conserved only for cylindrically symmetric field configuration since

$$\dot{\ell}_z = \beta c^2 \partial_\theta \phi. \quad (34)$$

2. Orders of magnitude

To put some numbers, the pulsation is given by Eq. (21) so that the radius of the trajectory in absence of a fifth force is

$$R_0 = 1.4 \times 10^{-4} \left(\frac{E_0}{1 \text{ eV}} \right)^{1/2} \left(\frac{m}{m_p} \right)^{1/2} Z^{-1} \left(\frac{B}{1 \text{ T}} \right)^{-1} \text{ m}. \quad (35)$$

3. Dynamics with no fifth force

We have already discussed the free motion in full generality. We just need to add the connection to the initial conditions and consider a new description of the motion.

Assume that at $t = 0$ the trajectory starts at (x_0, y_0) with velocity $(V_0 \cos \alpha, V_0 \sin \alpha)$, its equation is then

$$\begin{cases} x = x_c + R_0 \sin(\omega_0 t - \alpha) \\ y = y_c + R_0 \cos(\omega_0 t - \alpha) \end{cases} \quad (36)$$

with

$$R_0 = V_0/\omega_0, \quad \begin{cases} x_c = x_0 + R_0 \sin \alpha \\ y_c = y_0 - R_0 \cos \alpha \end{cases}. \quad (37)$$

R_0 can be negative with our convention. This is indeed trivial but it emphasizes that the center of the motion is not the center of the coordinates system because the magnetic force is not a central force. It is easily checked that

$$\ell_z = \frac{1}{2}(r_c^2 - R_0^2)\omega_0, \quad \mathcal{E} = \frac{1}{2}R_0^2\omega_0^2$$

so that $\mathcal{E} = V_0^2/2$ gives the relation between the radius of the orbit and the pulsation.

Since

$$\begin{cases} \frac{d\theta}{dt} = \frac{\ell_z}{r^2} - \frac{1}{2}\omega_0 \\ \left(\frac{dr}{dt} \right)^2 = 2\mathcal{E} - r^2 \left(\frac{\ell_z}{r^2} - \frac{1}{2}\omega_0 \right)^2, \end{cases} \quad (38)$$

the minimum and maximum radius of the trajectory are given by

$$r_{\pm} = \frac{\sqrt{2}}{\omega_0} \sqrt{2\mathcal{E} + \ell_z \omega_0 \pm 2\sqrt{\mathcal{E}(\mathcal{E} + \ell_z \omega_0)}}$$

that satisfy $r_+ - r_- = 2R_0$ as expected. Now, obviously θ is not constant so that the period of the motion cannot be extracted directly, however, since $dt = dr/\dot{r}$, we have from Eq. (38) that

$$t = \int \frac{dr}{\sqrt{2\mathcal{E} - r^2 \left(\frac{\ell_z}{r^2} - \frac{1}{2}\omega_0 \right)^2}},$$

so that the period of the motion is

$$\frac{T}{2} = \int_{r_-}^{r_+} \frac{2r dr / \omega_0}{\sqrt{(r_-^2 - r^2)(r^2 - r_+^2)}} = \frac{\pi}{\omega_0}. \quad (39)$$

Note also that Eq. (38) shows that the dynamics is the one of a point particle with a potential $(\omega_0^2 r^2/4 - \ell_z \omega_0)/2$, that is nothing but the centrifugal potential. This may sound as a

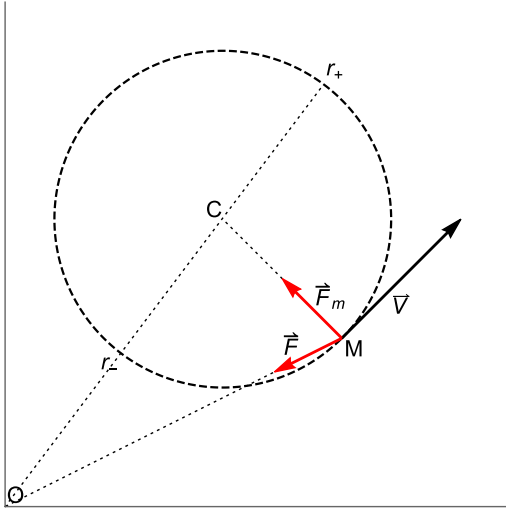


FIG. 1. The geometry of the problem. The magnetic force \mathbf{F}_m is perpendicular to the motion and thus points locally toward the center of curvature C of the trajectory. The dashed circle represents the pure magnetic trajectory. The perturbative force \mathbf{F} , even if it is central is not parallel to \mathbf{F}_m unless $C = O$. We call “radial” a force for which there exists a coordinate system such that $\phi(r)$, i.e., such that the force points toward O . The magnetic force points toward the local curvature center and is thus not radial but simply perpendicular to the trajectory.

complicated way of describing a simple result but this can be easily generalized to the case of a perturbing force.

4. Radial force

As can be trivially seen from Fig. 1, the magnetic force is indeed not radial. It points toward the local center of curvature. With our definition $\phi/M_p = \phi(r)$ the force per unit mass is $\mathbf{F} = \beta c^2 \phi'(r) \mathbf{e}_r$. Since the field enjoys a cylindrical symmetry, the angular momentum (33)–(34) is conserved. We deduce that

$$\begin{cases} \frac{d\theta}{dr} = \frac{\ell_z}{r^2} - \frac{1}{2}\omega_0 \\ \left(\frac{dr}{dt}\right)^2 = 2\mathcal{E} - r^2\left(\frac{\ell_z}{r^2} - \frac{1}{2}\omega_0\right)^2 - 2\beta c^2 \phi(r) \end{cases}, \quad (40)$$

which is a simple extension of Eq. (38). This shows that the dynamics is similar to the one of a point particle of unit mass in the effective potential

$$U_{\text{eff}} = \beta \phi(r) + \frac{r^2}{2} \left(\frac{\ell_z}{r^2} - \frac{1}{2}\omega_0 \right)^2.$$

The integration of Eq. (40) by quadrature gives

$$t = \int \frac{dr}{\sqrt{2(\mathcal{E} - \beta c^2 \phi(r)) - r^2\left(\frac{\ell_z}{r^2} - \frac{1}{2}\omega_0\right)^2}}, \quad (41)$$

$$\theta = \int \frac{(\ell_z/r^2 - \omega_0/2)dr}{\sqrt{2(\mathcal{E} - \beta c^2 \phi(r)) - r^2\left(\frac{\ell_z}{r^2} - \frac{1}{2}\omega_0\right)^2}} \quad (42)$$

which gives the equation of the trajectory in the parametric form $\{t(r), \theta(r)\}$. The turning points are solution of

$$\dot{r} = 0. \quad (43)$$

They delimit the domain of the allowed motion. If this domain is of the form $[r_-, r_+]$ then the trajectory is restricted to an annulus and, thanks to Bertrand theorem (1873), we know that the trajectory will be periodic only if $\phi \propto r^2$ or $1/r$.

Numerically, once we set the initial conditions (x_0, y_0) and $V_0(\cos \alpha, \sin \alpha)$ it is obvious that $r_0 = \sqrt{x_0^2 + y_0^2}$, $\theta_0 = \arctan(y_0/x_0)$, $\dot{\theta}_0 = (V_0/r_0) \sin(\alpha - \theta_0)$ so that the energy and angular momentum are $\mathcal{E} = V_0^2/2 + \beta c^2 \phi(r_0)$ and $\ell_z = r_0^2(\dot{\theta}_0 + \omega_0/2)$, which determines the annulus of allowed trajectories. As an example, we consider the potential $\phi = a/r$, with a a constant with units of length. When $a \rightarrow 0$ we recover the free trajectory which is then drifting along the center defined by the central force, as shown on Fig. 2 (the values of the parameters are not meant to be realistic but chosen to illustrate the properties of the trajectory). Note also that by tuning the initial conditions, we can either get a small trajectory drifting in between the cylinders or a large trajectory precessing around the inner cylinder.

Since the fifth force is small compared to the magnetic force, we can estimate the period of the drift from the fact that in the guiding center approximation [48], the drift velocity is

$$\mathbf{v}_{\text{drift}} = \frac{\mathbf{F} \wedge \mathbf{B}}{qB^2}, \quad (44)$$

which holds as long as the force can be considered constant on the scale of the gyroradius, a condition that is satisfied for our models. For a radial force $-m\beta c^2 \phi' \mathbf{e}_r$ and a magnetic field along \mathbf{e}_z this leads to an orthoradial velocity,

$$\mathbf{v}_{\text{drift}} = \frac{\beta c^2 \phi'}{\omega_0} \mathbf{e}_\theta \quad (45)$$

that is to the pulsation of the drift of the trajectory of C around O as

$$\omega_{\text{drift}} = \left. \frac{\beta c^2 \phi'}{r\omega_0} \right|_{r=r_c}. \quad (46)$$

This is indeed an approximation which works well when the force is small and when the gradient of the fifth force is

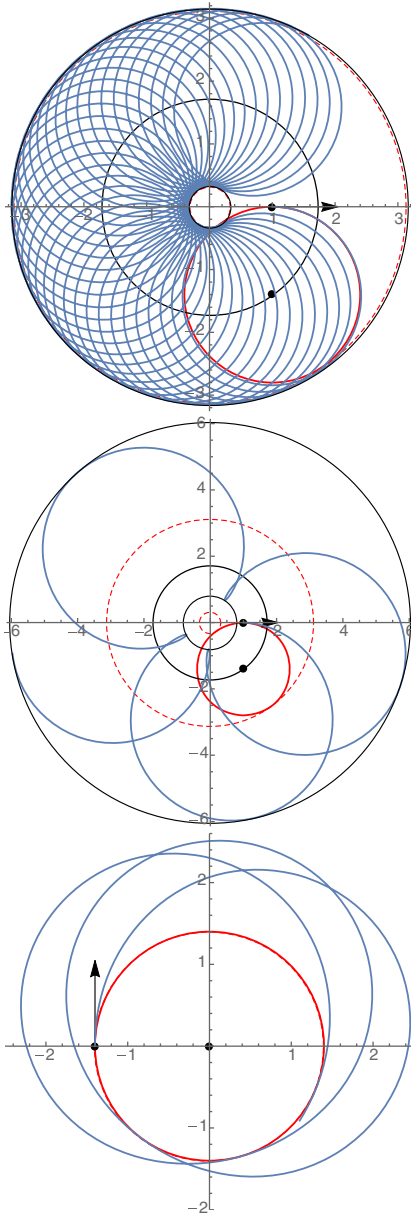


FIG. 2. Example of a central force $\varphi = a/r$. The solid red circle corresponds to the free motion ($a = 0$) while the dashed red circles define the annulus of allowed trajectory when there is no fifth force. We have represented the initial conditions (initial point and initial velocity) as well as the center of the magnetic trajectory (black dot). When $a \neq 0$ the two black circles represent the turning radii defining the annulus of allowed trajectories. When $\beta a c^2$ is small (top: $\beta a c^2 = 0.1 \text{ m}^3/\text{s}^2$) the free trajectory precesses slowly inside this annulus. When a is larger (middle: $\beta a c^2 = 1 \text{ m}^3/\text{s}^2$), the trajectory can explore regions forbidden in absence of the fifth force. The last example considers the case in which the center of the free magnetic motion is O so that it will the static circular trajectory is deformed in a precessing ellipse ($\beta a c^2 = -0.3 \text{ m}^3/\text{s}^2$). All plots assume $\omega_0 = 0.5 \text{ s}^{-1}$, $V_0 = 0.7 \text{ m/s}$ and $x_0 = 1 \text{ m}$.

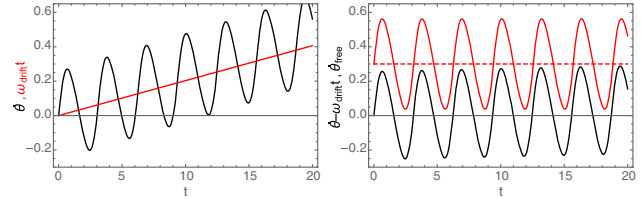


FIG. 3. Comparison of the variation of $\theta(t)$ with the drift $\omega_{\text{drift}}t$ [left] and of the residue $\theta - \omega_{\text{drift}}t$ to the $\theta(t)$ for the free motion with an arbitrary offset to compare the curves [right]. Parameters: $\omega_0 = 2$, $a = 0.1$, $V_0 = 0.7$, $x_0 = 1 \text{ m}$.

small on the scale of the gyroradius. Figure 3 shows that it gives an excellent estimation of the drift pulsation.

5. Radial chameleon

The previous analysis shows that a tiny central force will modify the cyclotron motion in two ways: (1) by extending the zone of allowed trajectories and (2) by making the trajectory drift. For a fifth force of small amplitude we are mostly interested by the latter effect.

The advantage of the chameleon field is that we can “engineer” the profile of the field inside the cavity. If the two cylinders have the same axis, then the experiment enjoys a cylindrical symmetry and $\varphi(r)$ so that the fifth force is radial. The simulations we are using [45,46] assume that $R_{\text{in}} = 0.2 \text{ m}$, $R_{\text{out}} = 0.6 \text{ m}$, $\rho_{\text{mat}} = 8.125 \text{ g.cm}^{-3}$ (typical of invar) for the cylinders and $\rho_{\text{in}} = 10^{-3}\rho$ for the intercylinder region. The theory assumes $\Lambda = 1 \text{ eV}$, $n = 2$, $\beta = 1$.

The free parameters at hand are ω_0 (fixed by the choice of the particle and the magnetic field) and V_0 (fixed by the initial kinetic energy. This defines the radius of the free trajectory. If we start from $(x_0, y_0) = (0.2, 0)$ [in meter] with $\alpha = \pi/2$ we need $R_0 = 0.2 \text{ m}$ for the trajectory to remain inside the two cylinders. Assume that

$$\varphi = (a/r) \quad (47)$$

so that $F = -\beta a c^2/r^2$ that we normalize to have an amplitude of $F_0 = \beta a c^2/r_c^2 \sim 10^{-7} \text{ N/kg}$ on $r_c = 0.4 \text{ m}$ so that $F = -F_0(r_c/r)^2$. It follows that we get

$$\omega_{\text{drift}} = \frac{F_0}{r\omega_0}.$$

This shows that the time for the orbit to drift from a distance R is $\tau = R/rc\omega_0$. We have the constraints that $V_0 < c$ while we want to optimize the drift. To get some insight let us consider the time for the orbit to drift from a length R and ask whether this could be smaller to a time scale of some hours. This sets the constraints

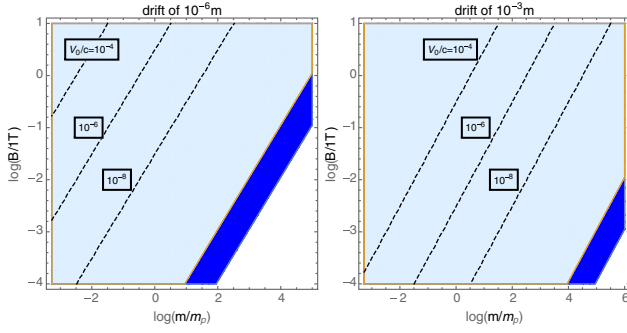


FIG. 4. Constraints on the free experimental parameters (B, m) for a particle of charge $Z = 1$ and a force of typical magnitude $F_0 \sim 10^{-7}$ N/kg for a drift of 10^{-6} m (left) or 10^{-3} m (right) over a time scale smaller than 1 hr (white region) or 10 hr (blue region) along the circle of radius r_c . The dashed lines indicate the values of V_0/c , showing that a nonrelativistic description is sufficient.

$$R_0\omega_0(B, m, Z) < c, \quad \tau(R, B, m, Z) = \frac{R\omega_0}{F_0} < T_{\text{exp}}, \quad (48)$$

T_{exp} being the duration of the experiment. The second relation implies that if $R \sim R_0$, i.e., a drift comparable to the gyroradius, then $R_0\omega_0 < 3.6 \times 10^{-4}$ m/s for $F_0 \sim 10^{-7}$ N/kg so that the first constraint will always be satisfied. Using Eq. (21), this implies

$$\left(\frac{B}{\text{T}}\right) \left(\frac{m}{m_p}\right)^{-1} < 3.8 \times 10^{-9} \frac{(T_{\text{exp}}/1 \text{ h})}{Z} \times \left(\frac{F_0}{10^{-7} \text{ N/kg}}\right) \left(\frac{R}{10^{-3} \text{ m}}\right)^{-1} \quad (49)$$

which gives the constraint on (B, m) that would allow one to observe a drift of R on a time scale of T_{exp} . As can be read from Fig. 4, a typical drift of $1 \mu\text{m}$ on a timescale smaller than 1 hr could be observed for a magnetic field of 1 mT and a particle of $100 m_p$. These orders of magnitude can be recovered from the distance drifted in a time τ as

$$\frac{R_{\text{drift}}}{1 \text{ cm}} = 3.8 \times 10^{-3} \left(\frac{B}{10^{-3} \text{ T}}\right)^{-1} \left(\frac{m}{100m_p}\right) Z^{-1} \left(\frac{\tau}{1 \text{ hr}}\right). \quad (50)$$

6. Generic chameleon

In Ref. [46], we have shown that we can generate a field profile that depends on θ by shifting the axis of the inner cylinder by δ . The amplitude of the monopoles were shown to be proportional to δ/R_{in} and to decrease with the multipole.

The main effect of an angular dependence is that the angular momentum will not be conserved since

$$\dot{\mathcal{E}} = 0, \quad \dot{\ell}_z = \beta c^2 \partial_\theta \varphi. \quad (51)$$

Since the angular momentum will vary along the trajectory, it implies that the inner and outer radius of the annulus of allowed trajectories will change over time. Indeed, it is still given as the root of Eq. (43) with \dot{r} given by Eq. (40) but ℓ_z is no more constant.

Then, the drift of the trajectory will not be orthoradial anymore as in Eq. (45). Assume for the sake of the argument that the field configuration is the sum of multipoles of the form

$$\varphi_n(r) = \Phi_n(r) \cos n\theta, \quad (52)$$

to which one shall add multipoles in $\sin n\theta$, that we omit since it does not modify our general argument. Then the fifth force will be the sum of the multipoles

$$\mathbf{F}_n = -\beta \left[\Phi'_n(r) \cos n\theta \mathbf{e}_r - n \frac{\Phi_n(r)}{r} \sin n\theta \mathbf{e}_\theta \right] \quad (53)$$

so that the drift velocity is

$$\mathbf{v}_{\text{drift}}^{(n)} = \frac{\beta}{\omega_0} \left[n \frac{\Phi_n(r)}{r} \sin n\theta \mathbf{e}_r + \Phi'_n(r) \cos n\theta \mathbf{e}_\theta \right]. \quad (54)$$

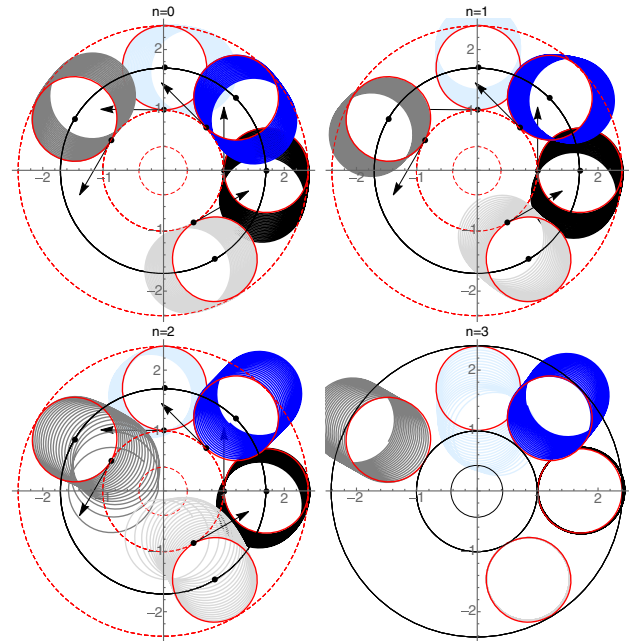


FIG. 5. Drift patterns for the 4 first multipoles ($n = 0 \dots 3$) assuming the form (52) for the field configuration with $\Phi_n = a/r$ for all n . All plots assume $\omega_0 = 1 \text{ s}^{-1}$, $V_0 = 0.7 \text{ m/s}$, and $\beta c^2 a = 0.01 \text{ m}^3/\text{s}^2$ tangent to the circle with $r = 1 \text{ m}$ initially with initial angle $\theta_0 = 0$ (black), $\pi/4$ (blue), $\pi/2$ (light blue), $5\pi/6$ (gray), $5\pi/3$ (light gray) so that the colors represent trajectories with same initial conditions.

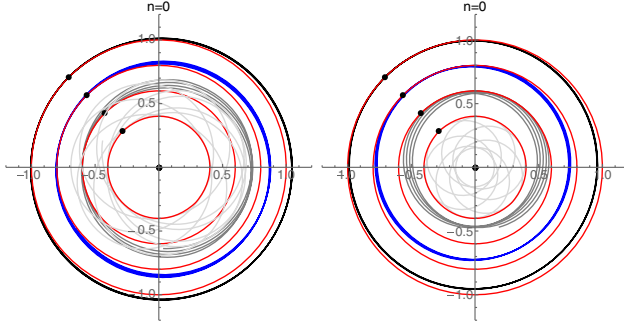


FIG. 6. Trajectories tuned such that the gyrocenter coincides with the center of symmetry O initially. In absence of fifth force the trajectory shall be a circle of center O . With a fifth force, the trajectory will deviate from this “free” trajectory in a couple of gyro-periods. All plots assume $\omega_0 = 2 \text{ s}^{-1}$, $V_0 = 0.7 \text{ m/s}$, and $\beta c^2 a = 0.1 \text{ m}^3/\text{s}^2$ [left] and $\beta c^2 a = -0.1 \text{ m}^3/\text{s}^2$ [right] tangent to the circle with $r = 1 \text{ m}$, 0.8 m , 0.6 m and 0.4 m initially with initial angle $\theta_0 = \pi/4$.

If $\Phi_n = a_n/r$ as assumed in our previous example, then the fifth force induced drift will make an angle $\alpha_n = \arctan[n \tan n\theta]$ with respect to the radial direction so that the radial drift is boosted by a factor n compare to the orthoradial drift. This is illustrated on Fig. 5. This opens new ways of testing the fifth force since instead of monitoring the drift, one can monitor the charge of the inner or outer cylinder that will change due to the inward or outward drifts of the particle that otherwise would have remained inside the two cylinders.

To finish, let us also illustrate the effect of the fifth force on trajectories that would be circles of center O in absence of a fifth force. In that case, the guiding center approximation will not hold and the effect of the fifth force can only be investigated numerically. Figure 6 gives some examples of trajectories for a monopole, comparing an attractive and repulsive force. Indeed it assumes a fifth force with an unrealistically large magnitude for the sake of the illustration. The effect of larger multipoles enlarge the landscape of possible trajectories. The question of the best experimental strategy and the design of the field distribution remain to be discussed.

IV. MACROSCOPIC CONSEQUENCES

So far we have described the microscopic effects of the fifth force on the dynamics of charged particles. Let us now show that it has a macroscopic side related to the drift current associated with the fifth force.

A. One-dimensional current

Let us consider two parallel plates as depicted on Fig. 7 of size $\ell \times L$ along the xz -direction and separated by a distance $2D$ along the y -axis and assume we impose a magnetic field Be_z . By symmetry the scalar field will have a

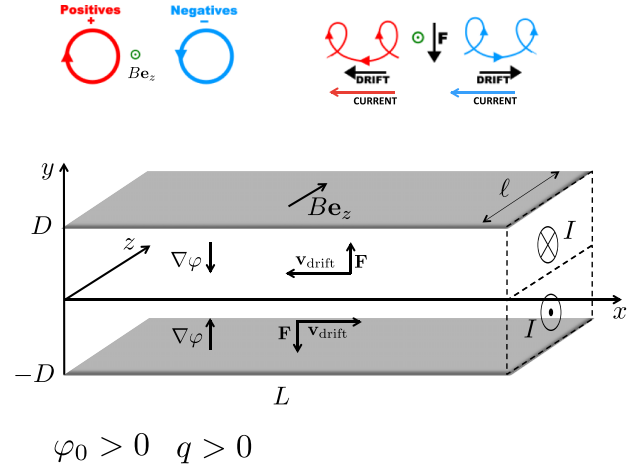


FIG. 7. Experimental design to generate macroscopic current from a fifth force. All quantities are defined in the text and are plotted assuming $\varphi_0 > 0$ and $q > 0$. Top pictures show that particles of opposite charges drift in opposite directions but generate a current in the same direction.

profile $\varphi(y)$ so that it generates a fifth force $F = -m\beta c^2 \partial_y \varphi \mathbf{e}_y$.

It follows from Eq. (44) that the particles enjoy a cyclotron motion of pulsation ω_0 drifting along the x axis at the velocity

$$\mathbf{v}_{\text{drift}} = -\frac{\beta c^2}{\omega_0} \mathbf{e}_x. \quad (55)$$

Now, if the density of charge is η_q , this generates a current density

$$\mathbf{j} = \eta_q q \mathbf{v}_{\text{drift}}(y) \quad (56)$$

flowing in opposite directions in the upper ($y > 0$) and lower ($y < 0$) parts, because $\partial_y \varphi > 0$ for $y < 0$ and $\partial \varphi < 0$ for $y > 0$. It follows that it will generate a total current

$$I = \ell \int_{-D}^D \mathbf{j}(y) \cdot \mathbf{e}_x dy. \quad (57)$$

In order to put numbers, let us assume that the profile of φ is given by

$$\varphi = \varphi_0 \left(1 - \frac{y^2}{D^2} \right) \quad (58)$$

so that the force is

$$\mathbf{F} = 2m \frac{\beta c^2 \varphi_0}{D} \frac{y}{D} \mathbf{e}_y$$

and we set $F_0 = 2\beta c^2 \varphi_0 / D \sim 10^{-7} \text{ N/kg}$. Hence, the current density is

$$\mathbf{j}(y) = -2q\eta_q \frac{\beta c^2 \varphi_0 y}{\omega_0 D D} \mathbf{e}_x \quad (59)$$

so that the current profile is

$$\frac{dI}{dy} = \ell j(y) \quad (60)$$

and the total current

$$\mathbf{I} = \mp q\eta_q \ell D \frac{\beta c^2 \varphi_0}{\omega_0 D} \mathbf{e}_x$$

in the upper/outer region respectively (if $q > 0$ and $\varphi_0 > 0$).

In order to estimate its amplitude, we need assume a typical value of the density. Assume we have a gas in standard conditions, its density is 1 mol/20 l, i.e.,

$$\eta_q = \eta_0 \sim 3 \times 10^{25} \text{ m}^{-3},$$

then

$$\frac{I}{1 \text{ nA}} = 5 \left(\frac{\eta_q}{\eta_0} \right) \left(\frac{B}{1 \text{ T}} \right)^{-1} \left(\frac{m}{m_p} \right) \left(\frac{S_{\perp}}{1 \text{ m}^2} \right) \left(\frac{F_0}{10^{-7} \text{ m/s}^2} \right) \quad (61)$$

with $S_{\perp} = \ell D$. First we note that the current is independent of the charge of the particle, simplify because qv_{drift} is, and proportional to the mass. The current reaches $0.5 \mu\text{A}$ for $m = m_p$ and $B = 0.01 \text{ T}$.

B. Effect on the field profile

Still, we need to be careful. In the microscopic analysis performed in Sec. III, we studied the effect of the fifth force on a test particle and the density inside the cavity was fixed externally. Now, we need to have a large number of particles, with a number density η_0 so that the mass density inside the cavity $\rho \sim 5 \times 10^{-2} (m/m_p) \text{ kg}\cdot\text{m}^{-3}$. As a consequence this will affect the profile inside the cavity since the Klein-Gordon equation is

$$\partial_y \phi(y) = n\Lambda^{n+4} [\phi_*^{-(n+1)} - \phi^{-(n+1)}] \quad (62)$$

in one-dimension, with

$$\phi_*^{n+1} = \frac{M_p \Lambda^{n+4} n}{\beta \rho}.$$

The field tends toward ϕ_* (ρ_{mat}) in the wall on a length scale of the order of the Compton length

$$\lambda = \sqrt{\frac{\phi_*^{n+2}}{n(n+1)\Lambda^{n+4}}}$$

of the order of $\lambda_{\text{wall}} = 2 \text{ cm}$. This shows that one will need to properly design the parameters of the experiment since one would want to increase m and η_q to get a higher current, but that would increase the density ρ_{in} so that $\phi_* \propto 1/\rho^{n+1}$ will decrease as well as $\lambda \propto 1/\rho^{1+n/2}$ so that the force will scale as

$$F \propto \partial_y \phi \propto \frac{\phi_*}{\lambda} \propto \rho_{\text{in}}^{-\frac{n+2}{2(n+1)}}.$$

Hence one can either adopt a model-independent approach and constrain F_0 for a chosen set (B, m, η_q) or one can try to constrain a given model, in which case the scaling above and the dependence of the force on the density of matter inside could be used to optimize the choice of (η_q, m) since it sets the amplitudes of the current but also affects F_0 through the mass density.

As an example, we provide the profile of the scalar field from which one can deduce the profile of the force and of the current density. These are depicted on Fig. 8.

C. Annular current inside the cylinders

Coming back to the case of the nested cylinders we studied earlier, the same reasoning shows that there shall exist an annular current along \mathbf{e}_{θ} given by

$$\mathbf{j}(r) = \eta_q q \frac{\beta c^2}{\omega_0} \varphi'(r) \mathbf{e}_{\theta}, \quad (63)$$

corresponding to a total current

$$\mathbf{I} = \eta_q q L \frac{\beta c^2}{\omega_0} \int_{R_{\text{in}}}^{R_{\text{ext}}} \varphi'(r) dr \mathbf{e}_{\theta}. \quad (64)$$

if L is the length of the cylinders. And, as expected from the Lenz law, it generates a magnetic field along the z -axis, with typical magnitude on the axis

$$B_{\text{drift}} = \mu_0 \eta_q q \frac{\beta c^2}{\omega_0} \int_{R_{\text{in}}}^{R_{\text{ext}}} \varphi'(r) dr. \quad (65)$$

With the ansatz (47) we get the typical magnitudes

$$\mathbf{I} = -\frac{\eta_q q}{\omega_0} F_0 (R_{\text{ext}} - R_{\text{in}}) L \mathbf{e}_{\theta} \quad (66)$$

$$\mathbf{B}_{\text{drift}} = \mu_0 \mathbf{I} / L \quad (67)$$

with the permeability of vacuum $\mu_0 = 4\pi \times 10^{-7} \text{ T}\cdot\text{m/A}$ and, again $F_0 = \beta a c^2 / R_{\text{ext}} R_{\text{in}}$. The typical order of magnitude is identical to the one of Eq. (61) with

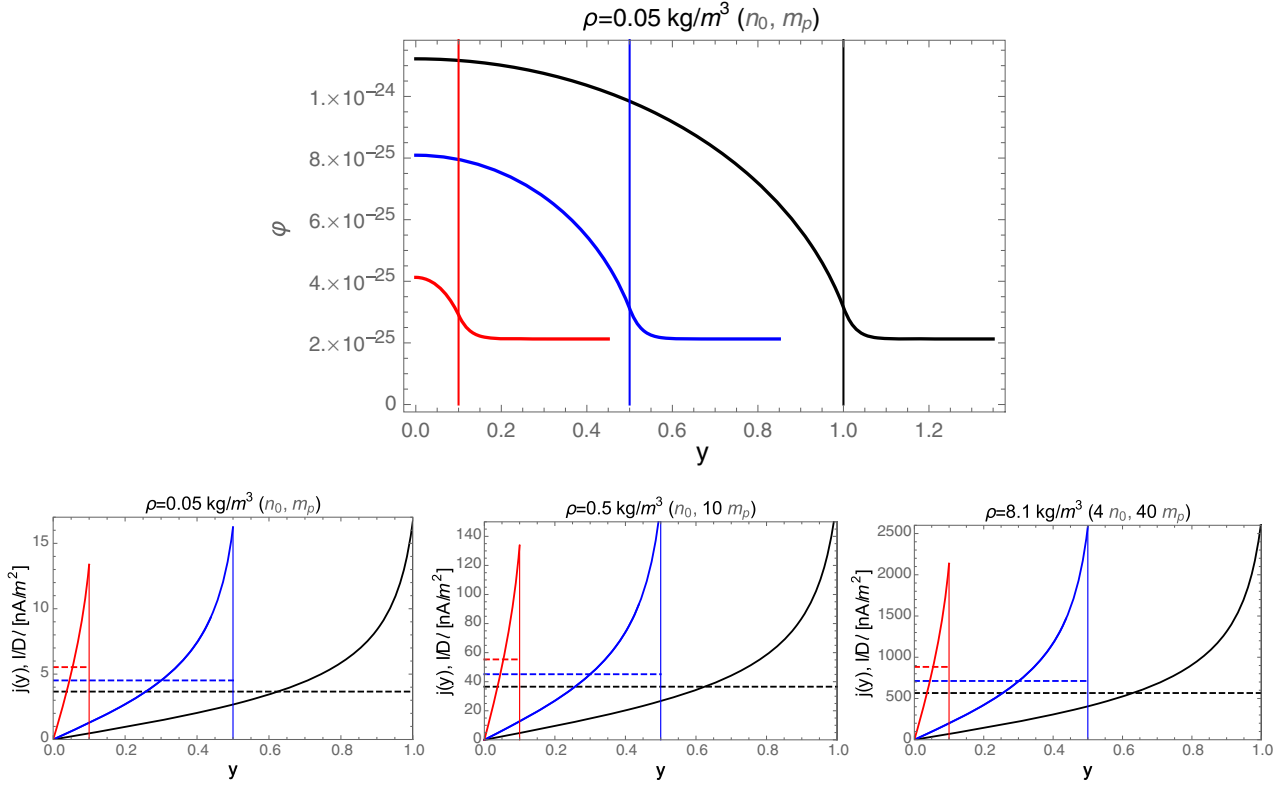


FIG. 8. Profile of the scalar field $\phi(y)$ for a chameleon model with $n = 2$, $\Lambda = 1 \text{ eV}$ and $\beta = 1$ assuming that $D = 1, 0.5, 0.1 \text{ m}$ (black, blue, red) and that the density inside the cavity is $\rho_0 = \eta_0 m_p = 0.05 \text{ kg/m}^3$ (top); the changes in the profile for $10\rho_0$ and $10^{-3}\rho_{\text{mat}}$ are not visible by eye. For the same models, we obtain the profile of the current density $j(y)$ (solid lines) and the total intensity per unit surface (dashed lines), both in nA/m^2 .

$S_{\perp} = 2L(R_{\text{ext}} - R_{\text{in}})$. It can then be checked that $B_{\text{drift}} \sim 10^{-18} \text{ T}$ so that it can be completely neglected compared to the experimental magnetic field.

D. Discussion

This shows that the effect of the fifth force on the dynamics of a charged particle at the microscopic level has several macroscopic consequences: (1) in 1 dimension, it generates a drift current between the parallel walls, (2) in 2 dimensions with cylindrical symmetry, it generates an annular current and (3) in 2 dimensions with no cylindrical symmetry, the particles drift inward and/or outward and may charge the walls of the cylinders, leading to the growth of a radial electric field.

Our numerical estimations (61) favor high mass particles, with no dependencies on its charge, while at the microscopic level, the drift effect favors large mass, low charge particles. A key issue is the *density* that can be reached in laboratory experiments. Plasma densities typically ranges from 10^3 to 10^{33} m^{-3} in nature. Pushing to 10^{20} m^{-3} will allow one to get a current larger than 1 nA . Note also that in the one-dimensional setup, one can in principle access $I(y)$. Such a measurement would be

extremely valuable since it will enable to get some information on the profile $\phi(y)$, i.e., it potentially gives access to a way to constrain the parameters of the model—see Eq. (60).

Note also that the *temperature* of the plasma is not a key issue since the drift is insensitive to the velocity of the particle. Nevertheless, we need it to be cold enough so that the gyroradius is much smaller than the typical size of the experiment, i.e., we shall demand that $\sqrt{2k_B T/m}/\omega_0^2 \ll 1 \text{ m}$, i.e., that $T < 10^{11} \text{ K}$, which is achieved easily for protons.

To finish let us remind that there is a force much larger than the fifth force that causes the particle to drift: the *standard gravitation* since its magnitude is of order $g = 10 \text{ m/s}^2$ and thus would cause a drift typically 9 orders of magnitude larger, at least, than the one induced by the fifth force. Luckily we can suppress this effect: since the drift (44) behaves as $\mathbf{F} \wedge \mathbf{B}$, aligning the magnetic field with the local gravitational field will ensure that it will not act on the particle. This can be done in a table-top experiment for a chameleon field since its profile is dictated by the geometry of the experiment and screened from the local environment. Actually, it offers a nice way to calibrate the experiment. Since $g \gg F_0$ one can first set the walls vertical so that the

magnetic field is horizontal and measure the current I_{\max} and then rotate the whole experiment until the magnetic field is vertical. Hence the current shall change as

$$I = I_{\max} \left[\sin \theta + \frac{F_0}{g} \right].$$

The measurement of I_{\max} and of the local gravity field allows one to evade the individual measurement of η_q and B . Then, any upper limit on $I(0)$ provides a constraint on F_0/g . Concerning the Newton force induced by the walls of the cavity, first let us remind that it will strictly vanish if the walls are infinite. Then, for large parallel walls, the residual gravity field has a component parallel to the magnetic field; it induces no drift while only its y -component has an effect that will modify the total current while the x -component will modify the profile of the current density. The amplitude of g_y is smaller than $G\rho_{\text{mat}}eD/L \sim 5 \times 10^{-8}(e/10 \text{ cm})(D/L) \text{ m/s}^2$ hence roughly 2 orders of magnitude smaller than the fifth force we try to measure. Hence to maximize the current, we need to maximize the surface, i.e., ℓD , while minimizing D/L in order to make the gravity of the walls completely negligible. As can be shown from Fig. 8 it also gives a higher mean current density.

Let us also stress that in the discussions of Sec. III we have not included the effect of the Newtonian gravitational field induced by the cylinders. First, if the cylinders are infinite the Newton force in the intercylinder space vanishes exactly. Then for finite length cylinders, for the radial setup, the gravitational force will be aligned with the axis of the cylinders, and thus with the magnetic field so that it will induce no drift. When the cylinders are not coaxial, there will be a small residual Newton force that will be, similarly to the case discuss in the previous paragraph, negligible.

To finish, let us mention a possible way to increase the sensitivity. As seen from Eq. (51) the angular profile of the force affects the evolution of the angular momentum which is not conserved anymore when there is no cylindrical symmetry. One can think of designing the shape of the inner and outer ‘‘cylinders’’ so that the profile exhibits sharp changes in $\partial_\theta \varphi$, similar to electric point effect. That could generate locally large gradients, the design of which could be controlled and hence distinguished from other forces. Such ideas need to be investigated later.

All these arguments convince us that this can provide a new experimental concept to detect fifth force in the laboratory. Indeed for now we just established orders of magnitude for such an experimental setup, the technological feasibility of which would need to be investigated in details, a task much beyond the scope of this work.

V. RADIATION DAMPING

Besides the fifth force and the magnetic force, the particle being accelerated shall undergo a reaction force,

the Abraham-Lorentz-Dirac force, the effect of which needs to be compared to the fifth force. The equations of motion have to be extended to

$$m\gamma^\mu = q(F_{\text{ext}}^{\mu\nu} + F_{\text{self}}^{\mu\nu})u_\nu, \quad (68)$$

in Gaussian units, where $F_{\text{ext}}^{\mu\nu}$ is the Faraday tensor of the electromagnetic field of the moving charge. The computation of the reaction forces requires to evaluate the self-retarded potential. This is detailed in chapter II.19 of Ref. [47]. It requires a regularization and many schemes are used in electrodynamics, see e.g., Ref. [49]. Using a regularization by averaging on the direction gives the radiation reaction force

$$F_{\text{self}}^{\mu\nu}u_\nu = \frac{2}{3}q(\dot{\gamma}^\mu - \gamma^2 u^\mu) \quad (69)$$

as proposed by Abraham, Lorentz and Dirac. In the nonrelativistic limit, the radiation reaction force takes the form

$$\mathbf{F}_{\text{reac}} = \frac{2}{3} \frac{q^2}{4\pi\epsilon_0 c^3} \dot{\mathbf{a}}, \quad (70)$$

once we put the international units back.

It is easily evaluated on the free trajectory since $\mathbf{V} = V_0(\cos \omega t - \alpha, \sin \omega t)$. It is indeed a damping force

$$\mathbf{F}_{\text{reac}} = -\frac{2}{3} \frac{q^2}{4\pi\epsilon_0 c^3} \omega_0^2 \mathbf{V}.$$

This implies that it does not induce a drift but a shrinking of the trajectory so that it cannot be confused with the effect of the fifth force. Nevertheless, it needs to be evaluated since it will limit the duration of the experiment.

VI. CONCLUSION

This article has investigated the effect of a small fifth force of scalar origin on the dynamics of a charged particle. It has derived the full relativistic equations of motion and conserved quantities and gave their nonrelativist limit. Then, it investigated the dynamics of a charge in a uniform magnetic field to show that the standard cyclotron motion enjoys a drift, similar to the one that can be observed if the magnetic field is not uniform. This drift is fully dictated by the profile of the scalar field. Focusing on profiles in between two nested cylinders, as studied in our previous works [45,46], we have shown that the drift is orthoradial if the configuration is cylindrically symmetric and has a more involved angular structure for a general profile.

One can control the cyclotron pulsation ω_0 by choosing the particle and tuning the magnetic field. Controlling the initial velocity of the particle determines its gyroradius. Then, the typical properties of the drift (timescale and direction) depend on the fifth force, that is on the profile

of the scalar field within the two cylinders. While the profile of a light scalar field cannot be tuned for a light dilaton, this is not the case for a chameleon field. Thanks to the environmental dependence, the field inside the cavity is screened from the outside and its profile will mostly depend on the local density in the cavity, the nature of the walls and the geometry of the cavity. This is a crucial property of these models, allowing one to engineer these fields (indeed if they exist). In particular, and as demonstrated in Refs. [45,46], shifting the axis of the cylinders allows one to design angular dependencies. The typical amplitude and profile of the force will depend on the parameters of the microscopic model (Λ, n, β) and the design of the experiment $(R_{\text{in}}, R_{\text{ext}}, \delta, \rho)$ and was shown to be typically of the order of 10^{-7} m/s^2 . We already mentioned in Ref. [45] that the force affects any experiment based on monitoring the trajectory of atoms inside a cylindrical cavity of free falling particles in space.

These effects on individual particles would require to monitor a drift, or relative drift, of single particles on the order of the gyroradius on a time scale of the hour for a force of 10^{-7} m/s^2 . As explained, there is a macroscopic side to these effects since the fifth force induces macroscopic currents that may be easier to measure. In that case we need to have a plasma within the cavity, which would affect the force and its profile since it modifies the local mass density inside the cavity. In the particular case of the one-dimensional experimental set-up proposed in this work shows that a fifth force of 10^{-7} m/s^2 can induce a drift current larger than 5 nA. This would require to push the density to the density of a gas in standard conditions while the density of plasma in nature can range from 10^3 to 10^{33} m^{-3} . Hence the density is one of the key parameters. Otherwise one would need to operate with a magnetic field of $1 \mu\text{T}$ and heavy particles. The temperature of the plasma plays no major role since the drift velocity is independent of the energy of the particle. Nevertheless we shall require that the gyroradius is much smaller than the typical size of the experiment. Setting $R_0 \sim \sqrt{2k_B T/m}/\omega_0 \ll 10^{-3} \text{ m}$ implies that the temperature be smaller than $5 \times 10^6 \text{ K}$, which is easily achieved—room temperature would correspond to $R_0 \sim 20 \mu\text{m}$. It is also important to remind that the effect of gravitation, that also induces a drift several orders of magnitude larger, can be screened by aligning the magnetic field with the local gravity field. As a consequence, it is not necessary to go to space. Then, the gravity of the walls of the cavity are roughly 2 orders of magnitude smaller than the nominal fifth force we could measure. Given these numbers, the feasibility or the existence of loopholes in our arguments would require to be investigated with care. Note also that the experiment may also enable to access the transverse profile of the chameleon field, directly related to the properties of the potential and coupling function, a possibility which has not been offered by any other proposed experimental setup so far.

Indeed, it would be bold to argue that it offers so far a new experimental design to test fifth force in laboratory. We have just used toy field profile to illustrate the physical effects and derive orders of magnitude. One would need to implement, and most probably optimize, field profiles, as shown in Ref. [46] and discuss the detectability of the drifts and of the current and all sources of noise that will unavoidably be present. The question of the alignment of the magnetic field with the local gravity field is crucial as well as a careful study of the gravity induced by the surrounding of the experiment. To finish, we note that we still have the freedom to let the magnetic field vary in time.

Nevertheless we believe that it opens a way of reflection to eventually reach such a new experimental setup. Let us also mention, to finish, that the equations of motion derived here are fully general and can also be applied to the propagation of cosmic rays.

ACKNOWLEDGMENTS

We thank Philippe Brax, Gilles Esposito-Farèse, Pierre Fleury, Julien Larena, Roland Lehoucq, Cyril Pitrou, and Manuel Rodrigues for their comments and insight. M. P. B. is supported by a CNES/ONERA PhD grant. This work is supported in part by the EU Horizon 2020 research and innovation programme under the Marie Skłodowska Grant No. 690575. We acknowledge the financial support of CNES through the APR program (“GMscope+” project). The work of J.-P. U. made in the ILP LABEX (under Reference No. ANR-10-LABX-63) was supported by French state funds managed by the ANR within the Investissements d’Avenir program under Reference No. ANR-11-IDEX-0004-02.

APPENDIX A: INITIAL CONDITIONS

The initial conditions can be fixed by either choosing $(\mathbf{x}_0, V_0, \alpha)$ or $(\mathbf{x}_0, \mathcal{E}, \ell_z)$. The first are more natural since one does not know the potential φ but the second allows one to compare motion with the same constants of motions.

One can easily shift from one to the other since

- (i) Starting from $(\mathbf{x}_0, V_0, \alpha)$, we have $r_0 = \sqrt{x_0^2 + y_0^2}$, $V_{x0} = V_0 \cos \alpha$, $V_{y0} = V_0 \sin \alpha$, $\mathcal{E} = V_0^2/2 + \beta\varphi(r_0)$, $\theta_0 = \arctan(y_0/w_0)$ so that $\dot{\theta}_0 = V_0 \sin(\alpha - \theta_0)/r_0$ and then $\ell_z = r_0^2(\dot{\theta}_0 + \omega_0/2)$.
- (ii) Starting from $(\mathbf{x}_0, \mathcal{E}, \ell_z)$, we have $r_0 = \sqrt{x_0^2 + y_0^2}$ so that $V_0 = \sqrt{2(\mathcal{E} - \beta\varphi(r_0))}$. Then, $\theta_0 = \arctan(y_0/w_0)$ and $\dot{\theta}_0 = (\ell_z/r_0^2 - \omega_0/2)$, $V_{\theta 0} = r_0 \dot{\theta}_0$ so that $\alpha = \theta_0 + \arcsin(V_{\theta 0}/V_0)$ and then $V_{x0} = V_0 \cos \alpha$, $V_{y0} = V_0 \sin \alpha$.

It is also interesting to rewrite the dynamical system by using the dimensionless time $\tau = \omega_0 t$ and rescaling the lengths in units of the gyroradius R_0 as

$$\begin{aligned}x'' &= y' - \gamma \frac{x}{r^3}, \\y'' &= -x' - \gamma \frac{y}{r^3},\end{aligned}\quad (\text{A1})$$

with the dimensionless parameter $\gamma = \beta c^2 a / \omega_0^2 R_0^3$ if the field configuration is given by $\varphi = a/r$. The initial conditions are then given by $v_0 = 1$ so that $(x'_0, y'_0) = (\cos \alpha, \sin \alpha)$ and (x_0, y_0) . Under such a form, the dimensional analysis implies that the drift pulsation can only be a function of (γ, r_c) .

It is easily checked that for $\gamma = 0$ we have a circular orbit, that is drifting when $\gamma \ll 1$ and tend to a precessing ellipse for large γ and a standard static ellipse for $\gamma = +\infty$.

APPENDIX B: PARTICLE IN AN ELECTRIC FIELD

For the sake of completeness, let us consider the case of a one-dimensional electric field between two plates, $\mathbf{E} = E\mathbf{e}_x$ so that the only non-zero component of the Faraday tensor is $F^{0x} = E$.

1. Standard acceleration

When the fifth force vanishes, it is clear from the equation of motion (5) that the 4-acceleration has a constant modulus

$$\gamma_\mu \gamma^\mu = \left(\frac{qE}{m}\right)^2 \equiv g^2. \quad (\text{B1})$$

This is indeed easy to understand since in the inertial frame tangent to the charge worldline, the electric field remains unchanged in a Lorentz transformation. It follows that $dU^x/d\tau = gU^0$, i.e., $d^2X/d\tau^2 = gdT/d\tau$ with the constraints $U_\mu U^\mu = -(dT/d\tau)^2 + (dX/d\tau)^2 = -1$. It can be integrated as

$$gT = \sinh g\tau, \quad gX = \cosh g\tau \quad (\text{B2})$$

giving the trajectory

$$gX = \sqrt{1 + g^2 T^2}. \quad (\text{B3})$$

2. Effect of the fifth force

We now consider that two parallel infinite plates so that the field configuration in between them is given by $\phi(x)$. Indeed since the force is extremely weak, typically smaller than 10^{-7} N/kg, see e.g., Ref. [45], it will always be subdominant. Nevertheless, it has been argued that such a small force may affect any experiment based on monitoring the trajectory of atoms inside a cavity [50]. Indeed the force has to be compared to gravity and it has been pointed out in Ref. [45] that in space, it is responsible for a drift of the particle inside a cylindrical cavity on timescales of the hour.

An idea could be constrain such a tiny force by considering a particle in an unstable inertial motion. An easy realization is to consider a charged particle inside a capacitor with its two parallel walls normal to \mathbf{e}_y with positions $y = \pm D$ and assume that there is a static electromagnetic field

$$\mathbf{E} = E\mathbf{e}_y, \quad \mathbf{B} = B\mathbf{e}_x.$$

A particle launched with the velocity $\mathbf{V}_0 = U\mathbf{e}_x$ will have a straight trajectory if

$$U = E/B. \quad (\text{B4})$$

This is the standard classical Hall effect.

Now, assume there is a fifth force. The profile of the scalar field will be of the form $\phi(y)$ with $\partial_y \phi_0 = 0$ by symmetry. Hence, it implies, working with the nonrelativistic equations of motion for the sake of simplicity, as

$$\ddot{X} = \frac{qB}{mA(\phi)} \dot{Y}, \quad (\text{B5})$$

$$\dot{Y} = \frac{qB}{mA(\phi)} (U - \dot{X}) - \frac{\beta}{M_P} \partial_y \phi. \quad (\text{B6})$$

We rely of the computations of the profile of the scalar field we presented in Ref. [45]. Since $\phi \ll M_P A$ will almost not vary within the walls so that $A = A[\phi(y=0)] \equiv 1$.

Then, consider a set of trajectories $\{X(t; h), Y(t; h)\}$ labeled by a parameter h , with initial conditions

$$(X, Y)_0 = (0, h), \quad (\dot{X}, \dot{Y})_0 = (U, 0).$$

The trajectory $h = 0$ will indeed be an inertial motion along $Y = 0$ but, contrary to the usual Hall effect, the trajectories starting from $h \neq 0$ will deviate from this standard trajectory.

Let us start by a toy profile mimicking the profile inside two walls, which has no analytic form,

$$\phi(y) = \phi_{\text{wall}} + \phi_0 \left(1 - \frac{y^2}{D^2}\right) \quad (\text{B7})$$

so that the force is

$$\mathbf{F} = 2 \frac{\phi_0 \beta c^2}{M_P D^2} y \mathbf{e}_y \equiv D \omega_0^2 \eta \frac{y}{D} \mathbf{e}_y \quad (\text{B8})$$

with $\eta = 2(\phi_0/M_P)\beta c^2/D\omega_0^2 \ll 1$ the relative extra acceleration induced by the fifth force.

If the gradient is constant within the plates, which indeed not the case but allows to illustrate the phenomena, the trajectories are simply given by

$$\begin{cases} X(t; h) = \left[U + \frac{\eta}{1-\eta} h \omega_0 \right] t - \frac{\eta}{1-\eta} h \frac{\sin \sqrt{1-\eta} \omega_0 t}{\sqrt{1-\eta}} \\ Y(t; h) = h \left[1 + \frac{\eta}{1-\eta} (1 - \cos \sqrt{1-\eta} \omega_0 t) \right] \end{cases} \quad (\text{B9})$$

for $\eta < 1$. We have the free parameters U (determined by E and B), ω_0 (determined by B , the charge and mass of the particle), $h = 1 \dots D$, D determined by the size of the experiment so that then $\eta = F_0/D\omega_0^2$ is the quantity we want to constraint. Since we expect $F_0 < 10^{-7}$, η is expected to be small compared to unity.

The main problem is that one would need an extremely long capacitor which makes such an experiment completely unrealistic. One solution may be to consider periodic orbits and then turn to 2-dimensional configurations.

-
- [1] T. Lee and C.-N. Yang, Conservation of heavy particles and generalized gauge transformations, *Phys. Rev.* **98**, 1501 (1955).
- [2] Y. Fujii, Dilaton and possible non-Newtonian gravity, *Nature (London)* **234**, 5 (1971).
- [3] G. Gibbons and B. F. Whiting, Constraints on unification theories imposed by measurements of Newtonian gravity, *Nature (London)* **291**, 636 (1981).
- [4] G. Nordström, Relativitätssprinzip und gravitation, *Phys. Z.* **13**, 1126 (1912); A. Einstein and A. D. Fokker, Nordstrom's theory of gravitation from the point of view of the absolute differential calculus, *Ann. Phys. (Berlin)* **44**, 321 (1914); **14**, 500 (2005).
- [5] T. Damour and G. Esposito-Farese, Nonperturbative Strong Field Effects in Tensor - Scalar Theories of Gravitation, *Phys. Rev. Lett.* **70**, 2220 (1993).
- [6] C. M. Will, *Theory and Experiment in Gravitational Physics* (Cambridge University Press, Cambridge, England, 2018).
- [7] C. M. Will, The confrontation between general relativity and experiment, *Living Rev. Relativity* **17**, 4 (2014).
- [8] E. Adelberger, B. R. Heckel, and A. Nelson, Tests of the gravitational inverse square law, *Annu. Rev. Nucl. Part. Sci.* **53**, 77 (2003).
- [9] E. Fischbach, D. Sudarsky, A. Szafer, C. Talmadge, and S. Aronson, Reanalysis of the Eötvös Experiment, *Phys. Rev. Lett.* **56**, 3 (1986); **56**, 1427(E) (1986).
- [10] E. Fischbach and C. Talmadge, *The Search for Non-Newtonian Gravity* (Springer Science & Business Media, New York, 1999).
- [11] J. Bergé, P. Brax, M. Pernot-Borràs, and J.-P. Uzan, Interpretation of geodesy experiments in non-Newtonian theories of gravity, *Classical Quantum Gravity* **35**, 234001 (2018).
- [12] B. Jain *et al.*, Novel probes of gravity and dark energy, [arXiv:1309.5389](https://arxiv.org/abs/1309.5389).
- [13] J. Bergé, P. Brax, G. Métris, M. Pernot-Borràs, P. Touboul, and J.-P. Uzan, MICROSCOPE Mission: First Constraints on the Violation of the Weak Equivalence Principle by a Light Scalar Dilaton, *Phys. Rev. Lett.* **120**, 141101 (2018).
- [14] P. Touboul *et al.*, MICROSCOPE Mission: First Results of a Space Test of the Equivalence Principle, *Phys. Rev. Lett.* **119**, 231101 (2017).
- [15] N. Deruelle, Nordstrom's scalar theory of gravity and the equivalence principle, *Gen. Relativ. Gravit.* **43**, 3337 (2011).
- [16] J.-P. Uzan, The fundamental constants and their variation: Observational status and theoretical motivations, *Rev. Mod. Phys.* **75**, 403 (2003).
- [17] J.-P. Uzan, Varying constants, gravitation and cosmology, *Living Rev. Relativity* **14**, 2 (2011).
- [18] J.-P. Uzan, Variation of the constants in the late and early universe, *AIP Conf. Proc.* **736**, 3 (2004).
- [19] T. Damour and K. Nordtvedt, General Relativity as a Cosmological Attractor of Tensor Scalar Theories, *Phys. Rev. Lett.* **70**, 2217 (1993).
- [20] T. Damour and A. Polyakov, The string dilation and a least coupling principle, *Nucl. Phys.* **B423**, 532 (1994).
- [21] K. Hinterbichler and J. Khoury, Screening Long-Range Forces through Local Symmetry Restoration, *Phys. Rev. Lett.* **104**, 231301 (2010).
- [22] J. Khoury and A. Weltman, Chameleon Fields: Awaiting Surprises for Tests of Gravity in Space, *Phys. Rev. Lett.* **93**, 171104 (2004).
- [23] J. Khoury and A. Weltman, Chameleon cosmology, *Phys. Rev. D* **69**, 044026 (2004).
- [24] A. Weltman, Testing Chameleon models in the laboratory, in *43rd Rencontres de Moriond: Cosmology* (Thê Gioi Publishers, Hanoi, Vietnam, 2008), pp. 329–332.
- [25] J. H. Steffen, A. Upadhye, A. Baumbaugh, A. S. Chou, P. O. Mazur, R. Tomlin, A. Weltman, and W. Wester, Laboratory Constraints on Chameleon Dark Energy and Power-Law Fields, *Phys. Rev. Lett.* **105**, 261803 (2010).
- [26] C. Burrage and J. Sakstein, Tests of chameleon gravity, *Living Rev. Relativity* **21**, 1 (2018).
- [27] P. Brax, C. Burrage, and A.-C. Davis, Laboratory tests of screened modified gravity, *Int. J. Mod. Phys. D* **27**, 1848009 (2018).
- [28] P. Brax and C. Burrage, Atomic precision tests and light scalar couplings, *Phys. Rev. D* **83**, 035020 (2011).
- [29] C. Burrage and E. J. Copeland, Using atom interferometry to detect dark energy, *Contemp. Phys.* **57**, 164 (2016).
- [30] D. Sabulsky, I. Dutta, E. A. Hinds, B. Elder, C. Burrage, and E. J. Copeland, Experiment to Detect Dark Energy Forces Using Atom Interferometry, *Phys. Rev. Lett.* **123**, 061102 (2019).
- [31] C. Burrage, E. J. Copeland, and E. A. Hinds, Probing dark energy with atom interferometry, *J. Cosmol. Astropart. Phys.* **03** (2015) 042.
- [32] B. Elder, J. Khoury, P. Haslinger, M. Jaffe, H. Müller, and P. Hamilton, Chameleon dark energy and atom interferometry, *Phys. Rev. D* **94**, 044051 (2016).
- [33] P. Hamilton, M. Jaffe, P. Haslinger, Q. Simmons, H. Müller, and J. Khoury, Atom-interferometry constraints on dark energy, *Science* **349**, 849 (2015).

- [34] S. Schlögel, S. Clesse, and A. Füzfa, Probing modified gravity with atom-interferometry: A numerical approach, *Phys. Rev. D* **93**, 104036 (2016).
- [35] P. Brax, C. van de Bruck, A.-C. Davis, D. F. Mota, and D. Shaw, Detecting chameleons through Casimir force measurements, *Phys. Rev. D* **76**, 124034 (2007).
- [36] C. Burrage, E. J. Copeland, and J. A. Stevenson, A proposed experimental search for chameleons using asymmetric parallel plates, *J. Cosmol. Astropart. Phys.* **08** (2016) 070.
- [37] S. Lamoreaux and W. Buttler, Thermal noise limitations to force measurements with torsion pendulums: Applications to the measurement of the Casimir force and its thermal correction, *Phys. Rev. E* **71**, 036109 (2005).
- [38] A. Lambrecht and S. Reynaud, Casimir and short-range gravity tests, in *Proceedings, 46th Rencontres de Moriond on Gravitational Waves and Experimental Gravity: La Thuile, Italy* (Thê Gioi Publishers, Hanoi, Vietnam, 2011), pp. 199–206.
- [39] P. Brax and G. Pignol, Strongly Coupled Chameleons and the Neutronic Quantum Bouncer, *Phys. Rev. Lett.* **107**, 111301 (2011).
- [40] A. N. Ivanov, R. Höllwieser, T. Jenke, M. Wellenzohn, and H. Abele, Influence of the chameleon field potential on transition frequencies of gravitationally bound quantum states of ultracold neutrons, *Phys. Rev. D* **87**, 105013 (2013).
- [41] D. F. Mota and D. J. Shaw, Strongly Coupled Chameleon Fields: New Horizons in Scalar Field Theory, *Phys. Rev. Lett.* **97**, 151102 (2006).
- [42] E. Adelberger, B. R. Heckel, S. A. Hoedl, C. Hoyle, D. Kapner, and A. Upadhye, Particle Physics Implications of a Recent Test of the Gravitational Inverse Square Law, *Phys. Rev. Lett.* **98**, 131104 (2007).
- [43] A. Upadhye, Dark energy fifth forces in torsion pendulum experiments, *Phys. Rev. D* **86**, 102003 (2012).
- [44] P. Brax, G. Pignol, and D. Roulier, Probing strongly coupled Chameleons with slow neutrons, *Phys. Rev. D* **88**, 083004 (2013).
- [45] M. Pernot-Borràs, J. Bergé, P. Brax, and J.-P. Uzan, General study of chameleon fifth force in gravity space experiments, *Phys. Rev. D* **100**, 084006 (2019).
- [46] M. Pernot-Borràs, J. Bergé, P. Brax, and J.-P. Uzan, Fifth force induced by a chameleon field on nested cylinders, *Phys. Rev. D* **101**, 124056 (2020).
- [47] N. Deruelle and J.-P. Uzan, *Relativity in Modern Physics*, Oxford Graduate Texts (Oxford University Press, Oxford, 2018).
- [48] G. Northrop, The guiding center approximation to charged particle motion, *Ann. Phys. (N.Y.)* **15**, 79 (1961).
- [49] T. Damour, A new and consistent method for classical renormalization, *Nuovo Cimento B* **26**, 157 (1975).
- [50] C. Llinares and P. Brax, Detecting Coupled Domain Walls in Laboratory Experiments, *Phys. Rev. Lett.* **122**, 091102 (2019).

Chapter conclusion

We proposed a new test of scalar fifth force by looking at the effect it causes on the trajectories of charged particles. We showed that it induces a shift to these trajectories that on the macroscopic scales shall induce a current. The case of the chameleon field between two plates have been used to illustrate this current. It could be measurable in the proper conditions.

044059-10

Chapter 7

Conclusion and perspectives

In this thesis we analysed the different aspects required to be studied in order to test the existence of scalar fifth forces with a given experiment. We placed ourselves in the scope of the MICROSCOPE mission which represents the first test of the weak equivalence principle in a laboratory in space. Partial results of this experiment allowed the improvement of the current precision on this test by an order of magnitude. Full results are to be published soon. The main aim of this study was to set constraints on scalar fifth forces by using this bound on the WEP or by seeking for effects different from a WEP violation in the MICROSCOPE data.

We first focused on unscreened scalar fields. These types of models are the most straightforward to constrain. This is due to the linearity of their dependency to the matter distribution. The only limitation in this analysis comes from the uncertainties on this distribution. In the case of the MICROSCOPE mission, the matter at play consists of the satellite's matter and the Earth. The satellite's mass distribution is well known but its fifth force effects are expected to be sub-dominant due to the low mass it represents compared with the Earth. Earth's mass distribution is estimated from the geodesic measurements of the spatial variation of its gravity field. This estimation being done by assuming Newtonian gravity, when considering a new gravitational force the estimation must be modified. We considered the cases of a dilaton-like massless scalar field and of a massive one that lead the fifth force to be finite-range through a Yukawa potential behaviour. By assuming a model for the Earth distribution of matter, as done in the literature of the current constraints, we showed that the first MICROSCOPE results improved the current bound on these models by nearly an order of magnitude. For massive scalar fifth force, this improvement occurs only for ranges that are greater than the distance between the satellite and the Earth center. Thence a space mission such as MICROSCOPE is not ideal to test short-ranged-forces i.e. more massive scalar field. A laboratory test in which the source mass and the test mass are closer, would be more appropriate to provide competitive constraints. An idea would be to perform torsion balances experiment – that provide the best bounds on short-ranged-forces – in space to enjoy the stable environment it provides. For longer-ranged-forces, the bounds from MICROSCOPE could be improved by increasing the precision of the experiment. We also studied how to go beyond the assumed mass distribution for Earth. We derived the mathematical tools needed for the derivation of a geoid model in the case of considering an additional Yukawa force. However constraining at the same time the geoid and the existence of a Yukawa force is degenerate. We showed that due to the finite-range of this force, this degeneracy can be broken by performing two geodesic missions at different orbits. Doing the same analysis with more general models of fifth force, such as the screened ones, was beyond the scope of this study as its analytical treatment is not as straightforward as for the Yukawa model.

In the second half of the thesis, we studied screened fifth forces and how to model them in an experiment such as MICROSCOPE. We considered the case of the chameleon field. We addressed the resolution of its dynamics numerically for different matter geometries. In this resolution we paid a specific attention to the way of setting boundary conditions of the problem. This allowed us to safely re-analyse the arguments for screening present in the literature. Many other aspects of this literature have been checked. We solved the case of a geometry of nested cylinders similar to the MICROSCOPE's one. We concluded that the matter constituting the MICROSCOPE experiment is screening any fifth force effect sourced by the Earth for most of the unconstrained parameter space of the chameleon model. For the remaining part of parameter space such a force could penetrate the satellite. Its quantification is nonetheless still an open issue. It requires taking into account a matter distribution including both the satellite and the Earth. We explored the way of solving it, but it requires subsequent computing resources which is out of the scope of this study. Limiting the effects of the screening of the experiment as encountered in MICROSCOPE is also still an open issue. It requires to find ways to free ourselves from the need of putting the experiment in a vacuum cavity and to increase the distance between the test masses and the means of measurement. In the case of the MICROSCOPE experiment, the fact of using a capacitive measurement precludes these possibilities. Besides, not using a vacuum cavity would lead to the possible difficulty of a least control of perturbations, that could induce lesser sensitivities. Testing chameleon gravity might require to find the correct balance between optimising screening and optimising the experiments' sensitivity.

To overcome this limited competitiveness of the MICROSCOPE mission on the test of the chameleon field, we also realised and pointed out for the first time the possibility of a fifth force sourced by the asymmetries in the matter distribution internal to the experiment. In MICROSCOPE, such an asymmetry can appear when one of its test mass cylinder is shifted from its rest position with respect to the others. We solved the chameleon field in this type of asymmetrical geometries. We found that the force the displacement creates is destabilising and behaves as a stiffness due to its linear scaling to the displacement. This stiffness is to be compared with the electrostatic stiffness present in the MICROSCOPE experiment. This stiffness has been measured and found to differ from the expected values from electrostatic models. We considered the use of this discrepancy to test the chameleon stiffness. For that matter, we analysed any other sources of such a stiffness with mainly the action of a gold wire fixed on the test masses to control their potential. The physical quantities of this wire are indeterminate, we estimated them with the results of these sessions. We used the residual stiffness, we obtained from the analysis, to constrain a Yukawa model – other possible source of stiffness – and the chameleon. We showed that the constraints are not competitive which is not surprising as it was not designed for this measurement. A way to improve the constraints would be to increase asymmetries in the device.

Finally with the help of the chameleon field profile obtained for cavities, we prospected for new type of experiment to test its existence. We indeed studied how a fifth force affects the trajectories of charged particles in a magnetic field. We showed that as long as the fifth force is strong enough, the trajectories of particles in a cavity get progressively shifted. When considering several charged particles such as in a plasma, this drift induces a macroscopic electrical current that could in principle be detectable. The feasibility of such experiment is still to be quantified.

To conclude, gravity tests in space are only at their beginning. They represent the most promising way of testing gravity beyond GR. Besides the significant improvement they allow on experimental sensitivities, they could provide possible phenomenological breakthrough. Space tests give access to regimes of gravity that have not been probed

yet with the precision of a laboratory experiment, leading to the possible detection of new effects of modified gravity. As we illustrated with the case of environment dependent theories, the testability of such effects is crucially dependent on the development of new numerical methods for a realistic modelling of their features. Proposals of new space tests flourish in the context of the democratisation of space. A successor to MICROSCOPE [6] is expected to improve the precision on the WEP test with a larger number of different materials. In the context of the ESA Voyage 2050 long term plan, a multi-scale test of gravity have been proposed [8] to probe gravity beyond the boundaries of the solar system. Ideas for novel tests are depending on new leaps in detection technologies and in numerical sciences.

Bibliography

- [1] B. P. Abbott and et al. Observation of gravitational waves from a binary black hole merger. *Phys. Rev. Lett.*, 116:061102, Feb 2016.
- [2] E. Adelberger, B. Heckel, and A. Nelson. Tests of the gravitational inverse-square law. *Annual Review of Nuclear and Particle Science*, 53(1):77–121, 2003.
- [3] E. G. Adelberger, C. W. Stubbs, B. R. Heckel, Y. Su, H. E. Swanson, G. Smith, J. H. Gundlach, and W. F. Rogers. Testing the equivalence principle in the field of the Earth: Particle physics at masses below 1 micro eV? *Physical Review D*, 42(10):3267–3292, Nov. 1990.
- [4] S. Baeßler, B. R. Heckel, E. G. Adelberger, J. H. Gundlach, U. Schmidt, and H. E. Swanson. Improved Test of the Equivalence Principle for Gravitational Self-Energy. *Physical Review Letters*, 83(18):3585–3588, Nov. 1999.
- [5] Q. Baghi. *Optimisation de l'analyse de données de la mission spatiale MICROSCOPE pour le test du principe d'équivalence et d'autres applications*. PhD thesis, 2016. Thèse de doctorat dirigée par Métris, Gilles Astronomie et Astrophysique Paris Sciences et Lettres 2016.
- [6] B. Battelier, J. Bergé, A. Bertoldi, L. Blanchet, K. Bongs, P. Bouyer, C. Braxmaier, D. Calonico, P. Fayet, N. Gaaloul, C. Guerlin, A. Hees, P. Jetzer, C. Lämmerzahl, S. Lecomte, C. L. Poncin-Lafitte, S. Loriani, G. Métris, M. Nofrarias, E. Rasel, S. Reynaud, M. Rodrigues, M. Rothacher, A. Roura, C. Salomon, S. Schiller, W. P. Schleich, C. Schubert, C. Sopena, F. Sorrentino, T. J. Sumner, G. M. Tino, P. Tuckey, W. von Klitzing, L. Wörner, P. Wolf, and M. Zelan. Exploring the foundations of the universe with space tests of the equivalence principle, 2019.
- [7] J. D. Bekenstein. Relativistic gravitation theory for the modified newtonian dynamics paradigm. *Phys. Rev. D*, 70:083509, Oct 2004.
- [8] J. Bergé, L. Baudis, P. Brax, S. wey Chiow, B. Christophe, O. Doré, P. Fayet, A. Hees, P. Jetzer, C. Lämmerzahl, M. List, G. Métris, M. Pernot-Borràs, J. Read, S. Reynaud, J. Rhodes, B. Rievers, M. Rodrigues, T. Sumner, J.-P. Uzan, and N. Yu. The local dark sector. probing gravitation's low-acceleration frontier and dark matter in the solar system neighborhood, 2019.
- [9] B. Bertotti, L. Iess, and P. Tortora. A test of general relativity using radio links with the Cassini spacecraft. *Nature*, 425(6956):374–376, Sept. 2003.
- [10] G. Boniolo. Theory and experiment. the case of eötvös' experiments. *The British Journal for the Philosophy of Science*, 43(4):459–486, 1992.
- [11] V. B. Braginskii and V. I. Panov. The Equivalence of Inertial and Gravitational Masses. *Soviet Physics Uspekhi*, 14(6):811, 1972.

- [12] C. Brans and R. H. Dicke. Mach's Principle and a Relativistic Theory of Gravitation. *Physical Review*, 124(3):925–935, Nov. 1961.
- [13] P. Brax, C. Burrage, and A.-C. Davis. Laboratory tests of screened modified gravity. *International Journal of Modern Physics D*, 06 2018.
- [14] P. Brax, C. van de Bruck, A.-C. Davis, D. F. Mota, and D. Shaw. Detecting chameleons through Casimir force measurements. *Phys. Rev. D*, 76(12):124034, Dec. 2007.
- [15] P. Brax, C. van de Bruck, A.-C. Davis, D. F. Mota, and D. Shaw. Testing chameleon theories with light propagating through a magnetic field. *Phys. Rev. D*, 76(8):085010, Oct. 2007.
- [16] J. D. Brown and L. L. Lowe. Multigrid elliptic equation solver with adaptive mesh refinement. *Journal of Computational Physics*, 209(2):582–598, Nov. 2005.
- [17] C. Burrage, E. J. Copeland, and E. Hinds. Probing dark energy with atom interferometry. *Journal of Cosmology and Astroparticle Physics*, 2015(03):042–042, mar 2015.
- [18] C. Burrage, E. J. Copeland, A. Moss, and J. A. Stevenson. The shape dependence of chameleon screening. *Journal of Cosmology and Astroparticle Physics*, 2018(01):056, 2018.
- [19] C. Burrage and J. Sakstein. Tests of chameleon gravity. *Living Rev Relativ*, 21(1):1, Dec. 2018.
- [20] R. R. Caldwell, R. Dave, and P. J. Steinhardt. Cosmological imprint of an energy component with general equation of state. *Phys. Rev. Lett.*, 80:1582–1585, Feb 1998.
- [21] R. Chhun. *Classical and Quantum Gravity*, in prep.
- [22] T. E. H. T. Collaboration. First M87 Event Horizon Telescope Results. I. The Shadow of the Supermassive Black Hole. *The Astrophysical Journal Letters*, 875(1):L1, Apr. 2019.
- [23] T. Damour and J. F. Donoghue. Equivalence principle violations and couplings of a light dilaton. *Physical Review D*, 82(8):084033, Oct. 2010.
- [24] T. Damour and K. Nordtvedt. General relativity as a cosmological attractor of tensor-scalar theories. *Physical Review Letters*, 70(15):2217–2219, Apr. 1993.
- [25] T. Damour and A. M. Polyakov. The string dilation and a least coupling principle. *Nuclear Physics B*, 423(2):532–558, July 1994.
- [26] C. de Rham. Massive Gravity. *Living Reviews in Relativity*, 17(1):7, Dec. 2014.
- [27] N. Deruelle and J.-P. Uzan. *Relativity in Modern Physics*. Oxford University Press, 2020.
- [28] H. Desmond, P. G. Ferreira, G. Lavaux, and J. Jasche. Fifth force constraints from galaxy warps. *Phys. Rev. D*, 98:083010, Oct 2018.
- [29] R. H. Dicke. Mach's Principle and Invariance under Transformation of Units. *Physical Review*, 125(6):2163–2167, Mar. 1962.

- [30] F. W. Dyson, A. S. Eddington, and C. Davidson. IX. A determination of the deflection of light by the sun's gravitational field, from observations made at the total eclipse of May 29, 1919. *Philosophical Transactions of the Royal Society of London. Series A, Containing Papers of a Mathematical or Physical Character*, 220(571-581):291–333, Jan. 1920.
- [31] A. Einstein. Die formale Grundlage der allgemeinen Relativitätstheorie. *Sitzungsberichte der Königlich Preussischen Akademie der Wissenschaften (Berlin)*, pages 1030–1085, Jan. 1914.
- [32] A. Einstein. Die Feldgleichungen der Gravitation. *Sitzungsberichte der Königlich Preussischen Akademie der Wissenschaften (Berlin)*, pages 844–847, Jan. 1915.
- [33] A. Einstein. Die Grundlage der allgemeinen Relativitätstheorie. *Annalen der Physik*, 354(7):769–822, 1915.
- [34] A. Einstein. Erklärung der Perihelbewegung des Merkur aus der allgemeinen Relativitätstheorie. *Sitzungsberichte der Königlich Preussischen Akademie der Wissenschaften (Berlin)*, pages 831–839, Jan. 1915.
- [35] A. Einstein. Näherungsweise Integration der Feldgleichungen der Gravitation. *Sitzungsberichte der Königlich Preussischen Akademie der Wissenschaften (Berlin)*, pages 688–696, Jan. 1916.
- [36] A. Einstein. Kosmologische Betrachtungen zur allgemeinen Relativitätstheorie. *Sitzungsberichte der Königlich Preussischen Akademie der Wissenschaften (Berlin)*, pages 142–152, Jan. 1917.
- [37] A. Einstein. *The Collected Papers of Albert Einstein, Volume 7 (English): The Berlin Years: Writings, 1918-1921. (English Translation of Selected Texts)*. Collected Papers of Albert Einstein. Princeton University Press, 1987.
- [38] B. Elder, J. Khoury, P. Haslinger, M. Jaffe, H. Müller, and P. Hamilton. Chameleon dark energy and atom interferometry. *Phys. Rev. D*, 94(4):044051, Aug. 2016.
- [39] G. Esposito-Farèse. *Motion in Alternative Theories of Gravity*, pages 461–489. Springer Netherlands, Dordrecht, 2011.
- [40] G. Esposito-Farèse and D. Polarski. Scalar-tensor gravity in an accelerating universe. *Phys. Rev. D*, 63:063504, Feb 2001.
- [41] G. Esposito-Farèse. Tests of scalar-tensor gravity. *AIP Conference Proceedings*, 736(1):35–52, 2004.
- [42] C. W. F. Everitt, D. B. DeBra, B. W. Parkinson, J. P. Turneaure, J. W. Conklin, M. I. Heifetz, G. M. Keiser, A. S. Silbergleit, T. Holmes, J. Kolodziejczak, M. Al-Meshari, J. C. Mester, B. Muhlfelder, V. G. Solomonik, K. Stahl, P. W. Worden, W. Bencze, S. Buchman, B. Clarke, A. Al-Jadaan, H. Al-Jibreen, J. Li, J. A. Lipa, J. M. Lockhart, B. Al-Suwaidan, M. Taber, and S. Wang. Gravity Probe B: Final Results of a Space Experiment to Test General Relativity. *Physical Review Letters*, 106(22):221101, May 2011.
- [43] P. Fayet. Extra $U(1)$'s and new forces. *Nuclear Physics B*, 347(3):743 – 768, 1990.
- [44] E. Fischbach and C. L. Talmadge. *The search for non-Newtonian gravity*. Springer, New York, 1999. OCLC: 828735653.

- [45] K. C. Freeman. On the Disks of Spiral and S0 Galaxies. *Astrophysical Journal*, 160:811, June 1970.
- [46] Y. Fujii and K. ichi Maeda. The scalar-tensor theory of gravitation. *Classical and Quantum Gravity*, 20(20):4503–4503, sep 2003.
- [47] G. Galilei. *Discourses and Mathematical Demonstrations Relating to Two New Sciences*. Dover, 1638.
- [48] M. Gasperini. Singularity prevention and broken lorentz symmetry. *Classical and Quantum Gravity*, 4(2):485–494, mar 1987.
- [49] P. Hamilton, M. Jaffe, P. Haslinger, Q. Simmons, H. Muller, and J. Khoury. Atom-interferometry constraints on dark energy. *Science*, 349(6250):849–851, Aug. 2015. arXiv: 1502.03888.
- [50] E. Hardy, A. Levy, M. Rodrigues, P. Touboul, and G. Métris. Validation of the in-flight calibration procedures for the MICROSCOPE space mission. *Advances in Space Research*, 52(9):1634–1646, Nov. 2013.
- [51] K. Hinterbichler and J. Khoury. Screening long-range forces through local symmetry restoration. *Phys. Rev. Lett.*, 104:231301, Jun 2010.
- [52] E. Hubble. A relation between distance and radial velocity among extra-galactic nebulae. *Proceedings of the National Academy of Sciences*, 15(3):168–173, 1929.
- [53] L. Hui, A. Nicolis, and C. W. Stubbs. Equivalence principle implications of modified gravity models. *Physical Review D*, 80(10):104002, Nov. 2009.
- [54] R. A. Hulse and J. H. Taylor. Discovery of a pulsar in a binary system. *Astrophysical Journal*, 195:L51–L53, Jan. 1975.
- [55] M. Ishak. Testing general relativity in cosmology. *Living Reviews in Relativity*, 22(1):1, Dec 2018.
- [56] M. Jaffe, P. Haslinger, V. Xu, P. Hamilton, A. Upadhye, B. Elder, J. Khoury, and H. Muller. Testing sub-gravitational forces on atoms from a miniature in-vacuum source mass. *Nature Physics*, 13:938, July 2017.
- [57] B. Jain, V. Vikram, and J. Sakstein. ASTROPHYSICAL TESTS OF MODIFIED GRAVITY: CONSTRAINTS FROM DISTANCE INDICATORS IN THE NEARBY UNIVERSE. *The Astrophysical Journal*, 779(1):39, Nov. 2013.
- [58] D. J. Kapner, T. S. Cook, E. G. Adelberger, J. H. Gundlach, B. R. Heckel, C. D. Hoyle, and H. E. Swanson. Tests of the gravitational inverse-square law below the dark-energy length scale. *Phys. Rev. Lett.*, 98:021101, Jan 2007.
- [59] J. Khoury and A. Weltman. Chameleon cosmology. *Phys. Rev. D*, 69(4):044026, Feb. 2004.
- [60] J. Khoury and A. Weltman. Chameleon Fields: Awaiting Surprises for Tests of Gravity in Space. *Phys. Rev. Lett.*, 93(17):171104, Oct. 2004.
- [61] S. B. Lambert and C. L. Poncin-Lafitte. Improved determination of γ by VLBI. *Astronomy & Astrophysics*, 529:A70, May 2011.
- [62] A. Lambrecht and S. Reynaud. Casimir effect: theory and experiments. *International Journal of Modern Physics A*, 27(15):1260013, June 2012.

- [63] P. Laplace. *Traité de mécanique céleste*. 1825.
- [64] U. J. Le Verrier. Theorie du mouvement de Mercure. *Annales de l'Observatoire de Paris*, 5:1, Jan. 1859.
- [65] J. Lense and H. Thirring. Über den Einfluß der Eigenrotation der Zentralkörper auf die Bewegung der Planeten und Monde nach der Einsteinschen Gravitationstheorie. *Physikalische Zeitschrift*, 19:156, Jan. 1918.
- [66] A. Linde. Chaotic inflation. *Physics Letters B*, 129(3):177 – 181, 1983.
- [67] E. Mach. *Die Mechanik in ihrer Entwicklung Historisch-Kritisch Dargestellt*. 1883.
- [68] P. MacNeice, K. M. Olson, C. Mobarry, R. de Fainchtein, and C. Packer. PARAMESH: A parallel adaptive mesh refinement community toolkit. *Computer Physics Communications*, 126(3):330–354, Apr. 2000.
- [69] F. K. Manasse and C. W. Misner. Fermi Normal Coordinates and Some Basic Concepts in Differential Geometry. *Journal of Mathematical Physics*, 4(6):735–745, June 1963.
- [70] J. Mester, R. Torii, P. Worden, N. Lockerbie, S. Vitale, and C. W. F. Everitt. The STEP mission: principles and baseline design. *Classical and Quantum Gravity*, 18(13):2475–2486, June 2001.
- [71] M. Milgrom. A modification of the Newtonian dynamics as a possible alternative to the hidden mass hypothesis. *Astrophysical Journal*, 270:365–370, July 1983.
- [72] T. W. Murphy. Lunar laser ranging: the millimeter challenge. *Reports on Progress in Physics*, 76(7):076901, June 2013.
- [73] I. Newton. *Philosophiæ Naturalis Principia Mathematica*, English translation (1729) by Andrew Motte. 1687.
- [74] A. M. Nobili, D. Bramanti, E. Polacco, I. W. Roxburgh, G. Comandi, and G. Catastini. Galileo Galilei (GG) small-satellite project: an alternative to the torsion balance for testing the equivalence principle on Earth and in space. *Classical and Quantum Gravity*, 17(12):2347–2349, June 2000.
- [75] G. Nordström. Zur theorie der gravitation vom standpunkt des relativitätsprinzips. *Annalen der Physik*, 347(13):533–554, 1913.
- [76] K. Nordtvedt. Equivalence Principle for Massive Bodies. I. Phenomenology. *Physical Review*, 169(5):1014–1016, May 1968.
- [77] K. Nordtvedt. Equivalence Principle for Massive Bodies. II. Theory. *Physical Review*, 169(5):1017–1025, May 1968.
- [78] K. Nordtvedt. Testing Relativity with Laser Ranging to the Moon. *Physical Review*, 170(5):1186–1187, June 1968.
- [79] J. Overduin, F. Everitt, J. Mester, and P. Worden. The science case for STEP. *Advances in Space Research*, 43(10):1532 – 1537, 2009.
- [80] R. Pail, S. Bruinsma, F. Migliaccio, C. Förste, H. Goiginger, W.-D. Schuh, E. Höck, M. Reguzzoni, J. M. Brockmann, O. Abrikosov, M. Veicherts, T. Fecher, R. Mayrhofer, I. Krasbutter, F. Sansò, and C. C. Tscherning. First GOCE gravity field models derived by three different approaches. *Journal of Geodesy*, 85(11):819, Oct. 2011.

- [81] S. Perlmutter, G. Aldering, G. Goldhaber, R. A. Knop, P. Nugent, P. G. Castro, S. Deustua, S. Fabbro, A. Goobar, D. E. Groom, I. M. Hook, A. G. Kim, M. Y. Kim, J. C. Lee, N. J. Nunes, R. Pain, C. R. Pennypacker, R. Quimby, C. Lidman, R. S. Ellis, M. Irwin, R. G. McMahon, P. Ruiz-Lapuente, N. Walton, B. Schaefer, B. J. Boyle, A. V. Filippenko, T. Matheson, A. S. Fruchter, N. Panagia, H. J. M. Newberg, W. J. Couch, and T. S. C. Project. Measurements of ω and λ from 42 High-Redshift Supernovae. *The Astrophysical Journal*, 517(2):565, June 1999.
- [82] F. Perrotta, C. Baccigalupi, and S. Matarrese. Extended quintessence. *Phys. Rev. D*, 61:023507, Dec 1999.
- [83] P. Peter and J.-P. Uzan. *Primordial cosmology*. Oxford Graduate Texts. Oxford Univ. Press, Oxford, 2009.
- [84] E. Poisson and C. M. Will. *Gravity: Newtonian, Post-Newtonian, Relativistic*. Cambridge University Press, 2014.
- [85] B. Ratra and P. J. E. Peebles. Cosmological consequences of a rolling homogeneous scalar field. *Phys. Rev. D*, 37(12):3406–3427, June 1988.
- [86] C. Reigber, H. Lühr, P. Schwintzer, and J. Wickert, editors. *Earth Observation with CHAMP: Results from Three Years in Orbit*. Springer-Verlag, Berlin Heidelberg, 2005.
- [87] C. Reigber, R. Schmidt, F. Flechtner, R. König, U. Meyer, K.-H. Neumayer, P. Schwintzer, and S. Y. Zhu. An Earth gravity field model complete to degree and order 150 from GRACE: EIGEN-GRACE02s. *Journal of Geodynamics*, 39(1):1–10, Jan. 2005.
- [88] J. Renner. Kísérleti vizsgálatok a tömegvonzás és a tehetetlenség arányosságáról. *Matematikai és Természettudományi Értesítő*, 53:542–568, 1935.
- [89] A. G. Riess, A. V. Filippenko, P. Challis, A. Clocchiatti, A. Diercks, P. M. Garnavich, R. L. Gilliland, C. J. Hogan, S. Jha, R. P. Kirshner, B. Leibundgut, M. M. Phillips, D. Reiss, B. P. Schmidt, R. A. Schommer, R. C. Smith, J. Spyromilio, C. Stubbs, N. B. Suntzeff, and J. Tonry. Observational Evidence from Supernovae for an Accelerating Universe and a Cosmological Constant. *The Astronomical Journal*, 116(3):1009, Sept. 1998.
- [90] P. G. Roll, R. Krotkov, and R. H. Dicke. The equivalence of inertial and passive gravitational mass. *Annals of Physics*, 26(3):442–517, Feb. 1964.
- [91] R. Rummel, W. Yi, and C. Stummer. GOCE gravitational gradiometry. *Journal of Geodesy*, 85(11):777, Aug. 2011.
- [92] P. R. Saulson. Thermal noise in mechanical experiments. *Phys. Rev. D*, 42:2437–2445, Oct 1990.
- [93] S. Schlamminger, K.-Y. Choi, T. A. Wagner, J. H. Gundlach, and E. G. Adelberger. Test of the Equivalence Principle Using a Rotating Torsion Balance. *Physical Review Letters*, 100(4):041101, Jan. 2008.
- [94] K. Schwarzschild. Über das Gravitationsfeld eines Massenpunktes nach der Einsteinschen Theorie. *Sitzungsberichte der Königlich Preußischen Akademie der Wissenschaften (Berlin)*, pages 189–196, Jan. 1916.

- [95] I. I. Shapiro. Fourth test of general relativity. *Physical Review Letters*, 13(26):789, 1964.
- [96] V. Springel, R. Pakmor, A. Pillepich, R. Weinberger, D. Nelson, L. Hernquist, M. Vogelsberger, S. Genel, P. Torrey, F. Marinacci, and J. Naiman. First results from the IllustrisTNG simulations: matter and galaxy clustering. *Monthly Notices of the Royal Astronomical Society*, 475(1):676–698, 12 2017.
- [97] A. O. Sushkov, W. J. Kim, D. A. R. Dalvit, and S. K. Lamoreaux. Observation of the thermal Casimir force. *Nature Physics*, 7:230, Feb. 2011.
- [98] M.-G. Torsten, N. Zehentner, B. Klinger, and A. Kvas. Itsg-grace2014: a new grace gravity field release computed in graz. 09 2014.
- [99] P. Touboul. The Microscope Mission and Its Uncertainty Analysis. *Space Science Reviews*, 148(1):455–474, Dec. 2009.
- [100] P. Touboul, B. Foulon, L. Lafargue, and G. Métris. The microscope mission. *Acta Astronautica*, 50(7):433–443, Apr. 2002.
- [101] P. Touboul, B. Foulon, M. Rodrigues, and J. P. Marque. In orbit nano-g measurements, lessons for future space missions. *Aerospace Science and Technology*, 8(5):431–441, July 2004.
- [102] P. Touboul, G. Métris, V. Lebat, and A. Robert. The MICROSCOPE experiment, ready for the in-orbit test of the equivalence principle. *Classical and Quantum Gravity*, 29(18):184010, Aug. 2012.
- [103] P. Touboul, G. Métris, M. Rodrigues, Y. André, Q. Baghi, J. Bergé, D. Boulanger, S. Bremer, P. Carle, R. Chhun, B. Christophe, V. Cipolla, T. Damour, P. Danto, H. Dittus, P. Fayet, B. Foulon, C. Gageant, P.-Y. Guidotti, D. Hagedorn, E. Hardy, P.-A. Huynh, H. Inchauspe, P. Kayser, S. Lala, C. Lämmerzahl, V. Lebat, P. Leseur, F. Liorzou, M. List, F. Löffler, I. Panet, B. Pouilloux, P. Prieur, A. Rebray, S. Reynaud, B. Rievers, A. Robert, H. Selig, L. Serron, T. Sumner, N. Tanguy, and P. Visser. MICROSCOPE Mission: First Results of a Space Test of the Equivalence Principle. *Physical Review Letters*, 119(23):231101, Dec. 2017.
- [104] P. Touboul, G. Métris, M. Rodrigues, Y. André, Q. Baghi, J. Bergé, D. Boulanger, S. Bremer, R. Chhun, B. Christophe, V. Cipolla, T. Damour, P. Danto, H. Dittus, P. Fayet, B. Foulon, P.-Y. Guidotti, E. Hardy, P.-A. Huynh, C. Lämmerzahl, V. Lebat, F. Liorzou, M. List, I. Panet, S. Pires, B. Pouilloux, P. Prieur, S. Reynaud, B. Rievers, A. Robert, H. Selig, L. Serron, T. Sumner, and P. Visser. Space test of the equivalence principle: first results of the MICROSCOPE mission. *Classical and Quantum Gravity*, 36(22):225006, Oct. 2019.
- [105] A. Upadhye. Dark energy fifth forces in torsion pendulum experiments. *Physical Review D*, 86(10):102003, Nov. 2012.
- [106] A. Upadhye, S. S. Gubser, and J. Khoury. Unveiling chameleon fields in tests of the gravitational inverse-square law. *Physical Review D*, 74(10):104024, Nov. 2006.
- [107] J.-P. Uzan. Varying Constants, Gravitation and Cosmology. *Living Reviews in Relativity*, 14(1):2, Dec. 2011.
- [108] L. v. Eötvös. Über die Anziehung der Erde auf verschiedene Substanzen. *Mathematische und Naturwissenschaftliche Berichte aus Ungarn*, 8:65, 1890.

- [109] L. v. Eötvös, D. Pekár, and E. Fekete. Beiträge zum gesetze der proportionalität von trägheit und gravität. *Annalen der Physik*, 373(9):11–66, 1922.
- [110] R. F. C. Vessot, M. W. Levine, E. M. Mattison, E. L. Blomberg, T. E. Hoffman, G. U. Nystrom, B. F. Farrel, R. Decher, P. B. Eby, C. R. Baugher, J. W. Watts, D. L. Teuber, and F. D. Wills. Test of Relativistic Gravitation with a Space-Borne Hydrogen Maser. *Physical Review Letters*, 45(26):2081–2084, Dec. 1980.
- [111] V. Viswanathan, A. Fienga, O. Minazzoli, L. Bernus, J. Laskar, and M. Gastineau. The new lunar ephemeris INPOP17a and its application to fundamental physics. *Monthly Notices of the Royal Astronomical Society*, 476(2):1877–1888, May 2018.
- [112] R. M. Wald. *General relativity*. Chicago Univ. Press, Chicago, IL, 1984.
- [113] J. Wang, L. Hui, and J. Khoury. No-Go Theorems for Generalized Chameleon Field Theories. *Physical Review Letters*, 109(24):241301, Dec. 2012.
- [114] C. M. Will. The Confrontation between General Relativity and Experiment. *Living Rev. Relativ.*, 17(1):4, Dec. 2014.
- [115] E. Willemenot and P. Touboul. On-ground investigation of space accelerometers noise with an electrostatic torsion pendulum. *Review of scientific instruments*, 71(1):302–309, 2000.
- [116] I. Zlatev, L. Wang, and P. J. Steinhardt. Quintessence, Cosmic Coincidence, and the Cosmological Constant. *Physical Review Letters*, 82(5):896–899, Feb. 1999.
- [117] F. Zwicky. Die Rotverschiebung von extragalaktischen Nebeln. *Helvetica Physica Acta*, 6:110–127, Jan. 1933.

Tester la gravité dans l'espace : Vers un traitement réaliste de la gravité Caméléon dans la mission MICROSCOPE

Résumé : Ce travail examine la testabilité par des expériences menées dans l'espace de théories de gravité alternatives à la Relativité Générale. Il profite du contexte offert par la mission MICROSCOPE qui a récemment amélioré la précision du test du principe d'équivalence faible, principe pilier de la Relativité Générale. Étant la première expérience qui réalise ce test de précision dans un laboratoire dans l'espace, ses résultats étaient attendus pour tester des modèles de gravité présentant une dynamique dépendante de l'environnement via un mécanisme d'écrantage. Nous étudions le cas des théories tenseur-scalaire. Nous commençons par considérer de simples modèles non écrantés, afin d'en obtenir leur contrainte par MICROSCOPE, et d'explorer l'intrication entre la gravité modifiée et notre connaissance de la distribution en masse de la Terre. Nous considérons ensuite le modèle écranté Caméléon. Les non-linéarités de son mécanisme d'écrantage rendent la dépendance à l'environnement ainsi qu'au dispositif expérimental difficile à évaluer. Nous développons de nouvelles méthodes pour calculer le profil du Caméléon. La survenue de l'écrantage de MICROSCOPE et donc d'une 5^{ème} force sourcée par l'extérieur est discutée. Nous explorons aussi l'émergence d'une 5^{ème} force résultante d'asymétries dans sa géométrie interne. Nous caractérisons cette force et utilisons des sessions de mesures de la raideur électrostatique pour contraindre son existence. Les résultats de ces méthodes nous permettent aussi de comprendre l'influence du champ Caméléon sur le mouvement de particules chargées afin de proposer un nouveau concept de test.

Mots clefs : Tests de gravité, gravité modifiée, spatial, principe d'équivalence, mécanisme d'écrantage, modèle caméléon.

Testing gravity in space: Towards a realistic treatment of chameleon gravity in the MICROSCOPE mission

Abstract: This work investigates the testability by space-based experiments of gravity theories alternatives to general relativity. It enjoys the context of the MICROSCOPE mission that recently improved the precision on the test of weak equivalence principle, pillar principle of general relativity. Being the first experiment to perform such a precision test in a laboratory in space, its results were awaited for testing gravity models that exhibit an environmental dependent dynamics through a screening mechanism. We study the case of scalar-tensor theories. We start by considering simple unscreened models, to obtain their constraints by MICROSCOPE and to explore the entanglement between modified gravity and our knowledge about the Earth mass distribution. We then consider the screened chameleon model. The non-linearities of its screening mechanism makes its dependence to the environment and to the experimental apparatus challenging to evaluate. We develop new methods to compute the chameleon profile. The occurrence of screening in MICROSCOPE and thus of an externally sourced WEP-violating fifth force are discussed. We also explore the emergence of a fifth force as the result of asymmetries in its internal geometry. We characterise this force and take the advantage of stiffness-measurement sessions from MICROSCOPE to constraint its existence. The results of our methods also allows us to understand the influence of the chameleon field on the motion of charged particles and to propose a new concept of test.

Keywords: Gravity tests, modified gravity, spatial science, equivalence principle, screening mechanism, chameleon model.